The Interplay of Superconducting Quantum Circuits and Propagating Microwave States

Jan Goetz

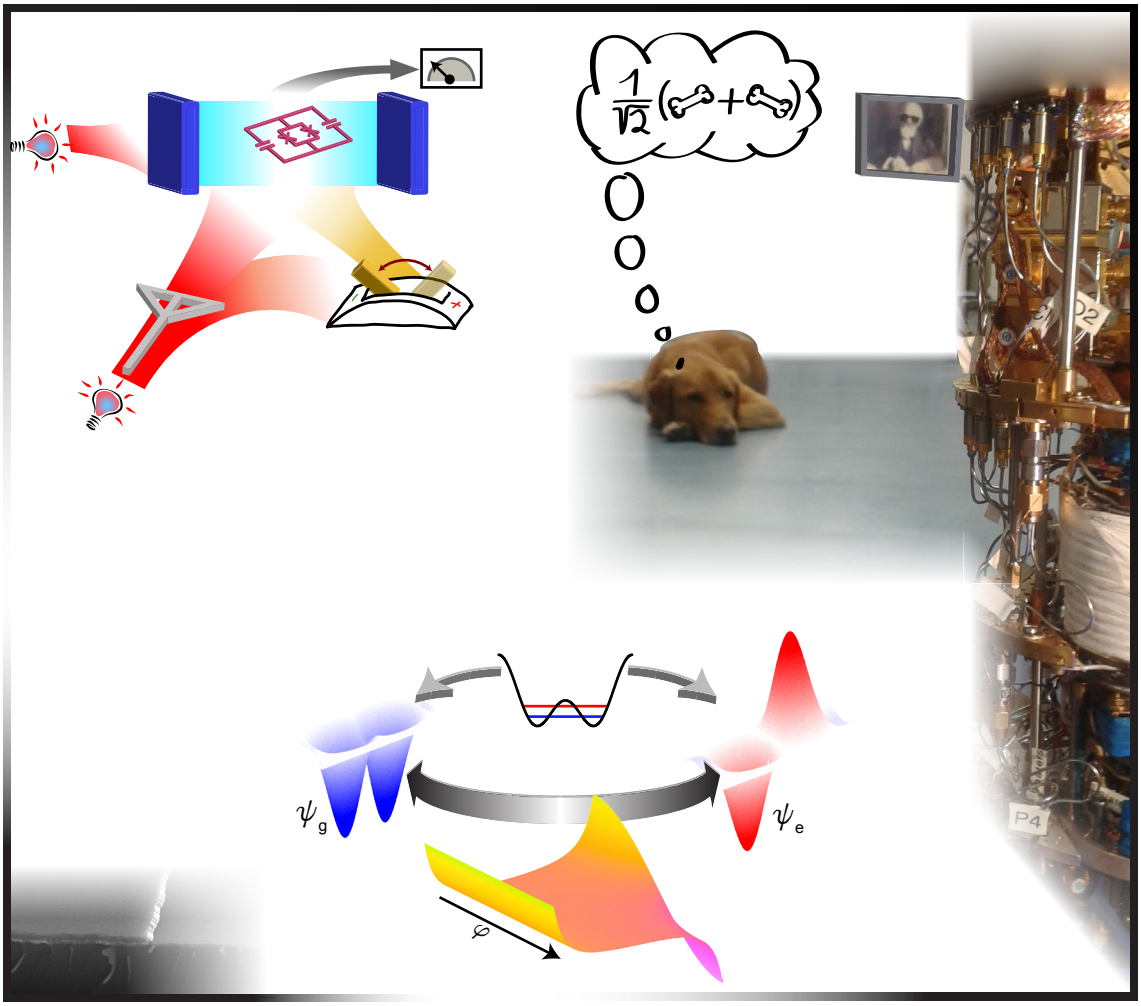

Dissertation

last revised version: 26.06.2017

TECHNISCHE UNIVERSITÄT MÜNCHEN

Lehrstuhl E23 für Technische Physik

Walther-Meißner-Institut für Tieftemperaturforschung
der Bayerischen Akademie der Wissenschaften

The Interplay of Superconducting Quantum Circuits and Propagating Microwave States

Jan Goetz

Vollständiger Abdruck der von der Fakultät für Physik der Technischen Universität München zur Erlangung des akademischen Grades eines

Doktors der Naturwissenschaften

genehmigten Dissertation.

Vorsitzender:		Prof. Dr. Frank Pollmann
Prüfer der Dissertation:	1.	Prof. Dr. Rudolf Gross
	2.	Hon.-Prof. Dr. Gerhard Rempe

Die Dissertation wurde am 29.09.2016 bei der Technischen Universität München eingereicht und durch die Fakultät für Physik am 22.06.2017 angenommen.

The gods had condemned Sisyphus to ceaselessly rolling a rock to the top of a mountain, whence the stone would fall back of its own weight. They had thought with some reason that there is no more dreadful punishment than futile and hopeless labor.

- Albert Camus, The Myth of the Sisyphus -

Choose a job you love, and you will never have to work a day in your life.

- Anonymous -

Abstract

Superconducting circuit quantum electrodynamics (QED) has developed into a powerful platform for studying the interaction between matter and different states of light. In this context, superconducting quantum bits (qubits) act as artificial atoms interacting with quantized modes of the electromagnetic field. The field can be trapped in superconducting microwave resonators or propagating in transmission lines. In this thesis, we particularly study circuit QED systems where microwave fields are coupled with superconducting flux and transmon qubits. We optimize the coherence properties of the resonators, by analyzing loss mechanisms at excitation powers of approximately one photon on average. We find that two-level fluctuators associated with oxide layers at substrate and metal surfaces and metal-metal interfaces represent the predominant loss channel. Furthermore, we show how broadband thermal photon fields influence the relaxation and dephasing properties of a superconducting transmon qubit. To this end, we study several second-order loss channels of the transmon qubit and find that the broadband fields introduce a larger decay rate than expected from the Purcell filter defined by the resonator. Additionally, we show that qubit dephasing at the flux-insensitive point as well as low-frequency parameter fluctuations can be enhanced by thermal fields. Finally, we study how artificial atoms react to changes in inherent properties of the light fields. We perform a detailed analysis of the photon statistics of thermal fields using their relation to the qubits coherence properties. We quantitatively recover the expected $n^2 + n$-law for the photon number variance and confirm this result by direct correlation measurements. We then show a novel technique for the in-situ conversion of the interaction parity in light-matter interaction. To this end, we couple spatially controlled microwave fields to a flux qubit with two degrees of freedom.

Kurzfassung

Das Gebiet der Quanten-Elektrodynamik von supraleitenden Schaltkreisen hat sich zu einer vielversprechenden Plattform zur Studie von Licht-Materie Wechselwirkung etabliert. In diesem Feld spielen supraleitende Quantenbits die Rolle von künstlichen Atomen, die mit propagierenden oder stationären Mikrowellenfeldern gefangen in einem Resonanzkörper interagieren. Wir untersuchen die Wechselwirkung zwischen Mikrowellenfeldern und supraleitenden Fluss und Transmon Quantenbits. Zur Probenoptimierung analysieren wir Verlustmechanismen in supraleitenden Resonatoren. Wir finden, dass Metall-Metall Grenzflächen und Metallschichten auf der Rückseite von Substraten zu Mikrowellenverlusten führen. Des Weiteren zeigen wir, dass breitbandige thermische Felder die Kohärenzeigenschaften eines supraleitenden Transmon Quantenbits beeinflussen. Anhand zweiter-Ordnung Verlustmechanismen zeigen wir, dass diese Felder stärkere Dissipation verursachen, als durch einen Purcell Filter zu erwarten wäre. Zusätzlich analysieren wir den Zusammenhang zwischen thermischen Feldern und zweiter-Ordnung Effekten bezüglich Dephasierung und niederfrequenten Qubitparameterfluktuationen. Schlussendlich behandeln wir den Zusammenhang zwischen intrinsischen Lichteigenschaften und der Wechselwirkung mit künstlichen Atomen. Wir überprüfen die Photonenstatistik von thermischen Feldern mittels Kohärenzeigenschaften des Transmon Quantenbits und können das erwartete $n^2 + n$-Gesetz reproduzieren. Wir vergleichen unsere Ergebnisse mit direkten Korrelationsmessungen des Mikrowellenfeldes. Weiterhin entwickeln wir eine Technik zur Kontrolle der Parität eines Wechselwirkungsoperators. Zu diesem Zweck untersuchen wir Auswahlregeln für ein Zweiniveausystem mit zwei Freiheitsgraden.

Contents

Chapter 1 Introduction

The manifold interplay between electromagnetic radiation (light) and matter has fascinated human beings from time immemorial. One particular reason are the everyday experiments on light-matter interaction that people can do with their bare eyes. For example, the thrill of thunderbolts, the admiration of rainbows, or the play of underwater colors reminds us of the fascinating properties of light. In fact, underwater vision is possible because the vanishing absorption spectrum of water coincides with the visible spectrum of human beings [1]. Hence, our eyes limit the frequency range to the visible spectrum of humans in these everyday experiments. Nevertheless, electromagnetic radiation covers the complete frequency spectrum ranging from γ-rays with picometer wavelengths [2] to extremely low radio frequencies with wavelengths of 10^8 m [3]. Using the skin as a detector, we can sense parts of this large spectrum as thermal radiation for example when feeling the sunlight. Apparently, the degradation of our skin is enhanced under the exposure of strong thermal radiation [4]. From a conceptual point of view, some of the experiments in this thesis are very similar to this sunburn scenario of human skin. The difference is that we use superconducting quantum circuits as detectors and black-body radiators with temperatures below 1.5 K instead of 5800 K of the sun as emitters. Furthermore, we operate at very low radiation levels down to the attowatt regime corresponding to the radiation of the sun absorbed by an area of only $10^{-21}\,\mathrm{m}^2$ [5].
All phenomena discussed above are completely classical, meaning that no quantization paradigm is required for their explanation. Moving beyond classical experiments, the quantum nature of light [6, 7] together with the quantized level structure of atoms builds the fascinating field of quantum electrodynamics (QED) [8, 9]. Prominent experiments in this field address the quantumness of the famous double-split experiments [10], quantum-teleportation [11, 12], or quantum computing algorithms [13, 14]. However, experiments studying the interaction between single atoms and freely propagating photons are very demanding due to the small scattering cross-section of atoms. Therefore, high quality factor optical cavities [15] are used as photon boxes to confine the light field to a small mode volume. This is the essence of the successful field of optical cavity QED, which is the state-of-the-art technique for experiments on a single quantum level. A powerful and complementary platform in the microwave regime are integrated superconducting circuits opening the field of circuit QED [16, 17]. In circuit QED experiments, superconducting qubits [18] act as artificial atoms, while high quality coplanar resonators [19] or three-dimensional cavities [20] provide suitable boxes for the quantized light field. The flexibility to engineer and scale these quantum circuits makes them promising for future applications in quantum computing [21–23]. Despite that, superconducting circuits allow for a strong [16, 24, 25],

ultrastrong [26–28], or even controllable [29–32] coupling to light and to other circuit elements. This flexibility together with the possibility to use off-the-shelf measurement electronics, allows one to study the interplay between superconducting quantum circuits and fundamental properties of microwave light with convenient circuit QED elements.
In this thesis, we characterize inherent properties of superconducting quantum circuits and microwave fields using state-of-the-art circuit QED setups. We give a basic introduction into the fundamentals of circuit QED setups in chapter 2. We then turn to the fabrication of circuit QED samples in chapter 3. Borrowing techniques from the standardized production of integrated circuits in semiconductors, we fabricate all samples using metallic thin films and multilayers. In particular, we use the superconductors niobium (Nb), aluminum (Al), and combinations thereof deposited on off-the-shelf silicon substrates. The typical level splitting observed in these superconducting quantum circuits is approximately 5 GHz corresponding to a temperature of approximately 250 mK. To observe quantum effects in these circuits, we therefore cool down the samples to very low temperatures. To this end, we have constructed a dilution refrigerator that reaches a base temperature of 25 mK suited for circuit QED experiments. For these experiments, we equipped the cryostat and a newly opened laboratory with advanced microwave electronics to prepare and read out quantum states in the circuits. We present the new refrigerator and all experimental details in chapter 4.
Because the performance of solid state quantum systems is typically limited by short coherence times of a few microseconds [20, 33–37], we perform a systematic study of loss mechanisms in superconducting resonators [38]. As presented in Sec. 5.1, we find that Nb/Al interfaces in the metallic thin film heterostructures and also metallic structures underneath the samples contribute significantly to microwave loss. We then turn to the interplay between superconducting circuits and microwave fields. We first probe second-order loss mechanisms due to thermal microwave fields in Sec. 5.2. We show [39] that the broadband character of thermal fields destroys the quantum coherence of a superconducting transmon qubit [40], even if it is protected by a cavity filter. We probe second-order noise in the low-frequency regime and demonstrate the expected T^3 temperature dependence of the qubit dephasing rate. Finally, we show that qubit parameter fluctuations due to two-level states are enhanced under the influence of thermal microwave states. In particular, we experimentally confirm the T^2-dependence of the fluctuation spectrum expected for noninteracting two-level states.
In chapter 6, we study fundamental properties of microwave light. We first analyze field correlations in Sec. 6.1 by measuring the photon number variance of thermal fields [41]. This variance is linked to the photon statistics and carries unique information on the intrinsic nature of the propagating light. Using the transmon qubit as photon detector, we find the well-known $n^2 + n$-law for thermal fields. In addition to thermal fields, coherent states as for example generated from a laser are of special interest in QED experiments. In circuit QED experiments, coherent fields typically induce level transitions through dipole interaction with the qubits. These level transitions can be allowed or forbidden due to parity conservation [42]. In Sec. 6.2, we probe this fundamental physical principle for qubits using a tunable gradiometric flux qubit which has two degrees of freedom. To this end, we develop a technique to change the symmetry of an on-chip microwave field in the near field of two antenna lines. With this setup, we can directly observe parity changes of interaction operators using either dipolar or quadrupolar selection rules. Finally, in chapter 7, we conclude this thesis and give a short outlook towards future experiments.

Chapter 2 Superconducting quantum circuits

In this chapter, we introduce the superconducting quantum systems that we use throughout this thesis. We present superconducting qubits and coplanar waveguide structures in Sec. 2.1 and Sec. 2.2, respectively. When coupling these systems to each other, one obtains the textbook problem of light-matter interaction, which can be described in the framework of circuit QED as presented in Sec. 2.3. Finally, we discuss decoherence processes in superconducting quantum circuits in Sec. 2.4.

2.1 Superconducting qubits

Superconducting qubits are one particular realization of quantum two-level systems next to a large series of other physical implementations [11, 13, 43–49]. We begin this section with a general description of quantum bits in Sec. 2.1.1 by introducing the physics of quantum two-level systems. For the superconducting version of qubits, we integrate concepts of superconductivity, fluxoid quantization, and Josephson junctions (see Sec. 2.1.2 and Sec. 2.1.3). The two workhorses of these circuits are a transmon qubit and a tunable gradiometric flux qubit, which are introduced in Secs. 2.1.4 – 2.1.6.

2.1.1 Quantum bits

A quantum bit (qubit) [50] is the quantum mechanical equivalent of a classical bit (basic unit of information). A classical bit resides either in the state 0 or in the state 1 so that we can imagine it as a pointer with only two possible positions [see Fig. 2.1 (a) and (b)]. In contrast, a qubit can be in a superposition state $|\Psi\rangle = p_\mathrm{g}\,|\mathrm{g}\rangle + p_\mathrm{e}\,|\mathrm{e}\rangle$, where p_g and p_e define the probabilities to find the qubit in the ground state $|\mathrm{g}\rangle$ or the excited state $|\mathrm{e}\rangle$, respectively. Consequently, they obey $|p_\mathrm{g}|^2 + |p_\mathrm{e}|^2 = 1$ [51]. The two qubit eigenstates are separated by the energy $\hbar\omega_\mathrm{q}$, where $\omega_\mathrm{q}/2\pi$ is the qubit transition frequency and $\hbar = 1.05 \times 10^{-34}\,\mathrm{J\,s}$ is the reduced Planck constant. To visualize the qubit state, we describe it as vector pointing to a certain position on a three-dimensional sphere with radius $0 \leq r \leq 1$, called the Bloch sphere. Points on this sphere are represented by the Bloch vector with coordinates $\mathbf{r} = (r\sin\theta\cos\varphi, r\sin\theta\sin\varphi, r\cos\theta)$ with $0 \leq \theta \leq \pi$ and $0 \leq \varphi \leq 2\pi$ as illustrated in Fig. 2.1 (c). The vector components denote the projections of the qubit state

$$|\Psi\rangle = \cos\frac{\theta}{2}\,|\mathrm{g}\rangle + e^{\imath\varphi}\sin\frac{\theta}{2}\,|\mathrm{e}\rangle = \begin{pmatrix} \cos\frac{\theta}{2} \\ e^{\imath\varphi}\sin\frac{\theta}{2} \end{pmatrix} \tag{2.1.1}$$

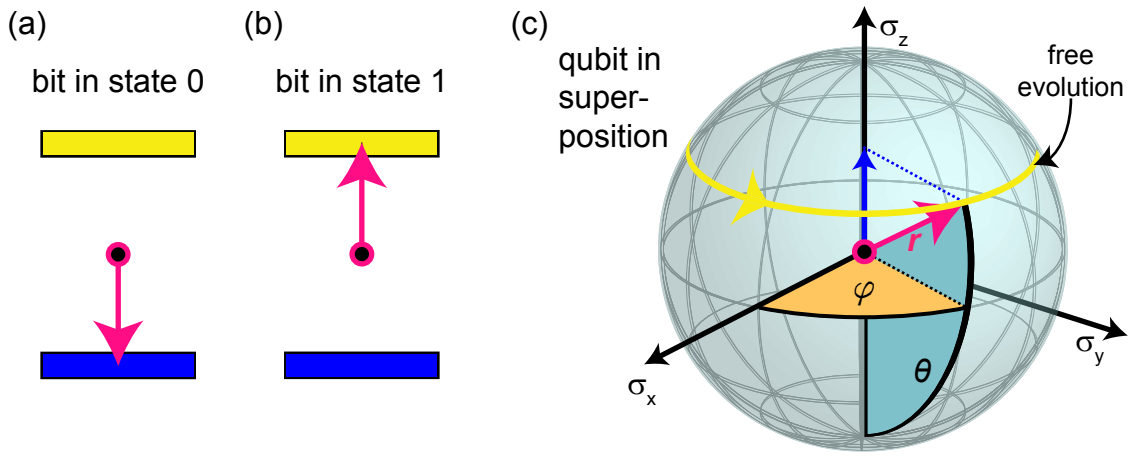

Figure 2.1: **(a)** and **(b)** Representation of the two possible states of a classical bit. **(c)** Representation of a qubit state vector on the Bloch sphere.

onto the intrinsic qubit axes σ_x, σ_y and σ_z. Projections onto these axes are equivalent to the expectation values of the Pauli operators $\langle\hat{\sigma}_x\rangle$, $\langle\hat{\sigma}_y\rangle$, and $\langle\hat{\sigma}_z\rangle$ [51]. In particular, we can express the operator $\langle\hat{\sigma}_z\rangle$ by the natural qubit eigenstates $|g\rangle$ and $|e\rangle$ as $\langle\hat{\sigma}_z\rangle = |p_g|^2 - |p_e|^2$. We use the quantization axis along σ_z to define the pure qubit Hamiltonian

$$\mathcal{H}_q = \frac{\omega_q}{2}\hat{\sigma}_z\,. \tag{2.1.2}$$

In the Bloch picture, points on the sphere surface ($|\mathbf{r}| = 1$) correspond to pure qubit states. Pure states are completely coherent, resulting in a well-defined phase relation between the basis states. Points inside the sphere ($|\mathbf{r}| < 1$) correspond to mixed states, which have partially lost their coherence properties due to decoherence processes. The transition from a pure state to a mixed state can be conveniently described by Lindblad master equation [52]. For the rest of this section, we stick to pure states and describe the influence of decoherence in Sec. 2.4.

Qubit dynamics - resonant case In the absence of decoherence, we describe the qubit dynamics by a time evolution $|\Psi\rangle(t)$ of the Bloch vector. This allows us to define qubit operations as rotations with certain angles carried out on the qubit state. To control the rotation angle, we use pulses of electromagnetic radiation with a certain length τ and frequency ω_d. We first consider the case of resonant driving, i.e., $\omega_d = \omega_q$. Then, the rotation frequency of the state vector, i.e., the Rabi frequency Ω_R depends solely on the drive amplitude Ω_d [53] and we can adjust the rotation angle by the energy $\Omega_R\tau$ irradiated to the qubit. We treat the irradiation classically by describing it with the Hamiltonian $\mathcal{H}_d = \hbar\Omega_d \cos(\omega_d t)\,\hat{\sigma}_x$. The general driven-qubit Hamiltonian reads

$$\mathcal{H}_{d,q} = \frac{\hbar}{2}\left[\omega_q\hat{\sigma}_z + 2\Omega_d \cos(\omega_d t)\,\hat{\sigma}_x\right] \tag{2.1.3}$$

which can be transformed into $\mathcal{H}'_d = \hbar\Omega_R\hat{\sigma}_x$ via a unitary transformation for the resonant case. Hence, we can rotate the state vector about the σ_x-axis in this way. We can apply rotations about the σ_y-axis by introducing a finite phase to the drive. In the following, we discuss the effect of a finite qubit-drive detuning.

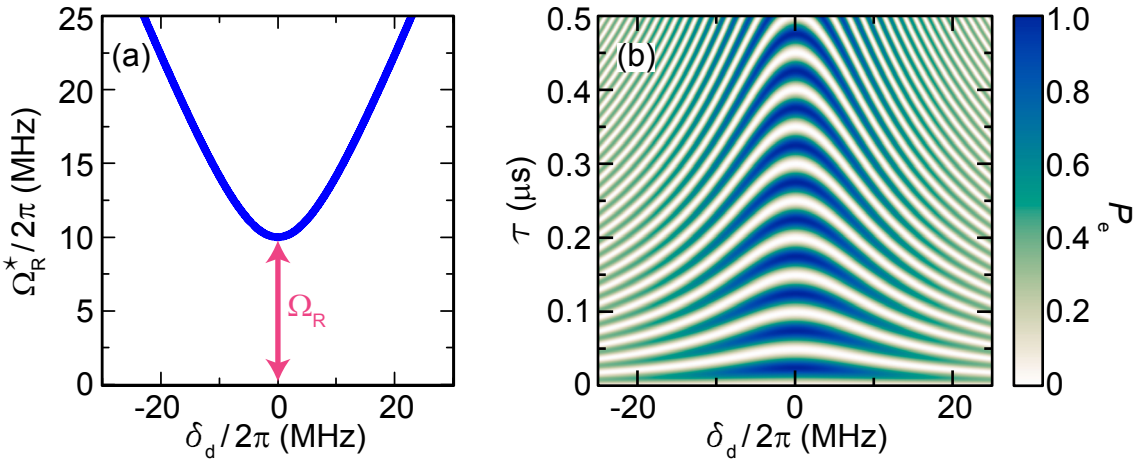

Figure 2.2: (a) Effective Rabi frequency $\Omega_\mathrm{R}^\star$ plotted versus detuning δ_d for $\Omega_\mathrm{R} = 10\,\mathrm{MHz}$. **(b)** Excited state probability in the absence of decoherence plotted versus detuning δ_d and pulse duration τ.

Non-resonant driving For a non-resonant drive with detuning $\delta_\mathrm{d} = \omega_\mathrm{q} - \omega_\mathrm{d}$, we transform Eq. (2.1.3) into a frame rotating with the drive frequency ω_d. That way, the time-independent interaction Hamiltonian in a rotating wave approximation can be expressed as [54] $\mathcal{H}_\mathrm{d}' = \hbar[\delta_\mathrm{d}\hat{\sigma}_\mathrm{z} + \Omega_\mathrm{d}\hat{\sigma}_\mathrm{x}]/2$. This Hamiltonian shows that the rotation frequency changes to $\Omega_\mathrm{R}^\star = \sqrt{\Omega_\mathrm{R}^2 + \delta_\mathrm{d}^2}$ [cf. Fig. 2.2 (a)]. Setting the global phase of the drive to zero, we obtain the rotation matrix [55]

$$\mathcal{R} = \begin{pmatrix} \cos\left(\Omega_\mathrm{R}^\star\tau\right) + \left(\frac{\Omega_\mathrm{R}}{\Omega_\mathrm{R}^\star}\right)^2 \mathcal{C} & -\frac{\delta_\mathrm{d}}{\Omega_\mathrm{R}^\star}\sin\left(\Omega_\mathrm{R}^\star\tau\right) & \left(\frac{\delta_\mathrm{d}\Omega_\mathrm{R}}{\Omega_\mathrm{R}^\star}^2\right)\left[1-\cos\left(\Omega_\mathrm{R}^\star\tau\right)\right] \\ -\frac{\delta_\mathrm{d}}{\Omega_\mathrm{R}^\star}\sin\left(\Omega_\mathrm{R}^\star\tau\right) & \cos\left(\Omega_\mathrm{R}^\star\tau\right) & -\frac{\Omega_\mathrm{R}}{\Omega_\mathrm{R}^\star}\sin\left(\Omega_\mathrm{R}^\star\tau\right) \\ \left(\frac{\delta_\mathrm{d}\Omega_\mathrm{R}}{\Omega_\mathrm{R}^\star}^2\right)\left[1-\cos\left(\Omega_\mathrm{R}^\star\tau\right)\right] & -\frac{\Omega_\mathrm{R}}{\Omega_\mathrm{R}^\star}\sin\left(\Omega_\mathrm{R}^\star\tau\right) & \cos\left(\Omega_\mathrm{R}^\star\tau\right) + \left(\frac{\delta_\mathrm{d}}{\Omega_\mathrm{R}^\star}\right)^2 \mathcal{C} \end{pmatrix}, \quad (2.1.4)$$

using $\mathcal{C} = [1 - \cos(\Omega_\mathrm{R}\tau)]$. Equation (2.1.4) shows that we can rotate the qubit state vector about all three axes of the Hilbert space. Rotations about the σ_z axis are induced by the free evolution of the qubit state vector [see Fig. 2.1 (c)]. The angular rotation with frequency δ_d is in analogy to the Lamor precession of a free spin [56]. Because the qubit exchanges no energy with the environment during the free evolution, the σ_z component of Ψ stays constant. However, the σ_z component starts oscillating, when applying a coherent (near) resonant drive. Under the condition $\delta_\mathrm{d} < \Omega_\mathrm{d}$, we calculate the angular dependence of the excited state probability

$$p_\mathrm{e} = |\langle e|\Psi(\tau)\rangle|^2 = \frac{\Omega_\mathrm{R}}{\Omega_\mathrm{R}^\star}\sin^2\left(\Omega_\mathrm{R}^\star\tau\right), \quad (2.1.5)$$

as illustrated in Fig. 2.2 (b).

2.1.2 Superconductivity and fluxoid quantization

Quantum bits can conveniently be realized as superconducting circuits that show quantum behavior [16, 57, 58]. Due to fabrication reasons, we use the superconductors niobium (Nb) and aluminum (Al) in this thesis, which have transition temperatures T_c in the kelvin range [59, 60]. To observe quantum behavior in these circuits, the qubit energy $\hbar\omega_\mathrm{q}$ must

be below $k_\mathrm{B}T_\mathrm{c}$, where $k_\mathrm{B} = 1.38 \times 10^{-23}\,\mathrm{J/K}$ is the Boltzmann constant. Furthermore, the thermal energy $E_\mathrm{th} = k_\mathrm{B}T$ must be sufficiently below $\hbar\omega_\mathrm{q}$. Hence, we need to perform experiments in the millikelvin regime to reduce intrinsic dissipation and observe quantum effects.[1] Next to the advantage of low dissipation, we make use of the superconducting energy gap Δ_0 which is much larger than the energy separation $\hbar\omega_\mathrm{q}$ of the superconducting qubits. Hence, we can explicitly address single energy levels of the quantum systems within this gap. Additionally, closed superconducting structures obey fluxoid quantization providing necessary boundary conditions for the operation of superconducting qubits.

Description of superconductors In a superconductor, all free electrons form a superconducting condensate [61], which we describe by a single coherent wave function [62] $\psi(\mathbf{r},t) = \sqrt{n_\mathrm{s}(\mathbf{r},t)}\exp[\imath\theta(\mathbf{r},t)]$. Here, $\theta(\mathbf{r},t)$ and $n_\mathrm{s}(\mathbf{r},t)$ are the space- and time-dependent macroscopic phase and the density of Cooper pairs defining the superconducting condensate. Following the theory of Bardeen, Cooper, and Schrieffer (BCS theory) [63, 64], Cooper pairs are electron pairs, which are bound in most cases by attractive electron-phonon interaction. For zero temperature, the Cooper pair density approaches $n_\mathrm{s} = n_\mathrm{tot}/2$, where n_tot is the total electron density. For the case of finite temperature however, there is always a finite quasiparticle density [65]

$$n_\mathrm{qp} = \frac{D(E_\mathrm{F})}{\mathcal{V}}\sqrt{2\pi k_\mathrm{B}T\Delta_0}\exp\left(-\frac{\Delta_0}{k_\mathrm{B}T}\right), \tag{2.1.6}$$

where $D(E_\mathrm{F})$ describes the two-spin density of states at the Fermi energy and $\mathcal{V}$ is the volume of the superconductor. If there is a strong background noise with a power spectral density $\mathcal{S}(\Delta_0)$ at the energy gap of the superconductor, the quasiparticle density additionally grows with [65] $\sqrt{S(\Delta_0)}$ as shown in Fig. 2.3 (a). One example for a strong $\mathcal{S}(\Delta_0)$ is thermal 4.2 K radiation, which has a maximum near the energy gap of Al. Due to the simultaneous existence of superconducting and normal conducting electrons, superconductivity can be described in the most simple way by a two-fluid model [61]. In this model, we describe the current density of the superconducting fluid by the supercurrent density $\mathbf{j}_\mathrm{s}$ and that of the normal conducting fluid by $\mathbf{j}_\mathrm{n}$ [66].

Surface resistance in the two-fluid model For superconductors, the surface resistance $\mathcal{R}_\mathrm{s}$ has contributions of both normal conducting and superconducting electrons. While $\mathcal{R}_\mathrm{s}$ scales linearly with frequency for a normal conductor at room temperature, it scales with ω^2 for a superconductor [67]. This $\mathcal{R}_\mathrm{s} \propto \omega^2$ dependence of superconductors arises from the BCS penetration depth λ_BCS characterizing the typical decay length of electromagnetic fields inside the superconductor. This penetration depth accounts for the BCS coherence length ξ_0, the London penetration depth λ_L, and the mean free path λ_ℓ of the superconducting electrons.[2] At finite temperatures, the penetration depth is modified due the generation of normal conducting electrons with skin depth λ_n [69]. In the dirty limit, we can combine the penetration depth and the skin depth to

$$\lambda_\mathrm{s} = \left(\frac{1}{\lambda_\mathrm{BCS}^2} + \frac{2\imath}{\lambda_\mathrm{n}^2}\right)^{-1/2}. \tag{2.1.7}$$

[1] A detailed description of dissipative effects in superconductors is given in Sec. 2.4.

[2] In addition to these dependencies, the surface resistance also strongly depends on the conductor geometry [68].

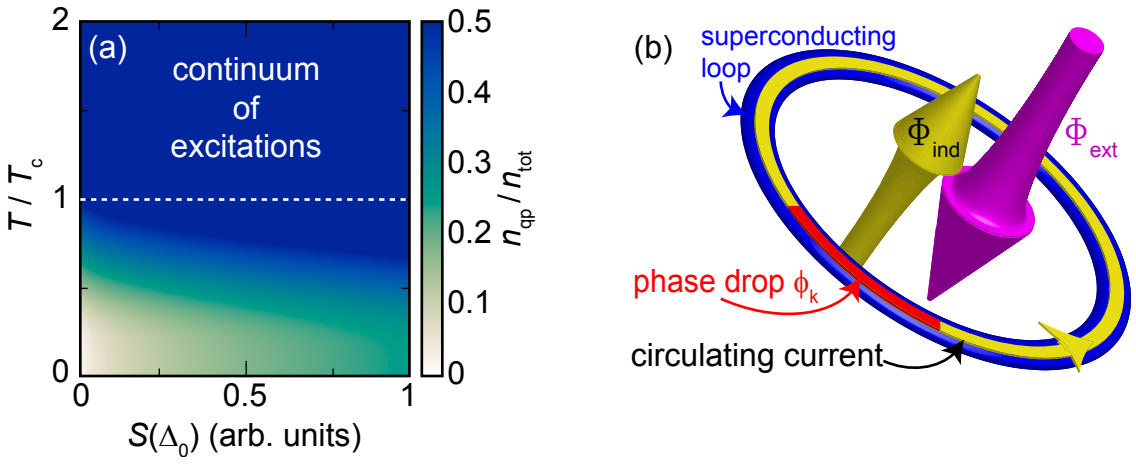

Figure 2.3: **(a)** Normalized quasiparticle density n_{qp} plotted versus noise at the energy gap $\mathcal{S}(\Delta_0)$ and temperature. At low temperatures and low noise, we achieve $n_{\mathrm{qp}} \simeq 0$ and can address single qubit levels. For $T > T_{\mathrm{c}}$, there is a continuum of possible excitations. **(b)** A thin superconducting loop with cross section smaller than the penetration depth provides fluxoid quantization partly via self-induced flux Φ_{ind} and partly via a phase drop ϕ_{k} in the condensate.

Because of thermal generation of quasiparticles described by Eq. (2.1.6), λ_{s} is temperature-dependent as predicted by BCS theory. It can be shown, however, that in the temperature regime between $T = 0$ and $T = T_{\mathrm{c}}/2$ the surface resistance simplifies to [70]

$$\mathcal{R}_{\mathrm{s}} \simeq A\, \lambda_{\mathrm{BCS}}^3 \frac{\omega^2}{T} \exp\left(-\frac{\Delta_0}{k_{\mathrm{B}} T}\right) . \tag{2.1.8}$$

Here, the exponential term is a Boltzmann factor resulting from quasiparticle generation and the prefactor A accounts for geometry and thickness effects [71, 72].
For sufficiently low temperatures and high frequencies, the mean free path of the normal conducting electrons can be larger than their skin depth. In this case, the local relationship between field and current (Ohms law) breaks down and there is a non-local relationship between electric field and current. This anomalous skin effect [73, 74] results in a surface resistance that scales with $\omega^{2/3}$ [75, 76]. The interplay between this $\omega^{2/3}$ relation and the ω^2 relation for superconductors highly depends on the specific properties of the superconductor. When the mean free path is, however, small compared to the coherence length ($\lambda_\ell \ll \xi_0$), the superconductor is in the dirty limit [77] and Eq. (2.1.8) is valid.[3]

Fluxoid quantization Fluxoid quantization is a fundamental effect in multiply connected superconductors describing quantization phenomena linked to the phase of the superconducting condensate [78]. An integral of the fluxoid along the path Γ in a closed superconducting loop, i.e.,

$$\oint_\Gamma \underbrace{\mu_0 \lambda_{\mathrm{L}}^2 \mathbf{j}_{\mathrm{s}}(\mathbf{r},t)\, \mathrm{d}s + \Phi_\ell}_{\text{fluxoid}} = N_\ell \cdot \Phi_0 \,, \tag{2.1.9}$$

always yields an integer amount of flux quanta $N_\ell \in \mathbb{Z}$. In Eq. (2.1.9), $\mu_0 = 4\pi \times 10^{-7}\,\mathrm{N/A^2}$ is the vacuum permeability, $\Phi_0 = (h/2e) \simeq 2\,\mathrm{fV\,s}$ is the flux quantum, and Φ_ℓ is the magnetic

[3] The thin film superconductors made of Nb and Al in this work can be treated in the dirty limit.

flux penetrating the loop. For superconductors with a cross section A_w much larger than the penetration depth, we can always find an integration path Γ where $\mathbf{j}_\mathrm{s}=0$. In this case, we obtain the limit of flux quantization [79, 80], where $\Phi_\ell = N_\ell \Phi_0$ and (possible) external flux Φ_ext is purely compensated by self-induced flux $\Phi_\mathrm{ind} = L_\mathrm{g} I_\ell$. Here, L_g is the geometric part of the loop inductance and $I_\ell = \int_{A_\mathrm{w}} \mathbf{j}_\mathrm{s}\,\mathrm{d}A$ is the current circulating in the loop. For the thin-film structures used in this work, however, the cross section of the loops is on the order of the penetration depth and the quantized value is the fluxoid because $\mathbf{j}_\mathrm{s}$ is finite in the complete cross section of the superconductor. In this case, it is convenient to use the reduced magnetic flux $\phi_\mathrm{g} = 2\pi\Phi_\mathrm{ind}/\Phi_0$ and $\phi_\mathrm{ext} = 2\pi\Phi_\mathrm{ext}/\Phi_0$, as well as the phase difference $\phi_\mathrm{k} = \oint_\Gamma \mu_0 \lambda_\mathrm{L}^2 I_\ell \cdot \mathrm{d}s$ [81] as depicted in Fig. 2.3 (b). The phase difference is attributed to a kinetic inductance $L_\mathrm{k} = \mu_0 \lambda_\mathrm{L}^2 s_\ell / A_\mathrm{w}$, where s_ℓ is the total loop length. Consequently, fluxoid quantization in the ring obeys

$$\overbrace{2\pi\frac{L_\mathrm{k} I_\ell}{\Phi_0}}^{\phi_\mathrm{k}} + \overbrace{2\pi\frac{\Phi_\mathrm{ext}}{\Phi_0}}^{\phi_\mathrm{ext}} + \overbrace{2\pi\frac{L_\mathrm{g} I_\ell}{\Phi_0}}^{\phi_\mathrm{g}} = 2\pi N_\ell\,. \tag{2.1.10}$$

Alternatively, we can apply the magnetic field during the transition of the ring into its superconducting state, which is a convenient method to flux-bias superconducting circuits [82, 83]. For an external loop frustration $f_\mathrm{ext} = \Phi_\mathrm{ext}/\Phi_0$, there is an inductive energy

$$E_\ell = \frac{1}{2}(L_\mathrm{g} + L_\mathrm{k}) I_\ell^2 = \frac{\Phi_0^2}{2(L_\mathrm{k} + L_\mathrm{g})}(f_\mathrm{ext} - N_\ell)^2\,. \tag{2.1.11}$$

stored in the loop, which can be used for flux trapping as follows. Applying an integer amount of j flux quanta to the ring ($f_\mathrm{ext} = N_j$) in the normal state and cooling it down to the superconducting state, the ring will prefer to stay in this N_j energy state. Due to Faradays law $\partial\mathbf{B}/\partial t = \nabla \times \mathbf{E} = 0$ ($\mathbf{E} = 0$ for superconductors), the magnetic flux cannot change. Hence, the ground state $N_\ell = 0$ cannot be reached and the ring remains frozen in the $N_\ell = N_j$ state. The energy required for an unintended phase slip is approximately given by [84–86] $E_{\Delta N} \approx \sqrt{6} I_{\ell,\mathrm{c}} \Phi_0 / 2\pi$, where $I_{\ell,\mathrm{c}}$ is the critical current of the loop. Assuming the critical current to be of the order of 1 mA the energy required for a phase slip corresponds to a temperature $T_\mathrm{slip} > 10^4$ K meaning that phase slipping processes are very unlikely.

2.1.3 Josephson junctions

Josephson junctions serve as non-linear circuit elements based on tunneling effects between two superconducting electrodes as depicted in Fig. 2.4. We use these elements to build electrical circuits with non-uniformly distributed level spacing. The non-linearity arises from the non-linear current-phase relation of Josephson junctions also known as Josephson effect. The Josephson effect describes the coherent tunneling of Cooper pairs through an insulating barrier as predicted by Brian D. Josephson [87]. After its first observation in 1963 [88] the Josephson effect was honored with the Nobel Prize in 1973.

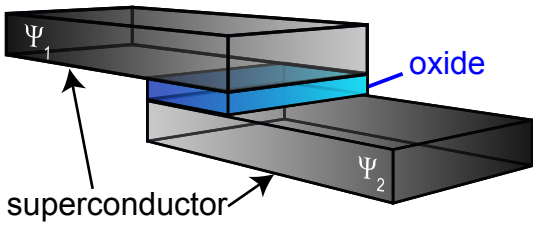

Figure 2.4: Sketch of a Josephson junction.

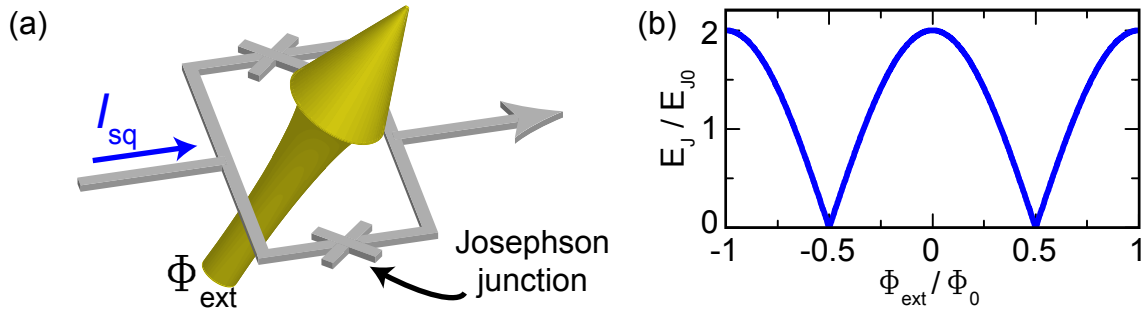

Figure 2.5: **(a)** Sketch of a DC SQUID, consisting of a superconducting loop intersected by two Josephson junctions. The maximum SQUID current I_c depends on the external magnetic flux Φ_ℓ threading the loop. For vanishing screening parameter β_ℓ, we have $\Phi_\ell \simeq \Phi_{ext}$. **(b)** Modulation of the Josephson energy plotted versus external magnetic flux for a negligible screening parameter β_ℓ.

The physics of a Josephson junction is highly dependent on the geometry of the junction. If the tunnel barrier is thin enough, the wave functions ψ_1 and ψ_2 of the two superconducting electrodes overlap, resulting in a finite supercurrent I_s across the insulating barrier [89]. A junction with area A_J can carry a maximum critical tunnel current $I_c = j_c A_J$, which is limited by a critical current density j_c. This critical current density depends exponentially on the barrier height and thickness [90].

Josephson equations and energy quantization The physics of Josephson junctions is defined by the two Josephson equations. The first Josephson equation describes the relation between the phase difference ϕ_J across the junction and the supercurrent as $I_s = I_c \sin(\phi_J)$. The second Josephson equation defines the time-dependent phase evolution $\partial\phi_J/\partial t = 2\pi V/\Phi_0$, where V denotes the voltage drop across the junction. Taking the time derivative of the first Josephson equation shows that the junction has a non-linear inductance [90]

$$L_J = \frac{\Phi_0}{2\pi I_c \cos\phi_J} = L_c \frac{1}{\cos\phi_J}\,. \tag{2.1.12}$$

The cosine term in the denominator leads to an adjustable Josephson inductance, which even can take negative values.
In the following, we discuss energy quantization in a Josephson junction. A Josephson junction is characterized by two characteristic energies, the Josephson coupling energy E_J and the charging energy E_c. In the zero voltage state, the potential energy of the junction

$$E_J = \frac{\Phi_0 I_c}{2\pi}(1-\cos\phi_J) = E_{J0}(1-\cos\phi_J) \tag{2.1.13}$$

is analog to the binding energy in molecules originating from the finite overlap of the wave functions of different electrons. The charging energy $E_c = e^2/2C_J$ is defined by the capacitance C_J of the junction, which can be approximated as a parallel plate capacitor [90]. Usually, a junction is in the regime $E_{J0} > E_c$ such that the charging energy defines the level splitting inside the junction potential. In the simplest case, the potential can be approximated by a parabola resulting in equidistant energy levels separated by the plasma energy $\hbar\omega_p = \sqrt{8E_J E_c}$ [91]. Consequently, quantization of energy levels becomes relevant if $E_{J0} > E_c \gg k_B T$. In this case, we can describe the junction dynamics by a phase particle in the lowest energy level oscillating with the plasma frequency ω_p.

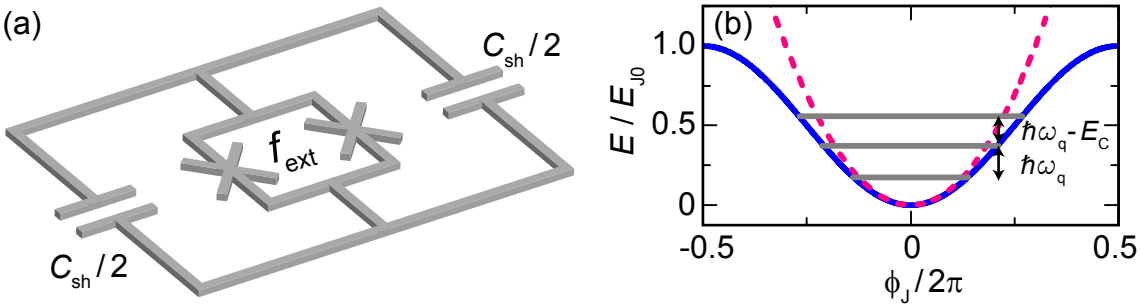

Figure 2.6: **(a)** Sketch of a transmon qubit that can be realized as a split Josephson junction (DC SQUID) shunted by two capacitors. **(b)** Potential energy of a transmon qubit at $\Phi_{\text{ext}} = 0$ plotted versus phase difference across the split junction. Due to a finite anharmonicity compared to a parabolic potential (dashed line), we can separate the first two energy levels.

DC SQUID The DC superconducting quantum interference device (DC SQUID) consists of two Josephson junctions connected in parallel [92] in a loop with inductance L_{sq} as depicted in Fig. 2.5 (a). The two parallel junctions act analogously to a single (split) junction with an adjustable critical current $I_{\text{sq}}(f_{\text{ext}})$. For a negligible screening parameter $\beta_\ell = 2I_{\text{c}}L_{\text{sq}}/\Phi_0 \ll 1$, the Josephson energy depends directly on the external magnetic frustration $f_{\text{ext}} = \Phi_{\text{ext}}/\Phi_0$ of the SQUID loop. This external frustration modulates the total supercurrent across the SQUID resulting in a coupling energy

$$E_{\text{J}}(f_{\text{ext}}) = 2\frac{\Phi_0 I_{\text{c}}}{2\pi}\left|\cos\left(\pi f_{\text{ext}}\right)\right| \tag{2.1.14}$$

of the SQUID as shown in Fig. 2.5 (b). In this thesis, we use DC SQUIDs to tune the Josephson energy E_{J0} of qubit junctions in order to vary the qubit transition frequency.

2.1.4 Transmon qubit

A transmission-line shunted plasma oscillation (transmon) qubit [40] belongs to the family of superconducting qubits [18] and is based on the energy level quantization in a Josephson junction. As derived above, the energy splitting of the levels is determined by the plasma frequency ω_{p}. To isolate the two lowest energy levels of a transmon qubit, the Josephson junction is shunted by a large capacitance C_{sh}. Furthermore, for the frequency tunable version of a transmon qubit, the single junction is replaced by a DC SQUID as illustrated in Fig. 2.6 (a). Then, the Hamiltonian of a transmon qubit reads

$$\mathcal{H}_{\text{q}} = \frac{1}{2}C_\Sigma\left(\frac{\Phi_0}{2\pi}\right)^2\frac{\partial\phi_{\text{J}}}{\partial t}^2 + E_{\text{J}}(f_{\text{ext}})[1-\cos(\phi_{\text{J}})]\,, \tag{2.1.15}$$

where $E_{\text{J}}(f_{\text{ext}})$ is given by Eq. (2.1.14) and $C_\Sigma = C_{\text{J}} + C_{\text{sh}}$ is the modified junction capacitance. To act as a qubit (two-level approximation), the level spacing must be sufficiently non-uniform what can be conveniently achieved by choosing a small ratio $E_{\text{J}}/E_{\text{c}}$ [40]. On the other hand, large values for $E_{\text{J}}/E_{\text{c}}$ are desirable because they lower the sensitivity to charge noise. As a trade-off, transmon qubits typically exhibit a ratio $E_{\text{J}}/E_{\text{c}} \simeq 50$ [93]. In this case, for calculating the lowest energy levels the cosine potential in Eq. (2.1.15) can be well approximated by the lowest terms of a Taylor expansion

$$\mathcal{H}_{\text{q}} = \frac{1}{2}C_\Sigma\left(\frac{\Phi_0}{2\pi}\right)^2\frac{\partial\phi_{\text{J}}}{\partial t}^2 + \frac{1}{2}E_{\text{J0}}\phi_{\text{J}}^2 - E_{\text{J0}}\frac{\phi_{\text{J}}^4}{24} + \mathcal{O}(\phi_{\text{J}}^6)\,, \tag{2.1.16}$$

which is equivalent to the Hamiltonian of a non-linear (Duffing) oscillator [94]. The first two terms in Eq. (2.1.16) describe a harmonic oscillator Hamiltonian, while the third term constitutes a small nonlinear perturbation resulting in an anharmonic potential shown in Fig. 2.6 (b). Considering only the harmonic terms in Eq. (2.1.16), we find that the qubit transition frequency [40]

$$\omega_{\mathrm{q}} = \omega_{\mathrm{p}} = \hbar^{-1}\sqrt{8E_{\mathrm{c}}E_{\mathrm{J0}}\left|\cos\left(\pi f_{\mathrm{ext}}\right)\right|}\,, \tag{2.1.17}$$

is given by the plasma frequency, which is adjustable via the external magnetic frustration f_{ext}. The perturbation term in Eq. (2.1.16) is responsible for the qubit anharmonicity [40] $\alpha \equiv E_{12} - E_{01} \approx -E_{\mathrm{c}}$ between the qubit states. Here, E_{ij} is the transition energy from level i to level j.

2.1.5 Flux qubit

For convenience, we first introduce the working principle of the standard three junction version of a flux [95–97] qubit depicted in Fig. 2.7 before discussing the gradiometric and tunable version in the next section. In contrast to the transmon qubit, the flux qubit operates in the regime $E_{\mathrm{J0}} \gg E_{\mathrm{c}}$ such that magnetic flux is the good quantum variable. For flux qubits, the two qubit states correspond to a superposition of circulating currents flowing clockwise and counterclockwise around a superconducting loop intersected by three Josephson junctions [96]. Two of the junctions have equal Josephson energies E_{J0} and the energy of the third junction is lowered by a factor α with $1/2 < \alpha < 1$. For a negligible loop inductance, the flux qubit potential can be written as the sum of the energies of three single Josephson junctions [55]. Due to fluxoid quantization, this potential reduces to [see Fig. 2.8 (a)]

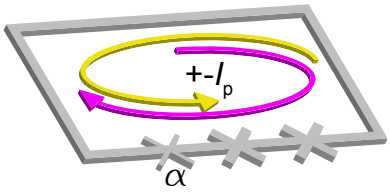

Figure 2.7: Sketch of a three junction flux qubit and the superposition of current states.

$$U_{\mathrm{q}} = E_{\mathrm{J0}}\left[2 + \alpha - \cos(\phi_1) - \cos(\phi_2) - \alpha\cos\left(\phi_{\mathrm{ext}} + \phi_1 - \phi_2\right)\right]. \tag{2.1.18}$$

Here, $\phi_{\mathrm{ext}} = 2\pi\Phi_{\mathrm{ext}}/\Phi_0$ is the reduced magnetic flux threading the qubit loop and ϕ_1, ϕ_2 are the phase differences across the two identical junctions. The third phase difference is eliminated due to the boundary condition imposed by fluxoid quantization. For $\alpha > 1/2$, a cut in the qubit potential along the line $\phi_2 = -\phi_1$ has the form of a double-well potential. As shown in Fig. 2.8 (b), this potential is symmetric for $f_{\mathrm{ext}} = N + 1/2$. The two minima can be identified with the two states of the persistent current $I_{\mathrm{p}} = \pm I_{\mathrm{c}}\sqrt{1-(2\alpha)^{-2}}$ flowing in opposite directions around the qubit loop. For $f_{\mathrm{ext}} = 1/2$, there is an energy degeneracy of the pure current states. A finite tunnel coupling through the potential leads to the formation of a symmetric and antisymmetric superposition state thereby lifting the degeneracy. For suitable qubit parameters, the tunneling rate Δ between the potential well is large enough to separate two qubit states. The tunneling rate [83]

$$\Delta(\alpha) = \frac{1}{\hbar}\sqrt{\frac{4E_{\mathrm{J}}E_{\mathrm{c}}(4\alpha^2-1)}{\alpha(1+2\alpha)}}\exp\left(-a(\alpha)\sqrt{4\alpha(1+2\alpha)\frac{E_{\mathrm{J}}}{E_{\mathrm{c}}}}\right), \tag{2.1.19}$$

depends on $a(\alpha) = \sqrt{1-(2\alpha)^{-2}} - [\arccos(1/2\alpha)/2\alpha]$ as depicted in Fig. 2.8 (c). In addition to the tunneling energy $\hbar\Delta$, there is a magnetic energy bias $\hbar\varepsilon = 2I_{\mathrm{p}}\Phi_0(f_{\mathrm{ext}} - 1/2)$ due to

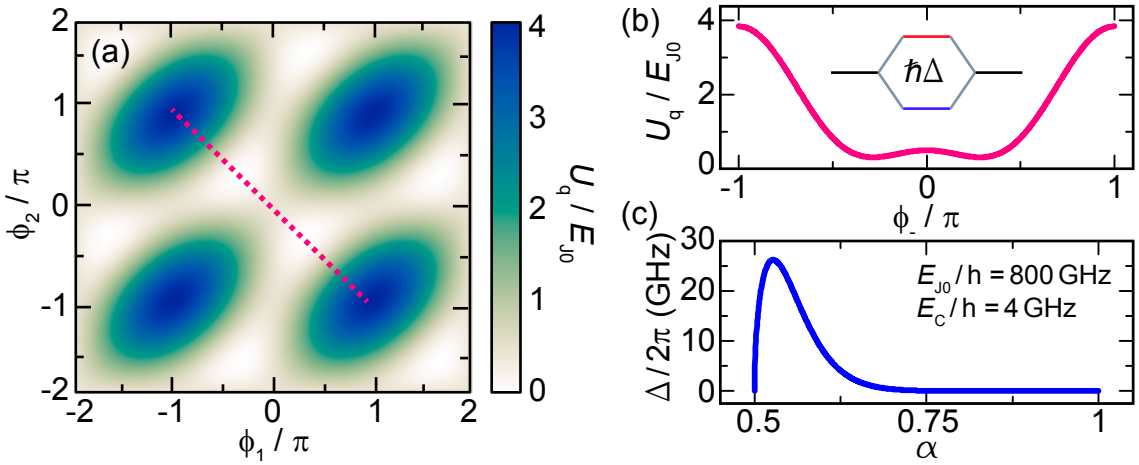

Figure 2.8: **(a)** Two-dimensional potential energy landscape of a flux qubit plotted versus phase difference across the two identical qubit junctions at $f_{\text{ext}} = 0$. Due to the symmetry of two junctions, the qubit is restricted to the case where $\phi_1 = -\phi_2$ indicated by the dashed line. **(b)** Qubit potential along the dashed line in panel (a). The two qubit eigenstates located in the two minima are energy degenerated, which is lifted by the tunneling matrix element Δ. **(c)** Qubit gap Δ plotted versus the ratio α.

an applied magnetic flux. This flux modifies the qubit energy for flux bias points away from the degeneracy point, i.e., $f_{\text{ext}} \neq N + 1/2$. Consequently, the effective Hamiltonian [95]

$$\mathcal{H}_{\text{q}} = \frac{\hbar\Delta}{2}\hat{\sigma}_{\text{x}} + \frac{\hbar\varepsilon}{2}\hat{\sigma}_{\text{z}} = \frac{\hbar}{2}\begin{pmatrix} \varepsilon & \Delta \\ \Delta & -\varepsilon \end{pmatrix} \tag{2.1.20}$$

has two degrees of freedom. Diagonalizing the Hamiltonian in Eq. (2.1.20) yields the eigenvalues $\pm 1/2\hbar(\varepsilon^2 + \Delta^2)^{1/2}$ defining the flux-dependent energy difference [95]

$$\hbar\omega_{\text{q}}(f_{\text{ext}},\alpha) = \hbar\sqrt{\varepsilon^2 + \Delta^2} = \sqrt{4I_{\text{c}}^2\Phi_0^2\left(1 - \left(\frac{1}{2\alpha}\right)^2\right)\left(f_{\text{ext}} - \frac{1}{2}\right)^2 + \Delta(\alpha)^2}\,. \tag{2.1.21}$$

This equation defines the well-known qubit hyperbola of a flux qubit. As apparent from Eq. (2.1.21), we can tune the qubit transition frequency by changing the magnetic energy bias $\hbar\varepsilon$ of the qubit. This method, however, drastically deteriorates the coherence properties of the qubit [33] because one leaves the flux sweet spot where $\partial\omega_{\text{q}}/\partial\Phi = 0$. Alternatively, we can tune the qubit gap Δ by replacing the α-junction by a DC SQUID. That way, we can always operate the qubit at the degeneracy point but are able to tune the transition frequency by varying an external parameter [83, 98]. At the degeneracy point, a finite flux Φ_α through the α-SQUID changes the α-value according to $\alpha = \alpha_0|\cos(\pi\Phi_\alpha/\Phi_0)|$. Here, α_0 is the ratio between the total coupling energy of the α-SQUID and that of one of the two identical qubit junctions. The qubit gap reacts to $\alpha(\Phi_\alpha)$ as described by Eq. (2.1.19).

2.1.6 Tunable-gap gradiometric flux qubit

The tunable-gap gradiometric flux qubit [83, 98], which we call *gradio qubit*, is a special version of the three junction flux qubit presented above. It comprises a gradiometric design

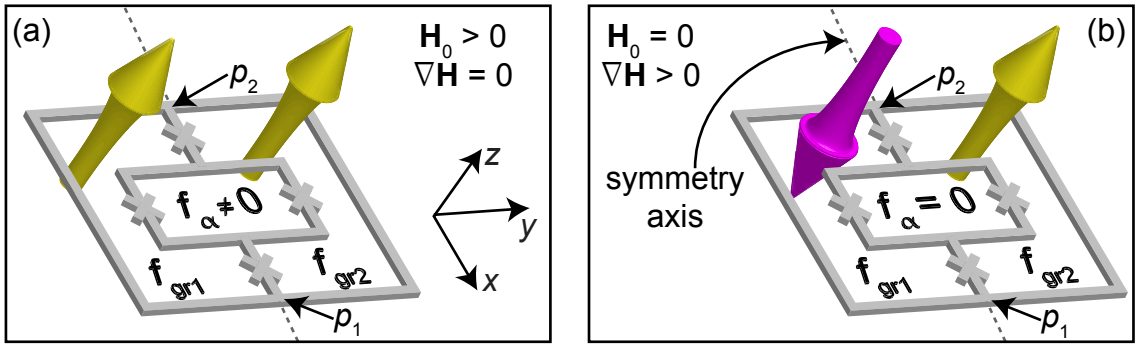

Figure 2.9: **(a)** Sketch of a gradio qubit penetrated by a homogeneous magnetic field $\mathbf{H}_0$. This field results in a finite frustration f_α of the SQUID loop, whereas the frustration f_{gr1} and f_{gr2} of the two gradiometer loops cancel each other. The qubit potential is defined by the phase difference between the two points p_1 and p_2 on the outer trap loop. **(b)** As in panel (a) but for a field gradient that has the qubits center line as symmetry axis. That way, there is no net frustration f_α of the SQUID loop, but a finite frustration difference $\delta f_{\mathrm{gr}} = f_{\mathrm{gr1}} - f_{\mathrm{gr2}}$ between the two gradiometer loops.

and a tunable α-junction. The gradiometric design consists of two equally sized loops with one shared line on the symmetry axis resulting in an eight-shaped geometry [99, 100]. In the following, we call the two equally sized loops the *gradiometer loops*, the larger outer loop the *trap loop*, and the loop of the α-SQUID the *SQUID loop*. The shared line of the two gradiometer loops can be interrupted by three Josephson junctions to form a flux qubit. We replace the center (α) junction by a DC SQUID to achieve tunability, which results in the design shown in Fig. 2.9. For a pedagogical description of the gradio qubit, we will separate external magnetic fields $\mathbf{H}_{\mathrm{ext}} = \mathbf{H}_0 + \nabla\mathbf{H}$ into a constant contribution $\mathbf{H}_0 \equiv (0, 0, H_0)$ and an ideal field gradient $\nabla\mathbf{H}$. For convenience, we construct this field gradient to have only a y-dependent z-component, i.e., $\nabla\mathbf{H} \equiv (0{,}0{,}\partial H_{\mathrm{z}}(y)/\partial y)$ from now on. That way, $\mathbf{H}_0$ couples symmetrically into the two gradiometer loops and $\nabla\mathbf{H}$ antisymmetrically. In a simplified picture, one can then say that $\nabla\mathbf{H}$ takes the role of f_{ext} in Eq. (2.1.18) and is therefore used to control $\varepsilon\hat{\sigma}_{\mathrm{z}}$ (it tilts the potential). The homogeneous field contribution is an additional control knob to tune $\Delta\hat{\sigma}_{\mathrm{x}}$.

Persistent current flow and qubit states The structure of a tunable-gap gradiometric flux qubit consists of four loops, which each have to obey fluxoid quantization (trap loop, two gradiometer loops, SQUID loop). In the following, we discuss how the persistent currents flow in these loops and how the qubit states are defined. For pedagogical reasons, we assume the simplest relevant situation that one flux quantum was trapped during the cooldown of the sample ($N_\ell = 1$) and that we apply zero magnetic field ($\mathbf{H}_0 = 0$) and also no field gradient ($\nabla\mathbf{H} = 0$). This situation is depicted in Fig. 2.10 (a). The resulting circulating loop current $I_\ell = \Phi_0/(L_{\mathrm{g}} + L_{\mathrm{k}})$ provides the dominating energy E_ℓ defined in Eq. (2.1.11). For a typical loop inductance $L_{\mathrm{g}} + L_{\mathrm{k}} \simeq 200\,\mathrm{pH}$, this energy is on the order of $h \times 100\,\mathrm{THz}$. We now discuss the current flow that results from the parabolic loop potential and from fluxoid quantization in all four loops.

– *SQUID reaction* – For simplicity, we assume an ideal α-SQUID that is perfectly symmetric and has identical junctions. For $N_\ell \neq 0$, there is a finite flux Φ_α applied to the SQUID loop due to the circulating current I_ℓ, which generates the SQUID frustration f_α. To satisfy fluxoid quantization in the SQUID loop, $\phi_1 - \phi_2 + 2\pi f_\alpha = 2\pi N$, where ϕ_1 and ϕ_2 are the

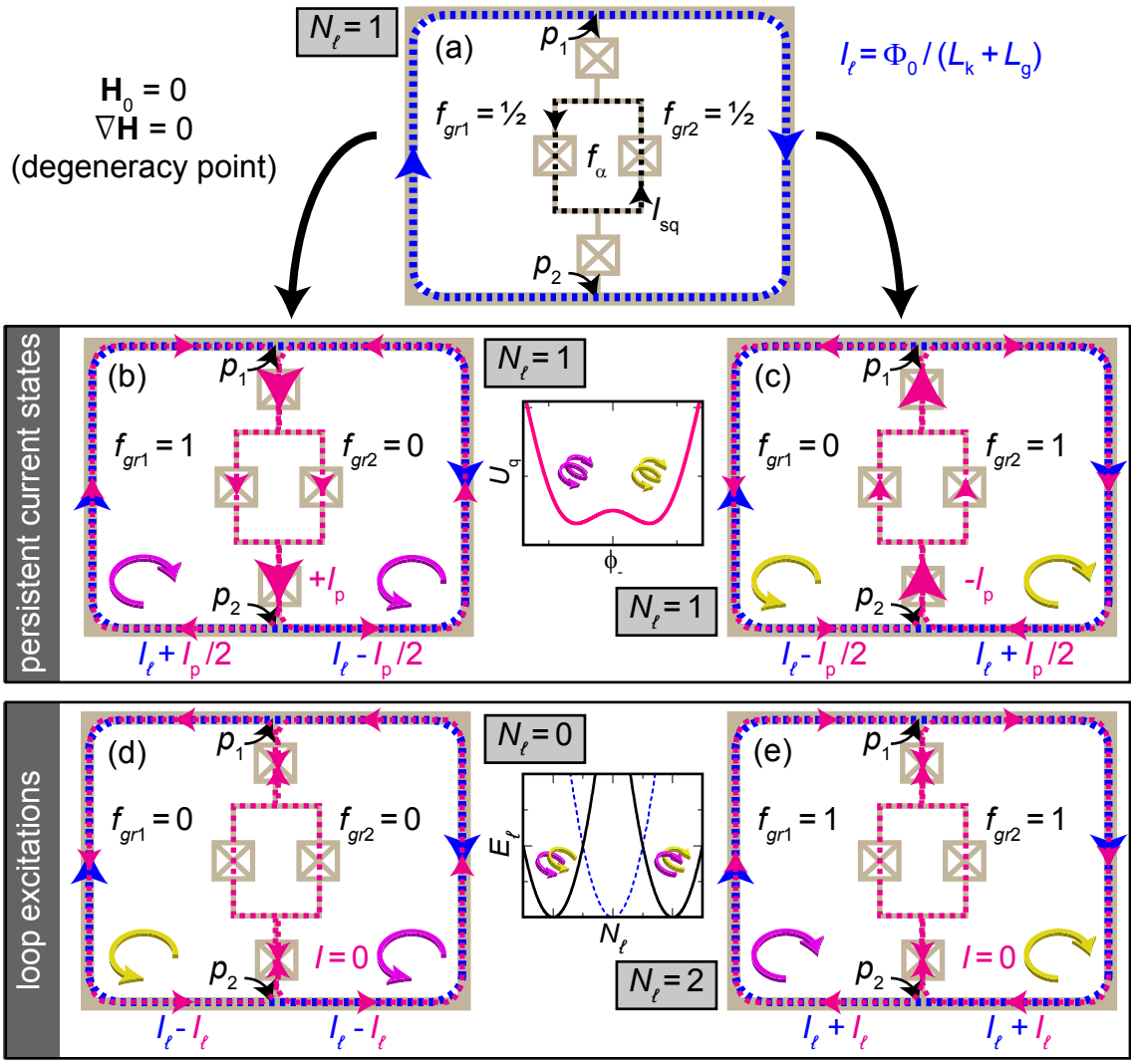

Figure 2.10: **(a)** Sketch of a tunable-gap gradiometric flux qubit and the currents I_ℓ around the trap loop and I_{sq} around the α-SQUID. Fluxoid quantization leads to formation of the two qubit states $|\mathrm{g_{gq}}\rangle$ in panel **(b)** and $|\mathrm{e_{gq}}\rangle$ in panel **(c)** due to the the persistent current I_{p} on the cneter line. Panel **(d)** and panel **(e)** show excitations of the trap loop, i.e., a change $\delta N_\ell = \pm 1$. This change can be induced if the qubit current I_{p} is on the order of I_ℓ and the current in both gradiometer loops is flowing in-phase. This situation is, however, very unlikely because $E_\ell \gg \hbar\omega_{\mathrm{q}}$.

phase differences across the SQUD junctions, there is a finite variation $\delta\phi = \phi_1 - \phi_2 = 2\pi f_\alpha$ between the phase difference across the SQUID junctions. This variation $\delta\phi$ results in a circulating supercurrent I_{sq} around the SQUID loop [see Fig. 2.10 (a)]. Because the SQUID is symmetric, the circulating current induces an equal amount of magnetic flux in the two gradiometer loops. We discuss SQUID imbalances in the following paragraph in terms of a multipole expansion. We also give a detailed description of the amount of induced flux accounting for screening effects further below.

– *Qubit states* – Fluxoid quantization and the symmetry of the trap loop result in a phase difference of $2\pi(N_\ell - 1/2)$ between the points p_1 and p_2 of the trap loop. For the specific case of $N_\ell = 1$ this means that there must be a phase difference of π across the three

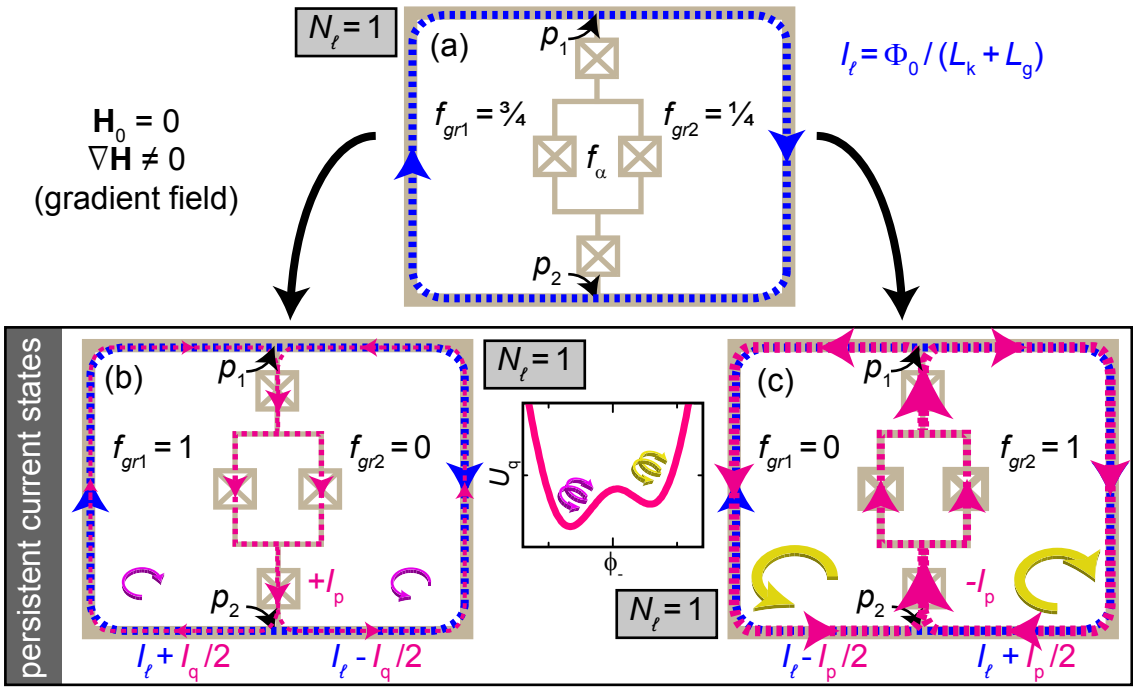

Figure 2.11: (a) - (c) Sketch of the current flow for a tunable-gap gradiometric flux qubit using a frustration difference $\delta f_{\rm gr} = f_{\rm gr1} - f_{\rm gr2} = 1/2$ as discussed in text.

Josephson junctions in the center line. This phase difference of π together with the phase difference of π resulting from the frustration $f_{\rm gr1} = f_{\rm gr2} = 1/2$ in the two gradiometer loops guarantees fluxoid quantization in both gradiometer loops. In the following, we characterize the gradiometer configuration by the state vector $|i, j\rangle \equiv |f_{\rm gr1}, f_{\rm gr2}\rangle$, i.e., $|1/2, 1/2\rangle$ for the situation discussed above and shown in Fig. 2.10 (a). When compensating for the π phase shift due to the half-integer flux quanta, the two configurations with lowest energies are depicted in Fig. 2.10 (b) and Fig. 2.10 (c). Due to the Josephson potential on the center line defined in Eq. (2.1.18), the enforced current along this line can be identified with the persistent current $I_{\rm p}$ of a regular flux qubit. This current creates an additional π phase shift corresponding to the frustration $f_{{\rm gr}j} = +1/2$ when flowing clockwise and $f_{{\rm gr}j} = -1/2$ when flowing counterclockwise ($j = 1, 2$). The resulting configurations $|1, 0\rangle$ in Fig. 2.10 (b) and $|0, 1\rangle$ in Fig. 2.10 (c) are the analog to the classical persistent current states $\pm I_{\rm p}$ in the untilted double-well potential of the flux qubit. Hence, at $\nabla\mathbf{H} = 0$ they form equal superposition states and the expectation value $I_{\rm q} = I_{\rm p}\langle\hat{\sigma}_{\rm z}\rangle$ vanishes. Because the wave function of the lower energy state in the untilted double-well potential is symmetric [95], we define the ground and the excited state

$$|{\rm g_{gq}}\rangle = \frac{|1, 0\rangle + |0, 1\rangle}{\sqrt{2}} \quad \text{and} \quad |{\rm e_{gq}}\rangle = \frac{|1, 0\rangle - |0, 1\rangle}{\sqrt{2}},$$

respectively. Just as for a regular flux qubit, these states are energy separated by the tunneling rate Δ.

– *Loop excitations* – The two situations discussed above are not the only current configurations that are compatible with fluxoid quantization in all loops. Additionally, there can be loop excitations as depicted in Fig. 2.10 (d) and Fig. 2.10 (e), which are, however,

very unlikely as discussed below. The first two excitations are characterized as $|0,0\rangle$ and $|1,1\rangle$. These states could occur either if the energy barrier [84–86] $E_{\Delta N} \approx \sqrt{6} I_{\ell,\mathrm{c}} \Phi_0 / 2\pi$ is overcome or if the inductive energy is very small and on the order of the qubit energy, i.e., $E_\ell \simeq \hbar\omega_\mathrm{q}$. Assuming a realistic qubit transition frequency $\omega_\mathrm{q} = 5\,\mathrm{GHz}$, this implies a very large loop inductance of approximately 1 µH as used for example in phase-slip flux qubits [85]. The requirement $E_\ell \simeq \hbar\omega_\mathrm{q}$ could also be satisfied for very large qubit energies. These transition frequencies, however, would exceed the energy gap Δ_0 by far and are therefore not feasible. Hence, for circuits presented in this work, loop excitations are not relevant.

– *Finite field gradient* – For a gradiometric qubit design, the control parameter for the magnetic energy bias $\hbar\varepsilon$ is the difference in frustration $\delta f_\mathrm{gr} \equiv f_\mathrm{gr1} - f_\mathrm{gr2}$ which can be created by a field gradient $\nabla\mathbf{H}$. A field gradient creates the situation $|1/2+\delta f_\mathrm{gr}/2,\ 1/2-\delta f_\mathrm{gr}/2\rangle$ shown in Fig. 2.11 (a) for the specific case $\delta f_\mathrm{gr} = 1/2$. This configuration creates a finite current flow $I_\mathrm{q} = I_\mathrm{p} \delta f_\mathrm{gr}$ over the Josephson junctions to ensure the states $|1,0\rangle$ [Fig. 2.11 (b)] and $|0,1\rangle$ [Fig. 2.11 (c)]. These states are separated by the additional magnetic energy $\hbar\varepsilon = 2 I_\mathrm{p} \delta f_\mathrm{gr} \Phi_0$. Even though the two qubit eigenstates $|\mathrm{g_{gq}}\rangle$ and $|\mathrm{e_{gq}}\rangle$ are still superposition states of $|1,0\rangle$ and $|0,1\rangle$, for $\varepsilon \gg \Delta$ they can be approximated by $|\mathrm{g_{gq}}\rangle \approx |1,0\rangle$ and $|\mathrm{e_{gq}}\rangle \approx |0,1\rangle$.

Screening and flux trapping So far, we have discussed the gradio qubit without applying a homogeneous field $\mathbf{H}_0$ and without considering screening effects of the superconducting loops. For an ideal gradiometer, $\mathbf{H}_0$ couples equally into both gradiometer loops as depicted in Fig. 2.9 (a). Hence, this field does not affect the frustration difference δf_gr. It changes, however, the field penetrating the SQUID loop used to tune the tunneling energy $\hbar\Delta$ and therefore couples to the $\hat{\sigma}_\mathrm{x}$ degree of freedom. Due to fluxoid quantization, the external field is screened proportional to the ratio of geometric to kinetic inductance $\beta = L_\mathrm{g}/L_\mathrm{k}$ of the trap loop [83, 101]. The factor β represents the ability of the loop to preserve its magnetic frustration f_tr. In other words, for $\beta \gg 1$, the loop always keeps its frustration even if the externally applied field is changed. On the other hand, for $\beta \ll 1$, the frustration directly follows the external field. A similar argument holds for a field $\mathbf{H}_\ell = N_\ell \Phi_0 / (\mu_0 A_\ell)$ that is generated by a finite amount of flux quanta N_ℓ trapped in the loop during the cooldown. For simplicity, we assume a homogeneous field generated inside the trap loop with area A_ℓ. The total field strength inside the loop therefore reads as

$$\mathbf{H}_0 = \frac{\mathbf{H}_\mathrm{ext}}{1+\beta} + \frac{\beta}{1+\beta} \frac{N_\ell \Phi_0}{\mu_0 A_\ell}\,, \tag{2.1.22}$$

where $\mathbf{H}_\mathrm{ext}$ is the field strength generated by the control circuitry. From Eq. (2.1.22) it follows that we can adjust $\mathbf{H}_0$ either continuously with an external magnetic field or stepwise via the number N_ℓ of trapped fluxoids. Please note that fluxoid quantization imposes a phase change of $2\pi N_\ell$ around the trap loop, resulting in a phase difference $\phi_\mathrm{q} = \pi N_\ell$ between points p_1 and p_2 by symmetry reasons. This circumstance shows that an odd number of trapped flux results in an equivalent half-integer flux bias of the gradio qubit. For an ideal qubit, these flux quanta result in a phase difference $\theta = 2\pi N_\ell$ between the two points p_1 and p_2 on the trap loop. Hence, the phase difference ϕ_q between these points is always πN_ℓ if an odd amount of fluxoid quanta is trapped.
The screening effect of the trap loop also screens the qubit against noise. Furthermore, a gradiometric qubit has the advantage of a reduced sensitivity to external flux noise [99, 102]. The reason is that flux noise emitted from a faraway object couples equally into the two loops and therefore introduce no fluctuations of the ε bias. Due to the quadrupolar structure

described below, the qubit is less sensitive to local fields that couple asymmetrically into the two loops because the quadrupolar coupling shows a $1/r^3$ dependence. This is in contrast to the standard flux qubit design, which interacts as a dipole that couples with $1/r^2$ to flux noise [103].

Multipole expansion for the gradio qubit The idealized, perfectly symmetric realization of a gradio qubit is hard to implement in reality due to imperfections in the fabrication process [83]. One convenient method to account for imperfections is a multipole expansion of the magnetic moment of the qubit as derived in detail in Sec. 2.1.7. The geometry of the gradio qubit results in a magnetic dipole moment $\boldsymbol{\mu}$ and in a quadrupole moment $\mathbf{Q}$. For an ideal gradio qubit, the dipole coupling reads $\boldsymbol{\mu}\cdot\mathbf{H}_0\hat{\sigma}_\mathrm{x}$ and the quadrupole coupling $\mathbf{Q}\cdot\nabla\mathbf{H}\hat{\sigma}_\mathrm{z}$. Imperfections in the geometry and in the Josephson junctions can be modeled by cross-coupling terms which have the form $\boldsymbol{\mu}_\mathrm{im}\cdot\mathbf{H}_0\hat{\sigma}_\mathrm{z}$ and $\mathbf{Q}_\mathrm{im}\cdot\nabla\mathbf{H}\hat{\sigma}_\mathrm{x}$.

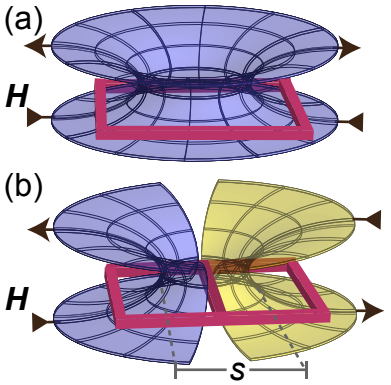

Figure 2.12: **(a)** Sketch of a dipole magnetic field $\mathbf{H}$ generated by a closed loop as for example the SQUID-loop. **(b)** Sketch of a quadrupolar magnetic field generated by an eight-shaped loop.

For our discussion, we assume that the qubit is placed in the plane perpendicular to the $\mathbf{e}_\mathrm{z}$-direction and that the origin of the coordinate system is in the center of the SQUID loop. Furthermore, we assume that the total current I flowing in a superconductor is uniformly distributed. That way, the general expression for the dipole moment $\boldsymbol{\mu} = I\int_A \mathrm{d}A'$ calculates to $\boldsymbol{\mu} = I\,A\,\mathbf{e}_\mathrm{z}$. The gradio qubit has two substructures that can generate such a dipole moment. First, the SQUID loop with area A_sq has a dipole moment $\boldsymbol{\mu}_\mathrm{sq} = I_\mathrm{sq}A_\mathrm{sq}\mathbf{e}_\mathrm{z}$ for a finite current I_sq circulating around the SQUID loop. This dipole moment generates a dipolar magnetic field as depicted in Fig. 2.12 (a) and couples to the $\hat{\sigma}_\mathrm{x}$ degree of freedom. Second, the trap loop has a large dipole moment $\boldsymbol{\mu}_\ell$. In the ideal case, this dipole moment does not couple to the qubit phase φ_q and is thus irrelevant for the qubit. However, a possible imbalance between the gradiometer loops introduces a dipole moment $\boldsymbol{\mu}_\mathrm{im} = I_\ell\delta A_\varepsilon\mathbf{e}_\mathrm{z}$. Here, δA_ε is the effective area difference between the gradiometer loops accounting for all possible imbalance sources such as difference in inductances, difference in the SQUID junctions, etc. In contrast to $\boldsymbol{\mu}_\mathrm{sq}$, this dipole moment couples to the $\hat{\sigma}_\mathrm{z}$ degree of freedom. In other words, for a finite $\boldsymbol{\mu}_\mathrm{im}$, we can increase the magnetic energy bias $\hbar\varepsilon$ also with homogeneous magnetics fields which is expressed in a finite quality of the gradiometer. With suitable control lines, however, we can compensate for this ε bias and operate the qubit again at its degeneracy point.

Similar to the dipole moment, the gradio qubit comprises a finite quadrupole moment $\mathbf{Q}$, which generates a quadrupolar magnetic field as depicted in Fig. 2.12 (b). In particular for the gradiometric design, we find the relevant component $\mathbf{Q}_\mathrm{yz} = 4/3sI_\mathrm{p}A_\ell$ [see Sec. 2.1.7 for details]. This quadrupole moment component couples to the $\hat{\sigma}_\mathrm{z}$ degree of freedom. Imperfections $\mathbf{Q}_\mathrm{im}$ in the quadrupole moment that couple to $\hat{\sigma}_\mathrm{x}$ are generated if a finite qubit current I_q changes the frustration of the SQUID. This could be due to differences in the mutual inductance between the gradiometer loops and the SQUID or due to differences in the SQUID junctions. The result of such an imperfection would be an asymmetric qubit hyperbola, because the qubit gap changes with δf_gr. Considering all four magnetic

moments, we obtain the total gradio qubit Hamiltonian

$$\mathcal{H}_{\mathrm{tot}}/\mu_0 = \underbrace{([\boldsymbol{\mu}_{\mathrm{sq}}\cdot\mathbf{H}_0]+\mu_0\Delta)\hat{\sigma}_{\mathrm{x}}}_{1/2\hbar\Delta\hat{\sigma}_{\mathrm{x}}} + \underbrace{[\mathbf{Q}_{\mathrm{yz}}\cdot\nabla\mathbf{H}]\hat{\sigma}_{\mathrm{z}}}_{+\ 1/2\hbar\varepsilon\hat{\sigma}_{\mathrm{z}}} + [\boldsymbol{\mu}_{\mathrm{im}}\cdot\mathbf{H}_0]\hat{\sigma}_{\mathrm{z}} + [\mathbf{Q}_{\mathrm{im}}\cdot\nabla\mathbf{H}]\hat{\sigma}_{\mathrm{x}}\,, \quad (2.1.23)$$
$$\underbrace{\qquad\qquad\qquad\qquad\qquad\qquad}_{\mathcal{H}_{\mathrm{q}}}$$

where the flux qubit Hamiltonian $\mathcal{H}_{\mathrm{q}}$ is defined in Eq. (2.1.20). Please note that we have added the zero-field splitting Δ of the qubit and have linearized the dependence $\Delta(\alpha)$ in Eq. (2.1.19) to $\boldsymbol{\mu}_{\mathrm{sq}}\cdot\mathbf{H}_0$ and $\mathbf{Q}_{\mathrm{im}}\cdot\nabla\mathbf{H}$, respectively.

2.1.7 Multipole expansion for superconducting circuits

In this section, we show how the multipole expansion for electromagnetic fields [104], typically utilized in light-matter interaction, can be mapped to superconducting circuits. For convenience, we first show the direct analogy between multiple point charges and transmon qubits. We then adapt this picture to flux qubits, where the magnetic moment of current-carrying loops takes the role of electrical charges and external magnetic fields correspond to electric fields in electrically induced state transitions of atoms. For these transitions, the interaction Hamiltonian between the atom and an electric field $\mathbf{E}_{\mathrm{d}}(t)=\mathbf{E}e^{\imath\omega_{\mathrm{d}}t}$ can be expanded to [105]

$$\begin{aligned}\mathcal{H}_{\mathrm{int}} =& \mathbf{p}\cdot\mathbf{E}(t) + [\mathbf{Q}\nabla]\cdot\mathbf{E}(t) + \mathcal{O}(\nabla^2)\\ =& p_xE_x + p_yE_y + p_zE_z +\\ & Q_{xx}\partial_xE_x + Q_{xy}\partial_yE_x + Q_{xz}\partial_zE_x +\\ & Q_{yx}\partial_xE_y + Q_{yy}\partial_yE_y + Q_{yz}\partial_zE_y +\\ & Q_{zx}\partial_xE_z + Q_{zy}\partial_yE_z + Q_{zz}\partial_zE_z + \mathcal{O}(\nabla^2)\,. \end{aligned} \quad (2.1.24)$$

Here, $\mathbf{p}=\int_{\mathcal{V}}\mathrm{d}^3r\cdot\rho(\mathbf{r})\mathbf{r}$ is the dipole moment of the electric charge distribution $\rho(\mathbf{r})$ of the atom and the rank-two tensor $\mathbf{Q}$ is the atoms electric quadrupole moment with components $Q_{ij}=\int_{\mathcal{V}}\mathrm{d}^3r\cdot\rho(\mathbf{r})[3r_ir_j-|\mathbf{r}|^2\delta_{ij}]$. In general, $\mathbf{Q}$ is symmetric ($Q_{ij}=Q_{ji}$) and traceless ($Q_{xx}+Q_{yy}+Q_{zz}=0$). Furthermore, in Eq. (2.1.24) $\partial_iE_j\equiv\partial E_j/\partial_i$ is the spatial derivative of the electric field component E_j. To simplify the situation, it is often useful to replace the charge distribution $\rho(\mathbf{r})$ by point-like charges at distinct positions $\mathbf{r}_k$. For k discrete charges q_k, one obtains $\mathbf{p}=\sum_k q_k\mathbf{r}_k$ and $Q_{ij}=\sum_k q_k[3r_{ik}r_{jk}-|\mathbf{r}_k|^2\delta_{ij}]$.
Using the discrete charge model, we can calculate the dipole and quadrupole moment for the two simple cases shown in Fig. 2.13 (a) and Fig. 2.13 (b), which we subsequently translate to superconducting qubits. For two oppositely charged particles, separated by a distance d in z-direction, we obtain a finite dipole moment $\mathbf{p}=(0,0,qd)$ but a vanishing quadrupole moment $Q_{ij}=0\,\forall\,i,j\in\{x,y,z\}$ [see Fig. 2.13 (a)]. For the situation of four alternating charged particles shown in Fig. 2.13 (b), the situation is opposite to two particles. In this quadrupole configuration the dipole moment $\mathbf{p}=(0,0,0)$ vanishes, but there is a finite component $Q_{yz}=3qd^2$ of the quadrupole moment. Hence, the interaction Hamiltonian for the two situations in Fig. 2.13 (a) and Fig. 2.13 (b) reads $\mathcal{H}_{\mathrm{int}}^{\mathbf{p}}=qdE_z$ and $\mathcal{H}_{\mathrm{int}}^{\mathbf{Q}}=6qd^2\partial_yE_z$, respectively.

Multipolar transmon qubits We now apply the concept of point-like charges to superconducting qubits, where we model the distributed nature of the circuits by effective

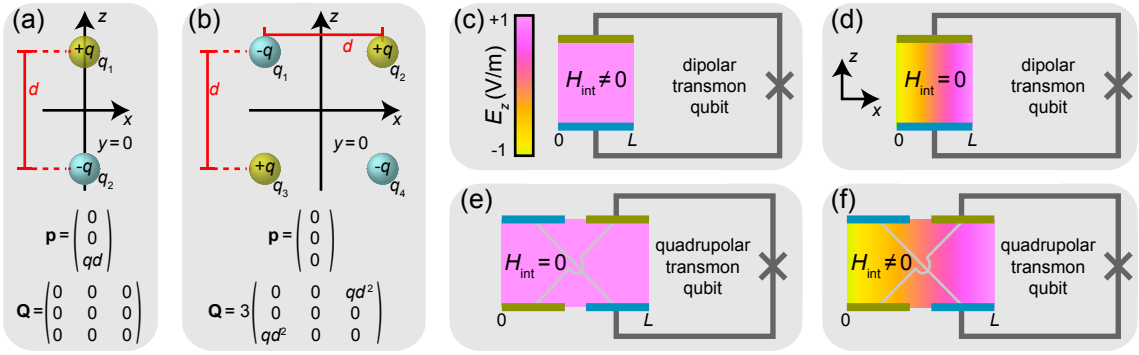

Figure 2.13: (a) Two point-like charges separated by a distance d create a finite electrical dipole moment $\mathbf{p}$ but zero quadrupole moment $\mathbf{Q}$. (b) Four alternating charges in a squared configuration create no dipole moment but have a finite quadrupole moment. (c) The two capacitor plates shunting the Josephson junction (cross) of a transmon qubit create an effective dipole moment $\mathbf{p}^{\text{eff}}$. This dipole moment couples to the z-component of the external drive field E_z (color code). (d) As in panel (c) but for a gradient field which has a node at half the capacitor length, $E_z(L/2) = 0$. (e) Gradiometric version of a transmon qubit exposed to a constant drive field. (f) As in panel (e) but for a gradient field.

dipole and quadrupole moments. As shown in Fig. 2.13 (c) and Fig. 2.13 (d), the two capacitors of a transmon qubit, shunting a Josephson junction, correspond to the situation of two oppositely charged particles in Fig. 2.13 (a). Hence, the transmon qubit has an effective dipole moment $\mathbf{p}^{\text{eff}} = (0,0,p_z^{\text{eff}})$. In this case, the z-component of the external drive is responsible for the finite interaction $\mathcal{H}_{\text{int}} = p_z^{\text{eff}} E_z^{\text{eff}} \hat{\sigma}_{\text{x}}$ when the qubit is expressed in the $\hat{\sigma}_{\text{z}}$-basis. Here, we use the effective field component $E_z^{\text{eff}} = L^{-1} \int_{-L/2}^{L/2} E_z(x) \mathrm{d}x$, where L is the capacitor length in x-direction. One immediately sees, that $E_z^{\text{eff}} = 0$ if the transmon qubit is exposed to a field gradient $\partial_y E_z = \text{const}$ with $E_z(L/2) = 0$ [see Fig. 2.13 (d)]. In this case, positive and negative E_z contributions cancel each other leading to a vanishing interaction Hamiltonian $\mathcal{H}_{\text{int}} = 0$. Similar to the situation depicted in Fig. 2.13 (b), it is possible to design transmon qubits with an effective quadrupole moment $\mathbf{Q}^{\text{eff}}$ by splitting the two capacitors in an alternating geometry as shown in Fig. 2.13 (e) and Fig. 2.13 (f). In this case, we obtain a quadrupolar interaction for effective field gradients $(\partial_y E_z)^{\text{eff}} = L^{-1} \int_0^L \partial_y E_z(x) \mathrm{d}x$ and the interaction strength vanishes for constant fields $E_z^{\text{eff}} = \text{const}$. The quadrupolar interaction is described by $\mathcal{H}_{\text{int}}^{\mathbf{Q}} = Q_{yz}^{\text{eff}} (\partial_y E_z)^{\text{eff}} \hat{\sigma}_{\text{x}}$.

Multipolar flux qubits The analogy between electrically induced state transitions in atoms described by Eq. (2.1.24) and in transmon qubits works well because both couple to the electric field. This is different for flux qubits, coupling to the external magnetic field $\mathbf{B}_{\text{d}}(t) = \mathbf{B} e^{i\omega_{\text{d}} t}$. Because also flux qubits act as artificial atoms, state transitions in these devices follow electric selection rules [42, 106]. Therefore, the interaction described by Eq. (2.1.24) is still valid when replacing $\mathbf{p} \leftrightarrow \boldsymbol{\mu}$, $\mathbf{Q} \leftrightarrow \mathbf{M}$, and $\mathbf{E} \leftrightarrow \mathbf{B}$. Here, $\boldsymbol{\mu}$ is the magnetic dipole moment and $\mathbf{M}$ is the magnetic quadrupole moment of the qubit. For a quasi-planar loop with area A carrying a circular current I, the magnetic dipole moment [104] $\boldsymbol{\mu} = (1/2) \int_{\mathcal{V}} \mathrm{d}^3 r\, \mathbf{r} \times \mathbf{j}$ can be simplified to $\boldsymbol{\mu} = (I/2) \int_{\partial A} \mathbf{r} \times \mathrm{d}\mathbf{r} = (0,0,IA)$ [see Fig. 2.14 (a)]. For the components of the magnetic quadrupole moment we obtain $M_{ij} = (2I/3) \sum_k \mu_{k,i} r_{k,j}$, where $\boldsymbol{\mu}_k$ is the k^{th} dipole positioned at $\mathbf{r}_k$. For a single loop ($k = 1$) and $\mathbf{r}_1 = (0,0,0)$, all components of $\mathbf{M}$ are zero. For the quadrupolar case shown in Fig. 2.14 (b), the dipole moment is zero and $\mathbf{M}$ has the finite component $M_{yz} = 4IAd/3$.

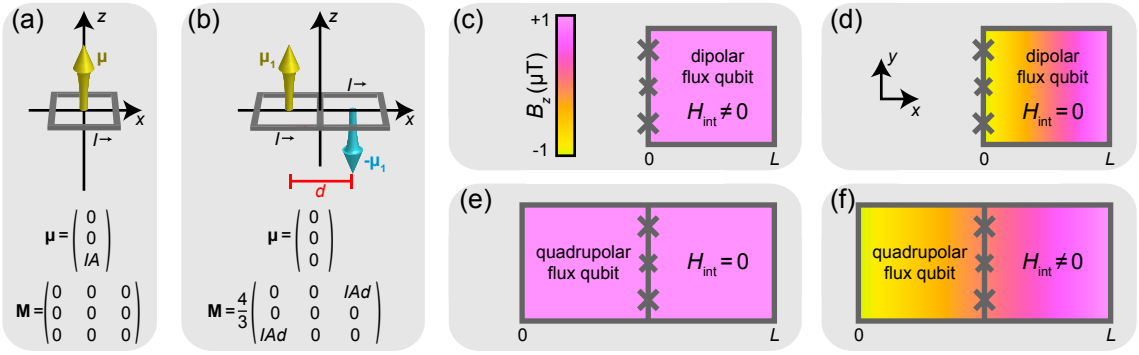

Figure 2.14: (a) A closed current-carrying loop with area A creates a finite magnetic dipole moment $\boldsymbol{\mu}$ but zero quadrupole moment $\mathbf{M}$. (b) Two loops carrying clockwise and counter clockwise currents $\pm I$ create no dipole moment but have a finite quadrupole moment. (c) Integrating three Josephson junctions into a superconducting loop forms a flux qubit with dipole moment $\boldsymbol{\mu}^{\mathrm{q}}$. This dipole moment couples to the z-component of the external magnetic drive field B_z (color code). (d) As in panel (c) but for a gradient field which has a node at half the qubit length, $B_z(L/2) = 0$. (e) Gradiometric version of a flux qubit exposed to a constant drive field. (f) As in panel (e) but for a gradient field.

Integrating three Josephson junctions with suitable parameters into a superconducting loop forms a flux qubit with persistent current I_{p} and area A_{q}. In the bare qubit basis, the dipolar interaction Hamiltonian between qubit and an oscillating magnetic field reads $\mathcal{H}_{\mathrm{int}}^{\mu} = B_z^{\mathrm{eff}} \mu_z^{\mathrm{q}} \hat{\sigma}_z$. Here, $\mu_z^{\mathrm{q}} = I_{\mathrm{p}} A_{\mathrm{q}}$ is the relevant dipole component of the qubit and $B_z^{\mathrm{eff}} = A_{\mathrm{q}}^{-1} \int_{A_{\mathrm{q}}} B_z(\mathbf{r}) \mathrm{d}^2 r$ is the effective magnetic field penetrating the qubit loop, which is finite for homogeneous magnetic fields [see Fig. 2.14 (c)]. When exposing the qubit to a constant field gradient in x-direction with $B_z(L/2) = 0$, the interaction strength vanishes as depicted in Fig. 2.14 (d). For quadrupolar coupling, the interaction Hamiltonian reads $\mathcal{H}_{\mathrm{int}}^{\mathbf{M}} = M_{yz}^{\mathrm{eff}} (\partial_y B_z)^{\mathrm{eff}} \hat{\sigma}_z$, where $(\partial_y B_z)^{\mathrm{eff}} = A_{\mathrm{q}}^{-1} \int_{A_{\mathrm{q}}} \partial_y B_z(\mathbf{r}) \mathrm{d}^2 r$ is the effective magnetic field gradient penetrating the qubit loop. Here, we restrict the situation two currents that flow in opposite direction in the two gradiometer loops. For structures with large loop inductance [107], also two in-phase currents are possible, generating a finite dipole moment for the structure shown in Fig. 2.14 (e).

2.2 Electromagnetic fields on coplanar waveguide transmission lines

Electromagnetic fields propagating on coplanar waveguide (CPW) transmission line structures are important to control and readout quantum states in superconducting circuits. In Sec. 2.2.1, we discuss basic concepts of transmission lines serving as one major building block in our experiments. Introducing boundary conditions into these lines can be used to generate resonant structures described in Sec. 2.2.2. Finally, we describe the most relevant states of light for this thesis in Sec. 2.2.3 and their correlation functions in Sec. 2.2.4.

2.2.1 Transmission line theory

Electromagnetic waves with gigahertz frequencies propagate freely in all directions of open space [108]. For technical applications, however, it is important to guide information encoded in these waves from a well-defined source to a particular destination. This task can

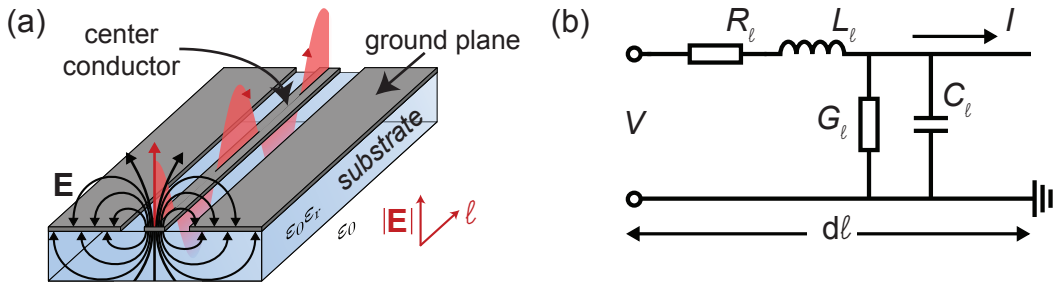

Figure 2.15: **(a)** Sketch of a piece of a CPW transmission line, which carries an electromagnetic wave that generates the electric field $\mathbf{E}$. **(b)** Equivalent lumped-element circuit for a piece of transmission line with infinitesimal length dℓ.

be achieved using waveguides such as two-dimensional CPWs [109], which can be thought of as a cut through a coaxial cable. In this thesis, we use thin Nb or Al films deposited on a silicon substrate for this purpose. A schematic of such a structure is shown in Fig. 2.15 (a) and the fabrication process is explained in detail in Sec. 3.2.

Wave propagation The wavelength of microwaves is on the same order as the lateral dimensions of the CPW structures which they live on. Therefore, we cannot apply the concept of lumped-element circuits where one assumes that the wavelength is substantially larger than the circuit itself. Instead, we describe voltage and current as propagating waves which travel over a certain length ℓ [110]. Nevertheless, we can model each individual point of a transmission line as a lumped-element circuit of infinitesimal length dℓ. In Fig. 2.15 (b), we show the equivalent lumped-element circuit for a transmission line structure with series inductance L_ℓ, series resistance R_ℓ, and shunt capacitance and conductance C_ℓ and G_ℓ, each per unit length. From Kirchhoff's laws [111] in the limit $\mathrm{d}\ell \to 0$, one can derive the well-known telegrapher's equations [110]. Solving these equations for a sinusoidal steady-state condition, we obtain wave equations for the voltage $V(\ell,t) = V(\ell)\, e^{\imath\omega t}$ and the current $I(\ell,t) = I(\ell)\, e^{\imath(\omega t + \pi/2)}$ with $\omega/2\pi$ being the wave frequency. In these expressions, we have defined the time-independent amplitudes

$$V(\ell) = V_0^+ e^{-\gamma\ell} + V_0^- e^{\gamma\ell}, \tag{2.2.1}$$

$$I(\ell) = I_0^+ e^{-\gamma\ell} + I_0^- e^{\gamma\ell}, \tag{2.2.2}$$

where $e^{\pm\gamma\ell}$ describes the spatial wave propagation in both directions of the line, while $V_0^\pm$ and $I_0^\pm$ define the amplitude at $\ell = 0$. The complex propagation constant

$$\gamma = \gamma_\Re + \imath\gamma_\Im = \sqrt{(R_\ell + \imath\omega L_\ell)(G_\ell + \imath\omega C_\ell)} \tag{2.2.3}$$

is in general frequency-dependent and defines the amplitude decrease after the wave has travelled a certain distance. The real part $\gamma_\Re$ characterizes the attenuation of the signal, whereas the imaginary part $\gamma_\Im$ describes the propagation properties of the line. To characterize these properties, we compare the amplitude at a certain point 1 to the amplitude at a point 2. Such a scenario is modeled as a two-port network, that we describe by a scattering matrix [110]

$$\begin{pmatrix} V_1^- \\ V_2^- \end{pmatrix} = \begin{pmatrix} S_{11} & S_{12} \\ S_{21} & S_{22} \end{pmatrix} \begin{pmatrix} V_1^+ \\ V_2^+ \end{pmatrix}, \tag{2.2.4}$$

where each element S_{ij} describes a scattering parameter of the network. For most of the measurements presented in this thesis, we analyze the transmission magnitude $\mathcal{T} \equiv |S_{21}|^2$ of a network structure.

Line impedance When designing CPW structures, one has a large freedom to choose different dimensions of and distances between adjacent structures. Changing the relative size of the waveguide structures has an impact on the relative dielectric constant ε_r and on the line impedance [109]. The line impedance is a typical figure of merit for a transmission line defined as [112]

$$Z_0 = \frac{V_0^+}{I_0^+} = \sqrt{\frac{R_\ell + \imath\omega L_\ell}{G_\ell + \imath\omega C_\ell}}\,. \tag{2.2.5}$$

For superconducting CPW transmission lines, the surface resistance (cf. Sec. 2.1.2) of the thin films is the main contribution to R_ℓ, which is negligible for frequencies below 10 GHz. Furthermore, for low temperatures and insulating substrates, also G_ℓ can be neglected. Hence, we obtain $\gamma_\Re \simeq 0$ and Eq. (2.2.5) simplifies to $Z_0 = \sqrt{L_\ell/C_\ell}$. Since most of the commercially available microwave equipment has a 50 Ω impedance, we also design our transmission line structures with a 50 Ω impedance to avoid reflections. This is achieved by using a 12 µm wide center conductor and a gap between center conductor and ground plane of 20 µm (for more details see Sec. 3.2).

Quantization of the electromagnetic field For very low excitation energies and very low temperatures, quantization of the electromagnetic fields on a transmission line becomes relevant. Starting from classical electrodynamics, we can use Maxwell's equations [113] to derive the quantization of electromagnetic field [7, 114]. We start from a vector potential $\mathbf{A}(\mathbf{x},t)$, satisfying the wave equation $c^2\nabla^2\mathbf{A} = \partial^2\mathbf{A}/\partial t^2$ in a given volume $\mathcal{V}$, where c is the speed of light. We can describe the vector potential as a sum of vector mode functions $\mathbf{u}_k(\mathbf{x})$ corresponding to a certain frequency ω_k for the k^{th} mode. Then, the electric field

$$\mathbf{E}(\mathbf{x},t) = -\frac{\partial \mathbf{A}}{\partial t} = \imath \sum_k \left(\frac{\hbar\omega_k}{2\varepsilon_0}\right)^{1/2} \left[a_k \mathbf{u}_k(\mathbf{x}) e^{-\imath\omega_k t} - a_k^\dagger \mathbf{u}_k^\star(\mathbf{x}) e^{\imath\omega_k t}\right] \tag{2.2.6}$$

is defined by the sum of all vector mode functions weighted by certain amplitudes a_k and $a_k^\dagger$. Using the relation $\mathbf{B} = \nabla \times \mathbf{A}$, we can find a similar relation for the magnetic field $\mathbf{B}(\mathbf{x},t)$. Field quantization can be accomplished by defining $a_k^\dagger$ and a_k as mutually adjoint operators $\hat{a}_k^\dagger$ and $\hat{a}_k$. These bosonic creation and annihilation operators follow the boson commutation relations $[\hat{a}_k,\hat{a}_{k'}] = [\hat{a}_k^\dagger,\hat{a}_{k'}^\dagger] = 0$ and $[\hat{a}_k,\hat{a}_{k'}^\dagger] = \delta_{kk'}$ [7]. The Hamiltonian of the system

$$\mathcal{H}_\mathrm{em} = \frac{1}{2}\int_\mathcal{V} \mathrm{d}^3x \left(\varepsilon_0 \mathbf{E}^2 + \frac{\mathbf{B}^2}{\mu_0}\right) = \sum_k \hbar\omega_k \left(\hat{a}_k^\dagger \hat{a}_k + \frac{1}{2}\right)\,. \tag{2.2.7}$$

comprises the sum of electric and magnetic energy. Here, the average occupation number of each mode is $n_k = \langle \hat{a}_k^\dagger \hat{a}_k \rangle$. The term $\hbar\omega_k/2$ in Eq. (2.2.7) is the omnipresent energy offset due to the vacuum fluctuations. Although we restrict ourselves to a finite volume in this derivation, field quantization also results from an open space approach [114].
A special case of field quantization occurs when only a single mode is allowed on the transmission line, i.e., in the case of a single mode resonator. Even though on a transmission

line there are always higher harmonics, we can restrict ourselves to a single mode if all higher harmonics are sufficiently far frequency shifted. In this case, the single mode Hamiltonian reads

$$\mathcal{H}_\mathrm{r} = \hbar\omega_\mathrm{r}\left(\hat{a}^\dagger\hat{a} + \frac{1}{2}\right). \tag{2.2.8}$$

This Hamiltonian plays an important role in the game of (circuit) quantum electrodynamics studied in detail in Sec. 2.3.

2.2.2 Superconducting transmission line resonators

Superconducting microwave transmission line resonators are widely used in circuit quantum electrodynamics (QED) to study light-matter interaction [26, 115], as quantum bus [116, 117] or photon storage devices [118]. In this section, we introduce the main concepts of resonant transmission line structures. In contrast to waves that propagate freely on transmission lines, in the following we force the electromagnetic field to standing waves with discrete frequencies by introducing boundary conditions. This frequency selection has several advantages for the application of microwave circuits. It allows for example to use resonators as strong filters [119], sensitive readout devices [24], or efficient memories [118]. The most convenient method to introduce boundary conditions into a transmission line structure is to generate either a short to ground or an open-circuit, i.e., a cut in the center conductor. While a short to ground forces the voltage at this position to zero, an open-circuit structure results in a vanishing current.

Half- and quarter-wavelength resonators We realize half-wavelength resonators by integrating two open-circuits into the transmission line, separated by a distance ℓ_r [see Fig. 2.16 (a)]. This setup causes the electromagnetic field to interfere constructively if its wavelength is equal to $\lambda_n = 2\,\ell_\mathrm{r}/k$, $k \in \mathbb{N}$. For all other wavelengths, the field interferes destructively, which strongly suppresses these modes inside the resonator. The frequency

$$\omega_{\mathrm{r},k} = \frac{1}{\sqrt{L_\ell C_\ell}}\frac{k}{2\ell_\mathrm{r}} = \frac{c}{\sqrt{\varepsilon_\mathrm{eff}}}\frac{k}{2\ell_\mathrm{r}} \tag{2.2.9}$$

of the standing waves depends on the characteristic transmission line parameters $\varepsilon_\mathrm{eff}, L_\ell$, and C_ℓ. If we apply a sinusoidal readout signal across the resonator, we have the textbook problem of a driven damped harmonic oscillator [120]. The transmission through a half-wavelength resonator is characterized by magnitude and phase

$$\mathcal{T}(\omega) = L_0\frac{{}^1\!/_4\,\kappa_\mathrm{tot}^2}{\left(\omega-\omega_{\mathrm{r},k}\right)^2 + {}^1\!/_4\,\kappa_\mathrm{tot}^2}, \tag{2.2.10}$$

$$\phi(\omega) = \left[\tan^{-1}\left(\frac{\omega\kappa_\mathrm{tot}}{\omega^2-\omega_{\mathrm{r},k}^2}\right) \bmod \pi\right] - \frac{\pi}{2}, \tag{2.2.11}$$

Here, L_0 and κ_tot are the insertion loss and the bandwidth (full width at half maximum) of the resonator leading to the Lorentzian line shape displayed in Fig. 2.16 (b) and the phase respective shown in Fig. 2.16 (c). Along the distributed circuit, the electromagnetic field is enveloped by the spatial functions $u(x) \propto \cos(k\pi x/\ell_\mathrm{r})$ and $j(x) \propto \sin(k\pi x/\ell_\mathrm{r})$. This spatial envelope defines the capacitive and inductive coupling strength to other electrical circuits on the chip. We can use the position inside the resonator at which we place the additional circuit to control the ratio between inductive and capacitive coupling.

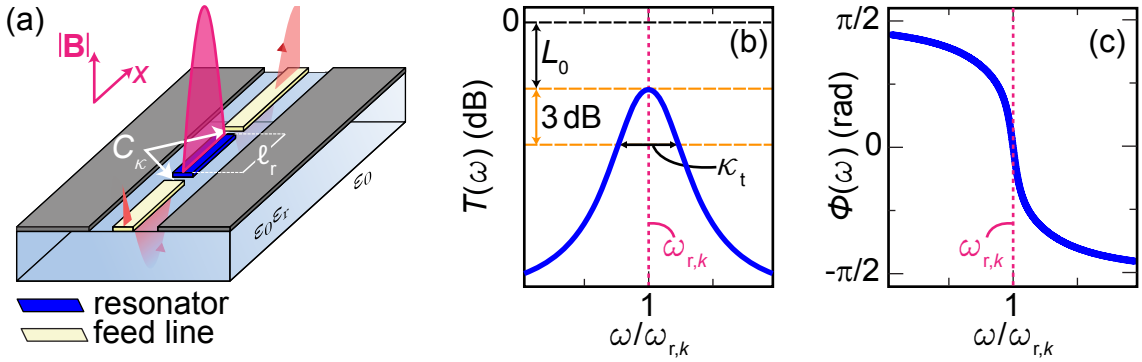

Figure 2.16: **(a)** Sketch of a half-wavelength resonator coupled to a CPW transmission line. The magnetic field $\mathbf{B}$ follows the spatial current distribution j. **(b)** Transmission magnitude of a half-wavelength resonator plotted versus readout frequency. **(c)** Phase response of a half-wavelength resonator plotted versus readout frequency.

In contrast to the half-wavelength resonator discussed above, for a quarter-wavelength resonator we replace one of the open-circuits by a short to ground. That way, we save one halve of the resonator allowing for smaller sample sizes. In addition, a quarter-wavelength resonator is typically read out in reflection, providing the complex reflection coefficient [121]

$$\Gamma = \frac{(\omega - \omega_{\mathrm{r},k})^2 + \imath\kappa_\mathrm{i}(\omega - \omega_{\mathrm{r},k}) + (\kappa_\mathrm{i}^2 - \kappa_\mathrm{x}^2)/4}{\omega - \omega_{\mathrm{r},k} + \imath(\kappa_\mathrm{i} - \kappa_\mathrm{x})/2} \,. \tag{2.2.12}$$

Here, κ_i and κ_x are the internal and external loss rates of the resonator as introduced in the following section.

Quality factor The resonance frequency of transmission line resonators can vary over a wide frequency range. To compare the performance of resonators with different frequencies, we can use their respective quality factor [110]

$$Q = 2\pi \frac{\text{average energy stored}}{\text{energy loss/cycle}} = \frac{\omega_\mathrm{r}}{\kappa_\mathrm{tot}} \,.$$

The resonator line width κ_tot comprises all dissipative loss channels of the device and the intended coupling to the external transmission lines. Consequently, the inverse loaded quality factor

$$\frac{1}{Q_\ell} = \frac{1}{Q_\mathrm{i}} + \frac{1}{Q_\mathrm{x}} = \frac{\kappa_\mathrm{i} + \kappa_\mathrm{x}}{\omega_\mathrm{r}} \tag{2.2.13}$$

is defined by the sum of the internal loss rate κ_i and external coupling rate κ_x. For simplicity, we model the transmission line resonator as a lumped element LCR circuit as shown in Fig. 2.17 (a). This lumped element model can be linked to the distributed element model of a transmission line via the definitions $L \equiv 2L_\ell \ell_\mathrm{r} (k\pi)^{-2}$ and $C \equiv 1/2\, C_\ell \ell_\mathrm{r}$ [112]. In the following, we show the independence of different loss mechanisms that lower the internal quality factor of a superconducting resonator. We assume low loss in the transmission lines such that the complex propagation constant defined in Sec. 2.2.1 can be approximated as [110]

$$\gamma \simeq \imath\omega\sqrt{L_\ell C_\ell}\left[1 - \frac{\imath}{2}\left(\frac{R_\ell}{\omega L_\ell} + \frac{G_\ell}{\omega C_\ell}\right)\right] \,. \tag{2.2.14}$$

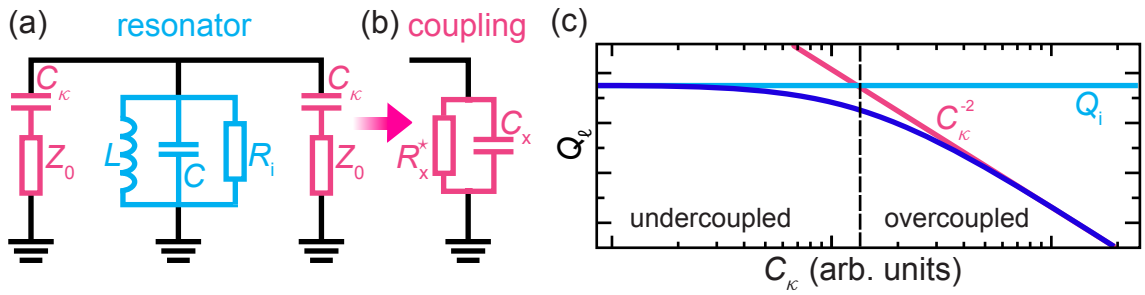

Figure 2.17: **(a)** Equivalent lumped-element LCR circuit diagram of a half-wavelength resonator coupled to two $Z_0 = 50\,\Omega$-matched feedlines with coupling capacitance C_κ. **(b)** Norton equivalent of the coupling capacitor that can be described as a parallel RC-circuit with coupling capacitance C_κ. **(c)** Loaded quality factor plotted versus coupling capacitance. In the undercoupled regime, the quality factor approaches the internal quality factor Q_i.

The internal resistance $R_\mathrm{i} = Z_0(\gamma_\Re \ell_\mathrm{r})^{-1}$ of the LCR-circuit model displayed in Fig. 2.17 (a) is defined by the real part $\gamma_\Re$ of the propagation constant and the internal quality factor reads [112] $Q_\mathrm{i} = \omega_{\mathrm{r},n} R_\mathrm{i} C = \pi[2\ell_\mathrm{r}\gamma_\Re]^{-1}$. The attenuation constant itself is a sum of different influences such as surface resistance [122, 123], loss from two-level-states [124, 125], quasiparticle generation in the superconducting material from stray infrared light [65] or thermal activation [126] (see Sec. 2.4.2 for details). Since all loss mechanisms add a finite resistance, we can write

$$\gamma_\Re = \sum_j \gamma_{\Re,j} \quad \Longleftrightarrow \quad \frac{1}{Q_\mathrm{i}} = \sum_j \frac{1}{Q_{\mathrm{i},j}}\,.$$

Due to the independence of loss mechanisms, we can investigate a single loss channel by selectively tuning a particular experimental parameter while leaving the remaining experimental environment untouched.

External coupling rate We couple the resonators to external feedlines for readout purposes. Even though the coupling mechanism is capacitive, we can model it with an effective parallel RC-circuit [112] shown in Fig. 2.17 (b). The Norton equivalent of each coupling capacitor yields an effective resistance and capacitance

$$R_\mathrm{x}^\star = \frac{1 + (\omega_{\mathrm{r},k} C_\kappa Z_0)^2}{(\omega_{\mathrm{r},k} C_\kappa)^2 Z_0}\,, \qquad C_\kappa^\star = \frac{C_\kappa}{1 + (\omega_{\mathrm{r},k} C_\kappa Z_0)^2}\,,$$

respectively, when assuming $R_\mathrm{i} = 0$. For typical CPW resonators $C \gg C_\kappa$ holds and the external quality factor is well approximated by [112]

$$Q_\mathrm{x} = \frac{\omega_{\mathrm{r},k} R_\mathrm{x}^\star C}{2} = \frac{\omega_{\mathrm{r},k} C}{2}\left[\frac{1 + (\omega_{\mathrm{r},k} C_\kappa Z_0)^2}{(\omega_{\mathrm{r},k} C_\kappa)^2 Z_0}\right]. \tag{2.2.15}$$

This equation shows that we can control the external quality factor by adjusting the coupling capacitance C_κ as depicted in Fig. 2.17 (c). For very large external quality factors, however, we cannot neglect internal loss rates anymore. In this regime, the internal quality factor limits the total quality of the resonator. Hence, we can distinguish two regions in the dependence of Q_ℓ on C_κ, which are the undercoupled regime ($Q_\mathrm{i} < Q_\mathrm{x}$) and the

overcoupled regime ($Q_\mathrm{i} > Q_\mathrm{x}$). The resonator's critical coupling point, $Q_\mathrm{i} = Q_\mathrm{x}$, separates the two regimes and we can approximate their limits as

$$Q_\ell \approx \begin{cases} Q_\mathrm{i} \simeq \text{const.} & Q_\mathrm{x} \gg Q_\mathrm{i} \quad \text{(undercoupled)} \\ Q_\mathrm{x} \propto C_\kappa^{-2} & Q_\mathrm{x} \ll Q_\mathrm{i} \quad \text{(overcoupled)}\,. \end{cases}$$

From these conditions, we directly recognize the importance of optimizing the internal quality factor when aiming for high quality resonators.

2.2.3 States of electromagnetic radiation

States of electromagnetic radiation such as thermal or coherent states can conveniently be described in a phase space representation of light [127]. In classical mechanics, we can characterize a physical system by a point in phase space, e.g., with its position $\mathbf{x}$ and momentum $\mathbf{p}$. That is, a single point in phase space defines the state of the system at a particular moment in time. On the contrary, in quantum mechanics the Heisenberg uncertainty [128, 129] $\Delta x \Delta p \geq 1/4$ introduces an omnipresent uncertainty between the two conjugate variables. This uncertainty smears out the single point in phase space prohibiting a simultaneous measurement of conjugate variables. Nevertheless, we can use the Wigner quasi-probability distribution [130] $W(\mathbf{x},\mathbf{p})$ to find the system in state $(\mathbf{x},\mathbf{p})$. This concept can be translated to any pair of conjugate variables that behave equivalently to position and momentum [131]. For the case of an electromagnetic field, we can express two conjugate operators using $\hat{a}$ and $\hat{a}^\dagger$, which leads to [7]

$$\hat{x} = (\hat{a} + \hat{a}^\dagger)/2 \quad \text{and} \quad \hat{p} = (\hat{a} - \hat{a}^\dagger)/(2\imath)\,.$$

The eigenstates $|x\rangle$ and $|p\rangle$ of $\hat{x}$ and $\hat{p}$ define the density matrix $\hat{\rho}$ of the system. Because $\hat{\rho}$ completely describes the physical system, also the Wigner function [127, 130, 132]

$$W(x,p) \equiv \frac{1}{2\pi} \int_{-\infty}^{+\infty} \mathrm{d}\xi \left\langle x - \frac{\xi}{2} \middle| \hat{\rho} \middle| x + \frac{\xi}{2} \right\rangle e^{(\imath p \xi)}\,, \tag{2.2.16}$$

completely describes the physical system. In Eq. (2.2.16), ξ is a real-valued integration variable such that the definition of the Wigner function is well-defined and normalized to $\int\int W(x,p) = 1$ [129].

Having full knowledge of the density operator or the Wigner function is equivalent to the knowledge on all moments $\langle (\hat{a}^\dagger)^m \hat{a}^n \rangle$ with $m,n \in \mathbb{N}_0$ [134–136]. Theoretically, an infinite number of moments must be known to fully reconstruct a quantum state but in many scenarios the reconstruction of a state is possible from a finite number of moments [135–137]. In particular, the most relevant class of Gaussian states are completely described by moments up to the second order ($m+n \leq 2$) [138–140]. Since the Wigner function is a quasi-probability distribution, it can become negative and indicate the quantumness of a state [141]. To reconstruct a (partially) negative Wigner function of a quantum state requires at least the knowledge of moments up to the fourth order [129, 142].

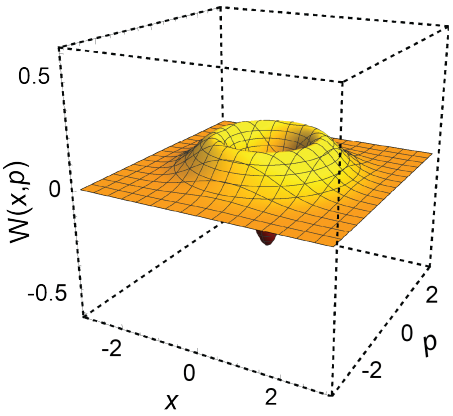

Figure 2.18: Wigner function of a Fock state $|1\rangle$. Picture taken from Ref. 133.

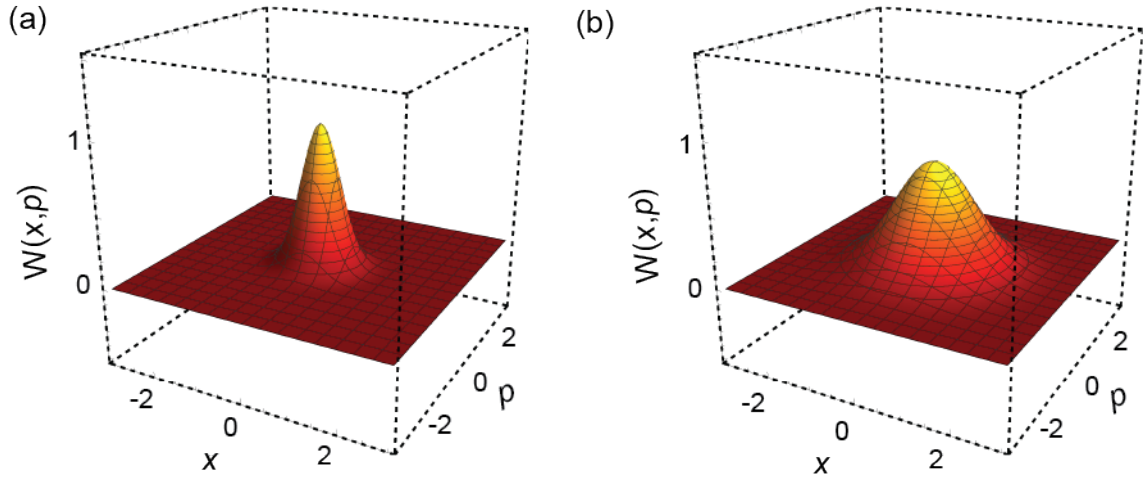

Figure 2.19: **(a)** Wigner function of a vacuum state $|0\rangle$. **(b)** Wigner function of a thermal state with $n_{\mathrm{th}} = 0.2$ photons on average. This photon number corresponds to 135 mK when operating at 5 GHz. Pictures taken from Ref. 133.

Fock States From a conceptual point of view, Fock or number states are important because they can be used as an orthonormal basis for the Hilbert-space in quantum mechanics [7]. Hence, we can describe any state of light by a superposition of Fock states. Furthermore, these non-classical states are the basis for many quantum computing protocols [117, 143, 144] and serve as toolbox for a series of quantum mechanical operations [50, 51]. Fock states $|n\rangle$ are the eigenstates of the number operator $\hat{n} = \hat{a}^\dagger \hat{a}$ and obey [145] $\hat{n}\,|n\rangle = n\,|n\rangle$. We obtain different Fock states by applying the creation and annihilation operators to an initial Fock state

$$\hat{a}\,|n\rangle = \sqrt{n}\,|n-1\rangle\ , \qquad \hat{a}^\dagger\,|n\rangle = \sqrt{n+1}\,|n+1\rangle\ .$$

In contrast to the Poissonian distribution expected for a harmonic oscillator, these equations show that Fock states belong to a discrete number of excitations in a single mode. A Fock state can for example be reached by relaxing an excitation from a resonant two-level-state into a single mode resonator [118]. We show the exemplary Wigner function for the Fock state $|1\rangle$ in Fig. 2.18. The fact that the Wigner function becomes negative towards the origin of the phase space clearly reveals the quantumness of Fock states.

Vacuum state The vacuum state $|0\rangle$ of a certain mode ω_k is the lowest order Fock state for which any excitations, e.g., thermal or coherent excitations, are absent. In a classical picture, such a state would contain zero photons, i.e., zero energy, and would be physically irrelevant. However, from the field theory described by Eq. (2.2.7) we see that vacuum fluctuations are always present [146] due to Heisenberg's uncertainty principle [128]. In Fig. 2.19 (a), we show the Gaussian envelope of the Wigner function $W(x,p) = \exp(-x^2 - p^2)/\pi$ corresponding to vacuum fluctuations around the origin. The $1/e$ contour of the Wigner function has the radius $1/4$ meaning that the vacuum state fulfills the Heisenberg principle with a minimum uncertainty. Since the vacuum state represents the $T = 0$ case, it cannot be realized in an experiment. However, if the experimental settings fulfill the condition $k_{\mathrm{B}}T \ll \hbar\omega$, we can well approximate the thermal state as a vacuum state [129]. Nevertheless, also the vacuum state has physical consequences and measurable effects, such as the Casimir effect [147].

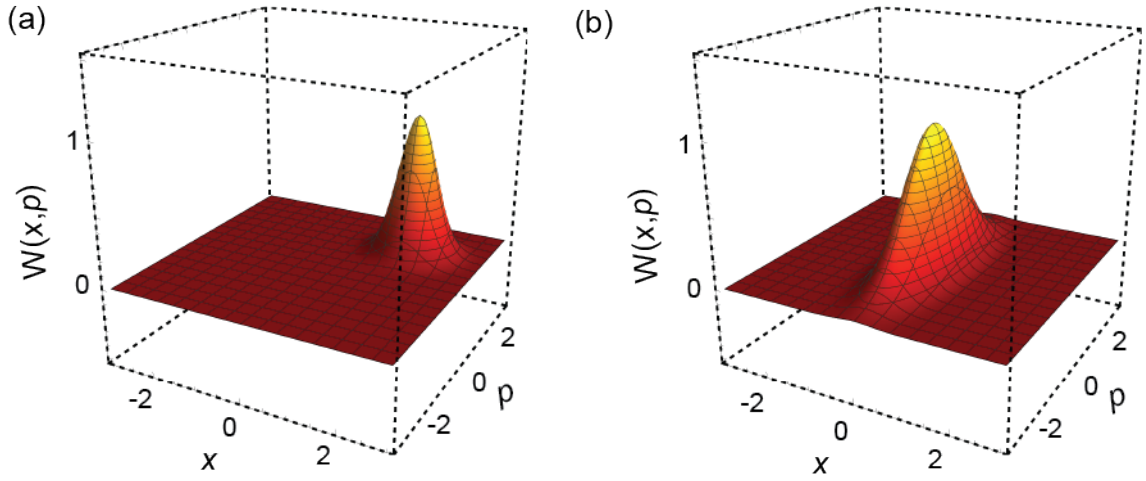

Figure 2.20: **(a)** Wigner function of a coherent state $|\alpha\rangle$ with $x_0 = p_0 = 1.5$. **(b)** Wigner function of a squeezed state with $\sigma_x = 1.5$ and $\sigma_p = 0.5$. Pictures taken from Ref. 133.

Thermal states As stated above, for a finite temperature we always expect a certain number of photons on average to be present. Hence, each state that we detect is superimposed by a thermal state [148]. Thermal states are emitted from black-body radiators of finite temperature T [129, 139] and have only negligible coherence [149–151]. They follow the Bose-Einstein distribution [145] defining the mean photon number

$$n_{\mathrm{th}} = \frac{1}{\exp(\hbar\omega/k_{\mathrm{B}}T) - 1} \tag{2.2.17}$$

at a certain frequency ω. From Eq. (2.2.17) we see that n_{th} becomes zero for $T = 0$ and asymptotically follows a linear trend with T for $\hbar\omega \ll k_{\mathrm{B}}T$. The Gaussian Wigner function $W(x,p) = \exp[-x^2 - p^2/(n_{\mathrm{th}} + 1/2)]/\pi(n_{\mathrm{th}} + 1/2)$ broadens with increasing temperature, as shown in Fig. 2.19 (b). Because of this broadening, thermal states do not belong to the class of minimum uncertainty states.

Coherent states In addition to thermal states consisting of incoherent photons as described above, coherent states have a well-defined frequency and phase. In practice, we generate these Gaussian states by phase-matched microwave sources, which operate analogously to a laser in optics. Coherent states are eigenstates of the annihilation operator, thus obeying [7] $\hat{a}\,|\alpha\rangle = \alpha\,|\alpha\rangle$. The complex eigenvalue $\alpha = x_0 + \imath p_0$ describes the amplitude $\mathcal{A} = \sqrt{x_0^2 + p_0^2}$ and the phase $\varphi = \arctan(p_0/q_0)$ of a sinusoidal electromagnetic wave. We can define a coherent state

$$|\alpha\rangle = \hat{D}(\alpha)\,|0\rangle = \exp(\alpha\hat{a}^\dagger - \alpha^*\hat{a})\,|0\rangle \tag{2.2.18}$$

by applying the displacement operator $\hat{D}(\alpha) \equiv \exp(\alpha\hat{a}^\dagger - \alpha^*\hat{a})$ to the vacuum state $|0\rangle$. Mathematically, the displacement $\alpha = x + \imath p$ is a complex number describing the point (x,p) in phase space to which $\hat{D}(\alpha)$ displaces. This fact also manifests itself in the Wigner function $W(x,p) = \exp[-(x - x_0)^2 - (p - p_0)^2]/\pi$ of a coherent state shown in Fig. 2.20 (a). A coherent state fulfills the Heisenberg principle with a minimum uncertainty.

Squeezed states Squeezed states also belong to the class of Gaussian states with minimum uncertainty [114, 127, 129]. Their name relates to the fact that their Wigner function can be squeezed below the radius of the vacuum state in one direction of the phase space [139, 152]. We cannot, however, beat the Heisenberg limit with a squeezed state since the unsqueezed quadrature grows in a way that the area underneath the Wigner function $W(x,p) = \exp(-x^2/\sigma_x^2 - p^2/\sigma_p^2)/\sigma_x\sigma_p$ obeys $\Delta x \Delta p \geq 1/4$ [cf. Fig. 2.20 (b)]. Here, σ_x, σ_p are the squeezing factors in x and p direction, respectively. Consequently, the Wigner function of a squeezed state is not rotationally symmetric but has an elliptical shape. A squeezed vacuum state

$$|\xi\rangle = \hat{S}(\xi)\,|0\rangle = \exp\left(\frac{1}{2}\xi^*\hat{a}^2 - \frac{1}{2}\xi(\hat{a}^\dagger)^2\right)|0\rangle \tag{2.2.19}$$

can be generated by applying the squeeze operator [7] $\hat{S}(\xi)$ to the vacuum (or any other input state). Here, the squeezing parameter ξ is a complex number defining the direction and the amount of squeezing.

Photon statistics The statistical nature of photons emitted from a light source, usually referred to as photon statistics, is described by a probability distribution either in terms of the number states or in terms of moments. For the latter, the variance $\mathrm{Var}(\langle\hat{a}^\dagger\hat{a}\rangle)$ of the mean photon number $\langle\hat{a}^\dagger\hat{a}\rangle$ is closely linked to the photon statistics [7]. The photon number variance can be measured in photon counting experiments similar to the famous experiment of Hanbury Brown and Twiss (HBT) [153]. In photon counting experiments, one measures the probability $P(n)$ to count n photons for an expected value $\langle n\rangle \equiv \langle\hat{a}^\dagger\hat{a}\rangle$. In particular, one finds a Poisson distribution for coherent states [7] and the Bose-Einstein distribution [154] for thermal states. For equal expectation values $\langle n\rangle$, these distributions are clearly distinguishable as shown in Fig. 2.21 (a) and expressed in

$$P(n) = \begin{cases} \dfrac{\langle n\rangle^n}{n!}e^{-\langle n\rangle} & \text{coherent state} \qquad (2.2.20a) \\ \dfrac{1}{\langle n\rangle + 1}\left(\dfrac{\langle n\rangle}{\langle n\rangle + 1}\right)^n & \text{thermal state}\,. \qquad (2.2.20b) \end{cases}$$

The Poissonian distribution is a threshold to separate between super-Poissonian, i.e., classical emitters and sub-Poissonian, i.e., quantum emitters. Classical fields can be generated from thermal emitters [41, 155–158], while quantum emitters are typical single photon sources [159–161] or generators of squeezed light [159, 162]. Since a direct measurement of $P(n)$ is experimentally challenging, typically the second-order correlation function

$$g^{(2)}(\tau) \equiv \frac{\langle\hat{a}^\dagger(t)\hat{a}^\dagger(t+\tau)\hat{a}(t+\tau)\hat{a}(t)\rangle}{\langle\hat{a}^\dagger(t+\tau)\hat{a}(t+\tau)\rangle\langle\hat{a}^\dagger(t)\hat{a}(t)\rangle}\,, \tag{2.2.21}$$

$$\tau \mapsto 0 \;\&\; \text{stationary field}: \qquad g^{(2)}(0) = \frac{\mathrm{Var}(\hat{a}^\dagger\hat{a}) - \langle\hat{a}^\dagger\hat{a}\rangle}{\langle\hat{a}^\dagger\hat{a}\rangle^2} + 1 \tag{2.2.22}$$

is measured in an HBT configuration [155, 156, 158]. For a coherent field, the variance is given as $\mathrm{Var}(\hat{a}^\dagger\hat{a}) = |\alpha|^2$ and also the expectation value is $\langle a^\dagger a\rangle = |\alpha|^2$. Hence, from Eq. (2.2.22), we obtain $g^{(2)}(0) = 1$. For a pure thermal field, we find $\mathrm{Var}(n_\mathrm{th}) = n_\mathrm{th}^2 + n_\mathrm{th}$ from the Bose-Einstein distribution in Eq. (2.2.17), and $\langle a^\dagger a\rangle = n_\mathrm{th}$. Hence, from Eq. (2.2.22),

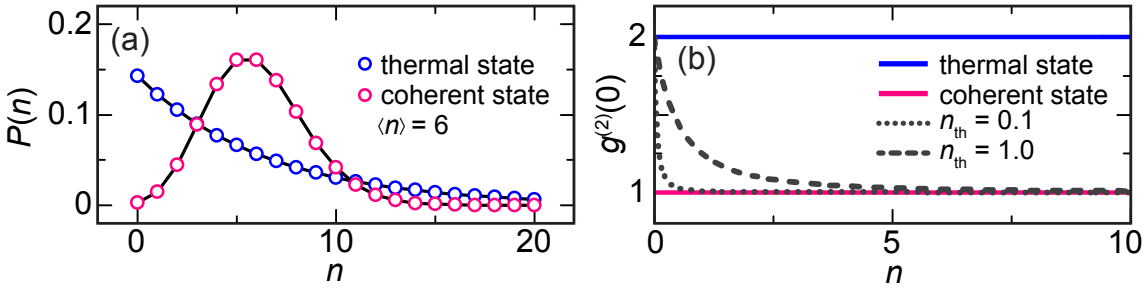

Figure 2.21: (a) Probability $P(n)$ to find n photons in a counting experiment for an expectation value $\langle n\rangle = 6$ photons. **(b)** Second-order correlation function $g^{(2)}(0)$ plotted versus photon number. The dotted and the dashed line are calculations for coherent states which also have a finite thermal contribution n_{th}.

we obtain $g^{(2)}(0) = 2$ which is independent of the photon number as it is also the case for the coherent state [see Fig. 2.21 (b)]. For high photon numbers, we consider the thermal field to be classical. In this regime the variance $n_{\mathrm{th}}^2 + n_{\mathrm{th}}$ can be approximated as n_{th}^2. The photon number expectation value is again $\langle n\rangle = n_{\mathrm{th}}$. Hence, we obtain $g^{(2)}(0) = (n_{\mathrm{th}}^2 - n_{\mathrm{th}})n_{\mathrm{th}}^{-2} + 1$. This behavior approaches $g^{(2)}(0) = 2$ for large photon numbers.
Real coherent fields always have a finite thermal contribution meaning that for $|\alpha|^2 < n_{\mathrm{th}}$ there must be a transition from $g^{(2)}(0) = 1$ to $g^{(2)}(0) = 2$. For a quantitative analysis, we have to calculate the corresponding variance and expectation values of the combined fields. In the following, we describe the thermal field by the operators $\hat{\xi}^\dagger\hat{\xi}$ and the coherent drive by the expression $\hat{c}^\dagger c$. The combined field is given as $\hat{a}^\dagger\hat{a} = \hat{\xi}^\dagger\hat{\xi} + \hat{c}^\dagger c$ and we assume that the two fields are uncorrelated. Hence, variance and expectation value are given as

$$\mathrm{Var}(\hat{a}^\dagger\hat{a}) = \mathrm{Var}(\hat{\xi}^\dagger\hat{\xi}) + \mathrm{Var}(\hat{c}^\dagger c) = (n_{\mathrm{th}}^2 + n_{\mathrm{th}}) + |\alpha|^2\,, \tag{2.2.23}$$

$$\langle\hat{a}^\dagger\hat{a}\rangle = \langle\hat{\xi}^\dagger\hat{\xi}\rangle + \langle\hat{c}^\dagger\hat{c}\rangle = n_{\mathrm{th}} + |\alpha|^2\,. \tag{2.2.24}$$

If we use these expression in Eq. (2.2.22), we obtain

$$g^{(2)}(0) = \frac{n_{\mathrm{th}}^2}{(n_{\mathrm{th}} + |\alpha|^2)^2} + 1 \tag{2.2.25}$$

shown in Fig. 2.21 (b). As expected, there is a smooth transition from $g^{(2)}(0) = 1$ to $g^{(2)}(0) = 2$ that depends on the background thermal field.

2.2.4 Correlation functions of broadband microwave states

For typical circuit QED experiments, microwave fields are generated at room temperature and subsequently attenuated inside a cryostat to reach photon numbers on the order of unity [41]. In this section, we calculate the variance of the corresponding states based on a beam splitter model depicted in Fig. 2.22 (a). Additionally, we calculate the variance of an amplified thermal fields [see Fig. 2.22 (b)], which is relevant for reconstruction setups [121, 139, 163] using parametric amplifiers as preamplifiers as discussed in Sec. 6.1. For convenience, we first calculate the correlation function $\mathcal{C}^{\mathrm{th}}(t)$ for thermal fields without employing the beam splitter model, which is analogously to the way presented in Ref. 17.

For pure thermal fields, we find the correlation function

$$\begin{aligned}\mathcal{C}^{\mathrm{th}}(t) &= \langle[\hat{a}^\dagger(t)\hat{a}(t) - \langle\hat{a}^\dagger\hat{a}\rangle][\hat{a}^\dagger(0)\hat{a}(0) - \langle\hat{a}^\dagger\hat{a}\rangle]\rangle \\ &= [\underbrace{\langle\hat{a}^\dagger\hat{a}\hat{a}^\dagger\hat{a}\rangle}_{2n_{\mathrm{th}}^2+n_{\mathrm{th}}} - \underbrace{\langle\langle\hat{a}^\dagger\hat{a}\rangle\hat{a}^\dagger\hat{a}\rangle}_{n_{\mathrm{th}}^2} - \underbrace{\langle\hat{a}^\dagger\hat{a}\langle\hat{a}^\dagger\hat{a}\rangle\rangle}_{n_{\mathrm{th}}^2} + \underbrace{\langle\hat{a}^\dagger\hat{a}\rangle^2}_{n_{\mathrm{th}}^2}]\mathcal{F}_{\mathcal{C}}(t) = (n_{\mathrm{th}}^2 + n_{\mathrm{th}})\mathcal{F}_{\mathcal{C}}(t)\,, \quad (2.2.26)\end{aligned}$$

which yields the $n_{\mathrm{th}}^2 + n_{\mathrm{th}}$ variance of thermal fields. Here, $\mathcal{F}_{\mathcal{C}}(t)$ is the characteristic decay function of the environment discussed in the following paragraph. Furthermore, in Eq. (2.2.26), we use the moments [121, 164] $\langle(\hat{a}^\dagger)^k\hat{a}^\ell\rangle_{\mathrm{th}} = \ell! n_{\mathrm{th}}^\ell \delta_{k\ell}$ of a thermal state.

Correlator for incoherently driven resonators To derive the photon number correlator $\mathcal{C}(\tau)$ inside the resonator for shot-noise, thermal, and coherent states, we use input-output theory for a single mode $\hat{a}$ of the resonator described by the Hamiltonian $\mathcal{H}_{\mathrm{r}} = \hbar\omega_{\mathrm{r}}\hat{a}^\dagger\hat{a}$. We start with deriving the correlator for broadband white noise, which could be thermal (i.e. super-Poissonian) or shot noise (i.e. Poissonian). The noise field occupies incoming modes $\hat{b}_{\mathrm{in}}(\omega,t)$ of an open transmission line, which is coupled to the resonator via a coupling capacitor with strength $\tilde{g}(\omega)$. Using the resonator density of states $D(\omega)$, the amplitude-damping of the resonator is given as $\kappa_{\mathrm{x}}/2 = \pi D(\omega_{\mathrm{r}})|\tilde{g}(\omega_{\mathrm{r}})|^2$. The transmission line modes describe a force [165] $F(t) = \imath\sum_\omega \tilde{g}(\omega)\hat{b}_{\mathrm{in}}(\omega,0)e^{-\imath\omega t}$ acting on the resonator such that the equation of motion becomes [166] $\partial\hat{a}/\partial t = -[\imath\omega_{\mathrm{r}} + \kappa_{\mathrm{x}}/2]\hat{a}(t) - F(t)$. In the Markov approximation, this equation solves in the Heisenberg picture to

$$\hat{a}(\tau) = e^{-(\imath\omega_{\mathrm{r}}+\kappa_{\mathrm{x}}/2)\tau}\left[\hat{a}(0) - \int_0^\tau \mathrm{d}t\; e^{-(\imath\omega_{\mathrm{r}}+\kappa_{\mathrm{x}}/2)\tau}F(t)\right]. \quad (2.2.27)$$

Using this equation, we calculate the photon-photon time correlator

$$\begin{aligned}\mathcal{C}(\tau) &\equiv \langle\delta n_{\mathrm{r}}(0)\delta n_{\mathrm{r}}(\tau)\rangle = \langle\hat{a}^\dagger(0)\hat{a}(0)\hat{a}^\dagger(\tau)\hat{a}(\tau)\rangle - \langle\hat{a}^\dagger(0)\hat{a}(0)\rangle^2 \\ &= \langle\hat{a}^\dagger(0)\hat{a}(0)\hat{a}^\dagger(0)\hat{a}(0)\rangle e^{-\kappa_{\mathrm{x}}\tau} - \langle\hat{a}^\dagger\hat{a}\rangle^2 \\ &- e^{-\kappa_{\mathrm{x}}\tau}\int_0^\tau \mathrm{d}t\;\langle\hat{a}^\dagger(0)\hat{a}(0)F^\dagger(t)\hat{a}(0)\rangle e^{(-\imath\omega_{\mathrm{r}}+\kappa_{\mathrm{x}}/2)t} \qquad (i) \\ &+ e^{-\kappa_{\mathrm{x}}\tau}\int_0^\tau \mathrm{d}t\;\langle\hat{a}^\dagger(0)\hat{a}(0)\hat{a}^\dagger(0)F(t)\rangle e^{(\imath\omega_{\mathrm{r}}+\kappa_{\mathrm{x}}/2)t} \qquad (ii) \\ &+ e^{-\kappa_{\mathrm{x}}\tau}\int_0^\tau\int_0^\tau \mathrm{d}t\mathrm{d}t'\;\langle\hat{a}^\dagger(0)\hat{a}(0)F^\dagger(t)F(t')\rangle e^{-\imath\omega_{\mathrm{r}}(t-t')}e^{\kappa_{\mathrm{x}}/2(t+t')} \qquad (iii)\,. \quad (2.2.28)\end{aligned}$$

Since external force and resonator are uncorrelated at $t = 0$, we write the two terms (i) and (ii) in Eq. (2.2.28) as [166]

$$\begin{aligned}(i) &= -\imath\sum_\omega \tilde{g}(\omega)e^{-\kappa_{\mathrm{x}}\tau}\int_0^\tau \mathrm{d}t\;\langle\hat{a}^\dagger(0)\hat{a}(0)\hat{a}(0)\rangle\;\langle\hat{b}_{\mathrm{in}}^\dagger(\omega,0)\rangle e^{\imath\omega t}e^{(-\imath\omega_{\mathrm{r}}+\kappa_{\mathrm{x}}/2)t} \\ (ii) &= +\imath\sum_\omega \tilde{g}(\omega)e^{-\kappa_{\mathrm{x}}\tau}\int_0^\tau \mathrm{d}t\;\langle\hat{a}^\dagger(0)\hat{a}(0)\hat{a}^\dagger(0)\rangle\;\langle\hat{b}_{\mathrm{in}}(\omega,0)\rangle e^{-\imath\omega t}e^{(\imath\omega_{\mathrm{r}}+\kappa_{\mathrm{x}}/2)t}\,.\end{aligned}$$

Here, one immediately sees that these expressions become zero for uncorrelated signals with zero mean (noise), characterized by $\langle\hat{b}_{\mathrm{in}}^\dagger\rangle = 0 = \langle\hat{b}_{\mathrm{in}}\rangle$. Hence, the relevant part for $\mathcal{C}(\tau)$ is determined by the last part (iii) in Eq. (2.2.28). Assuming that both thermal and shot noise have a white frequency distribution over the resonator bandwidth, i.e.,

$\langle F^\dagger(t)F(t')\rangle = \kappa_\mathrm{x}\langle \hat{b}^\dagger_\mathrm{in}(\omega,0)\hat{b}_\mathrm{in}(\omega,0)\rangle\delta(t-t')$, on resonance, part (iii) simplifies to

$$\begin{aligned}(iii) &= \kappa_\mathrm{x}\langle \hat{b}^\dagger_\mathrm{in}(\omega_\mathrm{r},0)\hat{b}_\mathrm{in}(\omega_\mathrm{r},0)\rangle\langle \hat{a}^\dagger(0)\hat{a}(0)\rangle e^{-\kappa_\mathrm{x}\tau}\int_0^\tau\int_0^\tau \mathrm{d}t\mathrm{d}t'\ \delta(t-t')e^{-\imath\omega_\mathrm{r}(t-t')}e^{\kappa_\mathrm{x}(t+t')/2}\\ &= \kappa_\mathrm{x}\langle \hat{b}^\dagger_\mathrm{in}(\omega_\mathrm{r},0)\hat{b}_\mathrm{in}(\omega_\mathrm{r},0)\rangle\langle \hat{a}^\dagger(0)\hat{a}(0)\rangle e^{-\kappa_\mathrm{x}\tau}\int_0^\tau \mathrm{d}t\ e^{\kappa_\mathrm{x}t}\\ &= \quad \langle \hat{b}^\dagger_\mathrm{in}(\omega_\mathrm{r},0)\hat{b}_\mathrm{in}(\omega_\mathrm{r},0)\rangle\langle \hat{a}^\dagger(0)\hat{a}(0)\rangle[1-e^{-\kappa_\mathrm{x}\tau}]\,. \end{aligned} \tag{2.2.29}$$

Using this expression, and equilibrium states, $\langle \hat{b}^\dagger_\mathrm{in}(\omega_\mathrm{r},0)\hat{b}_\mathrm{in}(\omega_\mathrm{r},0)\rangle = \langle \hat{a}^\dagger\hat{a}\rangle \equiv n_\mathrm{r}$, Eq. (2.2.28) simplifies to $\mathcal{C}(\tau) = [\langle \hat{a}^\dagger\hat{a}\hat{a}^\dagger\hat{a}\rangle - \langle \hat{a}^\dagger\hat{a}\rangle^2]\exp(-\kappa_\mathrm{x}\tau) = \mathrm{Var}(n_\mathrm{r})\exp(-\kappa_\mathrm{x}\tau)$. Hence, the correlator for white noise is given as the photon number variance which decays at the energy decay rate κ_x. Because we did not make any assumptions on the distribution of the noise (Poissonian, super-Poissonian, etc.), this statement holds for shot noise with $\mathrm{Var}(n_\mathrm{r}) = n_\mathrm{r}$ and $\mathcal{C}^\mathrm{sh}(\tau) = n_\mathrm{r}\exp(-\kappa_\mathrm{x}\tau)$ as well as for thermal noise with $\mathrm{Var}(n_\mathrm{r}) = n_\mathrm{r}^2 + n_\mathrm{r}$ and $\mathcal{C}^\mathrm{th}(\tau) = (n_\mathrm{r}^2 + n_\mathrm{r})\exp(-\kappa_\mathrm{x}\tau)$.

Attenuated thermal fields To calculate the photon number variance of an attenuated thermal field, we use the beam splitter model depicted in Fig. 2.22 (a). Here, we assume a thermal state generated at a higher temperature stage, which is subsequently attenuated inside the cryostat with attenuation $\eta \leq 1$. We describe the thermal state at high temperature with the bosonic operators $\hat{b}^\dagger$ and $\hat{b}$ and model the cryogenic attenuator as a beam splitter which mixes a weak thermal state described by $\hat{c}^\dagger$ and $\hat{c}$ to the incoming state. That way, we obtain the mixed state described with the operator $\hat{a}(t) = B\hat{b}(t) + C\hat{c}(t)$, where $B = \sqrt{\eta}$ and $C = \sqrt{1-\eta}$. We define the photon numbers $n_\mathrm{b} = \langle \hat{b}^\dagger\hat{b}\rangle$, $n_\mathrm{c} = \langle \hat{c}^\dagger\hat{c}\rangle$ and the total photon number $n_\mathrm{tot} = \langle \hat{a}^\dagger\hat{a}\rangle = B^2 n_\mathrm{b} + C^2 n_\mathrm{c}$. Then, the photon number variance is defined by the correlator

$$\begin{aligned}\mathcal{C}^\mathrm{th}(t) &= \langle[\hat{a}^\dagger(t)\hat{a}(t) - \langle \hat{a}^\dagger\hat{a}\rangle][\hat{a}^\dagger(0)\hat{a}(0) - \langle \hat{a}^\dagger\hat{a}\rangle]\rangle\\ &= \langle[\{B\hat{b}^\dagger(t) + C\hat{c}^\dagger(t)\}\{B\hat{b}(t) + C\hat{c}(t)\} - n_\mathrm{tot}]\times\\ &\quad [\{B\hat{b}^\dagger(0) + C\hat{c}^\dagger(0)\}\{B\hat{b}(0) + C\hat{c}(0)\} - n_\mathrm{tot}]\rangle\\ &= \langle[B^2\hat{b}^\dagger(t)\hat{b}(t) + BC\hat{b}^\dagger(t)\hat{c}(t) + BC\hat{c}^\dagger(t)\hat{b}(t) + C^2\hat{c}^\dagger(t)\hat{c}(t) - n_\mathrm{tot}]\times\\ &\quad [B^2\hat{b}^\dagger(0)\hat{b}(0) + BC\hat{b}^\dagger(0)\hat{c}(0) + BC\hat{c}^\dagger(0)\hat{b}(0) + C^2\hat{c}^\dagger(0)\hat{c}(0) - n_\mathrm{tot}]\rangle\,. \end{aligned} \tag{2.2.30}$$

Multiplying all terms yields

$$\begin{aligned}\mathcal{C}^\mathrm{th}(t) = [\ &\underbrace{B^4\langle \hat{b}^\dagger\hat{b}\hat{b}^\dagger\hat{b}\rangle}_{=B^4(2n_\mathrm{b}^2+n_\mathrm{b})} + \underbrace{B^3C\langle \hat{b}^\dagger\hat{b}\hat{b}^\dagger\hat{c}\rangle}_{=0} + \underbrace{B^3C\langle \hat{b}^\dagger\hat{b}\hat{c}^\dagger\hat{b}\rangle}_{=0} + \underbrace{B^2C^2\langle \hat{b}^\dagger\hat{b}\hat{c}^\dagger\hat{c}\rangle}_{=B^2C^2n_\mathrm{b}n_\mathrm{c}} - \underbrace{B^2n_\mathrm{tot}\langle b^\dagger\hat{b}\rangle}_{=B^2n_\mathrm{tot}n_\mathrm{b}}\\ &+ \underbrace{B^3C\langle \hat{b}^\dagger\hat{c}\hat{b}^\dagger\hat{b}\rangle}_{=0} + \underbrace{B^2C^2\langle \hat{b}^\dagger\hat{c}\hat{b}^\dagger\hat{c}\rangle}_{=0} + \underbrace{B^2C^2\langle \hat{b}^\dagger\hat{c}\hat{c}^\dagger\hat{b}\rangle}_{=B^2C^2n_\mathrm{b}(n_\mathrm{c}+1)} + \underbrace{BC^3\langle \hat{b}^\dagger\hat{c}\hat{c}^\dagger\hat{c}\rangle}_{=0} - \underbrace{BCn_\mathrm{tot}\langle \hat{b}^\dagger\hat{c}\rangle}_{=0}\\ &+ \underbrace{B^3C\langle \hat{c}^\dagger\hat{b}\hat{b}^\dagger\hat{b}\rangle}_{=0} + \underbrace{B^2C^2\langle \hat{c}^\dagger\hat{b}\hat{b}^\dagger\hat{c}\rangle}_{=B^2C^2n_\mathrm{c}(n_\mathrm{b}+1)} + \underbrace{B^2C^2\langle \hat{c}^\dagger\hat{b}\hat{c}^\dagger\hat{b}\rangle}_{=0} + \underbrace{BC^3\langle \hat{c}^\dagger\hat{b}\hat{c}^\dagger\hat{c}\rangle}_{=0} - \underbrace{BCn_\mathrm{tot}\langle \hat{c}^\dagger\hat{b}\rangle}_{=0}\\ &+ \underbrace{B^2C^2\langle \hat{c}^\dagger\hat{c}\hat{b}^\dagger\hat{b}\rangle}_{=B^2C^2n_\mathrm{b}n_\mathrm{c}} + \underbrace{BC^3\langle \hat{c}^\dagger\hat{c}\hat{b}^\dagger\hat{c}\rangle}_{=0} + \underbrace{BC^3\langle \hat{c}^\dagger\hat{c}\hat{c}^\dagger\hat{b}\rangle}_{=0} + \underbrace{C^4\langle \hat{c}^\dagger\hat{c}\hat{c}^\dagger\hat{c}\rangle}_{=C^4(2n_\mathrm{c}^2+n_\mathrm{c})} - \underbrace{C^2n_\mathrm{tot}\langle \hat{c}^\dagger\hat{c}\rangle}_{=C^2n_\mathrm{tot}n_\mathrm{c}}\\ &- \underbrace{B^2n_\mathrm{tot}\langle \hat{b}^\dagger\hat{b}\rangle}_{=B^2n_\mathrm{tot}n_\mathrm{b}} - \underbrace{BCn_\mathrm{tot}\langle \hat{b}^\dagger\hat{c}\rangle}_{=0} - \underbrace{BCn_\mathrm{tot}\langle \hat{c}^\dagger\hat{b}\rangle}_{=0} - \underbrace{C^2n_\mathrm{tot}\langle \hat{c}^\dagger\hat{c}\rangle}_{=C^2n_\mathrm{tot}n_\mathrm{c}} + n_\mathrm{tot}^2]\mathcal{F}_\mathcal{C}(t)\,. \end{aligned} \tag{2.2.31}$$

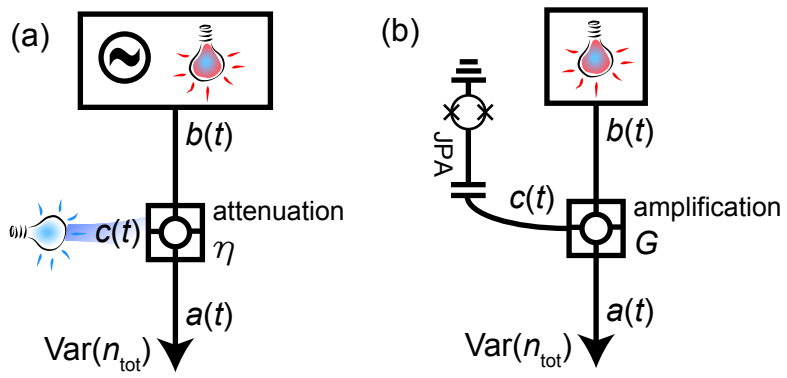

Figure 2.22: **(a)** Beam splitter model to calculate the variance of attenuated thermal and coherent fields. **(b)** Input-output model to calculate the variance of amplified thermal fields.

Here, we neglect all terms that are proportional to $\hat{b}$ and proportional to $\hat{c}$ because the first moment of thermal noise is zero. Also, we can neglect the fast rotating terms $\hat{b}\hat{b}$ and $\hat{c}\hat{c}$. That way, we obtain

$$\begin{aligned}\mathcal{C}^{\mathrm{th}}(t) = [&\eta^2 n_{\mathrm{b}}^2 + \eta n_{\mathrm{b}} + 2\eta(1-\eta)n_{\mathrm{b}}n_{\mathrm{c}} \\ &+ (1-\eta)^2 n_{\mathrm{c}}^2 + (1-\eta)n_{\mathrm{c}}]\mathcal{F}_{\mathcal{C}}(t)\,,\end{aligned} \tag{2.2.32}$$

This equation shows that the beam splitter model predicts the thermal photon statistics of the incoming field n_{b} for $\eta \mapsto 1$ (no attenuation) and the thermal photon statistics of the cold attenuator for $\eta \mapsto 0$ (strong attenuation).

Correlator for coherently driven resonators For coherently driven resonators, it is convenient to describe the transmission line modes as $\hat{b}_{\mathrm{in}}(\omega,t) = e^{\imath\omega t}[\bar{b}_{\mathrm{in}} + \hat{\xi}(t)]$. Here, $\bar{b}_{\mathrm{in}}^{(\star)}$ describes a classical coherent drive with frequency $\omega = \omega_{\mathrm{r}} - \delta_{\mathrm{r}}$. For a coherent input field, we assume that $\hat{\xi}^{(\dagger)}(t)$ are just vacuum fluctuations [17, 165, 167]. In a frame rotating at ω, the field inside the cavity is given as $\hat{a}(\tau) = \bar{a} + \hat{d}(\tau)$, where [167]

$$\bar{a} = \frac{-\sqrt{\kappa}}{\imath\delta_{\mathrm{r}} + \kappa/2}\bar{b}_{\mathrm{in}}\,, \tag{2.2.33}$$

$$\hat{d}(\tau) = -\sqrt{\kappa}\int_{-\infty}^{\tau} \mathrm{d}t\, e^{-(\imath\delta_{\mathrm{r}}+\kappa/2)(\tau-t)}\hat{\xi}(t)\,. \tag{2.2.34}$$

We can use this expression to calculate the correlator $\mathcal{C}^{\mathrm{coh}}(\tau) = n_{\mathrm{r}}\langle\hat{d}(0)\hat{d}^{\dagger}(\tau)\rangle$, which decays at the amplitude decay rate $\kappa_{\mathrm{x}}/2$ since [17, 167] $\langle\hat{d}^{\dagger}(0)\hat{d}(t)\rangle = \exp(-\imath\delta_{\mathrm{r}}t - \kappa_{\mathrm{x}}|\tau|/2)$. Hence, on resonance, the correlator for a coherent state $\mathcal{C}^{\mathrm{coh}}(\tau) = n_{\mathrm{r}}\exp(-\kappa_{\mathrm{x}}|\tau|/2)$ decays twice as slow as the correlator for white noise.

Attenuated coherent fields To calculate the photon number variance of an attenuated coherent field, we use the field operator $\hat{b} = \alpha(t) + \hat{d}(t)$, which describes a vacuum ($\hat{d}^{\dagger}\hat{d} = 0$) which is displaced by $|\alpha|^2 = n_{\mathrm{b}}$. A coherently driven resonator has the decay function $\mathcal{F}_{\mathcal{C}}(t) = \exp(-\kappa_{\mathrm{x}}t/2)$ [17, 168]. In the same manner as above, we define the total photon number $n_{\mathrm{tot}} = \langle\hat{a}^{\dagger}\hat{a}\rangle = B^2 n_{\mathrm{b}} + C^2 n_{\mathrm{c}}$. We want to note that the calculations below are also valid for shot noise, which has a Poisson statistics. In this case however, one has to use the characteristic decay function $\mathcal{F}_{\mathcal{C}}(t) = \exp(-\kappa_{\mathrm{x}}t)$ [17, 166]. That way, we calculate the

correlator

$$\begin{aligned}
\mathcal{C}^{\mathrm{coh}}(t) &= \langle[\hat{a}^\dagger(t)\hat{a}(t) - \langle\hat{a}^\dagger\hat{a}\rangle][\hat{a}^\dagger(0)\hat{a}(0) - \langle\hat{a}^\dagger\hat{a}\rangle]\rangle \\
&= \langle[\{B(\alpha^\star(t) + \hat{d}^\dagger(t)) + C\hat{c}^\dagger(t)\}\{B(\alpha(t) + \hat{d}(t)) + C\hat{c}(t)\} - n_{\mathrm{tot}}]\times \\
&\quad [\{B(\alpha^\star(0) + \hat{d}^\dagger(0)) + C\hat{c}^\dagger(0)\}\{B(\alpha(0) + \hat{d}(0)) + C\hat{c}(0)\} - n_{\mathrm{tot}}]\rangle \\
&= \langle[B^2|\alpha(t)|^2 + B^2\alpha^\star(t)\hat{d}(t) + BC\alpha^\star(t)\hat{c}(t) \\
&\quad + B^2\hat{d}^\dagger(t)\alpha(t) + B^2\hat{d}^\dagger(t)\hat{d}(t) + BC\hat{d}^\dagger(t)\hat{c}(t) \\
&\quad + BC\hat{c}^\dagger(t)\alpha(t) + BC\hat{c}^\dagger(t)\hat{d}(t) + C^2\hat{c}^\dagger(t)\hat{c}(t) - n_{\mathrm{tot}}]\times \\
&\quad [B^2|\alpha(0)|^2 + B^2\alpha^\star(0)\hat{d}(0) + BC\alpha^\star(0)\hat{c}(0) \\
&\quad + B^2\hat{d}^\dagger(0)\alpha(0) + B^2\hat{d}^\dagger(0)\hat{d}(0) + BC\hat{d}^\dagger(0)\hat{c}(0) \\
&\quad + BC\hat{c}^\dagger(0)\alpha(0) + BC\hat{c}^\dagger(0)\hat{d}(0) + C^2\hat{c}^\dagger(0)\hat{c}(0) - n_{\mathrm{tot}}]\rangle\,. \qquad (2.2.35)
\end{aligned}$$

Again multiplying all terms yields the non-vanishing terms

$$\begin{aligned}
\mathcal{C}^{\mathrm{coh}}(t) = [&\underbrace{B^4|\alpha|^4}_{=B^4 n_{\mathrm{b}}^2} + \underbrace{B^2C^2|\alpha|^2\langle\hat{c}^\dagger\hat{c}\rangle}_{=B^2C^2 n_{\mathrm{b}} n_{\mathrm{c}}} - \underbrace{B^2|\alpha|^2 n_{\mathrm{tot}}}_{=B^2 n_{\mathrm{b}} n_{\mathrm{tot}}} + \underbrace{B^4\langle\alpha^\star\hat{d}\hat{d}^\dagger\alpha\rangle}_{=B^4 n_{\mathrm{b}}} \\
&+ \underbrace{B^2C^2\langle\alpha^\star\hat{c}\hat{c}^\dagger\alpha\rangle}_{=B^2C^2(n_{\mathrm{b}}n_{\mathrm{c}}+n_{\mathrm{b}})} + \underbrace{B^2C^2\langle\hat{c}^\dagger\alpha\alpha^\star\hat{c}\rangle}_{=B^2C^2(n_{\mathrm{b}}n_{\mathrm{c}}+n_{\mathrm{c}})} + \underbrace{B^2C^2\langle\hat{c}^\dagger\hat{d}\hat{d}^\dagger\hat{c}\rangle}_{=B^2C^2 n_{\mathrm{c}}} + \underbrace{B^2C^2|\alpha|^2\langle\hat{c}^\dagger\hat{c}\rangle}_{=B^2C^2 n_{\mathrm{b}} n_{\mathrm{c}}} \\
&+ \underbrace{C^4\langle\hat{c}^\dagger\hat{c}\hat{c}^\dagger\hat{c}\rangle}_{=C^4(2n_{\mathrm{c}}^2+n_{\mathrm{c}})} - \underbrace{C^2 n_{\mathrm{tot}}\langle\hat{c}^\dagger\hat{c}\rangle}_{=C^2 n_{\mathrm{c}} n_{\mathrm{tot}}} - \underbrace{B^2|\alpha|^2\langle n_{\mathrm{tot}}\rangle}_{=B^2 n_{\mathrm{b}} n_{\mathrm{tot}}} - \underbrace{C^2 n_{\mathrm{tot}}\langle\hat{c}^\dagger\hat{c}\rangle}_{=C^2 2n_{\mathrm{c}} n_{\mathrm{tot}}} + n_{\mathrm{tot}}^2]\mathcal{F}_{\mathcal{C}}(t). \qquad (2.2.36)
\end{aligned}$$

After simplifying Eq. (2.2.36), we obtain the correlation function

$$\mathcal{C}^{\mathrm{coh}}(t) = [\eta n_{\mathrm{b}} + 2\eta(1-\eta)n_{\mathrm{b}}n_{\mathrm{c}} + (1-\eta)^2 n_{\mathrm{c}}^2 + (1-\eta)n_{\mathrm{c}}]\mathcal{F}_{\mathcal{C}}(t)\,, \qquad (2.2.37)$$

which approaches the variance of a coherent state for $\eta \mapsto 1$ (no attenuation) and the thermal photon statistics of the cold attenuator for $\eta \mapsto 0$ (strong attenuation).

Amplified thermal fields In reconstruction setups for propagating microwaves [121, 139, 152, 169] often Josephson parametric amplifiers are used as preamplifiers, which amplify the signal with a power gain G. Similar to the calculations of attenuated propagating microwaves, we calculate the variance of an amplified thermal field using a beam splitter model as depicted in Fig. 2.22 (b). In this model, we describe the amplified field by the operator [169, 170] $\hat{a}(t) = B\hat{b} + C\hat{c}^\dagger$, where $B = \sqrt{G}$ and $C = \sqrt{G-1}$. That way, we obtain the total photon number $n_{\mathrm{tot}} = Gn_{\mathrm{b}} + (G-1)n_{\mathrm{c}} + (G-1)$ and the correlator

$$\begin{aligned}
\mathcal{C}^{\mathrm{jpa}}(\tau) &= \langle[\hat{a}^\dagger(\tau)\hat{a}(\tau) - \langle\hat{a}^\dagger\hat{a}\rangle][\hat{a}^\dagger(0)\hat{a}(0) - \langle\hat{a}^\dagger\hat{a}\rangle]\rangle \\
&= \langle[\{B\hat{b}^\dagger(\tau) + C\hat{c}(\tau)\}\{B\hat{b}(\tau) + C\hat{c}^\dagger(\tau)\} - n_{\mathrm{tot}}]\times \\
&\quad [\{B\hat{b}^\dagger(0) + C\hat{c}(0)\}\{B\hat{b}(0) + C\hat{c}^\dagger(0)\} - n_{\mathrm{tot}}]\rangle \\
&= \langle[B^2\hat{b}^\dagger(\tau)\hat{b}(\tau) + BC\hat{b}^\dagger(\tau)\hat{c}^\dagger(\tau) + BC\hat{c}(\tau)\hat{b}(\tau) + C^2\hat{c}(\tau)\hat{c}^\dagger(\tau) - n_{\mathrm{tot}}]\times \\
&\quad [B^2\hat{b}^\dagger(0)\hat{b}(0) + BC\hat{b}^\dagger(0)\hat{c}^\dagger(0) + BC\hat{c}(0)\hat{b}(0) + C^2\hat{c}(0)\hat{c}^\dagger(0) - n_{\mathrm{tot}}]\rangle\,. \qquad (2.2.38)
\end{aligned}$$

Multiplying all terms yields the non vanishing terms

$$\begin{aligned}\mathcal{C}^{\mathrm{jpa}}(\tau) =&[\underbrace{B^4\langle\hat{b}^\dagger\hat{b}\hat{b}^\dagger\hat{b}\rangle}_{B^4(2n_\mathrm{b}^2+n_\mathrm{b})}+\underbrace{B^2C^2\langle\hat{b}^\dagger\hat{b}\hat{c}\hat{c}^\dagger\rangle}_{B^2C^2(n_\mathrm{b}n_\mathrm{c}+n_\mathrm{b})}-\underbrace{B^2n_\mathrm{tot}\langle\hat{b}^\dagger\hat{b}\rangle}_{B^4n_\mathrm{b}^2+B^2C^2n_\mathrm{b}n_\mathrm{c}+B^2C^2n_\mathrm{b}}+\underbrace{B^2C^2\langle\hat{b}^\dagger\hat{c}^\dagger\hat{c}\hat{b}\rangle}_{B^2C^2n_\mathrm{b}n_\mathrm{c}}\\&+\underbrace{B^2C^2\langle\hat{c}\hat{b}\hat{b}^\dagger\hat{c}^\dagger\rangle}_{B^2C^2(n_\mathrm{b}n_\mathrm{c}+n_\mathrm{b}+n_\mathrm{c}+1)}+\underbrace{B^2C^2\langle\hat{c}\hat{c}^\dagger\hat{b}^\dagger\hat{b}\rangle}_{B^2C^2(n_\mathrm{b}n_\mathrm{c}+n_\mathrm{b})}+\underbrace{C^4\langle\hat{c}\hat{c}^\dagger\hat{c}\hat{c}^\dagger\rangle}_{C^4(2n_\mathrm{c}^2+3n_\mathrm{c}+1)}\\&-\underbrace{C^2n_\mathrm{tot}\langle\hat{c}\hat{c}^\dagger\rangle}_{\substack{B^2C^2(n_\mathrm{b}n_\mathrm{c}+n_\mathrm{b})\\+C^4(n_\mathrm{c}^2+2n_\mathrm{c}+1)}}-\underbrace{B^2n_\mathrm{tot}\langle\hat{b}^\dagger\hat{b}\rangle}_{\substack{B^4n_\mathrm{b}^2+B^2C^2n_\mathrm{b}n_\mathrm{c}\\+B^2C^2n_\mathrm{b}}}-\underbrace{C^2n_\mathrm{tot}\langle\hat{c}\hat{c}^\dagger\rangle}_{\substack{B^2C^2(n_\mathrm{b}n_\mathrm{c}+n_\mathrm{b})\\+C^4(n_\mathrm{c}^2+2n_\mathrm{c}+1)}}+n_\mathrm{tot}^2]\mathcal{F}_\mathcal{C}(t).\end{aligned} \tag{2.2.39}$$

After simplifying Eq. (2.2.39), we obtain the correlation function

$$\begin{aligned}\mathcal{C}^{\mathrm{jpa}}(t) =& [G^2n_\mathrm{b}^2+G^2n_\mathrm{b}+G(G-1)n_\mathrm{b}+2G(G-1)n_\mathrm{b}n_\mathrm{c}\\&+(G-1)^2n_\mathrm{c}^2+(G-1)^2n_\mathrm{c}+G(G-1)n_\mathrm{c}+G(G-1)]\mathcal{F}_\mathcal{C}(t)\,,\end{aligned} \tag{2.2.40}$$

which approaches the variance $n_\mathrm{b}^2+n_\mathrm{b}$ of a thermal state for $G\mapsto 1$ (no amplification). For strong amplification ($G\gg 1$), we obtain

$$\mathcal{C}^{\mathrm{jpa}}(t) = G^2[n_\mathrm{b}+n_\mathrm{c}+1]^2\mathcal{F}_\mathcal{C}(t)\,. \tag{2.2.41}$$

2.3 Circuit QED

While in cavity quantum electrodynamics (QED) real atoms are used to study light-matter interaction [7] as depicted in Fig. 2.23 (a), electrical circuits are used in circuit QED experiments [16, 17, 26] as depicted in Fig. 2.23 (b). In these experiments, superconducting qubits play the role of artificial atoms while a superconducting resonator provides the quantized modes of the electromagnetic field with typical frequencies in the microwave regime. In this section, we introduce a general framework for light-matter interaction in Sec. 2.3.1. In Sec. 2.3.2, we derive the dipole and quadrupole coupling between quantized field modes and superconducting qubits. Finally, we discuss selection rules and the appearance of sidebands in Sec. 2.3.3.

2.3.1 Interaction between light and a two-level system

In a general context, the interaction between light and a two-level system can be described within the quantum Rabi model [171]. In this model, a quantum two-level system, represented by the Hamiltonian in Eq. (2.1.2), couples to a quantized resonator mode, represented by the Hamiltonian in Eq. (2.2.8). In the absence of loss terms, the quantum Rabi Hamiltonian [172]

$$\mathcal{H}_\mathrm{QR} = \frac{\hbar\omega_\mathrm{q}}{2}\hat{\sigma}_z+\hbar\omega_\mathrm{r}\left(\hat{a}^\dagger\hat{a}+\frac{1}{2}\right)+\underbrace{\hbar g\left(\hat{\sigma}_+ +\hat{\sigma}_-\right)\left(\hat{a}+\hat{a}^\dagger\right)}_{\mathcal{H}_\mathrm{int}} \tag{2.3.1}$$

describes a coherent coupling between the two entities. The corresponding interaction Hamiltonian $\mathcal{H}_\mathrm{int}$ is based on the qubit raising and lowering operators $\hat{\sigma}_+$ and $\hat{\sigma}_-$, respectively. In Eq. (2.3.1), the coupling rate g describes the interaction strength between the

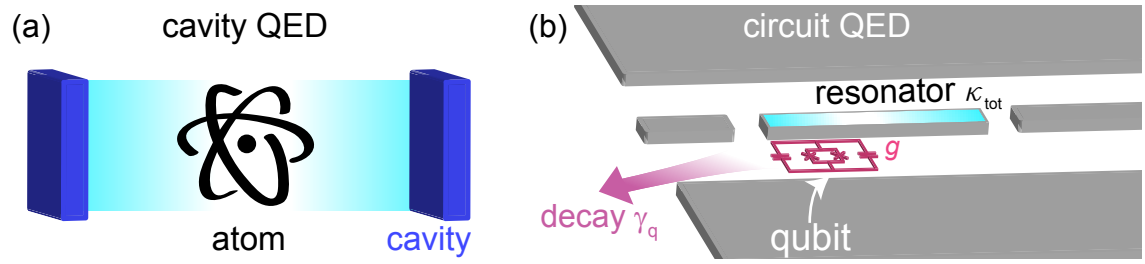

Figure 2.23: **(a)** Typical cavity QED setup, where a real atom is placed inside an optical cavity. **(b)** Typical setup for a circuit QED experiment, where an artificial atom (qubit) is placed inside a superconducting resonator. This setup is well-suited to reach the strong coupling limit, where qubit decay rate γ_q and resonator loss κ_{tot} are smaller than the mutual coupling g.

quantized field and the qubit. In the strong coupling regime, where the coupling rate is larger than all loss rates of the system but significantly lower than all eigenfrequencies, the quantum Rabi model can conveniently be approximated by the Jaynes-Cummings model [173] with corresponding Hamiltonian

$$\mathcal{H}_{JC} = \frac{\hbar\omega_q}{2}\hat{\sigma}_z + \hbar\omega_r\left(\hat{a}^\dagger\hat{a} + \frac{1}{2}\right) + \underbrace{\hbar g(\hat{\sigma}_+\hat{a} + \hat{\sigma}_-\hat{a}^\dagger)}_{\mathcal{H}_{int}} . \tag{2.3.2}$$

In the Jaynes-Cummings Hamiltonian, we can either excite the qubit by absorbing a photon ($\hat{\sigma}_+\hat{a}$) or take one excitation from the qubit and generate a photon ($\hat{\sigma}_-\hat{a}^\dagger$). In the basis of the uncoupled qubit and resonator eigenstates $|e,n_r\rangle$ and $|g,n_r+1\rangle$ using the resonator photon number n_r, the system Hamiltonian [17]

$$\mathcal{H}_{JC,n} = \frac{\hbar}{2}\begin{pmatrix} 2n_r\omega_r + \omega_q & g\sqrt{n_r+1} \\ g\sqrt{n_r+1} & (n_r+1)\omega_r - \omega_q \end{pmatrix} . \tag{2.3.3}$$

yields the eigenfrequencies $\omega_{\pm,n} = (n_r + 1/2)\omega_r \pm 1/2\sqrt{\delta^2 + 4g^2(n_r+1)}$ and the ground state is $\omega_{-,0} = -\delta/2$. Here, $\delta \equiv \omega_q - \omega_r$ is the detuning between the bare qubit and the resonator eigenfrequency. The eigenfrequencies of Eq. (2.3.3) show that there is a finite coupling between the eigenstates of the uncoupled system depending strongly on the detuning δ as depicted in Fig. 2.24. The new dressed eigenstates of the system are the superposition states $|+,n_r\rangle = \cos\Theta_{n_r}|e,n_r\rangle + \sin\Theta_{n_r}|g,n_r\rangle$ and $|-,n_r\rangle = \cos\Theta_{n_r}|g,n_r+1\rangle - \sin\Theta_{n_r}|e,n_r\rangle$. Here, the mixing angle $\Theta_n = \tan^{-1}(2g\sqrt{n_r+1}/\delta)/2$ is a measure for the degree of entanglement between qubit and resonator states.

Resonant regime When qubit and light mode are on resonance, i.e., $\delta \simeq 0$, the mixing angle $\Theta_n = \pi/4$ is maximum and consequently there is strong entanglement. In this regime, a coherent exchange of excitations between qubit and resonator occurs with the vacuum Rabi frequency $2g$. This interaction lifts the degeneracy of the corresponding eigenenergies by $2g\sqrt{n_r+1}$ to the new doublet eigenstates shown in Fig. 2.24 (a).

Dispersive regime In the dispersive regime, the detuning between qubit and resonator frequency is much larger than the coupling, i.e., $\delta \gg g$. In this regime, there is no exchange of excitations anymore but virtual photons mediate a dispersive interaction between qubit and light field. This interaction leads to frequency shifts of the qubit and resonator eigenfrequencies. The dressed states are either more photon-like or more atom-like. For the atom-like

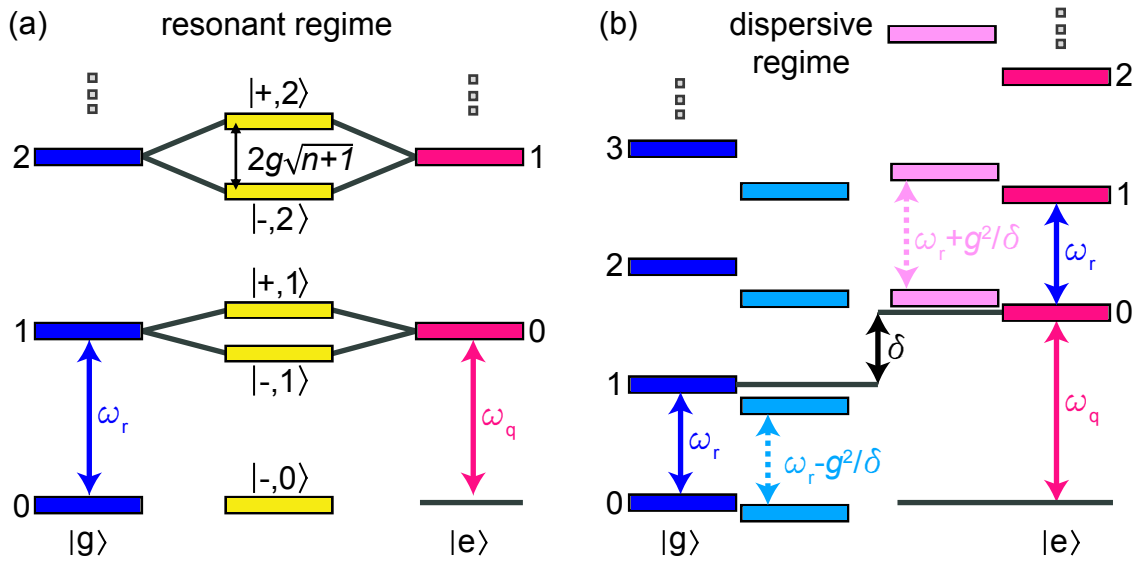

Figure 2.24: **(a)** Jaynes-Cummings ladder in the resonant regime where $\omega_\mathrm{r} \simeq \omega_\mathrm{q}$ and thus $\delta \simeq 0$. The strong coupling between the qubit and resonator states results in symmetric and antisymmetric superposition states (dressed states) with eigenenergies separated by $2g\sqrt{n_\mathrm{r}+1}$ thereby lifting the degeneracy of the uncoupled states. **(b)** Jaynes-Cummings ladder in the dispersive regime for the specific case $\omega_\mathrm{q} > \omega_\mathrm{r}$, i.e., a positive detuning δ. Then, the resonator states experience a downward shift when the qubit is in $|\mathrm{g}\rangle$ and an upward shift when the qubit is in $|\mathrm{e}\rangle$ by $\pm\,(2n+1)\,g^2/\delta$.

states, we use the unitary transformation $\mathcal{U}\mathcal{H}_\mathrm{JC}\mathcal{U}^\dagger$ with $\mathcal{U} = \exp\left[(g/\delta)\left(\hat{a}\hat{\sigma}_+ - \hat{a}^\dagger\hat{\sigma}_-\right)\right]$ to calculate the dispersive Jaynes-Cummings Hamiltonian [17]

$$\mathcal{H}_\mathrm{disp} \approx \hbar\omega_\mathrm{r}\left(\hat{a}^\dagger\hat{a} + 1/2\right) + \hbar/2\left(\omega_\mathrm{q} + 2\chi\hat{a}^\dagger\hat{a} + \chi\right)\hat{\sigma}_\mathrm{z}\,. \tag{2.3.4}$$

As apparent from Eq. (2.3.4), the qubit transition frequency ω_q has a constant Lamb shift $\chi \equiv g^2/\delta$ and further depends on the photon-number defined by the ac-Stark shift $2\chi\langle\hat{a}^\dagger\hat{a}\rangle$ [cf. Fig. 2.24 (b)]. In the photon-like case, we obtain the effective Hamiltonian [6]

$$\mathcal{H}_\mathrm{disp,r} \approx \hbar\omega_\mathrm{q}\hat{\sigma}_\mathrm{z}/2 + \hbar\left(\omega_\mathrm{r} + \chi\hat{\sigma}_\mathrm{z}\right)\left(\hat{a}^\dagger\hat{a} + 1/2\right)\,, \tag{2.3.5}$$

describing the qubit state-dependent resonator frequency, which we use for readout purposes. Because a transmon qubit is no true two-level system and has only a small anharmonicity α, the dispersive shift becomes [40] $\chi \equiv [g^2/\delta][\alpha/(\delta+\alpha)]$ because higher qubit levels have a significant influence.

Coupling between transmon qubit and resonator Due to its large shunt capacitors, a transmon qubit has a dominating electric dipole moment that couples to the oscillating electric field of the resonator. When calculating the coupling strength, it is convenient to return to a circuit representation of the system such as the one given in Fig. 2.25. The transmon qubit couples to the oscillating gate voltage [174] $V_\mathrm{g} = V_\mathrm{vac}(\hat{a}^\dagger + \hat{a})$ of the resonator. Here, $V_\mathrm{vac} = (\hbar\omega_\mathrm{r}/2C_\mathrm{r})^{1/2}$

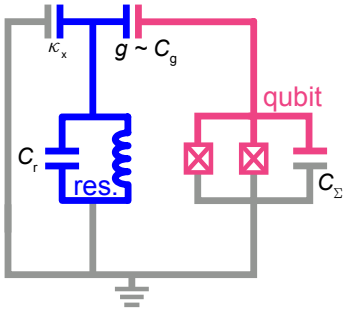

Figure 2.25: Equivalent circuit diagram of a transmon qubit coupled capacitively to a resonator, which itself is coupled to a readout line.

is the vacuum rms voltage of the resonator, which has a capacitance C_r. The coupling is mediated via the effective gate capacitance C_g between qubit and resonator. This capacitance results in the vacuum coupling strength [40]

$$\hbar g = \sqrt{2}\frac{C_\mathrm{g}}{C_\Sigma}\left(\frac{E_\mathrm{J}}{8E_\mathrm{c}}\right)^{1/4} eV_\mathrm{vac}\,, \tag{2.3.6}$$

where C_Σ is the total capacitance of the qubit.

2.3.2 Coupling between gradio qubit and resonator

So far, we have encountered light-matter interaction by assuming a point-like dipole coupling $\boldsymbol{\mu}\cdot\mathbf{H}_\mathrm{r}$ between the qubit dipole moment $\boldsymbol{\mu}$ and the resonator generating an oscillating field with amplitude $\mathbf{H}_\mathrm{r}$.[4] In this context, point-like means that the wavelength of the oscillating field is much larger than the qubit size. Further, dipole coupling means that the oscillating field is described in the far field approximation. In this approximation, a plane wave with constant amplitude represents the oscillating field. For a micrometer-sized qubit, the dipole approximation is justified and we can straightforwardly derive the dipole coupling. To this end, we apply a quantum model of the electric dipole coupling by using the quantum mechanical equivalents $\boldsymbol{\mu}\mapsto\langle\mathrm{e}|\boldsymbol{\mu}|\mathrm{g}\rangle\,(\hat{\sigma}_+ + \hat{\sigma}_-)$ and $\mathbf{H}_\mathrm{r}\mapsto H_\mathrm{vac}\mathbf{e}_\mathrm{z}(\hat{a}+\hat{a}^\dagger)$ [174]. Here, we use the vacuum magnetic field strength H_vac as well as the vector $\mathbf{e}_\mathrm{z}$ along the quantization axis of the qubit. Restating the dipole interaction in the quantum mechanical formalism reproduces the interaction Hamiltonian $\mathcal{H}_\mathrm{int} = \hbar g(\hat{\sigma}_+ + \hat{\sigma}_-)(\hat{a}+\hat{a}^\dagger)$ [see Eq. (2.3.1)] with single photon dipole coupling constant $g = \langle\mathrm{e}|\boldsymbol{\mu}|\mathrm{g}\rangle\, H_\mathrm{vac}\mathbf{e}_\mathrm{z}/\hbar$.
Generally, the coupling accounts also for higher magnetic moments of the qubit, such as the quadrupole moment $\mathbf{Q}$ introduced in Sec. 2.1.6. Furthermore, the oscillating field generated by the resonator can have a field gradient $\nabla\mathbf{H}_\mathrm{r}$ across the qubit area. The two most symmetric coupling schemes between a gradio qubit and a CPW resonator are sketched in Fig. 2.26 (a) and Fig. 2.26 (b). While in Fig. 2.26 (a), the oscillating current creates a field gradient coupling to $\hat{\sigma}_\mathrm{z}$ (transverse), in Fig. 2.26 (b) the magnetic field couples only into the SQUID loop resulting in a longitudinal $\hat{\sigma}_\mathrm{x}$ coupling. In the following, we focus on the transverse coupling scheme but we account for imbalances of the magnetic moments of the qubit (see Sec. 2.1.6 for details). The interaction Hamiltonian obtained from a standard multipole expansion [175, 176] can thus be written as

$$\mathcal{H}_\mathrm{int}/\mu_0 = \overbrace{[\mathbf{Q}\cdot\nabla\mathbf{H}_\mathrm{r}]\hat{\sigma}_\mathrm{z}}^{\text{(i): } g_\mathrm{t}} + \overbrace{[\mathbf{Q}_\mathrm{im}\cdot\nabla\mathbf{H}_\mathrm{r}]\hat{\sigma}_\mathrm{x} + [\boldsymbol{\mu}_\mathrm{sq}\cdot\mathbf{H}_\mathrm{r}]\hat{\sigma}_\mathrm{x}}^{\text{(ii): } g_\ell} + \overbrace{[\boldsymbol{\mu}_\mathrm{im}\cdot\mathbf{H}_\mathrm{r}]\hat{\sigma}_\mathrm{z} + \mathcal{O}(\nabla^2\cdot\mathbf{H}_\mathrm{r})}^{\text{(iii): } \approx 0}\,. \tag{2.3.7}$$

In the following, we discuss the three contributions (i) - (iii) highlighted in Eq. (2.3.7).

Transverse coupling The first contribution (i) in Eq. (2.3.7) is related to the transverse coupling strength g_t, which is the intended coupling in the scheme depicted in Fig. 2.26 (a). Hence, this coupling strength is dominating while the contributions from (ii) and (iii) are perturbative corrections. The transverse coupling to the $\hat{\sigma}_\mathrm{z}$ degree of freedom is provided by the field gradient $\nabla\mathbf{H}_\mathrm{r}$ generated by the resonator current, which changes the qubit phase φ_q defined between the two points p_1 and p_2. For the transverse coupling scheme, the

[4] Even though we are discussing the coupling between an electric dipole moment $\mathbf{d}$ and an electric field $\mathbf{E}$ so far, it can be shown [106] that this mechanism is equivalent to an magnetic dipole coupling $\boldsymbol{\mu}\cdot\mathbf{H}_\mathrm{r}$.

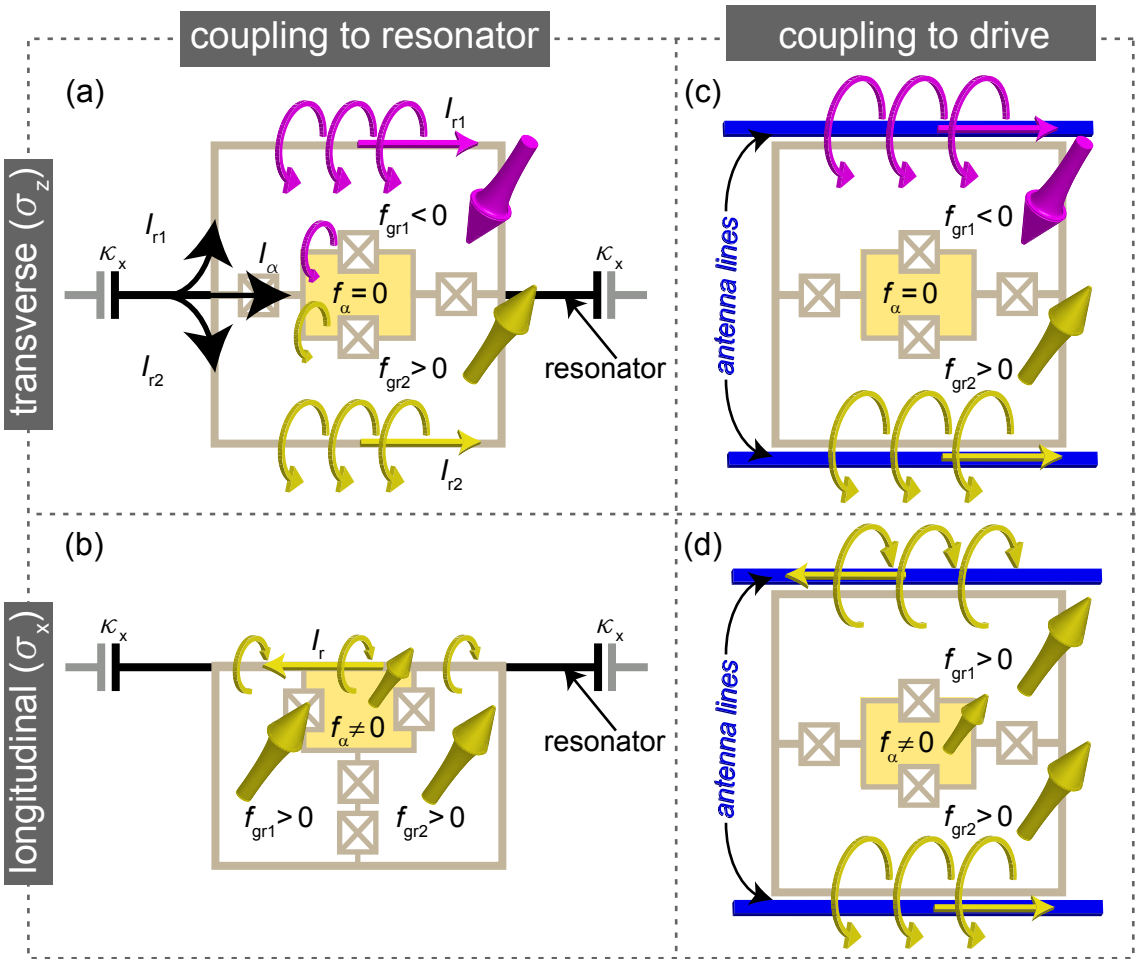

Figure 2.26: **(a)** Transverse coupling scheme and resulting current flow for a gradio qubit coupled to a resonator. **(b)** As in panel (a) but for longitudinal coupling. **(c)** Transverse coupling scheme between a gradient drive field and a gradio qubit. **(d)** As in panel (c) but for longitudinal coupling to a homogeneous drive field.

total resonator current $I_\mathrm{r} = I_\mathrm{vac}(\hat{a}+\hat{a}^\dagger)$ splits up into the three currents $I_\mathrm{r} = I_{\mathrm{r}1} + I_{\mathrm{r}2} + I_\alpha$. As depicted in Fig. 2.26 (a) each of these currents contributes to the total field gradient. We can calculate the individual currents $I_{\mathrm{r}j} = I_\mathrm{r} L_\mathrm{tot}/(L_{\mathrm{k}j} + L_{\mathrm{g}j})$, where $j = 1, 2, \alpha$. Here,

$$L_\mathrm{tot} = \left[\frac{1}{L_{\mathrm{k}1}+L_{\mathrm{g}1}} + \frac{1}{L_{\mathrm{k}2}+L_{\mathrm{g}2}} + \frac{1}{L_{\mathrm{k}\alpha}+L_{\mathrm{g}\alpha}+\sum_\mathrm{junctions} L_\mathrm{J}}\right]^{-1} \tag{2.3.8}$$

is the total inductance. Because the sum of the Josephson junction inductance dominates the loop inductance of the two gradiometer loops, the value of I_α is negligible. Furthermore, we assume equal values $I_{\mathrm{r}1} = I_{\mathrm{r}2} = I_\mathrm{r}/2$ and equal inductance values $L_{\mathrm{k}1} + L_{\mathrm{g}1} = L_{\mathrm{k}2} + L_{\mathrm{g}2}$. Therefore, the resonator current induces a flux difference $\delta\Phi_\mathrm{gr} = (L_{\mathrm{k}1} + L_{\mathrm{g}1})(I_\mathrm{vac}/2)(\hat{a}+\hat{a}^\dagger)$ and the field gradient reads $\mu_0 \nabla \mathbf{H}_\mathrm{r} = \delta\Phi_\mathrm{gr}/(A_\ell s)$, where $A_\ell s$ is the geometry factor defined in Sec. 2.1.6. Deviations from these assumptions generate an effective homogeneous field $\mathbf{H}_\mathrm{r}$, which introduces a longitudinal coupling as discussed below. Together with the quadrupole moment $\mathbf{Q} = A_\ell s (I_\mathrm{p}/2)$ defined in the same section, the transverse interaction Hamiltonian

in the bare basis reads as

$$\mathcal{H}_{\mathrm{int,t}} = (L_{\mathrm{k1}} + L_{\mathrm{g1}})\frac{I_{\mathrm{vac}}}{2}\frac{I_{\mathrm{p}}}{2}(\hat{a}+\hat{a}^\dagger)\hat{\sigma}_{\mathrm{z}} \equiv \hbar g_{\mathrm{t}}(\hat{a}+\hat{a}^\dagger)\hat{\sigma}_{\mathrm{z}}\,. \tag{2.3.9}$$

This interaction Hamiltonian has the same form as the interaction Hamiltonian for a regular flux qubit coupled to a resonator [26].

Longitudinal coupling The second part (ii) in Eq. (2.3.7) describes a longitudinal coupling between qubit and resonator. Both terms, $\mathbf{Q}_{\mathrm{im}} \cdot \nabla \mathbf{H}_{\mathrm{r}}$ and $\boldsymbol{\mu}_{\mathrm{sq}} \cdot \mathbf{H}_{\mathrm{r}}$, are strongly suppressed compared to the transverse coupling strength g_{t}. The gradient term is suppressed because it couples only to the qubit imbalance and the dipolar term is suppressed because the resonator does not create a homogeneous field to first order.
However, a real gradiometer has imbalances between the two loops due to fabrication imperfections [83, 177, 178] resulting in a homogeneous field $\mathbf{H}_{\mathrm{r}}$. This field induces a net frustration $\delta f_{\alpha,\mathrm{gr}} = \delta M_{\alpha,\mathrm{gr}} I_{\mathrm{vac}}(\hat{a}+\hat{a}^\dagger)/\Phi_0$ due to the dipole moment $\boldsymbol{\mu}_{\mathrm{sq}}$ of the α-SQUID. Here, $\delta M_{\alpha,\mathrm{gr}}$ is the difference between the mutual inductance $M_{\alpha 1} - M_{\alpha 2}$ between the SQUID and each gradiometer loop. This difference can be made as small as 0.2 % [83] by standard fabrication processes resulting in a negligible cross coupling. We expect a stronger effect of longitudinal coupling if a finite current I_α ($\propto \nabla \mathbf{H}_{\mathrm{r}}$) splits asymmetrically into the SQUID arms because of different inductance values of the two SQUID junctions. This effect results in a finite quadrupole imbalance $\mathbf{Q}_{\mathrm{im}}$, which converts a field gradient into additional flux through the SQUID loop. We assume that the current I_α across the SQUID splits proportional to the asymmetry factor $\delta L_{\mathrm{J}\alpha} = |L_{\mathrm{J}\alpha 1} - L_{\mathrm{J}\alpha 2}|$ and the longitudinal interaction reads

$$\mathcal{H}_{\mathrm{int},\ell} = \delta L_{\mathrm{J}\alpha} I_\alpha I_{\mathrm{vac}}(\hat{a}+\hat{a}^\dagger)\hat{\sigma}_{\mathrm{x}} \equiv \hbar g_\ell(\hat{a}+\hat{a}^\dagger)\hat{\sigma}_{\mathrm{x}}\,. \tag{2.3.10}$$

For realistic parameters $\delta L_{\mathrm{J}\alpha} = 100\,\mathrm{pH}$, $I_{\mathrm{vac}} = 20\,\mathrm{nA}$, $I_\alpha = 1\,\mathrm{nA}$, we obtain a longitudinal coupling strength $g_\ell/2\pi \simeq 3\,\mathrm{MHz}$. At the degeneracy point ($\varepsilon = 0$), a qubit-resonator system with purely longitudinal coupling in the bare basis is described as

$$\mathcal{H}_{\mathrm{sys,b}} = \frac{\hbar\Delta}{2}\hat{\sigma}_{\mathrm{x}} + \hbar\omega_{\mathrm{r}}\hat{a}^\dagger\hat{a} + \hbar g_\ell(\hat{a}+\hat{a}^\dagger)\hat{\sigma}_{\mathrm{x}}\,. \tag{2.3.11}$$

For this Hamiltonian, we cannot perform the usual transformation into the dispersive Jaynes-Cummings Hamiltonian. Instead, we rotate into the qubit eigenbasis and perform a polaron transformation [179–182] $\tilde{\mathcal{H}}_{\mathrm{sys,q}} = \mathcal{U}\mathcal{H}_{\mathrm{sys,b}}\mathcal{U}^\dagger$ using $\mathcal{U} = \exp\left[\hat{\sigma}_{\mathrm{z}}(\hat{a}^\dagger - \hat{a})g_\ell/\omega_{\mathrm{r}}\right]$. This transformation exactly diagonalizes the system Hamiltonian defined in Eq. (2.3.11) to the energy eigenbasis [183, 184]

$$\tilde{\mathcal{H}}_{\mathrm{sys,q}} = \frac{\hbar\Delta}{2}\hat{\sigma}_{\mathrm{z}} + \hbar\omega_{\mathrm{r}}\hat{a}^\dagger\hat{a} - \frac{g_\ell^2}{\omega_{\mathrm{r}}}\mathbb{1}\,. \tag{2.3.12}$$

This Hamiltonian exhibits no qubit-state-dependent ac-Stark shift but a constant frequency shift $g_\ell^2/\omega_{\mathrm{r}}$.

System Hamiltonian The last therm (iii) in Eq. (2.3.7) is negligible because it is a product of two second-order contributions. First, the resonator does not generate a strong homogeneous fiel $\mathbf{H}_\mathrm{r}$, and second the imbalance dipole element $\boldsymbol{\mu}_\mathrm{im}$ is small. Therefore, the system Hamiltonian in the bare basis reads as

$$\begin{aligned}\mathcal{H}_\mathrm{sys,b} =& \mathcal{H}_\mathrm{q} + \mathcal{H}_\mathrm{r} + \mathcal{H}_\mathrm{int,t} + \mathcal{H}_\mathrm{int,\ell} \\ =& \frac{\hbar\Delta}{2}\hat{\sigma}_\mathrm{x} + \frac{\hbar\varepsilon}{2}\hat{\sigma}_\mathrm{z} + \hbar\omega_\mathrm{r}\hat{a}^\dagger\hat{a} + \hbar g_\mathrm{t}(\hat{a}+\hat{a}^\dagger)\hat{\sigma}_\mathrm{z} + \hbar g_\ell(\hat{a}+\hat{a}^\dagger)\hat{\sigma}_\mathrm{x}\,. \end{aligned} \tag{2.3.13}$$

Because the transverse coupling dominates over the longitudinal coupling $g_\mathrm{t} \gg g_\ell$, we use the standard Jaynes-Cummings notation and transfer Eq. (2.3.13) to the eigenbasis of the qubit

$$\begin{aligned}\mathcal{H}_\mathrm{sys,q} =& \frac{\hbar\omega_\mathrm{q}}{2}\hat{\sigma}_\mathrm{z} + \hbar\omega_\mathrm{r}\hat{a}^\dagger\hat{a} \\ &+ \hbar g_\mathrm{t}\cos\theta(\hat{a}+\hat{a}^\dagger)\hat{\sigma}_\mathrm{z} - \hbar g_\mathrm{t}\sin\theta(\hat{a}+\hat{a}^\dagger)\hat{\sigma}_\mathrm{x} \\ &+ \hbar g_\ell\cos\theta(\hat{a}+\hat{a}^\dagger)\hat{\sigma}_\mathrm{x} + \hbar g_\ell\sin\theta(\hat{a}+\hat{a}^\dagger)\hat{\sigma}_\mathrm{z}\,, \end{aligned} \tag{2.3.14}$$

where we use the Bloch angle $\theta = \tan^{-1}(\Delta/\varepsilon)$ and $\omega_\mathrm{q} = \sqrt{\Delta^2+\varepsilon^2}$. At the degeneracy point, we find $\theta = \pi/2$ and $\{\cos\theta, \sin\theta\} = \{0, 1\}$.

2.3.3 Selection rules

A selection rule constrains the possible transition between two qubit states induced by an external drive due to the conservation of several quantum numbers such as angular momentum or parity [51]. Originating from quantum optics, these rules are also valid for circuit QED experiments [42, 106, 185, 186]. For electromagnetically induced transitions, the parity $\hat{\Pi}$ of initial and final state separates between forbidden and allowed transitions. For flux qubits, the ground state $|\mathrm{g}\rangle$ has even parity, while the excited state $|\mathrm{e}\rangle$ has odd parity [95]. In the same way as for $\hat{\Pi}$, we define an even operator $\hat{A}_+$ if it commutes with $|\mathrm{g}\rangle$ and vice versa. Even operators cannot induce transitions between states of different parities, which is expressed in the vanishing matrix element

$$\langle \mathrm{e}|\hat{A}_+|\mathrm{g}\rangle = 0\,. \tag{2.3.15}$$

On the other hand, an odd operator $\hat{A}_-$ can induce transitions between $|\mathrm{g}\rangle$ and $|\mathrm{e}\rangle$, i.e.,

$$\langle \mathrm{e}|\hat{A}_-|\mathrm{g}\rangle \neq 0\,. \tag{2.3.16}$$

In the following, we analyze transitions between the qubit ground and excited states based on the parity of the drive field. We describe this field quantum mechanically with the odd parity dipole operator $(\hat{d}^\dagger + \hat{d})$. Consequently, transitions between different qubit states can be treated as electric-dipole transitions in natural atoms [106]. This means, according to Eq. (2.3.15) and Eq. (2.3.16), one-photon assisted transitions are allowed for dipolar qubits as shown in Fig. 2.27 (a). If the qubit is not at its degeneracy point, the parity of the Jaynes-Cummings Hamiltonian is not well-defined and one- and multi-photon transitions are allowed [cf. Fig. 2.27 (b)].
For the tunable gradiometric flux qubit, these selection rules do no longer follow this simple picture because the qubit has a dipole moment coupling to $\hat{\sigma}_\mathrm{x}$ and a quadrupole

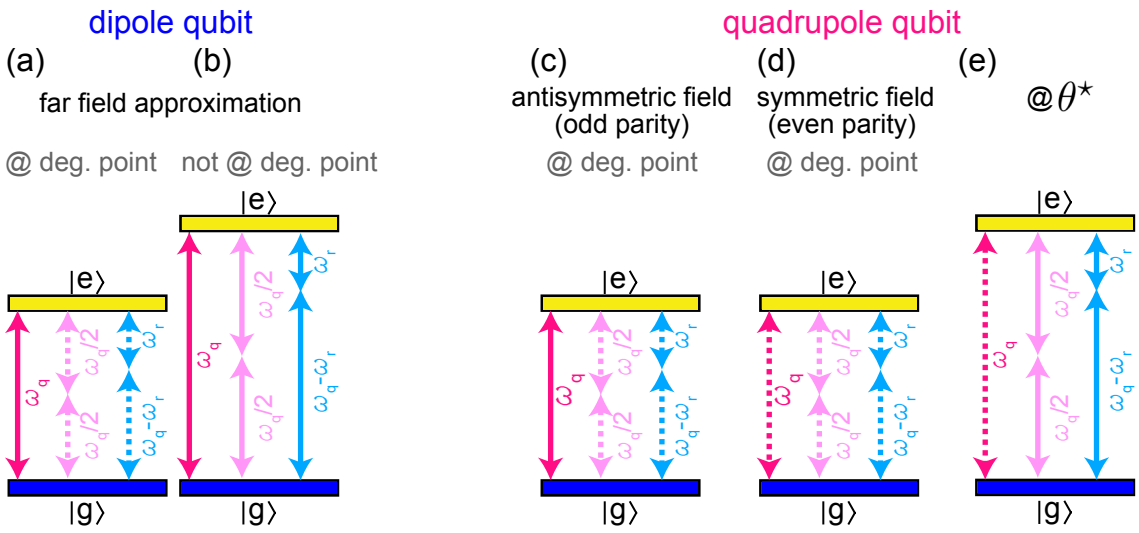

Figure 2.27: Selection rules for one- and multi-photon transitions for a dipole qubit **[(a),(b)]** and a quadrupole qubit **[(c)-(e)]**. Solid lines indicate allowed transitions while dashed lines represent forbidden transitions.

moment coupling to $\hat{\sigma}_z$. At the qubit degeneracy point, state transitions are excited by an antisymmetric field $\nabla\mathbf{H}_d$ depicted in Fig. 2.26 (c), while a (weak) symmetric drive depicted in Fig. 2.26 (d) has no effect. As shown in Fig. 2.27 (c) and Fig. 2.27 (d), two-photon assisted transitions are neither allowed for antisymmetric nor for symmetric drives. In the following, we derive a quantitative description of the transition matrix elements. In particular, we find a certain operating point $\theta^\star$ away from the degeneracy point, where dipolar and quadrupolar drive cancel each other [see Fig. 2.27 (e)].

One-photon transitions under a mixed drive For the gradio qubit placed between two antennas as depicted in Fig. 2.26 (c) and (d), we can drive the $\hat{\sigma}_x$ term in Eq. (2.3.13) with a symmetric, in the ideal case spatially homogeneous, microwave drive $(\mathbf{H}_d) = (0,0,H_z)$. Furthermore, we can drive the $\hat{\sigma}_z$ term with an antisymmetric, i.e., purely gradient microwave drive $(\nabla\mathbf{H}_d) = (0,0,\tilde{H}_z y)$. We describe the two drives in terms of their creation and annihilation operators $\hat{\ell}^\dagger,\hat{\ell}$ (longitudinal drive) and $\hat{t}^\dagger,\hat{t}$ (transversal drive), respectively. Hence, the operator $\hat{\ell}$ creates a symmetric field distribution, while $\hat{t}$ creates an antisymmetric field distribution. The respective interaction can be expressed as

$$\mathcal{H}_{\mathrm{int},\ell} = \hbar g_{\ell,\mathrm{d}} e^{i\omega_\mathrm{d} t}(\hat{\ell}^\dagger + \hat{\ell})\hat{\sigma}_x \overset{\text{c.l.}}{\approx} \hbar\frac{\Omega_\ell}{2}\cos(\omega_\mathrm{d} t)\hat{\sigma}_x\,, \tag{2.3.17}$$

$$\mathcal{H}_{\mathrm{int,t}} = \hbar g_{\mathrm{t,d}} e^{i\omega_\mathrm{d} t}(\hat{t}^\dagger + \hat{t})\hat{\sigma}_z \overset{\text{c.l.}}{\approx} \hbar\frac{\Omega_\mathrm{t}}{2}\cos(\omega_\mathrm{d} t)\hat{\sigma}_z\,. \tag{2.3.18}$$

Here, $g_{\ell,\mathrm{d}}$ and $g_{\mathrm{t,d}}$ denote the longitudinal and transversal vacuum coupling strength between the microwave drive and the qubit, respectively. In the classical limit (c.l.) on the right hand side, the drive is expressed as a coherent state $|\beta_{\ell,\mathrm{t}}\rangle$, where $\hat{\ell}\,|\beta_\ell\rangle = \beta_\ell\,|\beta_\ell\rangle$ and $\hat{t}\,|\beta_\mathrm{t}\rangle = \beta_\mathrm{t}\,|\beta_\mathrm{t}\rangle$. That way, the drives with frequency ω_d are characterized by their amplitudes $\Omega_\ell = 4\hbar g_{\ell,\mathrm{d}}\beta_\ell$ and $\Omega_\mathrm{t} = 4\hbar g_{\mathrm{t,d}}\beta_\mathrm{t}$, respectively. Then, applied to the eigenstates $|\mathrm{g_{gq}}\rangle$ and $|\mathrm{e_{gq}}\rangle$ defined in Sec. 2.1.6, one finds that $\hat{\Omega}_\ell$ has even parity and $\hat{\Omega}_\mathrm{t}$ has odd parity at the degeneracy point of the gradio qubit. For a superposition of both drives and away from the degeneracy point, however, the parity is not well-defined and transitions

can occur as discussed below.
In the following calculations, we derive transition matrix elements for qubit transitions under a mixed $(\Omega_\ell + \Omega_\mathrm{t})$ drive. We find that the selection rules known for circuit QED setups [185] must be modified taking the longitudinal drive into account. We start our calculations by adding the two drives to the system Hamiltonian defined in Eq. (2.3.13), which results in the bare basis to

$$\begin{aligned}\mathcal{H}_\mathrm{sys,b} = \frac{\hbar\Delta}{2}\hat{\sigma}_\mathrm{x} + \frac{\hbar\varepsilon}{2}\hat{\sigma}_\mathrm{z} + \hbar\omega_\mathrm{r}\hat{a}^\dagger\hat{a} + \hbar g_\mathrm{t}(\hat{a}+\hat{a}^\dagger)\hat{\sigma}_\mathrm{z} + \hbar g_\ell(\hat{a}+\hat{a}^\dagger)\hat{\sigma}_\mathrm{x} \\ + \frac{\hbar\Omega_\mathrm{t}}{2}\cos(\omega_\mathrm{d}t)\hat{\sigma}_\mathrm{z} + \frac{\hbar\Omega_\ell}{2}\cos(\omega_\mathrm{d}t)\hat{\sigma}_\mathrm{x}\,. \end{aligned} \tag{2.3.19}$$

Because we want to analyze qubit transitions, we restate the latter Hamiltonian in the energy eigenbasis of the qubit, i.e.,

$$\begin{aligned}\mathcal{H}_\mathrm{sys,q} = \frac{\hbar\omega_\mathrm{q}}{2}\hat{\sigma}_\mathrm{z} + \hbar\omega_\mathrm{r}\hat{a}^\dagger\hat{a} \\ + \hbar g_\mathrm{t}\cos\theta(\hat{a}+\hat{a}^\dagger)\hat{\sigma}_\mathrm{z} - \hbar g_\mathrm{t}\sin\theta(\hat{a}+\hat{a}^\dagger)\hat{\sigma}_\mathrm{x} \\ + \hbar g_\ell\cos\theta(\hat{a}+\hat{a}^\dagger)\hat{\sigma}_\mathrm{x} + \hbar g_\ell\sin\theta(\hat{a}+\hat{a}^\dagger)\hat{\sigma}_\mathrm{z} \\ + \frac{\hbar\Omega_\mathrm{t}}{2}\cos\theta\cos(\omega_\mathrm{d}t)\hat{\sigma}_\mathrm{z} - \frac{\hbar\Omega_\mathrm{t}}{2}\sin\theta\cos(\omega_\mathrm{d}t)\hat{\sigma}_\mathrm{x} \\ + \frac{\hbar\Omega_\ell}{2}\cos\theta\cos(\omega_\mathrm{d}t)\hat{\sigma}_\mathrm{x} + \frac{\hbar\Omega_\ell}{2}\sin\theta\cos(\omega_\mathrm{d}t)\hat{\sigma}_\mathrm{z}\,. \end{aligned} \tag{2.3.20}$$

Next, we cancel the time-dependent terms $1/2\Omega_\mathrm{t}\cos\theta\cos(\omega_\mathrm{d}t)\hat{\sigma}_\mathrm{z}$ and $1/2\Omega_\ell\sin\theta\cos(\omega_\mathrm{d}t)\hat{\sigma}_\mathrm{z}$ by moving to a nonuniformly rotating frame, where $\mathcal{H}_\mathrm{rot} = \mathcal{U}\mathcal{H}_\mathrm{sys,q}\mathcal{U}^\dagger - \imath\hbar\partial\mathcal{U}\partial\mathcal{U}^\dagger/\partial t$, and we chose

$$\mathcal{U} = \exp\left[\frac{\imath}{2}\hat{\sigma}_\mathrm{z}\sin(\omega_\mathrm{d}t)\left(\frac{\Omega_\mathrm{t}}{\omega}\cos\theta + \frac{\Omega_\ell}{\omega}\sin\theta\right)\right]. \tag{2.3.21}$$

That way, the effective Hamiltonian reads

$$\begin{aligned}\mathcal{H}_\mathrm{rot} = \frac{\hbar\omega_\mathrm{q}}{2}\hat{\sigma}_\mathrm{z} + \hbar\omega_\mathrm{r}\hat{a}^\dagger\hat{a} + \hbar g_\mathrm{t}\cos\theta(\hat{a}+\hat{a}^\dagger)\hat{\sigma}_\mathrm{z} + \hbar g_\ell\sin\theta(\hat{a}+\hat{a}^\dagger)\hat{\sigma}_\mathrm{z} \\ + \hbar\left[g_\ell\cos\theta(\hat{a}+\hat{a}^\dagger) - g_\mathrm{t}\sin\theta(\hat{a}+\hat{a}^\dagger) + \frac{\Omega_\ell}{2}\cos\theta\cos(\omega_\mathrm{d}t) - \frac{\Omega_\mathrm{t}}{2}\sin\theta\cos(\omega_\mathrm{d}t)\right] \\ \times\left[\hat{\sigma}_+ e^{-\imath\phi} + \hat{\sigma}_- e^{+\imath\phi}\right], \end{aligned} \tag{2.3.22}$$

where $\phi = -\sin(\omega_\mathrm{d}t)(\Omega_\mathrm{t}\cos\theta + \Omega_\ell\sin\theta)/\omega_\mathrm{d}$. We now move to the interaction picture with respect to qubit and resonator, which yields in rotating wave approximation

$$\begin{aligned}\mathcal{H}_\mathrm{eff} = \hbar\Big[g_\ell\cos\theta(\hat{a}e^{-\imath\omega_\mathrm{r}t} + \hat{a}^\dagger e^{+\imath\omega_\mathrm{r}t}) - g_\mathrm{t}\sin\theta(\hat{a}e^{-\imath\omega_\mathrm{r}t} + e^{+\imath\omega_\mathrm{r}t}\hat{a}^\dagger) \\ + \frac{\Omega_\ell}{2}\cos\theta\cos(\omega_\mathrm{d}t) - \frac{\Omega_\mathrm{t}}{2}\sin\theta\cos(\omega_\mathrm{d}t)\Big] \times\left[\hat{\sigma}_+ e^{+\imath\omega_\mathrm{q}t}e^{-\imath\phi} + \hat{\sigma}_- e^{-\imath\omega_\mathrm{q}t}e^{+\imath\phi}\right]. \end{aligned}$$

We can split this interaction Hamiltonian into a qubit-resonator term $\mathcal{H}_\mathrm{eff,r}$ and into a qubit-driving term $\mathcal{H}_\mathrm{eff,q}$ given as

$$\begin{aligned}\mathcal{H}_\mathrm{eff,r} = \hbar\Big[g_\ell\cos\theta(\hat{a}e^{-\imath\omega_\mathrm{r}t} + \hat{a}^\dagger e^{+\imath\omega_\mathrm{r}t}) - g_\mathrm{t}\sin\theta(\hat{a}e^{-\imath\omega_\mathrm{r}t} + e^{+\imath\omega_\mathrm{r}t}\hat{a}^\dagger)\Big] \\ \times\left[\hat{\sigma}_+ e^{+\imath\omega_\mathrm{q}t}e^{-\imath\phi} + \hat{\sigma}_- e^{-\imath\omega_\mathrm{q}t}e^{+\imath\phi}\right] \end{aligned} \tag{2.3.23}$$

$$\mathcal{H}_\mathrm{eff,q} = \hbar\left[\frac{\Omega_\ell}{2}\cos\theta - \frac{\Omega_\mathrm{t}}{2}\sin\theta\right]\cos(\omega_\mathrm{d}t)\left[\hat{\sigma}_+ e^{+\imath\omega_\mathrm{q}t}e^{-\imath\phi} + \hat{\sigma}_- e^{-\imath\omega_\mathrm{q}t}e^{+\imath\phi}\right]. \tag{2.3.24}$$

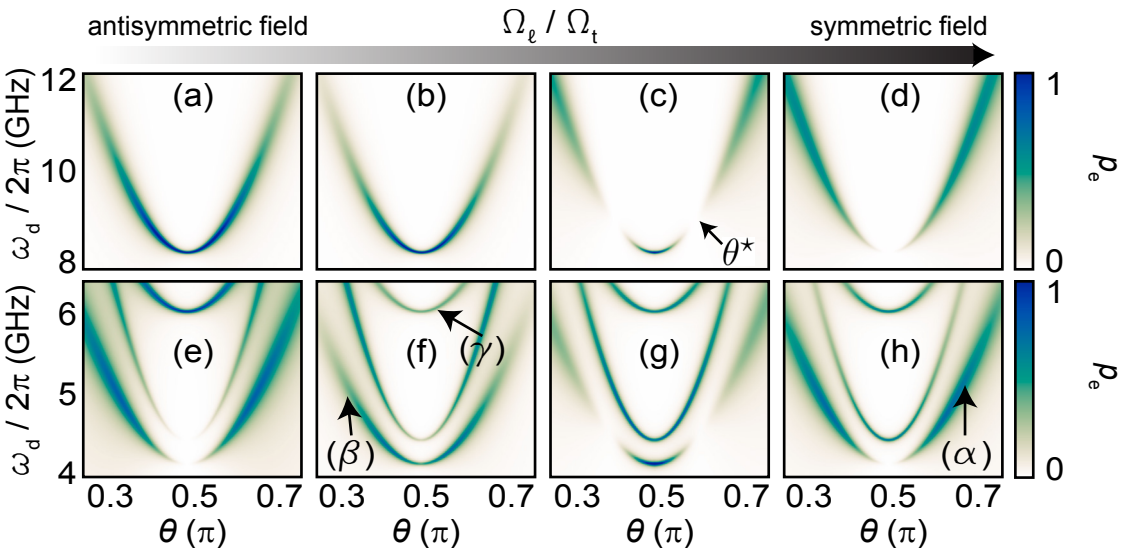

Figure 2.28: Top row from **(a)** to **(d)**: Color encoded excitation spectra for the direct one-photon transition of a quadrupolar qubit plotted versus Bloch angle θ and drive frequency. From panel (a) to panel (e) we increase the ratio $\Omega_\ell/\Omega_\mathrm{t}$. To model the qubit linewidth, we superimpose the qubit hyperbola [Eq. (2.1.21)], with a Lorentzian lineshape. In panel **(c)**, the ratio $\Omega_\ell/\Omega_\mathrm{t}$ provides the situation that there is an angle $\theta^\star$ at which longitudinal and transverse drive cancel each other. Bottom row from **(e)** to **(h)**: Color encoded excitation spectra for the two-photon process (α), the red sideband (β), and the two-photon process of the blue sideband (γ) for a resonator frequency $\omega_\mathrm{r} = 4\,\mathrm{GHz}$.

For low power (one-photon) driving, the transition Hamiltonian can be approximated using Bessel functions, which results in

$$\mathcal{H}_{\mathrm{trans},1} = \frac{\hbar}{2}\left[\frac{\Omega_\ell}{2}\cos\theta - \frac{\Omega_\mathrm{t}}{2}\sin\theta\right][J_0(\lambda) + J_2(\lambda)]\hat{\sigma}_\mathrm{x} \approx \frac{\hbar}{2}\left[\frac{\Omega_\ell}{2}\cos\theta - \frac{\Omega_\mathrm{t}}{2}\sin\theta\right]\hat{\sigma}_\mathrm{x}\,. \tag{2.3.25}$$

Here, J_k is the k^{th} Bessel function of the first kind and $\lambda = (\Omega_\mathrm{t}\cos\theta + \Omega_\ell \sin\theta)/\omega_\mathrm{d}$. Equation (2.3.25) means that we can drive one-photon transitions at the degeneracy point via an antisymmetric magnetic field due to the $\sin\theta$ term. This effect becomes weaker when we move away from the degeneracy point. However, in this case the longitudinal drive starts to activate transitions via the $\cos\theta$-term. Additionally, there is a certain angle $\theta^\star$, for which both drives cancel each other. In Figs. 2.28 (a) – (d), we show numerical calculations of the one-photon transition using Eq. (2.3.25) (with Bessel functions). Moving from (a) to (d), we increase the impact of the longitudinal drive, while staying in the low power (one-photon) limit, where $\Omega_\ell, \Omega_\mathrm{t} \ll \omega_\mathrm{r}$. As apparent, the coupling at the degeneracy point becomes weaker when increasing the ratio between longitudinal and transversal drive, implementing a controllable selection rule.

Multi-photon transitions For increasing drive power, we can activate multi-photon transitions by shining electromagnetic fields of frequency ω_q/n. In the case $n = 2$, the two photons have frequency $\omega_\mathrm{d} = \omega_\mathrm{q}/2$ and a combined even parity. Therefore, according to Eq. (2.3.15), two-photon processes are forbidden at the qubit degeneracy point for transverse and for longitudinal drives. For the general n-photon case, we can express the parity as $(\hat{\Pi}\hat{A}_-\hat{\Pi})^n = (-1)^n \hat{A}_-^n$ [185]. If we move away from the qubit degeneracy point, we can derive the effective Hamiltonian via a Schrieffer-Wolff transformation [42, 55]. For

possible two-photon transitions in the bare basis, i.e., $\omega_\mathrm{d} = \Delta/\sin\theta$, we find

$$\begin{aligned}\mathcal{H}_\mathrm{trans,2} &= \frac{\hbar}{2}\left[\frac{\Omega_\ell}{2}\cos\theta - \frac{\Omega_\mathrm{t}}{2}\sin\theta\right][-J_1(\lambda) - J_3(\lambda)]\hat{\sigma}_\mathrm{x} \\ &\approx \frac{\hbar}{2}\left[\frac{\Omega_\ell}{2}\cos\theta - \frac{\Omega_\mathrm{t}}{2}\sin\theta\right]\left[-\frac{\Omega_\mathrm{t}}{2\omega_\mathrm{d}}\cos\theta - \frac{\Omega_\ell}{2\omega_\mathrm{d}}\sin\theta\right]\hat{\sigma}_\mathrm{x} \\ &= \frac{\hbar}{8}\left[\left(\Omega_\mathrm{t}^2 - \Omega_\ell^2\right)\sin^2\theta\cos\theta + \Omega_\ell\Omega_\mathrm{t}\left(\sin^3\theta - \cos^2\theta\sin\theta\right)\right]\hat{\sigma}_\mathrm{x}\,. \end{aligned} \tag{2.3.26}$$

This Hamiltonian consists of two parts. First, a part proportional to $\sin^2\theta\cos\theta$, which is well-known from circuit QED experiments studying symmetry breaking of two-photon processes [42, 185]. For a mixed drive, this term is modified by a mixed $\Omega_\ell\Omega_\mathrm{t}$, which also depends strongly on the Bloch angle as shown in Figs. 2.28 (e) – (h).

Sidebands In the one-photon case, the red sideband transition ($\omega_\mathrm{q} - \omega_\mathrm{r}$) and the blue sideband transition ($\omega_\mathrm{q} + \omega_\mathrm{r}$) are forbidden for a transversal $\hat{\sigma}_\mathrm{x}$-like drive. However, due to the even parity of the $\hat{\sigma}_\mathrm{z}$ operator, sideband transitions are allowed for $\hat{\sigma}_\mathrm{z}$ drives [187]. To calculate the transition matrix element, we chose a unitary transformation via

$$\mathcal{U} = \exp\left[-\imath\frac{\Delta' t}{2}\hat{\sigma}_\mathrm{z} - \imath(\omega_\mathrm{r}t)\hat{a}^\dagger\hat{a}\right], \tag{2.3.27}$$

where $\Delta' = \Delta + (\gamma_+ + \gamma_-)/2$ with $\gamma_\pm = g_\mathrm{t}/(\Delta \pm \omega_\mathrm{r})$. In this frame, within a RWA, the sideband Hamiltonians read [184]

$$\mathcal{H}_\mathrm{red} = \hbar g_\mathrm{t}(\gamma_+ + \gamma_-)\hat{\sigma}_\mathrm{z}\hat{a}^\dagger\hat{a} - \frac{\hbar}{2}\left[\frac{\Omega_\ell}{2}\sin\theta - \frac{\Omega_\mathrm{t}}{2}\cos\theta\right]2\gamma_-[\hat{a}^\dagger\hat{\sigma}_- + \hat{a}\hat{\sigma}_+]\,, \tag{2.3.28}$$

$$\mathcal{H}_\mathrm{blue} = \hbar g_\mathrm{t}(\gamma_+ + \gamma_-)\hat{\sigma}_\mathrm{z}\hat{a}^\dagger\hat{a} - \frac{\hbar}{2}\left[\frac{\Omega_\ell}{2}\sin\theta - \frac{\Omega_\mathrm{t}}{2}\cos\theta\right]2\gamma_+[\hat{a}^\dagger\hat{\sigma}_+ + \hat{a}\hat{\sigma}_-]\,. \tag{2.3.29}$$

As shown in Figs. 2.28 (e) - (h), the transition probability for sideband transitions is opposite compared to the one-photon transition depicted in Figs. 2.28 (a) - (f).

Strong longitudinal drives A quantum two-level system described by the Hamiltonian in $\mathcal{H}_\mathrm{q} = \hbar\Delta\hat{\sigma}_\mathrm{z}/2 + \hbar\varepsilon\hat{\sigma}_\mathrm{x}/2$ is subjected to a longitudinal coupling to external drives when it is operated away from the degeneracy point. The reason is the finite value of the $\cos\theta$ term when transforming $\mathcal{H}_\mathrm{q}$ into the eigenbasis of the qubit. For the gradio qubit, there can be longitudinal coupling even at the degeneracy point due to the $\hat{\sigma}_\mathrm{z}$ of the SQUID loop. In this case, one has to perform the Polaron transformation described in Eq. (2.3.11) for the qubit-drive Hamiltonian. Such a transformation yields the effective Hamiltonian [188]

$$\mathcal{H}_\mathrm{eff} = \frac{\hbar\varepsilon}{2}\hat{\sigma}_\mathrm{z} + \hbar\omega_\mathrm{r}\hat{a}^\dagger\hat{a} + \frac{\hbar\Omega_\ell}{2}\hat{\sigma}_\mathrm{z}\cos(\omega_\mathrm{d}t) + \frac{\hbar\Delta}{2}\left\{\hat{\sigma}_+\exp\left[\frac{2g_\ell}{\omega_\mathrm{r}}(\hat{a}^\dagger - \hat{a})\right] + \mathrm{H.c.}\right\}. \tag{2.3.30}$$

Applying another time-dependent unitary transformation $\mathcal{U} = \exp[-\imath\Omega_\ell\hat{\sigma}_\mathrm{z}\sin(\omega_\mathrm{d}t)/2\omega_\mathrm{d}]$ yields the Hamiltonian

$$\mathcal{H}_\mathrm{eff'} = \frac{\hbar\varepsilon}{2}\hat{\sigma}_\mathrm{z} + \hbar\omega_\mathrm{r}\hat{a}^\dagger\hat{a} + \frac{\hbar\Delta}{2}\sum_{k=-\infty}^{\infty}\{J_k(x_\mathrm{d})\hat{\sigma}_+ B_k(t) + \mathrm{H.c.}\}\,, \tag{2.3.31}$$

where $J_k(x_\mathrm{d})$ is the k^th Bessel function of the first kind, $x_\mathrm{d} = \Omega_\ell/\omega_\mathrm{d}$ is the normalized drive amplitude, and $B_k(t) = \exp\left[2g_\ell/\omega_\mathrm{r}(\hat{a}^\dagger - \hat{a}) + \imath k\omega_\mathrm{d} t\right]$. We can expand Eq. (2.3.31) into the interaction picture, which yields

$$\mathcal{H}_\mathrm{int} = \frac{\hbar\Delta}{2} \sum_{k,m,n} \left\{ J_k^{m,n}(t)\hat{\sigma}_+ \hat{a}^{\dagger m}\hat{a}^n + \mathrm{H.c.} \right\} , \tag{2.3.32}$$

with

$$J_k^{m,n}(t) = \frac{(-1)^n J_k(x_\mathrm{d})}{m!n!} \left(\frac{2g_\ell}{\omega_\mathrm{r}}\right)^{m+n} \exp\left[-\frac{1}{2}\left(\frac{2g_\ell}{\omega_\mathrm{r}}\right)^2\right] \times \exp[\imath(k\omega_\mathrm{d} t + (m-n)\omega_\mathrm{r} t + \varepsilon t)] . \tag{2.3.33}$$

Equation (2.3.32) shows that depending on the order of n and m as well as depending on the drive amplitude, the resonance condition can be fulfilled for more than one drive frequency expressed in the Bessel functions $J_k(x_\mathrm{d})$.

2.4 Decoherence in superconducting circuits

Decoherence describes fundamental processes in physics that tend to destroy information on a certain (superposition) state in form of dephasing and depolarization [189–193]. While depolarization, i.e., energy decay, is an irreversible and dissipative loss mechanism into a bosonic heat bath [194–196], dephasing describes the loss of ordering information between the phase of two states forming a quantum superposition [197]. Decoherence addresses many fundamental questions in quantum mechanics such as the measurement problem [198, 199], the arrow of time [200–202], or whether and how the classical world may emerge from a quantum world [203, 204]. Technically speaking, decoherence arises from the intended [205, 206] or unintended [207, 208] interaction of the quantum system with its environment. In particular for solid state systems, decoherence is a limiting factor due to the dense environment [209–211] compared to atoms in ultra-high vacuum traps [212]. In the rest of this section, we will first introduce a general formalism to describe decoherence of a quantum bit in Sec. 2.4.1 and introduce main noise sources in Sec. 2.4.2. Finally, we describe loss mechanisms of superconducting resonators in Sec. 2.4.3.

2.4.1 Decoherence in quantum two-level systems

The dynamics of quantum two-level systems or qubits can conveniently be described within the Bloch-Redfield theory [213–215] introducing the longitudinal relaxation (depolarization) rate $\gamma_1/2\pi = T_1^{-1}$ and the transverse relaxation (dephasing) rate $\gamma_2/2\pi = T_2^{-1}$. The dephasing process itself is a combination of energy decay and pure dephasing (homogeneous broadening), which obey

$$\gamma_2 = \frac{\gamma_1}{2} + \gamma_\varphi \tag{2.4.1}$$

characterized by the pure dephasing rate γ_φ. The origin for decay and dephasing are fluctuations in the environment that couple incoherently to the qubit. There is a large number of possible sources for fluctuations such as flux noise [33, 216–219], charge noise [40, 93, 220–223], or noise from quasiparticles [36, 65, 224–227]. Each of these noise sources can be described as a quantum emitter generating temporal fluctuations $\delta\lambda(t)$ [211], where λ is a normalized amplitude, e.g., Φ/Φ_0. The emitter is characterized by its

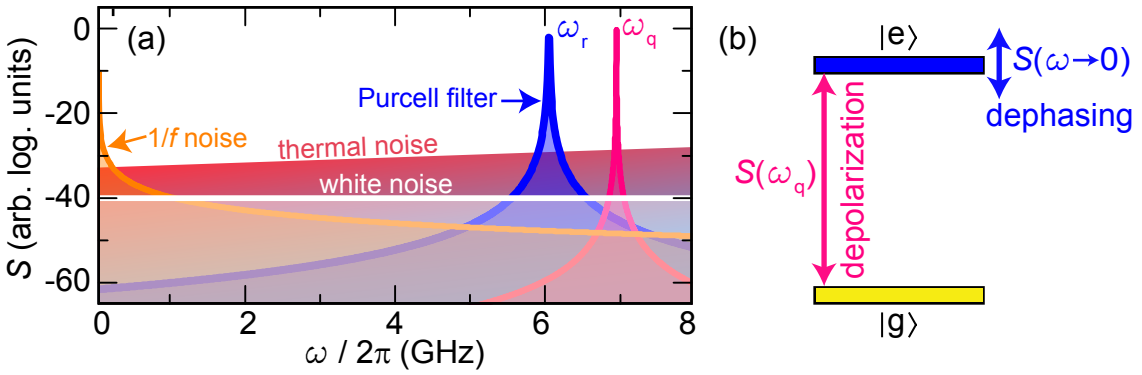

Figure 2.29: **(a)** Power spectral density for different noise sources and a Purcell filter plotted versus frequency. Additionally, we show the Lorentzian line shape of the qubit. **(b)** Level diagram of a qubit. A finite power spectral density $\mathcal{S}(\omega_\mathrm{q})$ at the qubit frequency introduces depolarization, while pure dephasing is caused by a spectral density $\mathcal{S}(\omega \mapsto 0)$ in the low-frequency limit.

autocorrelation function $\mathcal{C}_\lambda = \langle \delta\lambda(0)\delta\lambda(t)\rangle$. One prominent example is white noise, where the autocorrelation function is a δ-function meaning there is no coherence at all within the noise. Generally, the frequency distribution of the noise is characterized by the power spectral density $\mathcal{S}(\omega) = \hbar(2\pi)^{-1}\int \mathrm{d}t\, \mathcal{C}_\lambda e^{-\imath\omega t}$.

Please note that here and in the following, we use the power spectral density $\mathcal{S}(\omega)$ that has units W/Hz.

For colored noise, important examples are $1/f$ noise [228] with $\mathcal{S}(\omega) \propto \omega^{-1}$ on the hand, and thermal noise [229] with $\mathcal{S}(\omega) \propto \hbar\omega \coth(\hbar\omega/k_\mathrm{B}T)$ on the other hand [see Fig. 2.29 (a)]. In our description, we assume that the noise is weak [$\mathcal{S}(\omega) \ll \hbar\omega$], is Gaussian distributed, and has a short ranged autocorrelation function, i.e., it is Markovian [190, 230]. This Markovian approximation provides the foundation for the Bloch-Redfield theory but has to be modified if the qubit is coupled too strong to the heat bath [231–233].
To study the effect of environmental fluctuations, we model the qubit-bath system via the Hamiltonian $\mathcal{H}_\mathrm{sys} = (\hbar/2)[\Delta\hat{\sigma}_\mathrm{x} + \varepsilon\hat{\sigma}_\mathrm{z}] + \mathcal{H}_\mathrm{bath}$, where the bath Hamiltonian $\mathcal{H}_\mathrm{bath}$ provides the fluctuations $\delta\lambda$. At the qubit sweet spot, fluctuations acting on ε vanish to first-order, but second-order contributions can have a significant influence [234, 235]. Hence, we expand $\mathcal{H}_\mathrm{sys}$ to second-order in $\delta\lambda$ which yields in the eigenbasis of the qubit [211]

$$\mathcal{H}_\mathrm{sys} \approx \frac{\hbar}{2}\left[\omega_\mathrm{q}\hat{\sigma}_\mathrm{z} + \delta\omega_\mathrm{z}\hat{\sigma}_\mathrm{z} + \delta\omega_\mathrm{x}\hat{\sigma}_\mathrm{x}\right] + \mathcal{O}(\delta\lambda^3)\,. \tag{2.4.2}$$

Here, $\delta\omega_\mathrm{z} = \mathcal{D}_{\lambda,\mathrm{z}}\delta\lambda + \mathcal{D}^{(2)}_{\lambda,\mathrm{z}}\delta\lambda^2/2$ and $\delta\omega_\mathrm{x} = \mathcal{D}_{\lambda,\mathrm{x}}\delta\lambda + \mathcal{D}^{(2)}_{\lambda,\mathrm{x}}\delta\lambda^2/2$ are transverse and longitudinal energy fluctuations, where we have used the coupling strengths $\mathcal{D}_\lambda = \partial\mathcal{H}_\mathrm{sys}/\partial\delta\lambda$ and $\mathcal{D}^{(2)}_\lambda = \partial^2\mathcal{H}_\mathrm{sys}/\partial\delta\lambda^2$ for first- and second-order noise, respectively. If the fluctuations $\delta\lambda$ have just contributions along σ_z, they are diagonal in the energy eigenbasis of the qubit and only modulate the qubit eigenvalues but not its eigenstates. Hence, such perturbations introduce pure dephasing but do not cause depolarization. Generally, fluctuations can also have contributions along the σ_x direction, which is perpendicular to the quantization axis, meaning they introduce both dephasing and depolarization. In the following, we describe depolarization, caused by a finite power spectral density $\mathcal{S}(\omega_\mathrm{q})$ at the qubit frequency and pure dephasing caused by the spectral density $\mathcal{S}(\omega \mapsto 0)$ in the low-frequency limit as depicted in Fig. 2.29 (b).

Depolarization Depolarization is induced by noise sources (fluctuations) that are resonant with the qubit and thus have a significant power spectral density $\mathcal{S}(|\omega_\mathrm{q}|)$. On the one hand, these fluctuations increase the radiative decay, i.e., the relaxation rate $\gamma_\downarrow$ due to stimulated emission (compared to the spontaneous emission rate [236] due to vacuum fluctuations). On the other hand, the fluctuations can excite the qubit with a certain rate $\gamma_\uparrow$. These two processes add up to the depolarization rate $\gamma_1 = \gamma_\downarrow + \gamma_\uparrow$. Using a golden rule approach [237, 238], we find the two transition rates [167, 229, 239]

$$\gamma_\uparrow = \frac{1}{2}\left[\frac{\mathcal{D}_{\lambda,\mathrm{x}}}{\hbar\omega_\mathrm{q}}\right]^2 \frac{\mathcal{S}(-\omega_\mathrm{q})}{\hbar} \equiv \frac{1}{2}\frac{\kappa_\lambda}{\omega_\mathrm{q}}\frac{\mathcal{S}(-\omega_\mathrm{q})}{\hbar}\,, \tag{2.4.3}$$

$$\gamma_\downarrow = \frac{1}{2}\left[\frac{\mathcal{D}_{\lambda,\mathrm{x}}}{\hbar\omega_\mathrm{q}}\right]^2 \frac{\mathcal{S}(+\omega_\mathrm{q})}{\hbar} \equiv \frac{1}{2}\frac{\kappa_\lambda}{\omega_\mathrm{q}}\frac{\mathcal{S}(+\omega_\mathrm{q})}{\hbar}, \tag{2.4.4}$$

where we have introduced the effective coupling κ_λ between the fluctuations and the qubit. These equations show that the qubit reacts with excitation to negative frequencies and with relaxation to positive frequencies. From a purely classical consideration, one expects a symmetric power spectral density [239], i.e., $\mathcal{S}(+\omega_\mathrm{q}) = \mathcal{S}(-\omega_\mathrm{q})$. This symmetric case would result in equal rates $\gamma_\uparrow = \gamma_\downarrow$ meaning that the qubit stays totally unpolarized. Due to the detailed balance of a qubit in thermal equilibrium, however, the transition rates obey [167] $\gamma_\uparrow/\gamma_\downarrow = \exp(-k_\mathrm{B}T/\hbar\omega_\mathrm{q})$ which in turn forces the asymmetric case $\mathcal{S}(-\omega_\mathrm{q}) = \exp(-k_\mathrm{B}T/\hbar\omega_\mathrm{q})\mathcal{S}(+\omega_\mathrm{q})$. Hence, we find the total decay rate

$$\gamma_1 = \gamma_\downarrow + \gamma_\uparrow = \frac{1}{2}\frac{\kappa_\lambda}{\omega_\mathrm{q}}\frac{\mathcal{S}(\omega_\mathrm{q})}{\hbar}\left[1 + \exp\left(\frac{k_\mathrm{B}T}{\hbar\omega_\mathrm{q}}\right)\right]\,, \tag{2.4.5}$$

which leads to a decay function $g(t) = \exp(-\gamma_1 t/2\pi)$. At low temperatures $T \ll \hbar\omega_\mathrm{q}/k_\mathrm{B}$, the excitation rate $\gamma_\uparrow$ is exponentially suppressed and $\gamma_1 \simeq \gamma_\downarrow$. Because qubit experiments are typically performed at $k_\mathrm{B}T \ll \hbar\omega_\mathrm{q}$, we use the expression relaxation rate also for γ_1 processes. The direct proportionality between decay rate and power spectral density has been used in a large variety of experiments to measure the frequency dependence of the environmental background noise [35, 119, 219, 221, 240–243].

Purcell effect The above derivation for relaxation assumes that the qubit is exposed to the complete ohmic frequency spectrum of the environment. If we place the qubit inside a resonator, the spectral density can be strongly reduced due to the Purcell effect [240, 244–247]. The reason for the reduced density of states is the resonator filter, which only allows states within its Lorentzian frequency distribution [7]

$$\mathcal{F}_\mathrm{L}(\omega) = \frac{\kappa_\mathrm{tot}/2}{(\omega - \omega_\mathrm{r})^2 + (\kappa_\mathrm{tot}/2)^2} \tag{2.4.6}$$

that has to be multiplied to the qubit's linewidth [cf. Fig. 2.29 (a)]. If qubit and resonator are close to resonance, the spontaneous emission rate is enhanced by the resonators quality factor, i.e., larger than in the case of a free space environment. For a large qubit-resonator detuning δ, however, the low density of states suppresses the radiative decay. We can express the Purcell filtered relaxation rate of the qubit as [247]

$$\gamma_\mathrm{P}(\delta) = \frac{\kappa_\mathrm{x}}{2} - \frac{\sqrt{2}}{2}\sqrt{-A + \sqrt{A^2 + (\kappa\delta)^2}} \approx \frac{\kappa_\mathrm{x} g^2}{\delta^2} \tag{2.4.7}$$

with $A = \delta^2 + 4g^2 - \kappa_\mathrm{x}^2/4$.

Pure dephasing Pure dephasing of superposition states in qubits is introduced by a power spectral density $\mathcal{S}(\omega \mapsto 0)$. These adiabatic fluctuations of the environmental bath modify the qubit transition frequency, which subsequently leads to dephasing of the superposition state. For noise with a sufficiently smooth distribution around $\omega = 0$, we can again use a golden rule approach and find [211] $\gamma_\varphi = \pi \mathcal{D}_{\lambda,\mathrm{z}}^2 \mathcal{S}(\omega = 0)/\hbar$. In particular, for thermal noise on ohmic microwave lines we find [210] $\gamma_\varphi = \alpha k_\mathrm{B} T/\hbar$, where the dimensionless dissipation parameter $\alpha = \lim_{\omega \mapsto 0} \mathcal{S}(\omega)/[\hbar\omega]$ characterizes the coupling strength to the environment. We have to perform a more elaborate analysis for noise that diverges at zero frequency, e.g., $1/f$ noise. For an arbitrary spectral density, the qubit coherence $\langle \hat{\sigma}_-(t) \rangle$ decays as [235]

$$|\langle \hat{\sigma}_-(t) \rangle| = \exp\left[-\frac{1}{2} \int \frac{\mathrm{d}\omega}{2\pi} \mathcal{S}(\omega) \frac{\sin^2(\omega t/2)}{(\omega/2)^2} \right] . \tag{2.4.8}$$

For $1/f$ noise and linear coupling $\propto \delta\lambda$, the decay is proportional to $\exp[(\delta\lambda t)^2 \ln(\omega_\mathrm{ir} t/2\pi)]$, where the infrared cut-off frequency ω_ir is set by experimental details (see Sec. 4.4.1). For solid-state based qubits, $1/f$ noise is typically a dominant source for decoherence. To decrease this effect, one can tune the qubit to its sweet spot. At the sweet spot the linear coupling to noise is suppressed to first-order, meaning the terms proportional to $\mathcal{D}_{\lambda,\mathrm{z}}$ and to $\mathcal{D}_{\lambda,\mathrm{x}}$ in Eq. (2.4.2) vanish. Nevertheless, even at the flux sweet spot, dephasing can be strong due to second-order coupling. In the following, we only discuss fluctuations $\delta\lambda^2$ coupling to the longitudinal part of the qubit Hamiltonian in Eq. (2.4.2), i.e., to $\mathcal{D}_{\lambda,\mathrm{z}}^{(2)}$. As above, we discuss the two relevant cases of thermal noise and of $1/f$ noise. Due to its singularity at zero frequency, $1/f$ noise typically dominates at the qubit sweet spot. Here, we find the quadratic power spectral density $\mathcal{S}_{\lambda^2} = (4/\pi)\delta\lambda^2 \ln|\omega/\omega_\mathrm{ir}|/|\omega|$ leading to a decay proportional to $\exp(-\delta\lambda^2 \ln|\omega_\mathrm{ir} t/\pi|^2)$ [234]. For thermal noise, the quadratic contribution to the power spectral density yields a dephasing rate proportional to T^3 [234] so that cooling has a stronger effect than in the case of linear coupling where $\gamma_\varphi \propto T$.

Qubit parameter fluctuations Next to relaxation and dephasing discussed above, there can be variations of intrinsic qubit parameters such as the qubit level splitting or the qubit decay rate over a long timescale on the order of hours [20, 248]. Even though fluctuations of the qubit parameters do not directly introduce decoherence, they can hamper the performance of larger scale systems needed for quantum computation algorithms. The slow-frequency fluctuations can originate from interacting two-level states in the vicinity of the qubit resulting in a $1/f$ distribution [248–250] and also from thermal states [41]. Assuming that the environmental fluctuations couple directly and linearly to the qubit parameters, i.e., $\gamma_1(t) \propto \mathcal{S}(\omega_\mathrm{q},t)$, we can measure the frequency spectrum of the fluctuations via repeating measurements of the relaxation rate [41, 248]. When recording time traces of the relaxation rate, only environmental fluctuations that are slower than the inverse measurement time $1/t_\mathrm{meas}$ of one decay trace contribute to recordable fluctuations of the decay rate. When recording many decay traces, the autocorrelation function $\langle \gamma_1(t)\gamma_1(0) \rangle$ characterizes the fluctuations. Hence, from the autocorrelation function we can extract the power spectral density by computing the Fourier transform $\mathcal{S}(\omega) = \hbar/2\pi \int \mathrm{d}t \, \langle \gamma_1(t)\gamma_1(0) \rangle e^{-\imath\omega t}$ as discussed above.

2.4.2 Noise sources for superconducting qubits

Solid-state based qubits are susceptible to noise from various sources in their direct microscopic environment but also to fluctuations in the electromagnetic background from emitters situated in the far field. In the following, we discuss thermal noise, charge noise, flux noise, and photon shot noise, which are the most relevant noise sources for this thesis. A further important noise source that is not discussed here is noise from quasiparticle tunneling [65, 223, 225, 251–253].

Thermal noise of the environment Thermal noise is always present at finite temperatures because there is a certain occupation of uncorrelated thermal photons n_{th} defined by Eq. (2.2.17). We describe these photons by a bosonic bath obeying the Hamiltonian $\mathcal{H}_{\mathrm{bath}} = \sum_k \hbar\omega_k \hat{b}_k^\dagger \hat{b}_k$. The individual field modes with frequency ω_k are described by the respective field operators $\hat{b}_k^\dagger, \hat{b}_k$. The field modes are coupled to the qubit via the interaction Hamiltonian $\mathcal{H}_{\mathrm{int}} = -\imath\hbar \sum_k [\kappa_k \hat{\sigma}_+ \hat{b}_k + \kappa_k^\star \hat{b}_k^\dagger \hat{\sigma}_-]$, where κ_k and $\kappa_k^\star$ denote the coupling between bath and qubit excitation and decay, respectively. For convenience, we split up the transmission-line modes into a classical part $\bar{b}_k$ originating from a (possible) coherent drive, and into a quantum part $\hat{\xi}_k$, such that $\hat{b}_k(t) = e^{-\imath\omega_k t}\bar{b}_k + \hat{\xi}_k(t)$ [165]. The quantum part describes voltage fluctuations emitted from all nearby lines and will be the focus of the following discussion. The lines induce a voltage $V(t) = V_{\mathrm{vac}}[\hat{\xi}_k(t) + \hat{\xi}_k^\dagger(t)]$, which is fluctuating in time and has a Gaussian amplitude distribution. Here, V_{vac} is the vacuum amplitude of the corresponding mode. For a finite temperature, the correlation function for the voltage fluctuations reads [149] $\mathcal{C}_V(t) = [3V_{\mathrm{vac}}^2/\pi^2]\left[\zeta\left(2, 1 - \imath t\frac{k_{\mathrm{B}}T}{\hbar}\right) + \zeta\left(2, 1 + \imath t\frac{k_{\mathrm{B}}T}{\hbar}\right)\right]$, where $\zeta(s,a) = \sum_{j=0}^{\infty}[j+a]^{-s}$ is the Hurwitz function [cf. Fig. 2.30 (a)]. For temperatures in the kelvin range, this description yields a sub-nanosecond, i.e., negligible coherence time of thermal fields defined by the width of the Hurwitz function [149, 150, 254]. The power spectral density of thermal fields can be obtained by a Fourier transform [229, 255]

$$\mathcal{S}(\omega_k) = \frac{\hat{\xi}_k^\dagger \hat{\xi}_k}{2\pi Z_0} \int \mathrm{d}t\, \mathcal{C}_V(t) e^{-\imath\omega t} = 2\hbar\omega_k \coth\left(\frac{\hbar\omega_k}{2k_{\mathrm{B}}T}\right) = 4\hbar\omega_k(n_{\mathrm{th}} + 1/2)\,, \tag{2.4.9}$$

which is shown in Fig. 2.30 (b) and Fig. 2.30 (c). The non-vanishing spectral density at zero temperature arises from vacuum fluctuations responsible for the term $+1/2$ in Eq. (2.4.9).

Thermal background radiation Next to thermal noise from the direct qubit environment, black-body emitters irradiate thermal fields that generate non-equilibrium quasiparticles in the superconductors [256, 257]. This noise is generated as stray infrared light at higher temperature stages inside the cryostat and enters the sample box via small lids and also via the coaxial cables [65, 252]. Due to the broadband radiation that also follows Eq. (2.4.9), there are two major origins for decoherence from stray infrared light. First, stray light that is on resonance with the qubit can directly induce relaxation as discussed for the golden rule approach above. In this case, thermal photons arriving at the qubit enhance the decay. It has been shown [252], however, that this effect alone cannot explain relaxation rates measured in superconducting qubits. The second decoherence channel arises from high energy photons with energy $\hbar\omega \simeq \Delta_0$ on the order of the superconducting energy gap Δ_0. For Al, the energy gap is approximately 80 GHz [60] corresponding to black-body radiation of a 4 K emitter. Since the whole cryostat inset is precooled by a

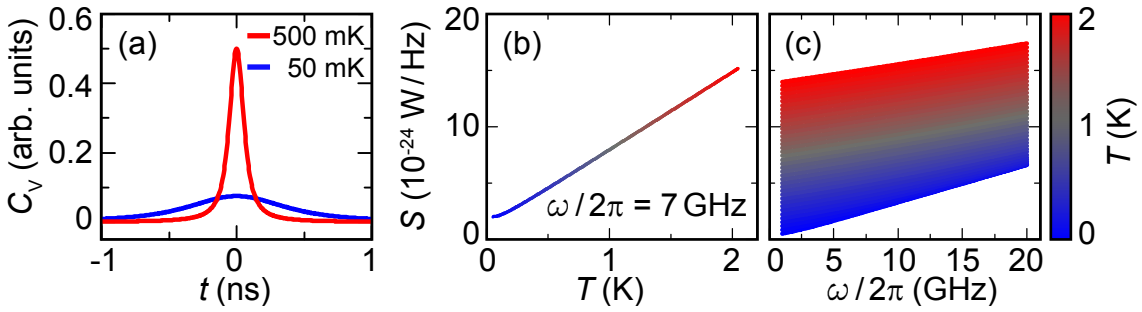

Figure 2.30: **(a)** Hurwitz correlation function applicable for thermal states. **(b)** Power spectral density for a thermal state plotted versus temperature. **(c)** Temperature-dependent power spectral density for thermal states plotted versus frequency.

liquid helium bath at 4.2 K, we expect a significant influence of this radiation [256, 258] if the sample is not efficiently shielded [65, 251].

Charge noise from two-level states Charge noise is one of the main sources for decoherence in Josephson junction based systems [40, 220–222, 248, 259, 260] since it couples directly to the two electrodes of a Josephson junction. The most prominent source for charge noise are two-level states (TLSs) [261–263] hopping between two bistable spatial configurations. These TLSs can be present either in the thin oxide layer of the junction itself [264–266] or in the dielectric environment of the qubit [267]. We describe each individual TLS with the double well Hamiltonian defined in Eq. (2.1.20), where each well corresponds to one spatial configuration of the TLS. From this description, we can derive the power spectral density via the coupling operator $\langle\hat{\sigma}_z\rangle = \tanh(\omega_{\text{tls}}/2k_BT)$, where ω_{tls} describes the level splitting of the TLS. In this framework, neglecting excitation of the qubit from the TLS, one finds the spectral density from a single TLS [248]

$$\mathcal{S}(\omega) = \cos^2\theta[1-\langle\hat{\sigma}_z\rangle^2]\frac{2\gamma_{1,\text{tls}}}{\gamma_{1,\text{tls}}^2+\omega^2} + \sin^2\theta\left[\frac{1+\langle\hat{\sigma}_z\rangle}{2}\right]\frac{2\gamma_{\varphi,\text{tls}}}{\gamma_{\varphi,\text{tls}}^2+(\omega-\omega_{\text{tls}})^2}, \qquad (2.4.10)$$

which we show in Fig. 2.31 (a). In Eq. (2.4.10), $\theta = \tan^{-1}(\Delta/\varepsilon)$ describes the TLS' mixing angle and $\gamma_{1,\text{tls}}$ and $\gamma_{\varphi,\text{tls}}$ are the TLS' relaxation and dephasing rate, respectively. The first term in Eq. (2.4.10) describes the low-frequency noise generated by a single TLS. The well-known $1/f$ spectral density of TLS noise in the low-frequency regime arises from the assumption that, due to the large number of TLSs, they are equally distributed across all frequencies (Dutta-Horn model) [228, 249, 268, 269]. The interaction between individual TLS depicted in Fig. 2.31 (b) also causes low-frequency fluctuations of qubit parameters [41, 248–250]. Additionally, the power spectrum is peaked around the Lorentzian line with center frequency ω_{tls} defined by the second term in Eq. (2.4.10). Due to the large number of TLSs adding up their power spectral density, one can assume a white frequency distribution over the complete qubit line width causing relaxation [260].

Flux noise Microscopic $1/f$ flux noise is one major source for superconducting circuits that include loops with Josephson junctions [33, 216–219, 270–272]. Analogously to charge noise, it has been shown that also flux noise has a microscopic origin [33]. For flux noise, unpaired electrons with a certain spin direction create a fluctuating magnetic moment [216]. As the fluctuations can be thermally activated, uncorrelated changes of spin directions again

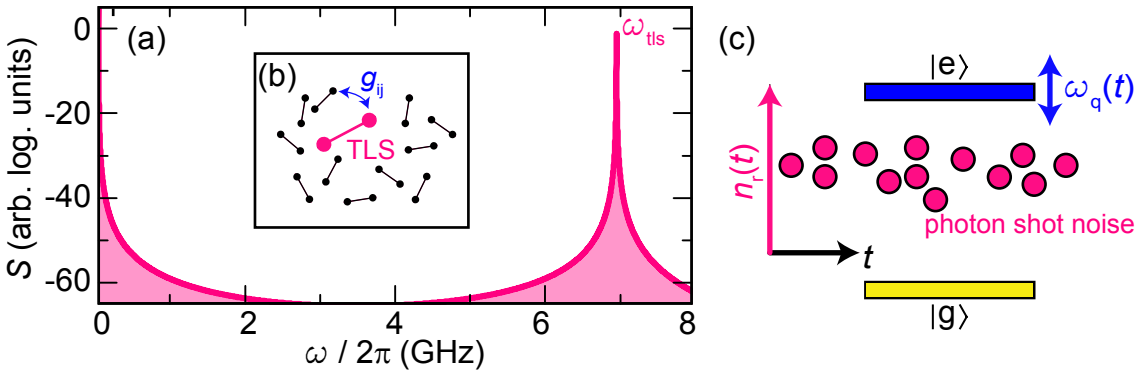

Figure 2.31: **(a)** Power spectral density for a single two-level state (TLS). **(b)** A TLS is typically surrounded by a large ensemble of other TLSs that couple to each other with coupling strength g_{ij}. **(c)** Schematics of decoherence due to photon shot noise. A fluctuating photon number $n_\mathrm{r}(t)$ results in fluctuations of the qubit frequency leading to dephasing.

yield a $1/f$ noise spectrum [273]. Hence, we can describe the power spectral density [33] $\mathcal{S}(\omega) = A_\Phi/|\omega|$, where A_Φ describes the noise amplitude. Since, in a typical configuration, the spin fluctuations couple via a dipole interaction to a superconducting loop, flux noise can be suppressed using a gradiometric design [99]. Due to the broad frequency spectrum of the thermally activated spin fluctuations, flux noise can also resonantly couple to the qubit, causing relaxation [33, 216, 274].

Photon shot noise Photon shot noise becomes relevant in coupled qubit-resonator systems, where the ac-Stark shift translates temporal photon-number fluctuations in the resonator directly into fluctuations of the qubit frequency proportional to $\chi \equiv g^2/\delta$ [see Fig.2.31 (c)]. The additional dephasing occurs because the qubit exhibits a phase shift $\delta\varphi_\mathrm{q}(\tau)$ from the fluctuations in n_r. This phase shift enters the correlation function [168] $\langle\hat{\sigma}_-(\tau)\hat{\sigma}_+(0)\rangle \approx \exp[-\gamma_2\tau - 2\chi^2 \int_0^\tau \mathrm{d}\tau' \mathcal{C}_{n_\mathrm{r}}(\tau')]$ of the qubit raising and lowering operators characterizing decoherence. One finds [17, 24] $\mathcal{C}^\mathrm{coh}_{n_\mathrm{r}}(\tau) = n_\mathrm{r}\exp(-\kappa_\mathrm{x}\tau/2)$ for coherent states inside a resonator and the super-Poissonian correlator [166] $\mathcal{C}^\mathrm{th}_{n_\mathrm{r}}(\tau) = (n_\mathrm{r}^2 + n_\mathrm{r})\exp(-\kappa_\mathrm{x}\tau)$ for thermal fields. From these correlation functions, we find the photon-number-dependent qubit dephasing rates [168, 275]

$$\gamma^\mathrm{coh}_{\varphi n}(n_\mathrm{r}) = 2n_\mathrm{r}\kappa_\mathrm{x}\theta_0^2 \tag{2.4.11}$$

$$\gamma^\mathrm{th}_{\varphi n}(n_\mathrm{r}) = (n_\mathrm{r}^2 + n_\mathrm{r})\kappa_\mathrm{x}\theta_0^2. \tag{2.4.12}$$

for a coherent and a thermal state, respectively. Here, [168] $\theta_0 = \tan^{-1}(2\chi/\kappa_\mathrm{x})$ is the accumulated phase of the injected photons due to the interaction with the qubit.

2.4.3 Microwave loss in superconducting resonators

Superconducting resonators have versatile applications in circuit QED experiments [26, 115–118]. For many of those applications, the coherence time limited by internal loss channels of the resonator should be as long as possible. In the single photon limit, TLSs located at the metal/substrate, metal/air, and substrate/air interfaces are considered to be the main contributors to microwave loss [124, 125]. In order to reduce these loss channels, much effort has been put into material development focusing on different metallization

compounds [276, 277] or substrate materials [278, 279]. Also, quasiparticle generation in the superconducting material from stray infrared light [65] or thermal activation [126] generates loss in these resonators. In addition to material choice and screening quality, the sample design itself can have a large influence on the internal quality factor of the resonator [280, 281]. This influence can arise from impedance mismatches at the coupling ports resulting in Fano resonances [19, 282], from parasitic modes in the substrate [283], or from additional resistive loss channels [284]. For efficiently shielded and well-designed setups based on optimized materials, internal quality factors above one million have been reached [19].
In the following, we introduce different microwave loss contributions that are relevant for our experiments. Dissipation on a quantum mechanical level can be introduced within the Caldeira-Leggett model [195]. In this model, one particular harmonic oscillator, which is the resonator in our case, couples to a bath of additional harmonic oscillators (noise). As above, we consider the coupling to be weak and we apply the Born-Markov approximation [285]. That way, we can describe the coupled resonator-bath system by the Hamiltonian [120]

$$\mathcal{H}_{\mathrm{CL}} = \hbar\omega_{\mathrm{r}}\hat{a}^\dagger\hat{a} + \sum_k \hbar\omega_k \hat{b}_k^\dagger\hat{b}_k + \hbar\sum_k [\kappa_k \hat{a}^\dagger\hat{b}_k + \kappa_k^\star \hat{b}_k^\dagger\hat{a}] + \hbar\sum_k \frac{1}{\omega_k}[\kappa_k\hat{a}^\dagger\hat{b}_k + \kappa_k^\star\hat{b}_k^\dagger\hat{a}]^2 \,. \quad (2.4.13)$$

Here, the second term describes the harmonic bath modes, the third term describes the short ranged coupling responsible for dissipation, and the last term is included to compensate for an energy shift of the bare resonator Hamiltonian [286]. In this formalism, dissipation is treated as a frictional force with a spectral density $\mathcal{S}(\omega) = (\hbar\pi/2)\sum_k \delta(\omega-\omega_k)\kappa_k^2/\omega_k$ [195, 287]. For typical configurations, the bath is ohmic [243], i.e., $\mathcal{S}(\omega)\propto\omega$. While Eq. (2.4.13) describes dissipative processes, in general there is also dephasing of a harmonic oscillator [120]. Dephasing is enhanced by temporal fluctuations $\delta\lambda(t)$, which couple to the electromagnetic field of the resonator as described within the fluctuation-dissipation theorem [288]. The linear coupling of these fluctuations to the resonator frequency results in the perturbed resonator Hamiltonian [120] $\mathcal{H}_{\mathrm{res}} = \hbar[\omega_{\mathrm{r}} + g_\lambda\delta\lambda(t)]\hat{a}^\dagger\hat{a}$ where g_λ describes the coupling between the electromagnetic field and the TLS. For superconducting CPW resonators used in this work, however, dephasing plays a negligible role. In the following, we describe the most relevant dissipative loss mechanisms of superconducting resonators.

Loss due to two-level states Loss due to two-level states (TLSs) is one of the most prominent sources for decoherence in superconducting thin film resonators [38, 276]. The TLSs arise from the unavoidable necessity to place the superconducting circuit on some kind of substrate. These substrates suffer from dielectric loss characterized by their loss tangent $\tan\kappa_{\mathrm{i}}$. The dielectric loss in turn originates from TLSs, e.g., defects or impurities, that can be excited with energies within the superconducting energy gap Δ_0. Each TLS absorbs photons from the electromagnetic field of the resonator and dissipates them back into the heat bath [289]. The total loss contribution of TLSs $\kappa_{\mathrm{tls}} = \sum_k p_k\kappa_{\mathrm{tls},k}$ consequently is a sum of many TLSs, contributing via their participation ratio p_k. The participation ratio depends on the one hand on the dipole moment of the TLS and, on the other hand, on the relative position inside the resonator. TLSs located at a voltage antinode of the resonator field contribute significantly stronger to TLS loss than TLSs located at a voltage node. Furthermore, TLSs that are already thermally excited cannot absorb photons of the

resonator anymore. Hence, the TLS loss rate

$$\kappa_{\mathrm{tls}}(\mathcal{P}_{\mathrm{r}},T) = \kappa_{\mathrm{tls}}^{0}\frac{\tanh\left(\hbar\omega_{\mathrm{r}}/2k_{\mathrm{B}}T\right)}{\sqrt{1+\left(\mathcal{P}_{\mathrm{r}}/\mathcal{P}_{\mathrm{c}}\right)^{\beta/2}}} \tag{2.4.14}$$

depicted in Fig. 2.32 (a) is strongest at very low temperatures and low excitation power. In Eq. (2.4.14), $\mathcal{P}_{\mathrm{r}} = \mathcal{P}Q_{\ell}^{2}/n\pi Q_{\mathrm{x}}$ is the power circulating inside the resonator [276] for the n^{th} mode and $\mathcal{P}$ is the power resonantly applied to the input of the resonator. The exponent β in Eq. (2.4.14) is known to be design-dependent [34] and $\mathcal{P}_{\mathrm{c}}$ is a characteristic power depending on the TLS properties [261, 279]. In the low temperature and low power limit, the internal loss rate approaches $\kappa_{\mathrm{tls}}^{0}$ defined by the unsaturated TLSs. The characteristic power $\mathcal{P}_{\mathrm{c}}$ defined in Eq. (2.4.14) is proportional to $\bar{\gamma}_{1,\mathrm{tls}}\bar{\gamma}_{\varphi,\mathrm{tls}}$, where $\bar{\gamma}_{1,\mathrm{tls}}$ and $\bar{\gamma}_{\varphi,\mathrm{tls}}$ represent the average relaxation and dephasing rate of the TLS ensemble, respectively. In the spin-boson model, the temperature dependence of $\bar{\gamma}_{1,\mathrm{tls}}$ follows a $\coth(\hbar\omega/2k_{\mathrm{B}}T)$ dependence [287, 290] that is proportional to T for $k_{\mathrm{B}}T \gg \hbar\omega$. Due to phonon-mediated interaction between the TLSs we expect

$$\bar{\gamma}_{\varphi,\mathrm{tls}} \propto \gamma_{\mathrm{ac}}T + \frac{\gamma_{\mathrm{op}}}{\left[\exp(\hbar\omega/k_{\mathrm{B}}T)-1\right]}\,, \tag{2.4.15}$$

where γ_{ac} and γ_{op} describe the TLS coupling rate to acoustic and optical phonons, respectively [291, 292]. For low temperatures, $k_{\mathrm{B}}T \ll \hbar\omega$, the interaction is predominantly mediated by the term accounting for acoustic phonons $\gamma_{\mathrm{ac}}T$. However, in the regime $\hbar\omega \simeq k_{\mathrm{B}}T$ that is relevant for our experiments, a power law $\propto T^{\alpha}$ has been found for both, $\bar{\gamma}_{1,\mathrm{tls}}$ and $\bar{\gamma}_{\varphi,\mathrm{tls}}$ [261–263, 266, 290–293]. Therefore, the temperature dependence of the characteristic power can be approximated as [261]

$$\mathcal{P}_{\mathrm{c}}(T) = \frac{3\hbar^{2}\varepsilon\gamma_{\mathrm{ac}}\bar{\gamma}_{1,\mathrm{tls}}}{2d^{2}}\coth\left(\frac{\hbar\omega_{\mathrm{r}}}{2k_{\mathrm{B}}T}\right)T^{\alpha}\,, \tag{2.4.16}$$

where $\varepsilon = \varepsilon_{0}\varepsilon_{\mathrm{r}}$ is the absolute permittivity of the dielectric and d is the effective dipole moment of the TLSs.

Loss due to thermal quasiparticles In the following, we focus on thermally induced quasiparticle loss described by the loss rate $\kappa_{\mathrm{qp}}(T)$. Whereas dielectric loss dominates at very low temperatures, loss related to the superconducting material typically becomes dominant when the sample temperature exceeds approximately 10 % of the critical temperature T_{c} of the superconductor [279]. In the temperature range of our experiments, we expect a considerable quasiparticle contribution only for samples containing Al, while Nb samples are better protected against this loss mechanism [294]. Assuming that the superconducting material is in the dirty or local limit, the quasiparticle contribution can be described with the Matthis-Bardeen theory [73, 126],

$$\frac{\kappa_{\mathrm{qp}}(T)}{\omega_{\mathrm{r}}} = \frac{2\mathcal{K}}{\pi}\frac{e^{-\zeta}\sinh(\xi)K_{0}(\xi)}{1-e^{-\zeta}\left(\sqrt{2\pi/\zeta}-2e^{-\xi}J_{0}(\xi)\right)}\,. \tag{2.4.17}$$

Here, $\mathcal{K}$ is the ratio of kinetic inductance to total inductance of the conductor, $\zeta = \Delta_{0}/k_{\mathrm{B}}T$ with the superconducting energy gap Δ_{0}, $\xi = \hbar\omega_{\mathrm{r}}/2k_{\mathrm{B}}T$, and $J_{0}\,, K_{0}$ are the modified Bessel function of the first and second kind, respectively.

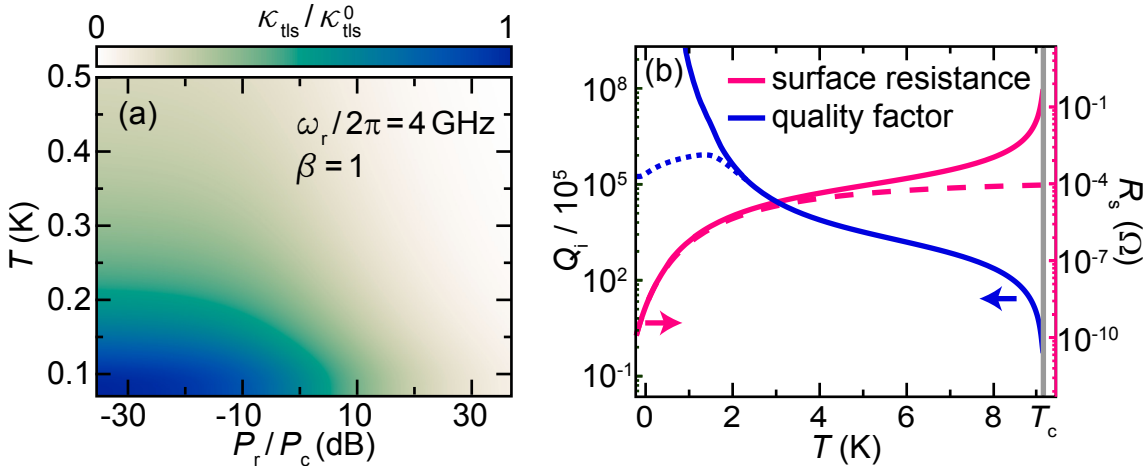

Figure 2.32: **(a)** Normalized TLS loss contribution $\kappa_{\rm tls}/\kappa^0_{\rm tls}$ plotted versus readout power and temperature. **(b)** Left axis: Calculated internal quality factor of a Nb resonator plotted versus temperature (solid blue line). The dotted blue line also takes TLS loss into accout, which becomes relevant in the low temperature regime $k_{\rm B}T < \hbar\omega$. Right axis: Surface resistance calculated for a 100 nm thick Nb film plotted versus temperature (solid pink line). For the solid pink line, we use the complete Matthis-Bardeen integrals [68], while the dashed pink line is a calculation based on Eq. (2.1.8).

Eddy current loss at the superconductor surface In addition to the various sources of microwave loss mentioned above, there can be loss due to eddy currents in the surface of the superconducting material [38]. This loss arises from the oscillating magnetic field $\mathbf{H}\exp(\imath\omega_{\rm r}t)$, generated by the resonator current. Due to the finite penetration depth $\lambda_{\rm s}$ of the superconductor defined in Eq. (2.1.7), there is also a magnetic field $\mathbf{H}_{\rm s}$ inside the superconducting material. For microwave frequencies, the field decays within the penetration depth, thus $\mathbf{H}_{\rm s} = \mathbf{H}_0\exp(-|z|/\lambda_{\rm s})$, where $\mathbf{H}_0 \equiv \mathbf{H}(z{=}0)$ denotes the field strength at the surface of the superconductor. Using Maxwell's equation $\nabla\times\mathbf{E} \propto -\partial\mathbf{H}_{\rm s}/\partial t$, the magnetic field induces eddy currents proportional to Ohms law $\mathbf{j} = \sigma_0\mathbf{E}$ [111].[5] Here, σ_0 is the conductivity at $T = 0$ in the Drude model [90]. In the two-fluid model described in Sec. 2.1.2, the eddy currents have a superconducting and a normal conducting contribution, which leads to the total current density [295]

$$\mathbf{j}_{\rm tot} = \mathbf{j}_{\rm s} + \mathbf{j}_{\rm n} = \sigma_0\left[n_{\rm qp} - \frac{\imath}{\omega_{\rm r}\tau}n_{\rm s}\right]\mathbf{E}\,, \tag{2.4.18}$$

where τ describes the mean free time of the electrons. The dissipated power in a volume $\mathcal{V}$ inside the superconductor [295]

$$\mathcal{P}_{\rm s} = \frac{1}{2}\int \mathrm{d}\mathcal{V}\,\Re(\mathbf{j}_{\rm tot}\cdot\mathbf{E}) = \frac{1}{2}\mathcal{R}_{\rm s}H_0^2 \tag{2.4.19}$$

is directly connected to the surface resistance $\mathcal{R}_{\rm s}$ defined in Eq. (2.1.8). In Eq. (2.4.19), the magnetic field component $H_0 \equiv H_{\rm y}(z{=}0)$ points along the surface of the superconductor perpendicular to the current flow in x-direction [see Fig. 2.34 for details]. The specific temperature dependence $\mathcal{R}_{\rm s}(T)$ shown in Fig. 2.32 (b) translates directly into the temperature dependence of eddy current loss $1/Q_{\rm i} = \mathcal{P}_{\rm s}/\mathcal{P}_{\rm r}$. Because the field intensity H_0^2 is

[5] A correct treatment of the field-current relation must account for the anomalous skin effect and requires the application of Boltzmann's transport equation [90]. For simplicity, we assume a local interaction between field and current here.

directly proportional to the readout power $\mathcal{P}_\mathrm{r}$, we expect that the eddy current loss rate $\kappa_\mathrm{s}/\omega_\mathrm{r} = \mathcal{P}_\mathrm{s}/\mathcal{P}_\mathrm{r} \propto \mathcal{R}_\mathrm{s}$ is power-independent.

Eddy current loss in the substrate material In the remainder of this chapter, we show that there can also be eddy current loss in the conductive material used to fix the samples in a sample box. This loss originates from a residual magnetic field $\mathbf{H}_h \equiv \mathbf{H}(z{=}-h)$ on the backside of the substrate with height h as shown in Fig. 2.33 (a). Therefore, we also find a finite field $\mathbf{H}_\mathrm{s}$ in the volume of the silver glue used to fix our samples in the sample box. Inside the silver glue volume, the field decays exponentially in z-direction for microwave frequencies within the skin depth λ_s, thus $\mathbf{H}_\mathrm{s} = \mathbf{H}_h \exp(-|z-h|/\lambda_\mathrm{n})$. The dissipated power due to eddy currents reads [296] $\mathcal{P}_\mathrm{s} = (1/2\sigma_\mathrm{r}) \int (\nabla{\times}\mathbf{H}_\mathrm{s})^2 \,\mathrm{d}\mathcal{V}$, where σ_r is the electrical conductivity at the resonator frequency and $\mathcal{V}$ is the volume of the conductive material on the backside of the substrate. In the following, we first calculate the field distribution generated from the CPW and finally use this expression to derive the resulting loss rate.
We calculate the components of a magnetic field $\mathbf{H}(y,z)$, which is induced by an oscillating current $I = \sqrt{2} I_\mathrm{r} \cos(\omega_\mathrm{r} t)$ flowing in the center conductor of the resonator. For simplicity, we neglect the time dependence of this current and assume that the field is created by the effective amplitude I_r. Furthermore, we neglect the vanishing x-component of the resonator field. We divide the magnetic field components into a field amplitude $H_h = \sqrt{(1+\varepsilon_\mathrm{r}) P_\mathrm{r} Z_0/2}\,(Z_\mathrm{vac} w)^{-1}$ [297] and a spatial distribution $\mathbf{k}(y,z)$. Here, w is the center conductor width and $Z_\mathrm{vac} \simeq 377\,\Omega$ is the vacuum impedance. Then, the magnetic field $\mathbf{H}(y,z) = H_h \mathbf{k}(y,z)$ is symmetric with respect to $y=0$ but depends on the dielectric material and on the boundary conditions given by the sample box. At the vacuum side of the CPW, the two relevant field components read

$$k_\mathrm{y}^\mathrm{vac} = \sum_{j>0}^{\infty} \frac{2}{F_j} \left[\frac{\sin(j\pi\xi/2)}{j\pi\xi/2} \sin(j\pi\tilde{\xi}/2) \right] \cos(j\pi y/b) e^{-\gamma_j |z|}, \tag{2.4.20}$$

$$k_\mathrm{z}^\mathrm{vac} = \underbrace{\sum_{j>0}^{\infty} \frac{2}{F_j} \left[\frac{\sin(j\pi\xi/2)}{j\pi\xi/2} \sin(j\pi\tilde{\xi}/2) \right] \sin(j\pi y/b)}_{\approx b/w \text{ for } y \ll b} e^{-\gamma_j |z|}. \tag{2.4.21}$$

Here, $\xi = w/b$ and $\tilde{\xi} = (s{+}w)/b$ are geometry parameters defined in Fig. 2.34. Further, $F_j = b\gamma_j/j\pi$ with $\gamma_j = j\pi\sqrt{1 + (2bv/j\lambda_\mathrm{vac})^2}/b$, $v = \sqrt{(\lambda_\mathrm{vac}/\lambda_\mathrm{cpw})^2 - 1}$. The two wavelengths $\lambda_\mathrm{cpw} = 2\pi c/\omega_\mathrm{r}\sqrt{(1+\varepsilon_\mathrm{r})/2}$ and $\lambda_\mathrm{vac} = 2\pi c/\omega_\mathrm{r}$ are defined by the speed of light c on the CPW and in free space, respectively. We calculate the field inside the substrate by introducing suitable boundary conditions, i.e., an electric wall at the backside of the substrate (see Fig. 2.34). The electric wall forces the z-component of $\mathbf{H}$ to vanish at $z=-h$ by multiplying it with $\sin(\pi z/h)$. Consequently, we find the components of the field distribution inside the substrate

$$\begin{aligned} k_\mathrm{y}^\mathrm{sub} = &- \sum_{j>0}^{\infty} \frac{2}{F_{j1}} \left[\frac{\sin(j\pi\xi/2)}{j\pi\xi/2} \sin(j\pi\tilde{\xi}/2) \right] \cos(j\pi y/b) \\ &\times \left\{ \left[\frac{F_{j1}^2 \coth(q_j) - \varepsilon_\mathrm{r} (2b/j\lambda_\mathrm{vac})^2 \tanh(r_j)}{1 + (2b/j\lambda_\mathrm{cpw})^2} \right] \cosh(\gamma_{j1} z) - \sinh(\gamma_{j1} z) \right\}, \end{aligned} \tag{2.4.22}$$

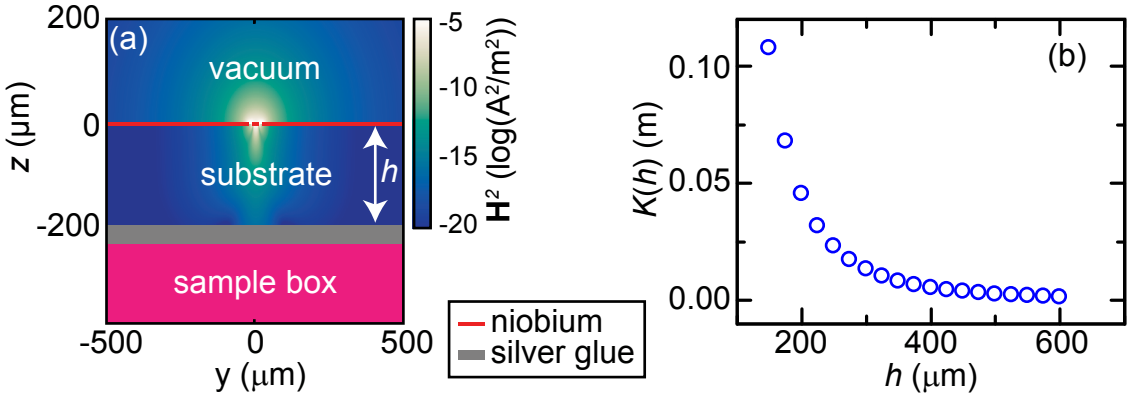

Figure 2.33: **(a)** Magnetic field intensity $\mathbf{H}^2(y,z)$ along a yz-cut through a CPW sample with substrate thickness $h = 200\,\mu\text{m}$ for $I_\text{r} = 4.5\,\text{mA}$ and $\varepsilon_\text{r} = 11.9$. Depicted in red is the Nb resonator at $z = 0$ with its center conductor at $y = 0$. Underneath the sample, we use silver glue to attach the substrate to the sample box. **(b)** Substrate thickness dependence of $K(h)^2$.

$$k_\text{z}^\text{sub} = \sum_{j>0}^{\infty} \frac{2}{F_{j1}} \left[\frac{\sin(j\pi\xi/2)}{j\pi\xi/2} \sin(j\pi\tilde{\xi}/2)\right] \sin(j\pi y/b) \times \left\{\cosh(\gamma_{j1} z) - \coth(q_j)\sinh(\gamma_{j1} z)\right\} \sin(\pi z/h). \tag{2.4.23}$$

In these equations, we use the terms $\gamma_{j1} = j\pi\sqrt{1-(2bvu/j\lambda_\text{vac})^2}/b$, $u = \sqrt{\varepsilon_\text{r} - (\lambda_\text{vac}/\lambda_\text{cpw})^2}$, $F_{j1} = b\gamma_{j1}/j\pi$, $r_j = \gamma_{j1}h + \tanh^{-1}(F_{j1}/\varepsilon_\text{r}F_j)$ and $q_j = \gamma_{j1}h + \text{cotanh}^{-1}(F_j/F_{j1})$.
Because Eqs. (2.4.20) - (2.4.23) are numerical approximations, we have to find suitable computation parameters. These parameters are the distance b at which we place the magnetic walls, the maximum number of iterations j_max, and the area in the yz-plane in which we perform the computations. As shown in Fig. 2.33 (a), we restrict the calculations to the area between $y_0 = 500\,\mu\text{m}$ and $z_0 = \pm h$. For reproducible results, we place the magnetic walls at $(y = 0)$ and at $b = \pm 2\pi h$. For a convenient numerical result we typically sum up to a maximum iteration step $j_\text{max} = 1000$.
So far, we have calculated the magnetic field at one slice in x-direction of the resonator. We now calculate the total integrated field over the length ℓ_r of the resonator. Assuming a sinusoidal current distribution between the two coupling capacitors, we find the field $|\mathbf{H}_h(x,y)| = H_h k(y,h)\sin(\pi x/\ell_\text{r})$ on the backside of the substrate. Assuming that this field generates the field $\mathbf{H}_\text{s}$ inside the lossy conductor, we calculate the dissipated power

$$\begin{aligned} P_\text{s}(h) &= \int_0^{\ell_\text{r}} \text{d}x \int_{-\infty}^{\infty} \text{d}y \int_0^{-\infty} \text{d}z \frac{(\nabla\times\mathbf{H}_\text{s})^2}{2\sigma_\text{r}} = \int \frac{\text{d}\mathcal{V}}{2\sigma_\text{r}} \left(\nabla\times\hat{e}_\text{y}\frac{H_h k(y,h)\sin(\pi x/\ell_\text{r})}{\exp(|z|/\lambda_\text{s})}\right)^2 \\ &= \int \frac{\text{d}\mathcal{V}}{2\sigma_\text{r}} \frac{H_h^2 k(y,h)^2}{\exp(2|z|/\lambda_\text{s})} \left(\hat{e}_\text{z}\frac{\pi\cos\left(\frac{\pi x}{\ell_\text{r}}\right)}{\ell_\text{r}} - \hat{e}_\text{x}\frac{\sin\left(\frac{\pi x}{\ell_\text{r}}\right)}{\lambda_\text{s}}\right)^2 \\ &\overset{\ell_\text{r}\gg\lambda_\text{s}}{\approx} \frac{H_h^2}{2\lambda_\text{s}^2\sigma_\text{r}} \int_0^{\ell_\text{r}} \text{d}x \sin^2\left(\frac{\pi x}{\ell_\text{r}}\right) \int_{-\infty}^{\infty} \text{d}y \cdot k(y,h)^2 \int_0^{\infty} \text{d}z \exp(-2|z|/\lambda_\text{s}) \\ &= \frac{(1+\varepsilon_\text{r})P_\text{r}Z_0}{4\lambda_\text{s}^2\sigma_\text{r}(Z_\text{vac}w)^2}\frac{\ell_\text{r}}{2}K(h)^2\frac{\lambda_\text{s}}{4} = \frac{(1+\varepsilon_\text{r})P_\text{r}Z_0\ell_\text{r}}{32\lambda_\text{s}\sigma_\text{r}(Z_\text{vac}w)^2}K(h)^2 = \sqrt{\frac{\omega_\text{r}\mu}{2\sigma_\text{r}}}\frac{(1+\varepsilon_\text{r})P_\text{r}Z_0\ell_\text{r}}{32(Z_\text{vac}w)^2}K(h)^2. \end{aligned} \tag{2.4.24}$$

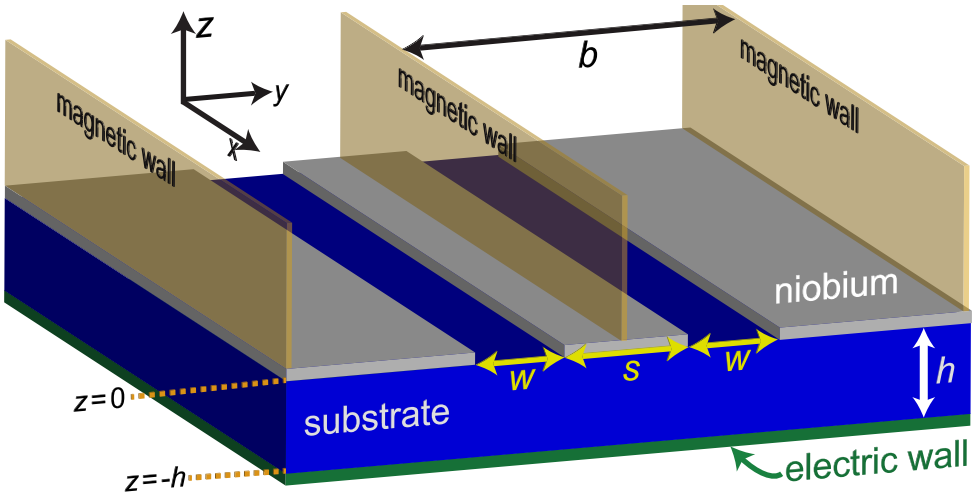

Figure 2.34: Sketch of a piece CPW transmission line to illustrate the relevant directions and length scales used for the calculation of the electromagnetic field distribution. For the metal structures, we use a fixed center strip width $w = 20\,\mu\text{m}$ and a distance to the ground planes $s = 12\,\mu\text{m}$. In our simulations, we place magnetic walls at the positions $y = \{-b, 0, b\}$ as well as an electric wall at the sample backside to provide suitable boundary conditions for the electromagnetic field.

In the above expression, we use $\int \mathrm{d}\mathcal{V} = \int_0^{\ell_\mathrm{r}} \mathrm{d}x \int_{-\infty}^{\infty} \mathrm{d}y \int_0^{-\infty} \mathrm{d}z$,[6] the absolute permeability of the conductive $\mu \simeq \mu_0$ material, and $\lambda = \sqrt{2/\omega_\mathrm{r}\mu\sigma_\mathrm{r}}$ [298]. To evaluate the total field intensity that enters the silver glue volume underneath the sample, we integrate[7] $K(h)^2 = \int_{-y_0}^{y_0} \mathrm{d}y [k_\mathrm{y}^\mathrm{sub}(y)]^2$ at $z = -h$ along the y-direction. The resulting thickness dependence of $K(h)^2$ shown in Fig. 2.33 (b) has the expected increase for thinner substrates. Finally, we obtain the substrate-thickness-dependent loss rate $\kappa_\mathrm{s}(h)$ defined as $\mathcal{P}_\mathrm{s}/\mathcal{P}_\mathrm{r}$, the ratio of the power dissipated in the system to stored power. From our calculations, we find

$$\frac{\kappa_\mathrm{s}(h)}{\omega_\mathrm{r}} = \sqrt{\frac{\omega_\mathrm{r}\mu}{2\sigma_\mathrm{r}}} \frac{(1+\varepsilon_\mathrm{r}) Z_0 K(h)^2 \ell_\mathrm{r}}{32 (Z_\mathrm{vac} w)^2}\,, \tag{2.4.25}$$

which is independent of the power circulating inside the resonator.

[6] Please note that our calculations are independent of the mode number k because $\int_0^{\ell_\mathrm{r}} \mathrm{d}x \sin(k\pi x/\ell_\mathrm{r})^2 = 1/2$, $\forall k \in \mathbb{N}$.

[7] We integrate our data numerically using the `trapz` function in MATLAB

Chapter 3 Sample fabrication

In this chapter, we introduce all relevant fabrication steps and detailed fabrication parameters for our samples. The most important development concerning sample fabrication within this thesis is the transition from Nb/Al two-layer samples to samples fabricated in an all-Al process.[1] That way, we significantly increase the coherence times of our samples and simultaneously reduce the number of fabrication steps.
In Sec. 3.1 of this chapter, we describe the fabrication of Josephson junctions, which is based on electron beam lithography and double-angle shadow-evaporation. In Sec. 3.2, we introduce the fabrication process for thin film CPW structures based on optical lithography. Details on all samples investigated in thesis are provided in Sec. 3.3.

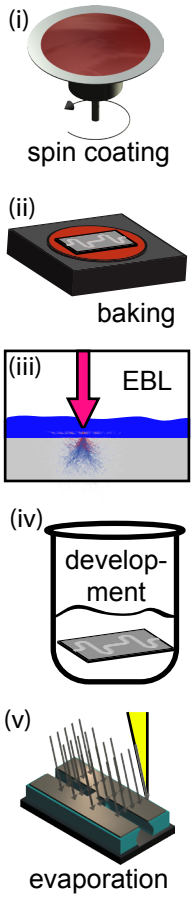

Figure 3.1: Main fabrication steps for Al based Josephson junctions.

3.1 Fabrication of Josephson junctions

In this section, we outline the different fabrication steps necessary for the fabrication of Al-based Josephson junctions depicted in Fig. 3.1. Because the actual junction size and shape strongly defines the physical properties of the junction in later experiments, it is important to have good control over the resist system. To improve the quality of the junction fabrication process at the WMI, we investigate the spin-coating process and the necessary baking steps in Sec. 3.1.1, which is based on the work presented in Ref. 299. The Josephson junctions are patterned using electron beam lithography (EBL). During this work, we have been strongly engaged in the exchange of the electron beam facility and in the adaption of all fabrication steps presented in Sec. 3.1.2.[2] In this context, we modify the established patterning processes developed in Ref. 299 to a large extend. The modification includes the introduction of ghost layers and a temperature controlled development process.[3] Finally, we introduce the Al evaporation, which is based on double-angle shadow evaporation [302, 303], and oxidation steps in Sec. 3.1.3.

[1] We develop the all-Al process in close collaboration with M. Haeberlein.
[2] In the course of this thesis we have replaced a 30 keV `FEI XL30sFEG` by a 100 keV `NanoBeam Limited nB5` electron beam lithography system.
[3] These fabrication processes are largely developed in Ref. 300 and Ref. 301.

3.1.1 Resist system - spin coating and baking

In the following, we introduce the resist system used for the fabrication of Josephson junctions as well as the different steps to generate a spatially homogeneous resist film on top of a substrate.

Resist system The resist system used to transfer nm-sized patterns to the evaporated Al thin films consists of a double-layer structure. We use two types of polymethylmethacrylate (PMMA), which is a well-established resist system for electron sensitive applications [304–306]. The first resist layer has a stronger sensitivity to electron radiation and is used to form a suitable undercut, which is crucial for the shadow evaporation technique. This resist is a PMMA copolymerized with methyl methacrylate-methacrylic acid (MA) that is dissolved in 1-methoxy-2-propanole in a ratio PMMA/MA = 33 %.[4] For the top layer, we use a resist with a high resolution allowing for nanometer accuracy for the junction process.[5] We use a spin coating process as described below to apply a thin, pattern-defining layer and a thicker bottom layer of approximately 70 nm and 700 nm, respectively.

Spin coating A common method to apply thin resist films onto a substrate is spin coating [307] as depicted in Fig. 3.2. Since the actual film thickness and the homogeneity of the resulting resist is crucial for the reliable fabrication of Josephson junctions, we describe the spatial and temporal development of the surface height distribution of the resist $h(r,t)$ in the following. We assume a cylindrical system such that the local resist thickness only depends on the radial component r as shown in Fig. 3.2 (a). In a first step, the liquid resist is pipetted to a substrate rotating with frequency ω_{rot} which is typically some hundred hertz. This rotation instantaneously centrifugalizes most of the resist off the substrate. The resulting outflow dominates during the start of the process until the substrate is completely covered with resist [cf. Fig. 3.2 (b)]. Only accounting for flow dominated processes already yields a reasonable theory to model $h(r,t)$ [308]. However, to account for the different concentration of solids in different resists, one has to include the evaporation of the solvent [309]. In the following we introduce a formula for $h(r,t)$ including evaporation by a mass transfer equation for the solution [310, 311]. A detailed description of the fluid dynamics has been collected during the work presented in Ref. 299. Evaporation starts immediately after the deposition of the resist and takes place throughout the entire process of spin coating. The evaporation of the solvent can be modeled by the mass transfer equation $\partial m/\partial t = k(x_A^0 - x_A^\infty)$ with k being the mass transfer coefficient. Here, x_A^0 is the initial concentration of the solvent and x_A^∞ is the mass fraction of the solvent that would be in equilibrium with the mass fraction of the solvent in the bulk vapor [310]. In this model, we obtain the final film thickness [299]

$$h_{\mathrm{f}} = (1 - x_A^0)\left[\tilde{k}(x_A^0 - x_A^\infty)\right]^{\frac{1}{3}} \frac{1}{\sqrt{\omega_{\mathrm{rot}}}}\,, \tag{3.1.1}$$

where $\tilde{k}$ is a modified mass transfer coefficient. Equation (3.1.1) provides a deterministic description of the spin coating process where the final resist thickness is inversely proportional to the square root of the rotational frequency. This dependence is experimentally confirmed [309, 310, 312] but does not hold in general. Restrictions occur from the solvent

[4] We use `Allresist PMMA/MA = 33 % AR-P 617.08` resist for our process

[5] We use `Allresist PMMA 950k AR-P 679.02` resist for our process.

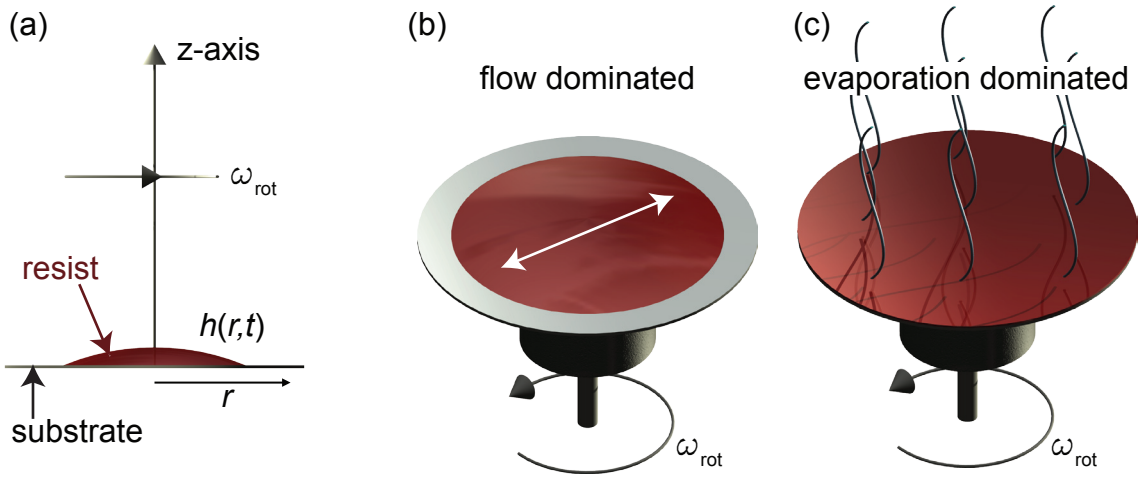

Figure 3.2: **(a)** Cross-sectional view of a substrate covered with liquid resist on a spin coater rotating with frequency ω_{rot}. We assume a rotational system symmetry such that the resist height h depends only on the radial distance r and the time t. **(b)** For short times after resist dripping, the resist height is flow dominated. **(c)** When the complete substrate is covered with resist, the surface dynamics is strongly determined by evaporation processes. Drawings taken from Ref. 299.

type, the solid content, and the viscosity of the resist. Furthermore, the usage of rectangular substrates with finite lateral dimensions and the application of a double-layer resist system introduce variations from Eq. (3.1.1).

Resist surface To evaluate the spin coating process, we measure the spatial distribution $h(r)$ of the resist surface [299]. In Fig. 3.3 (a), we show $h(r)$ of a Si substrate covered with the double-layer resist system. In contrast to circular wafers with 1 inch in diameter used in previous works [177] (see also Fig. 3.6), the rectangular $6 \times 10\,\mathrm{mm}^2$ substrates show thickness variations over the entire substrate. From a quantitative analysis,[6] we find that the average resist thickness fits nicely to the expected values of 700 nm and 770 nm for single-layer and double-layer systems, respectively [cf. Fig. 3.3 (b) and (c)]. There are, however, deviations in the resist thickness with peak-to-peak variations of approximately 25 %. In particular, we observe a significant influence of the rectangular substrate shape resulting in a significantly higher film thickness at the edges of the substrate (edge beads). Edge beads primarily originate from a larger surface tension at the edges of the substrate and from resist wave reflections [313]. Additionally, air friction enhances the evaporation process and supports the formation of edge beads in the case of non-rotational symmetric substrates. Since the edge bead formation is a complex process that is hard to control, the most promising solution to avoid them is the usage of large enough and circular substrates.

Resist defects In addition to edge beads, there is a series of other defects that can occur during a spin coating process [314–316]. Two prominent examples are striations [317, 318] and comets [319]. Comets are discontinuities in the resist that appear because the liquid outflow is disturbed by dirt particles on the substrate [see Fig. 3.3 (d)]. These particles are either already stuck on the substrate before resist is pipetted or are brought to the substrate via the resist. To avoid the formation of comets, we clean the substrates with

[6] We acknowledge the thickness measurements, which have been performed by the Sentech company.

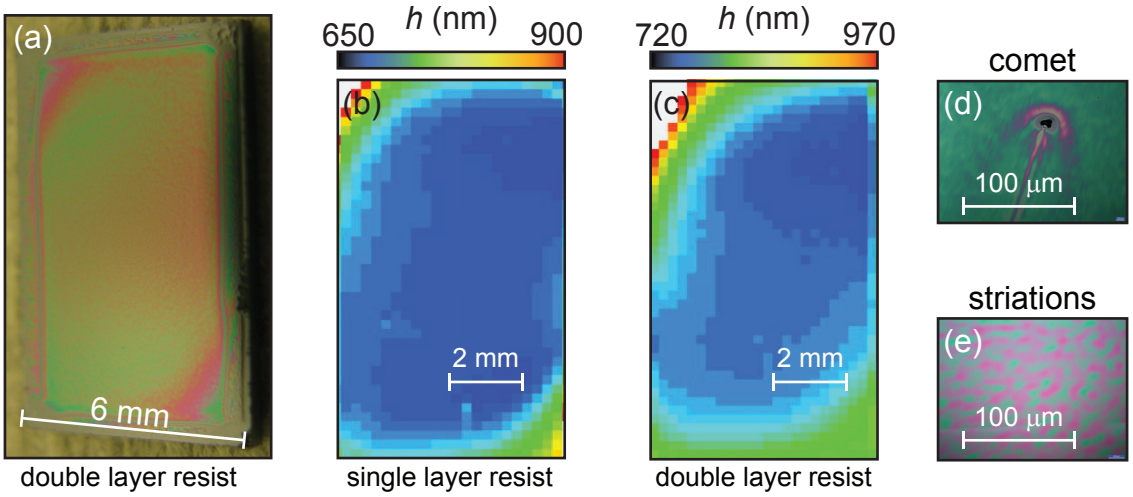

Figure 3.3: **(a)** Photograph of a $6 \times 10\,\mathrm{mm}^2$ sized Si substrate covered with a double-layer resist system. **(b)** Resist height h plotted for a single-layer resist system. **(c)** Resist height h plotted for a double-layer resist system. **(d)** Photograph of a comet. **(e)** Photograph of striations.

an O_2 plasma before spin coating. Striations are quasi-periodic modulations of the resist thickness with sub-millimeter period as shown in Fig. 3.3 (e). Even though the physical reason for striations is not completely understood, one prominent model [320–323] assumes local evaporation leading to surface tension variations. Due to the Marangoni effect [324], more resist flows to regions with higher surface tension and increases the thickness at these points. This effect is enhanced by less volatile solvents meaning that PMMA/MA 33 % with its low viscosity suffers strongly from striations. From a measurement with a DEKTAK profilometer, we find that the thickness variations are on the order of 20 nm, which is consistent with other measurements found in literature [318]. During the the work presented in Ref. 299, we show several methods to prevent striations, e.g., increase the rotation frequency or change the atmosphere above the substrate. These experiments have triggered the decision to install a new spin coater in the clean room facilities of the WMI that has a closed atmosphere.[7] Additionally, this spin coater suffers less from vibrations providing resist films without a significant amount of striations.

Resist baking After spin coating, the resist is heated above its glass temperature T_g on a hot plate to remove residual solvent in the resist layer and to changes the chemical properties of the polymers [299]. T_g is a resist-specific property and depends on the concentration of the remaining solvent and on the film thickness [325]. For PMMA, T_g is approximately 150 °C. In Fig. 3.4, we illustrate the chemical process during the baking step. The higher mobility of the resist constituents supports the diffusion of the solvents. Hence, the total length of the baking step is crucial for a complete removal of the solvents. A complete removal is limited by the resist thickness and by the molecular weight of the polymer [326]. In addition to solvent diffusion discussed above, there is a chemical transition of the PMMA during the baking step. The solvent dilution triggers this transition and leads to ring formation of new copolymers, which are bound by anhydride weak links. These copolymers have a significantly increased sensitivity to electron bombardment [327].

[7] We use a `Laurell WS-650-23B` spin coater.

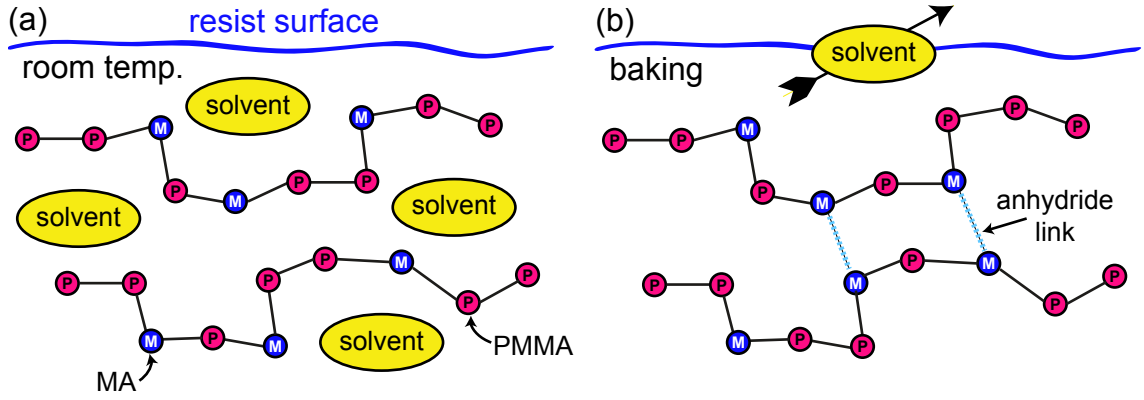

Figure 3.4: **(a)** Copolymer chains consisting of PMMA and MA that enclose residuals of the solvent at room temperature. **(b)** During the baking step, the residual solvents diffuse through the resist surface and there is a formation of anhydride links in-between the copolymer chains.

3.1.2 Electron beam lithography

Electron beam lithography (EBL) in combination with lift-off or reactive ion etching processes is a commonly used technique for fabricating nanometer-sized thin film structures [328]. In EBL processes, the high-energy beam electrons break up the long copolymer-chains in a suitable resist, which subsequently are washed away in a development step. That way, we form a well-defined pattern in the resist, serving as a mask in the subsequent thin film evaporation process for the Josephson junctions. The EBL process provides a spatial resolution that is well-suited for the fabrication of nm-sized junctions. Theoretically, the EBL resolution is limited by the de-Broglie wavelength [329] of the electrons, which is in the picometer range for keV electrons. This limit, however, is not achieved due to lens aberrations in the electron optics but also due the interaction of electrons within the electron beam [330] and with the resist/substrate materials. This electron-matter interaction results in a resolution for typical resist systems on the order of a few tens of nanometers [328, 331, 332]. In the following, we describe the relevant mechanisms of electron-matter interaction.

Elastic scattering We describe electron-matter interaction in the framework of scattering processes, where we differentiate between elastic and inelastic processes. Elastic scattering happens when the electrons feel the Coulomb potential of the resist- and substrate nuclei but when there is no energy transfer. Hence, elastic scattering does not break up the copolymer-chains but broadens the electron beam and consequently reduces the resolution. The elastic scattering of electrons can be well-described with a screened Rutherford cross-section σ_{tot} accounting for the screening β_{N} of the nucleus potential by the shell electrons. The screened Rutherford differential elastic cross-section [333]

$$\frac{\mathrm{d}\sigma_{\mathrm{tot}}}{\mathrm{d}\Omega} = \frac{\mathcal{Z}^2 e^4}{4E_{e^-}^2 (1 - \cos\theta + 2\beta_{\mathrm{N}})^2} \tag{3.1.2}$$

depends on the incident electron energy E_{e^-}, on the atomic number $\mathcal{Z}$, and on the polar scattering angle θ. Even though Eq. (3.1.2) must be modified for heavy elements [333] and holds only for high-energy electrons in the keV-range, it gives a reasonable intuition into the scattering process. A more advanced description of elastic scattering includes spin-orbit

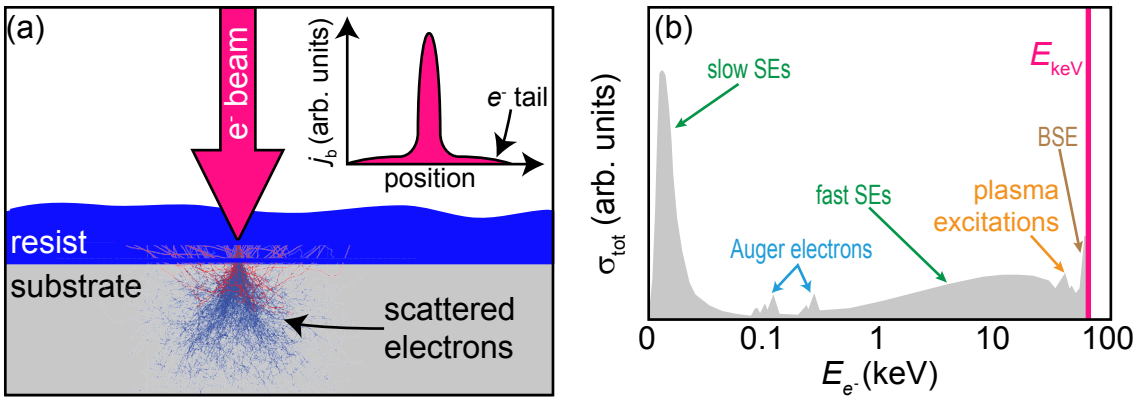

Figure 3.5: **(a)** Sketch of an electron beam irradiated to resist and substrate. The complex scattering paths of electrons inside resist and substrate are simulated using a Monte-Carlo method [299]. The inset shows the spatial distribution of the beam current density j_b. Next to the Gaussian profile, there is a tail of electrons broadening the beam profile. **(b)** Energy distribution of the total cross-section for electron matter interaction assuming a beam energy of $E_{e^-} = 80\,\mathrm{keV}$.

coupling and leads to the well-known Mott cross-section [334]. The main conclusion derived from Eq. (3.1.2) is the proportionality $\mathrm{d}\sigma_{\mathrm{tot}}/\,\mathrm{d}\Omega \propto E_{e^-}^{-2}$, meaning that low-energy electrons have a much larger cross-section than high-energy electrons. Consequently, low-energy electrons more likely undergo small-angle elastic scattering events, which subsequently broadens the beam as depicted in Fig. 3.5 (a). Moreover, the probability for large-angle scattering (back-scattering) is increased for low-energy electrons. These back-scattered electrons (BSEs) may re-emerge into the resist at some distance from where the beam entered. The beam broadening and the reemerging electrons lead to the proximity effect. Proximity effect means that the exposed pattern is wider than the scanned pattern [335–339]. Therefore, it is advantageous to use a high acceleration voltage for the writing process. The latter argument is one reason, to operate the nanobeam nB5 system installed during this thesis at 80 keV compared to the maximum 30 keV of the previous FEI system.

Inelastic scattering Even though elastic scattering events have a large influence on the actual shape of the electron beam inside the resist, inelastic scattering processes provide the energy that is necessary to break up the copolymer-chains. Since this energy is approximately 100 eV [340], most pair-breaking processes are induced by low-energy electrons. The most prominent inelastic scattering process is inner-shell ionization providing secondary electrons (SEs). Here, an incident electron transfers its energy to a bound inner-shell electron of a target atom and ejects the target electron to the vacuum level. The excess energy from the electron of a higher shell, occupying the vacancy, is then emitted either by X-ray photons or by Auger-electrons [341]. As shown in Fig. 3.5 (b), these processes occur for energies in the range of 100 eV to a few keV, which makes them the main source for pair-breaking in the PMMA/MA polymers. Further inelastic scattering processes include bremsstrahlung, cathodoluminescence, plasmon excitations, and electron-phonon interaction [see Ref. 341 for details]. The complex energy distribution of the scattering processes depicted in Fig. 3.5 (b) is simplified in a mean energy loss model, characterized by the stopping power [334, 342]

$$\mathcal{P} = \frac{\partial E}{\partial s} \propto \frac{\mathcal{Z}}{E_{e^-}} \ln\left(\frac{1.166 E_{e^-}}{d_1 \mathcal{Z}} + d_2\right), \tag{3.1.3}$$

which has the form of a modified Bethe equation. Here, d_1 and d_2 are material specific constants [343]. This loss model, which is frequently used for the simulation of electron-matter interaction [333, 344–349], assumes a constant energy loss per traveling distance $\partial E/\partial s$ of the electrons. The simulations based on this model use a Monte-Carlo method to describe the formation of secondary electrons as individual events occurring after a mean free path [344, 350]. During the work presented in Ref. 299, we perform a series of simulations of electron interaction in the double-layer resist system as the one shown in Fig. 3.5 (a). From these simulations, we gain detailed insight into the proximity effect in our system. This insight was an important achievement since the proximity effect provides the highly desirable undercut in the lower resist layer. Furthermore, the simulations provide the spatial distribution of the energy deposition of the electron beam defining the sensitivity of a resist as described in the following paragraph.

Sensitivity and contrast The energy-dependent break-up of copolymer chains as described above defines how sensitive a specific resist is to electron irradiation. The resist sensitivity accounts for the number of electrons at a given beam energy (dose) that is required to break up all copolymer chains in a certain area. This number of electrons scales inversely with the beam energy [cf. Eq. (3.1.3)]. Additionally, it depends on the resist thickness, on the particular developer [332], and on the monomer (MA) content in the resist [351]. Because the resist is very sensitive to low-energy electrons as described above, it is susceptible to SEs that re-emerge at a position away from the primary electron incident point. This fact lowers the contrast, i.e., the remaining film thickness as a function of the exposure dose. Ideally, the contrast is given by a step-function. For real EBL processes, however, this function has a finite slope and the contrast of the resist can be expressed as [328] $c_{\mathrm{res}} = \log(D_2/D_1)^{-1}$. Here, D_1 is the highest dose leaving the resist unaffected and D_2 is the dose where the entire resist is broken up. Since these doses are highly dependent on the particular fabrication process, we systematically measure the contrast of the two resist systems in Ref. 299. We find that the clearing dose of the approximately 700 nm thick PMMA/MA bottom layer is only slightly lower than for the double-layer resist system. This fact requires a careful dose-analysis when the shape or the size of an actual pattern is changed in order not to break the upper resist at adverse positions. In addition to SEs, the resist is sensitive to the tail of electrons next to the Gaussian beam profile shown in the inset of Fig. 3.5 (a). This tail originates from imperfect electron optics and noise in the magnetic focusing coils. Compared to the previously used FEI system, the nB5 system has a strongly reduced noise contribution resulting in a clear Gaussian beam profile. This beam profile provides a high reproducibility of the patterning process, when the beam is accurately focused to the substrate.

Beam focusing Optimizing the contrast during the EBL process not only requires an optimized dose selection but also a well-focused beam. During the work presented in Ref. 299, we establish a focusing method based on gold nanoparticles.[8] The nanometer diameter of these particles makes them well-suited to focus the electron beam on the resist surface as outlined in the following. Before transferring the sample to the electron beam system, we apply small droplets of gold nanoparticles onto the spin coated resist as shown in Fig. 3.6 (a). These droplets form large accumulations of circular crystals that

[8] We use `Sigma-Aldrich 753637` nano particles, which are dissolved in a stabilized suspension in 0.1 mmol phosphate buffered saline and have a spherical shape with 40 nm diameter.

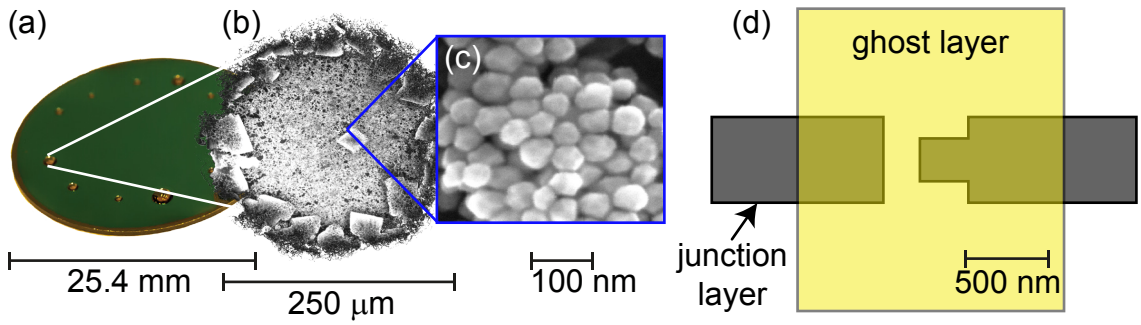

Figure 3.6: **(a)** Photograph of a circular Si substrate, where single droplets of a gold nanoparticle solution are applied to the spin-coated resist. **(b)** and **(c)** Scanning electron microscope image of the gold nanoparticles. Pictures taken from Ref. 299. **(d)** Schematic drawing of the pattern that is scanned for defining the resist pattern for the Josephson junction fabrication (junction layer). To generate the required undercut, we additionally irradiate a ghost layer with lower dose.

can be resolved with a scanning electron microscope [cf. Fig. 3.6 (b)]. We optimize the beam focus by zooming in on these crystals until single gold particles are resolvable [see Fig. 3.6 (c)]. Using this focusing procedure has strongly improved the reproducibility during the fabrication of Josephson junctions.

Ghost layer The well-focused beam with its clean Gaussian profile is a perfect resource to write patterns with nm accuracy. It has turned out, however, that the undercut required for shadow evaporation is no longer present because of the lack of the proximity effect. To reintroduce a sufficient undercut, we make two modifications to the established fabrication process presented in Ref. 299. First, we write an additional ghost layer in addition to the actual junction pattern [301] as depicted in Fig. 3.6 (d). For this layer, we use a substantially reduced dose compared to the junction layer ($D_{\text{ghost}}/D_{\text{junc.}} \simeq 0.15$) such that the resist in the ghost layer area is only partly activated. The second modification is a temperature-controlled development step [300] as described in the following paragraph.

Resist development Before we evaporate the Al thin films for the Josephson junctions, we remove the exposed resist areas in a two-stage development process. In a first step, a developer washes away all broken-up polymer chains, while the non-activated chains stick to the substrate. In a second step, we generate the required undercut using temperature controlled isopropanol (IPA). For the first step, we dip the sample completely into a developer, which we keep at ambient temperature. We use a developer for PMMA that is selective to the molecular weight of the broken-up polymers.[9] This step washes away only the part of the resist that is written as the junction layer [cf. Fig. 3.6 (d)]. The subsequent development step forms an undercut as shown in Fig. 3.7 (a). To this end, we use the fact that IPA itself works as weak developer for PMMA [352–354] and that the sensitivity to IPA of PMMA/MA (bottom layer) is enhanced compared to PMMA 950k (top layer) [299]. Furthermore, the sensitivity of the top layer strongly decreases for decreasing temperature [300]. While the first development step is performed at room-temperature, for the second development step we stabilize the IPA temperature at $(4.0 \pm 0.2)\,^{\circ}\text{C}$. That way, we achieve a selective development of only the lower resist layer.

[9] We use `Allresist AR-600-56` developer for the process. This particular developer is methyl-isobutyl-ketone (MIBK) diluted in IPA with an IPA : MIBK ratio of 3 : 1.

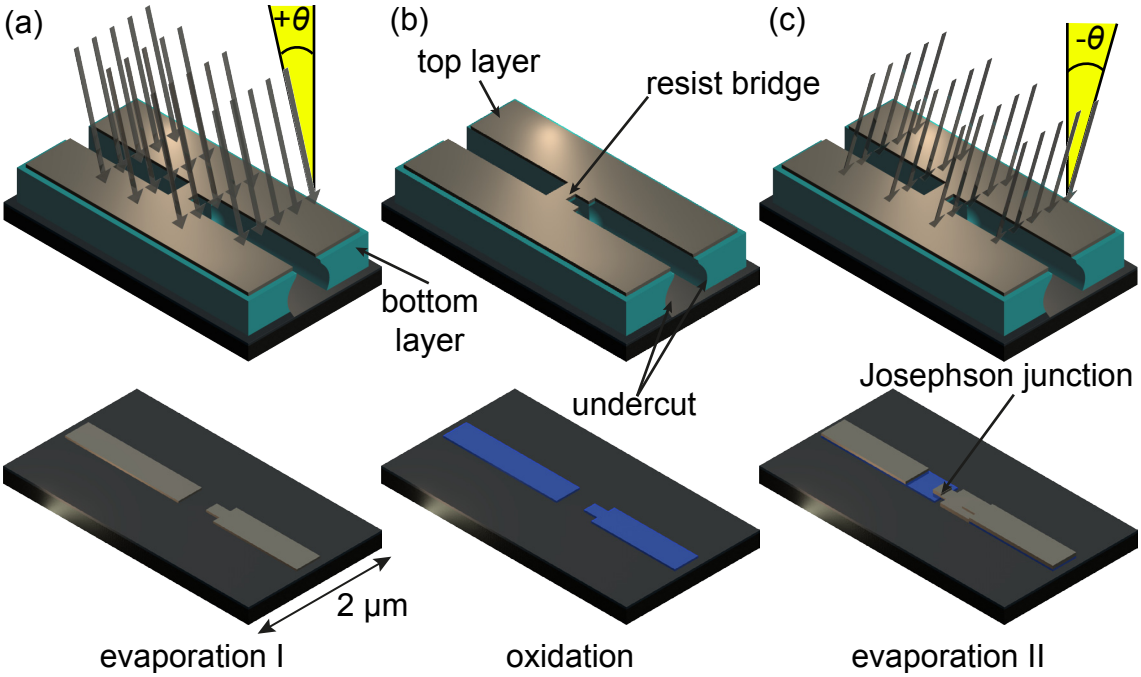

Figure 3.7: Different fabrication steps for Josephson junctions including both resist layers in the top row. These layers are omitted in the bottom row to show the resulting Al films. **(a)** First evaporation step at angle $+\theta$. **(b)** Oxidation of the evaporated Al-film. **(c)** Second evaporation step at angle $-\theta$. The overlap of the two Al films is determined by the evaporation angles, the width of the resits bridge, and the thickness of the lower resist layer. Drawings taken from Ref. 299.

3.1.3 Evaporation and oxidation of Al thin films

The electrical circuits for the Josephson junctions consist of thin Al films, which we evaporate on a dielectric substrate. We fabricate $Al/AlO_x/Al$ structures by integrating an oxidation step between two steps of Al evaporation (see Fig. 3.7). The two Al films have a thickness of 40 nm and 70 nm, respectively. By evaporating from two different angles $\theta = \pm 17°$, we generate an overlap between the upper and the lower Al film. This overlap is intersected by the oxide layer and thus forms the Josephson junction.

Al evaporation We use a thin film deposition system for thermal evaporation of Al [355]. To avoid contaminations of the Al films, the evaporator is placed inside an ultra-high vacuum chamber typically operating at 10^{-8} mbar. Furthermore, we use very pure Al with a purity of 99.999 % in the two evaporation steps. Before we deposit the Al onto the substrate, we evaporate a certain amount of Al onto a shutter to get rid of possible contamination in the Al crucible. Then, we open the shutter and record the mass change of a quartz crystal to monitor the film thickness of the evaporated Al. We use a growth rate of 12 Å/s to achieve a precise film thickness. We evaluate the film thickness using atomic force microscopy (AFM) images as the one shown in Fig. 3.8 (a). With our deposition system, we achieve a thickness accuracy of approximately ±5 nm for the individual Al films [300]. The root-mean-square surface roughness of the Al films is approximately 0.8 nm. For our process, the surface roughness is lowest for high evaporation rates [300], which is in contrast to other studies in this field [356].

Al oxidation The most crucial part in Josephson junction fabrication is the definition of the insulating tunneling barrier formed by the thin oxide layer. There are two main reasons for the importance of the oxidation step. The first reason is the exponential dependence of the junction critical current on the oxide thickness [357]. In particular flux qubits demand high critical current densities requiring thin oxides of only a few atomic layers. In such thin layers, inhomogeneous oxidation may easily lead to electrical shorts rendering the junction unusable. The junction's critical current density strongly depends on the duration and the oxygen pressure of the oxidation process. We again use the quartz crystal [300] to monitor the progress of the oxidation process. The process starts with an Al_2O_3 monolayer formation during the first seconds for typical pressures in the µbar regime [358]. This formation is followed by oxidation via tunneling of oxygen atoms characterized by a much lower oxidation rate. Since tunneling is a statistical process, which depends on many parameters (pressure, temperature, surface-roughness, etc.), the exact critical current density is hard to predict for thin oxide layers.

Junction parameters We perform DC SQUID measurements [177] to characterize the physical properties of the junctions from their current-voltage characteristics (IVCs). The purity of the Al is characterized by the zero-field voltage $V_g \simeq 360\,\mu V$ found for our Al films [177, 178]. This value is close to the theory value $V_g^{BCS} = 2 \times 1.764 k_B T_c \simeq 365\,\mu V$ [66], using $T_c = 1.2\,K$ for Al. Hence, we have only negligible influence of impurities in the Al. In addition, the junction capacitance [359] and critical current density determining the junction inductance can be extracted from IVC measurements. Since capacitance and inductance determine the characteristic energies E_J and E_c of the junctions, these values are crucial for the fabrication of different superconducting qubit types. For our junctions, typical values of the specific capacitance are on the order of several hundred $fF/\mu m^2$ [177, 178]. Depending on the oxidiation process, we find current densities of approximately $0.5\,kA/cm^2$ to $4\,kA/cm^2$ for flux qubit junctions and $100\,A/cm^2$ for transmon qubits.

3.2 Fabrication of CPW structures

In this section, we describe basic fabrication steps used for thin film CPW structures made from Nb using optical lithography. Because optical lithography is a well-established process at the WMI [68, 360, 361], we only describe the main concept in Sec. 3.2.1 and focus on various methods to clean the substrate in Sec. 3.2.2.

3.2.1 Optical lithography

Optical lithography works in close analogy to EBL described above. The two main differences are that we activate the resist with ultraviolet light instead of accelerated electrons, and that we use a negative patterning process.[10] The negative fabrication process comprises the following five steps. (i) We first deposit a 100 nm thick Nb film using sputter deposition. (ii) We spin coat a negative resist onto the substrate. (iii) We activate the relevant parts of the resist with ultraviolet light using a photomask that contains the CPW structure. (iv) We develop the resist. (v) We finally remove the metal in the activated areas using an etching process.

[10] A negative process means that we remove the not-activated resist, compared to the positive EBL process described above.

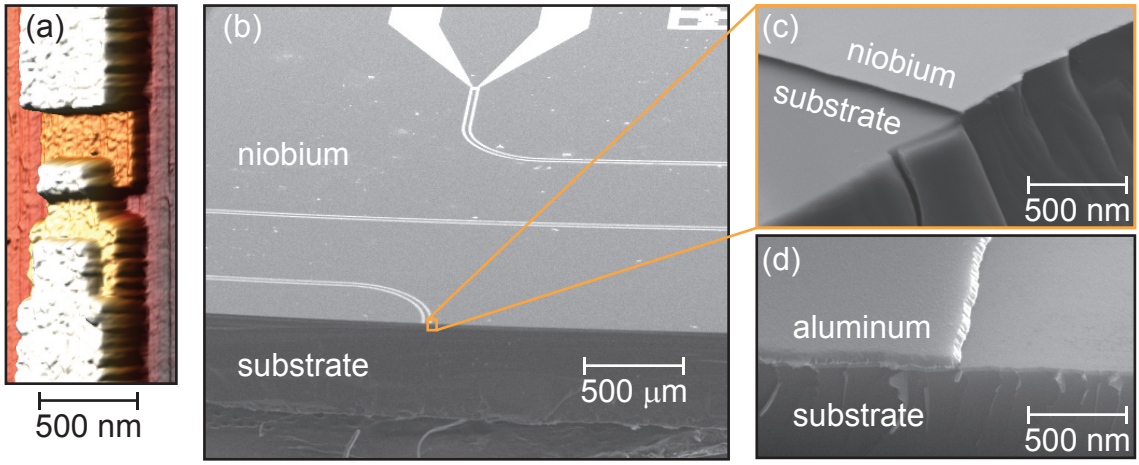

Figure 3.8: **(a)** Atomic force microscope image of a typical Josephson junction consisting of two Al layers with 40 nm and 70 nm height. **(b)** Scanning electron microscope image of a resonator sample which is broken into pieces to investigate the profile of the metal film. **(c)** Profile of a 100 nm thick RIE-etched Nb film fabricated with a negative process. **(d)** Profile of a 110 nm thick evaporated Al film fabricated with a positive process.

Negative process The reason to use a negative process is the high melting temperature and reactivity of Nb which prohibits an evaporation process. Therefore, sputtering is the suitable method to deposit thin Nb films. Sputtering in turn, is not compatible with a positive process for two reasons. First, sputtering is an isotropic deposition process, which covers the vertical edges of a resist in a positive process. These covered edges are hard to remove in a lift-off process. Second, sputtering on top of a resist results in edge defects and sharp Nb tips because the resist suffers from the strong electron and Nb bombardment. The resulting edge defects in turn lower the sample quality [122, 123, 125, 362, 363] because of the enhanced electromagnetic field strength at these positions. Hence, we use a negative process by etching the spare Nb away, which results in very clean edges as shown in Fig. 3.8 (c).

Reactive ion etching Our standard etching method is reactive ion etching (RIE),[11] where a chemical-reactive Ar/SF_6 plasma is used to remove the Nb from the substrate surface. We use an inductively coupled plasma (ICP), which is generated by a magnetic field at low pressure. Additionally, there is an RF bias to create directional electric fields near the substrate to accelerate the ions. This setup allows one to vary the plasma density independently from the energy of the ions. Hence, we can adjust the ratio between the chemical and the physical etching rates. We use this possibility because the acceleration power can effect the quality of superconducting resonators [124]. The reason is that a reduced RF power reduces the kinetic energy of the ions hitting the sample providing a reduced surface roughness. During the work presented in Ref. 364, we fabricate and characterize resonators with RF powers between 100 W and 30 W. For our samples, however, there is no significant influence of the RIE power on the sample quality. Hence, the sample quality of the resonators presented in this thesis is not limited by the etching process.

[11] We use a `Oxford Plasmalab 80 Plus` device with ICP plasma source for our process.

3.2.2 Substrate cleaning

As described in Sec. 2.4.2, superconducting resonators can suffer from significant loss due to two-level states (TLSs) at the substrate surface. Standard cleaning procedures based on acetone and IPA in an ultrasonic bath only superficially remove dirt on the substrate surface. They do not remove, however, TLSs embedded in the upper atomic layers of the substrate. We remove these TLSs from the sample by physically removing the substrate surface. We investigate two common methods for the latter type of surface cleaning during the work presented in Ref. 364 and Ref. 68. The first method is based on wet-etching the surface by dipping the sample into hydrofluoric acid (HF-dip) [364] and the second method is an ion-gun cleaning step before metallization [68].

HF-dip Except for some samples fabricated on sapphire, we use thermally oxidized Si as substrate material. To remove contaminations residing in the oxidized surface, one can use an HF-dip [124, 365]. After etching in a HF:H_2O solution, there is a pure Si surface leading to the formation of dangling bonds [366]. These dangling bonds get passivated by hydrogen atoms [367, 368], which protect the surface from contamination. This protection lasts for approximately half an hour [369, 370] limiting the time to transfer the sample into an evacuated environment, i.e., the load lock of the sputtering chamber. A successful HF-dip completely removes the Si oxide but does not etch away too much of the pure Si to keep the surface smooth. Hence, we use a suitable combination of the etch time and of the strength of the HF:H_2O solution. Finding such a combination is supported by the fact that the etch rate of HF is much higher for SiO_2 than for Si [371]. We find that for a ratio HF:$H_2O = 1{:}10$, an etch time of three minutes is a good trade-off to remove the 50 nm thermal oxide [364]. The complete removal of the SiO_2 surface can be controlled by the hydrophilic-to-hydrophobic transition of the sample. After the wet etch, we place the samples in deionized water to completely remove HF residuals. To benefit from the hydrogen passivated surface, we mount the samples in the load lock of our sputtering chamber within ten minutes after the HF-dip.

Ion gun treatment As an alternative to the etching process described above, we use ion-gun bombardment of the surface to remove contaminations [19, 372, 373]. One advantage of ion-gun cleaning compared to the HF-dip is that the ion-gun is located in the same vacuum cluster as the sputtering magnetron. Hence, the cleaned surface is hardly exposed to contaminations between the cleaning- and the metallization step. In our setup, the background pressure on the order of 10^{-9} mbar minimizes the contamination process. During the cleaning process, electrons are accelerated towards an argon-filled chamber with a pressure of 4×10^{-6} mbar. In this chamber, the electrons ionize the argon atoms that are subsequently accelerated towards the substrate. The voltage used to accelerate the ions towards the substrate is one crucial parameter during the cleaning process because the final velocity of the ions strongly determines the surface roughness of the substrate [374]. The surface roughness in turn has a strong effect on the quality of superconducting resonators [19, 296]. A second parameter affecting the surface roughness is the duration of the cleaning process. On the one hand, this time should be as short as possible to minimize the surface roughness. On the other hand, the cleaning time must be sufficient to remove the surface contamination completely. During the work presented in Ref. 68, we perform a systematic study of acceleration voltage and cleaning time to optimize the quality of superconducting resonators.

3.3 Fabricated samples

In this section, we present relevant fabrication parameters and the layout for the different samples analyzed during this thesis. Our samples can be divided into three groups as shown in Fig. 3.9. The first group (Sec. 3.3.1) comprises all transmission line and resonator samples without qubits. These samples all have the same geometry for the CPW structure except for one microstrip sample. We adapt the basic CPW structure for the gradio qubit sample presented in Sec. 3.3.2. Finally, in Sec. 3.3.3, we introduce the transmon qubit sample used to study second-order noise processes and photon statistics of thermal fields.

3.3.1 Resonator and transmission line samples

Fabrication parameters We first give a detailed summary of the fabrication parameters used for all resonator and open transmission line samples used in Sec. 4.3 and in Sec. 5.1. The resonators are half-wavelength resonators with a design as shown in Fig. 3.10. For the Nb CPW structures, we always use a fixed center strip width $w = 20\,\mu\text{m}$, a distance to the ground planes $s = 12\,\mu\text{m}$, and a film thickness of 100 nm (see Fig. 2.34 for details). The resonator length is $\ell_\text{r} \simeq 15.25\,\text{mm}$ resulting in a resonance frequency of approximately 4 GHz. We summarize the fabricated resonators in Tab. 3.1.[12] The samples are fabricated either on a SiO_2-covered SI, HF treated Si/SiO_2, or a sapphire substrate.[13] The 50 nm oxide on the Si substrates is thermally grown and the Si itself is undoped with a specific resistance larger than $1\,\text{k}\Omega\,\text{cm}$. All substrates have lateral dimensions of $6\,\text{mm} \times 10\,\text{mm}$ and are cleaned by a series of isopropanol and acetone dips in an ultrasonic bath. We sputter deposit the 100 nm thick Nb films with a deposition rate of 0.33 nm/s at an argon pressure of 275 µbar with an argon flow of 10 sccm. We spin the optical resist with 1000 rpm onto the Nb coated substrate.[14] We perform mask exposure to ultraviolet light after baking for 70 s at 110 °C. For reactive ion etching we use an Ar/SF_6 plasma with a flow of 10 sccm for Ar and 20 sccm for SF_6. We etch for 70 s at a pressure of 20 mbar using 50 W for the ICP plasma. The patterned samples are fixed with silver glue inside a gold-plated copper box as shown in Fig. 3.10 (b). To save sample space, we connect the feed lines directly to the coaxial cables using a transmission line to coaxial (CPW/SMA) adapter.[15] We use 10 µm gap capacitors as shown in Fig. 3.10 (c) resulting in an external coupling rate $\kappa_\text{x}/2\pi \simeq 15\,\text{kHz}$ (cf. Sec. 4.3.2).

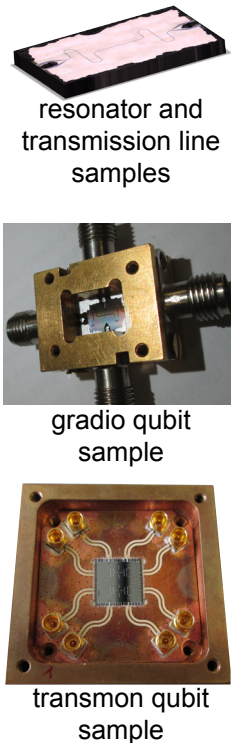

Figure 3.9: Different sample types fabricated during this work.

Modifications from the standard process We now list the modifications of the above described fabrication steps for the individual samples presented in Tab. 3.1.

[12] Most of the resonator samples summarized in Tab. 3.1 are fabricated during the work presented in Ref. 364

[13] We purchase all our wafers from `CrysTec GmbH`.

[14] We use `MicroChemicals AZ 5214 E` resist for our process.

[15] We use `Rosenberger 32K724-600S5` panel jack stripline adapters for that purpose.

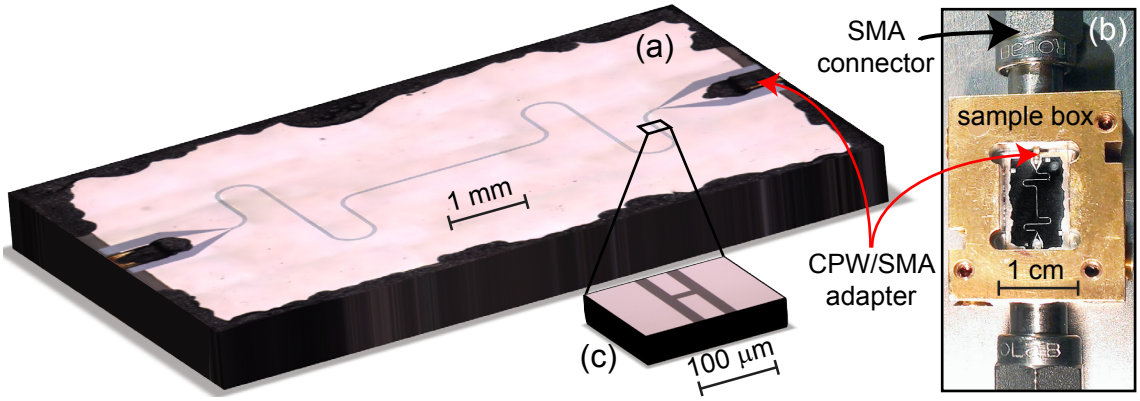

Figure 3.10: **(a)** Microscope image of a Nb resonator. This basic design with resonance frequency $\omega_r/2\pi \simeq 4\,\mathrm{GHz}$ is used for all samples except for the transmon qubit sample. The dark surrounding of the chip is the silver glue used to ground the superconducting ground plane. **(b)** Photograph of a resonator inside a sample box which is connected to an SMA connector via an CPW/SMA adapter. **(c)** Zoom into the area where one of the coupling capacitors is placed. The $10\,\mu\mathrm{m}$ wide gap yields an external quality factor of approximately 3×10^5.

- Sample III is patterned with an EBL process instead of optical lithography. To this end, we only use a single layer of the PMMA/MA resist spin-coated with 2000 rpm for one minute. Even though the etch resistance of PMMA is significantly lower compared to standard photo resists [351], the approximately 1 µm thick resist withstands the RIE process. For the large CPW structures, we use an electron beam with a beam current of 14.5 nA and apply a dose of $400\,\mu\mathrm{C/cm^2}$. We focus the beam using gold nanoparticles as described in Sec. 3.1.2 and align the write-fields at the corners of the rectangular substrate.

- For sample IV, we remove the SiO_2 layer on top of the Si substrate. To this end, we wet-etch for three minutes with a ratio $HF{:}H_2O = 1{:}10$. Afterwards, we rinse the sample with deionized water before placing it in the sputtering chamber within five minutes after the wet etch.

Table 3.1: Overview of the relevant resonators fabricated during this work. Sample IX has a superconducting ground plane on the backside of the substrate.

ID	Symbol in graphs	Substrate	thickness	Cleaning	Options
I	○	Si/SiO_2	250 µm	standard	–
II	●	Si/SiO_2	525 µm	standard	–
III	▲	Si/SiO_2	525 µm	standard	EBL
IV	◆	Si	250 µm	HF-dip	–
V	◀	Sapphire	200 µm	ion-gun	–
VI	▼	Si/SiO_2	525 µm	standard	gridded ground plane
VII	⬢	Si/SiO_2	250 µm	ion-gun	Al bridge
VIII	▶	Si/SiO_2	250 µm	standard	Al bridge
IX	■	Si/SiO_2	250 µm	standard	microstrip
X		Si/SiO_2	525 µm	standard	all-Al, gradio qubit

- Sample V has been fabricated during the work presented in Ref. 68 on a 200 µm thick sapphire substrate. The substrate is in-situ cleaned by Ar ion beam etching before Nb sputter deposition. The sapphire is orientated in (0001) direction and polished on both sides. We operate the ion-gun at an operating pressure of 4×10^{-6} mbar, a filament current of 2.7 A, and an emission current of 30 mA. The duration of ion-gun bombardment is 60 s with an acceleration voltage of 100 V.
- Sample VI has a gridded ground plane as one is shown in Fig. 3.11 (b). The square holes of sample VI have a width of 8 µm and are separated by 12 µm.
- Al evaporation for the center conductor part of sample VII and sample VIII is done at 2×10^{-7} mbar with 8 kV and a filament current of 400 mA providing an Al rate of 12 Å/s. To clean the Nb surface of sample VII, we use an Ar ion milling process for 60 s with an Ar flow of 0.5 sccm, an emission current of 20 mA, an extraction voltage of 600 V, and an acceleration voltage of 2.4 kV.
- Sample IX is a microstrip resonator, which has a conductor width of 200 µm and a 100 nm thick Nb layer on the backside of the substrate serving as ground.[16]
- Sample X is the resonator used to read-out the gradio qubit described in Sec. 3.3.2. Hence, it has a different coupling capacitor [cf. Fig. 3.11 (c)] and also the qubit and the antenna structures. Nevertheless, we use quality factor measurements to benchmark the performance of an $Al/ALO_x/Al$ sample.

3.3.2 Gradio qubit sample

In the following, we introduce the gradio qubit sample used to characterize the selection rules for quadrupolar fields in Sec. 6.2. In Fig. 3.11 (a), we show the complete sample mounted in a sample box. To connect the sample to coaxial cables, we use CPW/SMA adapters and silver glue as described above.

Sample layout The heart of the sample is a tunable-gap gradiometric flux qubit that can be controlled by two on-chip antennas as shown in Fig. 3.11 (b). Each of the gradiometer loops has a size of 20 µm × 20 µm and the SQUID loop has a 5 µm × 12 µm area. All qubit lines are 500 nm wide. The two larger junctions have areas of 250 nm × 200 nm [cf. Fig. 3.11 (c)] and the SQUID junctions have areas of 150 nm × 200 nm. The resonator has the same geometry as the samples introduced in Sec. 3.2 but with two modified coupling capacitors as shown in Fig. 3.11 (d). Additionally, we use rectangular 8 µm wide holes in the ground plane to trap possible magnetic flux vortices.

Spin coating parameters Before the spin coating, we clean the 525 µm thick Si/SiO_2 substrate with an oxygen plasma for five minutes to remove residual particles on the surface. We then place it for 10 min on a hotplate at 160 °C to evaporate possible humidity at the substrate surface. For spin coating of the lower, 680 nm thick, layer of PMMA/MA33 % resist, we use a rotation rate of 2000 rpm. We bake the resist at 160 °C for 10 min. In a second step, we coat the sample with 70 nm of PMMA950K resist spinning at a rate of 4000 rpm. Afterwards, we again bake out the resist at 160 °C for 10 min.

[16] We acknowledge sample fabrication by Marta Krawczyk in the context of her Master thesis [375].

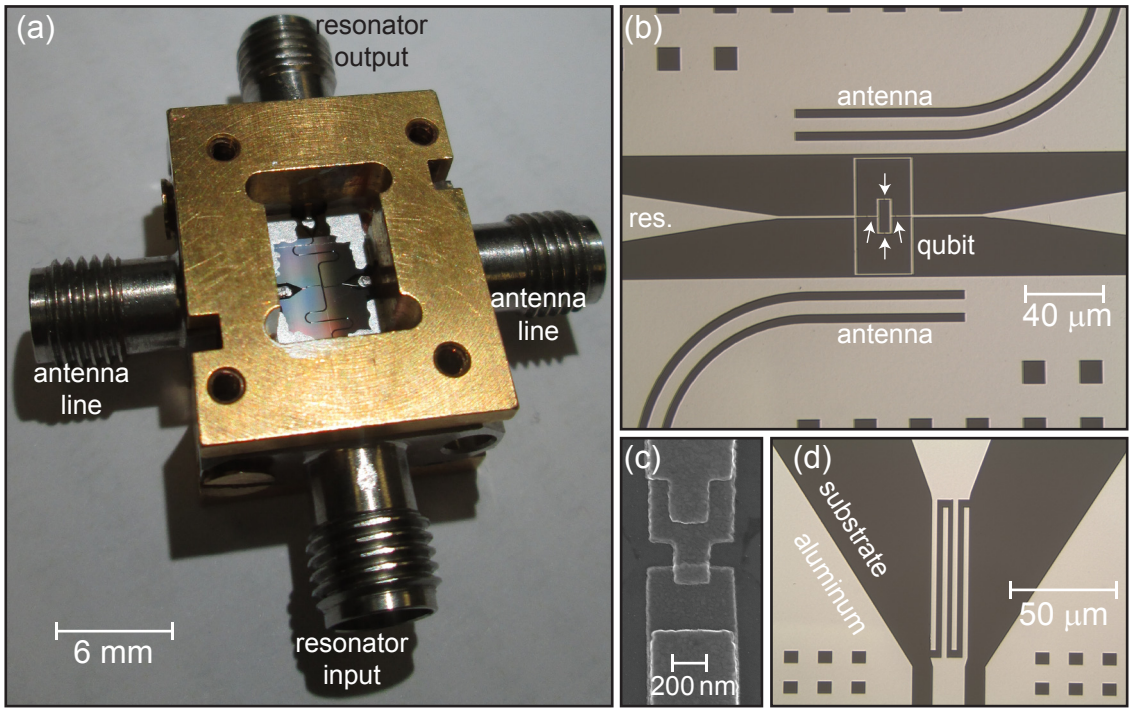

Figure 3.11: **(a)** Photograph of the sample box for the gradio qubit sample including four SMA connectors for the RF-lines and the actual sample in the center. At the corners of the substrate, the silver-glue is visible and from bottom to top, the resonator meanders across the substrate. **(b)** Microscope image of the area where the gradio qubit is located. The resonator center conductor runs from left to right and is galvanically coupled to the qubit. There are two antenna lines approaching from the bottom and from the top to shape the driving field. Arrows indicate the positions where Josephson junctions are located. **(c)** Scanning electron microscope image showing one of the two larger Josephson junctions. **(d)** Microscope image of one of the coupling capacitors confining the half-wavelength resonator.

EBL parameters The gradio qubit sample is fabricated in one fabrication step from an $Al/AlO_x/Al$ sandwich structure, i.e., there is no Nb for the CPW structure. That way, we omit the lossy Al/Nb interface to increase the sample coherence times (cf. Sec. 5.1). To pattern the structure in an EBL process, we use two independent electron beam exposures at an acceleration voltage of 80 kV. In the first step, we pattern the large CPW structures and in the second step, we pattern the qubit and the Josephson junctions. For both steps, we use the auto conjugate function of the nB5 device and focus on gold nanoparticles. For the ground plane structures, we use a beam current of 14.5 nA and a dose of $400\,\mu C/cm^2$, while the center conductor and the antenna lines are written with a dose of $480\,\mu C/cm^2$. Furthermore, we scale the main-fields with a factor 1.001 to avoid stitching errors. The qubit is written with a beam current of 2.6 nA and a dose of $800\,\mu C/cm^2$. We develop the sample in two steps. First, we wash away the activated structures in both resist layers using an AR600-56 developer for 45 s. Then, we immerse the sample in isopropanol at 4 °C for 120 s to selectively develop only the lower resist layer.

Evaporation parameters For metallization, we evaporate a 40 nm thick Al with 17° angle onto the previously patterned sample. This layer forms the bottom electrode of the Josephson junctions but also covers the complete CPW structure. We then oxidize the

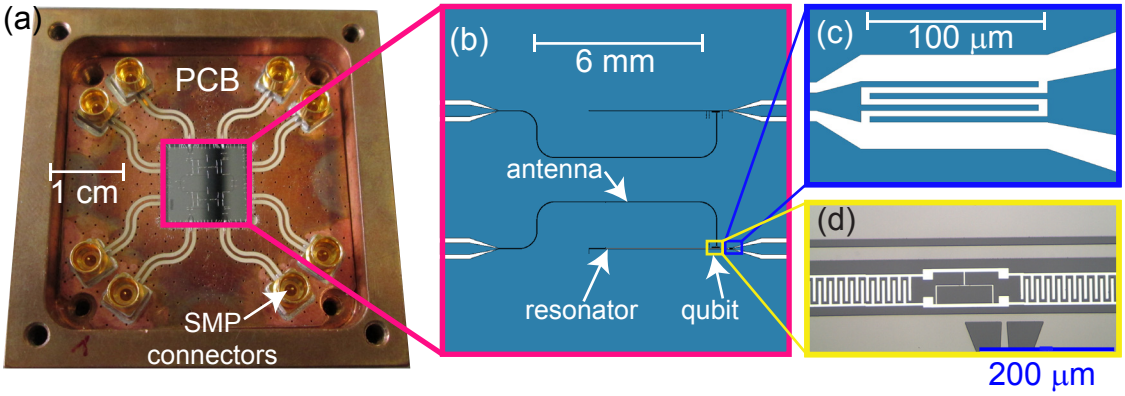

Figure 3.12: **(a)** Photograph of the sample box for the transmon qubit sample including a printed circuit board (PCB) with surface mount SMP connectors and the actual sample in the center. **(b)** Drawing of the sample including two identical qubit-resonator systems and on-chip antennas. For our experiments, we characterize only one of the two systems. **(c)** Coupling capacitor of the quarter-wavelength resonator. **(d)** Photograph of the transmon qubit (white) placed close to the center conductor of the resonator and coupled to an on-chip antenna approaching the qubit from the bottom.

sample for 3000 s at an oxygen pressure of 3.3×10^{-4} mbar aiming at a current density of approximately 500 A/cm^2. The oxygen flow is set to 3 sccm with a valve position of 45°. In a subsequent step, a second layer of Al of thickness 70 nm is evaporated onto the sample at angle $\theta = -17°$, creating the second electrode of the junction. To oxidize all surfaces without contamination from air, we oxidize the sample once more inside the evaporation chamber. We use the above mentioned oxidation parameters but with an oxygen flow of 8 sccm to build a clean oxide on all Al surfaces.

3.3.3 Transmon qubit sample

We now present the sample box, the layout, and the fabrication parameters of the transmon qubit sample used to characterize photon fields in Sec. 5.2 and Sec. 6.1.[17]

Sample holder The sample holder used for the transmon qubit measurements consist of two parts as shown in Fig. 3.12 (a). The first part is a 6 cm × 6 cm gold-plated copper box, which can be closed with a lid. The lid is designed in a way to provide only a small mode volume above the PCB to reduce the number of parasitic modes. Second, there is a printed circuit board (PCB) inside the box, which is equipped with coaxial SMP straight plug PCB connectors. These connectors are used for RF coaxial cables, which enter the box through small holes in the lid. The PCB is a 635 µm thick plate of Rogers 3010, a dielectric material with a dielectric constant $\varepsilon_r \simeq 11$. The dielectric is coated on both sides with a 35 µm thick layer of copper structured with CPW transmission lines leading from the chip to surrounding surface mount PCB connectors.[18]. The PCB ground plane contains copper-coated vias to suppress slotline modes in the transmission lines and wave propagation between top and bottom ground plane.

[17] We acknowledge sample fabrication by Javier Puertas Martínez in the context of his Master thesis [376].
[18] We use `Rosenberger 19S102-40ML5` connectors for that purpose.

Sample layout The transmon qubit sample consists of two equally designed parts, each containing a quarter-wavelength resonator, an on-chip antenna, and a transmon qubit as shown in Fig. 3.12 (b). The resonator is capacitively coupled to a feed line on the one end and shorted to ground on the other end [cf. Fig. 3.12 (c)]. The feed line ends in a contact pad of larger dimension to provide enough space for the Al bonds used to connect the feed line with the PCB. We use approximately five bonds to connect the center conductor on the chip and the center conductor on the PCB for optimum impedance matching [377], while the ground plane is connected by approximately 100 bonds. We place the transmon qubit in the gap of the CPW resonator as shown in Fig. 3.12 (d). It is located at a position close to the input capacitor, meaning at a voltage antinode. In addition to resonator and qubit, an on-chip antenna line runs from a second contact pad to a position next to the qubit, where it is grounded.

Fabrication parameters The sample is fabricated on a $12\,\mathrm{mm} \times 12\,\mathrm{mm} \times 525\,\mu\mathrm{m}$ large Si/SiO_2 substrate with 50 nm thermally grown oxide. While resonator and antenna are made from Nb using optical lithography, the qubit is patterned with electron beam lithography and metallized using Al evaporation as described above. Compared to the gradio qubit sample we use slightly different oxidation parameters. We oxidize the sample for 40 min at 7.3 µbar and 45° valve position aiming for a critical current density of approximately $100\,\mathrm{A/cm^2}$.

Chapter 4 Experimental techniques

From a technological point of view, the main achievement of this thesis is a significant contribution to the setup of a laboratory suitable for sensitive microwave experiments on superconducting quantum circuits and qubits (CIRQUS lab, see Fig. 4.1).[1] The heart of the laboratory is a dilution refrigerator designed and fabricated at WMI (see Fig. 4.2), which we wire up in a way to perform time-resolved measurements on superconducting quantum circuits at millikelvin temperatures. Apart from the normal effort of turning an empty room into the productive laboratory shown in Fig. 4.3, one particular challenge was the identification and removal of a leakage of suprafluid helium between the distillation chamber and the inner isolation vacuum.

Figure 4.1: Poster welcoming visitors and researchers in the CIRQUS lab.

We introduce the dilution refrigerator and its main components in Sec. 4.1. The time-domain measurement setup[2] with all its microwave components is discussed in detail in Sec. 4.2. Finally, in Sec. 4.3 and Sec. 4.4, we present preparatory measurements for the gradio qubit sample and the transmon qubit sample.

[1] The setup of the CIRQUS lab has been achieved in close collaboration with F. Wulschner [378], M. J. Schwarz [178], F. Deppe, and the cryogenics experts C. Probst, K. Neumeier, and J. Höss.

[2] We acknowledge a close collaboration with M. Häberlein on the time-domain setup.

4.1 Cryostat for experiments with quantum circuits

Circuit QED experiments work at millikelvin temperatures to avoid thermal excitation of the conducting quantum circuit. To reach such low temperatures, usually ^{3}He/^{4}He dilution refrigerators are used because they provide sufficient cooling power for all the required microwave equipment under continuous operation. The working principle of a dilution refrigerator is shown in Fig. 4.2. It is based on the fact that a liquid ^{3}He/^{4}He mixture separates into two coexisting phases with different ^{3}He concentration when precooled to temperatures below 870 mK [379, 380]. In practice, the ^{3}He concentrated phase floats on top of the ^{3}He dilute phase containing more ^{4}He. When pumping ^{3}He out of the dilute phase, ^{3}He has to diffuse over the phase boundary to restore equilibrium. In this process, the heat required for the dilution provides the cooling power of the refrigerator. Since the vapor pressure of ^{3}He becomes unreasonably small at millikelvin temperatures, the pump acts on the liquid surface at a higher temperature in the distillation chamber (still).
In Fig. 4.3 (a), we show a schematics of the laboratory including all components of the cryostat in the CIRQUS lab. On the one hand, there are several pumps and a gas handling system used for cooldown and the continuous operation of the cryostat. On the other hand, there is sophisticated measurement equipment installed in two racks and controlled by three computers. The refrigerator reaches a base temperature of 25 mK, is equipped with 24 coaxial and 48 twisted pair cables and has a cylindrical sample space of 12 cm diameter and 30 cm height. In the following, we describe the dilution insert, the cryogenic measurement components, and the shielding and filtering setup.

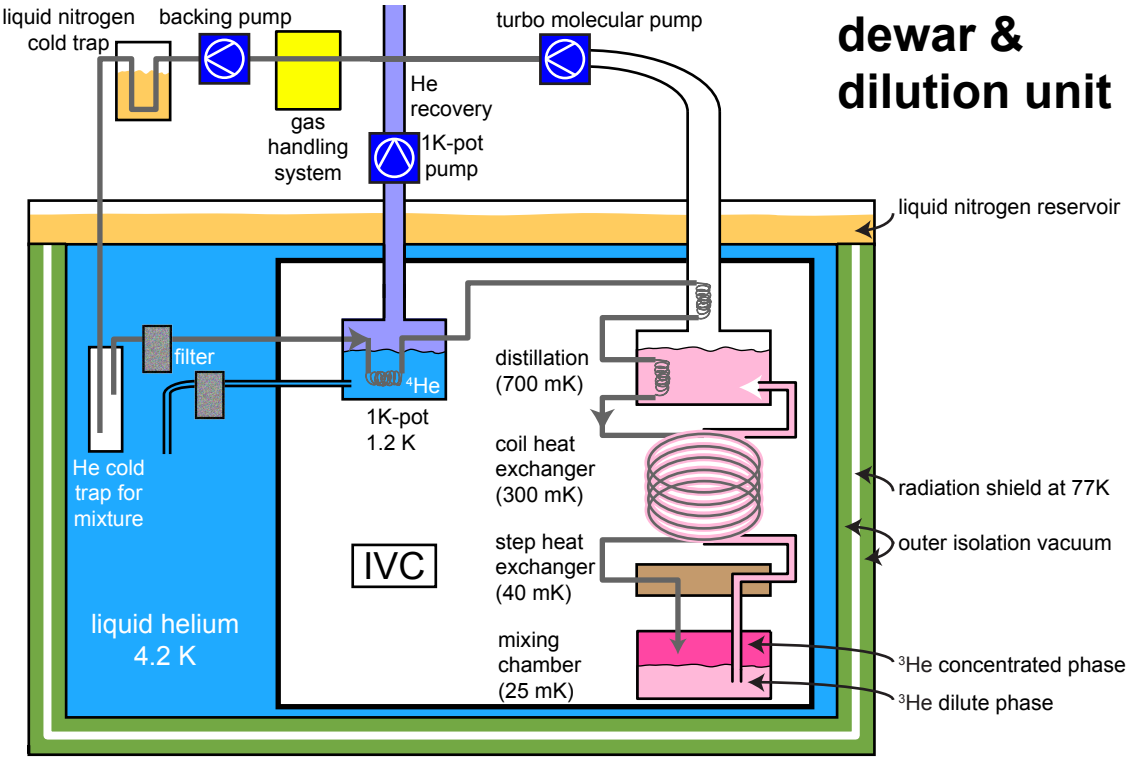

Figure 4.2: Schematics of the dilution refrigerator in the CIRQUS lab.

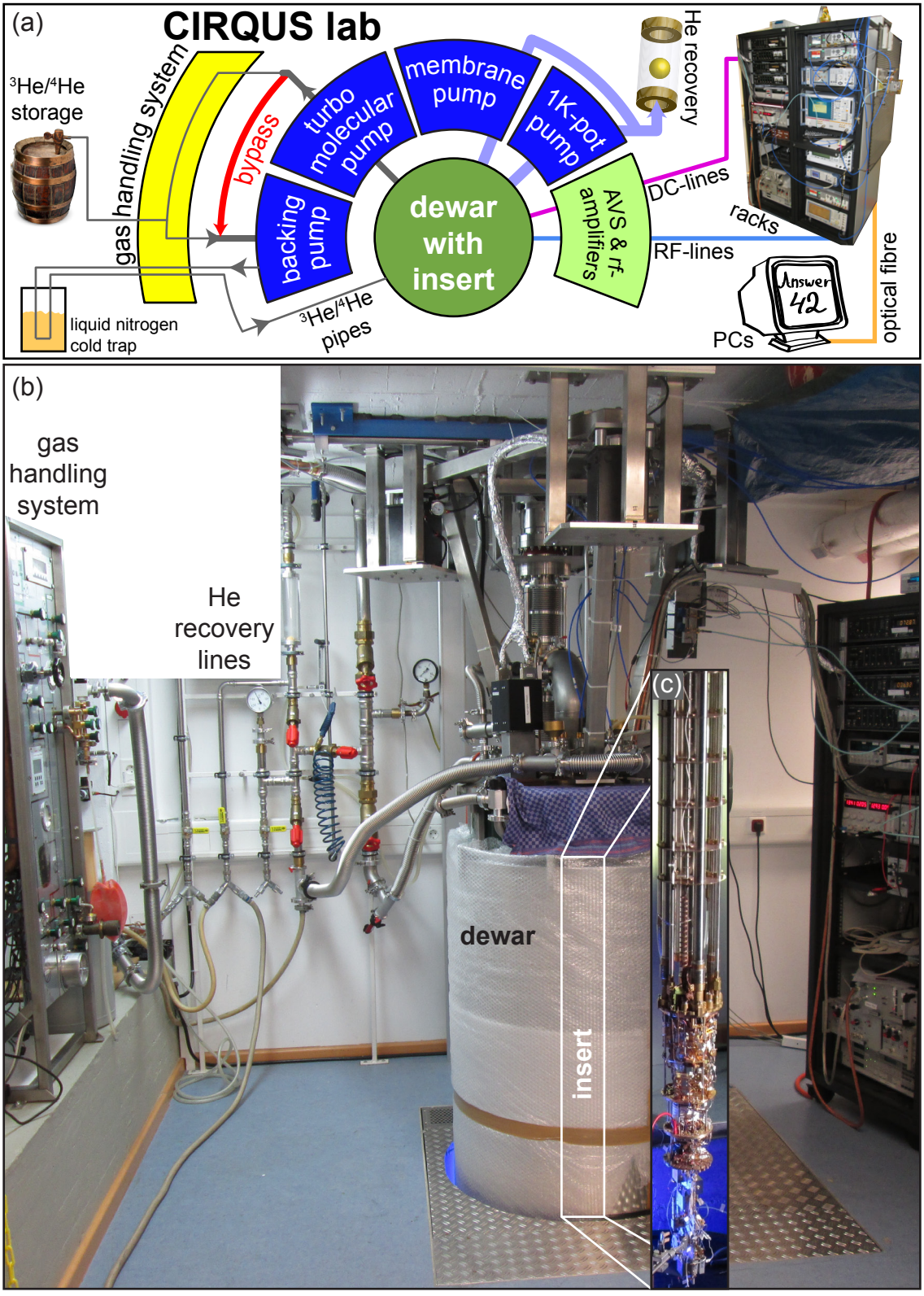

Figure 4.3: **(a)** Schematics of the CIRQUS lab. **(b)** Photograph of the closed cryostat under operation. We can lower the dewar into a $3\,\mathrm{m}$ deep hole to uncover the cryogenic insert shown in panel **(c)**.

4.1.1 Dilution refrigerator

Liquid helium dewar and cryogenic insert Our dilution refrigerator comprises a commercially obtained dewar[3] shown in Fig. 4.3 (b) and a custom-made insert (designed and fabricated at WMI) shown in Fig. 4.3 (c). The dewar is suspended on a vibration-isolation system to suppress mechanical motion induced by the building. We can precool the insert with liquid nitrogen and liquid helium using a membrane pump as depicted in Fig. 4.3 (a). Under normal operation, the time between two refills exceeds seven days for a dewar volume of 89 liter of liquid ^{4}He and 87 liter of liquid nitrogen. The insert into the liquid He dewar has a cylindrical shape with a diameter of 16 cm and a height of 1.2 m. At the bottom resides a cylindrical brass vacuum can. This inner vacuum chamber (IVC) has a diameter of 16 cm and a height of 65 cm. The IVC contains the dilution unit as well as space for experimental installations at various temperature stages. Notably, the dilution unit is mechanically decoupled from the experimental space. Several stainless steel tubes extend from the room temperature (RT) flange to or into the IVC. Two of these tubes are used to circulate the ^{3}He/^{4}He mixture, one to operate the 1K-pot, and one to evacuate the IVC. This evacuation tube as well as two other tubes are used to feed the microwave cables into the IVC. Furthermore, two tubes guide most of the twisted pair cables into the IVC via compact, homemade cold feedthroughs. These feedthroughs are 1.8×0.5 mm CuNi capillaries soldered into a copper lid and sealed with black Stycast 2850 GT. The DC cables for the cold amplifiers and the cold microwave switches lead through the ^{4}He bath and also enter the IVC through such feedthroughs. Inside and outside the stainless-steel tubes, copper baffles considerably reduce the effect of heat radiation from higher onto lower temperature stages.

1K-pot operation Before entering the actual dilution unit, the ^{3}He/^{4}He mixture is liquefied by means of evaporation cooling. To this end, ^{4}He from the bath is fed via a controlled impedance into a copper cylinder inside the IVC. This 1K-pot, shown in Fig. 4.4 (a), operates at a temperature of 1.2 K and a pressure of 0.5 mbar provided by a mechanical pump with a throughput of 110 m^3/h.[4] We design the 1K-pot with a large RT impedance $Z_{1\mathrm{K}} \simeq 6.6 \times 10^{11}\,\mathrm{cm}^{-3}$ to reduce helium consumption. To characterize the 1K-pot performance, we measure its temperature as a function of dissipated power in a 1 kΩ resistor attached to the vessel surface. We find a 1K cooling power $\mathcal{P}_{1\mathrm{K}} \simeq 20$ mW [cf. Fig. 4.4 (b)], which is sufficient to condense the circulating ^{3}He/^{4}He mixture at a condenser pressure of approximately 120 mbar. In order to avoid blockages of the impedance capillary, the ^{4}He from the bath is filtered using a combination of sintered metal powder and moose leather that has been soaked in a solution of toluol and alcohol to isolate a clean keratin structure.

Dilution unit The dilution unit provides the required cooling power at millikelvin temperatures that is necessary to cool the experimental installations. Important components of the dilution unit shown in Fig. 4.4 (a) are heat exchangers used to precool the condensed ^{3}He/^{4}He mixture after it has been precooled in the 1K-pot. The first two precooling steps are provided by winded capillaries exposed to the cold exhaust gas of the distillation chamber (still) and to the liquid mixture inside the still. The second capillary has a large RT impedance $Z_{\mathrm{still}} = 3.5 \times 10^{11}\,\mathrm{cm}^{-3}$ to decelerate the throughput of the superfluid

[3] We use a `Cryogenic Limited` stainless steel dewar.

[4] We use a `Leybold SC 110` mechanical pump for that purpose.

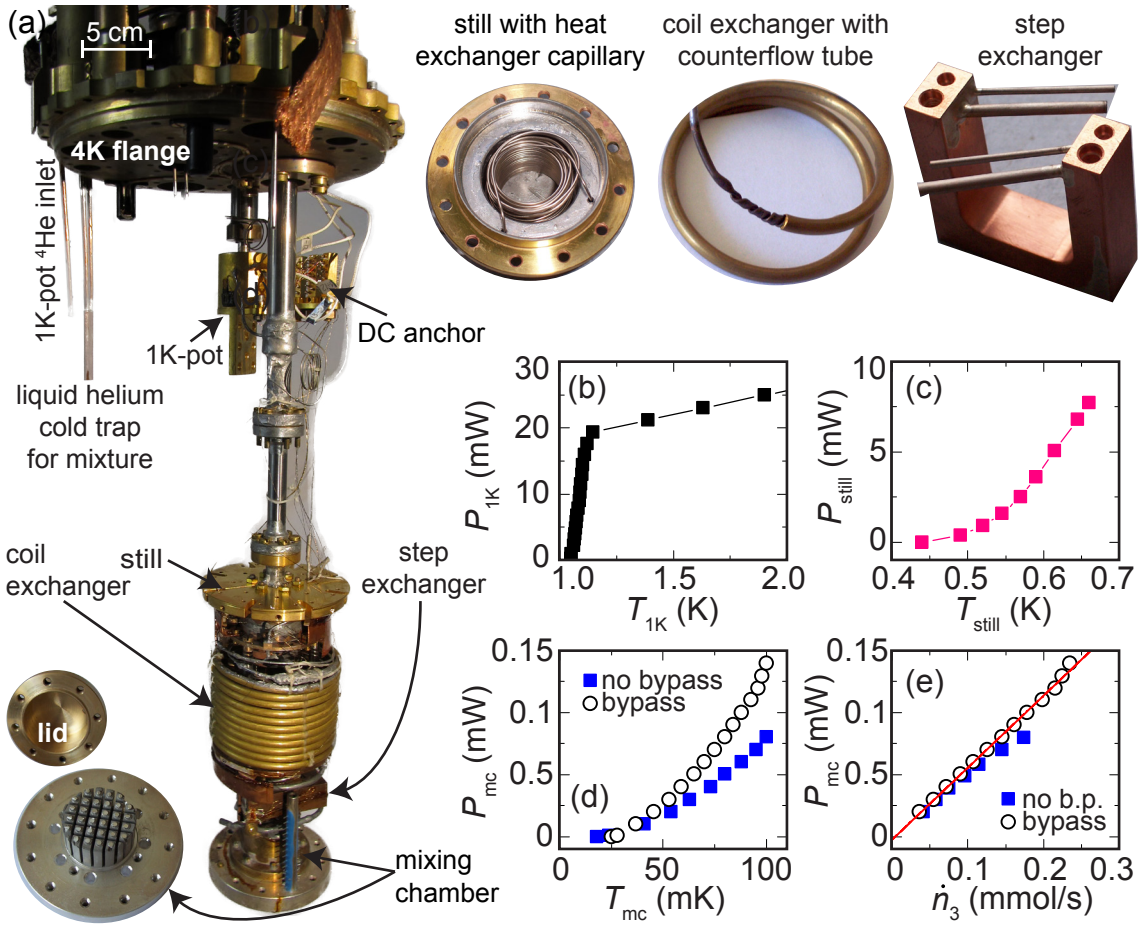

Figure 4.4: **(a)** Photograph of the dilution unit and its main components. **(b)** Cooling power of the 1K-pot as a function of vessel temperature. **(c)** Cooling power of the still as a function of its temperature. **(d)** Cooling power of the mixing chamber as a function of its temperature for a constant ^{3}He throughput $\dot{n}_3 = 175\,\mu\text{mol/s}$. **(e)** Cooling power of the mixing chamber as a function of the ^{3}He throughput measured at a mixing chamber temperature $T_{mc} = 100\,\text{mK}$. The solid line is a linear fit.

mixture. We adjust the throughput by heating a $1\,\text{k}\Omega$ resistor screwed to the still vessel and find a maximum cooling power of the still $\mathcal{P}_{still} \simeq 7\,\text{mW}$ at 675 mK [cf. Fig. 4.4 (c)]. For further precooling, the mixture enters a coil heat exchanger where a thin capillary wound into a long coil is put into a thicker capillary wound into a coil, too. While the coil exchanger has a large cross-section, we dimension the step exchanger placed below in a compact way to minimize the amount of ^{3}He for economic reasons. The two tubes of the horseshoe-shaped step exchanger are filled with a sintered copper powder to increase the effective surface area. With this design, the cryostat operates with a ^{3}He/^{4}He ratio of only 18 % and a total amount of 4 liter of ^{3}He gas. We determine the (unintended) ^{4}He flow of the cryostat to approximately 15 % at $T_{still} \simeq 675\,\text{mK}$ determined by a gas analysis using a leak detector. We take this ^{4}He flow into account when calculating the ^{3}He throughput from the pressure-dependent pumping power of our pumps. During operation, the phase boundary is located below all heat exchangers inside the mixing chamber, which contains silver pistils and is filled with a sintered silver powder.[5] The sinter is annealed at 100 °C

[5] We use `MaTeck 009388` powder with a grain size of approximately $(1.0 \pm 0.2)\,\mu\text{m}$ and a purity of 99.9 % inside the mixing chamber.

in a hydrogen atmosphere of 10 mbar for 4 h. In a subsequent step, the sinter is pressed between the silver pistils of the mixing chamber with a pressure of 6.3 kbar and annealed at 200 °C in a hydrogen atmosphere of 10 mbar for 4 h.

Cooling power We systematically analyze the mixing chamber performance, i.e., the temperature-dependent cooling power $\mathcal{P}_{\mathrm{mc}}(T)$, for varying ^{3}He/^{4}He throughput. During the first cooldowns of the cryostat without experimental installations, the cooling power at 100 mK has reached 80 µW and the base temperature fell below 14 mK [see Fig. 4.4 (d)]. We significantly improve this cooling power by installing a bypass between the exhaust of the turbo molecular pump[6] and the mechanical backing pump[7] as depicted in Fig. 4.3 (a). That way, we avoid pumping through the gas handling system with its large flow resistance. This impedance decrease causes a reduced vapor pressure inside the still allowing for a larger throughput due to the reduced still temperature. With this concept, the cooling power of the mixing chamber at 100 mK has improved to 140 µW. Even for this large still throughput, the linear dependence between cooling power and throughput remains unchanged. Hence, the cooling power is limited by the finite ^{3}He throughput $\dot{n}_3 = 175$ µmol/s of the mechanical backing pump. Theoretically, the cooling power [381–383] $\mathcal{P}_{\mathrm{mc}} = 82 T_{\mathrm{mc}}^2 \dot{n}_3$ depends on the temperature T_{mc} of the mixture entering the mixing chamber as well as on the throughput $\dot{n}_3$. For our setup, we find $\mathcal{P}_{\mathrm{mc}} \simeq 60 T_{\mathrm{mc}}^2 \dot{n}_3$ measured at a mixing chamber temperature $T_{\mathrm{mc}} = 100$ mK [cf. Fig. 4.4 (e)]. The slightly decreased cooling power is expected [384] because of the finite heat capacity of helium. We want to note that the minimum base temperature shown in Fig. 4.4 (d) has increased to 24 mK for the measurements including the bypass. The reason are the additional experimental installations, which are already mounted during these measurements. In particular the 24 coaxial cables add a significant heat leak to the mixing chamber causing the temperature increase.

4.1.2 Measurement equipment of the cryostat

48 twisted pair cables The twisted pair cabling of the cryostat is on the one hand used for thermometry, and on the other hand for power supply, i.e., heating purposes and the generation of static magnetic fields. A schematics of the twisted pair cabling is given in Fig. 4.5 (a). To avoid crosstalk, we physically separate the thermometer cables and the cables from heater, power supply, and coil current as much as possible by feeding them through different tubes. To supply the cryogenic amplifiers, we use 100 µm thick copper wires entering the cryostat through the He-exhaust tube [see Fig. 4.5 (c)].
Inside the IVC, the wires are thermalized at the 1K-stage by specially designed DC anchors as shown in Fig. 4.4 (a). Below the 1K-stage, we change the twisted pairs to superconducting Nb/Ti monofilament wires embedded in a phosphorous bronze matrix.[8] We thermalize the superconducting cables at different temperature stages by glueing them onto copper sheets as shown in Fig. 4.6 (d).[9]

DC filters and current supply Except for the power supply cables for the cryogenic amplifiers, we low-pass filter all twisted pair cables at the RT-flange to reduce the amount

[6] We use a `Pfeiffer TMU 521 DN160` turbo molecular pump with a sucking capacity of approximately 1200 m^3/h for ^{4}He.
[7] We use a `Leybold Trivac D40B` mechanical pump with a sucking capacity of 65 m^3/h.
[8] We purchase the superconducting wires from `Supercon Inc`.
[9] We use `Stycast 2850 FT Blue` epoxy for that purpose.

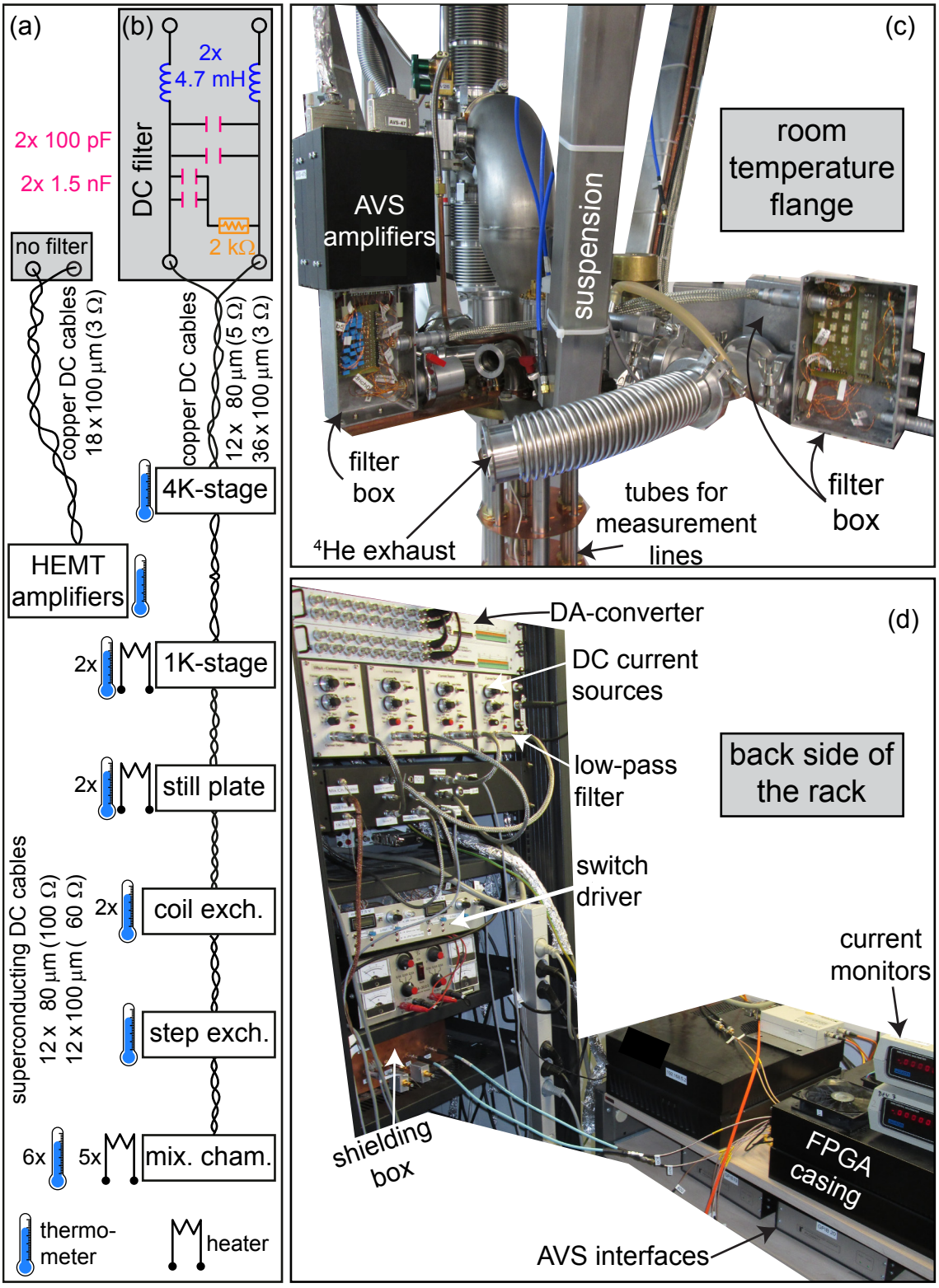

Figure 4.5: **(a)** Schematics of the DC cabling inside the cryostat. Resistance values correspond to room-temperature values. **(b)** Equivalent circuit diagram of the low-pass filters. **(c)** Photograph of the RT-flange of the cryostat. **(d)** Photograph of the backside of the rack.

of high-frequency noise entering the cryostat. To this end, we use homemade filters in shielded filter boxes right on top of the fridge as shown in Fig. 4.5. These *LRC* filters are realized as surface-mount devices (SMD) placed on a printed circuit board and have a cutoff frequency of approximately 100 kHz [385]. To reduce Johnson-Nyquist noise, the inductance coils in these filters have a low resistance of approximately 50 Ω. The 200 pF capacitance is a compromise between a large capacitance to achieve a low cutoff frequency and the incompatibility of the homemade current source with large capacitors [385]. These homemade current sources shown in Fig. 4.5 (d) are voltage controlled and have a maximum output current of 100 mA.[10] The ±1 V input range of the current sources results in a precision of 1.5 nA when operating the current source in the finest (1 µA) range with a 16-bit DA-converter.[11] To reduce crosstalk between high frequency noise of the DA-converters and the cryostat, we place commercial low-pass filters directly at the output of the current sources.[12]

Thermometry and temperature stabilization We use two independently controlled resistance (AVS) bridges to measure and stabilize different temperature stages of the cryostat.[13] At millikelvin temperatures, we measure the temperature by recording the resistance of certain materials such as carbon composites [386] or RuO_2 [387, 388]. In our cryostat, we use homemade thermometers that have been fabricated and calibrated in house. To avoid self-heating effects when measuring the resistance, we use very low excitation voltages in the µV regime and heavy filtering as explained above. The low-pass cutoff frequency of the SMD filters is sufficiently above the 13.7 Hz operating frequency of the AVS bridges but allows environmental noise with lower frequency to enter the cryostat. To minimize this effect, we mount the preamplifiers of our resistance bridges directly on top of the filter boxes sitting immediately at the cryostat as shown in Fig. 4.5 (c). In addition to the strong filtering, the cryostat is galvanically isolated from the power-grid. Specifically, we use an isolating transformer for electrical power and an independent ground connection for the cryostat.
Both AVS bridges are equipped with a multiplexing unit to read out the temperature of eight thermometers, which allows us to monitor the temperatures of up to four sample boxes in addition to all relevant components inside the cryostat. Alternatively, each bridge can stabilize the temperature of one thermometer via PID-controlled heating of a resistor. To stabilize the temperature of the sample stage or the sample boxes, we use 100 Ω thin-film resistors glued to a silver foil.[14] With optimized PID parameters, we reach a temperature precision of approximately 100 µK at 30 mK.
In addition to the cryogenic thermometers, we record and stabilize the temperature of several room-temperature components. Specifically, we stabilize the temperature of the microwave amplifiers to $(18.0 \pm 0.1)\,^{\circ}\mathrm{C}$ using a Peltier element [364].[15] This temperature stabilization is important to avoid amplitude and phase drifts of the coherent microwave signals. Furthermore, we record the temperature of the microwave amplifiers placed inside the shielding box presented in Sec. 4.2.2. Since the amplifiers are located inside the

[10] We thank U. Guggenberger to provide the four current sources for the CIRQUS lab.
[11] We use a `National Instruments PCIe-6353` DA converter for that purpose.
[12] We use `MiniCircuits BLP-1.9` filters with a cutoff frequency of 1.9 MHz for that purpose.
[13] We use `Picowatt AVS-47B` resistance bridges shown in Fig. 4.10 for thermometry and `Picowatt TS-530A` PID controllers for temperature stabilization.
[14] We use `Vishay/Beyschlag MCT 0603` resistors here.
[15] We use a `Laird Techn. DA-075-12-02` Peltier element for that purpose.

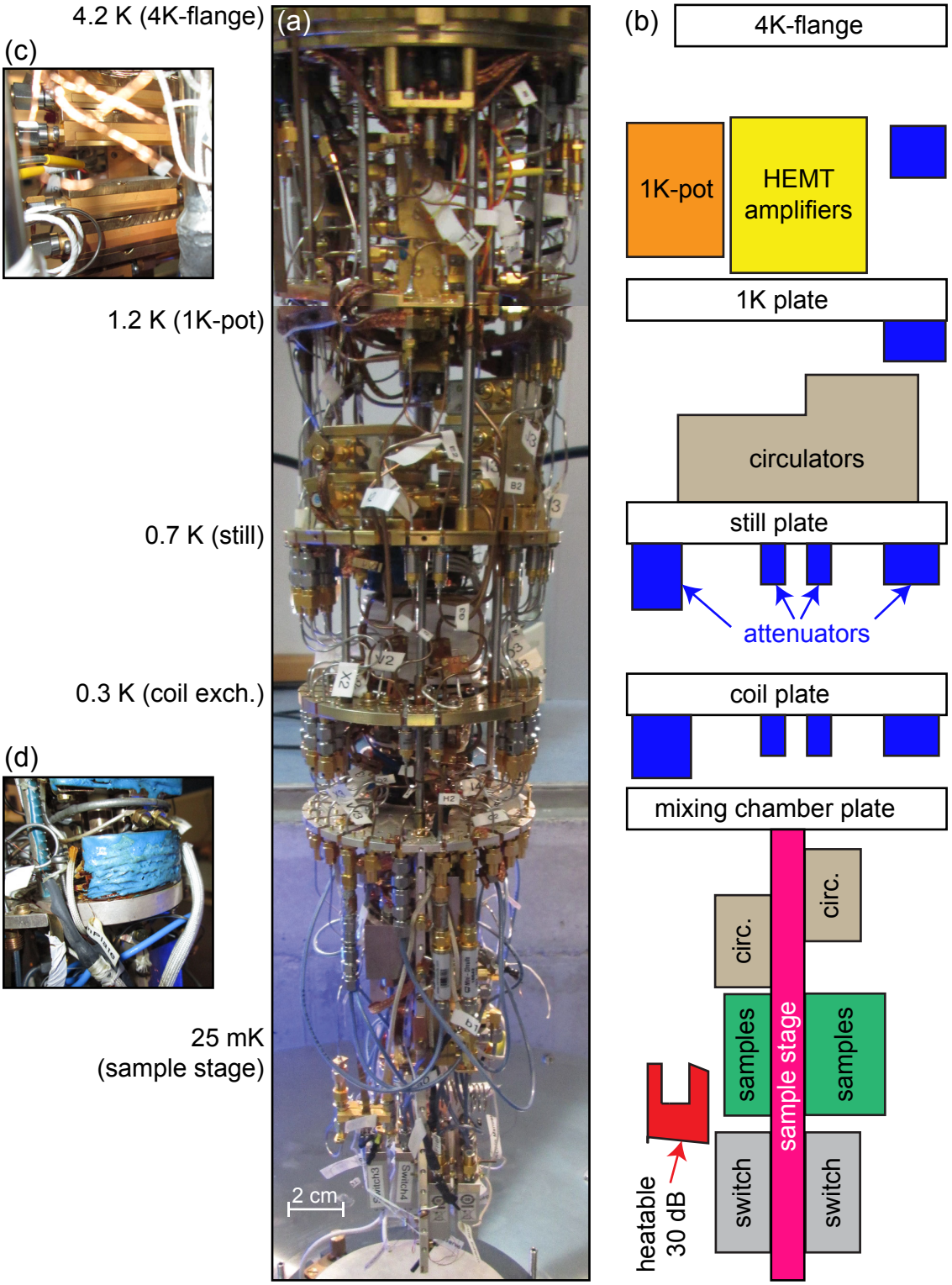

Figure 4.6: **(a)** Photograph of the cryostat inside the IVC below the 4K-flange. **(b)** Schematic drawing of the main components shown in panel (a). **(c)** Photograph of the HEMT amplifiers stacked on top of each other. **(d)** Photograph of a thermalization plate for the superconducting wires glued with blue Stycast.

copper box, which thermally isolates them from the environment, we couple the amplifiers to the box with a copper braid. That way, they operate at a constant temperature of approximately $(60 \pm 1)\,^{\circ}\mathrm{C}$, which is sufficient for our purposes.

RF input lines In the following, we describe the coaxial cabling used for the input lines of the cryostat. There are 24 semi-rigid coaxial cables entering the cryostat via RT feedthroughs to the inner isolation vacuum.[16] 16 of these cables are stainless steel cables with low heat conductivity but significant loss and are therefore used as input lines.[17] Below the 4K-flange, we use cables with a reduced diameter and a superconducting center conductor[18] to minimize thermal conductivity and, at the same time, strongly reduce microwave loss. We thermalize the cables with attenuators[19] at different temperature stages as shown in Fig. 4.6 (a).

RF output lines and cryogenic amplifiers For the output lines of the cryostat, it is important to minimize loss but also to achieve a sufficient thermalization of the cables. From RT to the 4K-flange, we use eight silver-coated seamless copper-clad steel cables (Cobras),[20] which have low loss (1 dB/m at 5 GHz) at cryogenic temperatures. For the cables connecting the 4K-stage with the sample stage, we use phosphor bronze cables with a superconducting Nb center conductor.[21] To thermalize the center conductors, we use several cryogenic circulators anchored to the still plate[22] and to the sample stage.[23]
We amplify the microwave signals with high electron mobility transistor (HEMT) amplifiers that are anchored to the 4K-flange. We use four amplifiers operating from 3 GHz to 8 GHz with a gain of 40 dB and one broadband amplifier with a gain of 35 dB between 4 GHz and 20 GHz.[24] The five amplifiers are stacked on top of each other as shown in Fig. 4.6 (c). The tight packing of the amplifiers results in a temperature increase of these devices to approximately 9 K due to the power consumption of 4 mW each. At this operating temperature, the amplifiers have a noise temperature of approximately 2 K as characterized in Sec. 4.4.3.

RF filters The performance of superconducting quantum circuits is typically limited by their short coherence times due to the noisy environment of the circuits. As derived in Sec. 2.4.2 and Sec. 2.4.3, one main noise channel are the microwave cables leading to the circuits. To protect the quantum circuits from this noise channel, we filter the broadband noise spectrum at low temperatures. To achieve sufficient filtering, we use different filter types shown in Fig. 4.7, which we characterize at cryogenic temperatures [364]. Depending on the experimental requirements, we use either band-pass filters with an insertion loss of more than 30 dB below 2.5 GHz and above 5.5 GHz[25] [see Fig. 4.7 (a)] or tubular low-pass

[16] We use `Rosenberger 02K641-KH0S3` feedthroughs for that purpose.
[17] We use UT-85 `Coax Co. Ltd SC-219-SS-SS` semi rigid cables for that purpose.
[18] We use UT-47 `Coax Co. Ltd SC-119-Nb-CN` cables for that purpose
[19] We use `Rosenberger 32AS102-K10S3` attenuators for that purpose.
[20] We use `Astrolab Cobra Flex 31086S` semi rigid cables for that purpose.
[21] We use UT-85 `Coax Co. Ltd SC-219-Nb-PBC` semi rigid cables for that purpose.
[22] We use `Raditek RADI-4.0-8.0-Cryo-S3-1WR` circulators with 18 dB isolation for that purpose.
[23] We use double-shielded `Quinstar CTH1 184-KS18` with 20 dB isolation for that purpose.
[24] We use `LowNoiseFactory LNC4_8A` and `LNC6_20B` amplifiers for that purpose.
[25] We use `MiniCircuits VBFZ 4000` band-pass filters for that purpose. Please note that for the transmon qubit sample, we use a resonator with $\omega_\mathrm{r}/2\pi \simeq 6\,\mathrm{GHz}$ and a `MiniCircuits VBFZ 5500` filter with a slightly higher pass band.

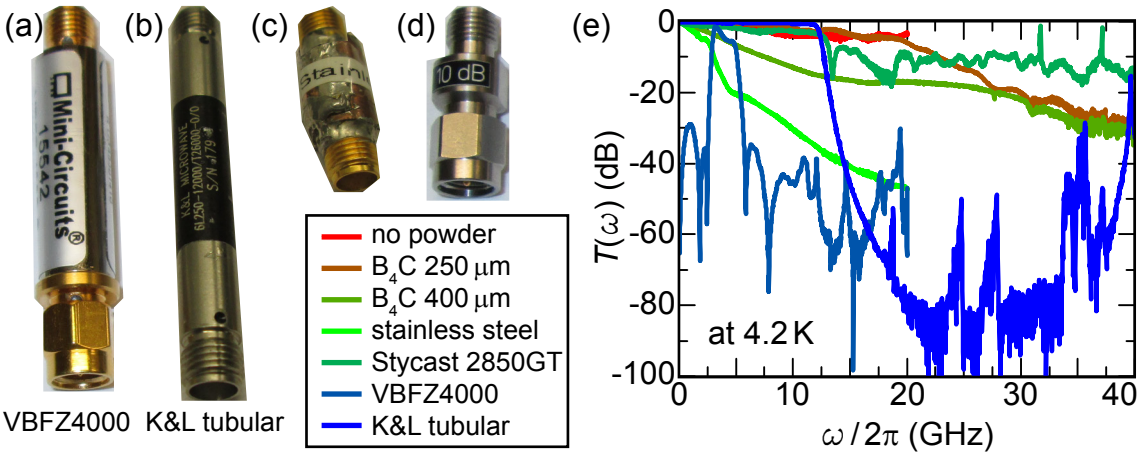

Figure 4.7: (a) – (d) Photographs of passive microwave components. From left to right: MiniCircuits VBFZ 4000 low-pass filter, K&L 6L-250-12000 tubular low-pass filter, homemade dissipative filter, Rosenberger attenuator. We fill the dissipative filters with different materials. We use boron carbide (B_4C) powder with grain sizes of $250\,\mu m$ and $400\,\mu m$, stainless steel powder, or Stycast. **(e)** Transmission magnitude of microwave filters measured at $4.2\,K$ plotted versus frequency.

filters shown in Fig. 4.7 (b) containing capacitively coupled dielectric spacers and a high precision surface topography.[26] These filters have a 3 dB cutoff frequency of 12 GHz and a typical insertion loss of 70 dB for frequencies up to 30 GHz [cf. Fig. 4.7 (e)]. For even higher frequencies the filters become transparent and are therefore not suited to block infrared radiation.

Infrared radiation filters As pointed out in Sec. 2.4.2, infrared radiation entering the sample box is a significant noise source that has to be filtered properly. Infrared radiation couples to the samples through the coaxial cables connected to the sample box. These cables use polytetrafluoroethylene (Teflon) as a dielectric, which shows a very good transmittance for infrared frequencies [389, 390]. Infrared frequencies are above the cutoff frequency of the transverse magnetic (TM) and the transverse electric (TE) modes in the coaxial cables [109, 391]. Therefore, infrared radiation can propagate in these modes, which distribute around the circumference of the cables. Technically, we cannot attenuate the TM and the TE modes with the microwave filters described above because they have spurious transmission resonances at these high frequencies [392]. Nevertheless, dissipative filters consisting of a metallic wire embedded in a metal powder [393] suppress these high-frequency modes [394–397]. Dissipation occurs because the ac noise induces dissipative eddy-currents in the powder, which damps these currents proportional to their frequency. Typical dissipative filters with stainless steel powder have an insertion loss of more than 20 dB at 5 GHz [see Fig. 4.7 (e)], which is not suited to operate circuits in the gigahertz range. Therefore, we use materials for the dielectric that do not suffer from eddy currents but that absorb infrared radiation. These materials can be Eccosorb CR-110 [398], black Stycast 2850 GT [399, 400], or different carbide types [65]. We fabricate several pipe-type coaxial filters with different filling materials [364]. The copper tubules used for these filters fit on the two SMA coaxial panel mount connectors as shown in Fig. 4.7 (c).[27] We design the length of the filter in such a way that the two pins inside the tubule touch and can be

[26] We use `K&L 6L-250-12000` low-pass filters for that purpose.
[27] We use `H+S 22SMA-50-0-15` connectors for that purpose.

soldered through a small hole in the outer shell. After inserting the filling material, we close the hole by soldering a copper lid on it. As filling material, we compare air (no powder), boron carbide (B_4C) with a grain size of 250 µm and 400 µm, stainless steel with a grain size of 400 µm, and Stycast 2850 GT. In the optical frequency range, all these materials are opaque meaning that terahertz radiation is suppressed strongly. In the infrared frequency range, the absorption of B_4C [401–403] and Stycast [399, 400] has been analyzed in several studies. When comparing the performance of the different fillings in the gigahertz range in Fig. 4.7 (e), we find that stainless steel has the strongest attenuation in the gigahertz regime as expected due to eddy-current loss. Also the 400 µm B_4C grains significantly absorb microwaves below 10 GHz, which is known for microwave sintering of ceramics [404]. The 250 µm B_4C grains, however, show a smooth frequency spectrum with negligible loss up to 20 GHz. Also the black Stycast is transparent up to 12 GHz. Hence, the latter two materials are well-suited for cryogenic infrared filters. From time-domain-reflectometry (TDR) measurements, we find a typical filter impedance of 55 Ω up to 60 Ω.

4.1.3 Radiation and magnetic flux shielding

To generate a clean electromagnetic environment inside the cryostat, we shield thermal radiation as well as magnetic noise. To this end, we use a combination of multi-stage shielding and absorbing coatings as described in the following paragraphs.

Radiation shielding We cascade different types of shielding around the sample space as depicted in Fig. 4.8 (a) to block thermal radiation. To protect the cryostat insert from 300 K-radiation, the dewar has an Al shield that is thermally anchored to the 77 K liquid nitrogen reservoir. The oxide surface of the high-purity Al is chemically cleaned to improve emissivity. To reduce radiation onto the Al shield, it is covered with a superinsulation blanket consisting of alternating layers of reflective aluminized mylar and nylon netting. The next shielding stage is at liquid helium temperature, where the helium reservoir made of stainless steel and the IVC made of brass reflect thermal radiation [cf. Fig. 4.8 (b)]. We protect the dilution unit and all measurement components anchored to it with a radiation shield made of copper that is thermally anchored to the still plate as shown in Fig. 4.8 (c). Additionally, we use the Al shield shown in Fig. 4.8 (d) anchored to the mixing chamber plate to protect our samples from radiation. Finally, the sample boxes themselves protect the superconducting circuits from external radiation.

Magnetic flux shielding To reduce magnetic flux noise, we place the dewar inside three μ-metal cans reaching almost up to the RT-flange.[28] To restore the alloy's metallurgical structure providing the intended magnetic properties, the shields are annealed for 4 h at 1150 °C. The heat treatment removes all impurities, e.g. carbides, sulfides, or nitrides, without adding oxidation. In addition, it increases the grain size and fixes the crystal structure of the alloy. With this treatment, the shields have a coercivity of 1.5 A/m and an approximate DC shielding of 5 dB each. Inside the helium reservoir the vacuum can is covered with a cryoperm shield with a 50 Hz permeability of 7×10^4 at cryogenic temperatures.[29] The shield has a thermal expansion of $1.3 \times 10^{-5}\,\mathrm{K}^{-1}$, a coercivity of

[28] We purchase these 1 mm-thick shields with a maximum permeability of 2.5×10^5 consisting of an 76.6 % Ni, 4.5 % Cu, 3.3 % Mo, 14.7 % Fe from `Meca Magnetic`.

[29] We purchase this shield consisting of an 77 % Ni, 4.5 % Cu, 2.5 % Mo, 15.1 % Fe alloy from `Meca Magnetic`.

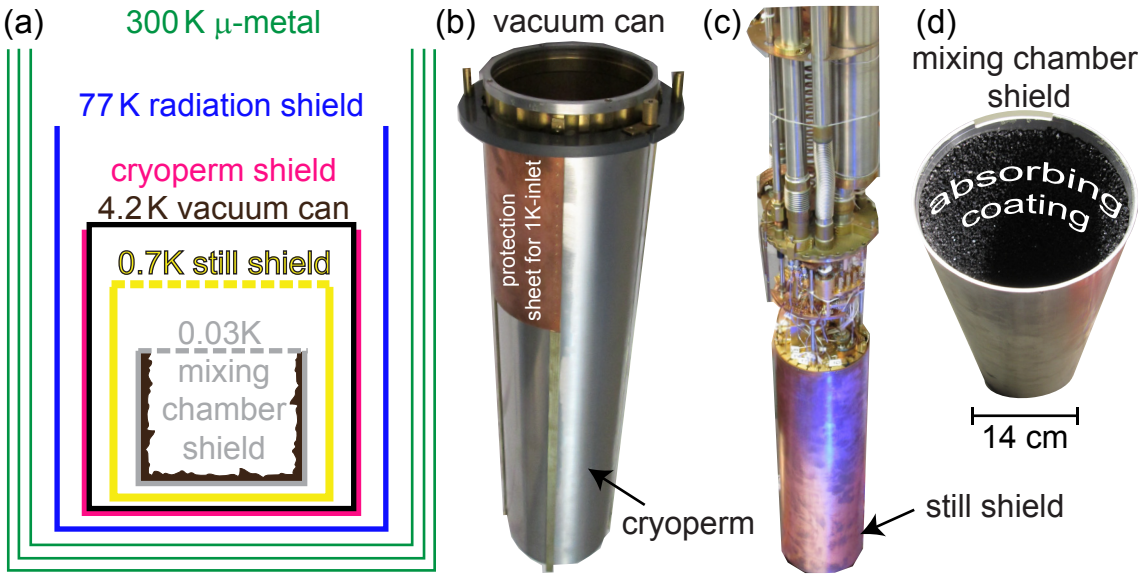

Figure 4.8: **(a)** Schematic drawing of the different shielding stages inside the cryostat. **(b)** Photograph of the inner vacuum can which is enclosed by a cryoperm μ-metal shield. **(c)** Photograph of the dewar insert with the still shield made from copper mounted to the still plate. **(d)** Photograph of the mixing chamber, which is covered with an absorbing coating.

2 A/m and an approximate DC shielding of 15 dB. Additionally, we make use of the superconducting properties of the mixing chamber shield, which sustains a constant magnetic flux inside. The shield is made of a 99.5 % pure Al alloy (AlMgSi), which becomes superconducting at 1.1 K [405]. To enable a homogeneous thermalization of the shield, we coat it with black Stycast 2850 Gt, which has a heat conductivity of approximately 0.01 W/(m K) at these low temperatures [406–409]. Additionally, the epoxy glue serves as an adherent layer for the absorbing coating described in the following paragraph.

Absorbing coating To absorb infrared radiation at the sample stage, we establish a technique to apply an absorbing coating to radiation shields during the work presented in Ref. 364. The coating has a rough surface as shown in Fig. 4.8 (d) to increase the total absorption rate by generating multiple reflections. For the coatings, we adapt a technique developed for the diffuse reflectors of the Herschel space platform [400], which has been shown to reduce loss in microwave circuits [65]. The coating consists of a mixture of SiC grains and Stycast 2850 GT,[30] where the SiC grains roughen the coating surface. The SiC itself has no absorption band in the sub-millimeter wavelength [400]. The absorption coefficient of Stycast 2850, however, increases from 8 cm^{-1} at 333 GHz to 19 cm^{-1} at 2.5 THz. We test the absorption properties of the coating in an experimental setup as shown in Fig. 4.9 (a) [364]. In this setup, we probe the transmission between two antennas in a closed copper can, which is prepared with the absorbing coating. We compare Stycast coating without grains and three different grain sizes to an uncoated reference can by measuring the transmission between the antennas at cryogenic temperatures. As shown in Fig. 4.9 (b), the pure Stycast coating does not significantly reduce the transmission between

[30] We use the GT version of the Stycast 2850 instead of the FT version used in Ref. 400. The Stycast 2850 GT is optimized to the thermal expansion of brass instead of copper and brass has an expansion coefficient close to that of Al.

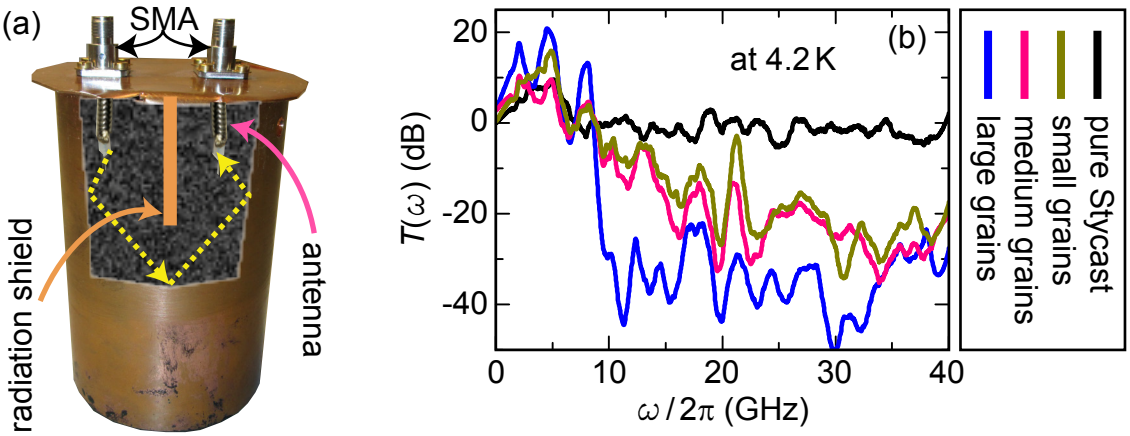

Figure 4.9: **(a)** Photograph of a closed copper can with two SMA feedthroughs. Inside the can, there are two antennas realized as semi-rigid coaxial cables where we remove the outer conductor and the isolation material for approximately 1 cm. To avoid direct crosstalk, we use a radiation shield between the two antennas. We coat the inside of the cans with different materials. **(b)** Normalized transmission magnitude from one antenna to the other plotted versus frequency for different coatings. We normalize our measurements to the transmission of an uncoated copper can.

the antennas. Hence, the Stycast coating with a smooth surface is not sufficient to absorb in the frequency range below 40 GHz. When roughening the surface with small (F30 0.6 mm) grains or with medium sized (F20 1 mm) grains, the absorption factor is approximately 20 dB between 15 GHz and 40 GHz. For even larger (F12 1.7 mm) grains, the absorption is reduced to almost 40 dB for frequencies higher than 10 GHz. For lower frequencies, we observe an increased transmission for all types of coatings. These frequency components must be screened by tight sample boxes and filters in the circuit. For terahertz radiation, we show the absorption of the absorbing coating in a similar experiment presented in Ref. 364. In these experiments, we measure the heating of a thermally isolated thermometer due to a nearby heater acting as a black-body radiator. We find that the thermometer heats up to a smaller extent in a coated surrounding for heater temperatures between 4.2 K and 12 K.

4.2 Time-resolved measurement setup

In addition to the cryogenic setup described in the previous section, we equip the CIRQUS lab with a measurement setup to perform time-resolved measurements (a photograph of the measurement equipment is shown in Fig. 4.10). The time-domain measurement setup resolves amplitude and phase variations of gigahertz signals on a nanosecond timescale [54]. This time-resolved measurement technique is crucial to detect the dynamics of superconducting quantum circuits [410] and for the characterization of microwave states of light [129]. The measurement setup presented here differs from other well-established setups [129, 410] in the chronology of averaging and homodyning. In our setup, the averaging step comes before the homodyne step as depicted in the operation principle of the time-domain setup in Fig. 4.11. The interchanged order of these steps is possible because we record coherent signals with a well-defined sinusoidal evolution rather than statistically distributed thermal states. Assuming that the detected signals follow well-defined amplitude and phase relations, we use an optimization protocol that dynamically adapts to variations and drifts in the carrier signal. That way, we omit any reference measurements to characterize

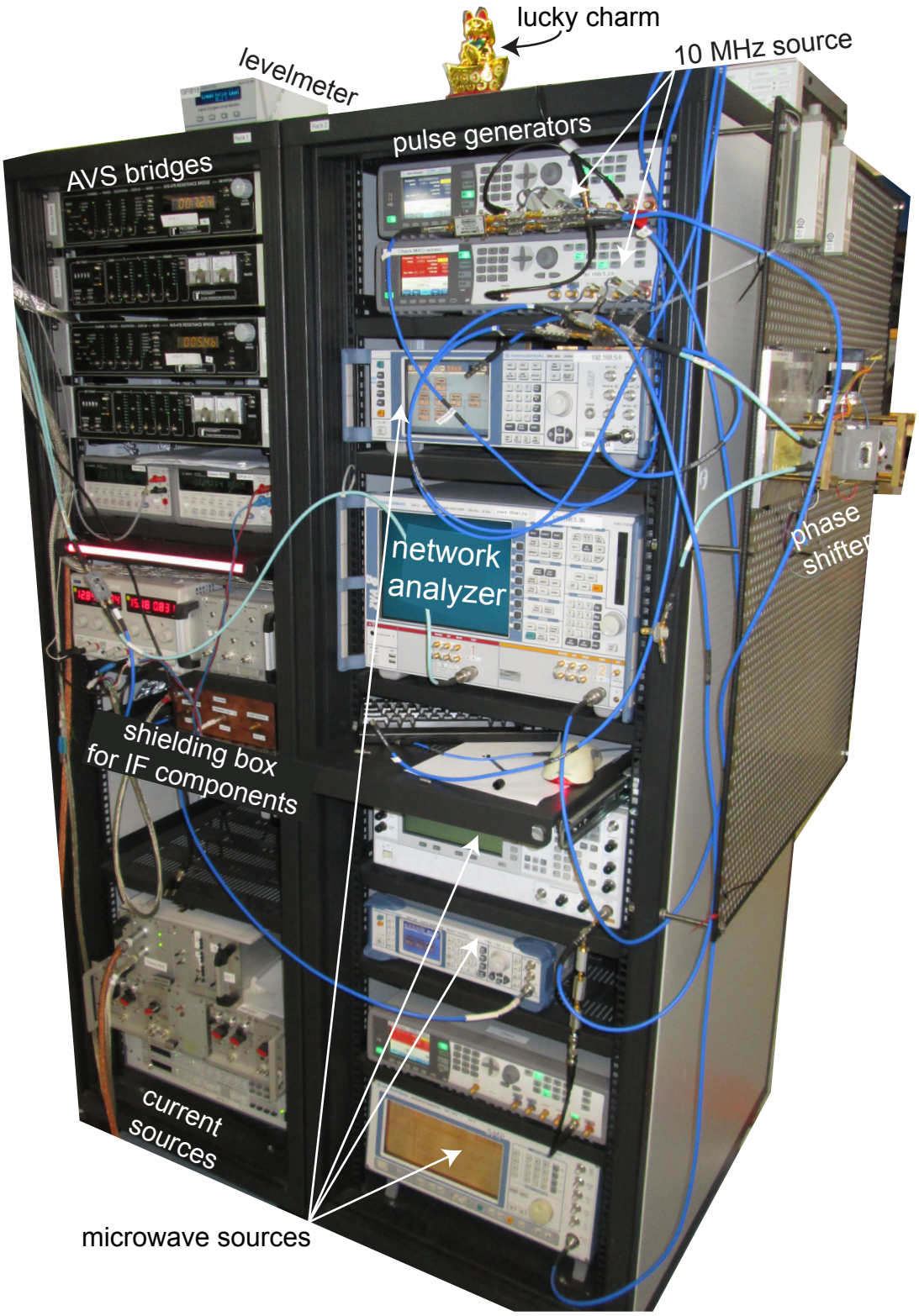

Figure 4.10: Photograph of the front side of the two racks containing most of the measurement equipment for the time domain setup described in the text.

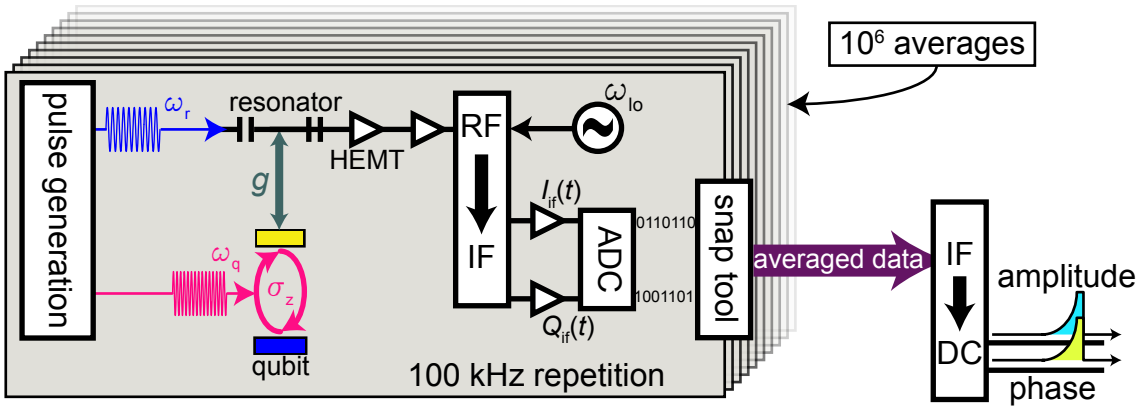

Figure 4.11: Schematic drawing of the measurement procedure used for time-resolved measurements of the qubit state. The single measurement traces including digitizing have a repetition rate of 100 kHz and are averaged approximately 10^6 times.

the detection path in our cryostat. For the specific case of a resonator used to read out a qubit in the strong coupling regime [see Eq. (2.3.2)], the protocol is as follows. First, we manipulate the qubit state by a series of drive pulses at or near the qubit transition frequency ω_q. To detect the qubit state, we read out the resonator with a second pulse at the resonator frequency ω_r. In the dispersive regime [see Eq. (2.3.5)], the ac-Stark shift changes the resonator eigenfrequency proportional to the σ_z-component of the qubit state. Due to the bandwidth of our analog-to-digital converters (ADCs), we convert the amplified gigahertz pulse (RF) to an intermediate (IF) frequency in the megahertz regime. To this end, we use $\mathcal{IQ}$-mixers supplying us with the in-phase and quadrature components $\mathcal{I}$ and $\mathcal{Q}$, respectively. After further amplification and low-pass filtering, we digitize the megahertz signals with ADCs. This procedure is repeated approximately 10^6 times and the single traces are averaged using a software code programmed in C++, which we call snap-tool. This strong averaging is necessary because the HEMT amplifiers add 10-20 noise photons to the readout signal, which typically contains one photon on average. In order to gain access to the quasi-DC envelopes of the megahertz signals, we perform a digital homodyning step and calculate amplitude and phase from $\mathcal{I}$ and $\mathcal{Q}$.
The rest of this section is structured as follows: We first present the pulse generation setup for drive- and readout pulses in Sec. 4.2.1. Second, in Sec. 4.2.2, we present the analog down-conversion setup. Averaging and digital homodyning is performed as described in Sec. 4.2.3.

4.2.1 Pulse generation and synchronization

The generation of pulsed sequences of gigahertz signals in a synchronized way is one main task for the time-resolved detection of quantum states in the microwave regime. In the following two paragraphs, we first discuss the technical implementation of such pulse sequences and subsequently address synchronization issues.

Pulse generation The technical realization of microwave pulse generation in the CIRQUS lab is depicted schematically in Fig. 4.12. We use two arbitrary function generators (AFGs), to generate the quasi-DC rectangular pulse envelopes.[31] To keep the flexibility of shaping

[31] We use `Agilent 81160A Pulse Function Arbitrary Noise Generator` for that purpose.

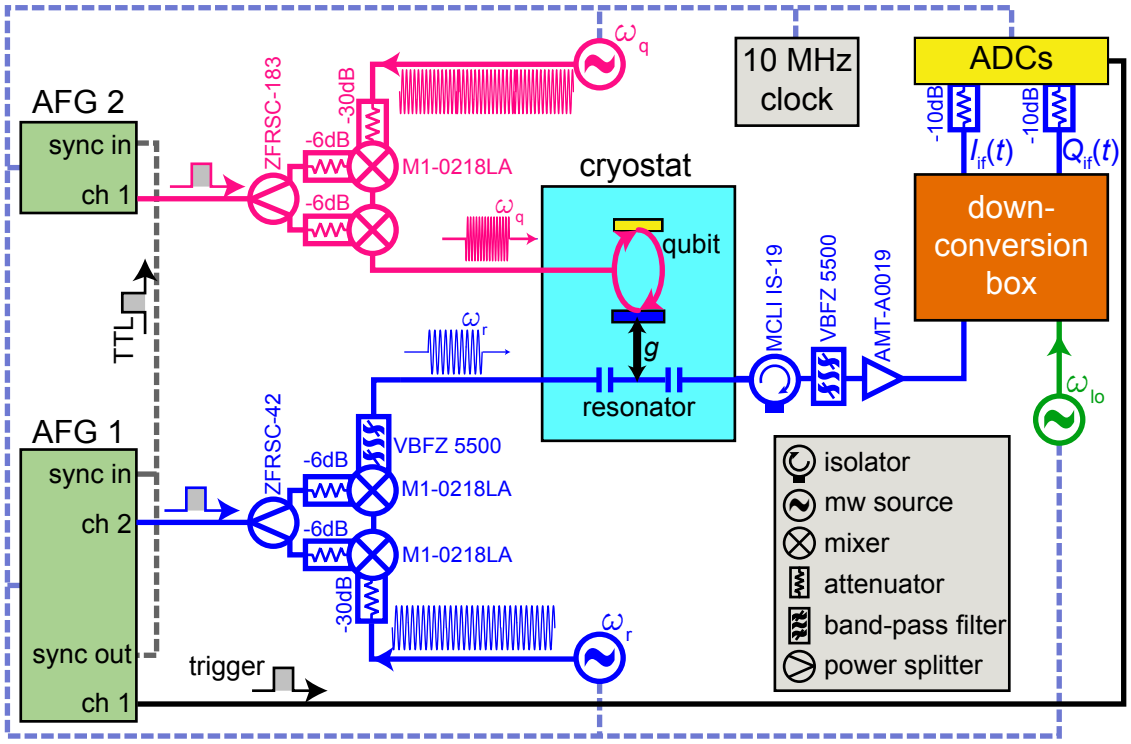

Figure 4.12: Time domain measurement setup. Pink and dark blue lines belong to the pulse generation and state detection setup, while dashed lines are synchronization lines. The down-conversion box is introduced in detail in Sec. 4.2.2.

more complex envelopes in the future, we digitally synthesize the waveforms loaded into the AFGs in our measurement software programmed as a LabView code. The code dynamically adapts the number of waveform points to the cycle length to keep a temporal precision of 1 ns. Hence, a waveform consists of 10^4 points for a typical cycle time of 10 µs. In Fig. 4.13 (a), we show the time evolution of a rectangular pulse used for triggering purposes. The finite rise time of 2 ns fits well to the 500 MHz bandwidth of of the AFG. For qubit state control and for a pulsed readout, we modulate the amplitudes of a sinusoidal gigahertz signal with the envelope pulses as shown in Fig. 4.13 (b).[32] To this end, we feed the continuous microwave signal from a microwave source as well as the rectangular pulse to the local oscillator (LO) and IF inputs of a double balanced harmonic mixer, respectively.[33] The mixers have an on/off ratio of approximately 20 dB and an insertion loss of 7 dB. To improve the on/off ratio, we use two mixers in series and split the rectangular pulse with a resistive power splitter.[34]

Synchronization A precise synchronization of all devices in the measurement setup is crucial for time-resolved measurements. In our setup, synchronization serves two tasks. First, each device must have exactly the same frequency standard and second, all pulses must arrive at the digitizer card precisely at the time when the card starts recording.

[32] For the qubit drive tone at frequency ω_q, we use a `Rohde&Schwarz SMF100A` microwave source, while an `Agilent PSG E8267D` source produces the readout tone at frequency ω_r.

[33] We use `Marki M1-0218LA` mixers for that purpose.

[34] We use `MiniCircuits ZFRSC-42` power splitters for that purpose.

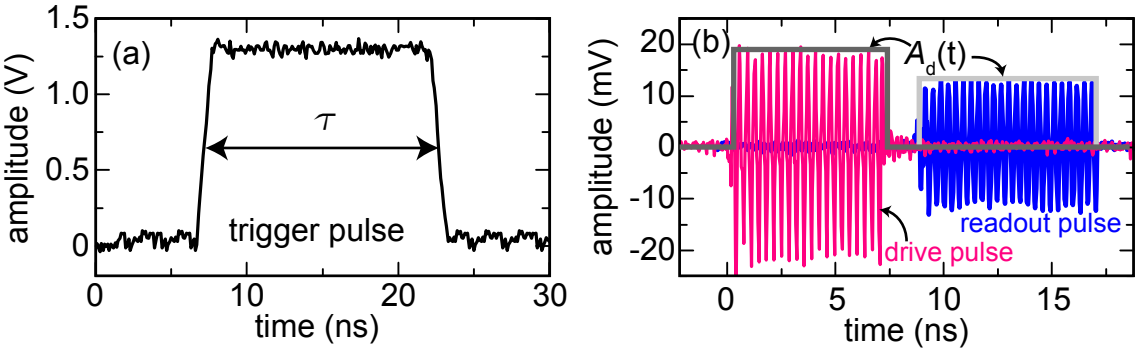

Figure 4.13: (a) Trigger pulse with pulse-width $\tau = 15\,\mathrm{ns}$ plotted versus time. (b) Microwave pulses and synthesized envelope function $\mathcal{A}_\mathrm{d}(t)$ plotted versus time. Both pulses have a frequency of 3.5 GHz and are detected before entering the cryostat with a fast oscilloscope.

Furthermore, because we average before the down-conversion, we must ensure that all recorded pulses always enter the digitizer card with an identical phase to avoid destructive interference. Each repetition of a 10 µs measurement cycle is triggered by one channel of an AFG as shown in Fig. 4.12. The TTL synchronization output of this channel triggers the output of the readout pulse and of the qubit drive pulse. To account for the propagation time of these pulses through the setup, we delay the actual pulse generated from that channel via the synthesized waveform. A typical time delay in our system for the trigger pulse is on the order of 150 ns. The common frequency standard is generated by an atomic clock based on rubidum-87 atoms.[35] This clock supplies a precise 10 MHz frequency reference that is connected to the synchronization input of all pulse generating devices and microwave sources [cf. Fig. 4.12]. The figures of merit for the synchronization are the phase-drift and the phase jitter between the different pulses. For a typical length of one measurement ($10\,\mu\mathrm{s} \times 10^6 = 10\,\mathrm{s}$), we observe no measurable phase drifts. Apart from phase drifts over this long timescale, however, the phase of the combined signals are subject to random jitter. To characterize this jitter, we record 10^6 traces with a fast oscilloscope and analyze deviations in the first rising edge of the pulses [54].[36] Calculating the standard deviation of the detected edge using the statistics function of the device, we find a rise time of 1.7 ns [cf. Fig. 4.13 (a)] and a jitter of 17 ps. For drive and readout pulse, we measure a jitter of 50 ps at the intermediate frequency $\omega_\mathrm{IF} = 62.5\,\mathrm{MHz}$ after down-conversion. This phase jitter corresponds to a phase noise of approximately 1°.

4.2.2 Analog down-conversion setup

We now describe the analog down-conversion step from the gigahertz frequencies used for readout to megahertz frequencies that our ADCs can resolve. We amplify the signal emerging from the cryostat at room temperature using an amplifier with a gain of 25 dB and a noise temperature below 60 K,[37] which is significantly below the broadband noise amplified by the HEMT amplifiers. This broadband noise also covers the carrier signal

$$s_\mathrm{out}(t) = \frac{1}{\sqrt{2}}[\underbrace{\mathcal{A}(t)\cos\left(\omega_\mathrm{r} t + \varphi(t)\right)}_{\mathcal{I}_\mathrm{rf}(t)} + \underbrace{\mathcal{A}(t)\sin\left(\omega_\mathrm{r} t + \varphi(t)\right)}_{\mathcal{Q}_\mathrm{rf}(t)}]\,, \tag{4.2.1}$$

[35] We use a `Stanford Research FS725` rubidium clock for that purpose.
[36] We use a `LeCroy Wavemaster 8600` oscilloscope for that purpose.
[37] We use an `Agile Microwave Technology Inc. AMT-A0019` amplifier for that purpose.

used for readout, which consists of the two components $\mathcal{I}_{\mathrm{rf}}$ and $\mathcal{Q}_{\mathrm{rf}}$. In Eq. (4.2.1), $\mathcal{A}(t)$ and $\varphi(t)$ are amplitude and phase of the carrier signal. This signal is physically down-converted using a double-balanced $\mathcal{IQ}$-mixer.[38] By modulation with a continuous local oscillator (LO) signal with frequency ω_{lo},[39] this mixer splits the carrier signal into high-frequency components $\mathcal{I}_+(t)$ and $\mathcal{Q}_+(t)$ and low-frequency components $\mathcal{I}_{\mathrm{if}}(t)$ and $\mathcal{Q}_{\mathrm{if}}(t)$ as shown in Fig. 4.14 (a). The frequency of the two resulting signals is given by the sum $\omega_+ = \omega_{\mathrm{r}} + \omega_{\mathrm{lo}}$ and by the difference $\omega_{\mathrm{if}} = \omega_{\mathrm{r}} - \omega_{\mathrm{lo}}$ of the two input frequencies. We use low-pass filters to suppress the undesired frequency contribution ω_+ and obtain

$$\mathcal{I}_{\mathrm{if}}(t) = \mathcal{A}(t)\cos(\omega_{\mathrm{if}}t + \varphi(t))\,, \tag{4.2.2}$$

$$\mathcal{Q}_{\mathrm{if}}(t) = \mathcal{A}(t)\sin(\omega_{\mathrm{if}}t + \varphi(t))\,. \tag{4.2.3}$$

Here, we assume a perfect mixer providing exactly 90° phase offset between $\mathcal{I}_{\mathrm{if}}$ and $\mathcal{Q}_{\mathrm{if}}$ and equal amplitudes at the two outputs. Deviations from this assumption are discussed in Sec. 4.2.3. Technically, we could down-convert s_{out} to zero frequency (homodyne) in order to save the additional step of digital homodyning and the need of a local oscillator. To avoid electronic $1/f$ noise and due to the ac-coupled ADCs, however, we chose an intermediate frequency $\omega_{\mathrm{if}} = 62.5\,\mathrm{MHz}$ in our experiments.
To optimize the performance of the down-conversion setup, the $\mathcal{IQ}$-mixer is placed together with additional microwave components inside a shielding box shown in Fig. 4.14 (b). This box is made of copper and isolates the microwave components inside from electromagnetic noise in the lab. The inner walls of the box are coated with an absorptive foil of rough surface to reduce the number of supported modes.[40] To make the lid of the box RF-tight, we place a conductive shielding gasket with a shielding efficiency of 80 dB at 100 MHz between cover and box.[41] To avoid that electromagnetic noise from the lab enters into the box through the measurement cables, we place an isolator at the input of the shielding box. The subsequent band-pass filter is used to reduce the bandwidth of incoming noise.[42] Without this filter, the noise bandwidth emitted from the cryostat is primarily determined by the amplification bandwidth of the HEMT amplifiers ranging from 3.5 GHz to 9 GHz. This large noise floor drives the IF amplifiers into compression if no band-pass filter is applied. To further reduce the noise spectrum, the down-converted signals $\mathcal{I}_{\mathrm{if}}$ and $\mathcal{Q}_{\mathrm{if}}$ pass a 90 MHz low-pass filter before and after the IF amplifiers.[43] That way, we keep a frequency window of 90 MHz open for the direct observation of coherent qubit oscillations, which are typically in the megahertz regime. Also in this respect, our setup differs from the narrow-band reconstruction method of microwave states discussed in Ref. 129. To make full use of the dynamic range of our ADCs, we use IF amplifiers with a typical gain of 65 dB and a noise temperature of 92 K.[44] To remove DC offsets and $1/f$ noise contributions from the amplified signals, they pass an additional high-pass filter with a cutoff frequency of 120 kHz.[45] The LO signal passes a 1.6 GHz high-pass filter and a circulator in order to avoid 10 MHz sidebands in the down-converted carrier signal.[46]

[38] We use a `Marki IQ-4509` mixer for that purpose.
[39] We use a `Rohde & Schwarz SMB 100A` microwave source for that purpose.
[40] We use `Kemet EFA(003)-240X240T0800 Fex Suppressor` foil for that purpose.
[41] We use a `Wurth Elektronik 3021005 Abschirmung Gasket` for that purpose.
[42] We use an `MiniCircuits VBFZ 5500` isolator for that purpose.
[43] We use `MiniCircuits SLP-90+` low-pass filters for that purpose.
[44] We use `MITEQ-AU-1525` amplifiers here.
[45] We use `MiniCircuits ZFHP-0R12` high-pass filters here.
[46] We use `MiniCircuits VHP16` high-pass filters for that purpose.

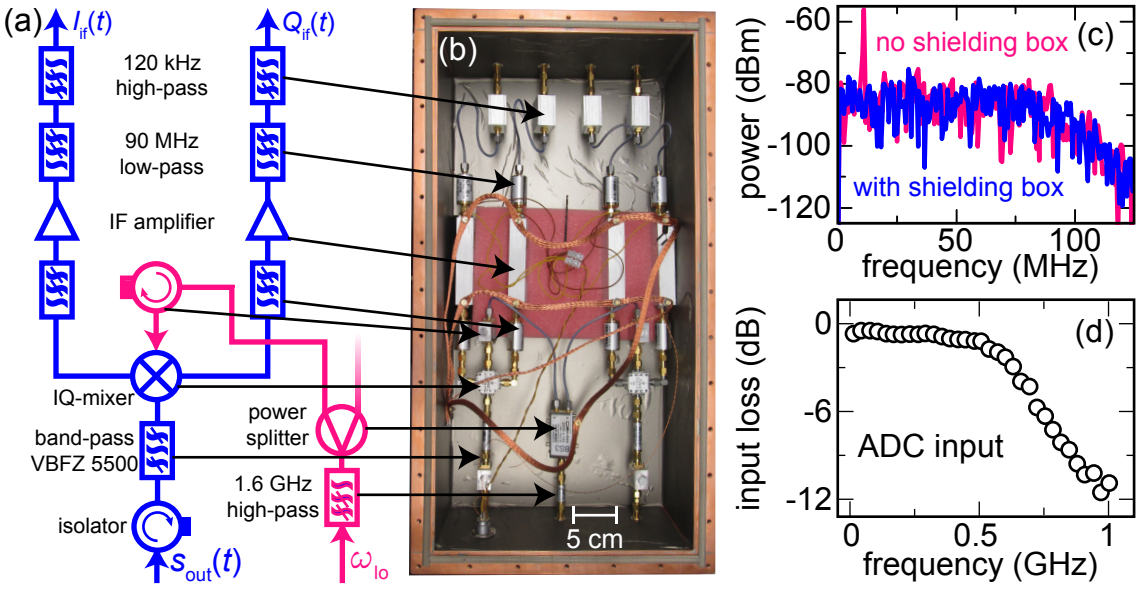

Figure 4.14: **(a)** Schematic drawing of the analog down-conversion setup. The black arrows point to equivalent microwave parts in the photograph of the opened shielding box shown in panel **(b)**. The box contains a second, identical setup for future use. **(c)** Noise power plotted versus frequency for setup placed in the open lab (no shielding box) or with shielding box. **(d)** Input loss of the ADCs of the X6-250m FPGA board measured above 1 MHz by `Innovative Integration` using an `Agilent N5181a` signal generator.

To characterize the measurement setup, we measure the noise spectrum of a 50 Ω termination screwed to the input of the shielding box. We record 10^6 averages of a 2.048 µs time trace with 4 ns steps and perform a Fourier transform into frequency space. When the lid of the shielding box is open, we measure a strong noise contribution at 10 MHz as shown in Fig. 4.14 (c). We benchmark the shielding efficiency of the box by repeating the noise measurement described above when the lid is closed. With the shielded setup, we significantly reduce the noise contribution at 10 MHz below the noise floor of the amplifiers [cf. Fig. 4.14 (c)]. The reduced noise level for frequencies higher than 100 MHz comes from the 90 MHz low-pass filters in the analog down-conversion setup.

4.2.3 Averaging and digital homodyning

We now describe the digital part of our setup where we average over single measurement traces and perform digital homodyning to a quasi-DC signal. Averaging is necessary since the carrier signal in a single readout trace is completely covered by noise. Nevertheless, since the noise is uncorrelated and has a zero arithmetic mean, we retrieve the in-phase and quadrature components of the carrier signal after strong averaging. While averaging is done in real using the snap-tool, digital homodyning is performed using a LabView code. The main advantage of our homodyne scheme compared to the schemes presented in Ref. 410 and Ref. 129 is the ability to dynamically adapt to frequency-dependent imbalances between the two amplification chains. That way, we are able to perform parameter sweeps without recalibrating offsets in the two components $\mathcal{I}_{\rm if}$ and $\mathcal{Q}_{\rm if}$.

Digitizing and averaging For digital data-processing, we digitize the two components $\mathcal{I}_{\rm if}(t)$ and $\mathcal{Q}_{\rm if}(t)$ with 250 MHz sampling rate and 14-bit resolution of the ±0.75 V input

range of the ADCs.[47] To reduce DC noise at the ADC inputs, the card is ac-coupled and has negligible input loss between 1 MHz and 250 MHz as shown in Fig. 4.14 (c). Even though our measurement card is equipped with an on-board FPGA,[48] we directly stream the data to a computer without using this FPGA functionality. The modular implementation of the measurement, however, allows for the integration of any real-time FPGA calculations in the future. A typical measurement trace consists of 512 points (2.048 µs) and is embedded into the 100 kHz (10 µs) cycling of the pulse generation setup. The data stream from the ADCs to the computer contains a header with channel information as well as the digitized data points. This data bundle is sent to the control computer via a single-lane PCIe 2.0 connection where it is post-processed within the 10 kHz repetition rate. In this configuration, we generate a streaming rate of 211 MByte/s, i.e., approximately half the maximum rate for a single-lane PCIe connection. Each trace of the data stream is received by the snap-tool, which subsequently averages the data by adding up the digitized traces in a memory buffer. When the maximum number of iterations $N_{\max}$ is reached, we calculate the mean value of each point in time by dividing the accumulated value by $N_{\max}$. We program the snap-tool in a way, that – in addition to averaging – any other computation with the digitized data can be performed. That way, we retain the flexibility for more advanced measurement routines. The averaged values $\mathcal{I}_{\text{if}}$ and $\mathcal{Q}_{\text{if}}$ are further processed in a LabView code as described in the following paragraph. To pass the data to the LabView code, the snap-tool provides a TCP/IP-based server.

Digital homodyning The digitized and averaged signals $\mathcal{I}_{\text{if}}$ and $\mathcal{Q}_{\text{if}}$ pass a homodyne routine programmed in LabView to remove the modulation with the IFcarrier frequency. To this end, we use a dynamic method that resolves the time dependency point by point using the optimization protocol depicted in Fig. 4.15. That way, we do not require additional calibration measurements.
In order to understand how the optimization protocol works, we first review the digital homodyning process itself. The final goal of this process is to get access to the time-dependent amplitude $\mathcal{A}(t)$ and phase $\varphi(t)$. In our discussion, it is more convenient to represent the IF signal as a trace in the phase space spanned by its field quadratures $\mathcal{I}_{\text{if}}(t)$ and $\mathcal{Q}_{\text{if}}(t)$. For an ideal signal defined by Eq. (4.2.2) and Eq. (4.2.3), this trace has the shape of a circle centered at the origin. Then, one can easily move to a rotating frame where the IF frequency is stationary using the rotation [410] $[\mathcal{I}_{\text{dc}}(t),\ \mathcal{Q}_{\text{dc}}(t)] = \mathcal{R}_{\text{if}}[\mathcal{I}_{\text{if}}(t),\ \mathcal{Q}_{\text{if}}(t)]$ with

$$\mathcal{R}_{\text{if}} = \begin{pmatrix} \cos(\omega_{\text{if}} t) & \sin(\omega_{\text{if}} t) \\ -\sin(\omega_{\text{if}} t) & \cos(\omega_{\text{if}} t) \end{pmatrix} . \tag{4.2.4}$$

With this rotation, the time-dependent quadrature amplitudes $\mathcal{I}_{\text{dc}}(t)$ and $\mathcal{Q}_{\text{dc}}(t)$ translate directly into $\mathcal{A}(t)$ and $\varphi(t)$. Due to the two individual amplification and filtering chains for $\mathcal{I}_{\text{if}}$ and $\mathcal{Q}_{\text{if}}$, however, there can be phase and amplitude deviations between the two channels resulting in the modified carrier signals

$$\mathcal{I}_{\text{if}}(t) = \mathcal{A}_{\mathcal{I}}(t) \cos(\omega_{\text{if}} t + \varphi(t)) + \delta\mathcal{I}_{\text{if}} \tag{4.2.5}$$

$$\mathcal{Q}_{\text{if}}(t) = \mathcal{A}_{\mathcal{Q}}(t) \sin(\omega_{\text{if}} t + \varphi(t) + \delta\varphi) + \delta\mathcal{Q}_{\text{if}} . \tag{4.2.6}$$

As shown in Fig. 4.15, these equations do not describe a circular trace anymore, but rather a twisted ellipse displaced from the origin by the amount $[\delta\mathcal{I}_{\text{if}},\ \delta\mathcal{Q}_{\text{if}}]$. In Eq. (4.2.5) and

[47] We use `Linear Technology LTC2157-14-Dual 14-Bit 250Msps` ADCs for that purpose.
[48] We use an `Innovative Integration X6-250M` board.

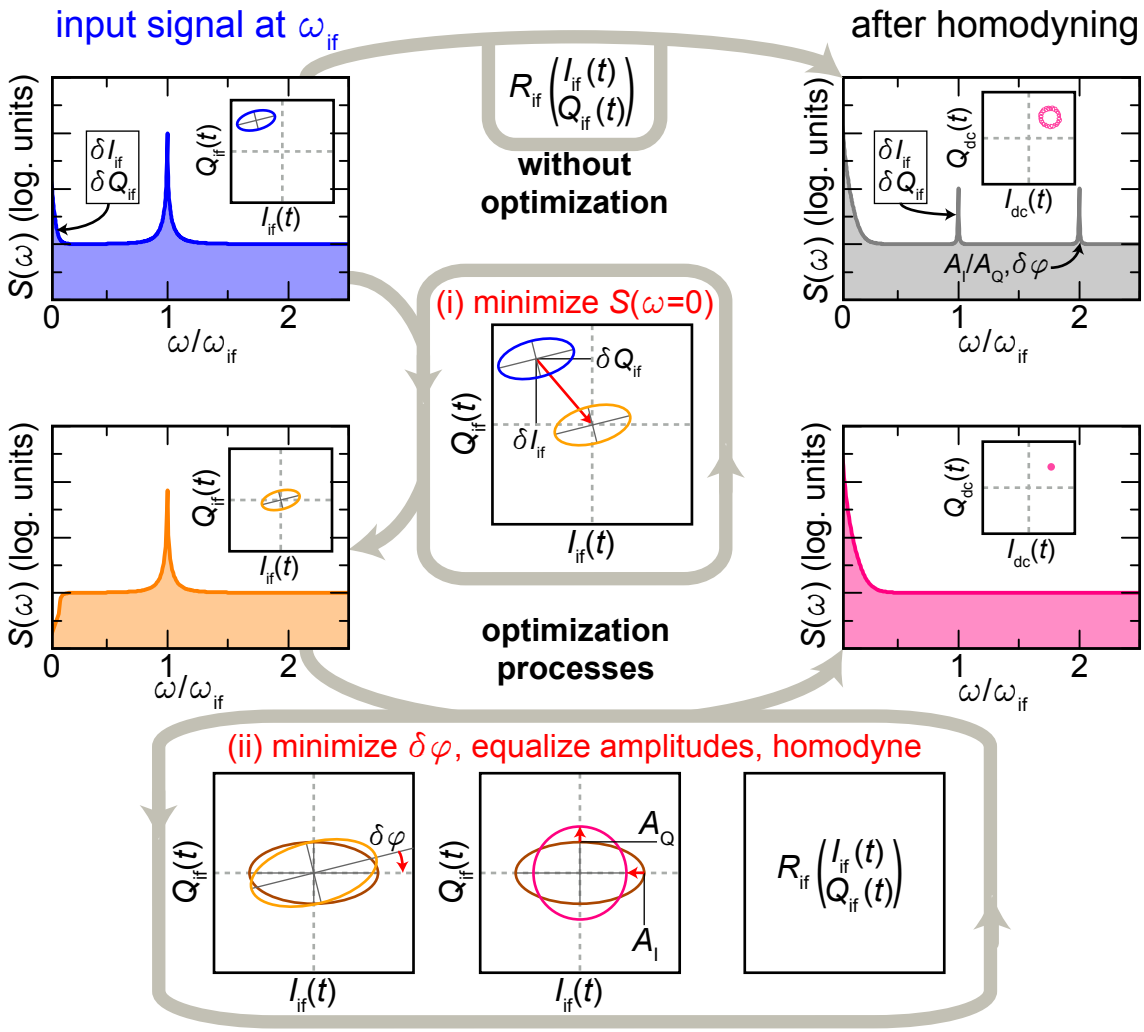

Figure 4.15: Sketch of the optimization process used for digital down-conversion. The insets of the spectral density plots show parametric plots of $\mathcal{I}_{\rm if}(t)$ vs. $\mathcal{Q}_{\rm if}(t)$.

Eq. (4.2.6), imperfections in the $\mathcal{IQ}$-mixer as well as in the two amplification chains result in different amplitudes $\mathcal{A}_\mathcal{I}(t)$ and $\mathcal{A}_\mathcal{Q}(t)$, respectively. Furthermore, the $\mathcal{IQ}$-mixer introduces a small phase offset $\delta\varphi$ between $\mathcal{I}_{\rm if}(t)$ and $\mathcal{Q}_{\rm if}(t)$, which typically depends on the frequency of both the carrier and the LO signal. Finally, the ADCs add the DC offsets $\delta\mathcal{I}_{\rm if}$ and $\delta\mathcal{Q}_{\rm if}$ to the digitized signals. When rotating Eq. (4.2.5) and Eq. (4.2.6) with $\mathcal{R}_{\rm if}$, the terms $\delta\mathcal{I}_{\rm if}$ and $\delta\mathcal{Q}_{\rm if}$ will rotate at the frequency $\omega_{\rm if}$. Furthermore, the amplitude ratio $\mathcal{A}_\mathcal{I}/\mathcal{A}_\mathcal{Q} \neq 1$ and also the phase offset $\delta\varphi$ result in spectral components at $2\omega_{\rm if}$. To correct for these artificial modulations, we use the optimization process described in the following. This optimization process consists of two important steps. In step (i) depicted in Fig. 4.15, we eliminate the DC offsets in the signals by subtracting the constant values $\delta\mathcal{I}_{\rm if}$ and $\delta\mathcal{Q}_{\rm if}$. We find the exact DC offsets by iteratively calculating the Fourier transforms of $(\mathcal{I}_{\rm if}(t) - \delta\mathcal{I}_{\rm if})$ and $(\mathcal{Q}_{\rm if}(t) - \delta\mathcal{Q}_{\rm if})$ for varying values of $\delta\mathcal{I}_{\rm if}$ and $\delta\mathcal{Q}_{\rm if}$ until a minimum at $\mathcal{S}(\omega{=}0)$ is reached.[49] After this step, we can assume $\delta\mathcal{I}_{\rm if} = \delta\mathcal{Q}_{\rm if} = 0$ in Eq. (4.2.5) and Eq. (4.2.6) and

[49] For the optimization process programmed in LabView we use the `Constrained Nonlinear Curve Fit.vi`, which is based on the Levenberg-Marquardt algorithm to find a set of parameters that best fit the theoretical model.

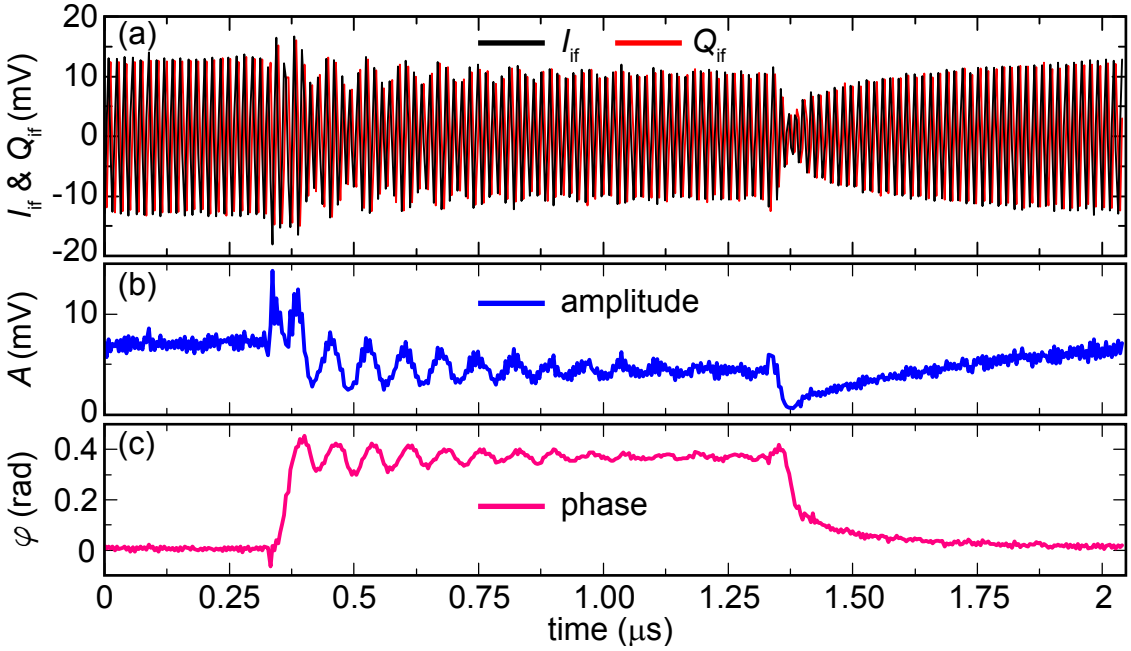

Figure 4.16: **(a)** Averaged time traces for $\mathcal{I}_{\rm if}(t)$ and $\mathcal{Q}_{\rm if}(t)$ at an IF frequency of 62.5 MHz showing the typical oscillatory behavior. **(c)** Amplitude $A(t)$ of the complex signal shown in (a) after homodyning. **(c)** Phase $\varphi(t)$ of the complex signal shown in (a) after homodyning.

continue with step (ii) of the optimization process. Step (ii) depicted in Fig. 4.15 contains three parallel tasks. The first task removes the phase offset between $\mathcal{I}_{\rm if}(t)$ and $\mathcal{Q}_{\rm if}(t)$, i.e., $\delta\varphi \mapsto 0$. The second task equalizes the amplitudes meaning that $\mathcal{A}_\mathcal{I} \mapsto \mathcal{A}_\mathcal{Q}$. If these tasks are performed precisely, we can finally homodyne the signal using the rotation matrix defined in Eq. (4.2.4). The optimization is based on calculations of amplitude and phase

$$\mathcal{A}(t) = \frac{1}{\sqrt{2}}\left[\frac{\alpha_\mathcal{I}\mathcal{I}_{\rm if}(t)}{\cos(\omega_{\rm if}t+\varphi(t))} + \frac{\alpha_\mathcal{Q}\mathcal{Q}_{\rm if}(t)}{\sin(\omega_{\rm if}t+\varphi(t)+\delta\varphi)}\right]^{1/2}, \tag{4.2.7}$$

$$\varphi(t) = \arctan\left[\frac{\frac{\alpha_\mathcal{Q}\mathcal{Q}_{\rm if}(t)}{\alpha_\mathcal{I}\mathcal{I}_{\rm if}(t)} - \sin(\delta\varphi)}{\cos(\delta\varphi)}\right] - \omega_{\rm if}t - \delta\varphi\,, \tag{4.2.8}$$

where $\alpha_\mathcal{I}$ and $\alpha_\mathcal{Q}$ are linear scaling factors. These scaling factors, as well as the phase offset $\delta\varphi$ are the free parameters, which are varied in the optimization process. In this process, we use the Levenberg-Marquardt algorithm to determine the set of parameters that best fit the spectral assumptions $\mathcal{A}(\omega_{\rm if},2\omega_{\rm if}) \simeq 0$ and $\varphi(\omega_{\rm if},2\omega_{\rm if}) \simeq 0$. In Fig. 4.16, we show the bare IF $\mathcal{I}_{\rm if}(t)$ and $\mathcal{Q}_{\rm if}(t)$ and the resulting amplitude and phase after demodulation. From a Fourier analysis of the demodulated signals, we find a typical signal/noise ratio of 40 dB for measurements using roughly one readout photon on average. With the dynamic optimization setup described above, we dynamically adapt the phase and DC offsets for each averaged measurement trace. That way, we omit any reference measurements to find calibration values for $\mathcal{A}_\mathcal{I}$,$\mathcal{A}_\mathcal{Q}$, and $\delta\varphi$.

The homodyne detection process described above works reliably for coherent signals with a larger amplitude than the averaged noise amplitude of the amplifiers. For the detection of thermal states without defined phase, however, the optimization process cannot be applied. Furthermore, the optimization is time-efficient only for weak measurements of

qubit states, where the averaging time is typically at least on the order of seconds and the additional computation time for the optimization process is negligible. When aiming for single shot measurements of superconducting qubits with a typical repetition rate of 100 kHz, the computing time of our protocol can strongly exceed the cycling time and limit the measurement efficiency. In this case, one could use one averaged calibration measurement, which is preceded to the actual single shot measurements.

4.3 Preparatory measurements for the gradio qubit experiments

In this section, we present preparatory measurements for the gradio qubit sample used in chapter 6. To this end, we first perform a systematic study of the circuit geometries. As shown in Fig. 4.17, all these characterization experiments are based on the same superconducting coplanar waveguide (CPW) transmission line structure patterned on a $6 \times 10\,\mathrm{mm}^2$ dielectric substrate.[50] In some cases, we add a pair of coupling capacitors into the center conductor of this basic structure to create a linear resonant circuit. In other cases, we add a pair of on-chip high-frequency antennas, to control a superconducting tunable-gap gradiometric flux qubit. In Sec. 4.3.1, we first characterize parasitic modes and properties of the fundamental transmission line structure. We then investigate the coupling capacitors used for our resonators and the loss induced by on-chip antennas (see Sec.4.3.2). Using these on-chip antennas, we show the formation of symmetric or antisymmetric RF fields in Sec. 4.3.3. This technique is essential to control a gradiometric-tunable flux qubit, which we integrate into the well characterized CPW structure as described in Sec. 4.3.4.

4.3.1 Characterization the transmission line structure

Because we use a He-bath cryostat operating between 1.8 K and 4.2 K[51] to characterize the transmission line structure, we use Nb thin films with $T_\mathrm{c} \simeq 9\,\mathrm{K}$ instead of Al. The samples are open transmission lines or resonator structures fabricated on silicon substrates as described in detail in Sec. 3.3.1. As depicted in Fig. 4.18 (a), we measure the transmission magnitude $\mathcal{T}(\omega)$ of these structures with a vector network analyzer (VNA).[52]

Parasitic modes of the transmission line sample A careful analysis of the transmission line characteristics is important to identify parasitic modes appearing as peaks or dips in a transmission spectrum. The transmission line geometry in Fig. 4.17 has a nearly constant transmission $\mathcal{T}(\omega) \simeq 1$ up to 10 GHz as shown in Fig. 4.18 (a). For frequencies above 10 GHz, we observe pronounced dips in the transmission spectrum. We attribute these dips to reflections and resonances in the sample box as well as in the substrate. Because all superconducting circuits presented in this thesis operate well below 10 GHz, these parasitic modes have no consequences in our experiments. Consequently, the transmission line structure presented here is well-suited to probe quantum effects in superconducting circuits.

[50] The transmon qubit, fabricated by J. Puertas Martínez [376], was initially planned by E. P. Menzel to serve as a single photon source and therefore has a different CPW structure.

[51] The cryostat is described in detail in Ref. 377.

[52] We use a `Hewlett-Packard 8722 D` network analyzer for that purpose.

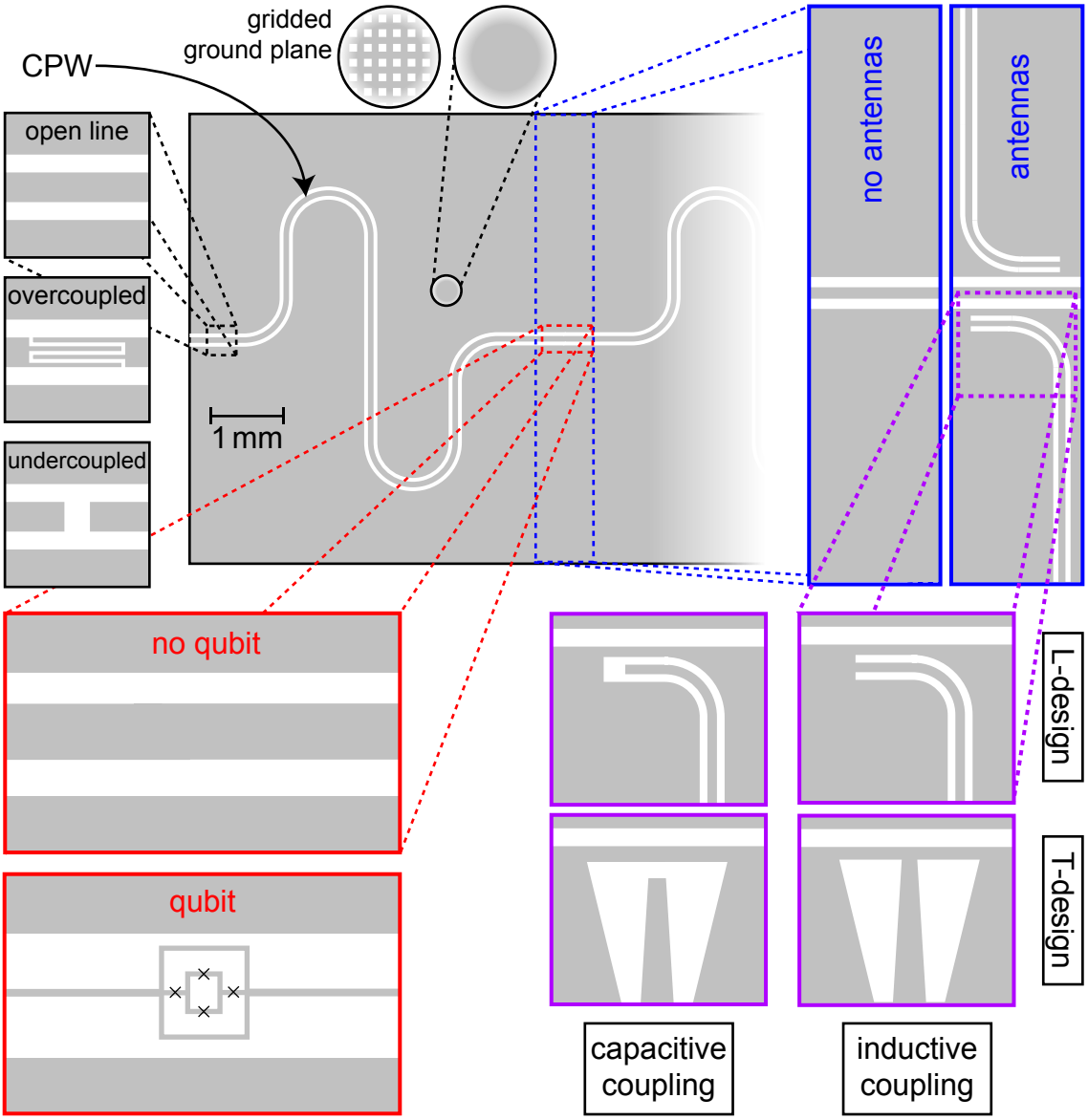

Figure 4.17: **(a)** Fundamental CPW structure used for most experiments in this work which has $20\,\mu m$ wide center conductor separated by $12\,\mu m$ from the ground plane. We can integrate coupling capacitors (zoom area marked by black dashed rectangle) or flux qubits (zoom area marked by red rectangle) into the center conductor. To control the qubit we can add a pair of antennas marked by the blue rectangle. We add either capacitively or inductively coupled antennas, which can have an L-design or a T-design. Furthermore, we can use a gridded ground plane to prevent flux vortices from moving across the sample frozen in the ground plane during cool-down.

Mean free path and penetration depth of Nb thin films More information about our superconducting Nb films is obtained by inserting two coupling capacitors into the center conductor of the transmission line and, in this way, creating a half-wavelength resonator. From the observed loss at 1.8 K and 4.2 K, we determine the mean free path λ_ℓ and the effective penetration depth λ_{BCS} defined in Sec. 2.1.2 of the Nb films. These important material parameters determine the surface resistance, and thus an important loss channel, of the Nb thin films. For our analysis, we measure the linewidth of a resonant

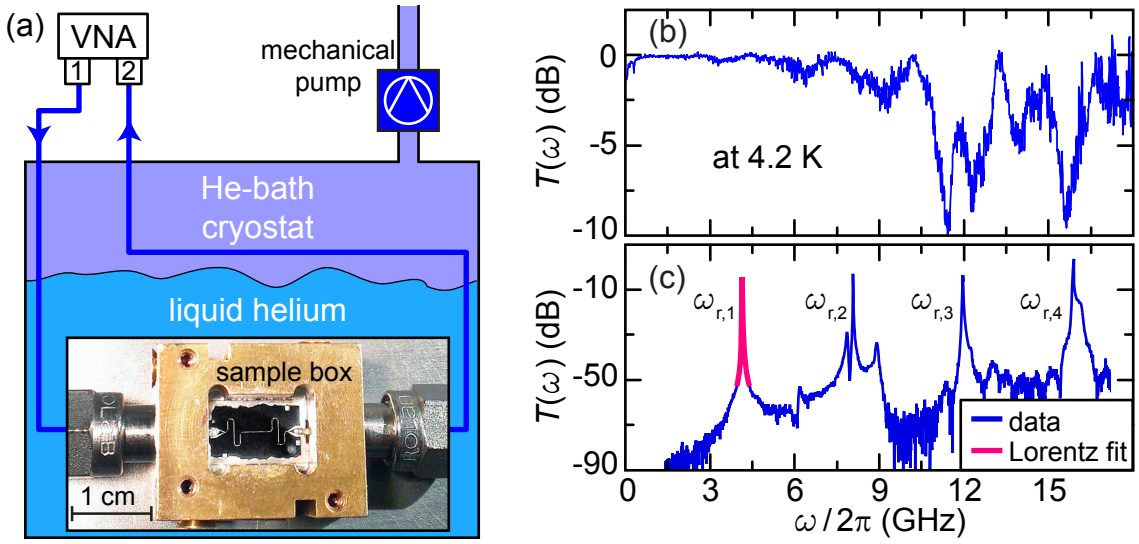

Figure 4.18: **(a)** Measurement setup for characterization measurements of transmission line structures using a vector network analyzer (VNA). The samples are mounted in a sample-box and cooled down in a He-bath cryostat. We can use a mechanical pump to reduce the vapor pressure and therefore the temperature of the liquid helium. **(b)** Transmission magnitude $\mathcal{T}(\omega)$ through an open transmission line sample plotted versus frequency. This measurement has been performed during the work presented in Ref. 361. **(c)** Transmission magnitude $\mathcal{T}(\omega)$ of an overcoupled resonator plotted versus frequency measured during the work presented in Ref. 68.

Nb structure defined by two coupling capacitors in the transmission line. The external coupling rate $\kappa_\mathrm{x}/2\pi \simeq 15\,\mathrm{kHz}$ of these capacitors is described in detail in Sec. 4.3.2. The two capacitors lead to standing waves with eigenfrequencies $\omega_{\mathrm{r},k}$ defined in Eq. (2.2.9) and shown in Fig. 4.18 (b). Away from these resonance frequencies, the transmission through the resonator is strongly suppressed due to the Lorentzian filter function. The bandwidth of the resonance peaks is determined by the total resonator loss $\kappa_\mathrm{tot} = \kappa_\mathrm{x} + \kappa_\mathrm{i}$ shown in Fig. 4.19 (a). At 4.2 K, we measure a resonator width $\kappa_\mathrm{tot}/2\pi \simeq 2.2\,\mathrm{MHz}$ for the fundamental mode $\omega_{\mathrm{r},1}$. Because the sample temperature of 4.2 K reaches almost 50 % of the critical temperature of Nb, we expect that a significant contribution to κ_tot comes from quasiparticle losses [279]. Consequently, we can reduce the resonator loss to $\kappa_\mathrm{tot}/2\pi \simeq 0.9\,\mathrm{MHz}$ by cooling the He bath cryostat from 4.2 K to 1.8 K.[53] In addition to the change in κ_tot, one expects a frequency shift of the resonance peak due to the change of the kinetic inductance [126]. A detailed analysis of this frequency shift and of the microwave loss allows one to derive the effective penetration depth and the mean free path of the Nb films. During the work presented in Ref. 68, we perform such an analysis and find a mean free path $\lambda_\ell \simeq 17\,\mathrm{nm}$ as well as the penetration depth $\lambda_\mathrm{BCS} \simeq 74\,\mathrm{nm}$. These values are comparable to those found in literature [411]. From these values, we estimate the loss rate due to surface resistance at mK temperatures to be significantly less than 1 kHz.

Current-induced quasiparticles In the previous paragraph, we analyze quasiparticle losses originating from thermally excited quasiparticles at relatively high temperatures ($T/T_\mathrm{c} > 0.1$). We now switch to the discussion of loss due to large oscillating currents inside

[53] To operate the helium-bath cryostat presented in Ref. 377 at 1.8 K, we reduce the vapor pressure to approximately 1 mbar using a mechanical pump.

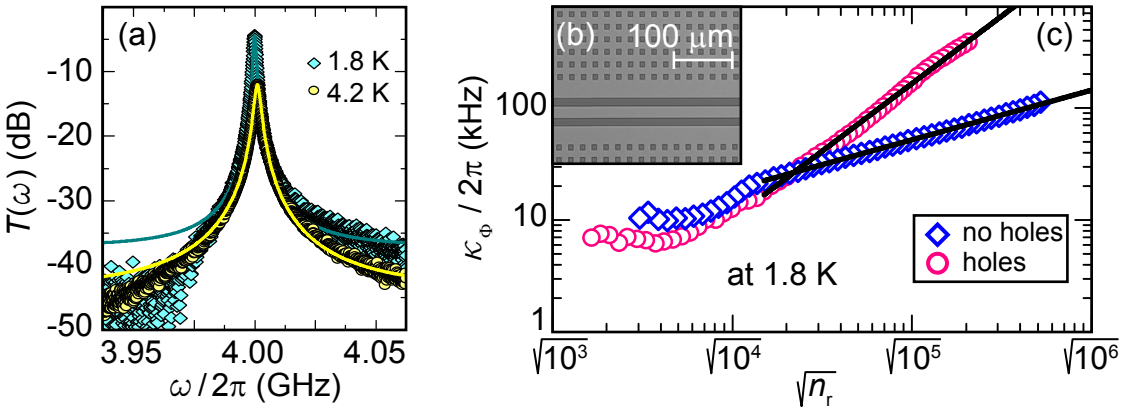

Figure 4.19: **(a)** Transmission magnitude of the fundamental mode of a superconducting Nb resonator measured at $4.2\,\mathrm{K}$ and $1.8\,\mathrm{K}$ sample temperature. Solid lines are Lorentzian fits. **(b)** Micrograph of the gridded ground plane used for the sample with holes. **(c)** Excess loss due to quasiparticles plotted versus field amplitude expressed as $\sqrt{n_\mathrm{r}}$. The solid lines are numerical fits as explained in text.

the resonator. From the loss model presented in Sec. 2.4.3, we expect no power dependence of the surface resistance loss. The loss model implies that the surface resistance itself shows no power dependence because the oscillating current does not generate additional quasiparticles. For very large readout power, however, the oscillating supercurrent may exceed the critical current at the sample edges thereby generating quasiparticles which contribute to the total loss rate of the resonator. These losses arise due to dissipative RF currents carried by quasiparticles. There are two possible candidates for quasiparticle induced losses. On the one hand, currents above the critical depinning current density could depin flux vortices, which subsequently dissipate power during their acceleration in the RF field. On the other hand, the local current density could exceed the critical depairing current density and generate normal conducting electrons.

The generation of loss due to flux vortices is as follows. Because Nb is a type-II superconductor, it enters the Shubnikov phase if the local magnetic field exceeds the critical field $B_{\mathrm{c1}} \simeq 200\,\mathrm{mT}$ [412]. For a superconducting thin film, however, the value of B_{c1} is strongly reduced due to demagnetization effects and can be as low as the earth magnetic field. The local magnetic field can be provided either from an external source or from the resonator itself. Based on the field calculations in Sec. 2.4.3, we expect, that vortex generation starts to form above approximately 10^6 photons. This number is based on the maximum calculated field strength $H_y^{\mathrm{max}} \simeq 5 \times 10^{-4}\,\mathrm{A/m}$ at the surface of the CPW structure generated from a single photon ($n_\mathrm{r} = 1$). This field strength corresponds to a magnetic field $B_y^{\mathrm{max}} \simeq 6.3 \times 10^{-7}\,\mathrm{mT}$. For a large enough oscillating current, especially the field components directly at the surface of the superconductor can exceed B_{c1} and generate vortices. Due to the resonator current density $\mathbf{j}_\mathrm{r}$, the vortices experience the force per vortex length [90] $\mathbf{F}_\Phi = \mathbf{j}_\mathrm{r} \times \mathbf{e}_\Phi \Phi_0$, where $\mathbf{e}_\Phi$ points in the direction of the magnetic flux in the vortex. Because superconductivity is suppressed in the core of a vortex, the resulting motion of the vortices leads to dissipation [413–415]. Their effect becomes manifest in the photon-number-dependent resonator loss $\kappa_{\mathrm{tot}}(n_\mathrm{r}) = \kappa_\mathrm{x} + \kappa_0 + \kappa_\Phi(n_\mathrm{r})$, where κ_0 accounts for all power-independent internal loss channels.

The generation of normal conducting electrons begins at positions where the local current density is enhanced due to geometry effects. Then, the current density can exceed the critical current density $j_\mathrm{c} \simeq 10^6\,\mathrm{A/cm^2}$ [416]. To identify which of the two processes is relevant

for our Nb thin films, we compare the power-dependent loss rates of two undercoupled Nb resonators. Both samples are fabricated on identical 525 µm thick Si/SiO_2 substrates using optical lithography. The relevant difference between them is that one sample has a continuous ground plane while the other one has a gridded ground plane. The square holes in the grid have a width of 8 µm and are separated by 12 µm as shown in Fig. 4.19 (b). The idea behind the grid is to provide a potential landscape where holes in the superconductor are potential minima for the vortices. Once a vortex is trapped in such a minimum it stays there until the trapping energy is again provided from an external source, e.g., thermal excitations. Hence, we would expect a smaller power dependence for the sample with gridded ground plane if flux motion is the source for the additional dissipation.
In Fig. 4.19 (c), we show the photon number dependence of the loss rate κ_Φ for the two resonators characterized at 1.8 K. Because we reach very high photon numbers ($n_\mathrm{r} > 10^5$), we can clearly observe additional loss due to crossing the critical current density. The additional loss rate increases stronger for the sample with gridded ground plane than for the sample with continuous ground plane. Hence, the additional loss is dominated by the generation of normal conducting electrons. The reason is the increased number of edges for the sample with gridded ground planes. At these edges, the quasiparticle generation is enhanced due to field elevation [417]. For the photon regime above $n_\mathrm{r} \simeq 1500$, we extract the excess loss per photon $\tilde{\kappa}_\Phi$ by fitting a power law $\kappa_\Phi = \tilde{\kappa}_\Phi \cdot n_\mathrm{r}^\beta$. In particular, we find $\tilde{\kappa}_{\Phi,\mathrm{grid}} \simeq 125\,\mathrm{kHz}/\sqrt{n_\mathrm{r}}$ and $\beta \simeq 1.22$ for the sample with gridded ground plane and $\tilde{\kappa}_{\Phi,\mathrm{cont}} \simeq 430\,\mathrm{kHz}/\sqrt{n_\mathrm{r}}$ and $\beta \simeq 0.43$ for the sample with continuous ground plane.

4.3.2 Coupling between transmission lines

In this section, we characterize coupling capacitors in half-wavelength CPW resonators and coupling coefficients of broadband on-chip antennas [418].

Coupling capacitors - point-like coupling We first evaluate the capacitance of the coupling capacitors used for the resonator structures throughout this work. The typical dimensions of these capacitors are small compared to the wavelength of the readout tone. Hence, we apply a lumped-element model imitating a point-like coupling. In general, this coupling between two structures A and B can be capacitively via their mutual capacitance C_κ or inductively via their mutual inductance M_κ. In both cases, Faraday's law describes the induced current and voltage

$$I_\mathrm{B} = -C_\kappa \frac{\partial V_\mathrm{a}}{\partial t} = -\imath\omega C_\kappa V_\mathrm{a} \exp(\imath\omega t)\,, \tag{4.3.1}$$

$$V_\mathrm{B} = -M_\kappa \frac{\partial I_\mathrm{a}}{\partial t} = -\imath\omega M_\kappa I_\mathrm{a} \exp(\imath\omega t + \imath\pi/2)\,. \tag{4.3.2}$$

Here, we assume that the signal oscillating at frequency ω in structure A is defined by the voltage amplitude V_a and the current amplitude I_a, respectively. In the case of coupling capacitors, the mutual capacitance determines the external quality factor of the resonator with total capacitance C (cf. Sec. 2.2.2). Since different experiments require different external quality factors, it is important to have well-founded knowledge of the mutual capacitance between two transmission lines. In addition to finite-element simulations, we extract the coupling capacity with two experimental methods. The first method is based on the frequency shift [112]

$$\delta\omega_\mathrm{r} = \frac{\omega_\mathrm{r}(C + C_\kappa) - \omega_\mathrm{r}(C)}{\omega_\mathrm{r}(C)} \approx -\frac{C_\kappa}{C} \tag{4.3.3}$$

induced from the additional capacitance at the coupling ports. The second method is to determine C_κ by measuring the resonator quality factor and apply Eq. (2.2.15). For this method, however, we have to make an assumption on the internal quality factor of our samples. During the work presented in Ref. 68, we perform a systematic study on the capacitance values for different capacitor geometries using both methods. From that study, we find the capacitor geometry used for the undercoupled resonators in Sec. 5.1 and the capacitor geometry used for the overcoupled resonators in Secs. 5.2 - 6.2. For the undercoupled resonators, we use gap-capacitors with a 10 µm wide gap and a capacitance $C_\kappa \simeq 1.1\,\mathrm{fF}$ resulting in a coupling strength $\kappa_\mathrm{x} \simeq 15\,\mathrm{kHz}$. This coupling corresponds to an external quality factor $Q_\mathrm{x} \simeq 3\times10^5$ at $\omega_\mathrm{r} \simeq 4\,\mathrm{GHz}$. For the experiments presented in Secs. 5.2 - 6.2, we use finger capacitors as shown in Fig. 3.12 (c) and in Fig. 3.11 (d). These capacitors result in a coupling strength $\kappa_\mathrm{x} \simeq 8.5\,\mathrm{MHz}$ for the quarter-wavelength resonator used in Sec. 6.1 and $\kappa_\mathrm{x} \simeq 2.5\,\mathrm{MHz}$ for the half-wavelength resonator used in Sec. 6.2.

Antenna coupling - distributed-coupling Even though we consider a purely capacitive and point-like coupling in the previous paragraph, generally the coupling has also inductive components and must be described in a distributed coupling model [419–422]. This model differs from the lumped-element model because voltage and current are distributed along the transmission lines meaning that there are regions where they coexist. In the distributed coupling model, we assume a spatial distribution $\widetilde{M}_\kappa(x)$ and $\widetilde{C}_\kappa(x)$ of the mutual inductance and capacitance per length, respectively (we consider the structure as quasi-one-dimensional). In addition to the spatial dependence of mutual capacitance and inductance, the amplitudes of current and voltage vary on the transmission lines due to interference and damping effects. We consider these effects using the space- and frequency-dependent envelopes $u(x,\omega)\in\{0,1\}$ and $j(x,\omega)\in\{0,1\}$. These envelopes account for several mechanisms that influence the spatial amplitude distribution. First, there is damping of the lines, i.e., $j_\mathrm{d}(x,\omega)=1/(1+\alpha_\mathrm{d}\sqrt{x\omega})$ with damping constant α_d.[54] Second, microwave attenuators placed in the input lines introduce a frequency-independent attenuation $j_\mathrm{a}=1/\alpha_\mathrm{a}$. Finally, there can be standing waves on resonant circuits, which enhance the envelope functions. Hence, we calculate the mutual inductance and capacitance as

$$M_\kappa(\omega)=\int_0^{\ell_\mathrm{c}}\widetilde{M}_\kappa(x)j_\mathrm{a}(x,\omega)j_\mathrm{B}(x,\omega)\,\mathrm{d}x \quad\text{and}\quad C_\kappa(\omega)=\int_0^{\ell_\mathrm{c}}\widetilde{C}_\kappa(x)u_\mathrm{a}(x,\omega)u_\mathrm{B}(x,\omega)\,\mathrm{d}x\,,$$

where, ℓ_c is the length of the coupling region. After computing $M_\kappa(\omega)$ and $C_\kappa(\omega)$, we treat the coupling region again as an effective point scatterer with impedance

$$Z_\kappa(\omega)=\frac{1}{1/R+2\imath\omega C_\kappa+1/(\imath\omega M_\kappa)}\,, \tag{4.3.4}$$

where R is the resistance of a (possible) galvanic connection between A and B. The transmission coefficient $2Z_\kappa(\omega)/[Z_0+Z_\kappa(\omega)]$ of this scatterer depends strongly on the ratio $Z_\kappa(\omega)/Z_0$. Taking into account the frequency-dependent damping, we find the transmission magnitude between A and B as

$$\mathcal{T}(\omega)=\left|\frac{1}{\alpha_\mathrm{a}(1+\alpha_\mathrm{d}\sqrt{x\omega})}\frac{2Z_\kappa(\omega)}{[Z_0+Z_\kappa(\omega)]}\right|^2\,. \tag{4.3.5}$$

[54] The same dependence holds, of course, also for the voltage envelope.

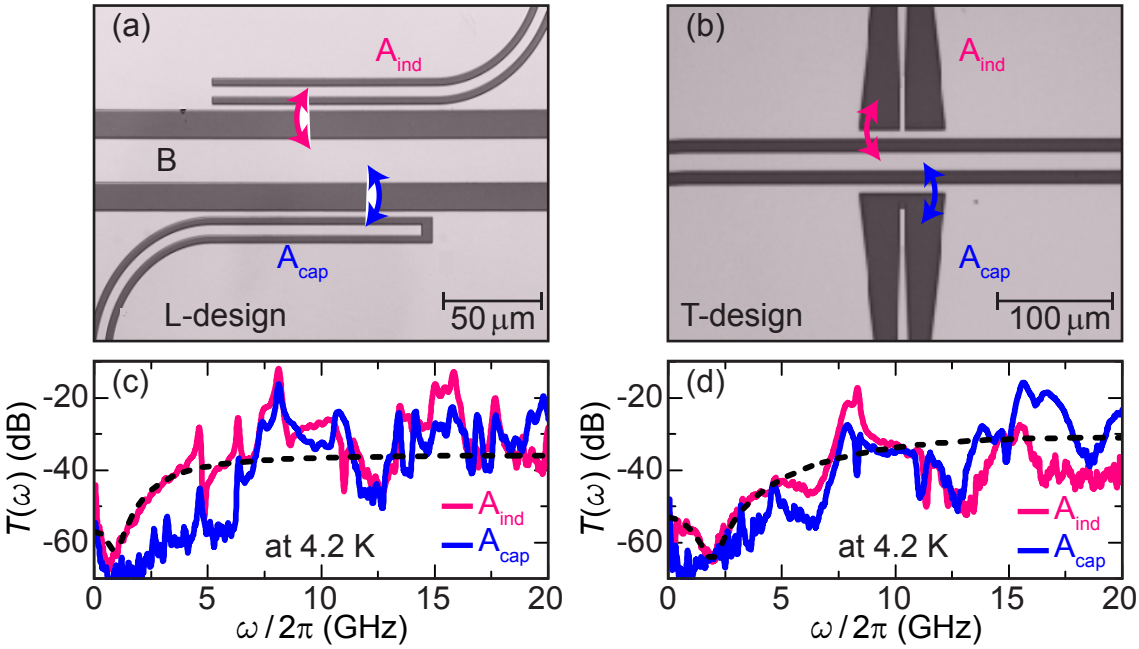

Figure 4.20: **(a)** Micrograph of a sample comprising two L-shaped antennas coupled to a transmission line (B). The antenna approaching from the top (A_{ind}) is inductively-coupled to an open transmission line, while the antenna approaching from the bottom (A_{cap}) is capacitively-coupled. **(b)** Experimental setup as shown in panel (a) but for two T-shaped antennas. **(c)** Calibrated transmission magnitude between the transmission line and the two antennas shown in panel (a) plotted versus frequency. **(d)** Calibrated transmission magnitude between the transmission line and the two antennas shown in panel (b) plotted versus frequency. Dashed lines are calculations based on Eq. (4.3.5).

To experimentally characterize the frequency-dependent transmission $\mathcal{T}(\omega)$ between different antenna structures and the central transmission line, we fabricate samples with several antenna designs. These designs are either inductively or capacitively coupled to an open transmission line (probe line) as shown in Fig. 4.20 (a) and (b). Here, the inductively coupled antennas are shorted to ground in the coupling region, while the capacitively coupled antennas have an open-circuit at this position. In Fig. 4.20 (c) and (d), we show $\mathcal{T}(\omega)$ between the antennas and the probe line measured at 4.2 K. The transmission magnitude shows large variations of more than 40 dB for both antenna designs and both coupling mechanisms. We observe several peak and dip structures arising from interference effects, i.e., standing waves on the chip. These peaks and dips are superimposed on a general trend described by Eq. (4.3.5). We show this trend for the inductively coupled antennas as dashed lines in Fig. 4.20 (c) and (d). Here, we set $1/R = 0$ because the antennas have no direct galvanic connection to the probe line and the silicon substrate is insulating at low temperatures. The calculations fit best to the data points if we set $M_\kappa = 1.5\,\mathrm{nH}$ and $C_\kappa = 1.3\,\mathrm{pF}$ for the L-design and $M_\kappa = 0.55\,\mathrm{nH}$ and $C_\kappa = 0.2\,\mathrm{pF}$ for the T-design. In both cases, the inductive contribution dominates the transmission, which is expected for the inductively coupled antenna. There is a reasonable quantitative agreement between the calculations and data for frequencies up to 5 GHz. For higher frequencies, however, interference effects dominate. For the capacitively coipled antennas, we observe a strongly reduced transmission for frequencies below 5 GHz compared to the inductively coupled antennas. Nevertheless, the measurements presented here are important to quantify the control pulses used for experiments with superconducting qubits.

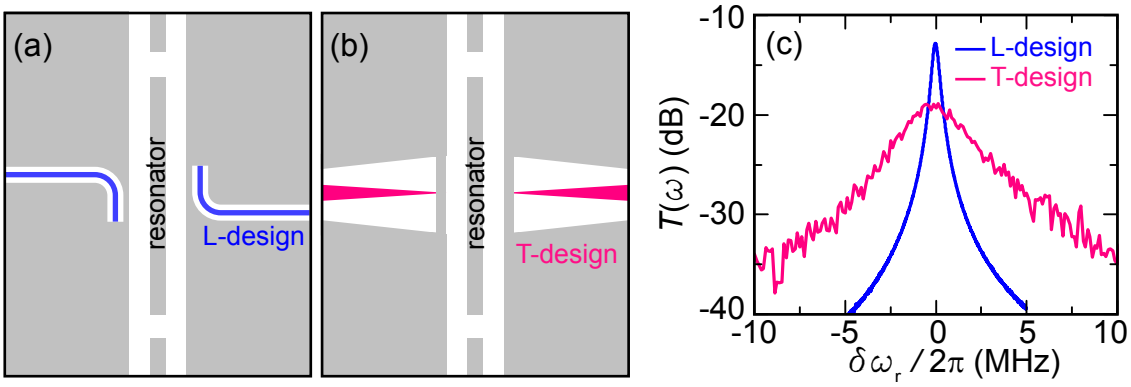

Figure 4.21: **(a)** Sketch of a CPW resonator coupled to two L-design antennas approaching the resonator from left and right, respectively. **(b)** Same as in panel (a) but for the T-design. **(c)** Transmission magnitude for resonators coupled to two antennas plotted versus detuning $\delta\omega_\mathrm{r} = \omega - \omega_\mathrm{r}$.

Resonator loss into antenna lines For many circuit QED experiments, qubits are coupled to CPW resonators. To control these qubits in a broadband frequency range, we use on-chip antennas as described above. However, the advantage of a broadband coupling to the qubit comes with the disadvantage that the coupling is also present at the resonator frequency. Especially, if inductively coupled antennas are placed at a current maximum of the resonator, photons can easily escape through the antenna lines. Consequently, the resonator quality decreases for strongly coupled antennas. Therefore, we must find a compromise between a small enough coupling to maintain the high resonator quality on the one hand, and a strong enough coupling for qubit control on the other hand. Here, strong enough means that we can induce enough signal into the superconducting circuits without heating the cryostat due to dissipating currents.
In the following, we compare the two antenna designs described above concerning the loss from the resonator into the antenna lines. The half-wavelength resonators depicted in Fig. 4.21 (a) and (b) have 10 µm gap capacitors resulting in an external coupling $\kappa_\mathrm{x} \simeq 15\,\mathrm{kHz}$. Since we perform the measurements at 1.8 K where internal loss rates are small, we approximate the loss rate κ_a into the antenna lines with the total loss rate κ_tot of the resonator, i.e., $\kappa_\mathrm{a} \approx \kappa_\mathrm{tot}$. Just as in the experiments presented in Sec. 6.2, we place one antenna on either side of the resonator. The first design (L-design) is shown in Fig. 4.21 (a). There, the antenna has a 50 Ω-matched CPW geometry until it is grounded in the close vicinity of the resonator. That way, we keep the overall structure size and consequently the crosstalk to the resonator small. For this design, we measure a loss rate into the antenna $\kappa_\mathrm{a}/2\pi \simeq 400\,\mathrm{kHz}$ corresponding to a loaded quality factor $Q_\ell \simeq 10^4$ [see Fig. 4.21 (c)]. The second antenna design (T-design) contravenes the 50 Ω-matching when approaching the resonator and widens up as shown in Fig. 4.21 (b). This geometry is larger and therefore shows more crosstalk to the resonator. Consequently, we measure an increased loss into the antenna $\kappa_\mathrm{a}/2\pi \simeq 2.6\,\mathrm{MHz}$ ($Q_\ell \simeq 1600$). Because this loss rate is approximately one order of magnitude higher than the loss rate of the L-design, we prefer the L-design for further experiments.

4.3.3 Formation of symmetric and antisymmetric microwave fields

For the control of quadrupolar artificial atoms, the spatial amplitude distribution of the electromagnetic field penetrating the circuits is important. In this thesis, we implement

quadrupolar artificial atoms as tunable-gap gradiometric flux qubits, which react to symmetric fields $\mathbf{H}_0$ and to antisymmetric fields $\nabla\mathbf{H}$ as introduced in Sec. 2.1.6 and Sec. 2.3.3. To control the amplitude distribution of the magnetic field penetrating the qubit, we place it between two symmetric antennas as shown in Fig. 4.22. That way, we generate a symmetric field with respect to the symmetry axis of the qubit as shown in Fig. 4.22 (a). This field configuration provides the symmetric magnetic field $\mathbf{H}_0$ required for RF control of the flux through the SQUID loop. On the other hand, an antisymmetric field as in Fig. 4.22 (b) provides the field gradient $\nabla\mathbf{H}$ in y-direction, which couples to the gradiometer part of the qubit. In the following, we show a way to generate RF fields with a spatial amplitude distribution that is either symmetric across the qubit area or RF fields that are antisymmetric. To calculate the amplitude distribution, we use a simple model based on Biot-Savarts law [423]. Our model does not include any boundary conditions from nearby ground planes, etc., but treats the undisturbed fields of current-carrying wires. We model each antenna as a single, thin wire of infinite length in x-direction. The wire is placed perpendicular to the yz-plane, crossing the plane at the coordinates $\mathbf{r}_1 = (0, y_1, 0)$. The magnetic field generated from this wire at a point $\mathbf{r}_0 = (x_0, y_0, z_0)$ in space reads $\mathbf{H}_1 = I_{\mathrm{d},1}/(2\pi|\mathbf{r}_0 - \mathbf{r}_1|)\mathbf{e}_\phi$ [423]. Here, $I_{\mathrm{d},1}$ is the current flowing through the wire and $\mathbf{e}_\phi$ is the unit vector in ϕ-direction when using a cylindrical coordinate system. This constant $1/|\mathbf{r}|$-dependence of a single antenna is not suited to manipulate the amplitude distribution. Thus, we sandwich the qubit in the near-field between two antennas, where the second antenna is placed at $\mathbf{r}_2 = (0, -y_1, 0)$. That way, the current $I_{\mathrm{d},2}$ enables either constructive or destructive interference of the two antenna fields. Since the qubit couples only to the z-component of the resulting field, we investigate the value

$$H_z(\mathbf{r}_0) = \frac{I_{\mathrm{d},1}}{2\pi}\frac{y_0 - y_1}{(y_0 - y_1)^2 + z_0^2} + \frac{I_{\mathrm{d},2}}{2\pi}\frac{y_0 + y_1}{(y_0 + y_1)^2 + z_0^2} \tag{4.3.6}$$

in the following. In Fig. 4.22 (c) and (d), we show $H_z(\mathbf{r}_0)$ for the two cases $I_{\mathrm{d},2} = I_{\mathrm{d},1}$ (symmetric field) and $I_{\mathrm{d},2} = -I_{\mathrm{d},1}$ (antisymmetric field) along the y-direction. Even though we have discussed only static solutions of the magnetic field so far, the line of argument also holds for oscillating currents if they have equal frequencies ω_d. We describe the oscillating currents as coherent drives $I_{\mathrm{d},1}(t) = I_1 \exp(\imath\omega_\mathrm{d} t)$ and $I_{\mathrm{d},2}(t) = I_2 \exp(\imath\omega_\mathrm{d} t + \imath\varphi_\mathrm{rel})$, respectively. We use the mean values $\langle I_{\mathrm{d},1}\rangle = I_1/\sqrt{2}$ and $\langle I_{\mathrm{d},2}\rangle = I_2\cos(\varphi_\mathrm{rel})/\sqrt{2}$ to calculate a quasistatic solution of the magnetic field using Eq. (4.3.6). Hence, we control the interference field with the amplitude ratio I_1/I_2 and with the relative phase φ_rel between the drives. In this formalism, the two scenarios in Fig. 4.22 (c) and (d) correspond to the situation where $I_1 = I_2$ and $\varphi_\mathrm{rel} = 0$ (symmetric field) and $\varphi_\mathrm{rel} = \pi$ (antisymmetric field).
To probe the amplitude shaping of microwave fields, we study on-chip interference effects of transmission line structures in much detail during the work presented in Ref. 361. We place a transmission line sample in an experimental setup as shown in Fig. 4.23 (a). The sample consists of a probe line, which runs symmetrically between the two on-chip antennas. We feed the antennas with a coherent drive generated from a VNA. We apply a phase shift in one of the arms using a motorized phase shifter.[55] Furthermore, we adjust the amplitudes I_1 and I_2 of the oscillating currents using attenuators in one of the lines. To probe the exact amplitude distribution of the field generated from the antennas, however, a sophisticated setup including SQUIDs or the like is required. Here, we use a simplified approach and measure the power $\mathcal{P}_\mathrm{t}$ transmitted to the probe line. Since the probe line sits symmetrically

[55] We use a motorized phase shifter constructed during the Diploma thesis of P. Eder [424].

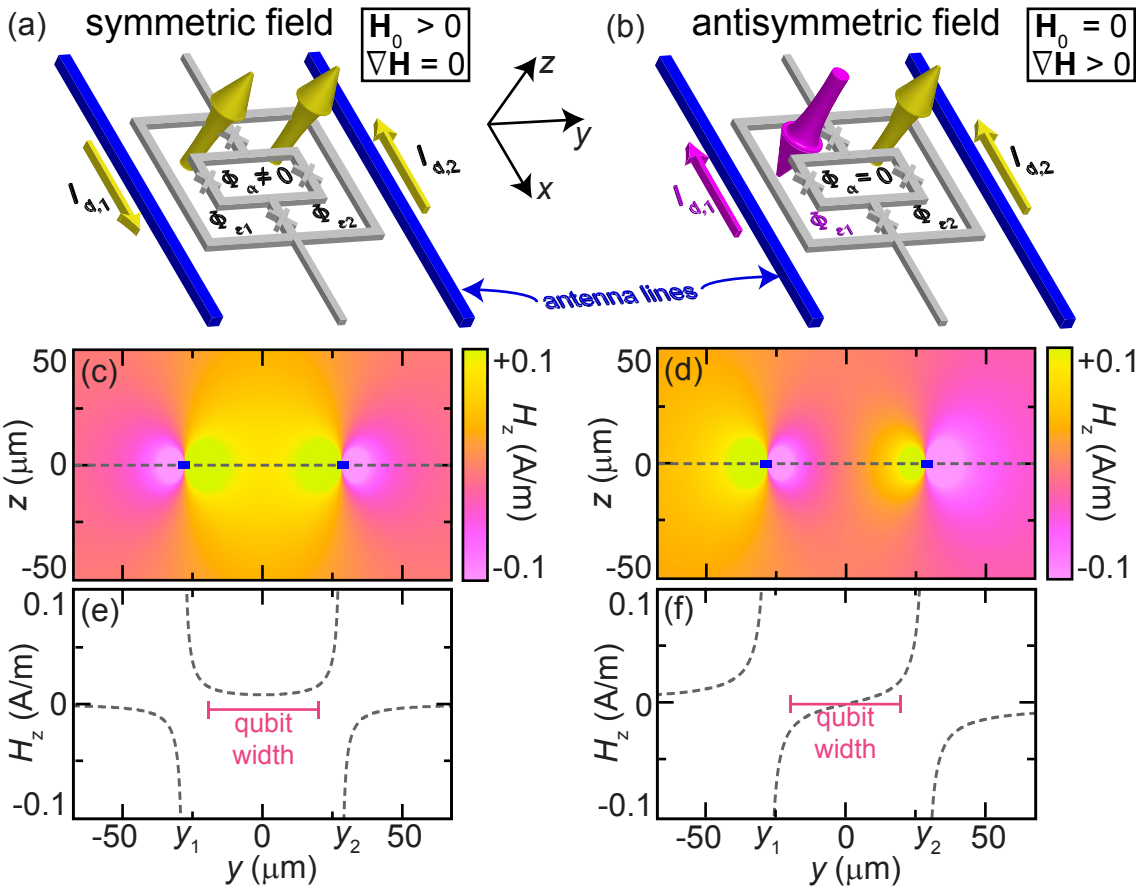

Figure 4.22: **(a)** Arrangement for the generation of symmetric magnetic fields penetrating a tunable-gap gradiometric flux qubit using two nearby antenna lines. The field is generated by the two oscillating currents $I_{\mathrm{d},1}$ and $I_{\mathrm{d},2}$. For the qubit, only the z-component H_{z} of the field depicted as the two circular arrows is relevant. **(b)** Same as in panel (a) but for an antisymmetric field. **(c)** Color-encoded z-component H_{z} of the magnetic field plotted versus position y (perpendicular to the qubit symmetry axes) and z for a symmetric magnetic field. The blue rectangles denote the position of the antenna lines. **(d)** Same as in panel (c) but for an antisymmetric field. **(e)** Magnetic field component H_{z} at the relevant height $z = 0$ indicated by the dashed line in panel (c) and panel (d). **(f)** Same as in panel (e) but for an antisymmetric field.

between the antennas, an antisymmetric field has an amplitude node at this position and no power is transmitted. A symmetric field, however, has a finite amplitude at the probe line position and the transmitted power has a maximum. In general, the power transmitted from the antennas to the probe line reads

$$\mathcal{P}_{\mathrm{t}}(\omega_{\mathrm{d}},\varphi_{\mathrm{rel}}) = Z_0 \mathcal{T}(\omega_{\mathrm{d}}) \left[I_{\mathrm{d},1}^2 + I_{\mathrm{d},2}^2 + 2 I_{\mathrm{d},1} I_{\mathrm{d},2} \cos\varphi_{\mathrm{rel}} \right] . \tag{4.3.7}$$

Here, we assume that the coupling $\mathcal{T}(\omega_{\mathrm{d}})$ defined in Eq. (4.3.5) between antenna and probe line, is equal for both antennas. When operating at a single drive frequency, we compensate for inequalities in $\mathcal{T}(\omega_{\mathrm{d}})$ by varying the attenuation in the lines. When sweeping the frequency, however, the situation becomes more complex as shown in Fig. 4.23 (b). Here, we observe an oscillatory behavior of the transmitted power versus frequency. This behavior arises from the phase shift φ_{rel} that increases linearly with frequency if the two arms have not the exact same electrical length. In this case, the phase evolution reads

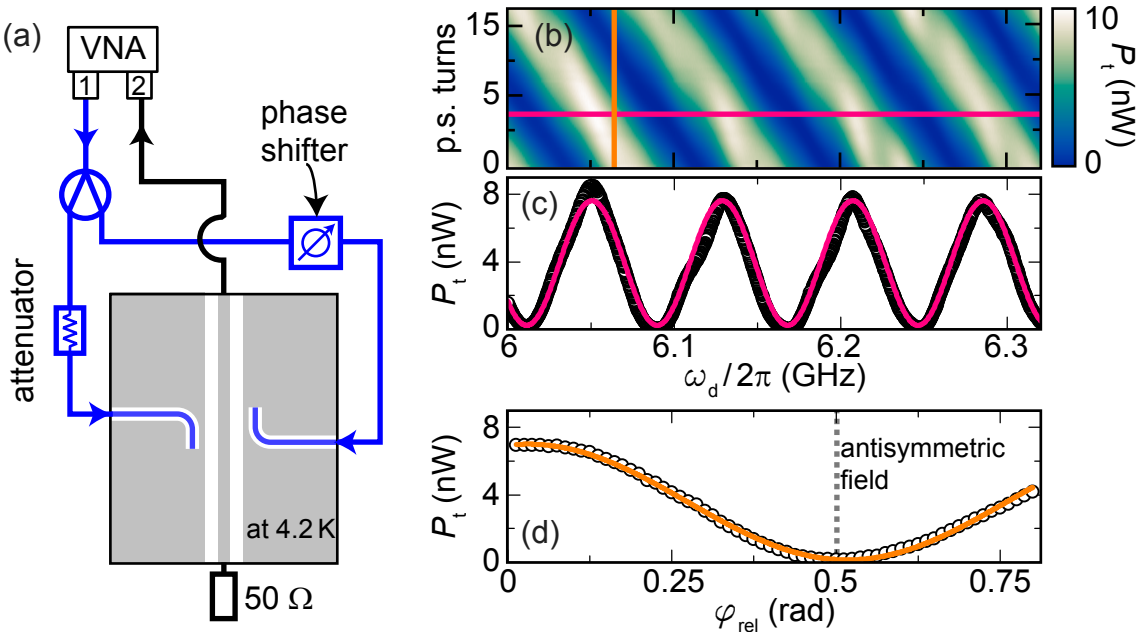

Figure 4.23: **(a)** Experimental setup to test the amplitude distribution of microwave fields. **(b)** Color-encoded power $\mathcal{P}_t$ transmitted from the two antennas to the probe line plotted versus drive frequency ω_d and phase shifter (p.s.) turns. Solid lines indicate where the traces shown in panel (c) and (d) are measured. **(c)** Power $\mathcal{P}_t$ transmitted from the two antennas to the probe line plotted versus drive frequency at 3 phase shifter turns. **(d)** Power $\mathcal{P}_t$ transmitted from the two antennas to the probe line plotted versus phase difference recorded at 6.06 GHz. In panel (c) and (d) solid lines are sinusoidal fits.

$\varphi_{rel}(\delta\ell) = \omega_d \delta\ell / c_{eff}$, where $\delta\ell$ is the length difference between the arms and c_{eff} is the effective speed of light in the measurement lines. As shown in Fig. 4.23 (c), this model explains the data in a reasonable way as indicated by the sinusoidal fit. A more controlled way to change the phase difference is to use the motorized phase shifter. That way, we achieve a clear sinusoidal behavior of the transmitted power as shown in Fig. 4.23 (d). As expected, we measure high transmission for $\varphi_{rel} = 0$ and a strongly reduced transmission for $\varphi_{rel} = \pi$ resulting in an on/off ratio of 55 dB. From this large on/off ratio, we conclude that we can efficiently control the amplitude distribution in the region between the two antenna lines. Consequently, we use this method to control the gradio qubit as presented in the next section.

4.3.4 Characterization of the gradio qubit

In this section, we introduce the measurement setup and characterization measurements for the sample used to study selection rules for quadrupolar qubits presented in Sec. 6.2.

Cryogenic sample setup We use a tunable gradiometric flux (gradio) qubit [83, 98] coupled to a half-wavelength CPW resonator as depicted in Fig. 4.24 (a). We place the qubit at the current antinode of the resonators fundamental mode and add a pair of inductively coupled on-chip antennas as described in Sec. 4.3.3. Qubit and resonator are made in one fabrication step from an Al/AlO_x/Al thin film as explained in detail in Sec. 3.3.2. That way, we remove loss due to Nb/Al transitions introduced in Sec. 2.4.3. For our experiments, we fix the sample with silver glue inside a gold-plated copper box [see Fig. 4.24 (b)] and

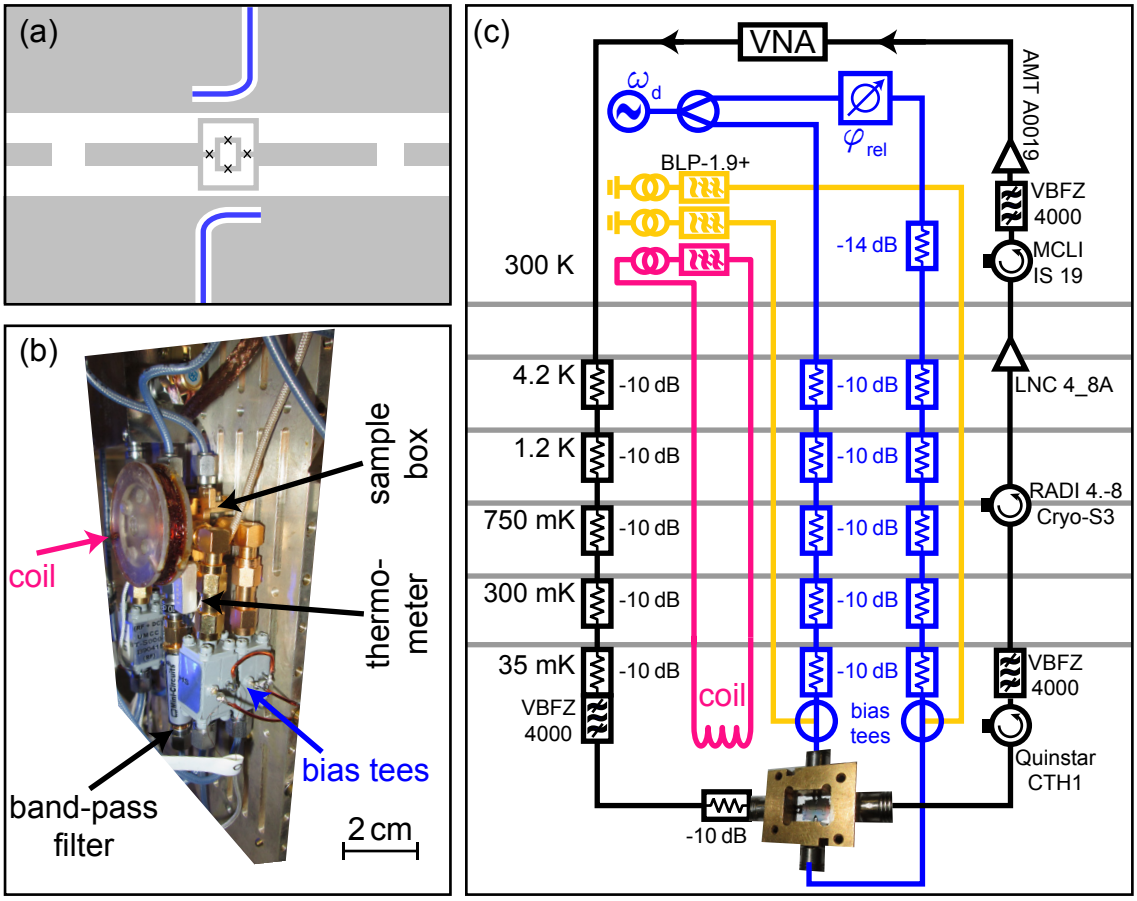

Figure 4.24: **(a)** Sketch of a gradio qubit galvanically coupled to a readout resonator and inductively coupled to two on-chip antennas. **(b)** Photograph of the cryogenic measurement setup. **(c)** Detailed measurement setup including microwave and DC components.

cool it to the base temperature of the cold-stage of our dilution refrigerator, i.e., 25 mK. Our low temperature setup has a sophisticated shielding against magnetic flux noise as described in Sec. 4.1.3. Additionally, we use a gridded ground plane for the CPW resonator to prevent the motion of flux vortices. The combination of strong shielding and a gridded ground plane yields a very high flux stability of the setup. This flux stability is a big advantage compared to earlier experiments [178, 425] with flux qubits that suffered from spatially unstable flux vortices.

Measurement setup The sample is connected to several RF and DC control lines, which we describe in detail in Sec. 4.1.2. We give a schematic overview of the cryogenic setup in Fig. 4.24 (c). We perform measurements either with a vector network analyzer (VNA)[56] or with the time domain setup described in Sec. 4.2. We filter input and output lines with `Minicircuit VBFZ 4000` band-pass filters at room temperature and at the sample stage to protect the qubit from noise. That way, we observe a very clean noise-floor for frequencies outside the band-pass region shown in Fig. 4.25 (a). We control the qubit using the two

[56] We use a `Rohde &Schwarz ZVA 24` network analyzer for that purpose. For a typical measurement, we use a bandwidth from 10 Hz to 100 Hz and average approximately 10 times.

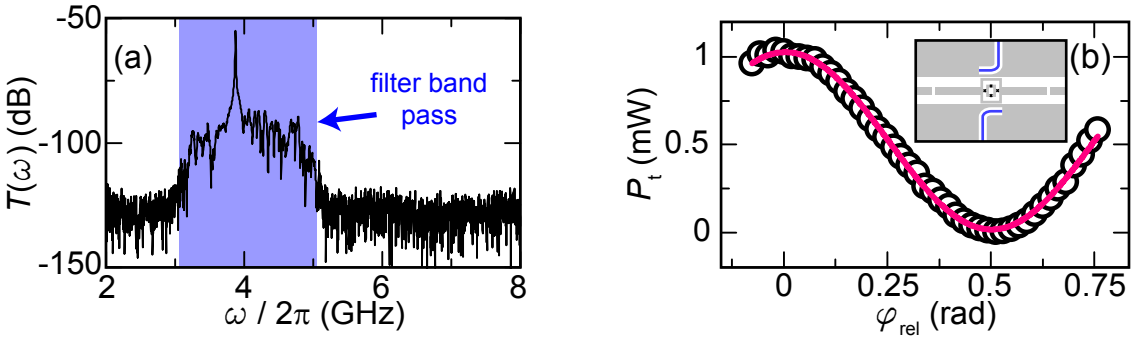

Figure 4.25: **(a)** Transmission magnitude measured through the resonator plotted versus readout frequency. **(b)** Power $\mathcal{P}_\mathrm{t}$ transmitted from the two antennas to the resonator plotted versus phase difference recorded at 3.99 GHz. The solid line is a sinusoidal fit and the insert depicts the experiment.

on-chip antennas, which are connected to bias tees [57] to allow for DC and RF control signals. These bias tees are specified to work between 2 GHz and 18 GHz for the RF input and have a 200 MHz bandwidth of the DC port. Hence, the DC cables are additionally low-pass filtered from the bias tees at cryogenic temperatures. Using the DC port of these bias tees, we generate on-chip static magnetic fields with a controlled spatial amplitude distribution. Additionally, we use the on-chip antennas to generate an RF field with varying spatial distribution. As described in the previous section, we use a room temperature phase shifter to control the phase difference φ_rel between the two antenna lines. In Fig. 4.25 (b), we show the precise control of the RF magnetic field, which is not affected by the usage of additional microwave components such as mixers, bias tees or filters. Quantitatively, we achieve an on/off ratio of 30 dB for 14 dB of additional attenuation in one of the antenna lines.

Resonator characterization In the following paragraphs, we characterize the sample using spectroscopic and time-resolved measurements. Spectroscopic measurements of qubit-resonator systems are a convenient method to access to the system's excitation spectrum [24, 26]. With our sample architecture, we can either populate the resonator with readout photons through the input line or excite the qubit through the antenna lines. We first characterize the resonator with a single tone transmission experiment to extract the resonator frequency $\omega_\mathrm{r}/2\pi = 3.88\,\mathrm{GHz}$ and the total loss rate $\kappa_\mathrm{tot}/2\pi = 2.5\,\mathrm{MHz}$. This loss rate is obtained from a Lorentzian fit to the resonator transmission spectrum and corresponds to a loaded quality factor $Q_\ell \simeq 1500$. The resonator is limited by its external loss rate $\kappa_\mathrm{x}/2\pi = 2.43\,\mathrm{MHz}$ and has an internal loss rate $\kappa_\mathrm{i}/2\pi \simeq 70\,\mathrm{kHz}$ (see Sec. 5.1.3 for details).

Magnetic flux control of the qubit Even though we shield the sample against external flux noise, we generate a static magnetic field using a superconducting coil attached to the sample holder to flux-bias the qubit. For the homemade coil with 1200 windings, we use 100 µm thick NbTi wire embedded in a phosphor bronze matrix. Because the coil dimensions are much larger than the qubit area, the generated field is spatially homogeneous across the qubit area. Hence, one expects the transition frequency of the gradio qubit to only depend on the magnetic flux through the α-SQUID. Due to a finite gradiometer quality described

[57] We use `BT-S000-HS` bias tees for that purpose.

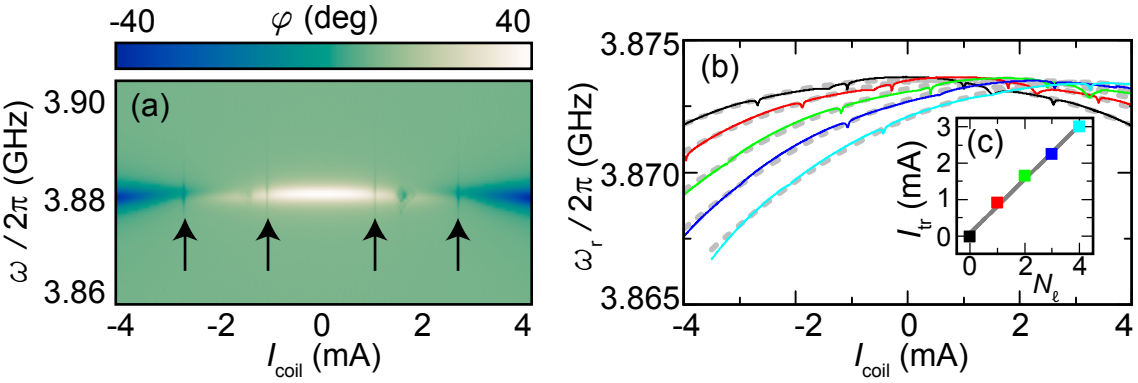

Figure 4.26: **(a)** Phase of the readout tone plotted versus readout frequency and magnetic field generated by the coil current. The arrows indicate anticrossings between qubit and resonator. **(b)** Resonator frequency plotted versus coil current for different numbers of flux quanta trapped. The dashed lines are parabolic fits as described in text. **(c)** Shift I_{tr} of the fitted parabolas plotted versus number of trapped flux quanta.

below, however, there is also a flux difference between the two gradiometer loops. This flux difference between the gradiometer loops arises mostly from the current circulating in the α-SQUID, which converts the homogeneous field to an effective field gradient (see Ref. 178 for details). To characterize the flux-dependent transition frequency of the qubit, we vary the magnetic field with a well-defined coil current in order to identify qubit-resonator anticrossings as shown in Fig. 4.26 (a). The anticrossings are located at $\delta\Phi_\varepsilon = N\Phi_0$, where $\delta\Phi_\varepsilon = \Phi_{\varepsilon 1} - \Phi_{\varepsilon 2}$ is the flux difference in the two gradiometer loops. From the spacing of the anticrossings, we calculate an effective mutual inductance $M_\varepsilon \simeq 0.625\,\Phi_0/\mathrm{mA} = 1.25\,\mathrm{pH}$, which describes the field difference between the two gradiometer loops induced by the external coil.

Flux trapping and gradiometer quality We characterize the gradiometer quality by comparing the total mutual inductance M_{tr} between external coil and trap loop to M_ε. That way, we extract the ratio between the actually applied field and the portion of the (homogeneous) field that is transformed into a flux difference $\delta\Phi_\varepsilon$. Hence, we measure the quality factor $Q_{\mathrm{tr}} = M_{\mathrm{tr}}/M_\varepsilon$ of the gradiometer. We measure M_{tr} by trapping certain amounts N_ℓ of flux quanta in the trap loop and evaluate how the resonance frequency is shifted with N_ℓ [see Fig. 4.26 (b)]. To trap the flux quanta, we apply a magnetic field during the transition to the superconducting state after we have heated the sample above T_{c}. We heat the sample using the DC cables to the antenna lines, which serve as local heat sources because of the finite resistance in the silver glue connectors. By applying a short current pulse of 10 mA, we locally heat the qubit above the critical temperature of Al in less than 1 s. Due to the short pulse duration, the total heat transferred to the sample stage is low and the temperature increase of the sample stage is approximately 50 mK. The flux-dependent frequency decrease for increasing I_{coil} shown in Fig. 4.26 (b) results from an parasitic inductance from circulating currents in the trap loop, which adds to the resonator inductance. We model this flux dependence using a parabolic function $\omega_{\mathrm{r}}(I_{\mathrm{coil}}) = \omega_{\mathrm{r},0} - K(I_{\mathrm{coil}} - I_{\mathrm{tr}})^2$, where $\omega_{\mathrm{r},0}$ is the maximum resonator frequency, I_{tr} is the current offset due to trapped flux quanta, and K is a conversion factor. Using the parabolic dependence in a numerical fit, we obtain the equidistant spacing for I_{tr} shown in Fig. 4.26 (c). The linear dependence yields a mutual inductance $M_{\mathrm{tr}} \simeq 1.391\,\Phi_0/\mathrm{mA} = 2.78\,\mathrm{pH}$. Hence, we

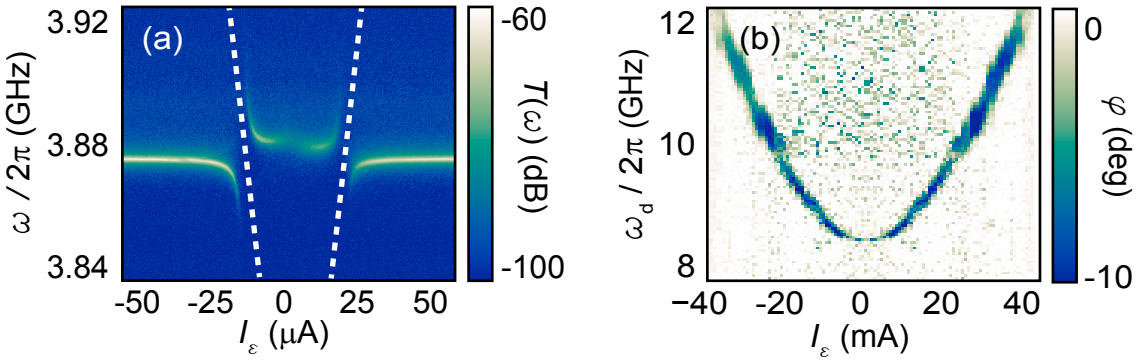

Figure 4.27: (a) Transmission magnitude of the readout tone plotted versus readout frequency and a gradient magnetic field generated by the on-chip ε-current flowing in one of the antenna lines. The dashed lines indicate the eigenfrequency of the qubit. **(b)** Phase of the readout tone plotted versus ε-current and frequency of a second drive tone.

achieve a gradiometer quality $Q_{\mathrm{tr}} \simeq 2.3$. This relatively low gradiometer quality is smaller by a factor 4 compared to previously characterized gradio qubits in a CPW architecture [178]. This quality degradation can be explained with the fact that we use a larger trap loop and place the qubit close to the ground plane of the resonator.

Qubit transition frequency For a suitable coil current, we observe a clear anticrossing between qubit and resonator frequency as shown in Fig. 4.27 (a). Here, we use the effective current value $I_\varepsilon = I_{\varepsilon 2} - I_{\varepsilon 1}$ flowing through the on-chip antennas to control the flux difference $\delta\Phi_\varepsilon$ between the two gradiometer loops. In particular, we feed a current through both antennas with a ratio $I_{\varepsilon 1}/I_{\varepsilon 2} = -1$ to generate an antisymmetric DC field. The anticrossing measured that way provides the transverse coupling strength $g_{\mathrm{t}}/2\pi \simeq 40\,\mathrm{MHz}$. We discuss the detailed mechanism of transverse coupling between the gradio qubit and the resonator in Sec. 2.3.2. The 40 MHz coupling strength exceeds the resonator loss $\kappa_{\mathrm{tot}}/2\pi$ and also the qubit coherence rate $\gamma_{\mathrm{q}}/2\pi \simeq 10\,\mathrm{MHz}$ measured below. Hence, the qubit-resonator system is in the strong coupling regime.
To further characterize the qubit, we perform qubit spectroscopy by applying an additional RF tone with frequency ω_{d} in a two-tone experiment as shown in Fig. 4.27 (b). For simplicity, we use only one of the antenna lines for the RF drive tone for all measurements presented in this section. We give a detailed discussion of effects using both antenna lines in Sec. 6.2. In the two-tone experiment, we utilize the qubit-state-dependent ac-Stark shift in the dispersive regime ($g_{\mathrm{t}}^2/\delta^2 \simeq 10^{-4}$) [cf. Eq. (2.3.5)], where $\delta \equiv \omega_{\mathrm{q}} - \omega_{\mathrm{r}}$. To control the operating point, we use a DC flux-bias generated by the external coil as well as a local magnetic field generated by the on-chip antenna lines. The on-chip control is particularly important to adjust the magnetic energy bias $\hbar\varepsilon$ of the qubit [cf. Eq. (2.1.20)]. By tuning this energy bias to zero, we determine the qubit gap Δ from the center frequency of a Lorentzian fit as shown in Fig. 4.28 (a). In additional qubit spectroscopy measurements at different operating points, we observe qubit gap frequencies up to a maximum $\Delta_{\mathrm{max}}/2\pi = 10.5\,\mathrm{GHz}$.

Readout photons Due to uncertainties in the transmission properties of both our measurement lines and the insertion loss of the resonator itself, we require an in-situ calibration of the resonator population. To this end, we determine the readout photon number $n_{\mathrm{r}} = \langle \hat{a}^\dagger \hat{a} \rangle$, using the photon number dependence of the qubit frequency defined in

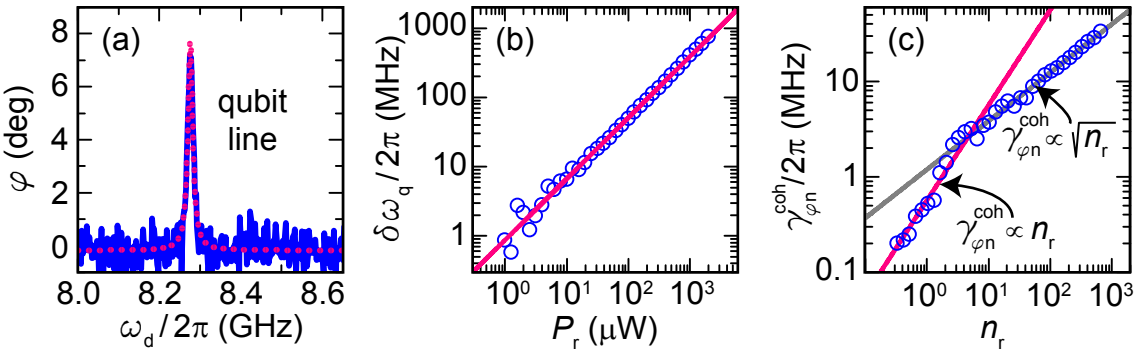

Figure 4.28: **(a)** Phase of the readout tone plotted versus frequency of the drive tone applied to the qubit in a two-tone experiment. The dashed line is a Lorentzian fit used to determine the qubit transition frequency and linewidth. **(b)** Shift of the qubit frequency $\delta\omega_\mathrm{q}$ plotted versus source power of the coherent readout tone. The solid line is a linear fit modelling the photon-number-dependent ac-Stark shift. **(c)** Measurement induced dephasing rate $\gamma_{\varphi n}^{\mathrm{coh}}$ plotted versus the number of readout photons. Solid lines are linear fits in the double logarithmic plot.

Eq. (2.3.4). We control n_r by varying the output power $\mathcal{P}_\mathrm{r}$ of the VNA and measure the frequency shift $\delta\omega_\mathrm{q} = 2n_\mathrm{r}g^2/\delta$ relative to the bare qubit transition frequency $\omega_{\mathrm{q},0}$ as shown in Fig. 4.28 (b). From the linear fit, we calculate a resonator population of 331 photons/mW power emitted from the VNA. A detailed description of the conversion between source power and photon number can be found in Ref. 133. All measurements presented in the following and in Sec. 6.2 are performed with 33 photons on average. This value is still well below the critical photon number [52] $n_\mathrm{crit} \equiv \delta^2/(2g)^2 \simeq 1900$ above which the dispersive limit breaks down. The finite number of readout photons can, however, increase the qubit dephasing rate according to Eq. (2.4.11) as discussed in the following paragraph.

Qubit linewidth and relaxation We determine the intrinsic (unbroadened) qubit linewidth γ_2 and the measurement induced dephasing rate $\gamma_{\varphi n}^{\mathrm{coh}}$ by varying the number of readout photons n_r. That way, we generate photon shot noise proportional to n_r [cf. Eq. (2.4.11)], which we can extrapolate to $n_\mathrm{r} \mapsto 0$ in order to find γ_2. By measuring the total qubit linewidth $\gamma_\mathrm{q}(n_\mathrm{r}) = \gamma_2 + \gamma_{\varphi n}^{\mathrm{coh}}(n_\mathrm{r})$, we extract $\gamma_2/2\pi \simeq 9.7\,\mathrm{MHz}$ and the measurement induced dephasing rate $\gamma_{\varphi n}^{\mathrm{coh}}(n_\mathrm{r})$ shown in Fig. 4.28 (c). In addition to the linear trend for low readout power, we observe a transition to a square root dependence $\gamma_{\varphi n}^{\mathrm{coh}} \propto \sqrt{n_\mathrm{r}}$. The reason is that for large readout power, the measurement rate exceeds κ_x leading to an inhomogeneously broadened Gaussian line [24]. This behavior is precisely displayed by the two fits $\gamma_{\varphi n}^{\mathrm{coh}}(n_\mathrm{r}) = \beta n_\mathrm{r}$ in Fig. 4.28 (c), which yield the slopes $\beta = 0.99 \pm 0.06$ and $\beta = 0.51 \pm 0.01$, respectively.

The intrinsic linewidth γ_2 is generated partly by the pure dephasing rate γ_φ^0 and partly by the relaxation rate γ_1. Using the time-resolved measurement setup introduced in Sec. 4.2, we characterize the qubit relaxation rate at different operating points. At all points, we bias the qubit at its degeneracy point to reduce the influence of flux noise. We find a maximum relaxation time $T_1 \simeq 2.6\,\mu\mathrm{s}$ corresponding to $\gamma_1/2\pi \simeq 385\,\mathrm{kHz}$ as shown in Fig. 4.29 (a). From measurements at different operating points, we find a scatter of the relaxation rate from 385 kHz to 665 kHz. In other words, the qubit is clearly dephasing-limited.

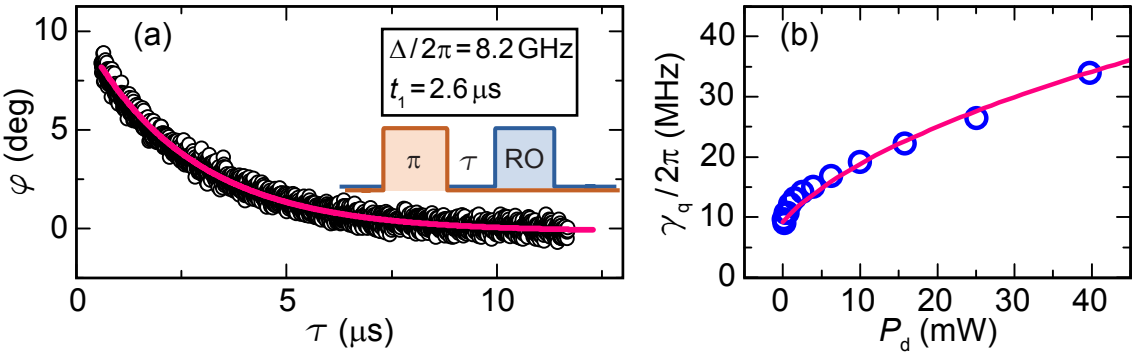

Figure 4.29: **(a)** Resonator phase plotted versus delay time τ in a T_1 measurement sequence as depicted in the insert. The solid line is an exponential fit. **(b)** Qubit linewidth plotted versus source power of the continuously applied drive tone. The solid line is a numerical fit of Eq. (4.3.8).

Qubit spectroscopy photons Finally, we calibrate the number of drive photons n_d that arrive at the qubit for a given source power $\mathcal{P}_\mathrm{d}$ used for the drive tone. Similar to the ac-Stark calibration used to calibrate n_r, we calibrate the drive photons by detecting the power broadening [24, 215]

$$\gamma_\mathrm{q} = \sqrt{\gamma_2^2 + n_\mathrm{d}(2g)^2 \frac{\gamma_2}{\gamma_1}} \tag{4.3.8}$$

of the qubit. We can extract the photon number by assuming a linear power-to-photon conversion α_d, i.e., $n_\mathrm{d} = \alpha_\mathrm{d}\mathcal{P}_\mathrm{s}$. Using $\gamma_2/2\pi = 9.7\,\mathrm{MHz}$ and $\gamma_1/2\pi = 385\,\mathrm{kHz}$ measured above, we obtain $\alpha_\mathrm{d} \simeq 0.16$ photons/mW [see Fig. 4.29 (b)].

4.4 Preparatory measurements for the transmon qubit experiments

In this section, we characterize the setup for all measurements concerning the transmon qubit sample. First, in Sec. 4.4.1, we discuss the transmon qubit and the resonator itself. We then introduce the heatable attenuators depicted in the measurement setup in Fig. 4.30 (b), which we use to generate broadband thermal microwave fields (see Sec. 4.4.3). Finally, in Sec. 4.4.4, we describe the dual-path reconstruction scheme used to measure the correlation functions of thermal fields presented in Sec. 6.1.

4.4.1 Characterization of the transmon qubit

The transmon qubit sample consists of a transmon qubit capacitively coupled to the voltage antinode of a quarter-wavelength resonator and to an on-chip antenna as depicted in Fig. 4.30 (a). The sample is fabricated and mounted into a sample box as described in detail in Sec. 3.3.3. We couple the sample box to the base temperature stage of the dilution refrigerator introduced in Sec. 4.1.

Resonator characterization We characterize the quarter-wavelength CPW resonator using reflection measurements with a VNA [see Fig. 4.30 (b)]. The 50 Ω-matched resonator has a resonance frequency $\omega_\mathrm{r}/2\pi \simeq 6.07\,\mathrm{GHz}$. The resonator is further characterized by the external loss rate $\kappa_\mathrm{x}/2\pi \simeq 8.5\,\mathrm{MHz}$ and the internal loss rate $\kappa_\mathrm{i}/2\pi \simeq 50\,\mathrm{kHz}$ extracted from the fit shown in Fig. 4.31 (a). These loss rates correspond to quality factors $Q_\mathrm{x} \simeq 714$

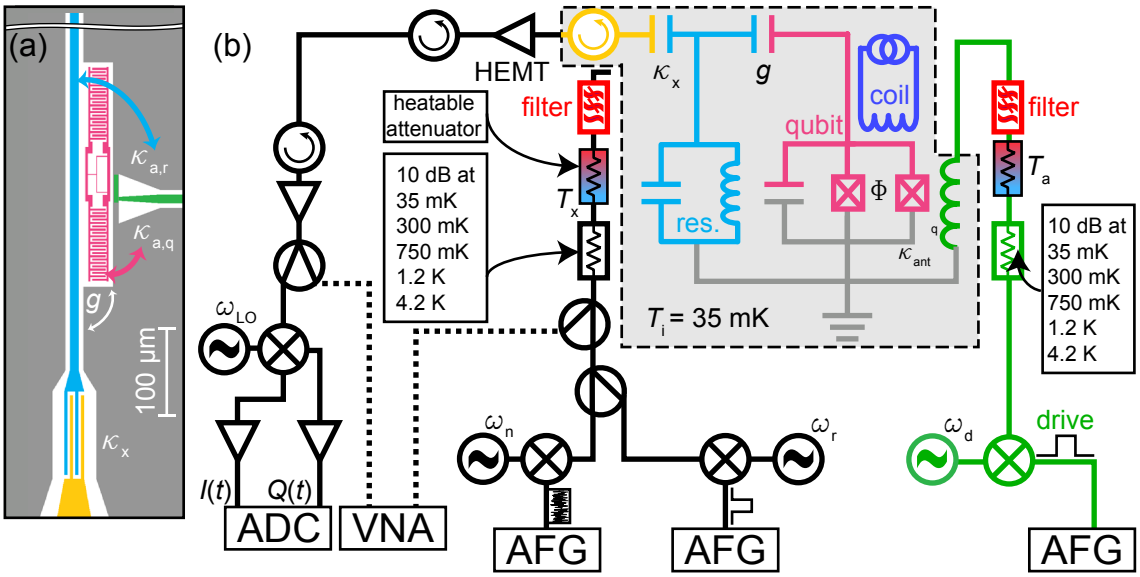

Figure 4.30: (a) Drawing of the transmon qubit sample. The frequency-tunable transmon qubit is capacitively coupled with coupling strength g to a readout resonator, which itself is coupled with κ_x to a readout-line. Further, the qubit is coupled with $\kappa_{a,q}$ to a $50\,\Omega$-matched on-chip antenna. (b) Schematic of the experimental setup. We inject thermal states into antenna and resonator by controlling the temperature T_x and T_a of heatable attenuators. We change the filters in the readout and the antenna line between two individual cooldowns.

and $Q_i \simeq 10^5$, respectively. The relatively high internal quality factor benefits from the fact that the transmon qubit has no galvanic connection to the resonator. In addition to the loss rates κ_x and κ_i, the resonator can decay with $\kappa_{a,r}/2\pi \simeq 30\,\text{kHz}$ to an on-chip antenna (see Sec. 5.2 for details). Because we stabilize the sample temperature to $T_i = 35\,\text{mK}$, there is only a small thermal occupation $n_i \simeq 2.5 \times 10^{-4}$ inside the resonator. We can change the thermal occupation using heatable attenuators or broadband shot noise from a room temperature AFG as depicted in Fig. 4.30 (b). A detailed description of the noise generation is given in Sec. 4.4.3.

Qubit characterization Because the qubit is flux tunable, we can extract the qubit-resonator coupling strength $g/2\pi \simeq 67\,\text{MHz}$ from the anticrossings shown in Fig. 4.31 (b). The magnetic flux Φ in the SQUID loop is induced via a superconducting coil outside the sample holder. For RF control of the qubit, we use the on-chip antenna shown in Fig. 4.30 (a). The RF signals induce state transitions of the transmon qubit due to a finite capacitive coupling between the antenna and the transmon capacitors. In Sec. 5.2, we determine the coupling rate $\kappa_{a,q}/2\pi \simeq 820\,\text{kHz}$ between antenna and qubit at the maximum qubit transition frequency $\omega_{q,0}/2\pi \simeq 6.92\,\text{GHz}$. We obtain this transition frequency from a two-tone experiment shown in Fig. 4.31 (c) and fitting a Lorentzian function to the dip in the transmission spectrum. Furthermore, the antenna can fine-tune the DC magnetic flux through the SQUID loop via the mutual inductance $M_a \simeq 1.3\,\text{pH}$.
We perform two cooldowns with different filter configurations used for the input and the antenna line, which result in different values for $\omega_{q,0}$. When using a pair of tubular low-pass filters introduced in Sec. 4.1.2 in antenna and readout line [see Fig. 4.30 (b)], we measure the maximum transition frequency $\omega_{q,0}/2\pi \simeq 6.92\,\text{GHz}$. Without these filters, we find that the transition frequency decreases by approximately 200 MHz [54, 376]. These results

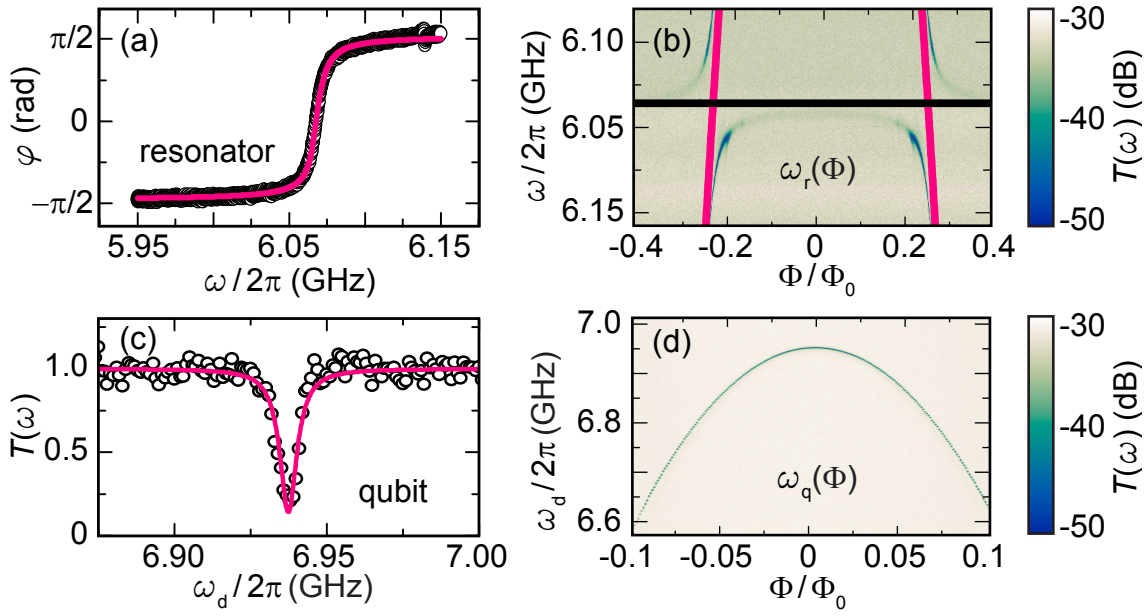

Figure 4.31: **(a)** Phase response of the resonator when the qubit is far detuned plotted versus frequency. The solid line is a fit using Eq. (2.2.12). **(b)** Color-encoded transmission magnitude $\mathcal{T}$ when probing the resonance frequency of the resonator as a function of magnetic flux in a single-tone experiment. Solid lines are calculations of the uncoupled qubit and resonator frequencies. **(c)** Transmission magnitude when probing the resonator in a two-tone experiment. The solid line is a Lorentzian fit to the dip in the transmission induced by the transmon qubit. **(d)** Transmission magnitude (color code) when probing at the resonator frequency and driving the qubit as a function of magnetic flux in a two-tone experiment.

show that efficient filtering of high frequencies are important to protect the junctions from noise at their plasma frequency and to protect noise at the transition frequency of the superconducting Al ($\omega_{c,Al}/2\pi \simeq 80\,\mathrm{GHz}$). Using the low-pass filtered setup, we find a maximum Josephson coupling energy $E_J/\hbar \simeq 2\pi \times 19.995\,\mathrm{GHz}$ calculated from Eq. (2.1.17) using the qubit anharmonicity $\alpha = -E_c/\hbar \simeq 2\pi \times 315\,\mathrm{MHz}$. We measure α with two-tone experiments at high drive power, where transitions to higher levels of the transmon circuit are visible [54, 376].

Weak quantum measurements The mapping of a qubit state onto the resonance frequency of the resonator constitutes a weak measurement [167, 426] as long as the qubit state is not completely projected to the σ_z axis. This projection occurs due to the back-action of the measurement apparatus on the quantum system, which drives the quantum state towards an eigenstate of the measurement operator [168]. Weak measurements cause only small back-action meaning they do not fully collapse the system's quantum superposition state [427]. In circuit QED, weak measurements are performed in the dispersive regime, where the back-action of the resonator is reduced by g/δ. Then, the measurement disturbs the qubit only marginally through measurement induced dephasing [52, 168]. From the experimentalists perspective, a weak measurement means to have only incomplete knowledge on the quantum state after a single measurement. In other words, the dispersively shifted Lorentzian lines of the resonator frequency must have a finite overlap to not be completely distinguishable.
In the dispersive limit, $|\chi| \equiv |[g^2/\delta][\alpha/(\delta+\alpha)]| \simeq 2\pi \times 3.11\,\mathrm{MHz} \ll g$, we use the system Hamiltonian $\mathcal{H}_{tot} = \mathcal{H}_{JC} + \mathcal{H}_d$ where $\mathcal{H}_d = \hbar\Omega_d \cos(\omega_d t)\hat{\sigma}_x$ represents an external drive (see

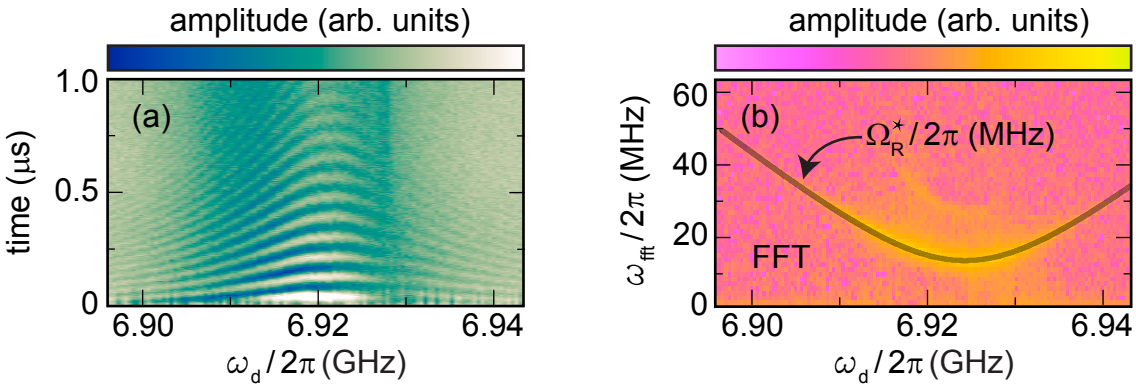

Figure 4.32: (a) Color-encoded transmission amplitude $\langle \mathcal{A} \rangle$ plotted versus time and drive frequency in weak quantum measurement (driven Rabi). **(b)** Fourier transform of the time traces shown in panel (a). The amplitude peaks follow the effective Rabi frequency $\Omega_{\mathrm{R}}^{\star}$.

Sec. 2.1.1) and $\mathcal{H}_{\mathrm{JC}}$ is the dispersive Jaynes-Cummings Hamiltonian defined in Eq. (2.3.2). The dispersive Hamiltonian leads to a shifted qubit frequency $\omega_{\mathrm{q}}^{\mathrm{d}} = \omega_{\mathrm{q}} + 2\chi n_{\mathrm{r}}$ and the shifted resonator frequency $\omega_{\mathrm{r}}^{\mathrm{d}} = \omega_{\mathrm{r}} + \chi\hat{\sigma}_{\mathrm{z}}$, which we use to detect the qubit state. Because $\chi < \kappa_{\mathrm{tot}}$, the requirement of a finite overlap of the two Lorentzian resonator lines is fulfilled for the transmon qubit sample. In a suitable rotating frame presented in Ref. 52, the effective qubit master equation in the dispersive limit is

$$\frac{\partial \hat{\rho}_{\mathrm{q}}^{\mathrm{d}}}{\partial t} = -\imath\frac{\omega_{\mathrm{q}}^{\mathrm{d}}}{2}[\hat{\sigma}_{\mathrm{z}},\hat{\rho}_{\mathrm{q}}^{\mathrm{d}}] + \frac{\gamma_{\varphi}^{\mathrm{eff}}}{2}\mathcal{D}(\hat{\sigma}_{\mathrm{z}})\hat{\rho}_{\mathrm{q}}^{\mathrm{d}} + \gamma_1\mathcal{D}(\hat{\sigma}_{-})\hat{\rho}_{\mathrm{q}}^{\mathrm{d}}\,. \tag{4.4.1}$$

Here, $\mathcal{D}(\hat{L}) = [2\hat{L}\hat{\rho}_{\mathrm{q}}^{\mathrm{d}}\hat{L}^{\dagger} - \hat{L}^{\dagger}\hat{L}\hat{\rho}_{\mathrm{q}}^{\mathrm{d}} - \hat{\rho}_{\mathrm{q}}^{\mathrm{d}}\hat{L}^{\dagger}\hat{L}]/2$ is the Lindblad operator [428] and $\hat{\rho}_{\mathrm{q}}^{\mathrm{d}} = \mathrm{Tr}(\hat{\rho}_{\mathrm{q}}^{\mathrm{d}})$ is the reduced density matrix of the qubit in the dispersive limit. The effective dephasing rate $\gamma_{\mathrm{eff}} = \gamma_{\varphi} + \gamma_{\varphi n}^{\mathrm{coh}}(n_{\mathrm{r}})$ depends on the pure dephasing rate γ_{φ} and on the measurement induced dephasing $\gamma_{\varphi n}^{\mathrm{coh}}(n_{\mathrm{r}})$ [see Eq. (2.4.11)]. For the transmon qubit sample, we expect additional measurement induced dephasing $\gamma_{\varphi n}^{\mathrm{coh}} \simeq 9.3\,\mathrm{MHz/photon}$. To observe coherent oscillations of the qubit state, we have to ensure that the total qubit decoherence rate is much smaller than the Nyquist-Shannon limit [429, 430] $\omega_{\mathrm{NS}}/2\pi = 125\,\mathrm{MHz}$ of our ADCs. Hence, we have to use a small photon number $n_{\mathrm{r}} \ll \omega_{\mathrm{NS}}/\gamma_{\varphi n}^{\mathrm{coh}} \simeq 13$. For the measurements presented in the following, we use a mean photon number $n_{\mathrm{r}} \simeq 0.1$ and operate at qubit-resonator detuning $\delta/2\pi \simeq 850\,\mathrm{MHz}$. That way, we clearly observe driven Rabi oscillations of the qubit state shown in Fig. 4.32 (a). The fact that the coherent oscillations of the qubit are not destroyed by the continuous readout tone shows that we apply only small back-action to the qubit without completely projecting the quantum state. We want to emphasize that the results presented here are no single-shot measurements, but averaged over 5×10^5 traces. Due to the averaging, we evaluate the amplitude expectation value $\langle \mathcal{A} \rangle$. For a quantitative analysis of the oscillations in $\langle \mathcal{A} \rangle$, we perform a Fourier transform of each time trace into the frequency domain as shown in Fig. 4.32 (b). In the Fourier spectrum appears a clear signature of the the Rabi frequency $\Omega_{\mathrm{R}}^{\star}$ [cf. Eq. (2.1.5)]. In particular, the minimum Rabi frequency $\Omega_{\mathrm{R}} = 12.3\,\mathrm{MHz}$ coincides precisely with the Rabi frequency obtained from a sinusoidal fit to the time trace at the qubit transition frequency in Fig. 4.32 (a). This fit also yields the Rabi decay rate $\gamma_{2,\mathrm{Rabi}}/2\pi = 3.1\,\mathrm{MHz}$. This decoherence rate coincides with the Lorentzian line width of the Fourier spectra in Fig. 4.32 (b).

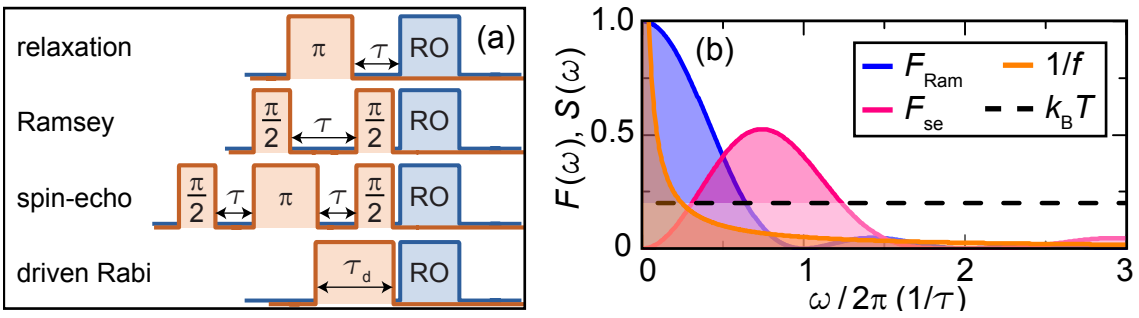

Figure 4.33: **(a)** Pulse sequences used to characterize the coherence properties of superconducting qubits. We typically perform a series of π and/or $\pi/2$ pulses, followed by a readout (RO) pulse. The control parameter to determine the qubit decay time the waiting time τ between the pulse or the pulse duration τ_d for the driven Rabi sequence. **(b)** Filter function of the Ramsey and the spin-echo sequence as well as the power spectral density for $1/f$ and white noise ($k_\mathrm{B}T$) plotted versus frequency in units of inverse pulse duration.

Pulsed qubit measurements The idea behind controlling a qubit with pulsed microwave signals is to rotate the qubit state about the σ_x-axis of the Bloch sphere. In such a scenario, the rotation angle depends in a linear way on the energy $E = \int_0^{\tau_\mathrm{d}} \mathcal{A}_\mathrm{d}(t)\,\mathrm{d}t$ stored in the pulse. Here, τ_d is the pulse duration and $\mathcal{A}_\mathrm{d}(t)$ is the time-dependent pulse amplitude. In the simplest approach, $\mathcal{A}_\mathrm{d}(t)$ is a square envelope that lasts from $t = 0$ to $t = \tau_\mathrm{d}$ and can be expressed as a window function

$$\mathcal{A}_\mathrm{d}(t) = \begin{cases} \mathcal{A}_0 & \text{if } 0 < t < \tau_\mathrm{d} \\ 0 & \text{else .} \end{cases} \tag{4.4.2}$$

That way, the rotation angle depends on both, the steady-state amplitude $\mathcal{A}_0$, and the length τ_d of the pulse. For qubit control and for the readout of a resonator, we modulate the pulse envelope $\mathcal{A}_\mathrm{d}(t)$ with the microwave frequencies ω_d and ω_r to follow $\mathcal{A}_\mathrm{d}(t)\cos(\omega_\mathrm{d,r}t)$, respectively. Even though there are more advanced pulse forms to optimize the qubit behavior [431–433], a rectangular envelope described by Eq. (4.4.2) already yields sufficient results for our purposes. In practice, we cannot reach a perfect rectangular envelope with infinitely steep edges due to the limited bandwidth of the AFGs. Instead, there is a finite rise time of the pulse, i.e., a ring-up until the pulse amplitude reaches its steady-state value. Mathematically, the ring-up of the rectangular pulse follows the decomposition of $\mathcal{A}_\mathrm{d}(t)$ into its spectral components [434] $\sum_{k=1}^{k_\mathrm{max}} \frac{1}{k}\sin(\pi k t/\tau_\mathrm{d})$. Here, the maximum number of iterations k_max is given by the 500 MHz bandwidth of the AFGs. Because the qubit transition frequency is several gigahertz, direct transitions induced from the spectral components are very unlikely. There can be, however, a finite leakage to higher levels of the transmon circuit [431, 435] because the qubit anharmonicity is only 315 MHz.
For the pulse sequences described in the following, we use rectangular RF pulses to control the qubit state and an additional RF readout pulse, which starts when all drive pulses are finished. A pulsed readout has the advantage that the photons in the resonator do not disturb the qubit evolution. The undisturbed qubit can then be manipulated via the different pulse sequences as shown Fig. 4.33 (a). The relaxation sequence is suited for noise spectroscopy in the high-frequency regime ($\omega \simeq \omega_\mathrm{q}$) providing the qubit relaxation rate $\gamma_1 \propto \mathcal{S}(\omega_\mathrm{q})$ [cf. Eq. (2.4.5)]. With the relaxation sequence, we measure the projection to the σ_z axis after exciting the qubit with a π pulse.
In order to probe noise in the low-frequency limit ($\omega \ll \omega_\mathrm{q}$) we use either a Ramsey or a

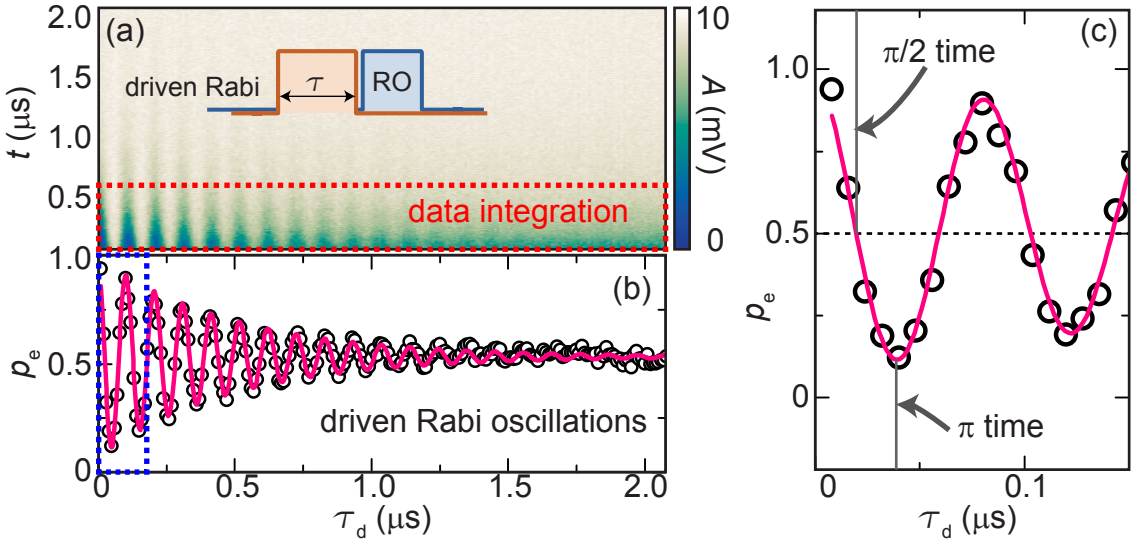

Figure 4.34: **(a)** Transmission amplitude (color code) plotted versus time and pulse duration in a pulsed driven Rabi experiment. For the analysis of the excited state probability, we take only data points from the area highlighted by the red dashed rectangle into account. **(b)** Excited state probability plotted versus pulse duration for the data shown in (a). **(c)** Zoom into the blue dashed rectangle in panel (b) to illustrate the $\pi/2$ and the π time.

spin-echo sequence, which provide the qubit decay rates $\gamma_{2,\mathrm{R}}$ and $\gamma_{2,\mathrm{se}}$, respectively. With the Ramsey sequence, the qubit is first excited with a $\pi/2$ pulse to a superposition of ground and excited state. After a certain waiting time τ, a second $\pi/2$ pulse is applied and the qubit state is measured. During the waiting time, the qubit accumulates the random phase [211] $\delta\varphi_\mathrm{q} = \mathcal{D}_{\lambda,\mathrm{z}} \int_0^\tau \mathrm{d}t\delta\lambda(t)$ due to fluctuations $\delta\lambda(t)$ coupling with the effective strength $\mathcal{D}_{\lambda,\mathrm{z}}$ as discussed in detail in Sec. 2.4.1. Furthermore, when averaging over several measurements, the fluctuations with frequencies down to the inverse of the total signal acquisition time τ_av contribute to the phase randomization [235]. Then, the decay function $g_\mathrm{Ram}(t)$ measured in a pulsed experiment is calculated by ensemble averaging [436]

$$g_\mathrm{Ram}(\tau) = \exp\left[-\tau^2\mathcal{D}_{\lambda,\mathrm{z}}^2 \int_{\omega_\mathrm{ir}}^{\omega_\mathrm{c}} \mathrm{d}\omega\ \mathcal{F}_\mathrm{Ram}(\omega,\tau)\mathcal{S}(\omega)/\hbar\right] = \exp\left[-\frac{\gamma_{2,\mathrm{R}}\tau}{2\pi}\right], \qquad (4.4.3)$$

where $\mathcal{F}_\mathrm{Ram}(\omega,\tau) = \sin^2(\omega\tau/2)/[\omega\tau/2]^2$ is a filter function that accounts for the pulse sequence [211, 436] and ω_ir, ω_c are cutoff frequencies discussed below. The decay function $g_\mathrm{se}(\tau)$ for the spin-echo sequence can be obtained in the same way, when replacing $\mathcal{F}_\mathrm{Ram}(\omega,\tau)$ in Eq. (4.4.3) by the spin-echo filter function $\mathcal{F}_\mathrm{se}(\omega,\tau) = \sin^4(\omega\tau/4)/[\omega\tau/4]^2$. As shown in Fig. 4.33 (b), the spin-echo sequence filters noise at $\omega \mapsto 0$, which is achieved by the additional π pulse that introduces a time reversal for the qubit evolution. Hence, for typically dominating $1/f$ noise, the spin-echo sequence yields a smaller dephasing rate than the Ramsey sequence [436], i.e., $\gamma_{2,\mathrm{se}} < \gamma_{2,\mathrm{R}}$.

The frequency range of the noise that is detected with the two sequences is between the lower (infrared) cutoff frequency ω_ir and the upper (ultraviolet) cutoff ω_c. The infrared cutoff $\omega_\mathrm{ir}/2\pi = 1/\tau_\mathrm{av}$ is set by the total duration of the measurement including averaging [437]. For our measurements with typical averaging times of 10 s, we therefore detect noise down to frequencies of 100 mHz. To characterize noise at even lower frequencies, we use correlation measurements as presented in Sec. 5.2. The limits for the ultraviolet cutoff is

not well understood so far [436], but the noise power depends only on a logarithmic scale on ω_c.
We obtain the π and $\pi/2$ times for a certain drive amplitude by performing a pulsed driven Rabi measurement as shown in Fig. 4.34 (a). To this end, we record the readout signal after applying a drive pulse of duration τ_d to the qubit. To evaluate the excited state probability p_e, we integrate the signal from $t=0$ to $t=500\,\mathrm{ns}$ [cf. Fig. 4.34 (a)] to obtain an average value $\langle \mathcal{A}_{int}(\tau_d)\rangle$. We calculate the excited state probability by applying an exponentially decaying sinusoidal fit $\mathcal{A}_{fit}(\tau_d) = \mathcal{A}_0 \cos(\Omega_R^\star \tau_d) + \mathcal{A}_1$ to $\langle \mathcal{A}_{int}(\tau_d)\rangle$.[58] From the resulting fit parameters $\mathcal{A}_0$ and $\mathcal{A}_1$, we calculate $p_e = -(\langle \mathcal{A}_{int}\rangle(\tau_d - \mathcal{A}_0)/2\mathcal{A}_1 + 1/2$. This analysis typically results in a clear oscillatory behavior of the calculated excited state probability p_e shown in Fig. 4.34 (b). From this data, we find the π time as the first minimum and the $\pi/2$ time as the first crossing between $p_e = 1/2$ and the data as shown in Fig. 4.34 (c).
We perform a detailed analysis, of relaxation, Ramsey, and spin-echo measurements during the work presented in Ref. 54. Furthermore, we use the pulsed measurement technique for the results presented in Sec. 5.2 and Sec. 6.1. At the flux sweet spot, the Ramsey rates $\gamma_{2,R}/2\pi \simeq (2.1 \pm 0.3)\,\mathrm{MHz}$ are obtained for typical qubit-drive detunings between 1 MHz and 20 MHz. In order to cut off noise in the DC limit, we perform spin-echo measurements. The spin-echo decay rate $\gamma_{2,se}/2\pi \simeq (1.9 \pm 0.3)\,\mathrm{MHz}$ is very close to the Ramsey decay rate, which means that the coherence of the transmon qubit is not limited by $1/f$ noise. This result is confirmed by the qubit relaxation rate $\gamma_1/2\pi = \simeq (3.9 \pm 0.5)\,\mathrm{MHz}$, which is approximately $2\gamma_{2,R}$. Hence, the transmon qubit is clearly T_1 limited because $T_2 \simeq 2T_1$. We want to note that the qubit is not Purcell limited because the rate [244, 247] $\gamma_P = \kappa_x g^2/\delta^2 \simeq 2\pi \times 53\,\mathrm{kHz}$ is far below γ_1.

4.4.2 Photon-number-dependent qubit dephasing rate

To derive the photon-number-dependent dephasing rate in the dispersive regime, we start with the system Hamiltonian $\mathcal{H}_{tot} = \mathcal{H}_{JC} + \mathcal{H}_d$ comprising the Jaynes-Cummings Hamiltonian $\mathcal{H}_{JC} = \mathcal{H}_r + \mathcal{H}_q + \mathcal{H}_g$ and a driving part $\mathcal{H}_d$. Here, $\mathcal{H}_q = \hbar\omega_q \hat{\sigma}_z/2$ is the bare qubit Hamiltonian, $\mathcal{H}_g = -\hbar g(\hat{a}^\dagger \hat{\sigma}_- + \hat{a}\hat{\sigma}_+)$ describes the qubit-resonator coupling using the Pauli operators $\hat{\sigma}_i$ and the resonator mode $\hat{a}$ with mean occupation $n_r = \langle \hat{a}^\dagger \hat{a}\rangle$. The external drive with amplitude $\varepsilon_j(t)$ reads $\mathcal{H}_d = \sum_j \hbar\varepsilon_j(t)(\hat{a}^\dagger e^{-\imath\omega_j t} + \hat{a}e^{+\imath\omega_j t})$. We use two different coherent drives, one to read out the resonator ($j = r$) and one to drive the qubit ($j = d$). Furthermore, the noise field $\hat{b}_{in}(\omega)$ can be treated as an incoherent external drive ($j = in$) such that $\varepsilon_{in}(t)e^{-\imath\omega_j t} \mapsto \pi^{-1}\kappa_x e^{-\imath\omega t} \int \mathrm{d}\omega\, D(\omega)\hat{b}_{in}^\dagger(\omega,t)\hat{b}_{in}(\omega,t)$. We assume that this drive is weak and δ-correlated in time, i.e., $\langle \varepsilon_{in}^\star(t)\varepsilon_{in}(t')\rangle \propto \delta(t-t')$. The dynamics of the qubit-resonator system can conveniently be described using the master equation [52, 168, 438]

$$\hbar\partial\hat{\rho}/\partial t = -\imath[\mathcal{H}_{tot},\hat{\rho}] + \kappa_x \mathcal{D}(\hat{a})\hat{\rho} + \gamma_1^{tot}\mathcal{D}(\hat{\sigma}_-)\hat{\rho} + \gamma_\phi^{tot}\mathcal{D}(\hat{\sigma}_z)\hat{\rho}/2\,. \tag{4.4.4}$$

Here, $\hat{\rho} = \mathrm{Tr}(\hat{\rho})$ is the system density matrix and $\mathcal{D}(\hat{L}) = [2\hat{L}\hat{\rho}\hat{L}^\dagger - \hat{L}^\dagger\hat{L}\hat{\rho} - \hat{\rho}\hat{L}^\dagger\hat{L}]/2$ is the Lindblad damping operator [428], which describes effects of the bath in the Markov approximation. The qubit is characterized by the total energy decay rate γ_1^{tot} and the total dephasing rate γ_ϕ^{tot}. To study the effect of photon number fluctuations, we transform $\mathcal{H}_{tot}$

[58] An equivalent result is obtained when performing this analysis using data for the averaged phase $\langle \varphi(\tau_d)\rangle$.

into the dispersive regime, which yields

$$\mathcal{H}_{\text{eff}} = \mathcal{H}_{\text{r}} + \mathcal{H}_{\text{q}} + \frac{\hbar}{2}(\chi + 2\chi\hat{a}^\dagger\hat{a})\hat{\sigma}_{\text{z}} + \sum_j \hbar\varepsilon_j(t)(\hat{a}^\dagger e^{-\imath\omega_j t} + \hat{a}e^{+\imath\omega_j t}) + \sum_j \frac{\hbar\varepsilon_j(t)}{\delta}(\hat{\sigma}_+ e^{-\imath\omega_j t} + \hat{\sigma}_- e^{+\imath\omega_j t})\,. \tag{4.4.5}$$

After this transformation and tracing out the resonator yields the laboratory frame master equation [Eq. (4.4.1)] for the qubit in the dispersive regime. In this regime, the total qubit decay rate γ_1^{tot} and dephasing rate γ_ϕ^{tot} are dependent on the photon number n_{r} in the resonator [52]. While the change of the qubit decay rate is due to dressing of states and due to frequency components at ω_{q}, the change of the dephasing rate is due to photon number fluctuations characterized by $\mathcal{C}(\tau)$. For a small cavity pull ($|\chi/\kappa_{\text{x}}| \ll 1$), we can make a Gaussian approximation for the dephasing rate $\gamma_{\varphi n}(n_{\text{r}})$ as discussed in the following paragraph. For our sample, we find $|\chi/\kappa_{\text{x}}| \simeq 0.35$, which leads to small corrections because the effective resonator frequency is different if the qubit is in the ground or the excited state. We discuss the corresponding corrections for broadband fields in the last paragraph of this section.

Qubit dephasing under the Gaussian approximation If we assume the resonator pull on the qubit to be weak ($|\chi/\kappa_{\text{x}}| \ll 1$), we can assume that after a time τ, the random phase accumulated [17] $\delta\varphi(\tau) = 2\chi\int_0^\tau \mathrm{d}t\,\delta n(t)$ is Gaussian distributed. In this case, the cumulant expansion is exact and one obtains [168]

$$\langle\hat{\sigma}_-(\tau)\hat{\sigma}_+(0)\rangle = \exp\left[-\gamma_2\tau - \frac{\langle\delta\varphi^2\rangle}{2}\right] = \exp\left[-\gamma_2\tau - 2\chi^2\int_0^\tau \mathrm{d}t\,\mathcal{C}(t)\right], \tag{4.4.6}$$

where $\gamma_2 = \gamma_1^{\text{tot}}/2 + \gamma_{\varphi 0}$. Equation (4.4.6) leads to the qubit dephasing rates defined in Eq. (2.4.11) and Eq. (2.4.12) defined above. To calibrate the mean photon number n_{r}, we measure the photon number dependent shift of the qubit frequency as a function of noise power in a steady state configuration. The externally applied broadband input field $\hat{b}_{\text{in}}$ is linked via Eq. (2.2.27), to the intra-resonator mode $\hat{a}$. Because we measure in a steady state, $\langle\hat{b}_{\text{in}}\rangle = 0$ and $\langle\hat{b}_{\text{in}}^\dagger\hat{b}_{\text{in}}\rangle$ has a constant mean. Further, because we assume white noise, $\hat{b}_{\text{in}}$ also has no frequency dependence in the relevant frequency regime. Within these limits and for negligible internal resonator losses, the broadband noise covering the resonator density of states $D(\omega)$ yields [39]

$$\delta\omega_{\text{q}} = 2\chi\hat{\sigma}_{\text{z}}\frac{\langle\hat{b}_{\text{in}}^\dagger\hat{b}_{\text{in}}\rangle}{\pi}\int \mathrm{d}\omega\, D(\omega) = 2\chi\hat{\sigma}_{\text{z}}\langle\hat{a}^\dagger\hat{a}\rangle \equiv 2\chi\hat{\sigma}_{\text{z}}n_{\text{r}}\,. \tag{4.4.7}$$

The above calibration method can also be obtained using a Wigner function approach[439] for the qubit off-diagonal elements in the small pull limit $|\chi|/\kappa_{\text{x}} \ll 1$. For larger pulls, this approach predicts a deviation from the linear trend predicted by Eq. (4.4.7). However, since we do not observe any non-linear trend in our Stark shift measurements, we conclude that our sample can be still treated in the small pull limit. Within this approximation, we do not separate between the two cases when the qubit is in the ground or the excited state such that $D(\omega)$ is simply given by the Lorentzian filter function $\mathcal{F}(\omega) = (\kappa_{\text{x}}/2)/[(\kappa_{\text{x}}/2)^2 + \delta_{\text{r}}^2]$, where $\delta_{\text{r}} = \omega_{\text{r}} - \omega$ is the detuning to the resonator frequency [see Fig. 4.35 (a)]. The broadband noise induces dephasing relative to photon number

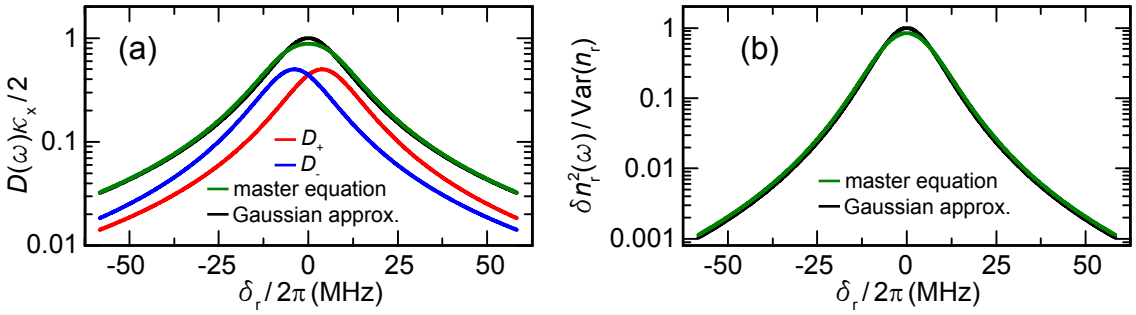

Figure 4.35: (a) Normalized resonator density of states $D(\omega)\kappa_\mathrm{x}/2$. (b) Photon fluctuations $\delta n_\mathrm{r}^2(\omega)$ calculated for the parameters used in panel (a).

fluctuations $\delta n_\mathrm{r}^2(\omega) = (\kappa_\mathrm{x}/2)^2 \mathcal{F}(\omega)^2 [\langle \hat{b}_\mathrm{in}^\dagger \hat{b}_\mathrm{in} \hat{b}_\mathrm{in}^\dagger \hat{b}_\mathrm{in}\rangle - \langle \hat{b}_\mathrm{in}^\dagger \hat{b}_\mathrm{in}\rangle^2]$ shown in Fig. 4.35 (b). Hence, the effective dephasing rate reads

$$\gamma_{\varphi n}^\mathrm{eff} = \theta_0^2 \frac{4}{\pi} \int \mathrm{d}\omega \, \delta n_\mathrm{r}^2(\omega) = \mathrm{Var}(n_\mathrm{r}) \kappa_\mathrm{x} \theta_0^2 \,. \tag{4.4.8}$$

Because the assumption of a Lorentzian line shape $D(\omega) = \mathcal{F}(\omega)$ is only approximately true for our experimental parameters ($|\chi/\kappa_\mathrm{x}| \simeq 0.35 \lesssim 1$), we evaluate corrections to Eq. (4.4.8) in the following paragraph. These corrections are due to the fact that the resonator has a different frequency when the qubit is in its ground or excited state.

Qubit dephasing using the full master equation For increasing cavity pull $|\chi/\kappa_\mathrm{x}|$, the effective resonator frequency is different if the qubit is in its ground or excited state. We account for this circumstance using the two different steady state fields [168] $\langle \hat{a}_\pm(\omega)\rangle = -\imath \langle \hat{b}_\mathrm{in}(\omega)\rangle \kappa_\mathrm{x}/(\kappa_\mathrm{x} \pm \imath 2\chi + 2\delta_\mathrm{r})$ if the qubit is in the excited (+) or ground (−) state, respectively. The two situations can be modelled by the resonator density of states

$$D_\pm(\omega) = \frac{\kappa_\mathrm{x}/2}{\kappa_\mathrm{x}^2/4 + (\delta_\mathrm{r} \pm \chi)^2} \tag{4.4.9}$$

shown in Fig. 4.35 (a). From $D_\pm(\omega)$, we calculate the mean photon numbers n_+ and n_- via Eq. (4.4.7) and calibrate the effective resonator occupation n_cal as follows. Because wo use a steady-state drive when calibrating the photon number, the qubit is in an equal superposition state leading to $n_\mathrm{cal} = (n_+ + n_-)/2$. In this case and for constant noise power $\langle \hat{b}_\mathrm{in}^\dagger \hat{b}_\mathrm{in}\rangle$, we obtain $n_\mathrm{cal} \approx n_\mathrm{r}$ to a very good approximation as indicated by the black and the green lines in Fig. 4.35 (a). Accounting for the frequency dependence of $\hat{a}_\pm$, we find for the photon number fluctuations [see Fig. 4.35 (b)]

$$\delta n_\mathrm{r}^2(\omega) = \frac{\kappa_\mathrm{x}^2}{4} \frac{[D_+(\omega) + D_-(\omega)]}{\kappa_\mathrm{x}^2/4 + \delta_\mathrm{r}^2 + \chi^2} [\langle \hat{b}_\mathrm{in}^\dagger \hat{b}_\mathrm{in} \hat{b}_\mathrm{in}^\dagger \hat{b}_\mathrm{in}\rangle - \langle \hat{b}_\mathrm{in}^\dagger \hat{b}_\mathrm{in}\rangle^2] \,. \tag{4.4.10}$$

With this expression, we calculate the dephasing rate $\gamma_{\varphi n}^\mathrm{m} = (2|\chi|/\kappa_\mathrm{x})^2 (\pi/4) \int \mathrm{d}\omega \, \delta n_\mathrm{r}^2(\omega)$. For the experimtal parameters stated above, we find the relative error $(\gamma_{\varphi n}^\mathrm{eff} - \gamma_{\varphi n}^\mathrm{m})/\gamma_{\varphi n}^\mathrm{eff} \simeq 0.04$. Hence, the Gaussian approximation made in the article is well justified.

4.4.3 Generation and detection of thermal fields

Thermal fields have a very smooth and well-defined power spectral density $\mathcal{S}(\omega)$ defined in Eq. (2.4.9). Therefore, they are well-suited for power calibration at cryogenic temperatures [139, 440] but can also serve as a known noise source [39, 41] as discussed in detail in Sec. 5.2. In the following, we discuss the generation and the detection of broadband thermal fields emitted from a heatable attenuator at cryogenic temperatures.

Generation of thermal fields To generate thermal states on the readout and on the antenna-line, we use heatable 30 dB attenuators[59] integrated into the feedlines as depicted in Fig. 4.30 (b). A photograph of the cryogenic setup is shown in Fig. 4.36 (a). Depending on its temperature, the attenuator emits voltage fluctuations into the coaxial cables, which are connected to the sample. For the thermal coupling between attenuator and the sample stage, we have to consider two requirements. On the one hand, the attenuator must thermalize well below 100 mK to reach the regime of negligible thermal fluctuations to uncover quantum fluctuations. On the other hand, we must heat up the attenuator above 1 K to reach considerable thermal photon numbers $n_{\mathrm{th}} > 1$ [cf. Eq. (2.2.17)] without affecting the sample temperature. Hence, we must ensure weak thermal coupling to the sample box but a moderate thermal coupling to the base temperature stage. We achieve this compromise using a brass stripe for thermalization, which is 20 cm long and has a 5 mm × 75 µm cross section.
For the coaxial cables connecting the attenuator to the sample box, we use 20 cm of Nb/CuNi UT47 cables. The temperatures T_{x} and T_{a} of the heatable attenuators used to vary the thermal photon number are controlled between (0.050 ± 0.001) K and (1.50 ± 0.01) K using an analog PID controller to heat a 100 Ω resistor. In addition to real thermal noise radiated from the attenuators, we can add noise generated from an AFG, which we up-convert to the desired noise frequency ω_{n} by mixing with a coherent microwave drive (see Fig. 4.30). For upconversion, we also enable amplitude-modulated moise at the microwave source to minimize the coherent portion in the signal. The AFG digitially generates shot noise with a 500 MHz bandwidth and a constant variance of 1 V into 50 Ω. The noise has a Gaussian amplitude distribution with a crest factor 3.1 and a Poissonian statistics. We additionally filter this noise before the up-conversion to the carrier frequency ω_{n} by two 100 MHz low-pass filters. That way, the noise has a bandwidth of 200 MHz and an on/off ratio of 35 dB.

Noise temperature of the amplification chain The well-defined power emitted from a heatable attenuator can be used to calibrate the gain G and the noise temperature T_{noise} of the amplification chain used to measure the small microwave signals. In such a calibration measurement, we sweep the attenuator temperature and measure the power [129]

$$P_{\mathrm{det}}(T_{\mathrm{x}}) = \frac{\langle \mathcal{I}_{\mathrm{dc}}^2(t)\rangle + \langle \mathcal{Q}_{\mathrm{dc}}^2(t)\rangle}{Z_0} = G \times B \left[\frac{\hbar\omega}{2}\coth\left(\frac{\hbar\omega}{2k_{\mathrm{B}}T_{\mathrm{x}}}\right) + k_{\mathrm{B}}T_{\mathrm{noise}}\right] \tag{4.4.11}$$

using the time-domain setup introduced in Sec. 4.2. Equation (4.4.11) can be derived from the Bose-Einstein distribution defined in Eq. (2.2.17) using the bandwidth $B \simeq 100$ MHz, which is defined by low-pass filters placed at the inputs of the ADCs. Compared to the setup in Sec. 4.2, for the power calibration the snap-tool additionally computes the

[59] We use `Rosenberger 32AS102-K10S3` attenuators for that purpose.

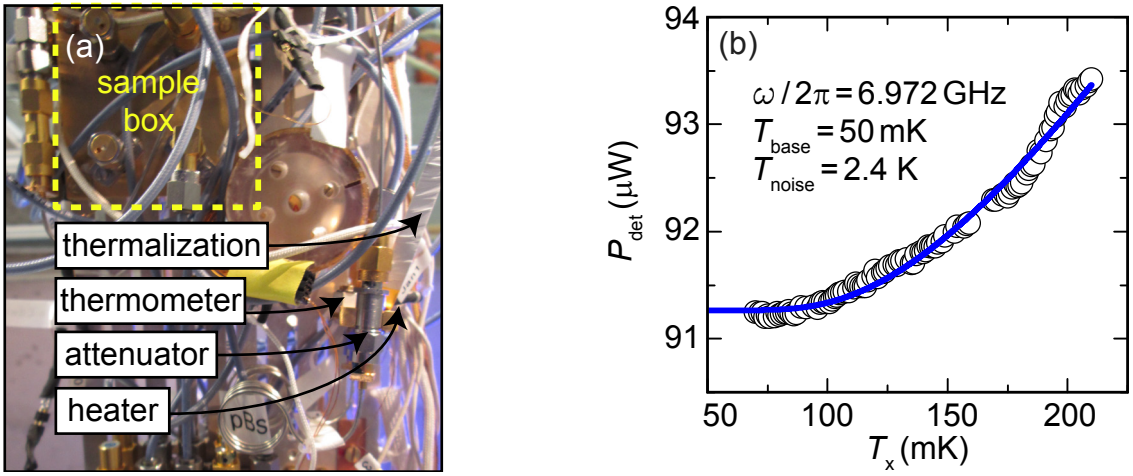

Figure 4.36: **(a)** Photograph of the experimental setup for the generation of thermal states. **(b)** Detected power plotted versus temperature of the heatable attenuator [133]. The solid line is a fit using Eq. (4.4.11).

correlation moments $\mathcal{I}_{\rm if}^2(t)$, $\mathcal{Q}_{\rm if}^2(t)$, and $\mathcal{I}_{\rm if}(t)\mathcal{Q}_{\rm if}(t)$. These moments are instantaneously averaged to $\langle\mathcal{I}_{\rm if}^2(t)\rangle$, $\langle\mathcal{Q}_{\rm if}^2(t)\rangle$, and $\langle\mathcal{I}_{\rm if}(t)\mathcal{Q}_{\rm if}(t)\rangle$. These averaged values are then digitally down-converted to $\langle\mathcal{I}_{\rm dc}^2(t)\rangle$, $\langle\mathcal{Q}_{\rm dc}^2(t)\rangle$, and $\langle\mathcal{I}_{\rm dc}(t)\mathcal{Q}_{\rm dc}(t)\rangle$ using the algorithms presented in Ref. 133. This approach differs from other well-established reconstruction protocols at the WMI [121, 129, 441] in the order of down-conversion and averaging. The permutation of these tasks is motivated by the question whether this approach is suitable for the reconstruction of microwave states with a relatively large bandwidth $B \simeq 100\,\mathrm{MHz}$. For a realistic test, the snap-tool also computes the average of the correlation moments $\langle\mathcal{I}_{\rm if}^k(t)\mathcal{Q}_{\rm if}^\ell(t)\rangle$ up to the fourth order, i.e., $k+\ell \leq 4$ for $k,\ell \in \mathbb{N}_0$. We find that the repetition rate during measurements with these additional computations is limited by the data transfer rather than by the computational power of the snap-tool. The reason is the increased $(36 \cdot 512)$ points long buffer of integers, which has to be transferred within the 100 kHz repetition rate to the main board of the computer.

We perform the calibration measurements in an extra cooldown where the thermal states can bypass the sample using a cryogenic microwave switch [133]. In Fig. 4.36 (b), we show the detected power at $\omega/2\pi = 6.972\,\mathrm{GHz}$ for a typical temperature sweep together with a fit of Eq. (4.4.11). We observe the expected $P_{\rm det}(T_{\rm x})$ dependence, which yields a power offset of approximately 91 µW. From a numerical fit, we obtain the noise temperature $T_{\rm noise} \simeq 2.4\,\mathrm{K}$ meaning that the amplifiers add $n_{\rm noise} = k_{\rm B}T_{\rm noise}/\hbar\omega \simeq 7$ noise photons on average. Additionally, we find a total gain $G \simeq 98\,\mathrm{dB}$, which agrees with the experimentally determined amplification values of our amplifiers [133]. Due to the 40 dB amplification of the HEMT amplifier, the 70 K noise temperature of the room temperature amplifiers can be neglected in our setup. From the experimental values for G and $T_{\rm noise}$ we convert the detected power to a certain number of photons by subtracting the noise power offset and subsequently dividing by G. Hence, we calculate the photon number conversion factor [129] $\mathrm{PNCF} = G \times B\hbar\omega$ in order to relate the detected power at the digitizer card to the number of photons in the open transmission line. For our specific setup, we obtain $\mathrm{PNCF} = 12.13\,\mu\mathrm{W}$ per photon, which corresponds to $n_{\rm th} = 0.08$ photons per µW detected power.

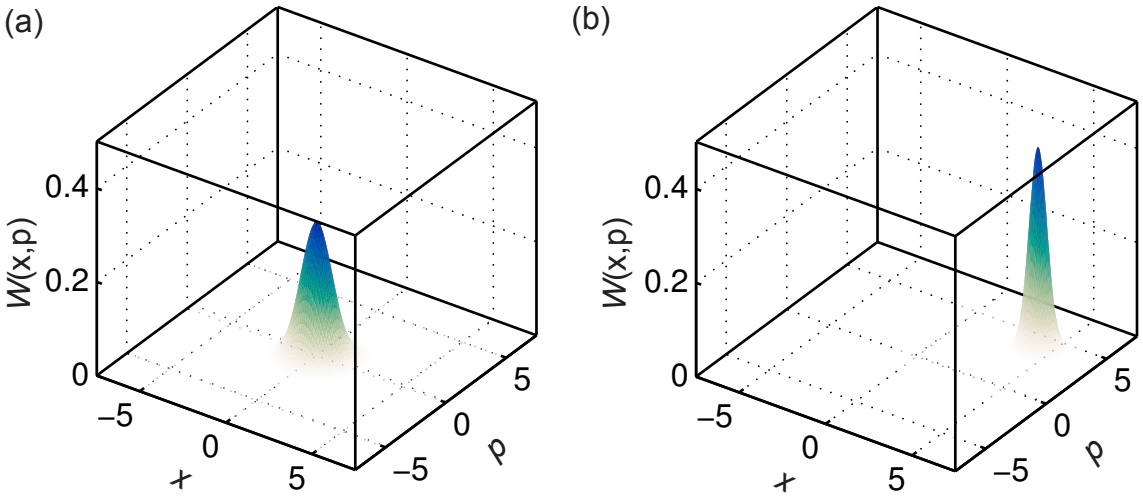

Figure 4.37: **(a)** Wigner function for a thermal microwave state of 206 mK and 6.972 GHz. **(b)** Wigner function for a coherent microwave state of approximately 30 photons at 6.972 GHz.

State reconstruction We now discuss the Wigner function reconstruction for a thermal and a coherent state using the photon number calibration of the previous paragraph. Even though these are just proof of principle experiments that have already been performed at the WMI with high accuracy [129, 139], we find important insight concerning the permutation of averaging and down-conversion. For state reconstruction, we first extract the relevant microwave power from the total detected power by subtracting the amplifier noise. For simplicity, we omit a check of the Gaussian criterion based on the cumulants up to the fourth order [138–140]. Second, we use the PNCF to convert the remaining power to a number of photons. This allows us to reconstruct the Wigner function for both, thermal and coherent, states following a standard reconstruction algorithm [129]. In Fig. 4.37 (a), we show the reconstructed Wigner function of a thermal state at $\omega/2\pi = 6.972\,\mathrm{GHz}$ and $T_\mathrm{x} = 206\,\mathrm{mK}$ corresponding to approximately 0.25 photons above the vacuum. Even though the reconstruction works qualitatively for the thermal states, a quantitative analysis of the expected broadening is not possible. The reason is that the in-situ calibration of the detection setup described in Sec. 4.2.3 is optimized for coherent states with a well-defined amplitude and phase. Hence, state reconstruction works sufficient for coherent states as shown in Fig. 4.37 (b).

4.4.4 Setup for correlation measurements with thermal fields

Due to the limitations in the detection of thermal states of the time-domain setup introduced in Sec. 4.2, we use a different setup[60] for the $g^{(2)}(\tau)$ correlation measurements presented in Sec. 6.1. This setup belongs to a dry dilution refrigerator in the BATMAN laboratory of the WMI, which is described in detail in Ref. 121. The BATMAN cryostat is equipped with heatable attenuators similar to the ones presented above. Furthermore, the cryostat is equipped with a dual-path setup which is well-suited for the analysis of propagating microwave states [163].
Using the dual-path setup in the BATMAN laboratory, we digitize the in-phase and

[60] We gratefully acknowledge the support by K. G. Fedorov and S. Pogorzalek who provide the data for the $g^{(2)}(\tau)$ measurements.

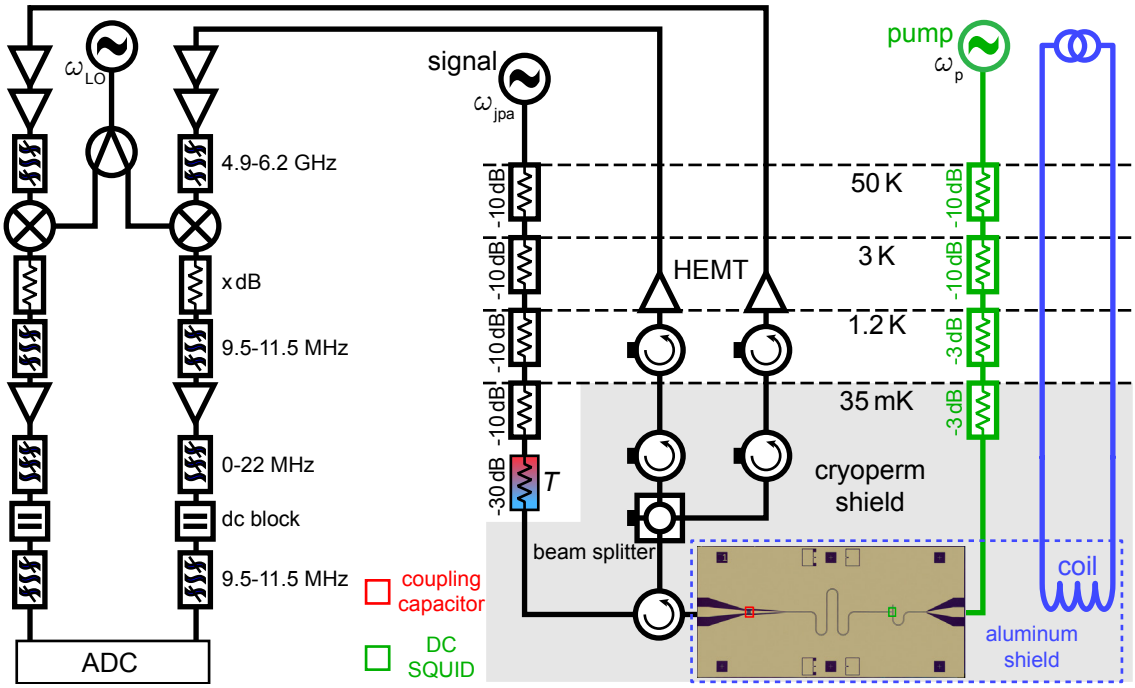

Figure 4.38: Schematics of the dual-path setup.

quadrature components $\mathcal{I}_{1,2}$ and $\mathcal{Q}_{1,2}$ of path 1 and path 2, respectively. From these components, we calculate the correlation moments $\langle \mathcal{I}_1^i \mathcal{I}_2^j \mathcal{Q}_1^k \mathcal{Q}_2^\ell \rangle$ up to the fourth order, i.e., $i+j+k+\ell \leq 4$ for $i,j,k,\ell \in \mathbb{N}_0$. This allows us to retrieve all the moments of the annihilation and creation operators, $\hat{a}$ and $\hat{a}^\dagger$, of the field modes by using beam splitter relations [169] and the independence of the noise contributions between the two detection paths. For uncorrelated input signals, i.e., vacuum and thermal states, the beam splitter does not affect the photon statistics of incident fields [442]. From the expectation value of the bosonic operators, we can calculate the second-order correlation function $g^{(2)}(\tau)$ defined in Eq. (2.2.22). Because this function is not well-suited for very low photon numbers due to the division by $\langle \hat{a}^\dagger \hat{a} \rangle^2$, we calculate the unnormalized correlation function $\tilde{g}^{(2)}(\tau) = g^{(2)}(\tau) \langle \hat{a}^\dagger \hat{a} \rangle^2$. Even though the dual-path setup provides the $g^{(2)}(\tau)$ function for variable time delays τ, we only analyze data for zero time delay, i.e., $g^{(2)}(\tau = 0)$.

JPA sample For the measurements based on the dual-path setup, we use the experimental setup presented in detail Ref. 121. Both Josephson parametric amplifier (JPA) samples were designed and fabricated at NEC Smart Energy Research Laboratories, Japan and RIKEN, Japan. The dual-path setup comprises a flux-driven JPA with gain G consisting of a quarter-wavelength transmission line resonator, which is short-circuited to ground by a DC SQUID (see Fig. 4.38). We couple an on-chip antenna inductively to the DC SQUID loop to apply a strong coherent pump tone ω_p at approximately twice the resonant frequency ω_jpa of the JPA. In this phase-insensitive mode, the two JPAs have a bandwidth of approximately 3 MHz, which we determine in a characterization measurement using a VNA [see Fig. 4.39 (a) and (b)]. Further specific parameters of the JPAs are summarized in Tab. 4.1.
In our photon statistics experiments, we use a cryogenic hybrid ring as beam splitter to

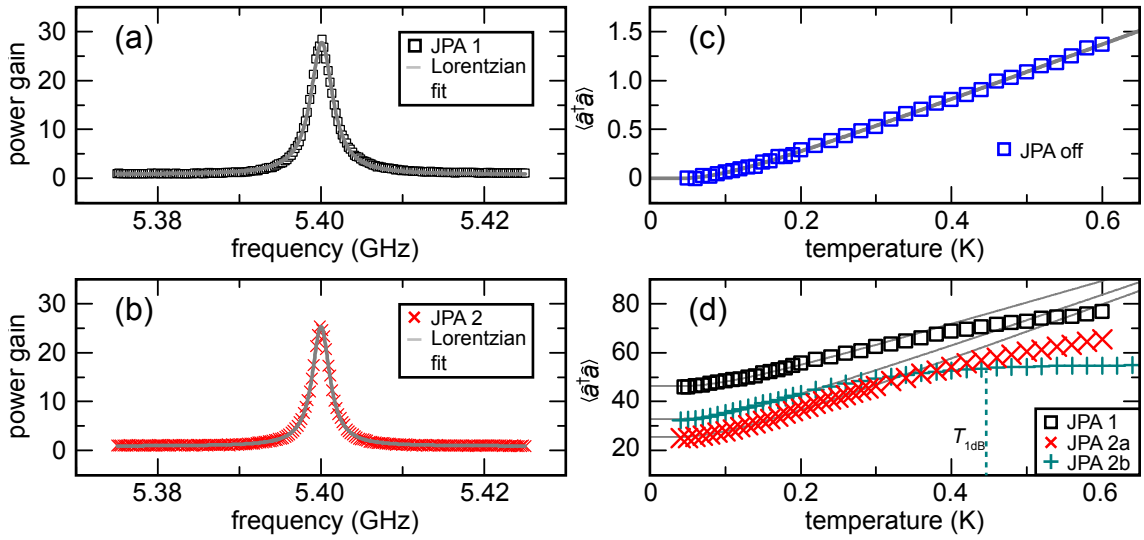

Figure 4.39: (a) JPA gain for a coherent drive measured in linear units versus frequency for JPA 1. The solid line is a Lorentzian fit used to determine the JPA bandwidth $B_{\rm jpa} \simeq 3.2\,\mathrm{MHz}$. (b) As in panel (a) but for JPA 2 which has a bandwidth of $2.6\,\mathrm{MHz}$. (c) Photon number $\langle \hat{a}^\dagger \hat{a} \rangle$ at the input of the beam splitter measured in a Planck spectroscopy experiment versus temperature of the thermal emitter. The solid lines is a fit of Eq. (4.4.12), which we use to determine the noise temperature and the gain of the amplification chain. (d) As in panel (c) but for the case that the JPA is turned on. By fitting Eq. (4.4.12) to the data points below $200\,\mathrm{mK}$, we obtain the gain and the noise photons added by the JPA. We also use this fit to determine the $1\,\mathrm{dB}$ compression point indicated by the dashed line for JPA 2b.

divide the signal into two amplification paths (dual-path method [443]). After strong but independent amplification in the two paths, the signal is downconverted to an intermediate frequency $\omega_{\rm if} = \omega_{\rm lo} - \omega_{\rm jpa} = 2\pi \times 11\,\mathrm{MHz}$ and enters an analog-to-digital conversion (ADC) card. The particular digitizing procedure to calculate all correction moments is described in detail in Ref. 163. From these calculations, we extract the signal moments $\langle (\hat{a}^\dagger)^n \hat{a}^m \rangle$. Thermal states are generated as described in detail in the previous subsection.

Photon number calibration To calibrate the photon number $\langle \hat{a}^\dagger \hat{a} \rangle$ at the input of the hybrid ring, we first perform a Planck spectroscopy experiment with the JPA turned off to relate the detected power $\mathcal{P}_{\rm det}$ and photon number $\langle \hat{a}^\dagger \hat{a} \rangle = \exp\left(\hbar\omega / k_{\rm B} T - 1\right)^{-1}$ via [440]

$$\mathcal{P}_{\rm det} = G_{\rm chain} \times B \times \hbar\omega \left[\langle \hat{a}^\dagger \hat{a} \rangle + \frac{1}{2} + k_{\rm B} T_{\rm chain} \right] . \tag{4.4.12}$$

Table 4.1: Overview of the JPA samples. We perform one measurement with JPA 1 and two individual measurements using JPA2 with different detuning $\delta_{\rm jpa} = \omega_{\rm jpa} - \omega_{\rm p}/2$ between JPA frequency $\omega_{\rm jpa}$ and pump frequency $\omega_{\rm p}$. The measurement bandwidth for all measurements is $\omega_{\rm jpa} \pm 200\,\mathrm{kHz}$. * We can only estimate the $1\,\mathrm{dB}$ compression point for JPA 1.

device	run	gain G	$B_{\rm jpa}$	$n_{\rm n}$	ρ	ξ	$\tilde{g}_{\rm n}^{(2)}(0)$	$\delta_{\rm jpa}/2\pi$	$\omega_{\rm jpa}/2\pi$	$T_{\rm 1dB}$	$\mathcal{P}_{\rm 1dB}$	$\kappa_{\rm x}$	$\kappa_{\rm i}$
JPA 1	–	14.3 dB	3.2 MHz	1.47	2.24	8.14	7.1	100 kHz	5.4 GHz	700 mK*	-127 dBm*	18.7 MHz	5.4 MHz
JPA 2	a	15.8 dB	2.6 MHz	0.66	2.23	3.29	1.1	100 kHz	5.4 GHz	590 mK	-129 dBm	14.9 MHz	0.2 MHz
JPA 2	b	15.2 dB	2.6 MHz	0.97	2.21	3.29	1.8	500 kHz	5.3 GHz	440 mK	-130 dBm	14.6 MHz	0.2 MHz

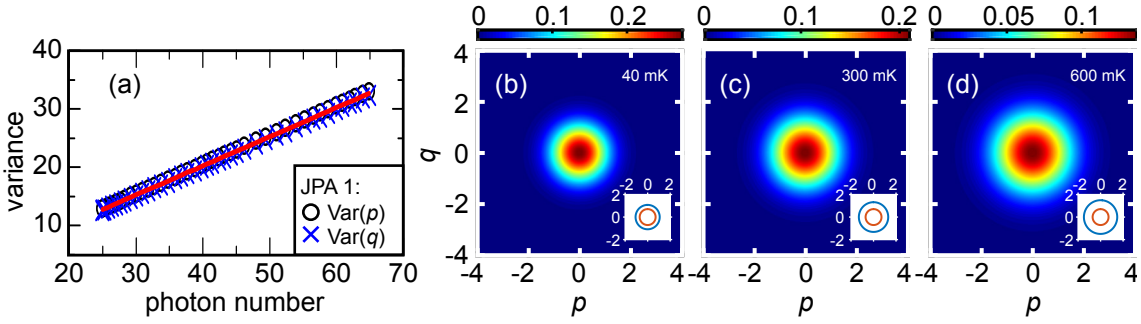

Figure 4.40: (a) Variance of $\hat{p}$ and of $\hat{q}$ plotted versus photon number. The solid line is a calculation based on Eq. (4.4.13). (b) - (d) Wigner functions of thermal states measured with JPA on referenced back to the input of the hybrid ring. The insets show the $1/e$-contour of the vacuum (red) and the thermal state (blue).

Here, G_{chain} is the total amplification of the setup, $B = 400\,\mathrm{kHz}$ is the measurement bandwidth, and T_{chain} is the effective noise temperature of the amplification chain. As shown in Fig. 4.39 (c), the data nicely follows Eq. (4.4.12) if the JPA is turned off. From this measurement, we obtain the noise temperature of the cryogenic amplifiers $T_{\mathrm{hemt}} \approx T_{\mathrm{chain}} \simeq 3\,\mathrm{K}$ and the gain $G_{\mathrm{chain}} \simeq 145\,\mathrm{dB}$. In order to characterize the JPA properties, we perform a temperature sweep when the JPA is turned on. As apperent from Fig. 4.39 (d), there is a constant photon number offset due to the noise photons n_{n} added by the devices. Furthermore, the JPAs run into compression when the field temperature exceeds approximately 400 mK. From the field temperature $T_{1\mathrm{dB}}$ at the 1 dB compression point (cf. Tab. 4.1), we calculate 1 dB values $\mathcal{P}_{1\mathrm{dB}} = \kappa_{\mathrm{x}}(2\pi)^{-1} k_{\mathrm{B}} T_{1\mathrm{dB}} \simeq -130\,\mathrm{dBm}$. Here, κ_{x} is the external coupling rate of the resonator, which strongly exceeds the internal loss rate κ_{i}. The values obtained for $\mathcal{P}_{1\mathrm{dB}}$ fit well to the 1 dB compression points measured for a coherent input state. For all measurements presented in this work, we use modest pump powers, such that we do not expect any non-linear effects [444] of the JPAs.

Variance of individual field quadratures We use Eq. (2.2.40) to describe the photon number variance of broadband amplified signals. When comparing the predicted values of $\xi = 4n_{\mathrm{n}} + 4$ and $\tilde{g}_{\mathrm{n}}^{(2)}(0) = 2(n_{\mathrm{n}} + 1)^2$, we observe that for both cases, the measured values are smaller than the expected values. To exclude that this effect is due to squeezing of the field quadratures, we analyze the variance of the individual quadrature components $\mathrm{Var}(\hat{p})$ and $\mathrm{Var}(\hat{q})$. Here, we define $\hat{p} = \imath(\hat{a}^\dagger - \hat{a})/2$ and $\hat{q} = (\hat{a}^\dagger + \hat{a})/2$. Then, at the input of the hybrid ring, one expects

$$\frac{\mathrm{Var}(\hat{p})}{G} = \frac{\mathrm{Var}(\hat{q})}{G} = \frac{\langle \hat{a}^\dagger \hat{a} \rangle}{2} + \frac{1}{4} \tag{4.4.13}$$

for unsqueezed thermal states. As shown in Fig. 4.40 (a), we observe the expected linear trend which fits very well to the expected behavior described in Eq. (4.4.13). Hence, we do not observe any squeezing effects in the field quadratures of the amplified thermal fields. This circumstance is also expressed in the circular Wigner functions shown in Figs. 4.40 (b) - (d).

Chapter 5
Loss mechanisms in superconducting quantum circuits

In this chapter, we present a detailed characterization of decoherence mechanisms in superconducting quantum circuits. We start with a systematic study of loss mechanisms in superconducting thin film microwave resonators in Sec. 5.1, which is based on Ref. 38. Section 5.2, which is based on Ref. 39, treats second-order decoherence mechanisms of a transmon qubit.

5.1 Loss mechanisms in superconducting thin film microwave resonators

This section is based on Ref. 38. The study of loss mechanisms in superconducting microwave resonators is a convenient method to evaluate loss channels affecting superconducting quantum circuits in general [19, 126, 276–281, 284]. In this section, we analyze a broad variety of microwave loss mechanisms which are relevant for the quantum circuits presented in Secs. 5.2 - 6.2. An overview of these contributions is given in Fig. 5.1. Our analysis is based on the nine samples summarized in Tab. 5.1. We describe the fabrication process of these samples in detail in Sec. 3.3.1. We focus on loss mechanisms which are relevant during experiments in the quantum regime, i.e., at low excitation numbers. Therefore, we cool down the resonators to millikelvin temperatures in the CIRQUS cryostat introduced in Sec. 4.1 and use readout signals down to approximately one photon on average. In Sec. 5.1.1, we compare TLS losses in different substrates and different metallic thin films. We find the well-known power and temperature dependence of TLS loss in CPW resonators [276]. Additionally, we observe a temperature dependence in the characteristic saturation power of the TLSs in agreement with TLS theory [263, 287]. From a material perspective, Nb and Al are the workhorse materials in circuit QED experiments. For this reason, it is particularly important to probe and quantify the different loss channels in these materials and combinations thereof (see Sec. 5.1.2). Because in circuit QED experiments, often Al based Josephson junctions are integrated into Nb CPW resonators [26, 31, 445], we focus on the influence of Nb/Al interfaces. Next to the fact that Josephson junctions itself can contribute to microwave loss [446], also the Nb/Al interfaces are possible loss channels. We find that these interfaces can be a dominant source for TLS loss. Due to our study of loss in Nb/Al interfaces, we change the fabrication process to an all-Al process resulting in an increased quality of the resonators (cf. Sec. 5.1.3). Nevertheless, above 200 mK Al

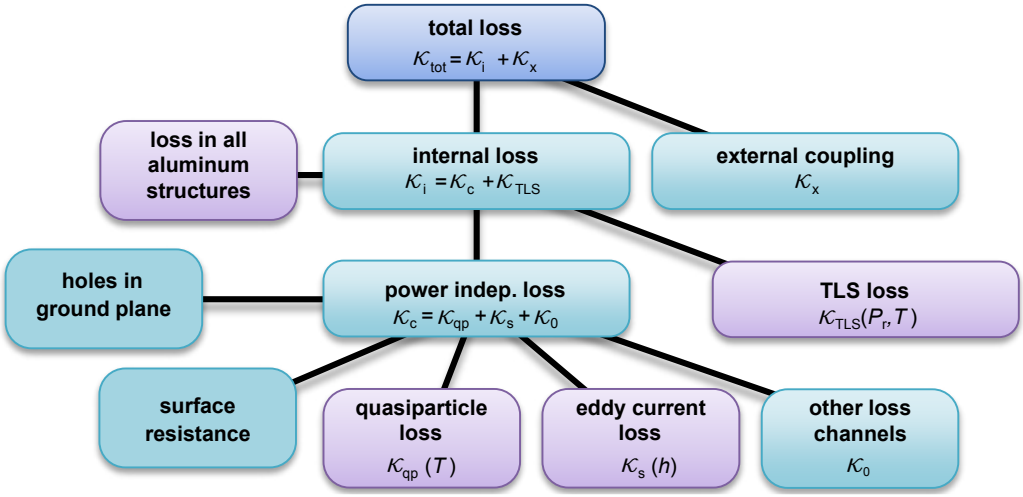

Figure 5.1: Microwave loss contributions in superconducting resonators. In this section, we discuss all loss contributions displayed as violet boxes.

based samples suffer from quasiparticle loss as discussed in Sec. 5.1.4. Galvanically coupled Josephson circuits are typically controlled via an external magnetic field, which can be a source for undesirable flux vortices in large superconducting structures [227]. Additionally, superconducting enclosures often interfere with the need of applying magnetic control fields. To solve these issues, one can use a normal conducting layer on the sample backside. To benchmark this solution, we analyze loss introduced by eddy currents in a conductive (silver glue) material on the sample backside in Sec. 5.1.5. Our analysis provides additional flexibility in the choice of sample package and fabrication process because we show that eddy currents can be avoided easily by means of a thick enough substrate.

Please note that in this section, we express all loss rates κ in terms of the corresponding dimensionless inverse quality factor $Q^{-1} = \kappa/\omega_r$.

Table 5.1: Overview of the samples analyzed in this section. The values of $\kappa^0_{tls}, \kappa_c, \beta$ and $\mathcal{P}_c$ are obtained by fitting Eq. (5.1.1) to a power sweep of each individual sample as shown in Fig. 5.2. We also list confidence intervals generated by the fits. We obtain α by fitting Eq. (2.4.16) to the values of $\mathcal{P}_c(T)$. Sample IX has a superconducting ground plane on the backside of the substrate.

ID		Purpose	$\kappa^0_{tls}/10^{-5}$	$\kappa_c/10^{-5}$	β	$\mathcal{P}_c$ (dBm)	α
I	○	reference	0.71	2.08	0.76	−97	2.3
II	●	thick substrate	0.89	1.04	1.25	−93	2.8
III	▲	patterned with EBL	0.34	0.33	1.06	−99	–
IV	◆	HF-dip	0.09	3.03	0.92	−83	2.0
V	◀	thin substrate	0.16	3.84	1.26	−83	2.8
VI	▼	gridded ground plane	1.19	0.99	1.2	−109	–
VII	⬢	Al bridge: Ion gun	0.86	1.75	1.28	−94	2.6
VIII	▶	Al bridge	19.02	2.78	1.04	−124	2.4
VIII	▶	Al bridge second harm.	0.69	1.69	0.88	−98	2.7
IX	■	microstrip	25.12	1.14	2.96	−110	–

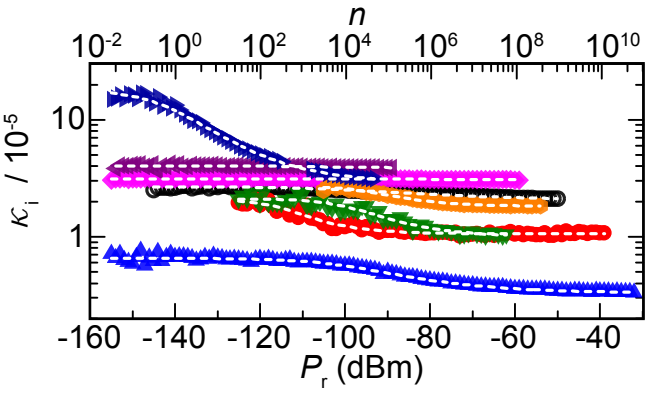

Figure 5.2: Internal loss rate for samples I – VIII plotted versus the microwave power circulating inside the resonator at 50 mK. Symbols are explained in Tab. 5.1. The average photon number on the top axis scale is calculated as $n = 2\pi\mathcal{P}_\mathrm{r}/\hbar\omega_\mathrm{r}^2$. Dashed lines are fits of Eq. (5.1.1) to the data.

5.1.1 Loss due to two-level states

Microwave loss due to two-level states (TLSs) is one of the most prominent source for decoherence in solid-state-based quantum systems [38, 267, 276]. They arise from the requirement to embed solids-state quantum systems into another solid-state environment, i.e., to place the superconducting circuit on some kind of substrate. These substrates suffer from dielectric loss characterized by their loss tangent $\tan\kappa_\mathrm{i}$. The dielectric loss is caused by defects, typically modeled by TLSs, which can be excited within the superconducting energy gap. This mechanism absorbs photons from the electromagnetic field of the resonator which are then dissipated into the environment [289]. The TLSs can be located inside the dielectric or at the dielectric/metal interfaces near the resonator. Each TLS contributes to the total TLS loss $\kappa_\mathrm{tls} = \sum_k p_k \kappa_{\mathrm{tls},k}$ with its participation ratio p_k. This ratio depends on the one hand on the dipole moment of the TLS and, on the other hand, on its relative position inside the resonator. Due to the distributed-element nature of the CPW resonator, TLS saturation does not occur uniformly across the sample but starts at voltage antinodes of the probed mode. Additionally, it depends on the center conductor width s as well as on the gap w between center conductor and ground plane. These geometry parameters determine the electric field strength [276, 447]. For our analysis, we split the internal loss rate into a power-independent term κ_c and a power- and temperature-dependent TLS contribution $\kappa_\mathrm{tls}(\mathcal{P}_\mathrm{r},T)$. Hence, the internal loss rate is described as

$$\kappa_\mathrm{i}(\mathcal{P}_\mathrm{r},T) = \kappa_\mathrm{tls}(\mathcal{P}_\mathrm{r},T) + \kappa_\mathrm{c}\,. \tag{5.1.1}$$

Here, $\mathcal{P}_\mathrm{r} = \mathcal{P}\omega_\mathrm{r}\kappa_\mathrm{x}/(k\kappa_\mathrm{tot}^2)$ is the power circulating inside the resonator [276] for the k^th mode and $\mathcal{P}$ is the power resonantly applied to the input of the resonator. In Eq. (5.1.1), $\kappa_\mathrm{tls}(\mathcal{P}_\mathrm{r},T)$ depends strongly on readout power and sample temperature as defined in Eq. (2.4.14). In the low temperature and low power limit, the internal loss rate approaches κ_tls^0 which is defined by the unsaturated TLSs.

In the following, we present experimental results starting with a comparison of TLS related loss. First, we discuss the TLS loss rates for samples I – VI (pure Nb resonators). We compare samples with different substrate thicknesses and surface treatments to our standard process for Nb on a 250 µm thick silicon substrate covered with 50 nm SiO_2 on both sides (cf. sample I in Tab. 5.1). As a surface treatment, we remove the SiO_2 layer on top of the silicon substrate for sample IV using hydrofluric acid (HF) as described in detail in Sec. 3.2.2. Fitting Eq. (5.1.1) to the power dependence of κ_i, we extract κ_tls^0, β and $\mathcal{P}_\mathrm{c}$ (see Fig. 5.2). The results are summarized in Table 5.1. For sample I, which serves as a reference sample, we find a TLS contribution $\kappa_\mathrm{tls}^0 \simeq 7.1 \times 10^{-6}$. We can study the influence

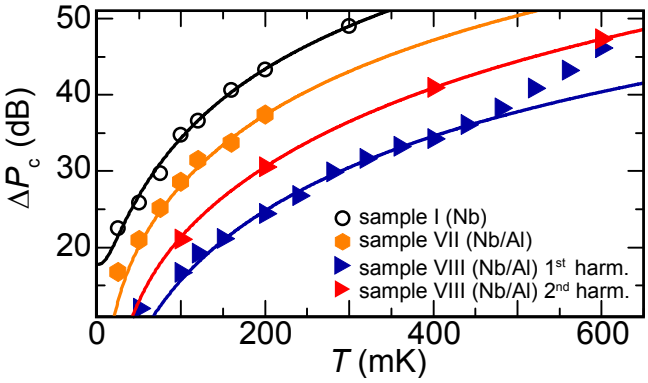

Figure 5.3: Relative change $\Delta\mathcal{P}_c$ of the characteristic power plotted versus temperature for different samples. Solid lines are fits of Eq. (2.4.16) to the data. For the first harmonic mode of sample VIII, we observe a strong increase for temperatures above 440 mK. For this dataset we fit only to data points below 440 mK. For better visibility, there is an offset of 6 dB between each dataset.

of TLSs near the surface using sample IV, where we have cleaned the surface with an HF-dip before metallization. For this sample, we measure $\kappa_{\mathrm{tls}}^{0} \simeq 9 \times 10^{-7}$, which is one order of magnitude lower than for sample I. Hence, we conclude that most of the TLS loss is introduced by the bulk SiO_2 layer, the SiO_2/metal, and SiO_2/air interfaces. In contrast, loss rates at the metal/air interface are significantly smaller ($\leq 9 \times 10^{-7}$). For sample VI (gridded ground plane) the TLS loss rates are comparable to those of a resonator with continuous ground plane.

The characteristic power $\mathcal{P}_c$ defined in Eq. (2.4.14) is proportional to $\bar{\gamma}_{1,\mathrm{tls}} \cdot \bar{\gamma}_{\varphi,\mathrm{tls}}$, where $\bar{\gamma}_{1,\mathrm{tls}}$ and $\bar{\gamma}_{\varphi,\mathrm{tls}}$ represent the average relaxation and dephasing rate of the TLS ensemble [261]. In the spin-boson model, the temperature dependence of $\bar{\gamma}_{1,\mathrm{tls}}$ follows a $\coth(\hbar\omega/2k_{\mathrm{B}}T)$ dependence [287, 290] which can be approximated by a linear dependence on T for $k_{\mathrm{B}}T \gg \hbar\omega$. Due to the phonon-mediated interaction between the TLSs, one expects the decoherence rate to scale with T for low temperatures as described in Eq. (2.4.15). However, in the regime $\hbar\omega \simeq k_{\mathrm{B}}T$ which is relevant for our experiments, a power law $\propto T^{\alpha}$ has been found [261–263, 266, 290–293] and the power dependence of $\mathcal{P}_c$ is expected to scale as T^{α}. To obtain further insight into the nature of the TLSs, we analyze the relative change $\Delta\mathcal{P}_c = \mathcal{P}_c(T) - \mathcal{P}_c(0)$, which is linked to TLS properties via Eq. (2.4.14). For each individual sample, we observe an increase in $\Delta\mathcal{P}_c$ for increasing temperature due to the temperature-dependent lifetime of the TLSs as shown in Fig. 5.3. From a fit based on Eq. (2.4.16), we find $\alpha \simeq 2.5 \pm 0.3$ (average over samples I – VIII). This value deviates from $\alpha = 1$ expected from the spin-boson model [287, 290] but is comparable to values reported for TLSs in glasses [261, 263] and phase qubits [266, 293]. This deviation can be attributed to the fact that our experiments are not in the low temperature limit, but rather in the intermediate regime $\hbar\omega \simeq k_{\mathrm{B}}T$.

5.1.2 Loss at Nb/Al interfaces

For resonators made from a single metal layer, the TLSs couple mainly to the electric field $\mathbf{E}_{\mathrm{r}}$ generated by the CPW structure. This situation changes for resonators including metal/metal interfaces, e.g., Nb/Al interfaces. In the case of a Nb/Al interface with an oxide layer of finite thickness h_{ox}, the interface forms a Josephson junction and the TLSs also couple to the electric field $|\mathbf{E}_{\mathrm{Nb/Al}}| = V_{\mathrm{J}}/h_{\mathrm{ox}}$ inside this junction [267]. Here, $V_{\mathrm{J}} = L_{\mathrm{J}}\partial I/\partial t$ is the voltage drop across the junction induced by the resonator current $I = I_{\mathrm{r}}\cos(\omega_{\mathrm{r}}t)$. Here, the Josephson inductance L_{J} is defined in Eq. (2.1.12). Assuming the junction as a

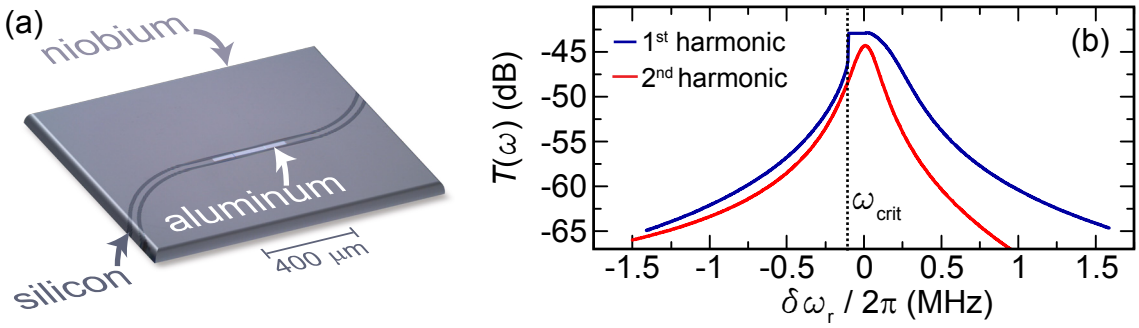

Figure 5.4: **(a)** Microscope image of the area where part of the Nb center conductor is replaced by an Al strip. **(b)** Transmission magnitude plotted versus $\delta\omega_\mathrm{r} \equiv \omega - \omega_\mathrm{r}$ for the first and second harmonic mode of sample VIII at $\mathcal{P}_\mathrm{r} \simeq -45\,\mathrm{dBm}$. For the first harmonic mode, the resonance shows a nonlinear behavior due to the presence of the Nb/Al interface forming a Josephson junction. We use the characteristic frequency ω_crit to determine the junctions critical current. The second harmonic mode does not couple to the the junction and therefore exhibits a Lorentzian peak.

parallel plate capacitor, the root mean square electric field inside the junction reads

$$E_\mathrm{Nb/Al}^\mathrm{rms} = \frac{\hbar\omega_\mathrm{r}}{2eh_\mathrm{ox}\cos\varphi}\frac{I_\mathrm{r}}{\sqrt{2}I_\mathrm{c}}\,. \tag{5.1.2}$$

This equation shows that a finite resonator current amplitude I_r leads to an electric field across the junction which can couple to TLSs in the junction. Therefore, we can apply Eq. (2.4.14) to describe the loss generated by TLSs inside a Josephson junction which is formed by an oxidized metal/metal interface incorporated into the center conductor of a CPW resonator.

We use sample VII and sample VIII, where an Al strip is placed at the current antinode of the fundamental mode, to study the influence of Nb/Al interfaces introduced into the center conductor of CPW resonators. Even though these interfaces are known to introduce loss in galvanically coupled Josephson junction based circuits[445, 446], the TLS effect on the internal quality factor of superconducting resonators has not yet been quantified. For this purpose, we replace a 150 µm long piece of the Nb center conductor by an Al strip of identical width and thickness as shown in Fig. 5.4 (a). The Al strip shares an 100 µm long overlap with the Nb center conductor and is evaporated in an extra fabrication step. For sample VII, we additionally clean the Nb surface by means of in-situ Ar-ion milling before the Al evaporation to remove oxides and resist residues from the Nb surface. More details on the fabrication process are given in Sec. 3.3. The transmission of the first harmonic mode of the resonator without ion gun treatment shows a deviation from the Lorentzian lineshape for large probe power [see Fig. 5.4 (b)]. As this behavior is typical for resonators including Josephson junctions [446, 448], we treat the Nb/Al interfaces as large-area Josephson junctions. As expected, the second harmonic mode, which has a current node at the interface position, shows a Lorentzian behavior. Due to the presence of the interfaces, we also observe a non-equidistant mode spacing, which is again typical for resonators including Josephson junctions [26]. Specifically, we find $\omega_{\mathrm{r},2}/\omega_{\mathrm{r},1} \simeq 1.93$, where $\omega_{\mathrm{r},k}$ is the resonance frequency of the k^th mode. In contrast, all samples without Nb/Al interface (samples I–VI) show an equidistant mode spacing, $\omega_{\mathrm{r},k}/\omega_{\mathrm{r},1} = k$ for $k \in 1{,}2{,}3$. The presence of the oxidized interfaces results in a large TLS loss rate. For the first harmonic mode of sample VIII, we observe an increase of more than one order of magnitude in κ_TLS^0 as compared to sample I (pure Nb) or sample VII (cleaned Nb/Al interface). Hence, we draw

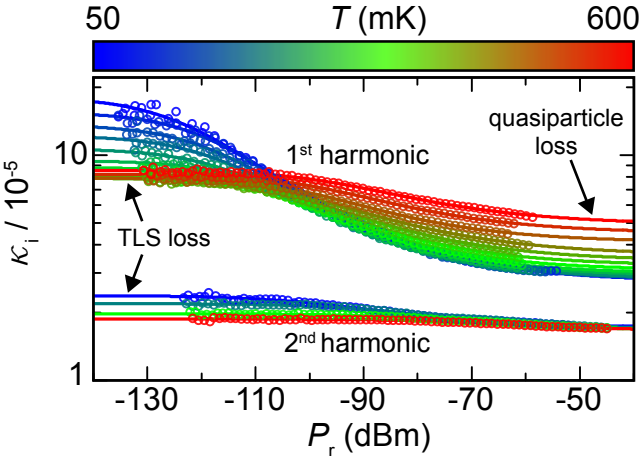

Figure 5.5: Internal loss rate plotted versus the circulating microwave power for the first two harmonic modes of sample VIII (no Ar ion cleaning) at temperatures between 50 mK and 600 mK. Solid lines are fits of Eq. (5.1.1) to the data. Arrows indicate the regions relevant for the analysis of TLS and quasiparticle loss.

two important conclusions. First, without cleaning step, the Nb oxides present at the interfaces are strong TLS sources. Second, these TLSs can cause significant loss. This behavior is not immediately obvious, because the Nb/Al interfaces are located at a voltage node of the first harmonic mode. Consequently, the TLSs associated with the Nb oxides at these interfaces are not expected to couple to the resonator electric field. Nevertheless, due to the electric field $\mathbf{E}_{\mathrm{Nb/Al}}$ between the Nb and the Al layer in the overlap area, we observe a pronounced power and temperature dependence of κ_{i} [see Fig. 5.5]. Actually, according to Eq. (5.1.2), $E^{\mathrm{rms}}_{\mathrm{Nb/Al}}$ is proportional to the resonator current and therefore maximum if the Nb/Al interface is placed at the current antinode (voltage node) of the resonator field. In the following, we discuss why the TLSs in the interfaces are not yet saturated by $E^{\mathrm{rms}}_{\mathrm{Nb/Al}}$ for a probe power corresponding to the vacuum current $I_{\omega_{\mathrm{r},1}} = (\hbar\omega_{\mathrm{r}}^2/2\pi^2 Z_0)^{1/2} \simeq 21\,\mathrm{nA}$, which is necessary to observe the power dependence shown in Fig. 5.5. From the critical frequency $\omega_{\mathrm{crit}}(\mathcal{P}_{\mathrm{r}})$ as indicated in Fig. 5.4, we can derive the critical current [448]

$$I_{\mathrm{c}} = \frac{\sqrt{3}(Z_0\Phi_0\mathcal{P}_{\mathrm{r}})^{1/3}}{2\pi\kappa_\ell L_{\mathrm{r}}(8\omega_{\mathrm{crit}})^{2/3}} \simeq 19.2\,\mu\mathrm{A}\,, \tag{5.1.3}$$

of the large Josephson junction. Here, $L_{\mathrm{r}} \simeq 6\,\mathrm{nH}$ is the total resonator inductance. With a junction area of approximately $2000\,\mu\mathrm{m}^2$, we obtain a current density $J_{\mathrm{c}} \simeq 0.96\,\mathrm{A/cm}^2$. This very low critical current density is expected, as the Nb was exposed to air for two days [357]. Nevertheless, we obtain $I_{\mathrm{c}} \gg I_{\omega_{\mathrm{r},1}}$ and can use the approximation $\cos\varphi = 1$ in Eq. (5.1.2). Assuming an oxide thickness on the order of 1 nm, we obtain $E^{\mathrm{rms}}_{\mathrm{Nb/Al}} \simeq 6\,\mathrm{V/m}$ from Eq. (5.1.2). On the one hand, this field strength is large enough to mediate a coupling between the TLSs and the resonator. On the other hand, it is small compared to the experimentally observed saturation field $|\mathbf{E}^{\mathrm{c}}_{\mathrm{Nb/Al}}| = 44\,\mathrm{V/m}$ given by the resonator current $I_{\mathrm{r}} \simeq (140 \pm 40)\,\mathrm{nA}$ for $\mathcal{P}_{\mathrm{c}} \simeq -124\,\mathrm{dBm}$.

In the next step, we confirm our model of TLS loss in the interfaces by analyzing the second harmonic mode of sample VIII, which has a voltage antinode at the interface position. As shown in Fig. 5.5, this mode shows a significantly smaller internal loss rate compared to the first harmonic mode. We measure $\kappa^0_{\mathrm{tls}}{=}7\times10^{-6}$ and $\kappa_{\mathrm{c}}{=}1.7\times10^{-5}$, that is, values comparable to those of the first harmonic mode of the pure Nb resonator (sample I). This observation is unexpected for loss based on a model considering only uniformly distributed loss mechanisms [112]. Instead, the effect can be explained by TLSs localized in the Nb/Al interfaces. Since for the second harmonic mode the interfaces are placed at the current

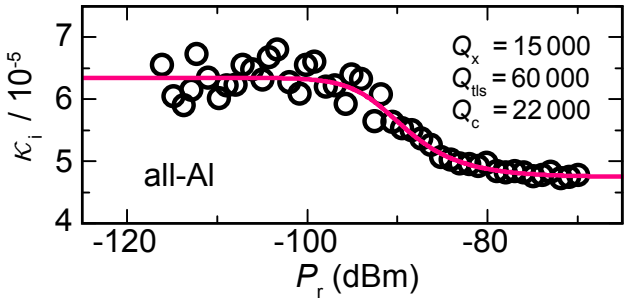

Figure 5.6: Internal loss rate plotted versus microwave power circulating inside an all-Al resonator. The solid line is a numerical fit based on Eq. (5.1.1).

node, $I_{\omega_{r,2}} \simeq 0$, the corresponding electric field $E^{\mathrm{rms}}_{\mathrm{Nb/Al}}$ is vanishingly small. Therefore, only the TLSs outside the interface, which couple to the resonator electric field, introduce loss rates comparable to those of sample I (pure Nb). We note that also the power-independent contribution κ_c is smaller for the second harmonic mode than for the first harmonic mode. This behavior indicates that the interfaces are not only strong sources for TLS loss but also for local resistive loss.
Finally, we find that local loss induced by the interfaces can be significantly reduced by in-situ ion gun treatment of the Nb surface before Al evaporation. In particular, we measure the loss rate $\kappa^0_{\mathrm{tls}} \simeq 9 \times 10^{-6}$ of the fundamental mode of sample VII (ion gun treatment), which is one order of magnitude larger than for sample VIII (no ion gun treatment). As expected, we find that κ^0_{tls} of sample VII is similar to κ^0_{tls} of both the second harmonic mode of sample VIII and the fundamental mode of sample I (pure Nb).

5.1.3 Loss in all-Al structures

The detailed discussion of loss in Nb/Al interfaces in Sec. 5.1.2 has triggered the effort to fabricate resonator samples consisting completely of an $\mathrm{Al/AlO_x/Al}$ structure. This techniques allows one to include Josephson junction based circuits without additional metal/metal or metal/oxide interfaces. The experimental challenge using this technique is the combination of a nanometer precision of the electron beam for Josephson junctions and the millimeter wide illumination for the CPW structures. As described in detail in Sec. 3.3.2, we achieve this by patterning the sample with two different parameter sets for the EBL process. Using the EBL process instead of optical lithography to pattern the resonators, we achieve very smooth edges of the Al thin films as shown in Fig. 3.8 (d).
To study the quality of resonators made from pure Al films, we use the sample containing the tunable gradiometric flux qubit, which we fabricate with an all-Al process. From a readout power sweep at 25 mK, we find a low-power loss $\kappa_{\mathrm{tls}} \simeq 6.4 \times 10^{-5}$, corresponding to $Q_{\mathrm{tls}} \simeq 6 \times 10^4$ (see Fig. 5.6). This quality factor is more than one magnitude higher than quality factors found for comparable samples with Nb/Al interface [178]. Furthermore, this quality factor exceeds typical external quality factors used in circuit QED experiments by two orders of magnitude (assuming $Q_x \simeq 600$). Hence, the internal loss rate of the all-Al resonator is negligible. Nevertheless, further improvements can be achieved by an advanced cleaning method of the substrate or by switching to intrinsic silicon (without thermal oxide layer) or sapphire substrates. These substrates have a smaller loss tangent resulting in even less internal loss [19]. To conclude, our results show that the careful analysis of Nb/Al interfaces and the experimental consequence to omit these interfaces, has really pushed the sample quality of integrated Josephson junction based circuits at the WMI.

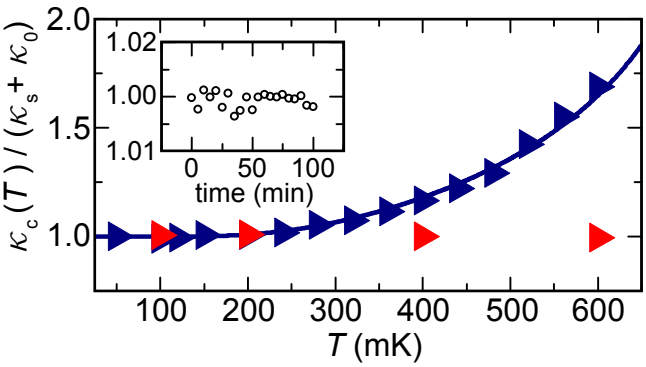

Figure 5.7: Normalized loss rate $\kappa_c(T)/(\kappa_s + \kappa_0)$ of sample VIII plotted versus sample temperature. Blue triangles correspond to the first and red triangles to the second harmonic mode. The solid line is a fit of $\kappa_c(T)$ using Eq. (5.1.4) based on calculations of $\kappa_{qp}(T)$. The inset shows the time dependence of $\kappa_c(T)/(\kappa_s + \kappa_0)$ at 50 mK.

5.1.4 Loss due to thermal quasiparticles

In the following, we focus on the high power regime where the internal losses are limited by

$$\kappa_c(T,h) = \kappa_{qp}(T) + \kappa_s(h) + \kappa_0 \,. \tag{5.1.4}$$

Here, $\kappa_{qp}(T)$ describes thermally induced quasiparticle loss and $\kappa_s(h)$ describes eddy current loss on the backside of the substrate. The term κ_0 comprises all other loss processes such as radiation [362], the finite surface resistance of superconductors [74], and non-thermal quasiparticles generated by stray infrared light [65, 126]. Quasiparticle loss rates are defined in Eq. (2.4.17) and become relevant when the temperature exceeds approximately 10 % of the critical temperature of the superconductor.

We first analyze the temperature dependence $\Delta\mathcal{P}_c(T)$ for both samples including a Nb/Al interface (sample VII and sample VIII). As shown in Fig. 5.3, the exponent α is in the same range as for all other samples (see Sec. 5.1.1). Specifically, we extract $\alpha \simeq 2.6$ (sample VII), $\alpha = 2.4$ (sample VIII, first harmonic), and $\alpha = 2.7$ (sample VIII, second harmonic). When extracting α for the first harmonic of sample VIII, we only take data points below 440 mK into account. We attribute the increased slope of $\mathcal{P}_c(T)$ above this temperature to self-heating processes [251, 449–451] inside the interfaces. This effect is not present in the second harmonic of sample VIII which has a current node at the interface position.

Next, we study the influence of the Nb/Al interfaces on κ_c, i.e., in the high power regime. For pure Nb resonators, we observe no significant change of κ_c in the temperature range between 50 mK and 600 mK. This behavior is expected because the number of quasiparticles is negligible for our experiments due to the critical temperature $T_c \simeq 9$ K of the Nb films. However, the situation is different for samples including an Al strip, which has a lower $T_c \simeq 1.2$ K. In Fig. 5.7, we show the temperature dependence of κ_c for the first two modes of sample VIII. For the first harmonic mode, we observe a quasiparticle induced increase of κ_c, which becomes relevant for temperatures above 200 mK. Using $\kappa_s + \kappa_0 = 2.8 \times 10^{-5}$ obtained from a power sweep at 50 mK where quasiparticles are negligible, we fit Eq. (5.1.4) to the data and find a kinetic inductance fraction of $\mathcal{K} \simeq 3.5 \times 10^{-4}$. This value is two orders of magnitude smaller than values reported in literature [126]. We explain this difference by the fact that the length of the Al strip is only 1/100 of the total length of the center conductor. In contrast to the first harmonic mode, κ_c of the second harmonic mode shows no temperature dependence because the current distribution of the resonator has a node at the Al position in this case. Hence, quasiparticles in the Al do not carry a significant amount of the current circulating inside the resonator. Therefore, we conclude that also with respect to quasiparticle loss it is advantageous to place such interfaces at current nodes.

Due to the reduced superconducting energy gap of Al compared to Nb, nonequilibrium quasiparticles generated by stray infrared light can be trapped in the Al layer [452, 453], which reduces the number of quasiparticles in the Nb part of the center conductor. This effect helps to decrease quasiparticle loss for resonator modes that have a current node at the position of the Al strip. Indeed, we measure $\kappa_c \simeq 1.65 \times 10^{-5}$ for the second harmonic mode of both samples including Al layers, which is smaller than $\kappa_c \simeq 2.2 \times 10^{-5}$ measured for the second harmonic mode of sample I (pure Nb resonator). Due to variations in the experimental environment, loss rates can vary as a function of time on a minutes timescale [248, 249]. In the inset of Fig. 5.7 we show the fluctuations of κ_c over a 100 minute time interval. From the statistics we evaluate a relatively small standard deviation 3.8×10^{-3}. Also over a period of several days, we do not observe any significant change in the resonator loss rate.

5.1.5 Eddy current loss

In addition to the various sources of microwave loss mechanisms mentioned above, we show that there can be eddy current loss in the conductive material used to fix our samples in the sample box. To this end, we rewrite κ_c from Eq. (5.1.4) for a constant temperature as the sum of a thickness-independent term $\kappa_{c,1}$ and a term $\kappa_s(h)$ depending on the substrate thickness h. That way, we obtain

$$\kappa_c(h) = \kappa_{c,1} + \kappa_s(h)\,. \tag{5.1.5}$$

The thickness dependence arises from a residual magnetic field $\mathbf{H}_0 \equiv \mathbf{H}(z{=}0)$ on the backside of the substrate. Therefore, we also find a finite field $\mathbf{H}_s$ in the volume of the silver glue used to fix our samples in the sample box. The thickness dependence of the eddy current loss rate is defined in Eq. (2.4.25). In the following, we experimentally analyze loss rates due to eddy currents. For this analysis, we compare all CPW samples fabricated by optical lithography. We observe that κ_c shows a significant dependence on the substrate thickness as displayed in Fig. 5.8. Assuming a negligible quasiparticle contribution $\kappa_{qp}(50\,\mathrm{mK}) \ll 10^{-6}$, a numerical fit based on Eq. (5.1.4) and Eq. (2.4.25) yields $\kappa_0 \simeq 8 \times 10^{-6}$ and a sheet conductivity $\sigma_r \simeq 7 \times 10^7\,\mathrm{S/m}$. This conductivity is approximately hundred times larger than the room temperature conductivity of our silver glue [454] and comparable to the room temperature conductivity of copper [298, 455]. Since our experiments are carried out at low temperatures where the conductivity of metals typically increases by a factor of 100 [456, 457], we can quantitatively explain the loss behavior shown in Fig. 5.8 by ohmic dissipation in the silver glue. The influence of eddy current loss depends on the material present underneath the sample. Compared to pure metals, silver glue has a relatively low conductivity and therefore larger loss rates. For samples with a substrate thickness of 525 µm, the loss rate is already enhanced by 13 % compared to κ_0 in the high power regime. Samples fabricated on 200 µm thick substrates show a loss increase by a factor of four compared to κ_0. The slight scatter in κ_c for $h = 250\,\mu\mathrm{m}$ is attributed to our assumption of a universal κ_0. This assumption is, of course, only a rough estimation because the samples are fabricated with different cleaning methods.

In summary, we can quantitatively explain loss due to eddy currents using numerical calculations of the **H**-field distribution in conductor backed CPW structures. The electrodynamical model suggests that it is advantageous to either use thick substrates or materials with high conductivity on the backside of the substrate. Therefore, enhanced loss rates caused by eddy currents can be avoided by using superconducting materials at this position.

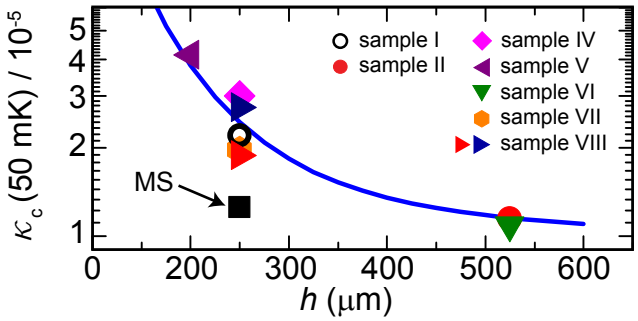

Figure 5.8: Power-independent loss rate κ_c measured at 50 mK plotted as a function of the substrate thickness. The solid line is a fit based on Eq. (5.1.4) and Eq. (2.4.25) not accounting for sample IX (MS), which has a superconducting layer at the sample backside.

This conclusion is supported by our measurements on the MS resonator (sample IX), which is fabricated on a 250 µm thick substrate and employs a superconducting ground plane. For this sample, we measure $\kappa_c \simeq 1 \times 10^{-5}$, which is reduced compared to the values of the other samples fabricated on a 250 µm thick substrate by a factor of two, despite the fact that the field at the bottom surface of the substrate is one order of magnitude larger as compared to the CPW samples.
In contrast to other groups [37], we observe a decrease of the power-independent loss rate κ_c by a factor of three for the sample fabricated with EBL (sample III) compared to sample II, which is fabricated with OL. There are two likely reasons for this observation. First, the Nb edges are smoother for the EBL sample than for the OL samples, resulting in a reduced field elevation at these positions. Second, compared to our OL process, the PMMA resist used for EBL may leave less resist residuals on the sample. Such resist residuals are known to introduce loss [37].

5.2 Second-order decoherence mechanisms of a transmon qubit

This section is based on Ref. 39. Solid-state based quantum circuits are attractive for quantum information systems due to their design flexibility and the possibility to engineer and tune interactions. This is particularly true for superconducting quantum circuits which are widely used for quantum computing [144] and quantum simulation [458], or the generation of quantum entanglement [163]. One advantage of superconducting circuits is that they provide strong [16, 459] or even ultrastrong [26–28] and well controllable [31, 32, 460–462] interaction. However, while strong interaction enables simple and fast manipulation of quantum circuits, it also goes along with strong coupling to environmental fluctuations (noise), thereby limiting the coherence properties. For superconducting quantum circuits, the impact of environmental noise has been widely studied both in theory and experiment. In particular, noise sources that couple coherently to qubits [264–266], as well as Markovian [35, 119, 241–243], or non-Markovian ($1/f$) noise sources [33, 216, 219, 221, 222, 463] have been analyzed. To optimize the coherence properties, several strategies to decouple a qubit from the environmental noise have been developed. In the first place, the most convenient way to suppress noise over a broad frequency range is to place the qubit inside a superconducting resonator [240]. This concept is efficient, when the qubit transition frequency is far detuned from the resonator frequency by an amount δ much larger than their coupling strength g. Nevertheless, even in this case, noise still couples to the qubit in second-order with strength g^2/δ. In the second place, fluctuations that modify the qubit transition frequency ω_q can be noticeably suppressed by tuning the qubit to an

operation point where the derivative of ω_q with respect to the fluctuating quantity vanishes [33, 40, 57, 219, 222]. Again, even at such a sweet spot, second-order coupling of environmental fluctuations can be a source for decoherence [234, 235, 464]. In addition to these decoherence processes, intrinsic qubit parameters such as its relaxation rate can be fluctuating in time [20, 248, 465, 466]. One prominent source for these fluctuations are interacting two-level states (TLSs) mediating low-frequency noise to the qubit.

The three second-order decoherence mechanisms mentioned above can be reliably studied with propagating thermal fields because their power spectral density $\mathcal{S}(\omega)$ can be adjusted with a high accuracy by controlling the temperature of a black-body radiator [139, 440, 443]. Furthermore, $\mathcal{S}(\omega)$ is white for low frequencies and sufficiently smooth at the qubit transition frequency, which allows for a quantitative analysis of second-order decoherence mechanisms. Besides the fact that thermal fields are an accurate control knob to study second-order effects of noise, their omnipresence in superconducting circuits [36, 38, 246, 252, 275, 276, 467] naturally results in a strong demand to investigate their second-order influence on the coherence properties of superconducting quantum circuits.

In this section, we systematically study the effect of the second-order coupling between thermal fields generated by a black-body radiator and a superconducting transmon qubit [40] placed in a superconducting resonator. We analyze the three individual decoherence mechanisms depicted in Fig. 5.9 (a). The novel aspect of our experiments is that we can irradiate the qubit either directly or via the resonator filter function with thermal noise of controllable power spectral density while keeping the qubit at the base temperature of a dilution refrigerator. This allows us to quantify the impact of thermal noise without suffering from parasitic effects such as quasiparticle generation in the superconducting circuits. We first derive basic concepts of this broadband coupling as well as experimental methods in Sec. 5.2.1. We analyze the first decoherence mechanism, which is relaxation of the qubit due to dispersively coupled thermal noise (see Sec. 5.2.2). In the dispersive Jaynes-Cummings regime, noise at the resonator frequency couples in second-order. In our experiments, we find a coupling to broadband fields which is enhanced as compared to that expected from the Purcell filter effect of the resonator. Furthermore, using coherent states and narrowband shot noise, we demonstrate the counter-intuitive effect that the qubit relaxation rate can be lowered for increasing field strengths. In Sec. 5.2.3, we discuss the situation when the thermal noise field is directly irradiated on the qubit via a near-field antenna without the cavity filter. At the flux sweet spot, this direct irradiation reveals the influence of second-order-coupled noise on the qubit dephasing rate. In particular, we observe the expected [235, 464] T^3 temperature dependence of the qubit dephasing rate. Finally, in Sec. 5.2.4, we show that low-frequency fluctuations of the qubit relaxation rate are related to the temperature of the black-body radiator if the field is not Purcell filtered. We can explain this effect by the presence of two-level fluctuators in the spatial vicinity of the qubit, which change the effective noise spectral density.

Our work establishes thermal fields as an important tool to probe the coherence properties of superconducting quantum circuits. In this way, we gain important insight into second-order decoherence mechanisms of superconducting qubits. Futhermore, our quantitative analysis of the decoherence rates is crucial to optimize the performance of superconducting qubits, which is necessary for many quantum computation and communication protocols.

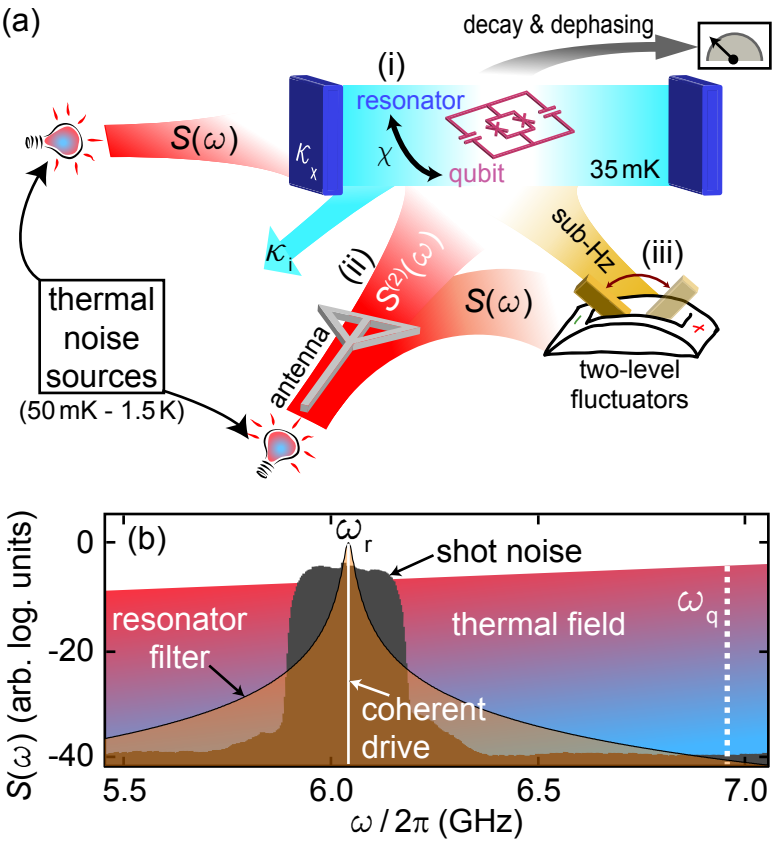

Figure 5.9: **(a)** Sketch of the experimental idea. We characterize the second-order coupling between a thermal noise source (black-body radiator of variable temperature) and a superconducting qubit by measuring the qubit decay and dephasing rate. The second-order coupling to the thermal noise field becomes relevant in the following situations: **(i)** When the qubit is dispersively coupled to a resonator acting as a filter for the noise field with spectral density $\mathcal{S}(\omega)$. **(ii)** When the qubit is directly irradiated by a noise field using a near-field antenna, but operated at a sweet spot making the second-order spectral density $\mathcal{S}^{(2)}(\omega)$ the leading contribution. **(iii)** When one or multiple two-level fluctuators change the noise spectral density in the sub-Hz regime. **(b)** Power spectral density of thermal fields, coherent states, and shot noise plotted versus frequency. All fields can be filtered by the Lorentzian filter function of a resonator. The dashed line shows the transition frequency of the qubit.

5.2.1 Specific theoretical and experimental foundations

Setup for second-order loss measurements using thermal states The experimental setup to study the effect of thermal noise on a superconducting transmon qubit is sketched in Fig. 5.9 (a). In two different cooldowns, we couple a thermal noise source either directly through a near-field antenna or indirectly via a superconducting resonator to a transmon qubit. In our experiments, we measure the qubit coherence properties as a function of the power spectral density of the noise source, which defines the average number of thermal photons. We generate the propagating thermal fields at low temperatures using a 50 Ω-matched 30 dB attenuator (see Sec. 4.4.3 for details). The attenuator is thermally decoupled from the sample box and only weakly coupled to the base temperature stage of a dilution refrigerator. The qubit is located inside a sample box as discussed in Sec. 3.3.3. We mount the sample to the base temperature stage of the CIRQUS cryostat (see Sec. 4.4.1) and stabilize it to $T_i = 35$ mK. Heating the attenuator

up to 1.5 K results in the emission of black-body radiation with a power spectral density controlled by the attenuator temperature. The average number of emitted thermal noise photons $n_{\mathrm{th}}(\omega,T) = [\exp(\hbar\omega/k_{\mathrm{B}}T) - 1)]^{-1}$ at frequency ω is given by the Bose-Einstein distribution [154] of a black-body radiator. The power spectral density of the propagating thermal fields emitted by a 50 Ω-matched attenuator into a 50 Ω-matched line reads [440]

$$\mathcal{S}(\omega,T) = \hbar\omega(n_{\mathrm{th}} + 1/2) = \frac{1}{2}\hbar\omega \coth\left(\frac{\hbar\omega}{2k_{\mathrm{B}}T}\right). \tag{5.2.1}$$

A physical understanding of this expression is obtained by writing the units as W/Hz. In this way, one immediately sees that $\mathcal{S}(\omega,T)$ describes the noise power per Hz of bandwidth. In Eq. (5.2.1), $\mathcal{S}(\omega,T)$ is reduced by a factor of four compared to the well-known [229, 255] Johnson-Nyquist noise $4k_{\mathrm{B}}T$ because we model the attenuator as a 50 Ω-matched noise source [110, 440]. We probe indicrectly coupled thermal fields by operating the qubit in the dispersive regime [case (i) in Fig. 5.9 (a)], where the detuning $\delta \equiv \omega_{\mathrm{q},0} - \omega_{\mathrm{r}}$ fulfills $g/\delta \ll 1$. Here, $g/2\pi \simeq 67\,\mathrm{MHz}$ is the qubit-resonator coupling strength, $\omega_{\mathrm{r}}/2\pi \simeq 6.07\,\mathrm{GHz}$ is the resonator frequency, and $\omega_{\mathrm{q},0}/2\pi \simeq 6.92\,\mathrm{GHz}$ is the qubit transition frequency at the flux sweet spot. For a transmon qubit, which is not a perfect two-level system, the dispersive shift of the qubit transition frequency [40] $\chi \equiv -g^2 E_{\mathrm{c}}/(\delta^2 - \delta E_{\mathrm{c}}) \simeq -2\pi \times 3.11\,\mathrm{MHz}$ depends on the transmon charging energy $E_{\mathrm{c}} \simeq h \times 315\,\mathrm{MHz}$. To probe dispersively coupled noise, we send the thermal fields through the coupling capacitor of the resonator. To analyze second-order contributions of thermal fields [case (ii) in Fig. 5.9 (a)], we use the on-chip antenna to directly irradiate the qubit with the thermal noise field without any cavity filtering. Since the antenna represents a short circuit of a 50 Ω line, the thermal noise field generates a thermal noise current, coupling thermal flux noise to the SQUID loop of the transmon qubit. Note that at the flux sweet spot, the second-order power spectral density [235, 464] (units to be read as W^2/Hz)

$$\mathcal{S}^{(2)}(\omega) = \omega\left[\frac{\hbar^2\omega^2 + 4\pi^2 k_{\mathrm{B}}^2 T^2}{12\pi}\right] \coth\left(\frac{\hbar\omega}{2k_{\mathrm{B}}T}\right) \tag{5.2.2}$$

of thermal fields is relevant because first-order fluctuations are strongly suppressed at the sweet spot. The second-order power spectral density, however, still couples intensity fluctuations to the qubit. Finally, we probe the influence of thermal fields on the low-frequency fluctuations of qubit parameters [case (iii) in Fig. 5.9 (a)] by repeatedly measuring the qubit relaxation rate on a timescale of three hours such that the lowest detectable switching frequency of the fluctuators is approximately 0.1 mHz. We perform these measurements for dispersively coupled noise and for noise, which couples directly through the antenna.

Thermal fields entering a resonator Based on the setup introduced above, we now derive how propagating voltage fluctuations on the feed lines influence the resonator population. Since we generate the thermal states outside the resonator, the mean photon population n_{r} inside the resonator can be calculated as a cavity field which is coupled to several bosonic baths each described by a Hamiltonian $\mathcal{H}_{\mathrm{bath}} = \sum_k \hbar\omega_k \hat{b}_{k,j}^\dagger \hat{b}_{k,j}$. Here, the respective field operators $\hat{b}_k^\dagger, (\hat{b}_k)$ create (annihilate) the individual field modes with frequencies ω_k. In our setup the three bosonic reservoirs ($j \in \{\mathrm{i,x,a}\}$) couple to the resonator modes described by the operators $\hat{a}, \hat{a}^\dagger$ via the interaction Hamiltonian $\mathcal{H}_{\mathrm{int}} = -\imath\hbar\sum_k[\kappa_{k,j}\hat{a}^\dagger\hat{b}_{k,j} - \kappa_{k,j}\hat{b}_{k,j}^\dagger\hat{a}]$. For convenience, we split up the transmission line modes into a classical part $\bar{b}_k$ originating from a coherent drive, and into a quantum part $\hat{\xi}_k$,

such that $\hat{b}_k(t) = e^{-\imath\omega_k t}\bar{b}_k + \hat{\xi}_k(t)$ [165]. The quantum part describes voltage fluctuations emitted from the heatable attenuators and will be the focus of the following discussion. The attenuators emit a voltage $V(t) = V_{\mathrm{vac}}[\hat{\xi}_k(t) + \hat{\xi}_k^\dagger(t)]$, which is fluctuating in time and has a Gaussian amplitude distribution. Here, V_{vac} is the vacuum amplitude of the corresponding mode. For a finite temperature, the correlation function for the voltage fluctuations reads [149]

$$\mathcal{C}_V(t) = \frac{3V_{\mathrm{vac}}^2}{\pi^2}\left[\zeta\left(2{,}1 - \imath t\frac{k_{\mathrm{B}}T}{\hbar}\right) + \zeta\left(2{,}1 + \imath t\frac{k_{\mathrm{B}}T}{\hbar}\right)\right], \tag{5.2.3}$$

where $\zeta(s,a) = \sum_{j=0}^{\infty}[j+a]^{-s}$ is the Hurwitz function. In Fig. 2.30 (a), we show the temporal correlation for a thermal excitation generated at two distinct temperatures. The width of the correlation function becomes smaller in time for higher temperatures, approaching a delta function, i.e., white noise, for very high temperatures. The coherence time τ_{rad} of thermal radiation can be defined as the full-width-half-maximum (FWHM) of the temporal correlation function. For temperatures in the kelvin range, this description yields a sub-nanosecond, i.e., negligible, coherence time of thermal fields defined by the width of the Hurwitz function [149, 150, 254]. The power spectral density of thermal fields $\mathcal{S}(\omega)$ in Eq. (5.2.1), which is shown in Fig. 2.30 (b) and Fig. 2.30 (c), can then be obtained by a Fourier transform [229, 255]. We now discuss how thermal fields described by $\mathcal{S}(\omega)$ enter the resonator. It can be shown that the power spectrum inside the resonator is the product of the resonator modes and the modes entering from outside [468]. Consequently, the relation between the field operator $\hat{a}$ inside the resonator and the input field reads [7]

$$\hat{a}(\omega_{\mathrm{r}}) = \sum_{j=\mathrm{i,x,ant}}\sum_{k}\frac{\sqrt{\kappa_{k,j}}\hat{b}_{k,j}(\omega_k)}{\kappa_{\mathrm{tot}}/2 - \imath[\omega_k - \omega_{\mathrm{r}}]}\,. \tag{5.2.4}$$

Due to the high density of modes, we take the continuum limit ($\sum_k \mapsto \int \mathrm{d}\omega_k$) and obtain the expression $n_{\mathrm{r}}(\omega,T) \approx \mathcal{F}_{\mathrm{L}}(\omega)\sum_j \kappa_j n_j(\omega,T)$. For a large qubit-resonator detuning $\delta \gg g,\kappa_{\mathrm{tot}}$, we can neglect the influence of qubit excitations entering the resonator. In this case, the Markovian master equation

$$\begin{aligned}\frac{\partial\hat{\rho}_{\mathrm{r}}}{\partial t} =& -\imath[\omega_{\mathrm{r}}\hat{a}^\dagger\hat{a},\hat{\rho}_{\mathrm{r}}] + \left\{n_{\mathrm{i}}\kappa_{\mathrm{i}} + n_{\mathrm{x}}\kappa_{\mathrm{x}} + n_{\mathrm{a}}\kappa_{\mathrm{a,r}}\right\}\mathcal{D}(\hat{a}^\dagger)\hat{\rho}_{\mathrm{r}} \\ &+ \left\{(n_{\mathrm{i}}+1)\kappa_{\mathrm{i}} + (n_{\mathrm{x}}+1)\kappa_{\mathrm{x}} + (n_{\mathrm{a}}+1)\kappa_{\mathrm{a,r}}\right\}\mathcal{D}(\hat{a})\hat{\rho}_{\mathrm{r}}\,,\end{aligned} \tag{5.2.5}$$

describes the resonator, where $\hat{\rho}_{\mathrm{r}}$ is the density matrix of the undisturbed resonator and $\mathcal{D}(\hat{L})$ is the Lindblad operator. In the steady state limit, Eq. (5.2.5) becomes

$$n_{\mathrm{r}} = \frac{n_{\mathrm{i}}\kappa_{\mathrm{i}} + n_{\mathrm{x}}\kappa_{\mathrm{x}} + n_{\mathrm{a}}\kappa_{\mathrm{a,r}}}{\kappa_{\mathrm{i}} + \kappa_{\mathrm{x}} + \kappa_{\mathrm{a,r}}}\,. \tag{5.2.6}$$

This equation shows that we can precisely control the power inside the resonator using thermal photons emitted from the heatable attenuators. Concerning power, the nature of the photons inside the resonator (e.g., thermal or coherent) makes no difference.

Photon number calibration We use the derivation for the resonator population in Eq. (5.2.6), to calibrate the photon number n_{r} and the coupling rate $\kappa_{\mathrm{a,r}}$. The coupling rates $\kappa_{\mathrm{x}} \simeq 8.5\,\mathrm{MHz}$ and $\kappa_{\mathrm{i}} \simeq 50\,\mathrm{kHz}$ are discussed in Sec. 4.4.1. Because of the low sample temperature, we neglect thermal photons coupling via κ_{i}. Then, on resonance, the steady state limit of the Markovian master equation [Eq. (5.2.5)] describing the resonator yields

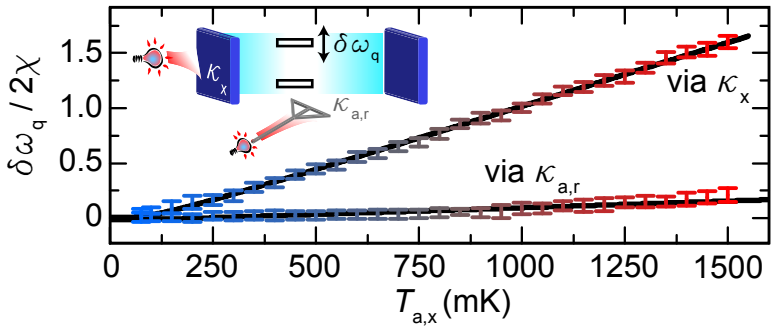

Figure 5.10: ac-Stark shift of the qubit transition frequency plotted versus temperature of the heatable attenuator in the readout line (via κ_x) or the antenna line (via $\kappa_\mathrm{a,r}$). Solid lines are fits using Eq. (5.2.7) and Eq. (5.2.8) while the inset depicts the experimental configuration.

$n_\mathrm{r}(\omega_\mathrm{r},T_\mathrm{x},T_\mathrm{a}) = [\alpha_\mathrm{x}\kappa_\mathrm{x} n_\mathrm{x}(\omega_\mathrm{r},T_\mathrm{x}) + \alpha_\mathrm{a}\kappa_\mathrm{a,r} n_\mathrm{a}(\omega_\mathrm{r},T_\mathrm{a})]/\kappa_\mathrm{tot}$. Here, the factors α_x and α_a account for losses in the microwave lines between attenuator and sample. Because we use the very same combination of attenuator and coaxial cables for the two cool-downs, we assume $\alpha_\mathrm{x} = \alpha_\mathrm{a} \equiv \alpha$ in the following. In the dispersive regime, we calibrate this factor by measuring the ac-Stark shift [24] of the qubit

$$\delta\omega_{\mathrm{q,x}}(T_\mathrm{x}) = 2\chi\alpha\kappa_\mathrm{x}\ n_\mathrm{x}(T_\mathrm{x})/\kappa_\mathrm{tot} + \delta\omega_{\mathrm{q,a}}(50\,\mathrm{mK})\,, \tag{5.2.7}$$

$$\delta\omega_{\mathrm{q,a}}(T_\mathrm{a}) = 2\chi\alpha\kappa_\mathrm{a,r} n_\mathrm{a}(T_\mathrm{a})/\kappa_\mathrm{tot} + \delta\omega_{\mathrm{q,x}}(50\,\mathrm{mK})\,. \tag{5.2.8}$$

From sweeping the temperature T_x of the feedline attenuator, we obtain $\alpha \simeq 4.1\,\mathrm{dB}$ using a numerical fit of Eq. (5.2.7) as shown in Fig. 5.10. From sweeping the antenna line attenuator, we extract the negligibly small coupling rate $\kappa_\mathrm{a,r}/2\pi \simeq 30\,\mathrm{kHz}$. We note that we also use coherent states and shot noise with the spectral density shown in Fig. 5.9 (b) in our experiments. These fields are generated at room temperature with state-of-the-art microwave equipment as discussed in Sec. 4.4.3. We calibrate the photon number of these fields with ac-Stark shift measurements similar to the ones discussed above.

Fundamental coherence properties of the transmon qubit In the absence of external microwave fields and at the flux sweet spot, the qubit is relaxation-limited with average coherence times of approximately 500 ns. In particular, we find typical values of the Ramsey decay rate $\gamma_{2,\mathrm{R}}/2\pi \simeq 2.1\,\mathrm{MHz}$, the spin-echo decay rate $\gamma_{2,\mathrm{se}}/2\pi \simeq 1.9\,\mathrm{MHz}$, and the energy decay (relaxation) rate $\gamma_1/2\pi \simeq 3.9\,\mathrm{MHz}$ [cf. Fig. 5.11 (a) – (c)]. This relaxation rate is a factor of ten larger than the expected Purcell rate and most likely dominated by loss into the $\mathrm{Si/SiO_2}$ substrate and into the on-chip antenna. The above numbers imply a pure dephasing rate $\gamma_\varphi = \gamma_{2,\mathrm{R}} - \gamma_1/2 \simeq 2\pi \times 150\,\mathrm{kHz}$. In general, we find that the irradiation of thermal states onto the qubit increases the decoherence rates, which is discussed in detail in Sec. 5.2.2 – Sec. 5.2.4.

We measure the coupling $\kappa_\mathrm{a,q}$ between antenna and qubit by irradiating the qubit with thermal noise (first-order coupling) through the antenna line. Thermal noise is Gaussian and weak [$\mathcal{S}(\omega) \ll \hbar\omega$] for average photon numbers $n_\mathrm{a} \approx 1$. Hence, we can apply the spin-boson model and Fermi's golden rule as in Sec. 2.4.1 to obtain $\gamma_1 = \mathcal{S}(\omega_\mathrm{q})/2\hbar$. This relation has been widely used to measure the frequency dependence $\mathcal{S}(\omega)$ of different noise sources by tuning the qubit transition frequency [35, 119, 219, 220, 240–243]. Here, we use a complementary approach and vary the magnitude of $\mathcal{S}(\omega_\mathrm{q} = \mathrm{const.})$ in a controlled way by varying the temperature of the black-body radiator (antenna line attenuator). The resulting qubit decay rate

$$\gamma_{1,\mathrm{a}}(T_\mathrm{a}) = \gamma_1 + \kappa_\mathrm{a,q} n_\mathrm{a}(\omega_\mathrm{q},T_\mathrm{a})/2 \equiv \gamma_1 + \delta\gamma_{1,\mathrm{a}}(T_\mathrm{a})\,, \tag{5.2.9}$$

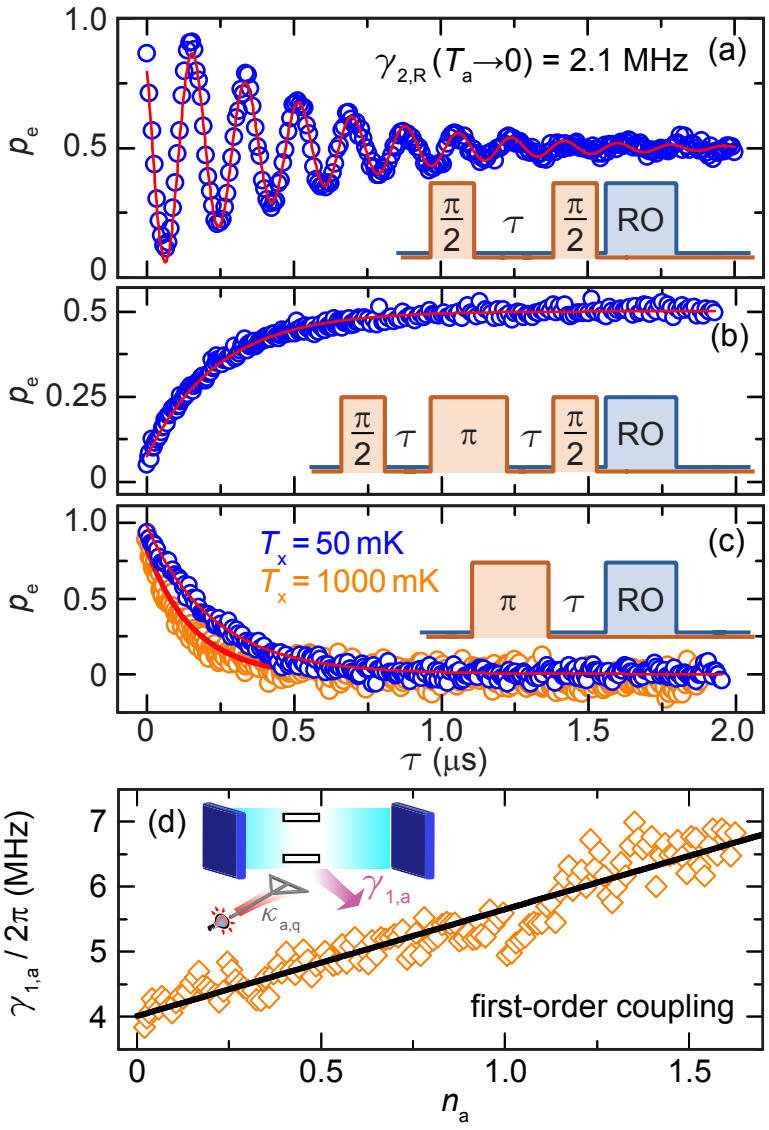

Figure 5.11: **(a)** Probability p_e to find the qubit in the excited state as a function of the free evolution time for the Ramsey pulse sequence (inset). Red envelopes indicate qubit control pulses, blue envelopes the readout pulse to the resonator. The solid lines are fits to the data points (circles). **(b)** As in panel (a), but for the spin-echo sequence. **(c)** As in panel (a), but for the relaxation sequence. T_x indicates the temperature of the readout line attenuator. **(d)** Qubit relaxation rate plotted versus the number of thermal photons emitted from the antenna line attenuator. The solid line is a linear fit and the inset depicts a sketch of the experimental setup.

is enhanced by $\delta\gamma_{1,a}$ compared to the intrinsic decay rate γ_1. We expect $\gamma_{1,a}$ to increase linearly with $\mathcal{S}(\omega_q)$ which is proportional to the average photon number n_a generated in the resonator by the thermal noise applied by the antenna. This is in very good agreement with the experimental data shown in Fig. 5.11 (d). From a linear fit of Eq. (5.2.9) to the data, we obtain the antenna qubit coupling rate $\kappa_{a,q} = 820\,\text{kHz}$, which means that approximately 1/5 of the total qubit relaxation can be attributed to decay into the antenna. The accuracy of the qubit acting as noise spectrometer is limited by the standard deviation $\sigma/2\pi \simeq 215\,\text{kHz}$ of the data obtained from the fit. This scatter can be attributed to additional low-frequency fluctuations of the relaxation rate discussed in detail in Sec. 5.2.4. We want to emphasize that changing the temperature of the thermal noise source has no effect on quasiparticle loss [224, 225] since the sample itself is kept at a constant temperature. Furthermore, radiation that directly generates quasiparticles, i.e., radiation with the gap frequency $\Delta_0/h \simeq 80\,\text{GHz}$ of Al is strongly suppressed in the coaxial cables.

5.2.2 Thermal fields in the dispersive Jaynes-Cummings regime

In contrast to the direct irradiation of the qubit by thermal noise as discussed above, in this section we study the effect of thermal noise, which we apply to the transmon qubit through a superconducting resonator. Then, the resonator acts as a narrow filter for the broadband thermal noise. Since the qubit is far detuned from the resonator frequency ($|\chi| \ll g$), noise couples only in second-order to the qubit, which can be described within the dispersive limit of the Jaynes-Cummings model. There, the power spectral density $\mathcal{S}(\omega_\mathrm{q})$ at the qubit frequency is strongly reduced due to the Lorentzian filter function of the resonator. Hence, we obtain the reduced vacuum Purcell decay rate [244, 247] $\gamma_\mathrm{P} = \kappa_\mathrm{x} g^2/\delta^2 \simeq 2\pi \times 53\,\mathrm{kHz}$. Nevertheless, also the thermal noise spectral density $\mathcal{S}(\omega_\mathrm{r})$ at the resonator frequency couples dispersively to the qubit with the coupling rate χ in second-order approximation [17]. In an elaborate treatment, the broadband nature of thermal fields requires an exact transformation of the dispersive Jaynes-Cummings Hamiltonian, which takes sideband decay into account [52]. This transformation yields the total relaxation rate in the dispersive regime

$$\begin{aligned}\gamma_1^\mathrm{d} = \gamma_1 \left[1 - \frac{|\chi|}{\delta}[2n_\mathrm{r}+1]\right] + \gamma_\mathrm{P}[2n_\mathrm{q}+1] \\ + 4\frac{|\chi|}{\delta}\frac{\mathcal{S}(\delta)}{\hbar} \times [2n_\mathrm{r}+1]\,,\end{aligned} \tag{5.2.10}$$

where the effective photon number at the qubit frequency is defined as $n_\mathrm{q} \equiv \alpha n_\mathrm{th}(\omega_\mathrm{q}, T_\mathrm{x})$. The first term in Eq. (5.2.10) is the main contribution to the total relaxation rate γ_1^d. The second term describes the Purcell decay rate due to the noise power $\mathcal{S}(\omega_\mathrm{q})$ at the qubit frequency. The last term accounts for a sideband decay resulting from the combined action of resonator photons at ω_r and thermal noise photons at $\delta \equiv \omega_\mathrm{q} - \omega_\mathrm{r} \simeq 850\,\mathrm{MHz}$ as shown in Fig. 5.12 (a). Interestingly, a reduction of the decay rate can be obtained with increasing resonator photon number n_r if $\gamma_1 > 4\mathcal{S}(\delta)/\hbar$ due to the mixing of qubit and resonator states [52].

Sideband spectral density and reduced qubit decay For a finite spectral density $\mathcal{S}(\delta)$, there can be sideband decay of the qubit as depicted in Fig. 5.12 (a). We calibrate the strength of the spectral density $\mathcal{S}(\delta)$ by selectively driving at the resonator frequency, which changes n_r while leaving n_q and $\mathcal{S}(\delta)$ in Eq. (5.2.10) constant. To this end, we use a coherent drive at the resonator frequency, and measure the change of the relaxation rate

$$\delta\gamma_{1,\mathrm{r}}(n_\mathrm{r}) = 2n_\mathrm{r}\frac{|\chi|}{\delta}\left[\frac{4\mathcal{S}(\delta)}{\hbar} - \gamma_1\right], \tag{5.2.11}$$

which is obtained by keeping only the n_r-dependent terms on the right hand side of Eq. (5.2.10). Equation (5.2.11) directly shows that for $4\mathcal{S}(\delta)/\hbar < \gamma_1$, we can reduce the qubit relaxation rate. As shown in Fig. 5.12 (b), we observe this decrease of the qubit relaxation rate for a coherent state that changes the resonator population in a controlled way. Using a numerical fit based on Eq. (5.2.11), we find a spectral density $\mathcal{S}(\delta) \simeq 1.32 \times 10^{-28}\,\mathrm{W/Hz}$. We obtain the same result when irradiating the resonator with shot noise that has a spectral density as shown in Fig. 5.9 (b). We note that the overall qubit decoherence rate given by $\gamma_2 = \gamma_\varphi + \gamma_1/2$ is nevertheless increasing due to the additional dephasing from photon shot noise as discussed in detail in Sec. 6.1.

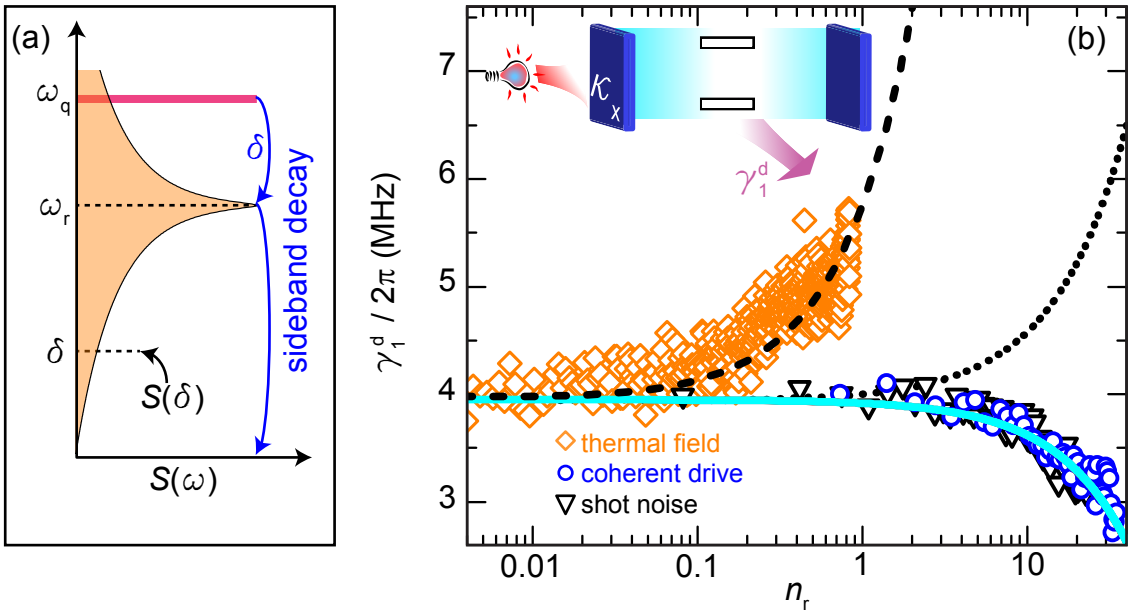

Figure 5.12: **(a)** Schematic drawing of sideband decay due to a finite noise power spectral density $\mathcal{S}(\delta)$ at the detuning frequency $\delta = \omega_\mathrm{q} - \omega_\mathrm{r}$. **(b)** Qubit relaxation rate for microwave fields coupling to the qubit through the resonator (see inset for setup sketch) plotted versus the average photon number n_r. The solid line is a numerical fit using Eq. (5.2.11). The dotted line is a calculation based on Eq. (5.2.10) modeling the expected increase due to thermal fields. For the dashed line we use a numerical fit of Eq. (5.2.10), where the enhanced relaxation rate is modeled by $n_\mathrm{q}(T_\mathrm{x})$ as a free parameter.

Broadband dispersive coupling When we apply broadband thermal fields through the resonator input, we experimentally verify the three competing mechanisms present in Eq. (5.2.11). First, the increasing noise power spectral density $\mathcal{S}(\omega_\mathrm{r})$ at the resonator frequency is reducing qubit relaxation due to the mixing of qubit and resonator states as discussed already above. Second, the increasing noise power spectral density at the qubit transition frequency attenuated by the Purcell filtering of the resonator, $\mathcal{S}(\omega_\mathrm{q})\mathcal{F}_\mathrm{L}(\omega_\mathrm{q})$, causes additional relaxation. Third, the increasing noise power spectral density at the detuning frequency δ attenuated by the Purcell filtering effect, $\mathcal{S}(\delta)\mathcal{F}_\mathrm{L}(\delta)$, causes additional relaxation. This mechanism can be viewed as a sideband decay. Hence, the overall relaxation rate increases with increasing number of thermal photons stored inside the resonator as shown in Fig. 5.12 (b). When comparing the measured total relaxation rate γ_1^d with a calculation according to Eq. (5.2.10) [dotted line in Fig. 5.12 (b)], we find that the measured decay rate is significantly larger than expected. Hence, we fit Eq. (5.2.10) to the data and use $n_\mathrm{q}(T_\mathrm{x})$ as a free parameter [dashed line in Fig. 5.12 (b)]. We find that the coupling of the thermal noise fields to the qubit is enhanced by a factor of 10. Because the qubit is galvanically decoupled from the resonator and the sample is stabilized at 35 mK, this additional coupling is most likely mediated by parasitic modes of the sample box [240, 469]. Among others, such modes can be slotline, parallel plane, and surface wave modes with resonance frequencies close to the qubit transition frequency. Our results show that this mechanism originating from the broadband nature of the noise fields can dominate over the Purcell rate originating from the finite bandwidth of the resonator. Therefore, great care must be taken in the microwave design of sample holders and chip layout in order to minimize losses from broadband fields.

5.2.3 Dephasing from thermal fields

In addition to the relaxation processes discussed above, the qubit can suffer from dephasing due to propagating thermal fields, even if the resonator filters them. The main contribution in this context is photon shot noise [24, 275, 467], which introduces dephasing by modulating the qubit frequency via the ac-Stark shift. We analyze the effect of photon shot noise due to thermal fields on the readout line for our sample in detail in Sec. 6.1. Here, we focus on dephasing caused by second-order intensity fluctuations of the thermal fields emitted from the heatable attenuator in the antenna line. The thermal noise fields themselves as current fluctuations on the short-circuited on-chip antenna, which couple magnetic flux noise into the SQUID loop of the transmon qubit [see Fig. 5.13]. Far away from the flux sweet spot, the qubit dephasing is dominated by the first-order noise power spectral density $\mathcal{S}(\omega \mapsto 0)$ defined in Eq. (5.2.1) due to the finite first-order transfer function. At the flux sweet spot, however, the first-order transfer function vanishes while second-order fluctuations can still introduce dephasing. These fluctuations are characterized by the second-order power spectral density $\mathcal{S}^{(2)}(\omega)$ defined in Eq. (5.2.2).

Coupling of thermally induced flux fluctuations First-order coupling between flux fluctuations $\delta\lambda \equiv \delta\Phi/\Phi_0$ and the qubit follow the Hamiltonian $\mathcal{H}_{\mathrm{sys}} = [\hbar/2][\omega_{\mathrm{q}}\hat{\sigma}_{\mathrm{z}} + \delta\omega_{\mathrm{q}}\hat{\sigma}_{\mathrm{z}}]$. Here, $\delta\omega_{\mathrm{q}} = \delta\lambda\mathcal{D}^{(1)}_{\lambda,\mathrm{z}}$ describes fluctuations of the qubit transition frequency leading to dephasing characterized by the first-order transfer function

$$\mathcal{D}^{(1)}_{\lambda,\mathrm{z}}(\lambda^\star) \equiv \frac{1}{\hbar}\left.\frac{\partial\mathcal{H}_{\mathrm{q}}(\lambda)}{\partial\lambda}\right|_{\lambda^\star} = -\left.\frac{\pi\omega_{\mathrm{q},0}}{2}\frac{\sin(\pi\lambda)}{\sqrt{\cos(\pi\lambda)}}\right|_{\lambda^\star}. \tag{5.2.12}$$

shown in Fig. 5.14 (a). Equation (5.2.12) is defined at flux operating points $\lambda^\star \in [-1/2, 1/2]$ using the transmon qubit Hamiltonian $\mathcal{H}_{\mathrm{q}} = \hbar\omega_{\mathrm{q},0}\sqrt{|\cos(\pi\lambda)|}$. To analyze the fluctuations $\delta\omega_{\mathrm{q}}$, we first derive how voltage fluctuations δV on the antenna line are converted into flux fluctuations $\delta\lambda$ in the SQUID loop. Because the antenna is short-circuited near the qubit by a finite inductance L_{a} as depicted in Fig. 5.13, we describe it as a first-order low-pass LR filter, i.e., $Z_{\mathrm{a}}(\omega) \approx \omega^2 L_{\mathrm{a}}^2/Z_0$ (similar to the way presented in Ref. 210). The finite inductance L_{a} of the short-circuit converts voltage fluctuations δV emitted from the attenuator into current fluctuations $\delta I = \delta V(\imath\omega L_{\mathrm{a}})^{-1}$. Via the mutual inductance M_{a} between antenna and SQUID loop, these current fluctuations cause flux fluctuations $\delta\lambda = M_{\mathrm{a}}\delta I/\Phi_0$. Using the transfer function in Eq. (5.2.12), we calculate the resulting change in transition frequency to

$$\delta\omega_{\mathrm{q}}(\lambda^\star) = \mathcal{D}^{(1)}_{\lambda,\mathrm{z}}(\lambda^\star) \times \delta\lambda = \mathcal{D}^{(1)}_{\lambda,\mathrm{z}}(\lambda^\star)\frac{M_{\mathrm{a}}}{\Phi_0}\frac{\delta V}{\imath\omega L_{\mathrm{a}}}. \tag{5.2.13}$$

This equation shows that thermally induced voltage fluctuations indeed lead to fluctuations $\delta\omega_{\mathrm{q}}$ of the qubit transition frequency. To calculate the resulting dephasing rate we use the spectral function

$$\begin{aligned}\langle\delta\omega_{\mathrm{q}}(t)\delta\omega_{\mathrm{q}}(0)\rangle_\omega &= \left[\frac{\mathcal{D}^{(1)}_{\lambda,\mathrm{z}}(\lambda^\star)M_{\mathrm{a}}}{\omega L_{\mathrm{a}}\Phi_0}\right]^2\langle\delta V(t)\delta V(0)\rangle_\omega \\ &= \left[\frac{\mathcal{D}^{(1)}_{\lambda,\mathrm{z}}(\lambda^\star)M_{\mathrm{a}}}{\omega L_{\mathrm{a}}\Phi_0}\right]^2 \mathrm{Re}\{Z_{\mathrm{a}}(\omega)\}\mathcal{S}(\omega) = \left[\mathcal{D}^{(1)}_{\lambda,\mathrm{z}}(\lambda^\star)\frac{M_{\mathrm{a}}}{\Phi_0}\right]^2\frac{\mathcal{S}(\omega)}{Z_0}\end{aligned} \tag{5.2.14}$$

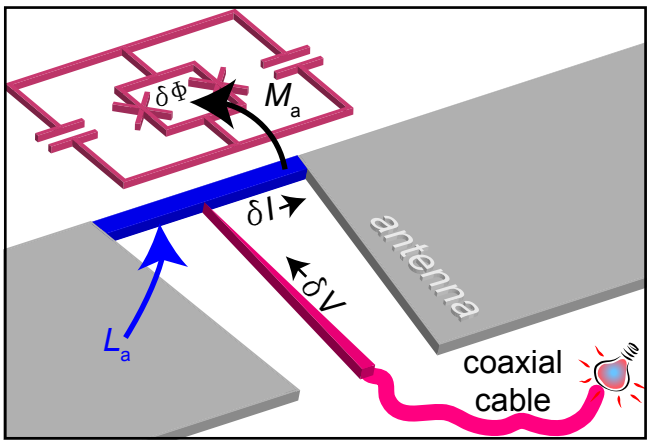

Figure 5.13: Sketch of the short-circuited antenna line, which converts voltage fluctuations δV into flux fluctuations $\delta\Phi$ inside the SQUID loop of the transmon. The region forming the short-circuit has an inductance L_a and a mutual inductance M_a to the SQUID loop. The propagating thermal fields are guided through a coaxial cable to the sample and are thus only located on the antenna structure.

of these fluctuations. Here, we use the well-known fluctuation dissipation theorem [429, 470] $\langle\delta V(t)\delta V(0)\rangle_\omega = \mathrm{Re}\{Z_\mathrm{a}(\omega)\}\mathcal{S}(\omega)$ to relate the voltage fluctuations to their power spectral density. The expression $\langle\delta V(t)\delta V(0)\rangle_\omega$ displays the spectral weight of the fluctuations with units V^2/Hz. The fluctuations of the qubit transition frequency defined in Eq. (5.2.14) lead to random fluctuations $\delta\varphi(t) = \int_0^t \mathrm{d}t'\delta\omega_\mathrm{q}(t')$ of the qubit phase relative to its mean phase $\bar{\varphi}$ in a rotating frame. Assuming thermal states to be Gaussian [235, 464] and $1/f$ contributions to be negligible, the phase fluctuations in turn lead to a single exponential decay function [168]

$$\begin{aligned}\langle\hat{\sigma}_-(t)\hat{\sigma}_+(0)\rangle &\approx \exp\left[-\gamma_2 t - \langle\delta\varphi^2\rangle/2\right] \\ &= \exp\left[-\gamma_2 t - \frac{1}{2}\int\int_0^t \mathrm{d}t_1\,\mathrm{d}t_2\langle\delta\omega_\mathrm{q}(t_1)\delta\omega_\mathrm{q}(t_2)\rangle\right] \\ &= \exp\left[-\gamma_2 t - \frac{1}{2}\left[\mathcal{D}^{(1)}_{\lambda,\mathrm{z}}(\lambda^\star)\frac{M_\mathrm{a}}{\Phi_0}\right]^2\frac{\mathcal{S}(\omega)}{Z_0}t\right]. \end{aligned} \tag{5.2.15}$$

Here, we make use of the fact that the correlation function $\langle\delta\omega_\mathrm{q}(t_1)\delta\omega_\mathrm{q}(t_2)\rangle$ is a δ-function at low frequencies (see Sec. 2.4.2). The additional decoherence due to thermal states on the antenna line is therefore given as

$$\gamma^{(1)}_{\varphi,\mathrm{a}} = \left[\mathcal{D}^{(1)}_{\lambda,\mathrm{z}}(\lambda^\star)\frac{M_\mathrm{a}}{\Phi_0}\right]^2\frac{\mathcal{S}(\omega)}{2Z_0} \approx \left[\mathcal{D}^{(1)}_{\lambda,\mathrm{z}}(\lambda^\star)\frac{M_\mathrm{a}}{\Phi_0}\right]^2\frac{k_\mathrm{B}T_\mathrm{a}}{Z_0}. \tag{5.2.16}$$

The approximation on the right-hand side of Eq. (5.2.16) reflects the low-frequency limit by setting $\mathcal{S}(\omega\mapsto 0) = k_\mathrm{B}T_\mathrm{a}$, which shows that dephasing due to propagating thermal fields is expected to increase linearly with the temperature T_a of the black-body radiator.
The above derivation of the qubit dephasing rate is equivalent to the result derived from the spin-boson model, where the dephasing is defined as [210] $\gamma^{(1)}_{\varphi,\mathrm{a}} = 2\pi\alpha\mathcal{S}(\omega\mapsto 0)/\hbar$. Here, the dimensionless dissipation parameter α is defined as [464]

$$\alpha = \frac{R_\mathrm{q}}{Z_0}\left[\hbar\mathcal{D}^{(1)}_{\lambda,\mathrm{z}}(\lambda^\star)\frac{\partial\lambda}{\partial\Phi}\frac{M_\mathrm{a}}{\Phi_0}\right]^2 = \frac{\hbar}{2\pi Z_0}\left[\mathcal{D}^{(1)}_{\lambda,\mathrm{z}}(\lambda^\star)\frac{M_\mathrm{a}}{\Phi_0}\right]^2 \tag{5.2.17}$$

and $R_\mathrm{q} \equiv h/4e^2$ is the quantum resistance for Cooper pairs. We note that the spin-boson model can be applied to calculate the dephasing rate because the antenna creates an ohmic environment if modeled as an LR-filter and because thermal noise has no $1/f$ contribution.

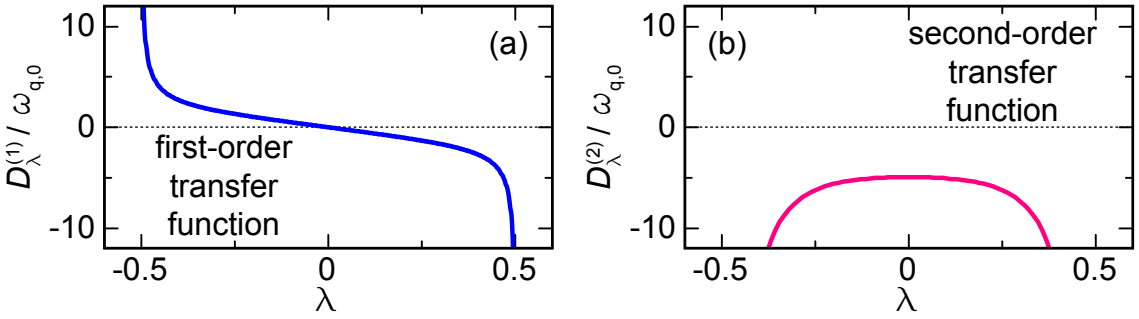

Figure 5.14: **(a)** First-order transfer function plotted versus the normalized control parameter $\lambda = \Phi/\Phi_0$. **(b)** Second-order transfer function plotted versus the control parameter λ.

Coupling of thermally induced intensity fluctuations When the transmon qubit is operated at the flux sweet spot, dephasing can be dominated from intensity fluctuations coupling in second-order to the qubit. These second-order fluctuations

$$\delta\lambda^2 \equiv \frac{\delta\Phi^2}{\Phi_0^2} = \frac{M_\mathrm{a}^{(2)}\delta I^2}{\hbar\omega_{\mathrm{q},0}} = \frac{M_\mathrm{a}^2}{L_\ell}\frac{\delta I^2}{\hbar\omega_{\mathrm{q},0}} \tag{5.2.18}$$

are normalized to the relevant energy scale $\hbar\omega_{\mathrm{q},0}$ of the qubit and scale with the second-order mutual inductance $M_\mathrm{a}^{(2)} = M_\mathrm{a}^2/L_\ell$ due to the inductive energy $E_\ell = \Phi_0^2/2L_\ell$ of the SQUID loop with inductance L_ℓ. The intensity fluctuations induce fluctuations $\delta\omega_\mathrm{q} = \mathcal{D}_{\lambda,\mathrm{z}}^{(2)}\delta\lambda^2/2$ of the qubit transition frequency leading to dephasing based on the system Hamiltonian $\mathcal{H}_\mathrm{sys}$ defined in the previous paragraph. The frequency fluctuations are characterized by the second-order derivative of the qubit transition frequency

$$\mathcal{D}_{\lambda,\mathrm{z}}^{(2)}(\lambda^\star) \equiv \frac{1}{\hbar}\frac{\partial^2\mathcal{H}_\mathrm{q}(\lambda)}{\partial\lambda^2}\bigg|_{\lambda=\lambda^\star} = -\frac{\pi^2\omega_{\mathrm{q},0}}{2}\sqrt{\cos(\pi\lambda)} - \frac{\pi^2\omega_{\mathrm{q},0}}{4}\frac{\sin^2(\pi\lambda)}{\cos^{3/2}(\pi\lambda)}\bigg|_{\lambda=\lambda^\star} \tag{5.2.19}$$

shown in Fig. 5.14 (b). Using this transfer function as well as $\delta V^2 = (\omega L_\mathrm{a})^2\delta I^2$, we can characterize fluctuations in the qubit transition frequency similar to Eq. (5.2.14) as

$$\begin{aligned}
\langle\delta\omega_\mathrm{q}(t)\delta\omega_\mathrm{q}(0)\rangle_\omega &= \left[\frac{\mathcal{D}_{\lambda,\mathrm{z}}^{(2)}(\lambda^\star)}{2}\right]^2\langle\delta\lambda^2(t)\delta\lambda^2(0)\rangle_\omega \\
&= \left[\frac{\mathcal{D}_{\lambda,\mathrm{z}}^{(2)}(\lambda^\star)}{2}\frac{M_\mathrm{a}^2}{L_\ell}\frac{1}{\omega^2L_\mathrm{a}^2}\right]^2\frac{\langle\delta V^2(t)\delta V^2(0)\rangle_\omega}{(\hbar\omega_{\mathrm{q},0})^2} \\
&= \left[\frac{\mathcal{D}_{\lambda,\mathrm{z}}^{(2)}(\lambda^\star)}{2}\frac{M_\mathrm{a}^2}{L_\ell}\frac{1}{\omega^2L_\mathrm{a}^2}\right]^2\mathrm{Re}\{Z_\mathrm{a}(\omega)\}^2\frac{\mathcal{S}^{(2)}(\omega)}{(\hbar\omega_{\mathrm{q},0})^2} \\
&= \left[\frac{\mathcal{D}_{\lambda,\mathrm{z}}^{(2)}(\lambda^\star)}{2}\frac{M_\mathrm{a}^2}{L_\ell}\right]^2\frac{\mathcal{S}^{(2)}(\omega)}{(\hbar\omega_{\mathrm{q},0})^2Z_0^2}\,.
\end{aligned} \tag{5.2.20}$$

where $\mathcal{S}^{(2)}(\omega)$ is the second-order spectral density defined in Eq. (5.2.2). To derive the dephasing rate using Eq. (5.2.20), we have to consider the statistical properties of $\mathcal{S}^{(2)}(\omega)$. Because the intensity fluctuations are not Gaussian distributed [464], applying an approach

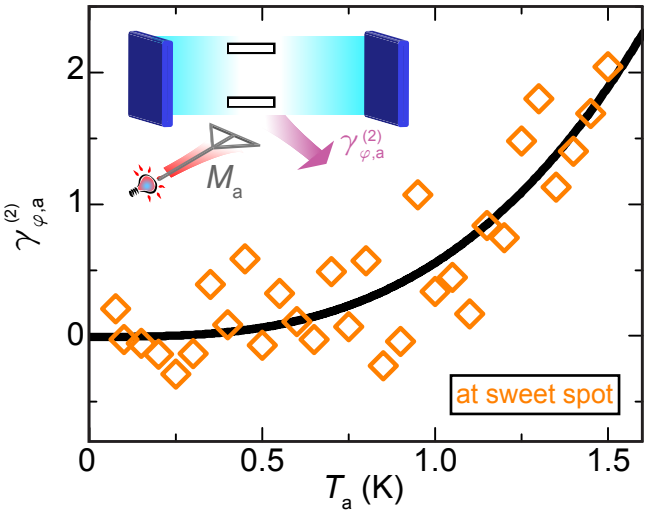

Figure 5.15: Thermally induced qubit dephasing rate $\gamma^{(2)}_{\varphi,\mathrm{a}}(T_\mathrm{a})$ measured as a function of the temperature T_a of the black-body radiator as depicted in the inset. To isolate second-order effects, we operate the qubit at the flux sweet spot of the transmon qubit. The solid line is a numerical fit using Eq. (5.2.22).

similar to the one in Eq. (5.2.15) to calculate the dephasing rate from second-order thermal fields is not valid in general. Performing only first-order pertubative analysis, we can, however, assume that the second-order fluctuations are Gaussian distributed with a width that is defined by $\mathcal{S}^{(2)}(\omega)$. Then, we find the additional dephasing rate due to second-order noise

$$\gamma^{(2)}_{\varphi,\mathrm{a}} = \left[\frac{\mathcal{D}^{(2)}_{\lambda,\mathrm{z}}(\lambda^\star)}{2}\frac{M_\mathrm{a}^2}{L_\ell}\right]^2 \frac{\mathcal{S}^{(2)}(\omega)}{(\hbar\omega_{\mathrm{q},0})^2 Z_0^2} \approx \underbrace{\left[\frac{\mathcal{D}^{(2)}_{\lambda,\mathrm{z}}(\lambda^\star)}{2\sqrt{3}}\frac{M_\mathrm{a}^2}{L_\ell Z_0}\right]^2}_{\alpha^{(2)}} \underbrace{\left[\frac{k_\mathrm{B}T_\mathrm{a}}{\hbar\omega_{\mathrm{q},0}}\right]^2}_{r} \frac{2\pi k_\mathrm{B}T_\mathrm{a}}{\hbar}, \tag{5.2.21}$$

taking the low-frequency limit $\mathcal{S}^{(2)}(\omega\mapsto 0)\approx 2\pi k_\mathrm{B}^3 T_\mathrm{a}^3/3\hbar$ obtained from Eq. (5.2.2). Just as the first-order dephasing rate, the second-order dephasing rate is equivalent to an approach based on the spin-boson model when using the second-order dissipation factor $\alpha^{(2)}$. When comparing Eq. (5.2.21) to Eq. (5.2.16), we see that second-order thermal noise is suppressed by the factor r if the thermal energy is lower than the qubit energy. Hence, we have to use temperatures $T_\mathrm{a} > \hbar\omega_{\mathrm{q},0}/k_\mathrm{B}$ or work at the flux sweet spot to observe the T^3 law.

Dephasing from second-order noise We discuss dephasing from second-order noise based on decoherence measurements at the flux sweet spot, i.e., $\lambda^\star \simeq 0$ where the qubit is insensitive to first-order flux noise. At this operating point, the second-order transfer function $\mathcal{D}^{(2)}_{\lambda,\mathrm{z}} = \pi^2\omega_{\mathrm{q},0}/2$ is relevant and we find the thermally induced qubit dephasing rate [cf. Eq. (5.2.21)]

$$\gamma^{(2)}_{\varphi,\mathrm{a}}(T_\mathrm{a}) = 2\pi\left[\frac{\pi^2}{4\sqrt{3}}\frac{M_\mathrm{a}^2}{L_\ell Z_0}\right]^2\left[\frac{k_\mathrm{B}T_\mathrm{a}}{\hbar}\right]^3, \tag{5.2.22}$$

which follows a T_a^3 dependence. Here, M_a describes the mutual inductance between qubit and antenna, L_ℓ is the inductance of the SQUID loop, and Z_0 is the line impedance. In Fig. 5.15, we plot the qubit dephasing rate $\gamma^{(2)}_{\varphi,\mathrm{a}}(T_\mathrm{a}) = \gamma_{2,\mathrm{R}}(T_\mathrm{a}) - \gamma_{2,\mathrm{R}}(T_\mathrm{a}\mapsto 0) - \delta\gamma_{1,\mathrm{a}}(T_\mathrm{a})/2$ caused by the intensity fluctuations of the thermal noise field at the flux sweet spot of the transmon qubit. The temperature independent decay rate $\gamma_{2,\mathrm{R}}(T_\mathrm{a}\mapsto 0)$ and the thermally induced relaxation rate $\delta\gamma_{1,\mathrm{a}}(T_\mathrm{a})$ are discussed in Sec. 5.2.1 [see Fig. 6.2 (a) and Fig. 6.2 (d), respectively]. The additional dephasing rate follows the expected T_a^3 dependence with a

scatter that is dominated by additional low-frequency fluctuations of the decay rate discussed in Sec. 5.2.4. Fitting Eq. (5.2.22) to the data, we find a loop inductance $L_\ell \simeq 50\,\mathrm{pH}$ which is in reasonable agreement with the value of 100 pH estimated from the loop geometry. Here, we have used the mutual inductance $M_\mathrm{a} = 1.3\,\mathrm{pH}$ obtained from measuring the induced flux shift of the qubit when applying a DC current through the antenna line. Our results show that second-order flux noise can induce residual dephasing in a transmon qubit, even if it is operated at the flux sweet spot. For typical temperatures ($T_\mathrm{a} < 50\,\mathrm{mK}$) used in circuit QED experiments, however, we find that additional intensity fluctuations introduce only negligible dephasing of approximately 100 Hz because of the quadratic suppression $(k_\mathrm{B}T_\mathrm{a}/\hbar\omega_{\mathrm{q},0})^2$ [cf. Eq. (5.2.21)]. Nevertheless, dephasing is not only determined by the relatively weak thermal contribution but also by stronger $1/f$ noise [33, 219]. Because $1/f$ noise also has a second-order contribution [235], our results show that this noise can be a possible source for the residual dephasing found for transmon qubits.

5.2.4 Fluctuating qubit parameters in the presence of thermal fields

In the following, we study the effect of thermal fields on the frequency spectrum of fluctuating qubit parameters. In particular, we analyze low-frequency variations of the relaxation rate of a transmon qubit. This phenomenon was also observed for flux qubits [465, 466], for transmon qubits in a 3D cavity and phase qubits [248], as well as for the resonance frequency of superconducting resonators [249]. One particular mechanism that can generate low-frequency fluctuations are TLSs [248, 250] in the spatial vicinity of the qubit. The fluctuation rate of the TLSs is influenced by the thermal field as depicted in Fig. 5.16.
Each individual TLS provides a Lorentzian shaped noise spectral density, which is centered around its excitation frequency $\omega_\mathrm{tls} = \sqrt{\varepsilon^2 + \Delta^2}$. Here, ε is the asymmetry energy and Δ is the tunnel splitting (see Sec. 2.4.2 for details). Because the TLSs are coupled to each other via dipole or strain-mediated interaction [471], each TLS eigenfrequency depends on the state of the other TLSs. The low-frequency variations of the TLS configuration results in low-frequency fluctuations of the noise power spectral density $\mathcal{S}(\omega_\mathrm{q},t)$ generated by the TLSs. Consequently, the qubit relaxation rate $\gamma_1(t) = \mathcal{S}(\omega_\mathrm{q},t)/2\hbar$ starts fluctuating. Since qubit parameter fluctuations are typically recorded in the sub-Hz regime where $\hbar\omega \ll k_\mathrm{B}T$, we assume a white spectrum proportional to $k_\mathrm{B}T$ for the contribution of the environmental heat bath. For a distribution $P(\varepsilon,\Delta)\,\mathrm{d}\varepsilon\,\mathrm{d}\Delta \propto \varepsilon^x \Delta^{-1}\,\mathrm{d}\varepsilon\,\mathrm{d}\Delta$ of TLSs, we expect a T^{2+x}-dependence to be the dominant contribution to the spectrum of γ_1 [248]. This contribution arises from those TLSs, which are detuned by $\delta\omega \equiv |\omega_\mathrm{q} - \omega_\mathrm{tls}| \gg \gamma_{2,\mathrm{R}}$. The exponent $x \geq 0$ is nonzero only for a finite interaction between the TLSs [248].
We experimentally characterize the fluctuations of the noise power spectral density by measuring fluctuations of the qubit relaxation rate $\gamma_1(t)$. To this end, we perform systematic long-time measurements of the relaxation rate as a function of the temperatures T_x and

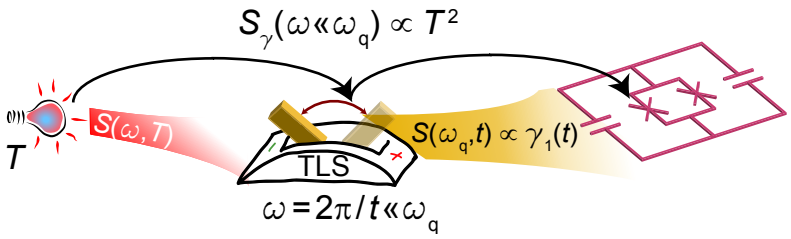

Figure 5.16: TLS-mediated relaxation rate fluctuations. The thermal field influences the TLS fluctuation rate causing fluctuations of the noise power spectral density $\mathcal{S}(\omega_\mathrm{q},t)$.

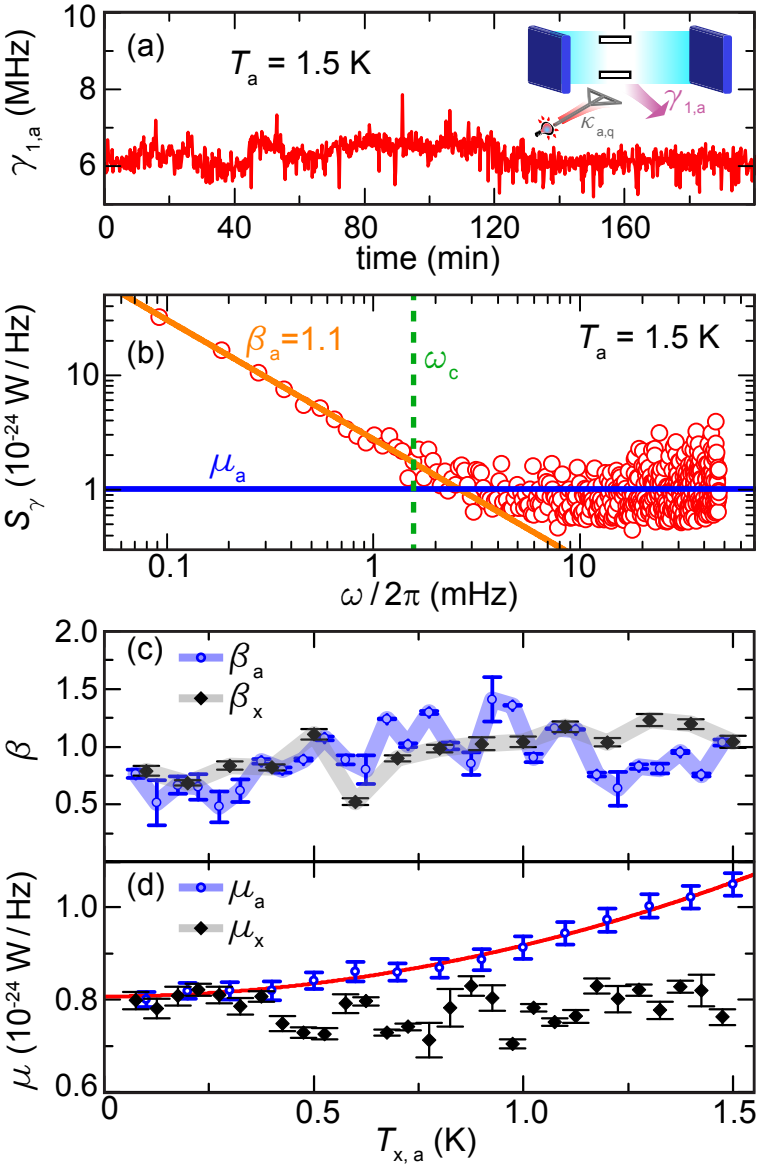

Figure 5.17: **(a)** Qubit relaxation rate recorded as a function of time recorded over a period of 200 min at $T_a = 1.5\,\mathrm{K}$. **(b)** Noise power spectral density for the data shown in panel (a). We obtain β from a fit to the data with frequencies below ω_c and μ as the mean value for points above ω_c. **(c)** Exponent β measured for $\omega < \omega_c$ versus temperature when applying thermal fields through the antenna or the resonator. Solid lines are guides to the eyes and error bars represent confidence intervals generated by the $\omega^{-\beta}$ fits. **(d)** Mean value μ of the white-noise contribution of thermal fields entering via the antenna or the resonator to $\mathcal{S}_\gamma$. The solid line is a fit as explained in text and error bars are the standard error of the mean.

of T_a ranging from 50 mK to 1500 mK. Each measurement is comprised of individual measurement traces taken at a repetition rate of 100 kHz, where the resonator is probed with 2 µs long traces with 250 MHz sampling rate. We average 4×10^5 of these measurements to extract the decay rate at a particular moment and then wait for 6 s such that individual data points are recorded at a rate of approximately 0.1 Hz. A typical series of relaxation measurements at $T_a = 1500\,\mathrm{mK}$ over 200 min is shown in Fig. 5.17 (a). Here, we observe a standard deviation $\sigma/2\pi \simeq 320\,\mathrm{kHz}$ from the mean relaxation rate $\langle\gamma_1\rangle/2\pi \simeq 6.25\,\mathrm{MHz}$. Even though the absolute value of σ seems large compared to other works [248], the relative scatter $\sigma/\langle\gamma_1\rangle \simeq 0.05$ is comparable. In our experiments, we observe no systematic influence of the temperature on σ for sweeps of T_a or T_x. To obtain more insight into the nature of the fluctuations, we investigate their spectral distribution. To this end, we calculate the Fourier transform $\mathcal{S}_\gamma(\omega) = \hbar/2\pi \int \mathrm{d}t\, \langle\gamma_1(t)\gamma_1(0)\rangle e^{-i\omega t}$ of the autocorrelation function $\langle\gamma_1(t)\gamma_1(0)\rangle$ as shown in Fig. 5.17 (b). For low frequencies, the data follows a $\omega^{-\beta}$-dependence, and crosses over into a frequency-independent tail for frequencies larger than a

characteristic frequency $\omega_c \simeq 1\,\mathrm{mHz}$. As shown in Fig. 5.17 (c), we find that $\beta_a \simeq 0.91 \pm 0.24$ and $\beta_x \simeq 0.96 \pm 0.19$ are approximately constant for thermal fields applied through antenna or resonator, respectively. This result is an extension of recent findings presented in Ref. 465, where $1/f$ fluctuations were analyzed up to a maximum temperature of 200 mK. Let us now turn to the white-noise contribution μ_a above the characteristic frequency ω_c exemplarily shown in Fig. 5.17 (c) and sytematically plotted as a function of the antenna line attenuator in Fig. 5.17 (d). We observe an increase of μ_a with the temperature T_a. From a numerical fit based on the function $\mu_a = \mu_{a0} + aT_a^{2+x}$, we find $\mu_{a0} = 0.81 \times 10^{-24}\,\mathrm{W/Hz}$, $a = 1.1 \times 10^{-25}\,\mathrm{W/(Hz\,K^2)}$, and $x = -0.01 \pm 0.13$. Hence, our results support the model presented in Ref. 248 where a bath of TLSs acts as a source for the fluctuations in the qubit relaxation rate. In particular, the negligible value of $x \simeq 0$ indicates that the TLSs relevant for our experiments are noninteracting. In contrast to μ_a, the white noise level μ_x is approximately independent of the thermal field [see Fig. 5.17 (d)]. In this case, the resonator filters the thermal fields and protects the TLSs from the external noise. Hence, from this model, a small resonator bandwidth and well-filtered feedlines are necessary in order to suppress externally activated switching of two-level fluctuators.

In summary, we have characterized the influence of propagating thermal microwaves onto second-order decoherence mechanisms of a transmon qubit in a resonator. Because we spatially and thermally separate the thermal emitter from the circuit QED sample, we are able to separate the influence of the thermal noise from the remaining loss channels of the qubit. This allows us to quantify three different second-order decoherence mechanisms. First, for the dispersive regime we find that the additional relaxation rate due to thermal fields applied via the resonator is larger than expected from Purcell filtering. This is a strong hint to the relevance of additional coupling channels such as parasitic on-chip modes. Second, we observe the expected T^3 dependence for the additional dephasing due to second-order noise at the flux sweet spot. This finding may explain the residual dephasing rates found for superconducting qubits with long coherence times. Finally, we investigate the influence of thermal fields on the low-frequency spectrum of qubit parameter fluctuations. We find that thermal fields enhance the white contribution of the noise power spectral density if applied broadband via an on-chip antenna. Our data confirms a model of thermally activated TLSs interacting with the qubit. The resonator, however, can filter this effect efficiently.

Chapter 6
Fundamental properties of microwave light

In this chapter, we study fundamental properties of propagating microwave states of light. First, in Sec. 6.1, we measure the photon statistics of weak thermal fields using two independent approaches. While the first method is based on a circuit QED architecture, the second method is a direct measurement of field correlations. Second, in Sec. 6.2, we explore the parity of interaction operators using shapeable microwave states. We achieve this by probing the manifold selection rules for a quadrupolar two-level system.

6.1 Photon statistics of weak thermal propagating microwaves

In this section, which is based on Ref. 41, we experimentally confirm the theoretically expected photon number variance $\mathrm{Var}(n)$ of thermal microwave fields for $0.05 \lesssim n \lesssim 1.5$ using two fundamentally distinct experimental setups. To this end, we first use a superconducting transmon qubit [40] interacting with the propagating fields via a dispersively coupled microwave resonator. Differently to approaches relying on the coherent dynamics [472–474], where decoherence is detrimental, the additional qubit dephasing rate induced by the field directly reflects the photon number variance in our experiments. We furthermore get access to finite time correlations for Poissonian noise fields due to the different decay constant of the photon-photon correlator. In particular, we find the expected factor of two between the dephasing rates caused by coherent states and shot noise. With the second setup, we extract the super-Poissonian photon statistics of propagating thermal microwaves from direct correlation measurements and from measurements using a near-quantum-limited Josephson parametric amplifier (JPA) [152, 475] as preamplifier. The results show that the noise added by the JPA inevitably alters the photon statistics of the amplified field. Our results provide a quantitative picture of propagating thermal microwaves, which is especially relevant for the characterization of more advanced quantum states in the presence of unavoidable thermal background fields. With respect to superconducting qubits, we gain systematic insight into a dephasing mechanism which may become relevant for state-of-the-art devices with long coherence times [246, 466].

6.1.1 Experimental idea

As propagating electromagnetic fields in general [11, 12, 14], propagating microwaves with photon numbers on the order of unity are essential for quantum computation [476, 477], communication [478], and illumination [479–482] protocols. Because of their omnipresence in experimental setups, the characterization of thermal states is especially relevant for many applications [483–486]. Specifically in the microwave regime, sophisticated experimental techniques for their generation at cryogenic temperatures, their manipulation, and detection have been developed in recent years. In this context, an important aspect is the generation of propagating thermal microwaves using thermal emitters [157, 440, 443]. These emitters can be spatially separated from the setup components used for manipulation and detection [139, 163], which allows one to individually control the emitter and the setup temperature. Due to the low energy of microwave photons, the detection of these fields typically requires the use of near-quantum-limited amplifiers [152, 487–489], cross-correlation detectors [139, 443, 489, 490], or superconducting qubits [39, 467, 491].

The unique nature of propagating fields is reflected in their photon statistics, which is described by a probability distribution either in terms of the number states or in terms of cumulants. The former were studied by coupling the field to an atom or qubit and measuring the coherent dynamics [472–474] or by spectroscopic analysis [492]. The cumulant-based approach, in practice, requires knowledge on the average photon number n and its variance $\mathrm{Var}(n)$ to distinguish many states of interest. To this end, the second-order correlation function $g^{(2)}(\tau)$ has been measured to analyze the photon statistics of thermal [155, 156, 158] or quantum [159–161] emitters ever since the ground-breaking experiments of Hanbury Brown and Twiss [153, 493]. While these experiments use the time delay τ as control parameter, at microwave frequencies the photon number n can be controlled conveniently [24, 157, 492, 494, 495]. In the specific case of a thermal field at frequency ω, the Bose-Einstein distribution yields $n(T) = [\exp(\hbar\omega/k_\mathrm{B}T) - 1]^{-1}$ and $\mathrm{Var}(n) = n^2 + n$, which can be controlled by the temperature T of the emitter. In practice, one wants to distinguish this relation from both the classical limit $\mathrm{Var}(n) = n^2$ and the Poissonian behavior $\mathrm{Var}(n) = n$ characteristic for coherent states [24] or shot noise [467, 496]. Hence, as shown in Fig. 6.1, the most relevant regime for experiments is $0.05 \lesssim n \lesssim 1$, which translates into temperatures between 100 mK and 1 K at approximately 6 GHz for the thermal emitter [39].

In our experiments, we generate the thermal fields using a temperature-controllable, 50 Ω-matched attenuator acting as a black-body emitter (see Sec. 4.4.3 for details). This emitter is thermally only weakly coupled to the 35 mK base temperature stage of a dilution refrigerator. Heating the attenuator up to 1.5 K results in the emission of thermal microwave radiation, which we guide to our detection setups. Experimentally, we achieve a high photon number stability $\delta n/n \lesssim 0.01$ due to the precise temperature stabilization of the emitter. In addition, we investigate coherent states emitted from a microwave source and white electronic shot noise. The latter is generated by upconverting the 200 MHz wide noise of an arbitrary function generator (AFG) to a center frequency of 6 GHz (see Ref. 4.4.3 for experimental details). Finally, we note an important correspondence of the results presented here to those discussed in Sec. 5.2. There, we have used the temperature of thermal microwave states as a novel control parameter to investigate the quantum coherence of superconducting circuits. Here, we apply the complementary approach: we use the coherence properties of superconducting circuits to extract information from thermal microwave fields.

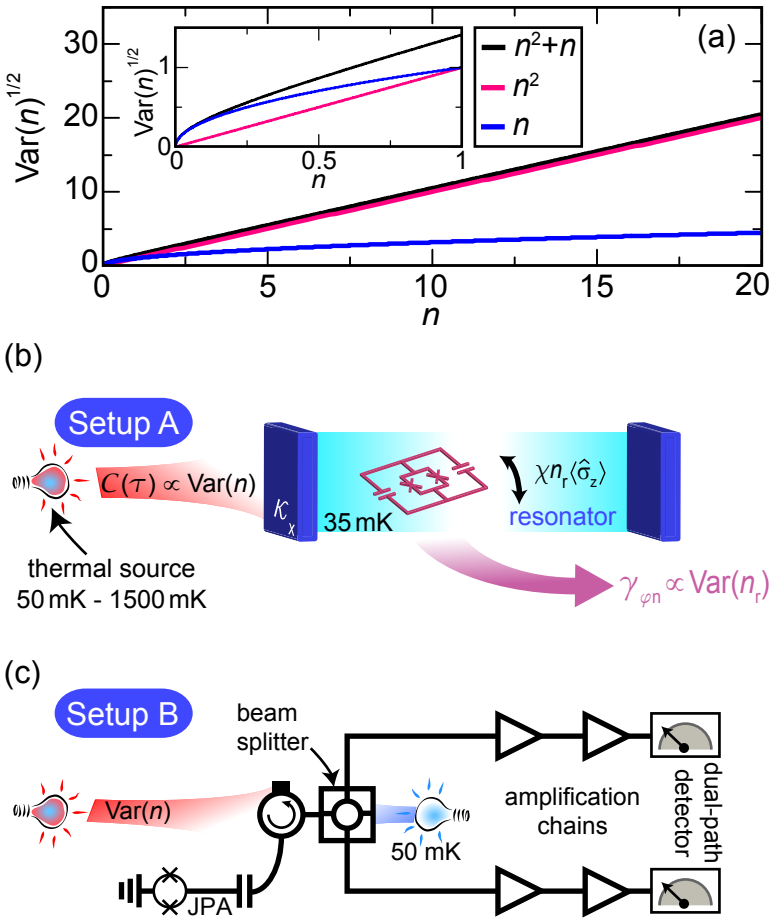

Figure 6.1: **(a)** Photon number correlations. $\mathrm{Var}(n)^{1/2}$ plotted versus photon number for thermal fields (black), their classical limit (red), and coherent states (blue). The inset shows the regime that we capture in our experiments. **(b)** Sketch of setup A: Here, we measure the photon number variance $\mathrm{Var}(n)$ of microwave fields encoded in the photon correlator $\mathcal{C}_n$ by detecting the dephasing rate γ_ϕ of a superconducting qubit. **(c)** Sketch of setup B, which is used to directly probe field correlations between two amplification chains behind a cryogenic microwave beam splitter. We can switch on and off the JPA.

Qubit setup We measure the photon number variance of propagating fields with the qubit setup depicted in Fig. 6.1 (b). To this end, we use a frequency-tunable transmon qubit operated at its maximum transition frequency $\omega_\mathrm{q}/2\pi = 6.92\,\mathrm{GHz}$ (see Sec. 4.4 for experimental details). The qubit is coupled with strength $g/2\pi \simeq 67\,\mathrm{MHz}$ to a quarter-wavelength coplanar waveguide resonator with resonance frequency $\omega_\mathrm{r}/2\pi = 6.07\,\mathrm{GHz}$ and external coupling rate $\kappa_\mathrm{x}/2\pi = 8.5\,\mathrm{MHz}$. Hence, the system is in the dispersive regime, where the detuning $\delta \equiv \omega_\mathrm{q} - \omega_\mathrm{r}$ fulfills $|\chi| \ll g$. Here, [40] $\chi \equiv [g^2/\delta][\alpha/(\delta+\alpha)] \simeq -2\pi \times 3.11\,\mathrm{MHz}$ and $\alpha/2\pi \simeq -315\,\mathrm{MHz}$ is the transmon anharmonicity. In the dispersive regime, the qubit couples to the photon number n_r in the resonator via the interaction Hamiltonian $\mathcal{H}_\mathrm{int} = \hbar\chi[n_\mathrm{r} + 1/2]\hat{\sigma}_\mathrm{z}$. We calibrate the photon number using the ac-Stark shift as presented in Sec. 5.2.1. Because the coupling is mediated by the Pauli operator $\hat{\sigma}_\mathrm{z}$, temporal fluctuations $n_\mathrm{r}(\tau)$ introduce qubit dephasing [17]. More precisely, the fluctuations are characterized by the correlator $\mathcal{C}(\tau) = \langle n_\mathrm{r}(0) n_\mathrm{r}(\tau)\rangle$ and generate a shift $\delta\varphi(\tau)$ of the qubit phase. While the first moment of this phase shift has a vanishing arithmetic mean, the second moment [168] $\langle\delta\varphi^2\rangle = 4\chi^2 \int_0^\tau \mathrm{d}\tau' \mathcal{C}(\tau')$ enters into the Ramsey decay envelope $\exp[-\gamma_1(n_\mathrm{r})\tau/2 - \gamma_{\varphi 0}\tau - \langle\delta\varphi^2\rangle/2]$. Here, $\gamma_1(n_\mathrm{r})$ is the total qubit relaxation rate and $\gamma_{\varphi 0}$ is the qubit dephasing rate due to all other noise sources except for those described by $\mathcal{C}(\tau)$. Because noise photons are stored in the field intensity, the super-Poissonian correlator $\mathcal{C}^\mathrm{th}(\tau) = (n_\mathrm{r}^2 + n_\mathrm{r})\exp(-\kappa_\mathrm{x}\tau)$ for thermal fields and the Poissonian correlator $\mathcal{C}^\mathrm{sh}(\tau) = n_\mathrm{r}\exp(-\kappa_\mathrm{x}\tau)$ for shot noise decay at the energy decay rate κ_x [see Sec. 2.2.4 for details]. On contrast, coherent states have a finite mean amplitude

such that $\mathcal{C}^{\mathrm{coh}}(\tau) = n_{\mathrm{r}} \exp(-\kappa_{\mathrm{x}}\tau/2)$ decays at the amplitude decay rate $\kappa_{\mathrm{x}}/2$. For all three states one obtains $\langle \delta\varphi^2 \rangle/2 = \gamma_{\varphi n}(n_{\mathrm{r}})\tau$, i.e., an exponential decay envelope. The photon-number-dependent dephasing rates are then defined by [24, 166, 168, 246, 275]

$$\gamma_{\varphi n}^{\mathrm{th}}(n_{\mathrm{r}}) = \kappa_{\mathrm{x}}\theta_0^2(n_{\mathrm{r}}^2 + n_{\mathrm{r}}) \equiv s_0^{\mathrm{th}}(n_{\mathrm{r}}^2 + n_{\mathrm{r}}), \tag{6.1.1}$$

$$\gamma_{\varphi n}^{\mathrm{coh}}(n_{\mathrm{r}}) = 2\kappa_{\mathrm{x}}\theta_0^2 n_{\mathrm{r}} \equiv s_0^{\mathrm{coh}} n_{\mathrm{r}}, \tag{6.1.2}$$

$$\gamma_{\varphi n}^{\mathrm{sh}}(n_{\mathrm{r}}) = \kappa_{\mathrm{x}}\theta_0^2 n_{\mathrm{r}} \equiv s_0^{\mathrm{sh}} n_{\mathrm{r}}. \tag{6.1.3}$$

Here, [168] $\theta_0 = \tan^{-1}(2\chi/\kappa_{\mathrm{x}})$ is the accumulated phase of the resonator photons due to the interaction with the qubit, resulting in $\kappa_{\mathrm{x}}\theta_0^2/2\pi = 3.4\,\mathrm{MHz}$. Remarkably, the factor of two between $\gamma_{\varphi n}^{\mathrm{coh}}$ and $\gamma_{\varphi n}^{\mathrm{sh}}$ is due to the fact that the photon-photon correlator decays faster for white noise than for coherent states. For thermal states, we control n_{r} via the temperature of the emitter, $n_{\mathrm{r}} \propto n(T)$. For coherent states and shot noise, we vary the microwave power P fed into the cryostat such that $n_{\mathrm{r}} \propto P$. We calibrate n_{r} via the Stark-shifted qubit frequency. The exact calibration procedure is presented in Sec. 5.2.1. As a consequence of Eqs. (6.1.1) - (6.1.3), measurements of the Ramsey decay rate $\gamma_2(n_{\mathrm{r}}) = \gamma_1(n_{\mathrm{r}})/2 + \gamma_{\varphi 0} + \gamma_{\varphi n}(n_{\mathrm{r}})$ allow us to extract the photon number variance as a function of n_{r}. We obtain $\gamma_1(n_{\mathrm{r}})$ from the relaxation measurements in Sec. 5.2.1. Furthermore, we emphasize that during our sweeps of the attenuator temperature, the sample box is stabilized at 35 mK. Also, all low-frequency components of the thermal field, usually responsible for dephasing, are strongly suppressed by the filter function of the resonator. Therefore, $\gamma_{\varphi 0}$ can be taken as a constant and we can extract $\gamma_{\varphi n}$ from a numerical fit to the decay envelope of a Ramsey time trace.

Dual-path setup With the dual-path setup depicted in Fig. 6.1 (c), we directly probe[1] field correlations using a reconstruction setup for microwaves [139, 169, 440, 443]. There, a cryogenic beam splitter equally divides the signal into two components, which are subsequently amplified independently. From the averaged auto- and cross-correlations, we retrieve all signal moments $\langle (\hat{a}^\dagger)^n \hat{a}^m \rangle$ up to fourth order ($0 \leq n+m \leq 4$ with $n,m \in \mathbb{N}_0$) in terms of the annihilation and creation operators, $\hat{a}$ and $\hat{a}^\dagger$. To calibrate the photon number $n_{\mathrm{bs}} = \langle \hat{a}^\dagger \hat{a} \rangle \propto n(T)$ at the input of the beam splitter, we perform a Planck spectroscopy experiment [440]. The dual-path setup also includes a near quantum-limited Josephson parametric amplifier (JPA), which can amplify the thermal field before it enters the beam splitter. The JPA consists of a quarter-wavelength transmission line resonator, which is short-circuited to the ground by a DC SQUID. This SQUID allows for the modulation of the resonator by applying an external magnetic flux. We couple an on-chip antenna inductively to the DC SQUID loop to apply a strong coherent pump tone ω_{p} at approximately twice the resonant frequency ω_{jpa} of the JPA. This pump scheme amplifies the incoming signal due to parametric effects [129, 152]. To calibrate the photon number n_{bs} at the input of the beam splitter, we perform a Planck spectroscopy experiment as described in the next paragraph.

Input loss calibration Both setups share the same technique for the generation of thermal fields. We use a cryogenic 50 Ω-matched 30 dB attenuator, which is thermally only weakly coupled to the 35 mK base temperature stage of a dilution refrigerator as discussed

[1] We greatfully acknowledge the experimental effort from S. Pogorzalek and K. G. Fedorov who conducted the correlation measurements presented in this section.

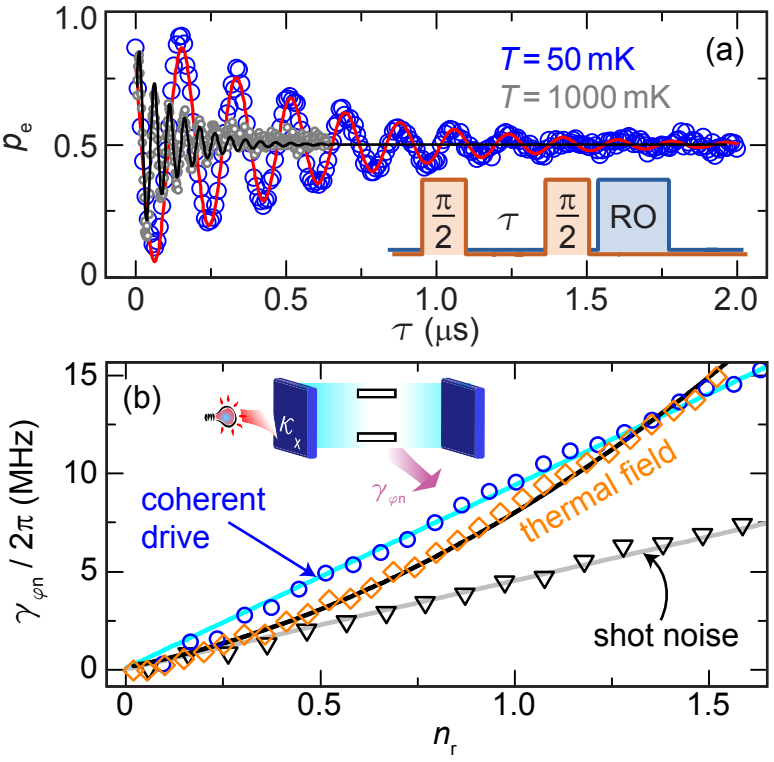

Figure 6.2: **(a)** Qubit excited state probability p_e for a Ramsey experiment plotted versus waiting time τ between two $\pi/2$ pulses. The solid lines are exponentially decaying sinusoidal fits. The inset shows the Ramsey pulse sequence followed by a readout (RO) pulse. **(b)** Qubit dephasing rates $\gamma_{\varphi n}$ of prototypical input fields plotted versus the average resonator population n_r. The super-Poissonian $n_r^2 + n_r$ statistics of thermal fields is fitted using Eq. (6.1.1). The blue and the grey line are fits of Eq. (6.1.2) and Eq. (6.1.3) to the data for coherent states and shot noise, respectively.

in Sec. 4.4.3. We achieve a high temperature stabilization $\delta T/T \simeq 0.01$ of the attenuator resulting in a comparable accuracy for n_{th}. In our experiments, we measure the variance of these thermal photons, which is characterized by the temporal fluctuations of the mean photon number. Because the reference point for these fluctuations, i.e., the resonator in setup A and the cryogenic beam splitter in setup B, is separated from the attenuator by coaxial cables, we carefully determine the loss $\alpha_{\mathrm{a,b}}$ in these cables in the following. With the qubit setup, we directly calibrate the loss of α_{b} using the photon-number-dependent ac-Stark shift as discussed in Sec. 5.2.1. With the dual-path setup, we perform a Planck spectroscopy experiment [440] for photon number calibration. To this end, we use the heatable attenuator as a black-body emitter. From these sweeps, we extract the cable loss $\alpha_{\mathrm{b}} \simeq 1.1\,\mathrm{dB}$.

6.1.2 Photon statistics detected with the transmon qubit

In the absence of external microwave fields, the transmon qubit is relaxation-limited with the rates $\gamma_1(n_r \simeq 0)/2\pi \simeq 4\,\mathrm{MHz}$ and $\gamma_2(n_r \simeq 0)/2\pi \simeq 2\,\mathrm{MHz}$. In Fig. 6.2 (a), we show the Ramsey time traces for the attenuator temperatures $T = 50\,\mathrm{mK}$ and $T = 1\,\mathrm{K}$. As expected, the latter shows a significantly increased Ramsey decay rate. A systematic temperature sweep reveals $\gamma_{\varphi n}^{\mathrm{th}}(n_r) \propto n_r^2 + n_r$ as displayed in Fig. 6.2 (b). For small photon numbers $n_r \lesssim 0.5$, we observe that the dephasing rate approaches a linear trend with slope $s_0^{\mathrm{th}} \equiv \partial \gamma_{\varphi n}^{\mathrm{th}} / \partial n_r|_{n_r = 0}$. This finite slope clearly allows us to rule out the validity of the classical limit $\mathrm{Var}(n_r) = n_r^2$ in this regime. From a fit of Eq. (6.1.1) to the data, we find $s_0^{\mathrm{th}}/2\pi = 3.9\,\mathrm{MHz}$, which is marginally enhanced compared to the expected value $\kappa_x \theta_0^2 / 2\pi$. We can quantitatively explain the slight enhancement by accounting for the constant thermal field emitted from attenuators at higher temperature stages leading to an enhanced Fano factor $\mathcal{F}$ [157, 489, 497]. Applying a beam splitter model to calculate

$\mathrm{Var}(n_\mathrm{r}+n_\mathrm{c}^\mathrm{th})$, we extract the reasonable contribution of $n_\mathrm{c}^\mathrm{th}=0.15$ corresponding to an effective mode temperature of approximately 140 mK.
As a cross-check for our setup, we confirm the well-explored [24, 168, 467] linear variance of fields with Poissonian photon statistics. To this end, we first expose the resonator to shot noise emitted by the AFG [498]. As shown in Fig. 6.2 (b), we indeed find a constant slope $s^\mathrm{sh}\equiv\partial\gamma_{\varphi n}^\mathrm{sh}/\partial n_\mathrm{r}\simeq 2\pi\times 4.6\,\mathrm{MHz}$. Also this value is slightly enhanced compared to $\kappa_\mathrm{x}\theta_0^2$. Again, we can understand this result by modeling the attenuation between the emitter inside the AFG and the qubit with a beam splitter adding a weak thermal state to the input field. A quantitative analysis using the beam splitter model yields the additional population $n_\mathrm{c}^\mathrm{sh}=0.19$, which coincides with n_c^th. In the next step, we investigate measurement-induced dephasing caused by coherent states as displayed in Fig. 6.2 (b). We again find a linear slope $s^\mathrm{coh}\equiv\partial\gamma_{\varphi n}^\mathrm{coh}/\partial n_\mathrm{r}=2\pi\times 9.3\,\mathrm{MHz}\simeq 2s^\mathrm{sh}$. The excellent quantitative agreement with the shot noise result is also reflected in $n_\mathrm{c}^\mathrm{coh}=n_\mathrm{c}^\mathrm{sh}$, i.e., identical Fano factors $\mathcal{F}=\langle\delta n_\mathrm{r}^2\rangle/\langle n_\mathrm{r}\rangle\simeq 1.1$. The enhancement of $s^\mathrm{coh}/s^\mathrm{sh}=2$ shows that the qubit dephasing rate reliably reflects the temporal dependence of photon-photon correlators.

6.1.3 Photon statistics detected with the dual-path setup

In order to complement our studies of thermal microwaves with the qubit setup, we directly probe field correlations with the dual-path state reconstruction setup depicted in Fig. 6.1 (c). Notwithstanding the very different experimental requirements in the microwave regime, direct correlation measurements on propagating light fields are inspired from quantum optics. For this reason, we characterize the photon number variance of the thermal microwave fields via the unnormalized correlation function

$$\tilde{g}^{(2)}(0)=n_\mathrm{bs}^2 g^{(2)}(0)=\mathrm{Var}(n_\mathrm{bs})-n_\mathrm{bs}+n_\mathrm{bs}^2\,, \tag{6.1.4}$$

which is $2n_\mathrm{bs}^2$ for a thermal state. As shown in Fig. 6.3 (a), the correlation function $\tilde{g}^{(2)}(0)$ of the thermal source follows the expected quadratic behavior. A numerical fit of the polynomial function $\tilde{g}^{(2)}(0)=\rho\, n_\mathrm{bs}^2$ using ρ as a free parameter yields $\rho=2.07$. This result coincides nicely with $\tilde{g}^{(2)}(0)=2n_\mathrm{bs}^2$ predicted for thermal states by Eq. (6.1.4). In the same way as with the qubit setup, we are therefore able to reliably map out the n^2+n dependence and not only the classical n^2 limit experimentally found in earlier work [157]. To lower the statistical scatter of the data points in Fig. 6.3 (a), we repeat the correlation measurement using a JPA operated in the phase insensitive mode. In this mode, the JPA works as a near-quantum-limited, phase-preserving amplifier [152] with power gain $G\gg 1$. At the input of the beam splitter, one then obtains $n_\mathrm{bs}\approx G(n_\mathrm{jpa}+n_\mathrm{n}+1)$. Here,

Table 6.1: Overview of the JPA samples. We perform one measurement with JPA 1 and two individual measurements using JPA2 with different detunings $\delta_\mathrm{jpa}=\omega_\mathrm{jpa}-\omega_\mathrm{p}/2$ between JPA frequency ω_jpa and pump frequency ω_p. The measurement bandwidth for all measurements is $\omega_\mathrm{jpa}\pm 200\,\mathrm{kHz}$.

device	run	input loss α	gain G_jpa	n_jpa	ρ	ξ	$\tilde{g}_\mathrm{jpa}^{(2)}(0)$	$\delta_\mathrm{jpa}/2\pi$	$\omega_\mathrm{jpa}/2\pi$
JPA 1	–	-1.07 dB	14.3 dB	1.71	2.24	8.14	7.1	100 kHz	5.4 GHz
JPA 2	a	-0.98 dB	15.8 dB	0.66	2.23	3.29	1.1	100 kHz	5.4 GHz
JPA 2	b	-0.98 dB	15.2 dB	0.97	2.21	3.29	1.8	500 kHz	5.3 GHz

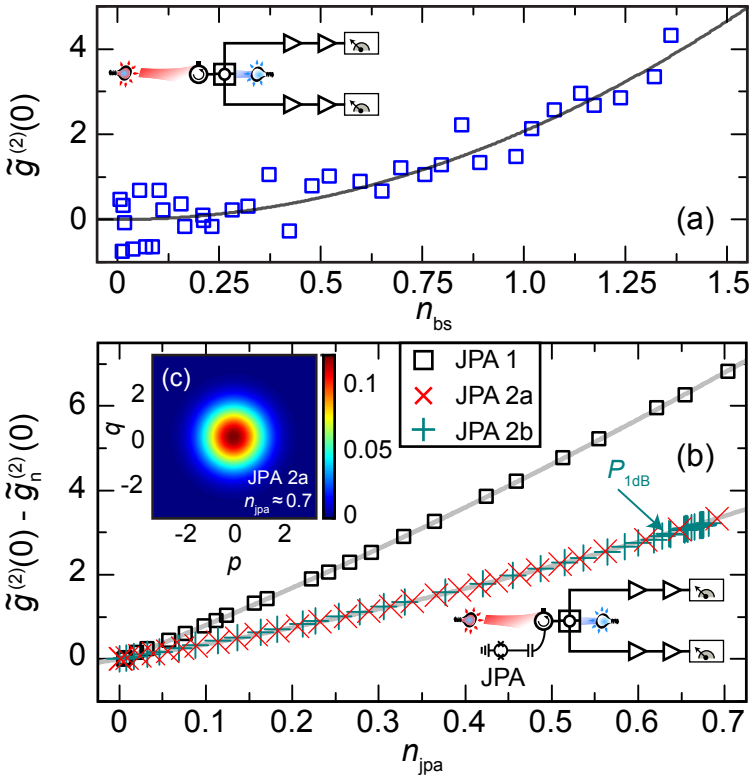

Figure 6.3: **(a)** Unnormalized second-order correlation function $\tilde{g}^{(2)}(0)$ plotted versus photon number n_{bs} at the beam splitter input without using the JPA. The solid line is a fit to the data using the function $\tilde{g}^{(2)}(0) = \rho\, n_{\mathrm{bs}}^2$. **(b)** Unnormalized second-order correlation function $\tilde{g}^{(2)}(0)$ corrected for the constant offset $\tilde{g}_{\mathrm{n}}^{(2)}(0)$ and plotted versus the photon number n_{jpa} at the JPA input. For the measurements of JPA 2a and JPA 2b we use slightly different operating points as summarized in Tab. 6.1. **(c)** Wigner function reconstruction referred back to the input of the JPA for an amplified thermal state.

$n_{\mathrm{jpa}} \propto n(T)$ are the signal photons and n_{n} are the noise photons added by the JPA, which we again obtain from a Planck spectroscopy experiment [440]. We compare measurements using two different JPAs (JPA 1 and JPA 2) based on frequency-tunable quarter wavelength resonators with operating frequencies $\omega_{\mathrm{jpa}}/2\pi \simeq 5.35\,\mathrm{GHz}$ and typical gains $G \simeq 15\,\mathrm{dB}$ (specific parameters are summarized in Tab. 6.1). To characterize the noise referred to the input of the JPA, we analyze the modified correlation function

$$\tilde{g}^{(2)}(0) = 2(n_{\mathrm{jpa}} + n_{\mathrm{n}} + 1)^2\,, \tag{6.1.5}$$

which can be derived from an input-output model for the JPA presented in Sec. 2.2.4. In Eq. (6.1.5), there is an n_{jpa}-independent offset $\tilde{g}_{\mathrm{n}}^{(2)}(0) = 2n_{\mathrm{n}}^2 + 4n_{\mathrm{n}} + 2$ due to the JPA gain and noise. In our model, we assume that the JPA noise is thermal, i.e., $\mathrm{Var}(n_{\mathrm{n}}) = n_{\mathrm{n}}^2 + n_{\mathrm{n}}$. In Fig. 6.3 (b) we plot the experimentally obtained correlations $\tilde{g}^{(2)}(0) - \tilde{g}_{\mathrm{n}}^{(2)}(0)$ versus the photon number n_{jpa} at the JPA input. From fits to the formula $\rho n_{\mathrm{jpa}}^2 + \xi n_{\mathrm{jpa}}$, we find $\rho \simeq 2.2$ in all three data sets in agreement with the expected value of $\rho = 2$. Therefore, also the JPA assisted measurements confirm a super-Poissonian statistics of the thermal fields. From the fits, we also find that the values ξ is reduced by a factor of approximately 2 compared to the expected value $4 + 4n_{\mathrm{n}}$. This observation is confirmed by the values extracted for $\tilde{g}_{\mathrm{n}}^{(2)}(0)$, which deviate to a similar extent. The reduced experimental values suggest that the amplified noise contains a significant contribution $\mathrm{Var}(n_{\mathrm{n}}) = n_{\mathrm{n}}^2$, an effect known for amplified thermal fields [157]. This classical contribution is power independent and also constant when the JPAs exceed their 1 dB compression point $\mathcal{P}_{1\mathrm{dB}} \simeq -130\,\mathrm{dBm}$ [see Fig. 6.3(b)]. We stress that the amplified fields are still Gaussian and show no squeezing effects between the two quadratures $\hat{p} = \imath(\hat{a}^\dagger - \hat{a})/2$ and $\hat{q} = (\hat{a}^\dagger + \hat{a})/2$ [see Fig. 6.3(c)]. As shown in Sec. 4.4.4, we find $\mathrm{Var}(\hat{p}) = \mathrm{Var}(\hat{q})$ for the complete temperature regime.

6.1.4 Comparison of the different measurement setups

Finally, we compare the performance of the qubit and the dual-path setup. Although we operate on and below the single photon level, the qubit and the dual-path setup (without JPA) systematically reproduce the n^2+n law with a high accuracy. Currently, the statistical spread for the qubit setup is one order of magnitude lower than the one for the dual-path setup. The accuracy of the qubit setup is limited by the Fano factor $\mathcal{F} \simeq 1.1$ of the setup and by the low-frequency variations of the qubit relaxation rate described in Sec. 5.2.4. Their standard deviation of 5 % well explains the spread of the experimental data points in Fig. 6.2 (b). Assuming that these variations decrease proportionally to the qubit decoherence rate, we estimate that for the best performing superconducting qubits [246], the accuracy can be improved by at least two orders of magnitude. The dual-path setup (without the JPA) is limited by the data processing rate of our digitizer card and by the noise temperature $T_\mathrm{n} \simeq 3\,\mathrm{K}$ of the cryogenic amplifiers. When the JPA is on, the noise temperature of these amplifiers is insignificant. Concerning adaptability, the dual-path setup in principle gives access to all signal moments, whereas the qubit is limited to amplitude and power correlations. While our measurements including a JPA decrease the statistical spread by two orders of magnitude, they also indicate that the statistics of the JPA noise can influence the statistics of the amplified field.
In conclusion, we have quantitatively characterized the photon number variance of propagating thermal microwaves using two fundamentally different approaches: indirect measurements with a superconducting qubit-resonator system and direct ones, with a dual-path detector. With both setups, we are able to quantitatively recover the n^2+n photon number variance of thermal fields in the single photon regime with a high resolution in comparison with existing experimental achievements [157]. In particular, we analyze the resolution limits and find that they can be improved by several orders of magnitude in both setups. For our current dual-path setup, we make the remarkable observation that noise added by the JPAs has a significant contribution with $\mathrm{Var}(n) = n^2$. Our results demonstrate that the three types of propagating microwaves we investigate can be reliably distinguished below the single photon level in an experiment by their photon statistics. Therefore, both setups are promising candidates to explore decoherence mechanisms possibly limiting high-performance superconducting qubits [246, 466] and the properties of more advanced quantum microwave states.

6.2 Engineering the parity of light-matter interaction with superconducting circuits

In physics, parity describes intrinsic symmetries of quantum states and operators, which has manifold applications in the standard model [499, 500], quantum information [501] and field [502, 503] theory. The latter includes quantum electrodynamics, where the parity of interaction operators defines selection rules for atomic state transitions [504–506]. Superconducting qubits are well-suited for systematic studies of selection rules, because the underlying symmetries can be tuned in-situ by external control parameters. For dipolar interactions such selection rules have been demonstrated experimentally [27, 42, 185]. We present a novel technique for the in-situ control of the interaction operator parity in superconducting quantum circuits. Using a tunable-gap gradiometric flux qubit, which exhibits both a dipole and a quadrupole moment, we precisely engineer the interaction parity with spatially shaped microwave fields. With our highly symmetric sample architecture,

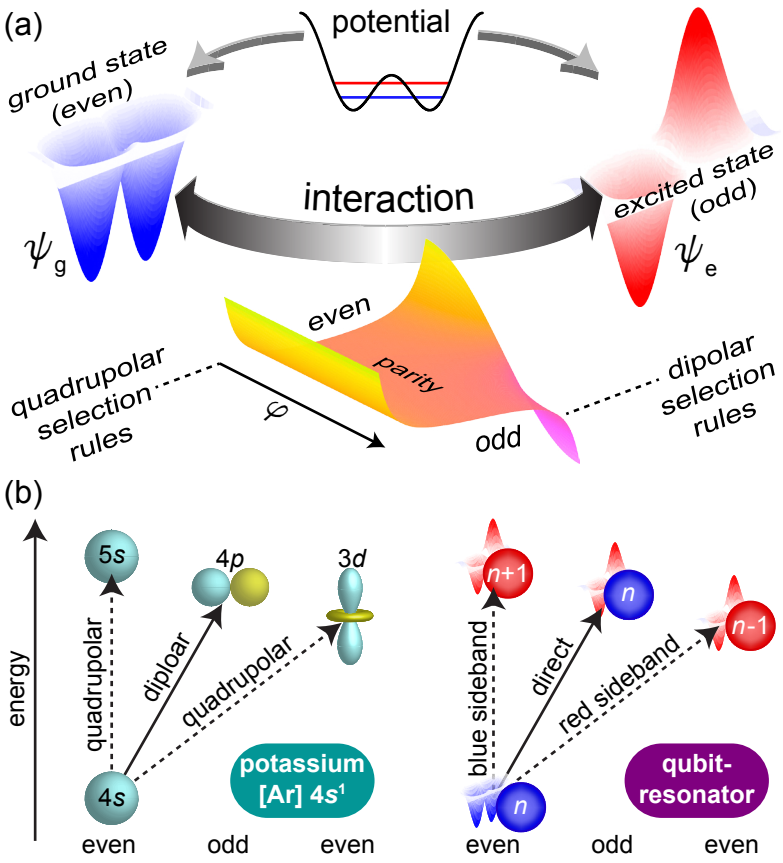

Figure 6.4: **(a)** At its degeneracy point, the symmetric double well potential of a flux qubit allows two states (ψ_g and ψ_e) with opposite parity. The interaction parity can be even, odd, or without specific symmetry controlled by a phase φ. For even interaction parity, quadrupolar selection rules apply and for odd interaction operators dipolar selection rules are valid. **(b)** Energy level diagram for ground and first three excited states for a potassium atom (left) and the qubit-resonator system (right).

we move from the $U(1)$ symmetry of Jaynes-Cummings interaction to the $\mathbb{Z}_2$ symmetry of the quantum Rabi Hamiltonian and even find longitudinal coupling-induced transparency reflecting the symmetry of the biased quantum Rabi model. In a second step, we couple the qubit to a resonator and, in this way, activate quadrupolar transitions in an artificial potassium-like atom. Our work paves the way towards parity based quantum simulation and physical applications relying on longitudinal interactions such as quantum annealers [507].

6.2.1 Experimental idea

Except for the weak interaction [499, 508], all physical interactions between elementary particles obey parity conservation. This concept is essential for promising technology, e.g., quantum computation based on the surface code [509–512] or for the seminal quantum Rabi model [171, 186, 513, 514] describing light-matter interaction. In both cases, however, parity is primarily used in a passive way, either as a direct observable or as a restricting quantity for rigorous selection rules between quantum states. These multifarious rules for atoms reduce to pure parity arguments for quasi-one-dimensional artificial atoms (qubits) made from superconducting circuits. For flux qubits, the two eigenstates $|\psi_g\rangle$ and $|\psi_e\rangle$ of their double-well potential have opposite parity and correspond to $1s$ and $2p$ orbitals in hydrogen-like atoms [see Fig. 6.4 (a)]. Therefore, selection rules are simply characterized by the parity product $\hat{\Pi}_{\mathrm{tot}} = \hat{\Pi}\,|\psi_g\rangle\,\hat{\Pi}(\mathcal{H}_{\mathrm{int}})\hat{\Pi}\,|\psi_e\rangle$, where $\mathcal{H}_{\mathrm{int}}$ is the interaction Hamiltonian. Parity conservation requires that $\hat{\Pi}_{\mathrm{tot}}$ is even for allowed transitions. This requirement leads to electric dipolar selection rules if $\mathcal{H}_{\mathrm{int}}$ is odd and anticommutes with $\hat{\Pi}$, $\{\mathcal{H}_{\mathrm{int}},\hat{\Pi}\} = 0$, and to electric quadrupolar selection rules if $\mathcal{H}_{\mathrm{int}}$ is even and commutes with $\hat{\Pi}$, $[\mathcal{H}_{\mathrm{int}},\hat{\Pi}] = 0$

(see Sec. 2.3.3 for details). While $\hat{\Pi}\,|\psi_\mathrm{g}\rangle$ and $\hat{\Pi}\,|\psi_\mathrm{e}\rangle$ are fixed for bare qubits, in principle one can vary $\hat{\Pi}(\mathcal{H}_\mathrm{int})$ to engineer selection rules. Since this task is experimentally challenging for atoms, where the amplitude distribution of an incident light beam has to be inverted within a few ångström, its realization in qubits is highly desirable.
Due to their design flexibility, superconducting circuits can be conveniently designed to have a finite quadrupole moment, which has been used to enable quantum gates [100], reduce flux noise [102] or radiative loss [515], and to study quantum transitions [516]. Placing a quadrupolar flux qubit in the nearfield of on-chip antennas makes the interaction parity a convenient control knob in quantum circuits. This powerful but yet unexplored tuning method allows us to engineer either dipolar or quadrupolar selection rules for one and the same qubit. Even more flexibility in our qubit provides its possible longitudinal coupling (via the Pauli operator $\hat{\sigma}_\mathrm{z}$) to electromagnetic fields, which is the unconventional alternative to the well-known transverse coupling via $\hat{\sigma}_\mathrm{x}$. We design our sample such that symmetric fields couple in a longitudinal fashion to the qubit and antisymmetric fields couple to the transverse degree of freedom. That way, we can for the first time probe selection rules for a quantum two-level system with two orthogonal degrees of freedom. In particular, we find distinctively unique selection rules apart the sweet spot, where the symmetry of the drive is broken in exactly the same way as the qubit potential.

With pure two-level systems, it is hard to simulate the multi-level structure of atoms. To overcome this issue, we introduce an additional degree of freedom provided by the photon number n in a microwave resonator coupled to the qubit. Because the Schrödinger equation for the resonator is solved by the Hermite polynomials, subsequent number states $|n\rangle$ of the resonator have opposite parity, $\hat{\Pi}_\mathrm{r} = e^{\imath\pi n}$. That way, the resonator acts as an effective orbital momentum ℓ in atoms where $\hat{\Pi}_\mathrm{a} = e^{\imath\pi\ell}$. Our quantum system is equivalent to a potassium atom with electron configuration [Ar]$4s^1$ [see Fig. 6.4 (b)]. Probing sideband transitions with $\Delta n = \pm 1$, we can activate the dipolar forbidden transitions to the $5s$ and $3d$ orbitals. These findings strongly extend the flexibility of qubits in possible quantum chemistry simulations of more complex molecules. Additionally, we implement truly longitudinal coupling mechanisms, which is useful for quantum state engineering [188, 517–520] or for simulations of relativistic physics. Finally, the parity of quantum microwave states is a promising encoding technique for error-correction-based quantum computing [512].

Our experimental setup contains three basic elements (qubit, resonator, antennas) as depicted in Fig. 6.5 (a) and introduced in detail in Sec. 4.3.4. We place a gap-tunable gradiometric flux qubit symmetrically between two on-chip antennas generating a magnetic field $\mathbf{H}$, which oscillates at the drive frequency ω_d. Our flux qubit has two degrees of freedom described by the Hamiltonian $\mathcal{H}_\mathrm{q} = \hbar(\Delta\hat{\sigma}_\mathrm{x} + \varepsilon\hat{\sigma}_\mathrm{z})/2$ because we replace one of the Josephson junctions by a SQUID. Due to the elaborate qubit geometry, the tunnel coupling Δ and the magnetic energy bias ε couple to different terms in a multipole expansion for the interaction Hamiltonian $\mathcal{H}_\mathrm{int} = \mu_0\boldsymbol{\mu}\mathbf{H}\hat{\sigma}_\mathrm{x} + \mu_0\mathbf{Q}\nabla\mathbf{H}\hat{\sigma}_\mathrm{z} + \mathcal{O}(\nabla^2\mathbf{H})$. Here, the SQUID dipole moment $\boldsymbol{\mu}$ defines the longitudinal coupling strength $\Omega_\ell = \mu_0\boldsymbol{\mu}\cdot\mathbf{H}/\hbar$ while the qubit quadrupole moment $\mathbf{Q}$ defines the transversal coupling strength $\Omega_\mathrm{t} = \mu_0\mathbf{Q}\nabla\cdot\mathbf{H}$. Because our two antennas generate strong field gradients, we can shape the amplitude distribution of $\mathbf{H}$ across the qubit area by introducing a phase shift φ_rel in one of the two paths [see Sec. 4.3.3 for details]. We obtain symmetric fields ($\Omega_\mathrm{t} = 0$) for $\varphi_\mathrm{rel} \in \{0,2\pi,...\}$ and antisymmetric fields ($\Omega_\ell = 0$) for $\varphi_\mathrm{rel} \in \{\pi,3\pi,...\}$ [see Fig. 6.5 (b)]. For arbitrary φ_rel, the total field is a superposition of both contributions. In the qubit eigenbasis where $\mathcal{H}'_\mathrm{q} = \hbar\omega_\mathrm{q}\hat{\sigma}_\mathrm{z}/2$ and

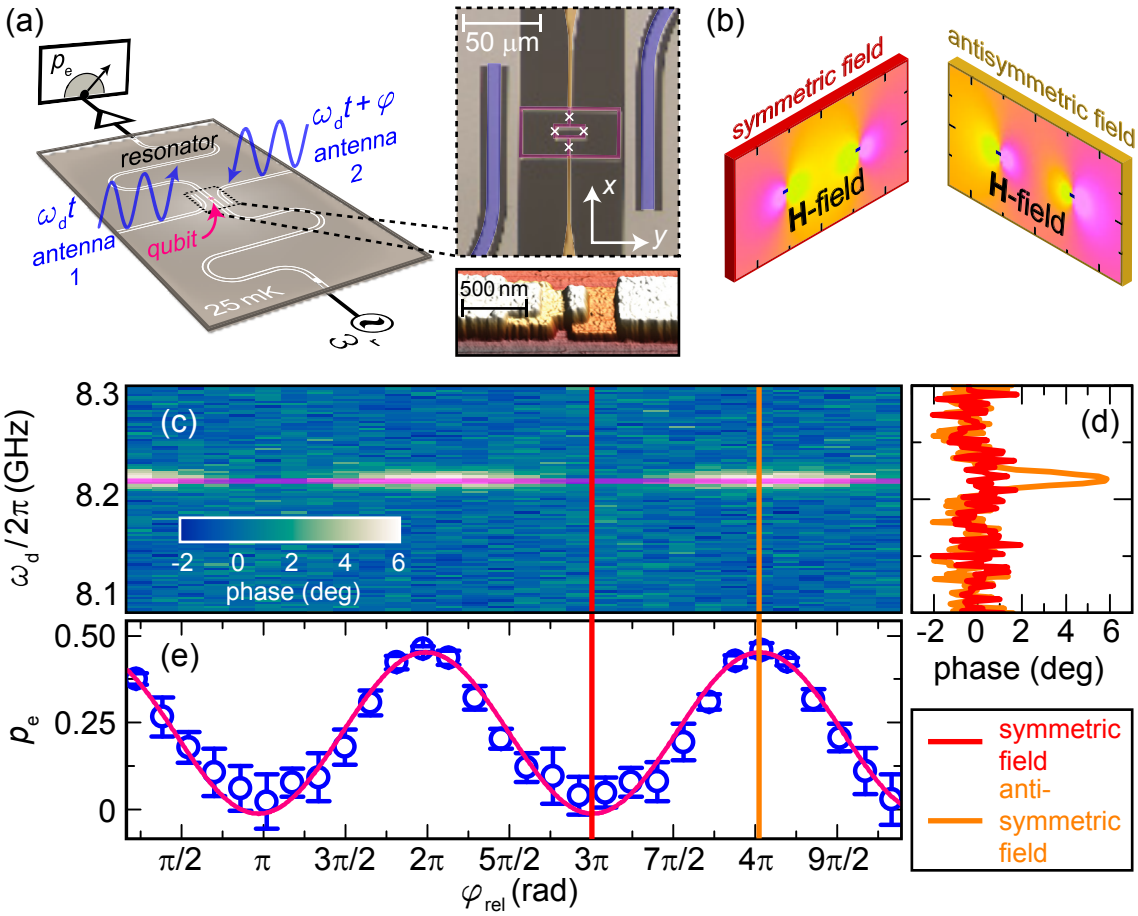

Figure 6.5: **(a)** Experimental architecture of chip layout and detection setup. The enlargement shows a micrograph of the relevant chip area with qubit, resonator and antennas. Crosses denote Josephson junctions as one is shown in the atomic force micrograph. **(b)** z-component H_z of the magnetic field generated by the two antennes for the symmetric and the antisymmetric case. **(c)** Phase response of the resonator plotted versus relative phase of the two microwave drives and versus drive frequency. Even multiples of π correspond to a symmetric RF drive while odd multiples of π correspond to antisymmetric RF fields. **(d)** Phase response $\phi(\omega_d)$ of the resonator plotted versus drive frequency at operating points corresponding to symmetric and antisymmetric RF fields indicated by the vertical lines in (c). **(e)** Qubit excited state probability plotted versus relative phase at $\omega_d = 8.218\,\mathrm{GHz}$. The solid line is sinusoidal fit.

$\omega_q = \sqrt{\Delta^2+\varepsilon^2}/\hbar$, the qubit-drive interaction Hamiltonian reads

$$\mathcal{H}'_{\rm int} = \hbar e^{i\omega_d t}[(\Omega_\ell \cos\theta - \Omega_t \sin\theta)\hat{\sigma}_x + (\Omega_t \cos\theta + \Omega_\ell \sin\theta)\hat{\sigma}_z]/2\,. \tag{6.2.1}$$

We can tune the Bloch angle $\theta = \tan^{-1}(\Delta/\varepsilon)$ by symmetric and antisymmetric DC fields applied through the two antennas. Equation (6.2.1) extends the QR model by the longitudinal coupling terms which are present in $\mathcal{H}_{\rm sys}$ even at the qubit degeneracy point $\theta = \pi/2$, where $\{\cos\theta, \sin\theta\} = \{0,1\}$. Therefore, the $\mathbb{Z}_2$ symmetry (parity conservation), usually present in the Rabi model [171], is broken due to the terms $\propto \hat{\sigma}_z$. We can, however, restore the $\mathbb{Z}_2$ symmetry of $\mathcal{H}_{\rm sys}$ by turning off the longitudinal coupling, i.e., $\Omega_\ell = \cos\theta = 0$. Then, transitions to the excited state are induced because the interaction is mediated via the odd parity operator $\hat{\sigma}_x$ (Fig. 2.13d). For pure longitudinal coupling ($\Omega_t = \cos\theta = 0$),

the conserved quantity of $\mathcal{H}_{\mathrm{sys}}$ is the qubit component $\hat{\sigma}_{\mathrm{z}}$ resulting in a nontrivial $U(1)$ symmetry. In that case, only the qubit gap Δ is modulated but no mixing of states is generated. For arbitrary drive symmetries ($\Omega_{\mathrm{t}} \neq 0 \neq \Omega_{\ell}$), the excited state probability follows a $\sin(\varphi/2)^2$-dependence. In the first part of this work, we use the resonator operating at $\omega_{\mathrm{r}} \simeq 3.9\,\mathrm{GHz}$ only to detect the qubit excited state probability p_{e} in a dispersive readout ($n = \mathrm{const}$).

6.2.2 One-photon assisted transitions

Interaction parity We use one-photon assisted transitions to show that selection rules for quadrupolar atoms depend on the parity of the interaction operator. For one-photon-assisted qubit state transitions, the symmetry of $\mathcal{H}'_{\mathrm{int}}$ is characterized by the parity operator $\hat{\Pi}_{\mathrm{int}} = -\hat{\sigma}_{\mathrm{z}}$. Therefore, only transitions via $\Omega_{\mathrm{t}}\hat{\sigma}_{\mathrm{x}}$ are allowed at the qubit degeneracy point while $p_{\mathrm{e}}(\Omega_{\ell}\hat{\sigma}_{\mathrm{z}}) \simeq 0$. For convenience, we first operate the qubit at its sweet spot, where $\omega_{\mathrm{q}} = \Delta$ and consequently the Jaynes-Cummings Hamiltonian defined in Eq. (2.3.2) has a well-defined parity. Hence, the probability to excite the qubit simplifies to $p_{\mathrm{e}} \propto \Omega_{\mathrm{t}}^2 \propto \sin^2(\varphi_{\mathrm{rel}}/2)$. When probing the qubit in a two-tone experiment, we clearly observe an oscillatory appearance of the qubit dip as shown in Fig. 6.5 (c). By analyzing the sweeps at $\varphi_{\mathrm{rel}} = 3\pi$ and $\varphi_{\mathrm{rel}} = 4\pi$, we extract an on/off ratio of more than 10 dB [see Fig. 6.5 (d)]. Hence, the qubit can be excited with a field of odd parity but not with even parity fields. To systematically analyze the qubit susceptibility to the parity of a microwave drive, we evaluate $p_{\mathrm{e}}(\varphi_{\mathrm{rel}})$. To increase the signal to noise ratio, we integrate the phase response $\phi_{\mathrm{tot}} = \int \phi(\omega_{\mathrm{d}})\,\mathrm{d}\omega$ over the FWHM of the qubit dip. The result shown in Fig. 6.5 (e) clearly follows a $\sin^2(\varphi_{\mathrm{rel}}/2)$ dependence, which supports our model prediction given by Eq. (6.2.1). We note that the total power $\mathcal{P}_{\mathrm{trans}} = \int [\Omega_{\ell} + \Omega_{\mathrm{t}}]^2\,\mathrm{d}A_{\mathrm{q}}$ transmitted to the qubit area A_{q} is approximately constant. We observe a small residual excitation probability at $\varphi_{\mathrm{rel}} = \pi, 3\pi$ in Fig. 6.5 (e). We attribute this to field imperfections due the superconducting ground planes and qubit lines as well as to a finite crosstalk between SQUID and gradiometer loop [178]. Despite that, the excellent agreement between data and theory shows that the gradiometric qubit is a well-suited circuit to study the parity of interaction operators.

Selection rules for a finite energy bias To emphasize that the oscillatory dependence in Fig. 6.5 (e) is truly related to the parity of $\mathcal{H}'_{\mathrm{int}}$, we investigate the symmetry properties (θ-dependence) of Eq. (6.2.1) in the following. Therefore, we analyze the selection rules for a quadrupolar qubit for finite magnetic energy bias $\hbar\varepsilon$, i.e., away from the qubit degeneracy point. This energy bias changes the qubit transition frequency and consequently also the Bloch angle θ in Eq. (6.2.2). Hence, the simple $\sin^2(\varphi_{\mathrm{rel}}/2)$ dependence shown in Fig. 6.5 (e) breaks down because we leave the operating point where $\sin\theta = 1$ and $\cos\theta = 0$. For purely antisymmetric fields ($\Omega_{\ell} = 0$), Eq. (6.2.1) describes the well-known $\hat{\sigma}_{\mathrm{x}}$ interaction for flux qubits (left column in Fig. 6.6). At the qubit degeneracy point (symmetric potential), $\hat{\sigma}_{\mathrm{x}}$ anticommutes with $\hat{\Pi}_{\mathrm{int}}$ resulting in dipolar selection rules. Apart the degeneracy point, the interaction parity is not well defined and the transition probability fades out due to the $\sin\theta$ term. In Fig. 6.6 (b), we also show numerical calculations of the qubit excited state probability.
For symmetric fields ($\Omega_{\mathrm{t}} = 0$), the interaction is purely mediated via $\hat{\sigma}_{\mathrm{z}}$, which commutes with $\hat{\Pi}_{\mathrm{int}}$ such that the transition probability vanishes at the degeneracy point (center column in Fig. 6.6). For increasing magnetic energy bias, however, the $\cos\theta$-term becomes finite and state transitions occur. In the intermediate regime ($\Omega_{\ell} \neq 0 \neq \Omega_{\mathrm{t}}$), there is an

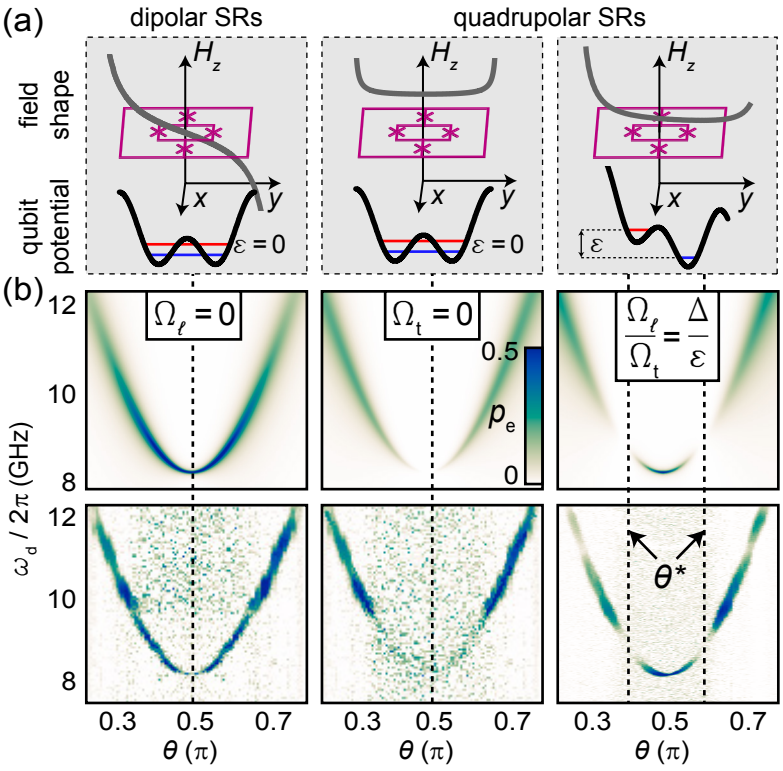

Figure 6.6: **(a)** Symmetry of the drive field and the qubit potential for three experimental contributions $(\Omega_\ell = 0, \Omega_t = 0)$ and $\Omega_\ell/\Omega_t = \Delta/\varepsilon$. **(b)** Expected (top row) and measured (bottom row) excited state probability p_e plotted versus Bloch angle θ and drive frequency ω_d. For the calculations in the top row, we use Eq. (6.2.2) in the low power (one-photon) limit $\Omega_\ell, \Omega_t \ll \omega_q$. The operating point defined by $\theta^\star$ defines the situation where the drive has the same symmetry as the qubit potential.

operating point $\theta^\star$ where the drive symmetry is broken in exactly the same way as the symmetry of the qubit potential (right column in Fig. 6.6). We can understand the vanishing transition matrix element at $\theta^\star$ by moving to a nonuniformly rotating frame where the effective interaction Hamiltonian becomes

$$\mathcal{H}_{\text{int}}^{\text{eff}} = \hbar \left[\frac{\Omega_\ell}{4} \cos\theta - \frac{\Omega_t}{4} \sin\theta \right] [J_0(\lambda) + J_2(\lambda)] \hat{\sigma}_x \,. \tag{6.2.2}$$

Here, J_k is the k^{th} Bessel function of the first kind and $\lambda = (\Omega_t \cos\theta + \Omega_\ell \sin\theta)/\omega_d$. From Eq. (6.2.2), one immediately sees that $\mathcal{H}_{\text{int}}^{\text{eff}} = 0$ if $\Omega_\ell/\Omega_t \equiv \tan\theta^\star = \Delta/\varepsilon$. In this case, we can rotate into a frame where drive and qubit potential have even parity such that the interaction is meditated via $\Omega_t \hat{\sigma}_z / \cos\theta^\star$ (quadrupolar selection rules). The appearance of this effect in our data is a clear evidence for parity induced selection rules applicable to qubits with two degrees of freedom.

6.2.3 Transitions in a potassium-like atom

So far, we have demonstrated tunable selection rules between two states of opposite parity, which corresponds to the $1s \mapsto 2p$ transition in hydrogen-like atoms. We now include the resonator into the interaction mechanism to generalize the concept of parity inversion. For the dressed levels of our artificial potassium atom, the parity $\hat{\Pi}_{\text{int}}^{\text{res}} = -\hat{\sigma}_z e^{\imath\pi n}$ is the product of the two subsystems [see Fig. 6.8 (a)]. The red and blue sidebands connect states of equal parity, $|\text{g},n\rangle \mapsto |\text{e},n\pm1\rangle$ [see Fig. 6.8 (b)], corresponding to the dipolar forbidden transitions $4s \mapsto 5s$ and $4s \mapsto 3d$. For the sideband transitions, the interaction parity is even because the qubit-resonator coupling is mediated by $\hat{\sigma}_x$ (odd) and also the drive photon couples typically via $\hat{\sigma}_x$ such that the parity product is even. With our parity inversion technique it is possible to activate the sideband transitions by changing from antisymmetric $(\Omega_\ell = 0)$

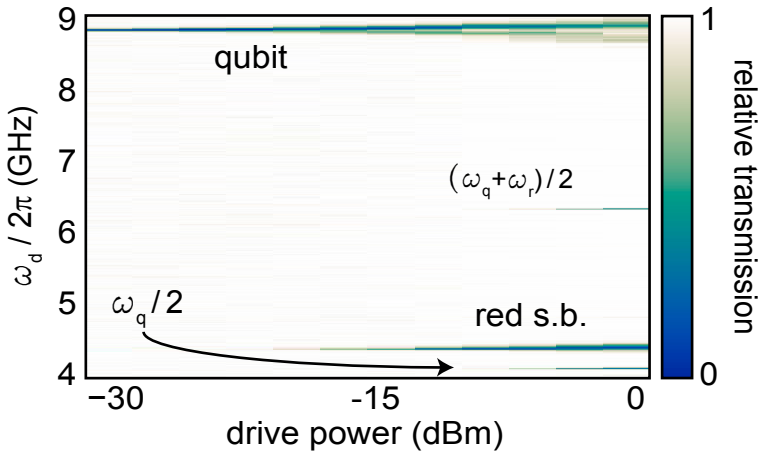

Figure 6.7: Two-tone spectroscopy at high drive power. The appearance of qubit splitting, red sideband, and two-photon transition is encoded in the transmission magnitude plotted versus drive power at the output of the microwave source.

to symmetric ($\Omega_t = 0$) drives. We show this based on the red sideband transition and based on the two-photon processes of the blue sideband and direct transition.
We activate sideband transitions by irradiating strong electromagnetic fields of frequency $(\omega_q - \omega_r)/n$ and $(\omega_q + \omega_r)/n$ for the n-photon red and blue sideband, respectively (see Fig. 6.7). Furthermore, multi-photon transitions of the direct process occur when irradiating strong electromagnetic fields of frequency ω_q/n. In the case $n = 2$, the qubit absorbs two photons of half the frequency.

Sideband transitions The red sideband transition can be seen as a two-photon process where one photon at frequency $\omega_q - \omega_r$ is taken from the drive and the second photon is taken from the resonator, $|g,n{+}1\rangle \mapsto |e,n\rangle$. As derived in detail in Sec. 2.3.3, this circumstance is expressed in the interaction Hamiltonian

$$\mathcal{H}_{\text{int}} = \frac{g}{\omega_q - \omega_r}\left[\frac{\Omega_\ell}{\Delta}\sin\theta - \frac{\Omega_t}{\Delta}\cos\theta\right](\hat{a} + \hat{a}^\dagger)\hat{\sigma}_x\,. \tag{6.2.3}$$

which yields a excited state probability $p_e \propto \mathcal{H}_{\text{int}}^2$. We see that the probability to drive red sideband transitions is reduced by $[g/(\omega_q - \omega_r)]^2 \simeq -40\,\text{dB}$ compared to the one-photon assisted transition. In Fig. 6.7 we show that the transition appears for drive powers 30 dB above the minimum drive power required to observe the one-photon transition. The flux dependence of this transition is directly opposite to that of one-photon transitions ($\sin\theta \mapsto \cos\theta$). For $\Omega_\ell = 0$, photons from the drive perform a parity swap and also photons from the resonator change the parity due to the $(\hat{a}^\dagger + \hat{a})\hat{\sigma}_x$ interaction. Hence, at the degeneracy point, transitions are forbidden. Due to a finite mixing angle θ, transitions can be induced when moving away from the degeneracy point. For the other extreme, $\Omega_t = 0$, the drive photon is emitted from a symmetric drive field, coupling to $\hat{\sigma}_z$. Nevertheless, the resonator photon still performs a parity swap via the $\hat{\sigma}_x$ interaction and the transition is allowed. Hence, the red sideband can be activated by changing the interaction operator for the drive photon from $\hat{\sigma}_x$ to $\hat{\sigma}_z$. This circumstance is expressed by the appearance of the red sideband at frequency $\delta = \omega_q - \omega_r \simeq 4.4\,\text{GHz}$ [case (i) in Fig. 6.8 (c)]. On contrast, when using two photons to drive a sideband, the interaction parity is always even. Consequently, the two-photon process of the blue sideband at frequency $(\omega_q + \omega_r)/2$ is allowed for antisymmetric and symmetric fields [case (ii) in Fig. 6.8 (c)]. The opposite is true for two-photon drives connecting states of opposite parity. In this case, the even interaction of the two-photon assisted transition $|g,n\rangle \mapsto |e,n\rangle$ is always forbidden [case (i) in Fig. 6.8 (c)].

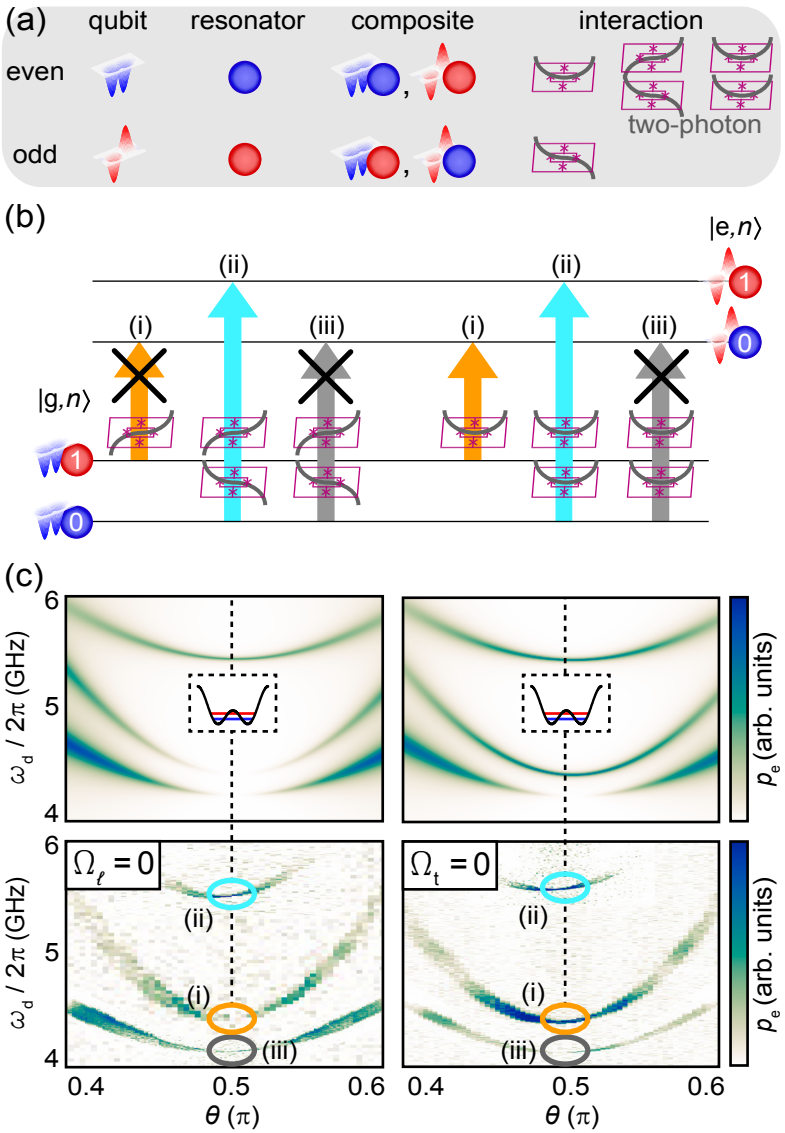

Figure 6.8: **(a)** Parity of qubit, resonator, and composite qubit-resonator states as well as of the interaction operator for one- and two-photon transitions. **(b)** Level scheme and corresponding parity of composite qubit-resonator states for multi-photon transitions $|\mathrm{g},n\rangle \mapsto |\mathrm{e},n\pm1\rangle$. Crossed out arrows denote forbidden transitions. **(c)** Expected (top row) and measured (bottom row) excited state probability p_e plotted versus Bloch angle θ and drive frequency ω_d. The circled areas show the red sideband (i), the two-photon transition (ii), and the two-photon transition of the blue sideband (iii), at the sweet spot (symmetric potential).

Two-photon transition In analogy to Eq. (2.3.26), we find the excited state probability for the direct two-photon process

$$\mathcal{H}''_\mathrm{int} = \frac{\hbar}{8}\left[\left(\Omega_\mathrm{t}^2 - \Omega_\ell^2\right)\sin^2\theta\cos\theta + \Omega_\ell\Omega_\mathrm{t}\left(\sin^3\theta - \cos^2\theta\sin\theta\right)\right]\hat{\sigma}_\mathrm{x}\,, \tag{6.2.4}$$

which can be derived from the two-photon driven Jaynes-Cummings Hamiltonian as derived in Eq. (2.3.26). Please note that Eq. (6.2.4) predicts the expected $\sin^2\theta\cos\theta$ dependence for the two-photon process of dipolar coupling for $\Omega_\ell = 0$. This process is suppressed by $(2g/\omega_\mathrm{q})^2 \simeq -40\,\mathrm{dB}$ compared to the one-photon process, which fits to the data shown in Fig. 6.7. Again, an intuitive picture of the excited state probability can be obtained when discussing the limits of symmetric and antisymmetric drive fields. At the degeneracy point and for $\Omega_\ell = 0$, two-photon transitions are forbidden due to the combined even parity, which is expressed by the $\cos\theta$ term [case (iii) in Fig. 6.8 (c)]. In contrast to the red sideband process, two-photon processes are also forbidden for $\Omega_\mathrm{t} = 0$ at the degeneracy point for parity reasons. Away from that point, two-photon transitions appear as expected from theory.

In conclusion we demonstrate a novel technique for the in-situ parity inversion to transform selection rules from dipolar to quadrupolar in superconducting circuits. By precisely shaping the amplitude distribution of microwave fields across the area of a quadrupolar flux qubit, we generate either longitudinal or transverse interaction mechanisms. That way, we can continuously tune transitions from allowed to forbidden at the qubit degeneracy point. Hence, we engineer either electric dipolar or electric quadrupolar selection rules for our qubit. When we break the symmetry of the qubit potential in exactly the same way as the symmetry of the microwave drive, we find new quadrupolar selection rules for a qubit with two degrees of freedom. Finally, we show that including a resonator into the interaction creates an artificial potassium. In this case, we activate quadrupolar interaction corresponding to the dipolar forbidden transitions $4s \mapsto 5s$ and $4s \mapsto 3d$. Our comprehensive study of parity tuning strongly enhances the understanding of coupling mechanisms in artificial atoms. The physics, however, is not restricted to these particular fields but applies generally to a quadrupolar two-level system exposed to a harmonic drive. This fact makes our study valuable for the various situations using two-level systems, reaching from optics [105], over trapped ions [521] and spin systems [522–524] to superconducting circuits [27, 100, 102, 515, 516]. Furthermore, we have not made any restrictions on the interaction mechanisms which also allows to apply our model to different coupling mediated for example by phonons [525] or magnons [526, 527]. Our study shows that quadrupolar interaction can be precisely engineered which leads towards more advanced studies such as phase transitions in Fermi gases [528].

Chapter 7
Conclusions and outlook

We sum up the key results of this thesis in Sec. 7.1 and give an outlook towards future experiments in Sec. 7.2. In the outlook, we focus on the possibility to squeeze a resonator mode using the tunable gradiometric flux qubit presented throughout this thesis.

7.1 Summary

In this thesis, we characterize inherent properties of superconducting quantum circuits and of electromagnetic radiation present in these circuits. To this end, we develop and improve comprehensive experimental techniques used for the characterization of quantum circuits.

Regarding the fabrication of superconducting quantum circuits, we have established a routine for qubit-resonator samples fabricated in an all-Al process. This task was triggered by a careful analysis of the loss mechanisms in CPW resonators based on a Nb/Al bilayer technology [38]. In our detailed study, we find that a significant loss contribution arises due to TLSs located in the thin oxide layer between the two metal structures. Consequently, we get rid of these interfaces by using all-Al resonators. This important step has pushed the quality of the qubit-resonator systems by one order of magnitude. The technical challenge to establish an all-Al fabrication of resonators with integrated Josephson junction-based circuits has benefit from a new EBL facility, which was purchased during this thesis. Based on this new device, we optimize our fabrication process mainly by using gold nanoparticles as focusing material. Using this technique together with an improved spin-coating process, sample fabrication has become a reliable resource for new experiments.

Throughout this thesis, we have put experimental effort into the construction of a new laboratory for quantum measurements (CIRQUS lab). In this new lab, we characterize superconducting quantum circuits at millikelvin temperature. Therefore, we have constructed a custom-built dilution refrigerator operating at 25 mK with a cooling power of 140 µW at 100 mK. To sustain large experimental flexibility, there are 24 coaxial lines mounted in the cryostat, which allow for larger scale circuit QED experiments in the future. Furthermore, we establish a measurement routine for time resolved measurements of qubit states. To this end, we use a heterodyne down-conversion setup and perform digital homodyning, which enables a broadband detection of quantum oscillations. Measurements performed with these setups build the heart of the experimental results presented in this thesis.

In order to systematically improve the performance of the superconducting quantum circuits studied in this thesis, we investigate geometry aspects and power dependencies of open

tranmission lines, resonators, and antenna structures. We find that resonators characterized in a helium bath cryostat significantly suffer from surface resistance loss, which is enhanced when using gridded groundplanes. When reducing power and temperature to the single photon regime, we show that the finite substrate thickness of 250 µm is a limiting factor in our experiments. We can quantitatively explain this fact with dissipative eddy currents in the conductive material on the backside of the substrate. Consequently, we adapt our fabrication process to 525 µm thick substrates. In addition to this eddy current loss, we show that quasiparticle loss in Al can be strong when heating the sample above 200 mK. Because this loss channel is also present in superconducting qubits, heating the sample is no option for a reliable study of the interaction between the thermal contribution of a noise field and a qubit. Therefore, we adapt a technique from state reconstruction setups [139] in order to generate propagating thermal microwave states. We use heatable attenuators in the feedlines, which are thermally only weakly coupled to the qubit and are therefore a well-defined control knob to tune the noise spectral density $\mathcal{S}(\omega)$. Using a transmon qubit, we find that the maximum coherence time of approximately 500 ns is strongly reduced when irradiating the qubit with propagating thermal fields [39]. In particular, utilizing a resonator as a Purcell filter for the qubit, we find that the qubit relaxation rate is enhanced by 13 dB compared to the value expected from the filter function of the resonator. When we send broadband thermal fields through an on-chip antenna, we find the expected T^3 law for dephasing due to second-order coupling at the qubit sweet spot. Finally, we investigate the influence of thermal fields on the low-frequency spectrum of qubit parameter fluctuations. We find that thermal fields enhance the white contribution of the noise power spectral density if applied broadband via an on-chip antenna. Our data confirms a model of thermally activated TLSs interacting with the qubit. The resonator, however, can filter this effect efficiently.

We use the transmon-resonator system discussed above to characterize the photon statistics of different propagating microwave fields. By varying the power of a coherent microwave drive, we quantitatively confirm the Poissonian statistics of coherent microwave fields. Furthermore, we show that a qubit-resonator system can be used to distinguish between the Poissonian statistics of coherent fields and the Poissonian statistics of shot noise. The reason is that the characteristic decay constant of the resonator is different for coherent and incoherent input fields. Finally, we use the qubit-resonator setup to quantify the super-Poissonian $n^2 + n$ law for thermal fields with high accuracy below one photon on average. We find that the accuracy of the qubit setup is limited by low-frequency fluctuations of the qubit relaxation rate. To test the efficiency of the qubit as a microwave detector, we compare our results to direct correlation measurements performened with a dual-path reconstruction setup. While also this setup quantitatively recovers the $n^2 + n$ statistics of thermal fields, there is a higher statistical error in these measurements when using only off-the-shelf components in the setup. Nevertheless, using a near-quantum-limited amplifier as preamplifier lowers the statistical error by two orders of magnitude. The preamplifier, however, introduces a finite systematical error due to the statistics of the amplifier noise. Our results provide fundamental insight into the nature of propagating thermal microwaves, which is especially relevant for the characterization of more advanced quantum states in the presence of unavoidable thermal background fields. With respect to superconducting qubits, we gain systematic insight into a dephasing mechanism which may become relevant for state-of-the-art, high-coherence devices.

Finally, we present a comprehensive study of selection rules for quadrupolar qubits based

on a parity concept for the interaction operator. To this end, we derive the transition probability for single- and multi-photon processes based on a drive with controllable amplitude distribution. For symmetric field configurations, the drive couples to the even $\hat{\sigma}_{\mathrm{z}}$ operator and for antisymmetric fields it couples to the odd $\hat{\sigma}_{\mathrm{x}}$ operator. We implement the parity inversion technique using a tunable gradiometric flux qubit, which is located in the near-field of two on-chip antennas. The well-defined amplitude distribution of these fields directly translates into the parity of the respective interaction operator. Our results show that the symmetry of the irradiated field is a convenient control knob for the interaction parity in circuit QED experiments. Because our study is generally valid for any quadrupolar two-level system coupled to a bosonic field, it provides important insight for a wide variety of physical applications.

7.2 Outlook: Squeezing with a gradio qubit

Within the last years, two research areas dealing with superconducting quantum circuits have emerged in parallel at the WMI. The first area is the study of light-matter interaction based on superconducting qubits [26, 28, 31, 39, 41, 83, 185, 243, 303] and the second area is the reconstruction and entangling of propagating microwave states [139, 152, 163, 440, 443]. However, as already presented in our study on photon statistics [41], there is a strong connection between the two fields. Moreover, it is straightforward to combine these two fields because they use the same microwave techniques at cryogenic and at room temperature. In the following, we present an experiment based on the gradio qubit, which has the ability to generate squeezed fields inside a resonator [517]. These fields can, on the one-hand, be detected with the dual-path setups developed at the WMI and, on the other hand, serve for entanglement processes that are required for quantum teleportation and illumination protocols based on propagating microwaves.

The idea of the experiment described in the following is to cool a particular mode ω_{r} of a superconducting transmission line resonator into a squeezed vacuum as presented in Ref. 517. To this end, we couple a tunable gradiometric flux (gradio) qubit galvanically to the resonator and use two antennas in exactly the way presented in Sec. 6.2. Squeezing occurs when driving red and blue sideband transitions simultaneously with controlled relative amplitudes η_1 and η_2 as depicted in Fig. 7.1 (a). Hence, the control parameter for the squeezing level will be the relative drive amplitude η_1/η_2 of the two coherent drives. Due to the two drives, we generate a superposition of sideband cooling and of sideband heating using the interaction of a qubit with a light field. If the decay rate γ_{q} of the qubit is large compared to the coupling rate g, the qubit continuously absorbs photons from but also emit photons to the resonator field and subsequently decays to the environment. This process performs a change of basis from the standard Jaynes-Cummings interaction $\mathcal{H}_{\mathrm{int}} = \hbar g(\hat{a} + \hat{a}^{\dagger})(\hat{\sigma}_{+} + \hat{\sigma}_{-})$ to a new base $\hat{b} = u\hat{a} + v\hat{a}^{\dagger}$ with $|u|^2 - |v|^2 = 1$. The resonator field is now a two-photon coherent state [529], which obeys $[\hat{b},\hat{b}^{\dagger}] = 1$. This means a unitary operator $\hat{S}$ can perform a transformation $\hat{b} = \hat{S}\hat{a}\hat{S}^{\dagger}$. In this formalism we obtain the state $|\beta\rangle = \hat{D}(\beta)\hat{S}\,|0\rangle$ by applying the displacement operator $\hat{D}(\beta)$ on the vacuum state $|0\rangle$. This operation is similar to the standard form of squeezing if we identify the operator $\hat{S}$ with the squeezing operator $\hat{S}(z)$ [7]. Here, $z = re^{\imath\phi}$ is the complex squeezing parameter where the phase ϕ determines the direction and the squeeze factor r the amount of squeezing. The difference to the usual definition of squeezing $|\alpha,z\rangle = \hat{S}(z)\hat{D}(\alpha)\,|0\rangle$ is the permutation of $\hat{S}$ and $\hat{D}$. Anyhow, both procedures yield the same state if the displacement parameters

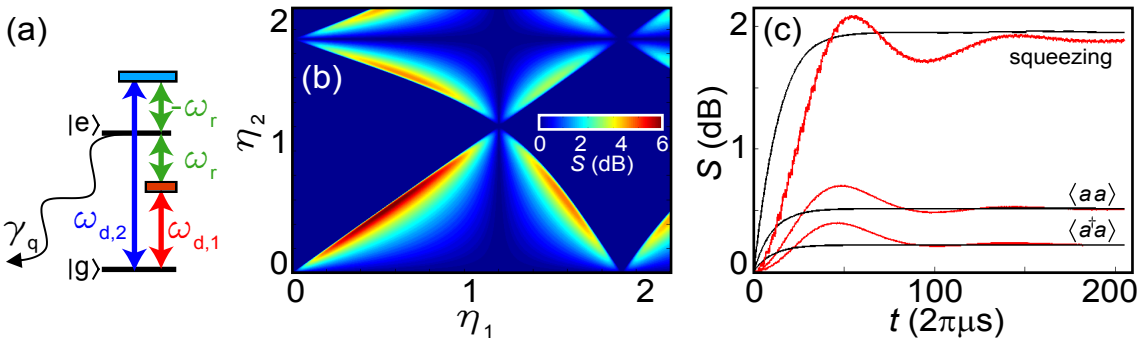

Figure 7.1: **(a)** Relevant drive frequencies to degenerate squeezing. **(b)** Color encoded squeezing level S of one resonator mode plotted versus relative amplitude of the two drives. The experimental parameters are $\omega_\mathrm{r}/2\pi = 4\,\mathrm{GHz}$, $\Delta/2\pi = 10\,\mathrm{GHz}$, $g/2\pi = 100\,\mathrm{MHz}$, $\gamma_\mathrm{q}/2\pi = 100\,\mathrm{MHz}$, $Q_\ell = 10^4$. **(c)** Sequeezing and second order cumulants $\hat{a}\hat{a}, \hat{a}^\dagger\hat{a}$ plotted versus time using an exact calculation (red line) and the effective master equation (black line). We acknowledge the discussions with D. Poras who provided the results shown in panel (b) and panel (c).

α and β obey $\alpha = u\beta - v\beta^\star$ which is the case for our notation. Engineering a coupling in the $\hat{b}$-basis, the qubit-field interaction is given as

$$\mathcal{H}_\mathrm{int,sq} = g(\hat{b}\hat{\sigma}_+ + \hat{b}^\dagger\hat{\sigma}_-) = g[(\sqrt{1+v^2}\hat{a} + v\hat{a}^\dagger)\hat{\sigma}_+ + (\sqrt{1+v^2}\hat{a}^\dagger + v\hat{a})\hat{\sigma}_-]\,. \tag{7.2.1}$$

meaning that the qubit can be excited by absorbing a photon with probability $\sqrt{1+v^2}$ and simultaneously creating a photon with probability v. Therefore, this type of coupling combined with a fast qubit decay cools the field mode to a squeezed vacuum $|0\rangle_b$, determined by the condition $\hat{b}\,|0\rangle_b = 0$. In the following, we show how we can implement this kind of coupling by driving the red and blue sideband simultaneously.
To induce sidebands we selectively drive the qubit gap Δ of the gradio qubit using a symmetric field configuration. The drive with frequency ω_d can be expressed as

$$\mathcal{H}_\mathrm{d}(t) = -\frac{\eta}{2}\omega_\mathrm{d}\left(e^{-\imath\omega_\mathrm{d}t} + e^{\imath\omega_\mathrm{d}t}\right)\hat{\sigma}_\mathrm{z}\,. \tag{7.2.2}$$

We assume that the drive modulates the coupling between qubit and resonator in the form

$$G(t) = g\left[1 - \eta\left(e^{-\imath\omega_\mathrm{d}t} + e^{\imath\omega_\mathrm{d}t}\right)\right]\,. \tag{7.2.3}$$

A scheme to implement this time-dependent coupling follows further below. As our driving explicitly introduces a time dependency, the drive rotates against qubit, resonator and interaction. The total system Hamiltonian is therefore given as $\mathcal{H}_\mathrm{t} = \mathcal{H}_0 + \mathcal{H}_\mathrm{d}(t) + \mathcal{H}_\mathrm{i}(t)$. Moving to the rotating frame with respect to $\mathcal{H}_0 + \mathcal{H}_\mathrm{d}(t)$ we apply the unitary transformation $U = \exp\left(-\imath\left[\mathcal{H}_0 + \mathcal{H}_\mathrm{d}(t)\right]\right)$. This transformation yields a Hamiltonian which has a time-dependent modulation of the coupling. If we chose the drive frequency $\omega_{\mathrm{d},1} = \Delta - \omega_\mathrm{r}$ and introduce a second drive at $\omega_{\mathrm{d},2} = \Delta + \omega_\mathrm{r}$, the resulting Hamiltonian in the interaction picture reads

$$\begin{aligned}\mathcal{H}_{\text{i.p.}} &= g\hat{\sigma}_+\left(\eta_1\hat{a}+\eta_2\hat{a}^\dagger\right)+\text{H.c.}\\ &\quad - g\hat{\sigma}_+\left(\eta_1\hat{a}e^{\imath 2\Delta t}+\eta_2\hat{a}^\dagger e^{\imath 2\Delta t}\right)+\text{H.c.}\\ &\quad + g\hat{\sigma}_+\left(\hat{a}e^{\imath\omega_{\text{d},1}t}-\eta_1\hat{a}^\dagger e^{i2\omega_{\text{d},1}t}\right)+\text{H.c.}\\ &\quad + g\hat{\sigma}_+\left(\hat{a}e^{\imath\omega_{\text{d},2}t}-\eta_2\hat{a}^\dagger e^{i2\omega_{\text{d},2}t}\right)+\text{H.c.}\\ &\quad + g\hat{\sigma}_+\left(\eta_2\hat{a}e^{i2\omega_{\text{r}}t}+\eta_1\hat{a}^\dagger e^{i2\omega_{\text{r}}t}\right)+\text{H.c.}\,. \end{aligned} \tag{7.2.4}$$

With respect to the first line all terms in Eq. (7.2.4) are rotating fast and can be neglected in a rotating wave approximation. Due to normalization, a rotating wave approximation of Eq. (7.2.4) can be transferred to the form of the squeezing interaction defined in Eq. (7.2.1) as follows:

$$\begin{aligned}\mathcal{H}_{\text{i.p.}} &= g\hat{\sigma}_+\left(\eta_1\hat{a}+\eta_2\hat{a}^\dagger\right)+\text{H.c.}\\ &= g\sqrt{\eta_1^2-\eta_2^2}\hat{\sigma}_+\left(\frac{\eta_1 g}{g\sqrt{\eta_1^2-\eta_2^2}}\hat{a}+\frac{\eta_2 g}{g\sqrt{\eta_1^2-\eta_2^2}}\hat{a}^\dagger\right)+\text{H.c.}\\ &= \bar{g}\hat{\sigma}_+\left(u\hat{a}+v\hat{a}^\dagger\right)+\text{H.c.}\,, \end{aligned} \tag{7.2.5}$$

using $\bar{g}=g\sqrt{\eta_1^2-\eta_2^2}$ and $u,v=\eta_{1,2}g/\bar{g}$. To obtain the interaction Hamiltonian in Eq. (7.2.5) we have to implement the time-dependent coupling of Eq. (7.2.3). This can be achieved by the driving explained above which creates a net magnetic flux at the $\alpha-$SQUID. The sinusoidal flux variation induces a modulation of qubit's α-value. The modulation transfers to the persistent current of the qubit, which reads

$$I_{\text{p}}(\alpha)=I_{\text{c}}\sqrt{1-\left(\frac{1}{2\alpha}\right)^2}=I_{\text{c}}\sqrt{1-\left(\frac{1}{2\left|\cos\left(\pi\frac{\Phi_{\text{s}}+\Phi_{\text{d}}(t)}{\Phi_0}\right)\right|}\right)^2}\,. \tag{7.2.6}$$

Here, we assume that the flux in the α-SQUID is composed of a static part Φ_{s} and an oscillating part $\Phi_{\text{d}}(t)$. For simplicity the following calculations are performed for a single drive frequency ω_{d} but can easily be extended to two ore more frequencies. As we have inductively coupled antennas the induced flux has the form $\Phi_{\text{d}}(t)=M_{\text{d}}I_{\text{d}}\cos(\omega_{\text{d}}t)$ where M_{d} is the mutual inductance between antenna and α-SQUID, and I_{d} is the current flowing through the antenna lines. If the amplitude of $\Phi_{\text{d}}(t)$ is small compared to Φ_0 we can Taylor expand Eq. (7.2.6) which yields

$$\begin{aligned}I_{\text{p}}(t) &= I_{\text{p}}(\alpha_0)+\underbrace{\frac{\partial I_{\text{p}}}{\partial\alpha}_{\alpha=\alpha_0}\frac{\partial\alpha}{\partial\Phi}_{\Phi=\Phi_{\text{s}}}M_{\text{d}}I_{\text{d}}}_{\eta}\cos(\omega_{\text{d}}t)+\mathcal{O}(\eta^2)\\ &= I_{\text{p}}(\alpha_0)\left(1-\frac{1}{I_{\text{p}}(\alpha_0)}\frac{I_{\text{c}}}{\sqrt{16\alpha_0^6-4\alpha_0^4}}\frac{\pi}{\Phi_0}\sin\left(\pi\frac{\Phi_{\text{s}}}{\Phi_0}\right)\Phi_{\text{d}}(t)\right)+\mathcal{O}(\eta^2)\,. \end{aligned} \tag{7.2.7}$$

Hence, we obtain a static persistent current $I_\mathrm{p}(\alpha_0)$ modulated by an effective amplitude η. The static value α_0 is connected to Φ_s by Eq. (7.2.6) and we obtain

$$\begin{aligned}\eta &= \frac{1}{\sqrt{1-\left(\frac{1}{2\alpha_0}\right)^2}} \frac{\pi}{\sqrt{16\alpha_0^6 - 4\alpha_0^4}} \frac{M_\mathrm{d} I_\mathrm{d}}{\Phi_0} \sin\left(\cos^{-1}(\alpha_0)\right) \\ &= \frac{-\pi}{\alpha_0 - 4\alpha_0^3} \sin\left(\cos^{-1}(\alpha_0)\right) \frac{M_\mathrm{d} I_\mathrm{d}}{\Phi_0} \,. \end{aligned} \tag{7.2.8}$$

This result shows that the modulation amplitude η depends on the one hand on α_0, i.e., on the static bias Φ_s and on the other hand on the induced RF field $M_\mathrm{d} I_\mathrm{d}$ and thus on Φ_d. In summary we have a persistent current that is modulated with frequency $\omega_\mathrm{d}/2\pi$ and amplitude η. Considering that g depends on the persistent qubit current, also the coupling strength is modulated in this way. Therefore, we achieve the desired time-dependent coupling $G(t) = g[1 - \eta\cos(\omega_\mathrm{d} t)] + \mathcal{O}(\eta^2)$ as required from Eq. (7.2.3).

List of publications

- Jan Goetz, P. Eder, M. Fischer, S. Pogorzalek, E. Xie, K. G. Fedorov, F. Deppe, A. Marx, R. Gross, "Parity-engineered selection rules in an artificial potassium atom", in preparation (2017).
- Jan Goetz, P. Eder, M. Fischer, S. Pogorzalek, E. Xie, K. G. Fedorov, F. Deppe, A. Marx, R. Gross, "Superconducting flux qubits with two degrees of freedom in a circuit-QED architecture", in preparation (2017).
- P. Eder, Jan Goetz, M. Fischer, S. Pogorzalek, E. Xie, K. G. Fedorov, F. Deppe, A. Marx, J.-J. Garcia-Ripoll, R. Gross, "Probing a superconducting on-chip interferometer with a transmon qubit", in preparation (2017).
- K. G. Fedorov, S. Pogorzalek, U. Las Heras, M. Sanz, P. Yard, P. Eder, M. Fischer, Jan Goetz, E. Xie, K. Inomata, Y. Nakamura, R. Di Candia, E. Solano, A. Marx, F. Deppe, R. Gross, "Finite-time quantum entanglement in propagating squeezed microwaves", ArXiv e-prints: 1703.05138 (2017).
- Jan Goetz, S. Pogorzalek, F. Deppe, K. G. Fedorov, P. Eder, M. Fischer, F. Wulschner, E. Xie, A. Marx, R. Gross, "Photon Statistics of Propagating Thermal Microwaves," Phys. Rev. Lett. **118**, 103602 (2017).
- Jan Goetz, F. Deppe, P. Eder, M. Fischer, M. Müting, J. Puertas Martínez, S. Pogorzalek, F. Wulschner, E. Xie, K. G. Fedorov, A. Marx, R. Gross, "Second-order decoherence mechanisms of a transmon qubit probed with thermal microwave states", Quant. Sci. Tech. **2**, 025002 (2017).
- S. Pogorzalek, K. G. Fedorov, L. Zhong, Jan Goetz, F. Wulschner, M. Fischer, P. Eder, E. Xie, K. Inomata, T. Yamamoto, Y. Nakamura, A. Marx, F. Deppe, R. Gross, "Flux-driven Josephson parametric amplifiers: hysteretic flux response and nondegenerate gain measurements", ArXiv e-prints: 1609.09041 (2016).
- F. Wulschner, Jan Goetz, F. R. Koessel, E. Hoffmann, A. Baust, P. Eder, M. Fischer, M. Haeberlein, M. J. Schwarz, M. Pernpeintner, E. Xie, L. Zhong, C. W. Zollitsch, B. Peropadre, J.-J. Garcia Ripoll, E. Solano, K. G. Fedorov, E. P. Menzel, F. Deppe, A. Marx, R. Gross, "Tunable coupling of transmission-line microwave resonators mediated by an rf SQUID", EPJ Quant. Tech. **3**, 10 (2016).
- K. G. Fedorov, L. Zhong, S. Pogorzalek, P. Eder, M. Fischer, Jan Goetz, E. Xie, F. Wulschner, K. Inomata, T. Yamamoto, Y. Nakamura, R. Di Candia, U. Las Heras, M. Sanz, E. Solano, E. P. Menzel, F. Deppe, A. Marx, R. Gross, "Displacement of Propagating Squeezed Microwave States", Phys. Rev. Lett. **117**, 020502 (2016).

- A. Baust, E. Hoffmann, M. Haeberlein, M. J. Schwarz, P. Eder, Jan Goetz, F. Wulschner, E. Xie, L. Zhong, F. Quijandria, D. Zueco, J.-J. Garcia Ripoll, L. Garcia-Alvarez, G. Romero, E. Solano, K. G. Fedorov, E. P. Menzel, F. Deppe, A. Marx, R. Gross, "Ultrastrong coupling in two-resonator circuit QED", Phys. Rev. B **93**, 214501 (2016).

- Jan Goetz, F. Deppe, M. Haeberlein, F. Wulschner, C. W. Zollitsch, S. Meier, M. Fischer, P. Eder, E. Xie, K. G. Fedorov, E. P. Menzel, A. Marx, R. Gross, "Loss mechanisms in superconducting thin film microwave resonators", J. Appl. Phys. **119**, 015304 (2016).

- M. Haeberlein, F. Deppe, A. Kurcz, Jan Goetz, A. Baust, P. Eder, K. G. Fedorov, M. Fischer, E. P. Menzel, M. J. Schwarz, F. Wulschner, E. Xie, L. Zhong, E. Solano, A. Marx, J.-J. Garcia Ripoll, R. Gross, "Spin-boson model with an engineered reservoir in circuit quantum electrodynamics", ArXiv e-prints: 1503.08065 (2015).

- A. Baust, E. Hoffmann, M. Haeberlein, M. J. Schwarz, P. Eder, E. P. Menzel, K. G. Fedorov, Jan Goetz, F. Wulschner, E. Xie, L. Zhong, F. Quijandria, B. Peropadre, D. Zueco, J.-J. Garcia Ripoll, E. Solano, F. Deppe, A. Marx, R. Gross, "Tunable and Switchable Coupling Between Two Superconducting Resonators", Phys. Rev. B **91**, 014515 (2015).

- M. J. Schwarz, Jan Goetz, Z. Jiang, T. Niemczyk, F. Deppe, A. Marx, R. Gross, "Gradiometric flux qubits with tunable gap", New J. Phys. **15**, 045001 (2013).

Danksagung

Diese Dissertation ist in den letzten viereinhalb Jahren meiner Zeit am Walther-Meißner-Institut (WMI) in Garching entstanden. In dieser Zeit wurde die Physik supraleitender Schaltkreise erforscht und wissenschaftlich diskutiert, es wurde aber auch gefeiert und gelacht. Alles Aktivitäten, die man ungern alleine im Labor macht, sondern die einen großen Kreis an Mitmenschen und Infrastruktur voraussetzen. Am WMI habe ich diese Voraussetzungen sowohl auf wissenschaftlicher, als auch auf persönlicher Ebene genießen dürfen. Diese Freude hat mir mein Doktorvater Rudolf Gross ermöglicht, der mit Weitsicht und hohem Arbeitsaufwand eine Forschungsgruppe zu supraleitenden Quantenschaltkreisen etabliert hat. Ich bin froh und dankbar, ein Teil dieser Gruppe zu sein und einen kleinen Beitrag zu deren Weiterentwicklung leisten zu dürfen. Ich habe in meiner Zeit am WMI sehr viel über Physik im Sinne der Wissenschaft, aber auch über den Forschungsalltag mit all seinen Hürden, Überraschungen und Faszinationen gelernt. Nicht zuletzt, weil wir Doktoranden immer offen und ehrlich in jegliche Gespräche mit eingebunden wurden. Ich bedanke mich herzlich für viereinhalb überaus wertvolle Jahre am WMI!
Aus wissenschaftlicher Sicht geht mein besonderer Dank an Frank Deppe und Achim Marx, die mir mit ihrem großem Erfahrungsschatz stets beratend und hilfreich zur Seite standen. Ihr habt mir in jeder Situation eine große Freiheit für meine eigenen Ideen und Pläne eingeräumt. Nichtsdestotrotz habt ihr mir auch immer dann weiter geholfen, wenn einmal etwas nicht so gut funktioniert hat. Mit euch ein neues Labor aufzubauen hat mich aus organisatorischer, aber auch aus technischer Hinsicht viele neue Dinge gelehrt. Gerade diese technischen Fragestellungen, die mit über zwei Jahren Dauer einen Großteil meiner Arbeit ausgemacht haben, waren für mich immer abwechslungsreich und voller unvorhersehbarer Herausfordungen. Die breite Aufgabenvielfalt hat mir die Experimentalphysik in meiner Zeit am WMI sehr ans Herzen gelegt.
Das Stemmen dieser Aufgabenvielfalt wäre sicherlich nicht ohne meinen Büro- und Laborgenossen Friedrich Wulschner möglich gewesen. Die unzähligen Stunden, die wir zusammen mit Hammer und Lötkolben im Labor verbracht haben, während wir uns mit Kaltgetränken im Loch über Wasser halten mussten, gehören sicherlich zu den prägendsten Eindrücken aus meiner Zeit am WMI. Es war schön, gemeinsam den CIRQUS Kryostaten aufzubauen und zu sehen, dass am Ende auch etwas sinnvolles damit erreicht werden kann.
Natürlich kann man eine Anlage, wie den Kryostaten im CIRQUS Labor nicht ohne die Vorkenntnisse und jahrelange Erfahrung diverser Experten am WMI aufbauen. Zum Gelingen des Projektes CIRQUS Labor haben auch maßgeblich die Kryo-Experten Christian Probst, Karl Neumeier und Sepp Höss beitragen. Insbesondere bei Christian Probst und Karl Neumeier möchte ich mich für den unermüdlichen Arbeitseinsatz bedanken, den sie in ihrer Freizeit erbracht haben. Ihre zahlreichen Ratschläge und ihre handwerkliche Unterstützung haben mir wesentlich beim Aufbau des Kryostaten geholfen.
Den Aufbau an sich, also das Fertigen aller Komponenten, hat in extrem zuverlässiger und präziser Weise die feinmechanische Werkstatt am WMI vollzogen. Es ist toll, dass man mit jedem Problem zu euch kommen kann und dass am Ende meistens eine simple und elegante Lösung gefunden wird, auf die wir Wissenschaftler vielleicht nicht direkt kommen

würden. Abseits der Werkstatt war es immer ein Vergnügen, mit euch beim Kaffee in der Küche, beim Ochsenbraten auf der Wiesn oder bei den diversen Institutsfesten Gedanken auszutauschen.
Wenn ein Kryostat einmal fertig gestellt ist, sollte er auch betrieben werden. Letzteres war nur durch die zuverlässige Versorgung mit kryogenen Flüssigkeiten der Heliumhalle möglich. Besonders bei Jan Naundorf möchte ich mich für seine stets unkomplizierte Hilfe und die Versorgung mit kryogenen Flüssigkeiten auf der Rampe bedanken!
Da man einen Kryostaten nur einkühlt, wenn man auch etwas sinnvolles zu messen hat, ist es wichtig, dass die Probenherstellung zuverlässig funktioniert. Die Fabrikation von Dünnschicht Proben hat zwei Säulen. Zum einen die Verfügbarkeit von allen benötigten Chemikalien sowie das Fachwissen zu ebendiesen. Mit ihrer Hilfsbereitschaft und ihren Ratschlägen waren Karen Helm-Knapp und Astrid Habel mir eine große Unterstützung. Zum anderen benötigt man funktionierende Depositationsanlagen und eine zuverlässige Reinraumtechnik. An dieser Stelle möchte ich mich bei Tom Brenninger und Sebastian Kammerer dafür bedanken, dass sie stets mit vollem Arbeitseinsatz unserer Vakuumcluster und die Reinraumtechnik in Stand gehalten haben.
Hat man dann einmal etwas an seinen Proben in einem Kryostaten gemessen, sollten die Ergebnisse offen und auf breiter Basis diskutiert werden. Neben den o.g. Rudolf Gross, Frank Deppe und Achim Marx habe ich stets ein offenes Ohr bei Kirill Fedorov und Hans Hübl gefunden. Ich habe sehr davon profitiert, dass ihr nicht nur wegen Kleo in mein Büro gekommen seid, sondern dass ihr immer auch auf die Fragen eingegangen seid, die bei mir gerade aktuell waren. Insbesondere die von Hans organisierten PhD Workshops waren jedes Mal eine fruchtbare Plattform für offene Diskussionen, die wir Doktoranden sehr genossen haben. Der leidenschaftliche, fast schon explosive Drang zur Physik hat mir stets einen sehr direkten Zugang zu oft komplexen Herausfordungen eröffnet.

Viele Ergebnisse, die in dieser Arbeit zusammen gefasst sind, beruhen auf der Anstrengung von Diplom-, Bachelor-, oder Masterstudenten mit denen ich zusammen arbeiten durfte. Allen voran Franz Sterr, der sich als “mein” erster Student zusammen mit Max Häberlein in die Tiefen der Elektronstrahllithographie gearbeitet hat. Die dabei von Franz etablierten Techniken setzen noch immer einen Standard bei unseren Fabrikationsprozessen. Abseits des Reinraums war Franz aber auch von Berlin bis München eine überaus motivierte und produktive Unterstützung. Die Ergebnisse zur Charakterisierung von supraleitenden Resonatoren bauen maßgeblich auf der Bachelorarbeit von Sebastian Meier und der Masterarbeit von Philipp Summer auf. Beide haben sich mit dem teils zähen Prozess der Qualitätsoptimierung in der Dünnschichttechnologie auseinander gesetzt. Die Antennencharakterisierung wurde von Hans-Peter Gürtner mit großer Sorgfalt durchgefürt und bildet die Grundlage für die Studie zur Auswahlregeln an quadrupolaren Quantenbits. Meine ersten Erfahrungen mit der Erzeugung und Detektion thermischer Mikrowellen-Zustände habe ich während der Bachelor Arbeit von Daniel Arweiler gesammelt. Insofern ist diese Arbeit der Keim für die Experimente, die wir mit dem Transmon Quantenbit durchgeführt haben. Die Fabrikation und eine erste Charakterisierung dieser Probe verdanke ich der Masterarbeit von Javier Puertas Martínez und Edwin Menzel, der als Postdoc damals die Koordination dieser Probe übernommen hat. Eine zeitaufgelöste Charakterisierung dieser Probe wäre nicht ohne die Masterarbeit von Miriam Müting möglich gewesen, die sich mit diesem komplexen Thema auseinander gesetzt hat. Insofern kann ich nicht ganz ohne Stolz sagen, dass sich alle Studenten, die mit mir zusammen gearbeitet haben, an diversen Stellen dieser Arbeit wiederfinden.

All diese Worte würden hier so nicht stehen, wären da nicht ein paar Personen, die mir eine Promotion am WMI schmackhaft gemacht hätten. An erster Stelle möchte ich hier Manuel Schwarz und Tomasz Niemczyk nennen. Dank euch hatte ich bereits eine super Zeit als Diplomand, die mir gezeigt hat, welche Möglichkeiten es am WMI gibt. Die rotierende Zeit in der Küche mit Louis, auf der Rampe mit August oder auf dem rollenden Fass im Untergrund werden sicherlich noch lange in Erinnerung bleiben. Nicht weniger prägend waren meine Erfahrungen mit Max Häberlein und Flo Kretzschmar. Wärend Max nicht nur ein guter Sparing-Partner bei der Diskussion über den Rand schwarzer Löcher war, hat Flo mir bis zum Ende seiner Promotion stets die Zeit im Büro versüßt. Auch wenn auf der Isar mal der ein- oder andere Ast im Weg war, haben wir uns doch immer wieder zusammen gerauft und sind Sieger beim Rundlauf in der Pingpong Bar geworden. Wenn wir mal keinen Pingpong Schläger dabei hatten, sind wir mit Peter Eder, der uns super beherbergt hat, zum Fußball beim FC Gröding gefahren. Ich möchte mich recht herzlich für das Rennen mit nackten Tatsachen und die Flutscheinwerferrechnung bedanken! Neben der gemeinsamen Zeit in Salzburg, möchte ich mich bei Peter aber für seine Gesellschaft bei hektoliterweisem Kaffeegenuss bedanken. Mit keinem anderen konnte man besser Schmuckkästchen suchen oder auf Lianen ausrutschen. Neben der oben beschriebenen gemeinsamen Arbeit im Labor war Friedrich Wulschner auch auf nichtwissenschaftlicher Ebene ein treuer Begleiter. Oft hat er mitgeholfen, den Cola-Mix aus dem Automaten zu ziehen, wenn abends mal wieder eine Motorhaube im Weg war oder man sich die Schärfe von Mexikanern verinnerlicht hat. Gegen Ende meiner Promotion wurden die Feierabendgespräche oft durch Philipp Schmidt und Stefan Klingler bereichert. Zwei Typen, bei denen die Maß stets halb voll und nicht halb leer ist, die weder vor Hartmut Engler zurück schrecken, noch vor dubiosen Szeneclubs in Berlin. Feierabendgespräche kann man auch super mit Matthias Opel führen, der einem immer wieder eine sehr erfrischende Sicht auf die kleinen und großen Probleme einer Promotion präsentiert.
Wenn einem das Mensa-Essen nicht so sehr liegt, muss man eben selber kochen. Das wäre alleine allerdings auch nur halb schön. An dieser Stelle geht mein Dank an die Küchencrew Zolli, Sybille, Peter, Max, Manuel, Frank, Stefan, Edwar und Kleo mit der die Mittagspause immer wie im Flug verging. Kleo war mir im Institut nicht nur in der Küche ein treuer Begleiter, sondern auch sonst immer, wenn die Arbeit mal wieder nicht so wollte, wie ich mir das vorgestellt habe. Da wo andere Institutsmitglieder gestresst oder betrübt reagieren, rollt sie sich mit einem lauten Schnaufen zusammen und träumt vom nächsten Mülleimer, den man ausräumen könnte. Auch wenn sie als Heliumschnüffler nie so richtig gut funktioniert hat, war sie doch stets zuverlässig, wenn das Käsebuffet leer gegessen werden sollte.

Natürlich gibt es während einer Promotion nicht nur das Leben am Institut. Einen sehr starken Rückhalt habe ich stets in meiner Familie gefunden. Auch wenn die räumliche Trennung die gemeinsame Zeit oft limitiert hat, konnte ich mich bei euch immer fallen lassen, wenn ich mal eine Pause brauchte. Nicht nur die Tatsache, dass diese Worte auf einer Zugfahrt zu euch geschrieben werden zeigt, wie wichtig ihr beim Gelingen dieser Arbeit seid! Ich bin dankbar, mit tollen Eltern, Großeltern, Geschwistern, Schwagern, Neffen und Nichten gesegnet zu sein, die mir eine große Sicherheit geben.
Der Grundstein für meine schöne Zeit in München wurde durch Linda gelegt, die es mir ermöglicht hat, ein selbständiges Leben zu führen. In meiner Zeit in München habe ich sicher von keiner Person mehr gelernt und mehr profitiert! Es war und ist immer schön, deine liebenswerte Sicht der Dinge zu erfahren. Du hast mir immer wieder gezeigt, dass es

mehr als Physik auf dieser Welt. Das Ende meiner Arbeit wurde maßgeblich von Miriam mitgetragen, die mir die Leichtigkeit am Leben wieder geschenkt hat. Deine pragmatische und unkomplizierte Art hat mir bei der Arbeit, aber auch auf privater Ebene gezeigt, wie man mit Rückschlägen umgehen kann. Du hast mir ungemein dabei geholfen wieder zu sein wie ich bin. Danke!

Bibliography

[1] S. M. Luria and J. A. S. Kinney, "Underwater Vision", Science **167**, 1454 (1970).

[2] E. Rutherford, *Philosophical Magazine*, vol. 5 of *6* (Taylor & Francis., 1903).

[3] M. W. Liemohn and A. A. Chan, "Unraveling the causes of radiation belt enhancements", EOS T. Am. Geophys. Un. **88**, 425 (2007).

[4] A. M. Kligman, "Early destructive effect of sunlight on human skin", JAMA-J. Am. Med. Assoc. **210**, 2377 (1969).

[5] G. Kopp and J. L. Lean, "A new, lower value of total solar irradiance: Evidence and climate significance", Geophy. Res. Lett. **38** (2011).

[6] C. Gerry and P. Knight, *Introductory Quantum Optics* (Cambridge University Press, 2005).

[7] D. Walls and G. Milburn, *Quantum Optics* (Springer Berlin Heidelberg, 2008).

[8] H. Mabuchi and A. C. Doherty, "Cavity Quantum Electrodynamics: Coherence in Context", Science **298**, 1372 (2002).

[9] N. Photon., "Quantum evolution", Nat. Photon. **3**, 669 (2009).

[10] A. Beige, "Quantum optics: A new take on the slit experiment", Nat. Photon. **10**, 290 (2016).

[11] D. Bouwmeester, J.-W. Pan, K. Mattle, M. Eibl, H. Weinfurter, and A. Zeilinger, "Experimental quantum teleportation", Nature **390**, 575 (1997).

[12] A. Furusawa, J. L. Sørensen, S. L. Braunstein, C. A. Fuchs, H. J. Kimble, and E. S. Polzik, "Unconditional Quantum Teleportation", Science **282**, 706 (1998).

[13] L. M. K. Vandersypen, M. Steffen, B. Gregory, C. S. Yannoni, M. H. Sherwood, and I. L. Chuang, "Experimental realization of Shor's quantum factoring algorithm using nuclear magnetic resonance", Nature **414**, 883 (2001).

[14] P. Kok, W. J. Munro, K. Nemoto, T. C. Ralph, J. P. Dowling, and G. J. Milburn, "Linear optical quantum computing with photonic qubits", Rev. Mod. Phys. **79**, 135 (2007).

[15] A. Imamoglu, D. D. Awschalom, G. Burkard, D. P. DiVincenzo, D. Loss, M. Sherwin, and A. Small, "Quantum Information Processing Using Quantum Dot Spins and Cavity QED", Phys. Rev. Lett. **83**, 4204 (1999).

[16] A. Wallraff, D. I. Schuster, A. Blais, L. Frunzio, R.-S. Huang, J. Majer, S. Kumar, S. M. Girvin, and R. J. Schoelkopf, "Strong coupling of a single photon to a superconducting qubit using circuit quantum electrodynamics", Nature **431**, 162 (2004).

[17] A. Blais, R.-S. Huang, A. Wallraff, S. M. Girvin, and R. J. Schoelkopf, "Cavity quantum electrodynamics for superconducting electrical circuits: An architecture for quantum computation", Phys. Rev. A **69**, 062320 (2004).

[18] J. Clarke and F. K. Wilhelm, "Superconducting quantum bits", Nature **453**, 1031 (2008).

[19] A. Megrant, C. Neill, R. Barends, B. Chiaro, Y. Chen, L. Feigl, J. Kelly, E. Lucero, M. Mariantoni, P. O'Malley, D. Sank, A. Vainsencher, J. Wenner, T. White, Y. Yin, J. Zhao, C. Palmström, J. M. Martinis, and A. Cleland, "Planar superconducting resonators with internal quality factors above one million", Appl. Phys. Lett. **100**, 113510 (2012).

[20] H. Paik, D. I. Schuster, L. S. Bishop, G. Kirchmair, G. Catelani, A. P. Sears, B. R. Johnson, M. J. Reagor, L. Frunzio, L. I. Glazman, S. M. Girvin, M. H. Devoret, and R. J. Schoelkopf, "Observation of High Coherence in Josephson Junction Qubits Measured in a Three-Dimensional Circuit QED Architecture", Phys. Rev. Lett. **107**, 240501 (2011).

[21] J. Q. You, J. S. Tsai, and F. Nori, "Scalable Quantum Computing with Josephson Charge Qubits", Phys. Rev. Lett. **89**, 197902 (2002).

[22] R. Barends, J. Kelly, A. Megrant, A. Veitia, D. Sank, E. Jeffrey, T. C. White, J. Mutus, A. G. Fowler, B. Campbell, Y. Chen, Z. Chen, B. Chiaro, A. Dunsworth, C. Neill, P. O'Malley, P. Roushan, A. Vainsencher, J. Wenner, A. N. Korotkov, A. N. Cleland, and J. M. Martinis, "Superconducting quantum circuits at the surface code threshold for fault tolerance", Nature **508**, 500 (2014).

[23] S. Boixo, T. F. Ronnow, S. V. Isakov, Z. Wang, D. Wecker, D. A. Lidar, J. M. Martinis, and M. Troyer, "Evidence for quantum annealing with more than one hundred qubits", Nat. Phys. **10**, 218 (2014).

[24] D. I. Schuster, A. Wallraff, A. Blais, L. Frunzio, R.-S. Huang, J. Majer, S. M. Girvin, and R. J. Schoelkopf, "ac Stark Shift and Dephasing of a Superconducting Qubit Strongly Coupled to a Cavity Field", Phys. Rev. Lett. **94**, 123602 (2005).

[25] J. D. Teufel, D. Li, M. S. Allman, K. Cicak, A. J. Sirois, J. D. Whittaker, and R. W. Simmonds, "Circuit cavity electromechanics in the strong-coupling regime", Nature **471**, 204 (2011).

[26] T. Niemczyk, F. Deppe, H. Hübl, E. P. Menzel, F. Hocke, M. J. Schwarz, J. J. Garcia-Ripoll, D. Zueco, T. Hümmer, E. Solano, A. Marx, and R. Gross, "Circuit quantum electrodynamics in the ultrastrong-coupling regime", Nat. Phys. **6**, 772 (2010).

[27] P. Forn-Díaz, J. Lisenfeld, D. Marcos, J. J. Garcia-Ripoll, E. Solano, C. J. P. M. Harmans, and J. E. Mooij, "Observation of the Bloch-Siegert Shift in a Qubit-Oscillator System in the Ultrastrong Coupling Regime", Phys. Rev. Lett. **105**, 237001 (2010).

[28] A. Baust, E. Hoffmann, M. Haeberlein, M. J. Schwarz, P. Eder, J. Goetz, F. Wulschner, E. Xie, L. Zhong, F. Quijandría, D. Zueco, J.-J. G. Ripoll, L. García-Álvarez, G. Romero, E. Solano, K. G. Fedorov, E. P. Menzel, F. Deppe, A. Marx, and

R. Gross, "Ultrastrong coupling in two-resonator circuit QED", Phys. Rev. B **93**, 214501 (2016).

[29] J. Majer, J. M. Chow, J. M. Gambetta, J. Koch, B. R. Johnson, J. A. Schreier, L. Frunzio, D. I. Schuster, A. A. Houck, A. Wallraff, A. Blais, M. H. Devoret, S. M. Girvin, and R. J. Schoelkopf, "Coupling superconducting qubits via a cavity bus", Nature **449**, 443 (2007).

[30] S. H. W. van der Ploeg, A. Izmalkov, A. M. van den Brink, U. Hübner, M. Grajcar, E. Il'ichev, H.-G. Meyer, and A. M. Zagoskin, "Controllable Coupling of Superconducting Flux Qubits", Phys. Rev. Lett. **98**, 057004 (2007).

[31] A. Baust, E. Hoffmann, M. Haeberlein, M. J. Schwarz, P. Eder, J. Goetz, F. Wulschner, E. Xie, L. Zhong, F. Quijandría, B. Peropadre, D. Zueco, J.-J. García Ripoll, E. Solano, K. Fedorov, E. P. Menzel, F. Deppe, A. Marx, and R. Gross, "Tunable and switchable coupling between two superconducting resonators", Phys. Rev. B **91**, 014515 (2015).

[32] F. Wulschner, J. Goetz, F. R. Koessel, E. Hoffmann, A. Baust, P. Eder, M. Fischer, M. J. Haeberlein, M. andSchwarz, M. Pernpeintner, E. Xie, L. Zhong, C. W. Zollitsch, B. Peropadre, J.-J. Garcia Ripoll, E. Solano, K. G. Fedorov, E. P. Menzel, F. Deppe, A. Marx, and R. Gross, "Tunable coupling of transmission-line microwave resonators mediated by an rf SQUID", EPJ Quant. Tech. **3**, 10 (2016).

[33] F. Yoshihara, K. Harrabi, A. O. Niskanen, Y. Nakamura, and J. S. Tsai, "Decoherence of Flux Qubits due to $1/f$ Flux Noise", Phys. Rev. Lett. **97**, 167001 (2006).

[34] H. Wang, M. Hofheinz, J. Wenner, M. Ansmann, R. C. Bialczak, M. Lenander, E. Lucero, M. Neeley, A. D. O'Connell, D. Sank, M. Weides, A. N. Cleland, and J. M. Martinis, "Improving the coherence time of superconducting coplanar resonators", Appl. Phys. Lett. **95**, 233508 (2009).

[35] V. Zaretskey, S. Novikov, B. Suri, Z. Kim, F. C. Wellstood, and B. S. Palmer, "Decoherence in a pair of long-lived Cooper-pair boxes", J. Appl. Phys. **114**, 094305 (2013).

[36] I. M. Pop, K. Geerlings, G. Catelani, R. J. Schoelkopf, L. I. Glazman, and M. H. Devoret, "Coherent suppression of electromagnetic dissipation due to superconducting quasiparticles", Nature **508**, 369 (2014).

[37] C. M. Quintana, A. Megrant, Z. Chen, A. Dunsworth, B. Chiaro, R. Barends, B. Campbell, Y. Chen, I.-C. Hoi, E. Jeffrey, J. Kelly, J. Y. Mutus, P. O'Malley, C. Neill, P. Roushan, D. Sank, A. Vainsencher, J. Wenner, T. C. White, A. N. Cleland, and J. M. Martinis, "Characterization and reduction of microfabrication-induced decoherence in superconducting quantum circuits", Appl. Phys. Lett. **105**, 062601 (2014).

[38] J. Goetz, F. Deppe, M. Haeberlein, F. Wulschner, C. W. Zollitsch, S. Meier, M. Fischer, P. Eder, E. Xie, K. G. Fedorov, E. P. Menzel, A. Marx, and R. Gross, "Loss mechanisms in superconducting thin film microwave resonators", J. App. Phys. **119**, 015304 (2016).

[39] J. Goetz, F. Deppe, P. Eder, M. Fischer, M. Müting, J. Puertas Martínez, S. Pogorzalek, F. Wulschner, E. Xie, K. G. Fedorov, A. Marx, and R. Gross, "Second-order

decoherence mechanisms of a transmon qubit probed with thermal microwave states", Quant. Sci. Tech. **2**, 025002 (2017).

[40] J. Koch, T. M. Yu, J. Gambetta, A. A. Houck, D. I. Schuster, J. Majer, A. Blais, M. H. Devoret, S. M. Girvin, and R. J. Schoelkopf, "Charge-insensitive qubit design derived from the Cooper pair box", Phys. Rev. A **76**, 042319 (2007).

[41] J. Goetz, S. Pogorzalek, F. Deppe, K. G. Fedorov, P. Eder, M. Fischer, F. Wulschner, E. Xie, A. Marx, and R. Gross, "Photon Statistics of Propagating Thermal Microwaves", Phys. Rev. Lett. **118**, 103602 (2017).

[42] F. Deppe, M. Mariantoni, E. P. Menzel, A. Marx, S. Saito, K. Kakuyanagi, H. Tanaka, T. Meno, K. Semba, H. Takayanagi, E. Solano, and R. Gross, "Two-photon probe of the Jaynes–Cummings model and controlled symmetry breaking in circuit QED", Nat. Phys. **4**, 686 (2008).

[43] J. I. Cirac and P. Zoller, "Quantum Computations with Cold Trapped Ions", Phys. Rev. Lett. **74**, 4091 (1995).

[44] H. Häffner, C. Roos, and R. Blatt, "Quantum computing with trapped ions", Phys. Rep. **469**, 155 (2008).

[45] M. S. Sherwin, A. Imamoglu, and T. Montroy, "Quantum computation with quantum dots and terahertz cavity quantum electrodynamics", Phys. Rev. A **60**, 3508 (1999).

[46] C. J. Hood, T. W. Lynn, A. C. Doherty, A. S. Parkins, and H. J. Kimble, "The Atom-Cavity Microscope: Single Atoms Bound in Orbit by Single Photons", Science **287**, 1447 (2000).

[47] R. Vrijen, E. Yablonovitch, K. Wang, H. W. Jiang, A. Balandin, V. Roychowdhury, T. Mor, and D. DiVincenzo, "Electron-spin-resonance transistors for quantum computing in silicon-germanium heterostructures", Phys. Rev. A **62**, 012306 (2000).

[48] J. M. Raimond, M. Brune, and S. Haroche, "Manipulating quantum entanglement with atoms and photons in a cavity", Rev. Mod. Phys. **73**, 565 (2001).

[49] A. Zrenner, E. Beham, S. Stufler, F. Findeis, M. Bichler, and G. Abstreiter, "Coherent properties of a two-level system based on a quantum-dot photodiode", Nature **418**, 612 (2002).

[50] M. A. Nielsen and I. L. Chuang, *Quantum Computation and Quantum Information* (Cambridge University Press, 2004).

[51] C. Cohen-Tannoudji, B. Diu, and F. Laloe, *Quantum Mechanics*, 2 (John Wiley & Sons, 2006).

[52] M. Boissonneault, J. M. Gambetta, and A. Blais, "Dispersive regime of circuit QED: Photon-dependent qubit dephasing and relaxation rates", Phys. Rev. A **79**, 013819 (2009).

[53] Y. Nakamura, Y. Pashkin, and J. S. Tsai, "Coherent control of macroscopic quantum states in a single-Cooper-pair box", Nature **398**, 786 (1999).

[54] M. Müting, "Time Domain Characterization of a Transmon Qubit", Master's thesis, TU München (2015).

[55] F. Deppe, "Superconducting flux quantum circuits: characterization, quantum coherence and controlled symmetrie breaking", PhD thesis, TU München (2009).

[56] M. Levitt, *Spin Dynamics: Basics of Nuclear Magnetic Resonance* (Wiley, 2001).

[57] D. Vion, A. Aassime, A. Cottet, P. Joyez, H. Pothier, C. Urbina, D. Esteve, and M. H. Devoret, "Manipulating the Quantum State of an Electrical Circuit", Science **296**, 886 (2002).

[58] F. Wilhelm, M. Storcz, C. van der Wal, C. Harmans, and J. Mooij, "Decoherence of Flux Qubits Coupled to Electronic Circuits", Adv. Solid State Phys. **43**, 763 (2003).

[59] D. Gerstenberg and P. M. Hall, "Superconducting Thin Films of Niobium, Tantalum, Tantalum Nitride, Tantalum Carbide, and Niobium Nitride", J. Electrochem. Soc. **111**, 936 (1964).

[60] J. F. Cochran and D. E. Mapother, "Superconducting Transition in Aluminum", Phys. Rev. **111**, 132 (1958).

[61] F. London, *Superfluids: Macroscopic theory of superconductivity*, Structure of matter series (Wiley, 1950).

[62] A. Taylor, "Wave equation for the macroscopic wave function in superconductors", J. Phys. C Solid State **3**, L52 (1970).

[63] L. N. Cooper, "Bound Electron Pairs in a Degenerate Fermi Gas", Phys. Rev. **104**, 1189 (1956).

[64] J. Bardeen, L. N. Cooper, and J. R. Schrieffer, "Theory of Superconductivity", Phys. Rev. **108**, 1175 (1957).

[65] R. Barends, J. Wenner, M. Lenander, Y. Chen, R. C. Bialczak, J. Kelly, E. Lucero, P. O'Malley, M. Mariantoni, D. Sank, H. Wang, T. C. White, Y. Yin, J. Zhao, A. N. Cleland, J. M. Martinis, and J. J. A. Baselmans, "Minimizing quasiparticle generation from stray infrared light in superconducting quantum circuits", Appl. Phys. Lett. **99**, 113507 (2011).

[66] W. Buckel and R. Kleiner, *Superconductivity: Fundamentals and applications* (Wiley-VCH, Weinheim, 2004).

[67] A. B. Pippard, "The Surface Impedance of Superconductors and Normal Metals at High Frequencies. V. Analysis of Experimental Results for Superconducting Tin", P. R. Soc. A **203**, 195 (1950).

[68] S. Meier, "Loss reduction of superconducting coplanar waveguide resonators on sapphire substrates", Bachelor's thesis, TU München (2014).

[69] R. Kaplan, A. H. Nethercot, and H. A. Boorse, "Frequency Dependence of the Surface Resistance of Superconducting Tin in the Millimeter Wavelength Region", Phys. Rev. **116**, 270 (1959).

[70] K. Saito and P. Kneisel, in *RF superconductivity: Accelerator technology for the 21st century* (2000).

[71] B. A. Mazin, "Microwave kinetic inductance detectors", PhD thesis, California Institute of Technology (2005).

[72] W. Weingarten, "Field-dependent surface resistance for superconducting niobium accelerating cavities", Phys. Rev. ST Accel. Beams **14** (2011).

[73] D. C. Mattis and J. Bardeen, "Theory of the Anomalous Skin Effect in Normal and Superconducting Metals", Phys. Rev. **111**, 412 (1958).

[74] T. Noguchi, M. Naruse, and Y. Sekimoto, "RF Conductivity and Surface Impedance of a Superconductor Taking into Account the Complex Superconducting gap Energy", Phys. Procedia **36**, 318 (2012).

[75] A. B. Pippard, "The Surface Impedance of Superconductors and Normal Metals at High Frequencies. II. The Anomalous Skin Effect in Normal Metals", P. R. Soc. A **191**, 385 (1947).

[76] G. E. H. Reuter and E. H. Sondheimer, "The Theory of the Anomalous Skin Effect in Metals", P. R. Soc. A **195**, 336 (1948).

[77] D. Belitz, "Theory for dirty superconductors. I. Strong-coupling equations", Phys. Rev. B **35**, 1636 (1987).

[78] D. Einzel, "50 Years of Fluxoid Quantization: 2e or Not 2e", J. Low Temp. Phys. **163**, 215 (2011).

[79] R. Doll and M. Näbauer, "Experimental Proof of Magnetic Flux Quantization in a Superconducting Ring", Phys. Rev. Lett. **7**, 51 (1961).

[80] B. S. Deaver and W. M. Fairbank, "Experimental Evidence for Quantized Flux in Superconducting Cylinders", Phys. Rev. Lett. **7**, 43 (1961).

[81] T. P. Orlando and K. A. Delin, *Foundations of applied superconductivity* (Addison Wesley, 1991).

[82] J. B. Majer, J. R. Butcher, and J. E. Mooij, "Simple phase bias for superconducting circuits", Appl. Phys. Lett. **80**, 3638 (2002).

[83] M. J. Schwarz, J. Goetz, Z. Jiang, T. Niemczyk, F. Deppe, A. Marx, and R. Gross, "Gradiometric Flux Qubits with a Tunable Gap", New J. Phys. **15**, 045001 (2013).

[84] C. N. Lau, N. Markovic, M. Bockrath, A. Bezryadin, and M. Tinkham, "Quantum Phase Slips in Superconducting Nanowires", Phys. Rev. Lett. **87**, 217003 (2001).

[85] J. E. Mooij and C. J. P. M. Harmans, "Phase-slip flux qubits", New J. Phys. **7**, 219 (2005).

[86] D. E. McCumber and B. I. Halperin, "Time Scale of Intrinsic Resistive Fluctuations in Thin Superconducting Wires", Phys. Rev. B **1**, 1054 (1970).

[87] B. Josephson, "Possible new effects in superconductive tunnelling", Phys. Lett. **1**, 251 (1962).

[88] P. W. Anderson and J. M. Rowell, "Probable Observation of the Josephson Superconducting Tunneling Effect", Phys. Rev. Lett. **10**, 230 (1963).

[89] M. Hermele, G. Refael, M. P. A. Fisher, and P. M. Goldbart, "Fate of the Josephson effect in thin-film superconductors", Nat. Phys. **1**, 117 (2005).

[90] R. Gross and A. Marx, *Festkörperphysik* (De Gruyter, 2014).

[91] J. M. Martinis, M. H. Devoret, and J. Clarke, "Energy-Level Quantization in the Zero-Voltage State of a Current-Biased Josephson Junction", Phys. Rev. Lett. **55**, 1543 (1985).

[92] J. Clarke and A. I. Braginski, *The SQUID Handbook*, vol. 1 (Wiley-VCH, 2004).

[93] A. A. Houck, J. Koch, M. H. Devoret, S. M. Girvin, and R. J. Schoelkopf, "Life after charge noise: recent results with transmon qubits", QIP **8** (2009).

[94] D. L. Mills, *Nonlinear optics: Basic concepts* (Springer, Berlin and New York, 1998).

[95] T. P. Orlando, J. E. Mooij, L. Tian, C. H. van der Wal, L. S. Levitov, S. Lloyd, and J. J. Mazo, "Superconducting persistent-current qubit", Phys. Rev. B **60**, 15398 (1999).

[96] J. E. Mooij, T. P. Orlando, L. Levitov, L. Tian, C. H. van der Wal, and S. Lloyd, "Josephson Persistent-Current Qubit", Science **285**, 1036 (1999).

[97] C. H. van der Wal, A. C. J. ter Haar, F. K. Wilhelm, R. N. Schouten, C. J. P. M. Harmans, T. P. Orlando, S. Lloyd, and J. E. Mooij, "Quantum Superposition of Macroscopic Persistent-Current States", Science **290**, 773 (2000).

[98] F. G. Paauw, A. Fedorov, C. J. P. M. Harmans, and J. E. Mooij, "Tuning the Gap of a Superconducting Flux Qubit", Phys. Rev. Lett. **102**, 090501 (2009).

[99] C. E. Wu, Y. Liu, and C. C. Chi, "The gradiometer flux qubit without an external flux bias", Supercond. Sci. Tech. **19**, 280 (2006).

[100] J. H. Plantenberg, P. C. de Groot, C. J. P. M. Harmans, and J. E. Mooij, "Demonstration of controlled-NOT quantum gates on a pair of superconducting quantum bits", Nature **447**, 836 (2007).

[101] F. Zwanenburg, "Superconducting electronics with phase biased SQUIDs", Master's thesis, TU Delft (2003).

[102] A. Fedorov, A. K. Feofanov, P. Macha, P. Forn-Díaz, C. J. P. M. Harmans, and J. E. Mooij, "Strong Coupling of a Quantum Oscillator to a Flux Qubit at Its Symmetry Point", Phys. Rev. Lett. **105**, 060503 (2010).

[103] J. Plantenberg, "Coupled superconducting flux qubits", PhD thesis, TU Delft (2007).

[104] R. E. Raab and O. L. De Lange, *Multipole theory in electromagnetism: classical, quantum, and symmetry aspects, with applications*, vol. 128 (Oxford University Press on Demand, 2005).

[105] M. Kasperczyk, S. Person, D. Ananias, L. D. Carlos, and L. Novotny, "Excitation of Magnetic Dipole Transitions at Optical Frequencies", Phys. Rev. Lett. **114**, 163903 (2015).

[106] Y. Liu, J. Q. You, L. F. Wei, C. P. Sun, and F. Nori, "Optical Selection Rules and Phase-Dependent Adiabatic State Control in a Superconducting Quantum Circuit", Phys. Rev. Lett. **95**, 087001 (2005).

[107] A. Kou, W. C. Smith, U. Vool, R. T. Brierley, H. Meier, L. Frunzio, S. M. Girvin, L. I. Glazman, and M. H. Devoret, "A fluxonium-based artificial molecule with a tunable magnetic moment", ArXiv e-prints: 1610.01094 (2016).

[108] F. E. Terman, *Radio Engineers' Handbook* (McGraw-Hill Book Company, 1943).

[109] R. Simons, *Coplanar Waveguide Circuits, Components, and Systems* (Wiley, 2004).

[110] D. M. Pozar, *Microwave engineering* (Wiley, 2012).

[111] G. Kirchhoff and L. Boltzmann, *Gesammelte Abhandlungen* (J. A. Barth, Leipzig, 1882).

[112] M. Göppl, A. Fragner, M. Baur, R. Bianchetti, S. Filipp, J. M. Fink, P. J. Leek, G. Puebla, L. Steffen, and A. Wallraff, "Coplanar waveguide resonators for circuit quantum electrodynamics", J. Appl. Phys. **104**, 113904 (2008).

[113] J. C. Maxwell, "A Dynamical Theory of the Electromagnetic Field", Philos. T. R. Soc. Lond. **155**, 459 (1865).

[114] M. O. Scully and M. S. Zubairy, *Quantum optics* (Cambridge University Press, Cambridge and New York, 1997).

[115] R. J. Schoelkopf and S. M. Girvin, "Wiring up quantum systems", Nature **451**, 664 (2008).

[116] Y. Kubo, C. Grezes, A. Dewes, T. Umeda, J. Isoya, H. Sumiya, N. Morishita, H. Abe, S. Onoda, T. Ohshima, V. Jacques, A. Dréau, J.-F. Roch, I. Diniz, A. Auffeves, D. Vion, D. Esteve, and P. Bertet, "Hybrid Quantum Circuit with a Superconducting Qubit Coupled to a Spin Ensemble", Phys. Rev. Lett. **107**, 220501 (2011).

[117] M. Mariantoni, H. Wang, R. C. Bialczak, M. Lenander, E. Lucero, M. Neeley, A. D. O'Connell, D. Sank, M. Weides, J. Wenner, T. Yamamoto, Y. Yin, J. Zhao, J. M. Martinis, and A. N. Cleland, "Photon shell game in three-resonator circuit quantum electrodynamics", Nat. Phys. **7**, 287 (2011).

[118] M. Hofheinz, H. Wang, M. Ansmann, R. C. Bialczak, E. Lucero, M. Neeley, A. D. O'Connell, D. Sank, J. Wenner, J. M. Martinis, and A. N. Cleland, "Synthesizing arbitrary quantum states in a superconducting resonator", Nature **459**, 546 (2009).

[119] N. T. Bronn, Y. Liu, J. B. Hertzberg, A. D. Corcoles, A. A. Houck, J. M. Gambetta, and J. M. Chow, "Broadband filters for abatement of spontaneous emission in circuit quantum electrodynamics", Appl. Phys. Lett. **107**, 172601 (2015).

[120] I. R. Senitzky, "Dissipation in Quantum Mechanics. The Harmonic Oscillator", Phys. Rev. **119**, 670 (1960).

[121] S. Pogorzalek, "Displacement of Squeezed Propagating Microwave States", Master's thesis, TU München (2015).

[122] C. L. Holloway and E. F. Kuester, "Edge shape effects and quasi-closed form expressions for the conductor loss of microstrip lines", Radio Sci. **29**, 539 (1994).

[123] C. L. Holloway and E. F. Kuester, "A quasi-closed form expression for the conductor loss of CPW lines, with an investigation of edge shape effects", IEEE Trans. Microwave Theory Techn. **43**, 2695 (1995).

[124] D. S. Wisbey, J. Gao, M. R. Vissers, F. C. S. da Silva, J. S. Kline, L. Vale, and D. P. Pappas, "Effect of metal/substrate interfaces on radio-frequency loss in superconducting coplanar waveguides", J. Appl. Phys. **108**, 093918 (2010).

[125] J. Wenner, R. Barends, R. C. Bialczak, Y. Chen, J. Kelly, E. Lucero, M. Mariantoni, A. Megrant, P. O'Malley, D. Sank, A. Vainsencher, H. Wang, T. C. White, Y. Yin, J. Zhao, A. N. Cleland, and J. M. Martinis, "Surface loss simulations of superconducting coplanar waveguide resonators", Appl. Phys. Lett. **99**, 113513 (2011).

[126] J. Gao, J. Zmuidzinas, A. Vayonakis, P. Day, B. Mazin, and H. Leduc, "Equivalence of the Effects on the Complex Conductivity of Superconductor due to Temperature Change and External Pair Breaking", J. Low Temp. Phys. **151**, 557 (2008).

[127] U. Leonhardt, *Measuring the Quantum State of Light*, Cambridge Studies in Modern Optics (Cambridge University Press, 1997).

[128] W. Heisenberg, "Über den anschaulichen Inhalt der quantentheoretischen Kinematik und Mechanik", Z. Phys. **43**, 172 (1927).

[129] E. P. Menzel, "Propagating Quantum Microwaves: Dual-path State Reconstruction and Path Entanglement", PhD thesis, TU München (2013).

[130] E. Wigner, "On the Quantum Correction For Thermodynamic Equilibrium", Phys. Rev. **40**, 749 (1932).

[131] J. E. Moyal, "Quantum mechanics as a statistical theory", Math. Proc. Cambridge **45**, 99 (1949).

[132] M. Hillery, R. O'Connell, M. Scully, and E. Wigner, "Distribution functions in physics: Fundamentals", Phys. Rep. **106**, 121 (1984).

[133] D. Arweiler, "Reconstruction of propagating and confined microwave states", Bachelor's thesis, TU München (2015).

[134] K. E. Cahill and R. J. Glauber, "Density Operators and Quasiprobability Distributions", Phys. Rev. **177**, 1882 (1969).

[135] A. Wünsche, "Reconstruction of operators from their normally ordered moments for a single boson mode", Quant. Opt. **2**, 453 (1990).

[136] V. Bužek, G. Adam, and G. Drobný, "Quantum state reconstruction and detection of quantum coherences on different observation levels", Phys. Rev. A **54**, 804 (1996).

[137] S. N. Filippov and V. I. Man'ko, "Measuring microwave quantum states: Tomogram and moments", Phys. Rev. A **84**, 033827 (2011).

[138] R. Schack and A. Schenzle, "Moment hierarchies and cumulants in quantum optics", Phys. Rev. A **41**, 3847 (1990).

[139] E. P. Menzel, R. Di Candia, F. Deppe, P. Eder, L. Zhong, M. Ihmig, M. Haeberlein, A. Baust, E. Hoffmann, D. Ballester, K. Inomata, T. Yamamoto, Y. Nakamura, E. Solano, A. Marx, and R. Gross, "Path Entanglement of Continuous-Variable Quantum Microwaves", Phys. Rev. Lett. **109**, 250502 (2012).

[140] C. Eichler, Y. Salathe, J. Mlynek, S. Schmidt, and A. Wallraff, "Quantum-Limited Amplification and Entanglement in Coupled Nonlinear Resonators", Phys. Rev. Lett. **113**, 110502 (2014).

[141] C. Ferrie, R. Morris, and J. Emerson, "Necessity of negativity in quantum theory", Phys. Rev. A **82**, 044103 (2010).

[142] A. Bednorz and W. Belzig, "Fourth moments reveal the negativity of the Wigner function", Phys. Rev. A **83**, 052113 (2011).

[143] S. Brattke, B. T. H. Varcoe, and H. Walther, "Generation of Photon Number States on Demand via Cavity Quantum Electrodynamics", Phys. Rev. Lett. **86**, 3534 (2001).

[144] E. Lucero, R. Barends, Y. Chen, J. Kelly, M. Mariantoni, A. Megrant, P. O'Malley, D. Sank, A. Vainsencher, J. Wenner, T. White, Y. Yin, A. N. Cleland, and J. M. Martinis, "Computing prime factors with a Josephson phase qubit quantum processor", Nat. Phys. **8**, 719 (2012).

[145] D. J. Griffiths, *Introduction to quantum mechanics* (Pearson Prentice Hall, Upper Saddle River, NJ, 2005).

[146] W. Dittrich and H. Gies, *Probing the Quantum Vacuum: Perturbative Effective Action Approach in Quantum Electrodynamics and its Application*, Springer Tracts in Modern Physics (Springer Berlin Heidelberg, 2000).

[147] D. A. R. Dalvit, "Quantum physics: Shaking photons out of the vacuum", Nature **479**, 303 (2011).

[148] B. E. A. Saleh and M. C. Teich, *Grundlagen der Photonik*, Lehrbuch Physik (Wiley-VCH, Weinheim, 2008).

[149] Y. Kano and E. Wolf, "Temporal Coherence of Black Body Radiation", P. Phys. Soc. **80**, 1273 (1962).

[150] C. Mehta, "Coherence-time and effective bandwidth of blackbody radiation", Il Nuovo Cimento **28**, 401 (1963).

[151] W. Eckhardt, "Anisotropy and temporal coherence of blackbody radiation", Phys. Rev. A **17**, 1093 (1978).

[152] L. Zhong, E. P. Menzel, R. Di Candia, P. Eder, M. Ihmig, A. Baust, M. Haeberlein, E. Hoffmann, K. Inomata, T. Yamamoto, Y. Nakamura, E. Solano, F. Deppe, A. Marx, and R. Gross, "Squeezing with a flux-driven Josephson parametric amplifier", New J. Phys. **15**, 125013 (2013).

[153] R. Hanbury Brown and R. Q. Twiss, "A Test of a New Type of Stellar Interferometer on Sirius", Nature **178**, 1046 (1956).

[154] S. Bose, "Plancks Gesetz und Lichtquantenhypothese", Z. Phys. **26**, 178 (1924).

[155] B. L. Morgan and L. Mandel, "Measurement of Photon Bunching in a Thermal Light Beam", Phys. Rev. Lett. **16**, 1012 (1966).

[156] F. Arecchi, E. Gatti, and A. Sona, "Time distribution of photons from coherent and Gaussian sources", Phys. Lett. **20**, 27 (1966).

[157] J. Gabelli, L.-H. Reydellet, G. Fève, J.-M. Berroir, B. Plaçais, P. Roche, and D. C. Glattli, "Correlations to Probe the Population Statistics of GHz Photons Emitted by Conductors", Phys. Rev. Lett. **93**, 056801 (2004).

[158] P. K. Tan, G. H. Yeo, H. S. Poh, A. H. Chan, and C. Kurtsiefer, "Measuring Temporal Photon Bunching in Blackbody Radiation", Astrophys. J. Lett. **789**, L10 (2014).

[159] R. Short and L. Mandel, "Observation of Sub-Poissonian Photon Statistics", Phys. Rev. Lett. **51**, 384 (1983).

[160] G. Rempe, F. Schmidt-Kaler, and H. Walther, "Observation of sub-Poissonian photon statistics in a micromaser", Phys. Rev. Lett. **64**, 2783 (1990).

[161] F. Treussart, R. Alléaume, V. Le Floc'h, L. T. Xiao, J.-M. Courty, and J.-F. Roch, "Direct Measurement of the Photon Statistics of a Triggered Single Photon Source", Phys. Rev. Lett. **89**, 093601 (2002).

[162] G. Breitenbach, S. Schiller, and J. Mlynek, "Measurement of the quantum states of squeezed light", Nature **387**, 471 (1997).

[163] K. G. Fedorov, L. Zhong, S. Pogorzalek, P. Eder, M. Fischer, J. Goetz, E. Xie, F. Wulschner, K. Inomata, T. Yamamoto, Y. Nakamura, R. Di Candia, U. Las Heras, M. Sanz, E. Solano, E. P. Menzel, F. Deppe, A. Marx, and R. Gross, "Displacement of Propagating Squeezed Microwave States", Phys. Rev. Lett. **117**, 020502 (2016).

[164] S. N. Filippov and V. I. Man'ko, "Evolution of microwave quantum states in terms of measurable ordered moments of creation and annihilation operators", Opt. Spectrosc. **112**, 365 (2012).

[165] M. Devoret, B. Huard, R. Schoelkopf, and L. Cugliandolo, *Quantum Machines: Measurement and Control of Engineered Quantum Systems: Lecture Notes of the Les Houches Summer School: Volume 96, July 2011*, Lecture Notes of the Les Houches Summer School (Oxford University Press, Oxford, 2014).

[166] P. Bertet, I. Chiorescu, C. Harmans, and J. Mooij, "Dephasing of a flux-qubit coupled to a harmonic oscillator", ArXiv e-prints: cond-mat/0507290 (2005).

[167] A. A. Clerk, M. H. Devoret, S. M. Girvin, F. Marquardt, and R. J. Schoelkopf, "Introduction to quantum noise, measurement, and amplification", Rev. Mod. Phys. **82** (2010).

[168] J. Gambetta, A. Blais, D. I. Schuster, A. Wallraff, L. Frunzio, J. Majer, M. H. Devoret, S. M. Girvin, and R. J. Schoelkopf, "Qubit-photon interactions in a cavity: Measurement-induced dephasing and number splitting", Phys. Rev. A **74**, 042318 (2006).

[169] R. Di Candia, E. P. Menzel, L. Zhong, F. Deppe, A. Marx, R. Gross, and E. Solano, "Dual-path methods for propagating quantum microwaves", New J. Phys. **16**, 015001 (2014).

[170] C. M. Caves, "Quantum limits on noise in linear amplifiers", Phys. Rev. D **26**, 1817 (1982).

[171] D. Braak, "Integrability of the Rabi Model", Phys. Rev. Lett. **107**, 100401 (2011).

[172] D. Ballester, G. Romero, J. J. García-Ripoll, F. Deppe, and E. Solano, "Quantum Simulation of the Ultrastrong-Coupling Dynamics in Circuit Quantum Electrodynamics", Phys. Rev. X **2**, 2160 (2012).

[173] E. Jaynes and F. Cummings, "Comparison of quantum and semiclassical radiation theories with application to the beam maser", Proceedings of the IEEE **51**, 89 (1963).

[174] J. Fink, "Quantum Nonlinearities in Strong Coupling Circuit QED", PhD thesis, ETH Zürich (2011).

[175] S. Datta, "Multipole expansion of the interaction hamiltonian between a charged particle and a non-uniform magnetic field", Eur. J. Phys. **5**, 243 (1984).

[176] S. Datta, "Multipole expansion of the interaction Hamiltonian between a charged particle and a non-uniform magnetic field: II. Exterior field", European Journal of Physics **6**, 257 (1985).

[177] J. Goetz, "Gradiometric flux quantum bits with tunable tunnel coupling", Diploma thesis, TU München (2011).

[178] M. J. Schwarz, "Gradiometric tunable-gap flux qubits in a circuit QED architecture", PhD thesis, TU München (2015).

[179] T. Holstein, "Studies of polaron motion", Ann. Phys. **8**, 325 (1959).

[180] R. Silbey and R. A. Harris, "Variational calculation of the dynamics of a two level system interacting with a bath", J. Chem. Phys. **80**, 2615 (1984).

[181] R. A. Harris and R. Silbey, "Variational calculation of the tunneling system interacting with a heat bath. II. Dynamics of an asymmetric tunneling system", J. Chem. Phys. **83**, 1069 (1985).

[182] C. K. Lee, J. Moix, and J. Cao, "Accuracy of second order perturbation theory in the polaron and variational polaron frames", J. Chem. Phys. **136**, 204120 (2012).

[183] F. Mei, V. M. Stojanović, I. Siddiqi, and L. Tian, "Analog superconducting quantum simulator for Holstein polarons", Phys. Rev. B **88**, 224502 (2013).

[184] P.-M. Billangeon, J. S. Tsai, and Y. Nakamura, "Circuit-QED-based scalable architectures for quantum information processing with superconducting qubits", Phys. Rev. B **91**, 094517 (2015).

[185] T. Niemczyk, F. Deppe, E. P. Menzel, M. J. Schwarz, H. Huebl, F. Hocke, M. Häberlein, M. Danner, E. Hoffmann, A. Baust, E. Solano, J. J. Garcia-Ripoll, A. Marx, and R. Gross, "Selection rules in a strongly coupled qubit-resonator system", ArXiv e-prints: 1107.0810 (2011).

[186] P. Forn-Díaz, G. Romero, C. J. P. M. Harmans, E. Solano, and J. E. Mooij, "Broken selection rule in the quantum Rabi model", Sci. Rep. **6**, 26720 (2016).

[187] A. Blais, J. Gambetta, A. Wallraff, D. I. Schuster, S. M. Girvin, M. H. Devoret, and R. J. Schoelkopf, "Quantum-information processing with circuit quantum electrodynamics", Phys. Rev. A **75**, 032329 (2007).

[188] Y.-J. Zhao, Y.-L. Liu, Y.-x. Liu, and F. Nori, "Generating nonclassical photon states via longitudinal couplings between superconducting qubits and microwave fields", Phys. Rev. A **91**, 053820 (2015).

[189] A. O. Caldeira and A. J. Leggett, "Influence of damping on quantum interference: An exactly soluble model", Phys. Rev. A **31**, 1059 (1985).

[190] D. F. Walls and G. J. Milburn, "Effect of dissipation on quantum coherence", Phys. Rev. A **31**, 2403 (1985).

[191] M. J. Collett, "Exact density-matrix calculations for simple open systems", Phys. Rev. A **38**, 2233 (1988).

[192] W. H. Zurek, "Decoherence and the Transition from Quantum to Classical", Phys. Today **44**, 36 (1991).

[193] H. J. Carmichael, *An open systems approach to quantum optics* (Springer-Verlag, Berlin Heidelberg, 1993).

[194] R. Feynman and F. Vernon Jr., "The theory of a general quantum system interacting with a linear dissipative system", Ann. Phys. **24**, 118 (1963).

[195] A. O. Caldeira and A. J. Leggett, "Influence of Dissipation on Quantum Tunneling in Macroscopic Systems", Phys. Rev. Lett. **46**, 211 (1981).

[196] K. Fujikawa and H. Terashima, "Fluctuation-dissipation theorem and quantum tunneling with dissipation at finite temperature", Phys. Rev. E **58**, 7063 (1998).

[197] C. J. Myatt, B. E. King, Q. A. Turchette, C. A. Sackett, D. Kielpinski, W. M. Itano, C. Monroe, and D. J. Wineland, "Decoherence of quantum superpositions through coupling to engineered reservoirs", Nature **403**, 269 (2000).

[198] H. D. Zeh, "On the interpretation of measurement in quantum theory", Found. Phys. **1**, 69 (1970).

[199] M. Schlosshauer, "Decoherence, the measurement problem, and interpretations of quantum mechanics", Rev. Mod. Phys. **76**, 1267 (2005).

[200] S. Saunders, "Time, quantum mechanics, and decoherence", Synthese **102**, 235 (1995).

[201] J. B. Hartle, "Quantum pasts and the utility of history", Phys. Scripta **1998**, 67 (1998).

[202] L. Maccone, "The Thermodynamic Arrow-of-time and Quantum Mechanics", Electron. Notes Theor. Comput. Sci. **270**, 75 (2011).

[203] W. H. Zurek, "Decoherence and the transition from quantum to classical – revisited", ArXiv e-prints: quant-ph/0306072 (2003).

[204] M. A. Schlosshauer, *Decoherence: and the quantum-to-classical transition* (Springer Science & Business Media, 2007).

[205] F. Verstraete, M. M. Wolf, and J. Ignacio Cirac, "Quantum computation and quantum-state engineering driven by dissipation", Nat. Phys. **5**, 633 (2009).

[206] H. Krauter, C. A. Muschik, K. Jensen, W. Wasilewski, J. M. Petersen, J. I. Cirac, and E. S. Polzik, "Entanglement Generated by Dissipation and Steady State Entanglement of Two Macroscopic Objects", Phys. Rev. Lett. **107**, 080503 (2011).

[207] M. Brune, E. Hagley, J. Dreyer, X. Maître, A. Maali, C. Wunderlich, J. M. Raimond, and S. Haroche, "Observing the Progressive Decoherence of the "Meter" in a Quantum Measurement", Phys. Rev. Lett. **77**, 4887 (1996).

[208] C. Roos, T. Zeiger, H. Rohde, H. C. Nägerl, J. Eschner, D. Leibfried, F. Schmidt-Kaler, and R. Blatt, "Quantum State Engineering on an Optical Transition and Decoherence in a Paul Trap", Phys. Rev. Lett. **83**, 4713 (1999).

[209] Y. Makhlin, G. Schön, and A. Shnirman, "Quantum-state engineering with Josephson-junction devices", Rev. Mod. Phys. **73**, 357 (2001).

[210] C. H. van der Wal, F. K. Wilhelm, C. J. Harmans, and J. E. Mooij, "Engineering decoherence in Josephson persistent-current qubits", Eur. Phys. J. B **31**, 111 (2003).

[211] G. Ithier, E. Collin, P. Joyez, P. J. Meeson, D. Vion, D. Esteve, F. Chiarello, A. Shnirman, Y. Makhlin, J. Schriefl, and G. Schön, "Decoherence in a superconducting quantum bit circuit", Phys. Rev. B **72**, 134519 (2005).

[212] T. Pellizzari, S. A. Gardiner, J. I. Cirac, and P. Zoller, "Decoherence, Continuous Observation, and Quantum Computing: A Cavity QED Model", Phys. Rev. Lett. **75**, 3788 (1995).

[213] R. K. Wangsness and F. Bloch, "The Dynamical Theory of Nuclear Induction", Phys. Rev. **89**, 728 (1953).

[214] A. G. Redfield, "On the Theory of Relaxation Processes", IBM J. Res. Dev. **1**, 19 (1957).

[215] A. Abragam, *The principles of nuclear magnetism*, 32 (Oxford university press, 1961).

[216] R. H. Koch, D. P. DiVincenzo, and J. Clarke, "Model for $1/f$ Flux Noise in SQUIDs and Qubits", Phys. Rev. Lett. **98**, 267003 (2007).

[217] R. Harris, M. W. Johnson, S. Han, A. J. Berkley, J. Johansson, P. Bunyk, E. Ladizinsky, S. Govorkov, M. C. Thom, S. Uchaikin, B. Bumble, A. Fung, A. Kaul, A. Kleinsasser, M. H. S. Amin, and D. V. Averin, "Probing Noise in Flux Qubits via Macroscopic Resonant Tunneling", Phys. Rev. Lett. **101**, 117003 (2008).

[218] S. Gustavsson, J. Bylander, F. Yan, W. D. Oliver, F. Yoshihara, and Y. Nakamura, "Noise correlations in a flux qubit with tunable tunnel coupling", Phys. Rev. B **84** (2011).

[219] J. Bylander, S. Gustavsson, F. Yan, F. Yoshihara, K. Harrabi, G. Fitch, D. G. Cory, Y. Nakamura, J.-S. Tsai, and W. D. Oliver, "Noise spectroscopy through dynamical decoupling with a superconducting flux qubit", Nat. Phys. **7**, 565 (2011).

[220] O. Astafiev, Y. A. Pashkin, Y. Nakamura, T. Yamamoto, and J. S. Tsai, "Quantum Noise in the Josephson Charge Qubit", Phys. Rev. Lett. **93**, 267007 (2004).

[221] O. Astafiev, Y. A. Pashkin, Y. Nakamura, T. Yamamoto, and J. S. Tsai, "Temperature Square Dependence of the Low Frequency $1/f$ Charge Noise in the Josephson Junction Qubits", Phys. Rev. Lett. **96**, 137001 (2006).

[222] J. A. Schreier, A. A. Houck, J. Koch, D. I. Schuster, B. R. Johnson, J. M. Chow, J. M. Gambetta, J. Majer, L. Frunzio, M. H. Devoret, S. M. Girvin, and R. J. Schoelkopf, "Suppressing charge noise decoherence in superconducting charge qubits", Phys. Rev. B **77**, 180502 (2008).

[223] D. Riste, C. C. Bultink, M. J. Tiggelman, R. N. Schouten, K. W. Lehnert, and L. DiCarlo, "Millisecond charge-parity fluctuations and induced decoherence in a superconducting transmon qubit", Nat. Commun. **4**, 1913 (2013).

[224] G. Catelani, J. Koch, L. Frunzio, R. J. Schoelkopf, M. H. Devoret, and L. I. Glazman, "Quasiparticle Relaxation of Superconducting Qubits in the Presence of Flux", Phys. Rev. Lett. **106**, 077002 (2011).

[225] M. Lenander, H. Wang, R. C. Bialczak, E. Lucero, M. Mariantoni, M. Neeley, A. D. O'Connell, D. Sank, M. Weides, J. Wenner, T. Yamamoto, Y. Yin, J. Zhao, A. N. Cleland, and J. M. Martinis, "Measurement of energy decay in superconducting qubits from nonequilibrium quasiparticles", Phys. Rev. B **84**, 024501 (2011).

[226] G. Catelani, S. E. Nigg, S. M. Girvin, R. J. Schoelkopf, and L. I. Glazman, "Decoherence of superconducting qubits caused by quasiparticle tunneling", Phys. Rev. B **86**, 184514 (2012).

[227] I. Nsanzineza and B. L. T. Plourde, "Trapping a Single Vortex and Reducing Quasiparticles in a Superconducting Resonator", Phys. Rev. Lett. **113** (2014).

[228] P. Dutta and P. M. Horn, "Low-frequency fluctuations in solids: $1/f$ noise", Rev. Mod. Phys. **53**, 497 (1981).

[229] J. M. Martinis, S. Nam, J. Aumentado, K. M. Lang, and C. Urbina, "Decoherence of a superconducting qubit due to bias noise", Phys. Rev. B **67**, 094510 (2003).

[230] R. Alicki, "Master equations for a damped nonlinear oscillator and the validity of the Markovian approximation", Phys. Rev. A **40**, 4077 (1989).

[231] D. P. DiVincenzo and D. Loss, "Rigorous Born approximation and beyond for the spin-boson model", Phys. Rev. B **71**, 035318 (2005).

[232] S. Shresta, C. Anastopoulos, A. Dragulescu, and B. L. Hu, "Non-Markovian qubit dynamics in a thermal field bath: Relaxation, decoherence, and entanglement", Phys. Rev. A **71**, 022109 (2005).

[233] A. A. Slutskin, K. N. Bratus', A. Bergvall, and V. S. Shumeiko, "Non-Markovian decoherence of a two-level system weakly coupled to a bosonic bath", Europhys. Lett. **96**, 40003 (2011).

[234] Y. Makhlin and A. Shnirman, "Dephasing of qubits by transverse low-frequency noise", J. Exp. and Theor. Phys. Lett. **78**, 0021 (2003).

[235] Y. Makhlin and A. Shnirman, "Dephasing of Solid-State Qubits at Optimal Points", Phys. Rev. Lett. **92**, 178301 (2004).

[236] A. Einstein, "Strahlungs-Emission und Absorption nach der Quantentheorie", Deutsche Physikalische Gesellschaft **18**, 318 (1916).

[237] P. A. M. Dirac, "The Quantum Theory of the Emission and Absorption of Radiation", P. R. Soc. Lond. A-Conta. **114**, 243 (1927).

[238] J. Orear and E. Fermi, *Nuclear Physics: A Course Given by Enrico Fermi at the University of Chicago*, Midway reprint (University of Chicago Press, 1950).

[239] R. J. Schoelkopf, A. A. Clerk, S. M. Girvin, K. W. Lehnert, and M. H. Devoret, "Noise and measurement backaction in superconducting circuits: qubits as spectrometers of quantum noise", Proc. SPIE **5115**, 356 (2003).

[240] A. A. Houck, J. A. Schreier, B. R. Johnson, J. M. Chow, J. Koch, J. M. Gambetta, D. I. Schuster, L. Frunzio, M. H. Devoret, S. M. Girvin, and R. J. Schoelkopf, "Controlling the Spontaneous Emission of a Superconducting Transmon Qubit", Phys. Rev. Lett. **101**, 080502 (2008).

[241] M. D. Reed, B. R. Johnson, A. A. Houck, L. DiCarlo, J. M. Chow, D. I. Schuster, L. Frunzio, and R. J. Schoelkopf, "Fast reset and suppressing spontaneous emission of a superconducting qubit", Appl. Phys. Lett. **96**, 203110 (2010).

[242] Z. Kim, B. Suri, V. Zaretskey, S. Novikov, K. D. Osborn, A. Mizel, F. C. Wellstood, and B. S. Palmer, "Decoupling a Cooper-Pair Box to Enhance the Lifetime to 0.2 ms", Phys. Rev. Lett. **106**, 120501 (2011).

[243] M. Haeberlein, F. Deppe, A. Kurcz, J. Goetz, A. Baust, P. Eder, K. Fedorov, M. Fischer, E. P. Menzel, M. J. Schwarz, F. Wulschner, E. Xie, L. Zhong, E. Solano, and J.-J. R. G. Marx, Achim García-Ripoll, "Spin-boson model with an engineered reservoir in circuit quantum electrodynamics", ArXiv e-prints: 1506.09114 (2015).

[244] E. M. Purcell, H. C. Torrey, and R. V. Pound, "Resonance Absorption by Nuclear Magnetic Moments in a Solid", Phys. Rev. **69**, 37 (1946).

[245] S. Filipp, A. F. van Loo, M. Baur, L. Steffen, and A. Wallraff, "Preparation of subradiant states using local qubit control in circuit QED", Phys. Rev. A **84**, 061805 (2011).

[246] C. Rigetti, J. M. Gambetta, S. Poletto, B. L. T. Plourde, J. M. Chow, A. D. Córcoles, J. A. Smolin, S. T. Merkel, J. R. Rozen, G. A. Keefe, M. B. Rothwell, M. B. Ketchen, and M. Steffen, "Superconducting qubit in a waveguide cavity with a coherence time approaching 0.1 ms", Phys. Rev. B **86**, 100506 (2012).

[247] E. A. Sete, J. M. Gambetta, and A. N. Korotkov, "Purcell effect with microwave drive: Suppression of qubit relaxation rate", Phys. Rev. B **89**, 104516 (2014).

[248] C. Müller, J. Lisenfeld, A. Shnirman, and S. Poletto, "Interacting two-level defects as sources of fluctuating high-frequency noise in superconducting circuits", Phys. Rev. B **92**, 035442 (2015).

[249] J. Burnett, L. Faoro, I. Wisby, V. L. Gurtovoi, A. V. Chernykh, G. M. Mikhailov, V. A. Tulin, R. Shaikhaidarov, V. Antonov, P. J. Meeson, A. Y. Tzalenchuk, and T. Lindström, "Evidence for interacting two-level systems from the 1/f noise of a superconducting resonator", Nat. Commun. **5**, 4119 (2014).

[250] L. Faoro and L. B. Ioffe, "Interacting tunneling model for two-level systems in amorphous materials and its predictions for their dephasing and noise in superconducting microresonators", Phys. Rev. B **91**, 014201 (2015).

[251] K. Lang, S. Nam, J. Aumentado, C. Urbina, and J. M. Martinis, "Banishing quasiparticles from Josephson-junction qubits: why and how to do it", IEEE T. Appl. Supercon. **13**, 989 (2003).

[252] A. D. Corcoles, J. M. Chow, J. M. Gambetta, C. Rigetti, J. R. Rozen, G. A. Keefe, M. Beth Rothwell, M. B. Ketchen, and M. Steffen, "Protecting superconducting qubits from radiation", Appl. Phys. Lett. **99**, 181906 (2011).

[253] S. Gustavsson, F. Yan, G. Catelani, J. Bylander, A. Kamal, J. Birenbaum, D. Hover, D. Rosenberg, G. Samach, A. P. Sears, S. J. Weber, J. L. Yoder, J. Clarke, A. J. Kerman, F. Yoshihara, Y. Nakamura, T. P. Orlando, and W. D. Oliver, "Suppressing relaxation in superconducting qubits by quasiparticle pumping", Science **354**, 1573 (2016).

[254] L. J. Klein, H. F. Hamann, Y.-Y. Au, and S. Ingvarsson, "Coherence properties of infrared thermal emission from heated metallic nanowires", Appl. Phys. Lett. **92**, 213102 (2008).

[255] R. J. Schoelkopf, P. J. Burke, A. A. Kozhevnikov, D. E. Prober, and M. J. Rooks, "Frequency Dependence of Shot Noise in a Diffusive Mesoscopic Conductor", Phys. Rev. Lett. **78**, 3370 (1997).

[256] P. J. de Visser, J. J. A. Baselmans, P. Diener, S. J. C. Yates, A. Endo, and T. M. Klapwijk, "Number Fluctuations of Sparse Quasiparticles in a Superconductor", Phys. Rev. Lett. **106**, 167004 (2011).

[257] O.-P. Saira, A. Kemppinen, V. F. Maisi, and J. P. Pekola, "Vanishing quasiparticle density in a hybrid Al/Cu/Al single-electron transistor", Phys. Rev. B **85**, 012504 (2012).

[258] R. Barends, S. van Vliet, J. J. A. Baselmans, S. J. C. Yates, J. R. Gao, and T. M. Klapwijk, "Enhancement of quasiparticle recombination in Ta and Al superconductors by implantation of magnetic and nonmagnetic atoms", Phys. Rev. B **79**, 020509 (2009).

[259] M. Kenyon, C. J. Lobb, and F. C. Wellstood, "Temperature dependence of low-frequency noise in Al–Al_2O_3–Al single-electron transistors", J. App. Phys. **88** (2000).

[260] M. Neeley, M. Ansmann, R. C. Bialczak, M. Hofheinz, N. Katz, E. Lucero, A. O'Connell, H. Wang, A. N. Cleland, and J. M. Martinis, "Process tomography of quantum memory in a Josephson-phase qubit coupled to a two-level state", Nat. Phys. **4** (2008).

[261] M. v. Schickfus and S. Hunklinger, "Saturation of the dielectric absorption of vitreous silica at low temperatures", Phys. Lett. A **64**, 144 (1977).

[262] U. Strom, M. von Schickfus, and S. Hunklinger, "Low-Temperature Anomalies in the Microwave Dielectric Properties of Na β-Alumina", Phys. Rev. Lett. **41**, 910 (1978).

[263] W. A. Phillips, "Two-level states in glasses", Rep. Progr. Phys. **50**, 1657 (1987).

[264] R. W. Simmonds, K. M. Lang, D. A. Hite, S. Nam, D. P. Pappas, and J. M. Martinis, "Decoherence in Josephson Phase Qubits from Junction Resonators", Phys. Rev. Lett. **93**, 077003 (2004).

[265] Y. Shalibo, Y. Rofe, D. Shwa, F. Zeides, M. Neeley, J. M. Martinis, and N. Katz, "Lifetime and Coherence of Two-Level Defects in a Josephson Junction", Phys. Rev. Lett. **105**, 177001 (2010).

[266] J. Lisenfeld, C. Müller, J. H. Cole, P. Bushev, A. Lukashenko, A. Shnirman, and A. V. Ustinov, "Measuring the Temperature Dependence of Individual Two-Level Systems by Direct Coherent Control", Phys. Rev. Lett. **105**, 230504 (2010).

[267] J. M. Martinis, K. B. Cooper, R. McDermott, M. Steffen, M. Ansmann, K. D. Osborn, K. Cicak, S. Oh, D. P. Pappas, R. W. Simmonds, and C. C. Yu, "Decoherence in Josephson Qubits from Dielectric Loss", Phys. Rev. Lett. **95**, 210503 (2005).

[268] E. Paladino, Y. M. Galperin, G. Falci, and B. L. Altshuler, "$1/f$ noise: Implications for solid-state quantum information", Rev. Mod. Phys. **86**, 361 (2014).

[269] A. L. Burin, S. Matityahu, and M. Schechter, "Low-temperature $1/f$ noise in microwave dielectric constant of amorphous dielectrics in Josephson qubits", Phys. Rev. B **92**, 174201 (2015).

[270] K. Kakuyanagi, T. Meno, S. Saito, H. Nakano, K. Semba, H. Takayanagi, F. Deppe, and A. Shnirman, "Dephasing of a Superconducting Flux Qubit", Phys. Rev. Lett. **98**, 047004 (2007).

[271] T. Kato, A. A. Golubov, and Y. Nakamura, "Decoherence in a superconducting flux qubit with a π-junction", Phys. Rev. B **76**, 172502 (2007).

[272] A. Ferrón and D. Domínguez, "Intrinsic leakage of the Josephson flux qubit and breakdown of the two-level approximation for strong driving", Phys. Rev. B **81**, 104505 (2010).

[273] S. Machlup, "Noise in Semiconductors: Spectrum of a Two-Parameter Random Signal", J. Appl. Phys. **25**, 341 (1954).

[274] F. Green, M. P. Das, and J. S. Thakur, in *SPIE's First International Symposium on Fluctuations and Noise*, edited by L. B. Kish, F. Green, G. Iannaccone, and J. R. Vig (SPIE, 2003), SPIE Proceedings.

[275] P. Bertet, I. Chiorescu, G. Burkard, K. Semba, C. J. P. M. Harmans, D. P. DiVincenzo, and J. E. Mooij, "Dephasing of a Superconducting Qubit Induced by Photon Noise", Phys. Rev. Lett. **95**, 257002 (2005).

[276] J. M. Sage, V. Bolkhovsky, W. D. Oliver, B. Turek, and P. B. Welander, "Study of loss in superconducting coplanar waveguide resonators", J. Appl. Phys. **109**, 063915 (2011).

[277] S. Ohya, B. Chiaro, A. Megrant, C. Neill, R. Barends, Y. Chen, J. Kelly, D. Low, J. Mutus, P. O'Malley, P. Roushan, D. Sank, A. Vainsencher, J. Wenner, T. C. White, Y. Yin, B. D. Schultz, C. J. Palmstrom, B. A. Mazin, A. N. Cleland, and J. M. Martinis, "Room temperature deposition of sputtered TiN films for superconducting coplanar waveguide resonators", Supercond. Sci. Tech. **27**, 015009 (2014).

[278] A. D. O' Connell, M. Ansmann, R. C. Bialczak, M. Hofheinz, N. Katz, E. Lucero, C. McKenney, M. Neeley, H. Wang, E. M. Weig, A. N. Cleland, and J. M. Martinis, "Microwave dielectric loss at single photon energies and millikelvin temperatures", Appl. Phys. Lett. **92**, 112903 (2008).

[279] M. Arzeo, F. Lombardi, and T. Bauch, "Microwave losses in MgO, $LaAlO_3$, and $(La_{0.3}Sr_{0.7})(Al_{0.65}Ta_{0.35})O_3$ dielectrics at low power and in the millikelvin temperature range", Appl. Phys. Lett. **104**, 212601 (2014).

[280] T. Lindström, J. E. Healey, M. S. Colclough, C. M. Muirhead, and A. Y. Tzalenchuk, "Properties of superconducting planar resonators at millikelvin temperatures", Phys. Rev. B **80**, 132501 (2009).

[281] M. S. Khalil, M. J. A. Stoutimore, F. C. Wellstood, and K. D. Osborn, "An analysis method for asymmetric resonator transmission applied to superconducting devices", J. Appl. Phys. **111**, 054510 (2012).

[282] U. Fano, "Effects of Configuration Interaction on Intensities and Phase Shifts", Phys. Rev. Lett. **124**, 1866 (1961).

[283] J. Wenner, M. Neeley, R. C. Bialczak, M. Lenander, E. Lucero, A. D. O'Connell, D. Sank, H. Wang, M. Weides, A. N. Cleland, and J. M. Martinis, "Wirebond crosstalk and cavity modes in large chip mounts for superconducting qubits", Supercond. Sci. Tech. **24**, 065001 (2011).

[284] J. M. Hornibrook, E. E. Mitchell, and D. J. Reilly, "Superconducting Resonators with Parasitic Electromagnetic Environments", ArXiv e-prints: 1203.4442 (2012).

[285] M. Born, "Quantenmechanik der Stoßvorgänge", Z. Phys. **38**, 803 (1926).

[286] V. Hakim and V. Ambegaokar, "Quantum theory of a free particle interacting with a linearly dissipative environment", Phys. Rev. A **32**, 423 (1985).

[287] A. J. Leggett, S. Chakravarty, A. T. Dorsey, M. P. A. Fisher, A. Garg, and W. Zwerger, "Dynamics of the dissipative two-state system", Rev. Mod. Phys. **59**, 1 (1987).

[288] R. Kubo, "The fluctuation-dissipation theorem", Rep. Prog. Phys. **29**, 255 (1966).

[289] L. Faoro and L. B. Ioffe, "Internal Loss of Superconducting Resonators Induced by Interacting Two-Level Systems", Phys. Rev. Lett. **109** (2012).

[290] J. Jäckle, "On the ultrasonic attenuation in glasses at low temperatures", Z. Phys. **257**, 212 (1972).

[291] S. Rudin, T. L. Reinecke, and B. Segall, "Temperature-dependent exciton linewidths in semiconductors", Phys. Rev. B **42**, 11218 (1990).

[292] P. Borri, W. Langbein, J. M. Hvam, and F. Martelli, "Well-width dependence of exciton-phonon scattering in $In_xGa_{1-x}As/GaAs$ single quantum wells", Phys. Rev. B **59**, 2215 (1999).

[293] J. Lisenfeld, A. Lukashenko, M. Ansmann, J. M. Martinis, and A. V. Ustinov, "Temperature Dependence of Coherent Oscillations in Josephson Phase Qubits", Phys. Rev. Lett. **99**, 170504 (2007).

[294] Y. Wang, P. Zhou, L. Wei, H. Li, B. Zhang, M. Zhang, Q. Wei, Y. Fang, and C. Cao, "Photon-induced thermal effects in superconducting coplanar waveguide resonators", J. Appl. Phys. **114**, 153109 (2013).

[295] H. Safa, "Surface resistance of a superconductor", Proceedings of the 5th Workshop on RF Superconductivity **2**, 771 (1987).

[296] S. P. Morgan, "Effect of Surface Roughness on Eddy Current Losses at Microwave Frequencies", J. Appl. Phys. **20**, 352 (1949).

[297] R. Simons and R. Arora, "Coupled Slot Line Field Components", IEEE T. Microw. Theory **30**, 1094 (1982).

[298] E. Maxwell, "Conductivity of Metallic Surfaces at Microwave Frequencies", J. Appl. Phys. **18**, 629 (1947).

[299] F. Sterr, "Optimization of Josephson Junction Nanofabrication for Superconducting Quantum Circuits", Diploma thesis, TU München (2013).

[300] E. Xie, "Optimized fabrication process for nanoscale Josephson junctions used in superconducting quantum circuits", Master's thesis, TU München (2015).

[301] L. Wang, "Fabrication Stability of Josephson Junctions for Superconducting Qubits", Master's thesis, TU München (2015).

[302] G. J. Dolan, "Offset masks for lift-off photoprocessing", Appl. Phys. Lett. **31**, 337 (1977).

[303] T. Niemczyk, F. Deppe, M. Mariantoni, E. P. Menzel, E. Hoffmann, G. Wild, L. Eggenstein, A. Marx, and R. Gross, "Fabrication technology of and symmetry breaking in superconducting quantum circuits", Supercond. Sci. Tech. **22**, 034009 (2009).

[304] M. Hatzakis, "PMMA copolymers as high sensitivity electron resists", J. Vac. Sci. Technol. **16**, 1984 (1979).

[305] N. Semaltianos and N. Semaltianos, "Spin-coated PMMA films", Microelectron. J. **38**, 754 (2007).

[306] K. Koshelev, M. Ali Mohammad, T. Fito, K. L. Westra, S. K. Dew, and M. Stepanova, "Comparison between ZEP and PMMA resists for nanoscale electron beam lithography experimentally and by numerical modeling", J. Vac. Sci. Technol. B **29**, 06F306 (2011).

[307] D. B. Hall, P. Underhill, and J. M. Torkelson, "Spin coating of thin and ultrathin polymer films", Polym. Eng. Sci. **38**, 2039 (1998).

[308] A. G. Emslie, F. T. Bonner, and L. G. Peck, "Flow of a Viscous Liquid on a Rotating Disk", J. Appl. Phys. **29**, 858 (1958).

[309] D. Meyerhofer, "Characteristics of resist films produced by spinning", J. Appl. Phys. **49**, 3993 (1978).

[310] D. E. Bornside, "Spin Coating of a PMMA Chlorobenzene Solution", J. Electrochem. Soc. **138**, 317 (1991).

[311] D. E. Bornside, R. a. Brown, P. W. Ackmann, J. R. Frank, A. a. Tryba, and F. T. Geyling, "The effects of gas phase convection on mass transfer in spin coating", J. Appl. Phys. **73**, 585 (1993).

[312] E. Mohajerani, F. Farajollahi, R. Mahzoon, and S. Baghery, "Morphological and thickness analysis for PMMA spin coated films", J. Optoelectron. Adv. M. **9**, 3901 (2007).

[313] T. Dobroth and L. Erwin, "Causes of edge beads in cast films", Polym. Eng. Sci. **26**, 462 (1986).

[314] L. W. Schwartz and R. V. Roy, "Theoretical and numerical results for spin coating of viscous liquids", Phys. Fluids **16**, 569 (2004).

[315] K. E. Holloway, P. Habdas, N. Semsarillar, K. Burfitt, and J. R. de Bruyn, "Spreading and fingering in spin coating", Phys. Rev. E **75**, 046308 (2007).

[316] D. P. Birnie, T. Schneller, R. Waser, M. Kosec, and D. Payne, *Chemical Solution Deposition of Functional Oxide Thin Films* (Springer, Vienna, 2013).

[317] X. Min, X. Orignac, and R. M. Almeida, "Striation-Free, Spin-Coated Sol-Gel Optical Films", J. Am. Ceram. Soc. **78**, 2254 (1995).

[318] H. Kozuka and M. Hirano, "Radiative Striations and Surface Roughness of Alkoxide-Derived Spin Coating Films", J. Sol-Gel Sci. Techn. **19**, 501 (2000).

[319] A. Mihi, M. Ocana, and H. Míguez, "Oriented Colloidal-Crystal Thin Films by Spin Coating Microspheres Dispersed in Volatile Media", Adv. Mater. **18**, 2244 (2006).

[320] D. Birnie and D. Haas, "Modeling of Striation Development in Spin Coating", 13^{th} International Coating Science and Technology Symposium (2006).

[321] D. E. Haas, J. N. Quijada, S. J. Picone, and D. P. Birnie III, "Effect of solvent evaporation rate on skin formation during spin coating of complex solutions", P. Soc. Photo-Opt. Ins. **280**, 280 (2000).

[322] D. Haas and D. Birnie, in *Proceedings of Am. Ceramic. Soc. Symposium on Sol-Gel* (2000).

[323] H. Kozuka, Y. Ishikawa, and N. Ashibe, "Radiative Striations of Spin-Coating Films: Surface Roughness Measurement and in-situ Observation", J. Sol-Gel Sci. Techn. **31**, 245 (2004).

[324] C. V. Sternling and L. E. Scriven, "Interfacial turbulence: Hydrodynamic instability and the marangoni effect", AICHE J. **5**, 514 (1959).

[325] K. Norrman, A. Ghanbari-Siahkali, and N. B. Larsen, "6 Studies of spin-coated polymer films", Annu. Rep. Prog. Chem., Sect. C: Phys. Chem. **101**, 174 (2005).

[326] J. Perlich, V. Körstgens, E. Metwalli, L. Schulz, R. Georgii, and P. Müller-Buschbaum, "Solvent Content in Thin Spin-Coated Polystyrene Homopolymer Films", Macromolecules **42**, 337 (2009).

[327] W. Moreau, D. Merritt, W. Moyer, M. Hatzakis, D. Johnson, and L. Pederson, "Speed enhancement of PMMA resist", J. Vac. Sci. Technol. **16**, 1989 (1979).

[328] P. Rai-Choudhury, *Handbook of Microlithography, Micromachining, and Microfabrication. Volume 1: Microlithography* (SPIE, 1997).

[329] L. Broglie, "The reinterpretation of wave mechanics", Found. Phys. **1**, 5 (1970).

[330] T. Groves, D. L. Hammond, and H. Kuo, "Electron-beam broadening effects caused by discreteness of space charge", J. Vac. Sci. Technol. **16**, 1680 (1979).

[331] A. Broers, A. Hoole, and J. Ryan, "Electron beam lithographie resolution limits", Microelectron. Eng. **32**, 131 (1996).

[332] M. A. Mohammad, K. P. Santo, S. K. Dew, and M. Stepanova, "Study of the interaction of polymethylmethacrylate fragments with methyl isobutyl ketone and isopropyl alcohol", J. Vac. Sci. Technol. B **30**, 06FF11 (2012).

[333] K. Murata, D. F. Kyser, and C. H. Ting, "Monte Carlo simulation of fast secondary electron production in electron beam resists", J. Appl. Phys. **52**, 4396 (1981).

[334] A. Jablonski, F. Salvat, and C. J. Powell, "Comparison of Electron Elastic-Scattering Cross Sections Calculated from Two Commonly Used Atomic Potentials", J. Phys. Chem. Ref. Data **33**, 409 (2004).

[335] S. Rishton and D. Kern, "Point exposure distribution measurements for proximity correction in electron beam lithography on a sub 100 nm scale", J. Vac. Sci. Technol. B **5**, 135 (1987).

[336] W. Patrick and P. Vettiger, "Optimization of the proximity parameters for the electron beam exposure of nanometer gate-length GaAs metal–semiconductor field effect transistors", J. Vac. Sci. Technol. B **6**, 2037 (1988).

[337] V. Aristov, B. Gaifullin, A. Svintsov, S. Zaitsev, H. Raith, and R. Jede, "Accuracy of proximity correction in electron lithography after development", J. Vac. Sci. Technol. B **10**, 2459 (1992).

[338] C. S. Ea and A. Brown, "Enhanced pattern area density proximity effect correction", J. Vac. Sci. Technol. B **19**, 1985 (2001).

[339] R. Wüest, P. Strasser, M. Jungo, F. Robin, D. Erni, H. Jäckel, R. Wüest, P. Strasser, M. Jungo, F. Robin, D. Erni, and H. Jäckel, "An efficient proximity-effect correction method for electron-beam patterning of photonic crystal devices", Microelectron. Eng. **67-68**, 182 (2003).

[340] A. R. Shultz, "High-energy radiation effects on polyacrylates and polymethacrylates", J. Polym. Sci. **35**, 369 (1959).

[341] F. Krumeich, "Properties of Electrons, their Interactions with Matter and Applications in Electron Microscopy"„ Tech. Rep., ETH Zürich (2011).

[342] D. C. Joy and S. Luo, "An empirical stopping power relationship for low-energy electrons", Scanning **11**, 176 (1989).

[343] A. Jablonski, S. Tanuma, and C. J. Powell, "Modified predictive formula for the electron stopping power", J. Appl. Phys. **103**, 063708 (2008).

[344] J. R. Lowney, "Monte Carlo simulation of scanning electron microscope signals for lithographic metrology", Scanning **18**, 301 (1996).

[345] Z. Tan and Y. He, "Monte Carlo calculation method on low energy electron scattering in polybasic medium", Chinese Sci. Bull. **43**, 171 (1998).

[346] Z. Tan, Y. Xia, X. Liu, and M. Zhao, "Monte-Carlo simulation of low-energy electron scattering in PMMA - using stopping powers from dielectric formalism", Microelectron. Eng. **77**, 285 (2005).

[347] P. Hovington, D. Drouin, and R. Gauvin, "CASINO: A new monte carlo code in C language for electron beam interactions - Part II: Description of the program", Scanning **19**, 1 (1997).

[348] D. Drouin, P. Hovington, and R. Gauvin, "CASINO: A new monte carlo code in C language for electron beam interactions - Part II: Tabulated values of the mott cross section", Scanning **19**, 20 (1997).

[349] H. Demers, N. Poirier-Demers, A. R. Couture, D. Joly, M. Guilmain, N. de Jonge, and D. Drouin, "Three dimensional electron microscopy simulation with the CASINO Monte Carlo software", Scanning **33**, 135 (2011).

[350] M. Kotera, R. Ijichi, T. Fujiwara, H. Suga, and D. B. Wittry, "A Simulation of Electron Scattering in Metals", JPN J. Appl. Phys. **29**, 2277 (1990).

[351] E. Reichmanis and L. F. Thompson, "Polymer materials for microlithography", Chem. Rev. **89**, 1273 (1989).

[352] M. J. Rooks, E. Kratschmer, R. Viswanathan, J. Katine, R. E. Fontana, and S. A. MacDonald, in *Papers from the 46th International Conference on Electron, Ion, and Photon Beam Technology and Nanofabrication* (2002), vol. 20, pp. 2937–2941.

[353] S. Yasin, D. Hasko, and H. Ahmed, "Comparison of MIBK/IPA and water/IPA as PMMA developers for electron beam nanolithography", Microelectron. Eng. **61**, 745 (2002).

[354] W. Jung-Sub, L. Hyo-Sung, and K.-B. K., "Enhanced Development Properties of IPA (Isopropyl Alcohol) on the PMMA Electron Beam Resist", Electron. Mater. Lett. **3**, 1 (2007).

[355] T. Brenninger, "A new thin thin film deposition system for the preparation of persistent current qubits", Master's thesis, TU München (2007).

[356] K. Bordo and H.-G. Rubahn, "Effect of Deposition Rate on Structure and Surface Morphology of Thin Evaporated Al Films on Dielectrics and Semiconductors", Mater. Sci. (2012).

[357] A. Kleinsasser, R. Miller, and W. Mallison, "Dependence of critical current density on oxygen exposure in Nb-AlO_x-Nb tunnel junctions", IEEE T. Appl. Supercon. **5**, 26 (1995).

[358] W. Krueger and S. Pollack, "The initial oxidation of aluminum thin films at room temperature", Surf. Sci. **30**, 263 (1972).

[359] F. Deppe, S. Saito, H. Tanaka, and H. Takayanagi, "Determination of the capacitance of nm scale Josephson junctions", J. Appl. Phys. **95**, 2607 (2004).

[360] F. Wulschner, "Nb/AlO_x/Nb Josephsonkontakte für supraleitende Quantenschaltkreise", Diploma thesis, TU München (2011).

[361] H. P. Gürtner, "Interfernce Effects on Superconducting Coplanar Waveguide Structures", Bachelor's thesis, TU München (2013).

[362] D. Kasilingam and D. Rutledge, in *Microwave Symposium Digest, IEEE MTT-S International* (1983), pp. 113–116.

[363] C. Neill, A. Megrant, R. Barends, Y. Chen, B. Chiaro, J. Kelly, J. Y. Mutus, O'Malley, P.J.J., D. Sank, J. Wenner, White, T. C., Y. Yin, A. N. Cleland, and J. M. Martinis, "Fluctuations from edge defects in superconducting resonators", Appl. Phys. Lett. **103**, 072601 (2013).

[364] P. Summer, "Characterization of superconducting coplanar waveguide resonators at millikelvin temperatures", Master's thesis, TU München (2014).

[365] A. Assmuth, *Photonenaktivierte Reinigungs-und Oxidationsprozesse für die Nanoelektronik* (Cuvillier, 2007).

[366] H. Dersch, J. Stuke, and J. Beichler, "Light-induced dangling bonds in hydrogenated amorphous silicon", Appl. Phys. Lett. **38**, 456 (1981).

[367] G. W. Trucks, K. Raghavachari, G. S. Higashi, and Y. J. Chabal, "Mechanism of HF etching of silicon surfaces: A theoretical understanding of hydrogen passivation", Phys. Rev. Lett. **65**, 504 (1990).

[368] E. Cartier, J. H. Stathis, and D. A. Buchanan, "Passivation and depassivation of silicon dangling bonds at the Si/SiO2 interface by atomic hydrogen", Appl. Phys. Lett. **63**, 1510 (1993).

[369] H. Hirayama and T. Tatsumi, "Hydrogen passivation effect in Si molecular beam epitaxy", Appl. Phys. Lett. **54**, 1561 (1989).

[370] S. S. Iyer, M. Arienzo, and E. de Fresart, "Low-temperature silicon cleaning via hydrogen passivation and conditions for epitaxy", Appl. Phys. Lett. **57**, 893 (1990).

[371] K. R. Williams, K. Gupta, and M. Wasilik, "Etch rates for micromachining processing-Part II", J. Microelectromech. S. **12**, 761 (2003).

[372] V. Gupta, J. Wu, and A. N. Pronin, "Effect of Substrate Orientation, Roughness, and Film Deposition Mode on the Tensile Strength and Toughness of Niobium-Sapphire Interfaces", J. Am. Ceram. Soc. **80**, 3172 (1997).

[373] A. Wildes, J. Mayer, and K. Theis-Brühl, "The growth and structure of epitaxial niobium on sapphire", Thin Solid Films **401**, 7 (2001).

[374] E. Chason and T. M. Mayer, "Low energy ion bombardment induced roughening and smoothing of SiO2 surfaces", Appl. Phys. Lett. **62**, 363 (1993).

[375] M. Krawczyk, "Microstrip Resonators for Circuit Quantum Electrodynamics", Master's thesis, TU München (2011).

[376] J. Puertas Martínez, "Circuit quantum electrodynamics with transmon qubits", Master's thesis, TU München (2015).

[377] M. Fischer, "On-chip Superconducting Microwave Interferometer", Master's thesis, TU München (2014).

[378] F. Wulschner, "Controlled interactions in superconducting quantum circuits", PhD thesis, Technische Universität München (2016).

[379] F. Pobell, *The ^{3}He-^{4}He Dilution Refrigerator* (Springer Berlin Heidelberg, Berlin, Heidelberg, 1996).

[380] A. T. A. M. de Waele, "Basic Operation of Cryocoolers and Related Thermal Machines", J. Low Temp. Phys. **164**, 179 (2011).

[381] J. Kuerten, C. Castelijns, A. de Waele, and H. Gijsman, "Thermodynamic properties of liquid ^{3}He-^{4}He mixtures at zero pressure for temperatures below 250 mK and 3He concentrations below 8%", Cryogenics **25**, 419 (1985).

[382] J. Kuerten, "^{3}He-^{4}He II mixtures: Thermodynamic and hydrodynamic properties", Ph. D Thesis, TU Eindhoven (1987).

[383] G. Chaudhry and J. G. Brisson, "Thermodynamic Properties of Liquid 3He-4He Mixtures Between 0.15 K and 1.8 K", J. Low Temp. Phys. **155**, 235 (2009).

[384] G. Chaudhry and G. Vermeulen, "Analysis of a Mixing Chamber Developed for Use in a Gravity-Independent Dilution Refrigerator", J. Low Temp. Phys. **169**, 90 (2012).

[385] G. Wild, "Macroscopic quantum tunneling in Josephson junctions - a method to characterise a well-shielded low temperature setup", Diploma thesis, TU München (2004).

[386] K. Neumaier, "Sample environment at low temperatures", Rev. Phys. Appl. (Paris) **19**, 677 (1984).

[387] I. Batko, K. Flachbart, M. Somora, and D. Vanicky, "Design of RuO_2-based thermometers for the millikelvin temperature range", Cryogenics **35**, 105 (1995).

[388] K. Uhlig, "Magnetoresistance of thick-film chip resistors at millikelvin temperatures", Cryogenics **35**, 525 (1995).

[389] F. Clarke and J. Larkin, "Measurement of total reflectance, transmittance and emissivity over the thermal IR spectrum", Infrared Physics **25**, 359 (1985).

[390] K. C. Camargo, A. F. Michels, F. S. Rodembusch, and F. Horowitz, "Multi-scale structured, superhydrophobic and wide-angle, antireflective coating in the near-infrared region", Chem. Commun. **48**, 4992 (2012).

[391] A. B. Zorin, "The thermocoax cable as the microwave frequency filter for single electron circuits", Review of Scientific Instruments **66**, 4296 (1995).

[392] D. Vion, P. F. Orfila, P. Joyez, D. Esteve, and M. H. Devoret, "Miniature electrical filters for single electron devices", J. Appl. Phys. **77**, 2519 (1995).

[393] F. P. Milliken, J. R. Rozen, G. A. Keefe, and R. H. Koch, "50 Ohm characteristic impedance low-pass metal powder filters", Rev. Sci. Instrum. **78**, 024701 (2007).

[394] A. Fukushima, A. Sato, A. Iwasa, Y. Nakamura, T. Komatsuzaki, and Y. Sakamoto, "Attenuation of microwave filters for single-electron tunneling experiments", IEEE T. Instrum. Meas. **46**, 289 (1997).

[395] K. Bladh, D. Gunnarsson, E. Hürfeld, S. Devi, C. Kristoffersson, B. Smalander, S. Pehrson, T. Claeson, P. Delsing, and M. Taslakov, "Comparison of cryogenic filters for use in single electronics experiments", Rev. Sci. Instrum. **74**, 1323 (2003).

[396] D. F. Santavicca and D. E. Prober, "Impedance-matched low-pass stripline filters", Meas. Sci. Technol. **19**, 087001 (2008).

[397] P. Forn-Díaz, R. N. Schouten, W. A. den Braver, J. E. Mooij, and C. J. P. M. Harmans, "Josephson squelch filter for quantum nanocircuits", Appl. Phys. Lett. **95**, 042505 (2009).

[398] K. Geerlings, "Improving Coherence of Superconducting Qubits and Resonators", PhD thesis, Yale University (2013).

[399] T. O. Klaassen, M. C. Diez, J. H. Blok, C.Smorenburg, K. J. Wildeman, and G. Jakob, in *Proceedings of the 12th International Symposium on Space Terahertz Technology*, edited by I. S. on Space Terahertz Technology (2001).

[400] T. O. Klaassen, J. H. Blok, J. N. Hovenier, G. Jakob, D. Rosenthal, and K. J. Wildeman, "Absorbing coatings and diffuse reflectors for the Herschel platform sub-millimeter spectrometers HIFI and PACS", pp. 32–35 (2002).

[401] H. Werheit, M. Laux, U. Kuhlmann, and R. Telle, "Optical Interband Transitions of Boron Carbide", Phys. Status Solidi **172**, K81 (1992).

[402] J. Sun, H. Ling, W. Pan, N. Xu, Z. Ying, W. Shen, and J. Wu, "Chemical Structure and Micro-Mechanical Properties of Ultra-Thin Films of Boron Carbide Prepared by Pulsed-Laser Deposition", Tribology Letters **17**, 99 (2004).

[403] M. Mortensen, P. Sorensen, O. Björkdahl, M. Jensen, H. Gundersen, and T. Bjornholm, "Preparation and characterization of Boron carbide nanoparticles for use as a novel agent in T cell-guided boron neutron capture therapy", Appl. Rad. Isotop. **64**, 315 (2006).

[404] J. D. Katz, "Microwave Sintering of Ceramics", Annu. Rev. Mater. Sci. **22**, 153 (1992).

[405] R. E. Mould and D. E. Mapother, "Effect of Precipitation Hardening on the Superconducting Properties of Aluminum", Phys. Rev. **125**, 33 (1962).

[406] D. Corzett, A. Keller, and P. Seligmann, "The thermal conductivity of manganin wire and Stycast 2850 GT between 1 K and 4 K", Cryogenics **16**, 505 (1976).

[407] C. Tsai, H. Weinstock, and W. Overton, "Low temperature thermal conductivity of stycast 2850FT", Cryogenics **18**, 562 (1978).

[408] J. Olson, "Thermal conductivity of some common cryostat materials between 0.05 and 2 K", Cryogenics **33**, 729 (1993).

[409] F. Rondeaux, P. Bredy, and J. M. Rey, "Thermal conductivity measurements of epoxy systems at low temperature", AIP Conference Proceedings **614**, 197 (2002).

[410] D. Schuster, "Circuit Quantum Electrodynamics", PhD thesis, Yale University (2007).

[411] A. Leo, G. Grimaldi, R. Citro, A. Nigro, S. Pace, and R. P. Huebener, "Quasiparticle scattering time in niobium superconducting films", Phys. Rev. B **84** (2011).

[412] H. R. Kerchner, D. K. Christen, and S. T. Sekula, "Critical fields H_c and H_{c2} of superconducting niobium", Phys. Rev. B **24**, 1200 (1981).

[413] C. Song, T. W. Heitmann, M. P. DeFeo, K. Yu, R. McDermott, M. Neeley, J. M. Martinis, and B. L. T. Plourde, "Microwave response of vortices in superconducting thin films of Re and Al", Phys. Rev. B **79**, 174512 (2009).

[414] C. Song, M. P. DeFeo, K. Yu, and B. L. T. Plourde, "Reducing microwave loss in superconducting resonators due to trapped vortices", Appl. Phys. Lett. **95**, 232501 (2009).

[415] D. Bothner, T. Gaber, M. Kemmler, D. Koelle, and R. Kleiner, "Improving the performance of superconducting microwave resonators in magnetic fields", Appl. Phys. Lett. **98**, 102504 (2011).

[416] R. Huebener, R. Kampwirth, R. Martin, T. Barbee, and R. Zubeck, "Critical current density in superconducting niobium films", IEEE Transactions on Magnetics **11**, 344 (1975).

[417] B. Chiaro, A. Megrant, A. Dunsworth, Z. Chen, R. Barends, B. Campbell, Y. Chen, A. Fowler, I. C. Hoi, E. Jeffrey, J. Kelly, J. Mutus, C. Neill, P. J. J. O'Malley, C. Quintana, P. Roushan, D. Sank, A. Vainsencher, J. Wenner, T. C. White, and J. M. Martinis, "Dielectric surface loss in superconducting resonators with flux-trapping holes", ArXiv e-prints: 1607.05841 (2016).

[418] I. B. Rajesh Mongia and P. Bhartia, *RF and Microwave Coupled-line Circuits*, vol. 44 (2001).

[419] S. Shiran, B. Reiser, and H. Cory, "A probabilistic method for the evaluation of coupling between transmission lines", IEEE Transactions on Electromagnetic Compatibility **35**, 387 (1993).

[420] Y. Kami and W. Liu, in *Electromagnetic Compatibility, 1998. 1998 IEEE International Symposium on* (1998), vol. 2, pp. 952–957 vol.2.

[421] L. Yin and L. He, "An Efficient Analytical Model of Coupled On-chip RLC Interconnects", Proc. Asia Automat. Conf. pp. 385–390 (2001).

[422] K. Agarwal, D. Sylvester, and D. Blaauw, "Modeling and analysis of crosstalk noise in coupled RLC interconnects", IEEE Transactions on Computer-Aided Design of Integrated Circuits and Systems **25**, 892 (2006).

[423] J. Jackson, *Classical Electrodynamics* (Wiley, 1998).

[424] P. Eder, "Dual-Path Receiver for State Reconstruction of Propagating Quantum Microwaves", Diploma thesis, TU München (2012).

[425] T. Niemczyk, "From strong to ultrastrong coupling in circuit QED architectures", PhD thesis, TU München (2011).

[426] K. W. Murch, R. Vijay, and I. Siddiqi, *Weak Measurement and Feedback in Superconducting Quantum Circuits* (Springer International Publishing, Cham, 2016).

[427] A. Wallraff, D. I. Schuster, A. Blais, L. Frunzio, J. Majer, M. H. Devoret, S. M. Girvin, and R. J. Schoelkopf, "Approaching Unit Visibility for Control of a Superconducting Qubit with Dispersive Readout", Phys. Rev. Lett. **95** (2005).

[428] G. Lindblad, "On the generators of quantum dynamical semigroups", Comm. Math. Phys. **48**, 119 (1976).

[429] H. Nyquist, "Thermal Agitation of Electric Charge in Conductors", Phys. Rev. **32**, 110 (1928).

[430] C. E. Shannon, "Communication in the Presence of Noise", Proc. IRE **37**, 10 (1949).

[431] F. Motzoi, J. M. Gambetta, P. Rebentrost, and F. K. Wilhelm, "Simple Pulses for Elimination of Leakage in Weakly Nonlinear Qubits", Phys. Rev. Lett. **103**, 110501 (2009).

[432] S. Gustavsson, O. Zwier, J. Bylander, F. Yan, F. Yoshihara, Y. Nakamura, T. P. Orlando, and W. D. Oliver, "Improving Quantum Gate Fidelities by Using a Qubit to Measure Microwave Pulse Distortions", Phys. Rev. Lett. **110** (2013).

[433] V. Vesterinen, O.-P. Saira, A. Bruno, and L. DiCarlo, "Mitigating information leakage in a crowded spectrum of weakly anharmonic qubits", ArXiv e-prints: 1405.0450 (2014).

[434] R. N. Bracewell, *The Fourier transform and its applications*, McGraw-Hill series in electrical and computer engineering. Circuits and systems (McGraw Hill, Boston, 2000).

[435] Z. Chen, J. Kelly, C. Quintana, R. Barends, B. Campbell, Y. Chen, B. Chiaro, A. Dunsworth, A. G. Fowler, E. Lucero, E. Jeffrey, A. Megrant, J. Mutus, M. Neeley, C. Neill, P. J. J. O'Malley, P. Roushan, D. Sank, A. Vainsencher, J. Wenner, T. C. White, A. N. Korotkov, and J. M. Martinis, "Measuring and Suppressing Quantum State Leakage in a Superconducting Qubit", Phys. Rev. Lett. **116**, 020501 (2016).

[436] S. M. Anton, C. Müller, J. S. Birenbaum, S. R. O'Kelley, A. D. Fefferman, D. S. Golubev, G. C. Hilton, H.-M. Cho, K. D. Irwin, F. C. Wellstood, G. Schön, A. Shnirman, and J. Clarke, "Pure dephasing in flux qubits due to flux noise with spectral density scaling as $1/f^{\alpha}$", Phys. Rev. B **85**, 224505 (2012).

[437] F. Deppe, M. Mariantoni, E. P. Menzel, S. Saito, K. Kakuyanagi, H. Tanaka, T. Meno, K. Semba, H. Takayanagi, and R. Gross, "Phase coherent dynamics of a superconducting flux qubit with capacitive bias readout", Phys. Rev. B **76**, 214503 (2007).

[438] J. Gambetta, A. Blais, M. Boissonneault, A. A. Houck, D. I. Schuster, and S. M. Girvin, "Quantum trajectory approach to circuit QED: Quantum jumps and the Zeno effect", Phys. Rev. A **77**, 012112 (2008).

[439] A. A. Clerk and D. W. Utami, "Using a qubit to measure photon-number statistics of a driven thermal oscillator", Phys. Rev. A **75**, 042302 (2007).

[440] M. Mariantoni, E. P. Menzel, F. Deppe, M. A. Araque Caballero, A. Baust, T. Niemczyk, E. Hoffmann, E. Solano, A. Marx, and R. Gross, "Planck Spectroscopy and Quantum Noise of Microwave Beam Splitters", Phys. Rev. Lett. **105**, 133601 (2010).

[441] L. Zhong, "Generation and Reconstruction of Propagating Quantum Microwaves", PhD thesis, TU München (2015).

[442] R. A. Campos, B. E. A. Saleh, and M. C. Teich, "Quantum-mechanical lossless beam splitter: SU(2) symmetry and photon statistics", Phys. Rev. A **40**, 1371 (1989).

[443] E. P. Menzel, F. Deppe, M. Mariantoni, M. A. Araque Caballero, A. Baust, T. Niemczyk, E. Hoffmann, A. Marx, E. Solano, and R. Gross, "Dual-Path State Reconstruction Scheme for Propagating Quantum Microwaves and Detector Noise Tomography", Phys. Rev. Lett. **105**, 100401 (2010).

[444] B. A. Kochetov and A. Fedorov, "Higher-order nonlinear effects in a Josephson parametric amplifier", Phys. Rev. B **92**, 224304 (2015).

[445] A. V. Shcherbakova, K. G. Fedorov, K. V. Shulga, V. V. Ryazanov, V. V. Bolginov, V. A. Oboznov, S. V. Egorov, V. O. Shkolnikov, M. J. Wolf, D. Beckmann, and A. V. Ustinov, "Fabrication and measurements of hybrid Nb/Al Josephson junctions and flux qubits with π-shifters", Supercond. Sci. Tech. **28**, 025009 (2015).

[446] M. Watanabe, K. Inomata, T. Yamamoto, and J.-S. Tsai, "Power-dependent internal loss in Josephson bifurcation amplifiers", Phys. Rev. B **80**, 174502 (2009).

[447] J. Gao, M. Daal, J. M. Martinis, A. Vayonakis, J. Zmuidzinas, B. Sadoulet, B. A. Mazin, P. K. Day, and H. G. Leduc, "A semiempirical model for two-level system noise in superconducting microresonators", Appl. Phys. Lett. **92**, 212504 (2008).

[448] V. E. Manucharyan, E. Boaknin, M. Metcalfe, R. Vijay, I. Siddiqi, and M. Devoret, "Microwave bifurcation of a Josephson junction: Embedding-circuit requirements", Phys. Rev. B **76**, 014524 (2007).

[449] E. A. Tholen, A. Ergül, E. M. Doherty, F. M. Weber, F. Gregis, and D. B. Haviland, "Nonlinearities and parametric amplification in superconducting coplanar waveguide resonators", Appl. Phys. Let. **90**, 253509 (2007).

[450] H. B. Wang, T. Hatano, T. Yamashita, P. H. Wu, and P. Müller, "Direct observation of self-heating in intrinsic Josephson junction array with a nanoelectrode in the middle", Appl. Phys. Lett. **86**, 023504 (2005).

[451] S. Guénon, M. Grünzweig, B. Gross, J. Yuan, Z. G. Jiang, Y. Y. Zhong, M. Y. Li, A. Iishi, P. H. Wu, T. Hatano, R. G. Mints, E. Goldobin, D. Koelle, H. B. Wang, and R. Kleiner, "Interaction of hot spots and terahertz waves in $Bi_2Sr_2CaCu_2O_8$ intrinsic Josephson junction stacks of various geometry", Phys. Rev. B **82**, 214506 (2010).

[452] N. Booth, P. Brink, R. Gaitskell, D. Goldie, A. Hahn, G. Salmon, and A. Swift, "Superconducting tunnel junctions and quasiparticle trapping", J. Low Temp. Phys. **93**, 521 (1993).

[453] N. A. Court, A. J. Ferguson, R. Lutchyn, and R. G. Clark, "Quantitative study of quasiparticle traps using the single-Cooper-pair transistor", Phys. Rev. B **77**, 100501 (2008).

[454] "Product No. 16062 - PELCO Conductive Silver Paint"„ Tech. Rep., TED PELLA. INC. (2013).

[455] J. Thorp, "R.F. conductivity in copper at 8 mm wavelengths", Proc. of the IEEI - Part III: Radio and Communication Engineering **101**, 357 (1954).

[456] R. A. Matula, "Electrical resistivity of copper, gold, palladium, and silver", J. Phys. Chem. Ref. Data **8**, 1147 (1979).

[457] M. Fouaidy and N. Hammoudi, "RRR of copper coating and low temperature electrical resistivity of material for TTF couplers", Physica C **441**, 137 (2006).

[458] A. A. Houck, H. E. Türeci, and J. Koch, "On-chip quantum simulation with superconducting circuits", Nat. Phys. **8**, 292 (2012).

[459] C. W. Zollitsch, K. Mueller, D. P. Franke, S. T. B. Goennenwein, M. S. Brandt, R. Gross, and H. Huebl, "High cooperativity coupling between a phosphorus donor spin ensemble and a superconducting microwave resonator", Appl. Phys. Lett. **107**, 142105 (2015).

[460] T. Hime, P. A. Reichardt, B. L. T. Plourde, T. L. Robertson, C.-E. Wu, A. V. Ustinov, and J. Clarke, "Solid-State Qubits with Current-Controlled Coupling", Science **314**, 1427 (2006).

[461] A. O. Niskanen, K. Harrabi, F. Yoshihara, Y. Nakamura, S. Lloyd, and J. S. Tsai, "Quantum Coherent Tunable Coupling of Superconducting Qubits", Science **316**, 723 (2007).

[462] R. C. Bialczak, M. Ansmann, M. Hofheinz, M. Lenander, E. Lucero, M. Neeley, A. D. O'Connell, D. Sank, H. Wang, M. Weides, J. Wenner, T. Yamamoto, A. N. Cleland, and J. M. Martinis, "Fast Tunable Coupler for Superconducting Qubits", Phys. Rev. Lett. **106**, 060501 (2011).

[463] G. Burkard, "Non-Markovian qubit dynamics in the presence of $1/f$ noise", Phys. Rev. B **79**, 125317 (2009).

[464] A. Shnirman, Y. Makhlin, and G. Schön, "Noise and Decoherence in Quantum Two-Level Systems", Phys. Scripta **2002**, 147 (2002).

[465] F. Yan, J. Bylander, S. Gustavsson, F. Yoshihara, K. Harrabi, D. G. Cory, T. P. Orlando, Y. Nakamura, J.-S. Tsai, and W. D. Oliver, "Spectroscopy of low-frequency noise and its temperature dependence in a superconducting qubit", Phys. Rev. B **85**, 174521 (2012).

[466] F. Yan, S. Gustavsson, A. Kamal, J. Birenbaum, A. P. Sears, D. Hover, T. J. Gudmundsen, D. Rosenberg, G. Samach, S. Weber, J. L. Yoder, T. P. Orlando, J. Clarke, A. J. Kerman, and W. D. Oliver, "The flux qubit revisited to enhance coherence and reproducibility", Nat. Comm. **7**, 12964 (2016).

[467] A. P. Sears, A. Petrenko, G. Catelani, L. Sun, H. Paik, G. Kirchmair, L. Frunzio, L. I. Glazman, S. M. Girvin, and R. J. Schoelkopf, "Photon shot noise dephasing in the strong-dispersive limit of circuit QED", Phys. Rev. B **86**, 180504 (2012).

[468] K. Ujihara, "Quantum theory of a one-dimensional optical cavity with output coupling. II. Thermal radiation field and the fluctuation-dissipation theorem", Phys. Rev. A **18**, 659 (1978).

[469] C. Schuster and W. Fichtner, "Parasitic modes on printed circuit boards and their effects on EMC and signal integrity", IEEE T. Electromagn. C. **43**, 416 (2001).

[470] H. B. Callen and T. A. Welton, "Irreversibility and Generalized Noise", Phys. Rev. **83**, 34 (1951).

[471] J. Lisenfeld, G. J. Grabovskij, C. Müller, J. H. Cole, G. Weiss, and A. V. Ustinov, "Observation of directly interacting coherent two-level systems in an amorphous material", Nat. Commun. **6**, 6182 (2015).

[472] D. M. Meekhof, C. Monroe, B. E. King, W. M. Itano, and D. J. Wineland, "Generation of Nonclassical Motional States of a Trapped Atom", Phys. Rev. Lett. **76**, 1796 (1996).

[473] M. Brune, F. Schmidt-Kaler, A. Maali, J. Dreyer, E. Hagley, J. M. Raimond, and S. Haroche, "Quantum Rabi Oscillation: A Direct Test of Field Quantization in a Cavity", Phys. Rev. Lett. **76**, 1800 (1996).

[474] M. Hofheinz, E. M. Weig, M. Ansmann, R. C. Bialczak, E. Lucero, M. Neeley, A. D. O'Connell, H. Wang, J. M. Martinis, and A. N. Cleland, "Generation of Fock states in a superconducting quantum circuit", Nature **454**, 310 (2008).

[475] T. Yamamoto, K. Inomata, M. Watanabe, K. Matsuba, T. Miyazaki, W. D. Oliver, Y. Nakamura, and J. S. Tsai, "Flux-driven Josephson parametric amplifier", Appl. Phys. Lett. **93**, 042510 (2008).

[476] S. L. Braunstein and P. van Loock, "Quantum information with continuous variables", Rev. Mod. Phys. **77**, 513 (2005).

[477] U. L. Andersen, J. S. Neergaard-Nielsen, P. van Loock, and A. Furusawa, "Hybrid discrete- and continuous-variable quantum information", Nat. Phys. **11**, 713 (2015).

[478] R. Di Candia, K. G. Fedorov, L. Zhong, S. Felicetti, E. P. Menzel, M. Sanz, F. Deppe, A. Marx, R. Gross, and E. Solano, "Quantum teleportation of propagating quantum microwaves", EPJ Quant. Tech. **2**, 25 (2015).

[479] S. Lloyd, "Enhanced Sensitivity of Photodetection via Quantum Illumination", Science **321**, 1463 (2008).

[480] S.-H. Tan, B. I. Erkmen, V. Giovannetti, S. Guha, S. Lloyd, L. Maccone, S. Pirandola, and J. H. Shapiro, "Quantum Illumination with Gaussian States", Phys. Rev. Lett. **101**, 253601 (2008).

[481] E. D. Lopaeva, I. Ruo Berchera, I. P. Degiovanni, S. Olivares, G. Brida, and M. Genovese, "Experimental Realization of Quantum Illumination", Phys. Rev. Lett. **110**, 153603 (2013).

[482] S. Barzanjeh, S. Guha, C. Weedbrook, D. Vitali, J. H. Shapiro, and S. Pirandola, "Microwave Quantum Illumination", Phys. Rev. Lett. **114**, 080503 (2015).

[483] N. Y. Yao, L. Jiang, A. V. Gorshkov, Z.-X. Gong, A. Zhai, L.-M. Duan, and M. D. Lukin, "Robust Quantum State Transfer in Random Unpolarized Spin Chains", Phys. Rev. Lett. **106**, 040505 (2011).

[484] N. Y. Yao, Z.-X. Gong, C. R. Laumann, S. D. Bennett, L.-M. Duan, M. D. Lukin, L. Jiang, and A. V. Gorshkov, "Quantum logic between remote quantum registers", Phys. Rev. A **87**, 022306 (2013).

[485] J. B. Brask, G. Haack, N. Brunner, and M. Huber, "Autonomous quantum thermal machine for generating steady-state entanglement", New J. Phys. **17**, 113029 (2015).

[486] Z.-L. Xiang, M. Zhang, L. Jiang, and P. Rabl, "Intra-city quantum communication via thermal microwave networks", ArXiv e-prints: 1611.10241 (2016).

[487] F. Mallet, M. A. Castellanos-Beltran, H. S. Ku, S. Glancy, E. Knill, K. D. Irwin, G. C. Hilton, L. R. Vale, and K. W. Lehnert, "Quantum State Tomography of an Itinerant Squeezed Microwave Field", Phys. Rev. Lett. **106**, 220502 (2011).

[488] C. Macklin, K. O'Brien, D. Hover, M. E. Schwartz, V. Bolkhovsky, X. Zhang, W. D. Oliver, and I. Siddiqi, "A near–quantum-limited Josephson traveling-wave parametric amplifier", Science **350**, 307 (2015).

[489] S. Virally, J. O. Simoneau, C. Lupien, and B. Reulet, "Discrete photon statistics from continuous microwave measurements", Phys. Rev. A **93**, 043813 (2016).

[490] C. Eichler, D. Bozyigit, C. Lang, L. Steffen, J. Fink, and A. Wallraff, "Experimental State Tomography of Itinerant Single Microwave Photons", Phys. Rev. Lett. **106**, 220503 (2011).

[491] K. W. Murch, S. J. Weber, K. M. Beck, E. Ginossar, and I. Siddiqi, "Reduction of the radiative decay of atomic coherence in squeezed vacuum", Nature **499**, 62 (2013).

[492] D. I. Schuster, A. A. Houck, J. A. Schreier, A. Wallraff, J. M. Gambetta, A. Blais, L. Frunzio, J. Majer, B. Johnson, M. H. Devoret, S. M. Girvin, and R. J. Schoelkopf, "Resolving photon number states in a superconducting circuit", Nature **445**, 515 (2007).

[493] R. Hanbury Brown and R. Q. Twiss, "Correlation between Photons in two Coherent Beams of Light", Nature **177**, 27 (1956).

[494] A. A. Houck, D. I. Schuster, J. M. Gambetta, J. A. Schreier, B. R. Johnson, J. M. Chow, L. Frunzio, J. Majer, M. H. Devoret, S. M. Girvin, and R. J. Schoelkopf, "Generating single microwave photons in a circuit", Nature **449**, 328 (2007).

[495] J.-C. Forgues, C. Lupien, and B. Reulet, "Emission of Microwave Photon Pairs by a Tunnel Junction", Phys. Rev. Lett. **113**, 043602 (2014).

[496] Y. Blanter and M. Büttiker, "Shot noise in mesoscopic conductors", Phys. Rep. **336**, 1 (2000).

[497] C. Beenakker and M. Patra, "Photon shot noise", Mod. Phys. Lett. **13**, 337 (1999).

[498] J. M. Fink, L. Steffen, P. Studer, L. S. Bishop, M. Baur, R. Bianchetti, D. Bozyigit, C. Lang, S. Filipp, P. J. Leek, and A. Wallraff, "Quantum-To-Classical Transition in Cavity Quantum Electrodynamics", Phys. Rev. Lett. **105**, 163601 (2010).

[499] R. N. Mohapatra and G. Senjanović, "Neutrino Mass and Spontaneous Parity Nonconservation", Phys. Rev. Lett. **44**, 912 (1980).

[500] H. Haber and G. Kane, "The search for supersymmetry: Probing physics beyond the standard model", Phys. Rep. **117**, 75 (1985).

[501] C. H. Bennett and D. P. DiVincenzo, "Quantum information and computation", Nature **404**, 247 (2000).

[502] R. H. Brandenberger, "Quantum field theory methods and inflationary universe models", Rev. Mod. Phys. **57**, 1 (1985).

[503] F. Wilczek, "Quantum field theory", Rev. Mod. Phys. **71**, S85 (1999).

[504] K. Bergmann, H. Theuer, and B. W. Shore, "Coherent population transfer among quantum states of atoms and molecules", Rev. Mod. Phys. **70**, 1003 (1998).

[505] M. Bhattacharya, C. Haimberger, and N. P. Bigelow, "Forbidden Transitions in a Magneto-Optical Trap", Phys. Rev. Lett. **91**, 213004 (2003).

[506] D. Tong, S. M. Farooqi, E. G. M. van Kempen, Z. Pavlovic, J. Stanojevic, R. Côté, E. E. Eyler, and P. L. Gould, "Observation of electric quadrupole transitions to Rydberg *nd* states of ultracold rubidium atoms", Phys. Rev. A **79**, 052509 (2009).

[507] J. Brooke, D. Bitko, F. T. Rosenbaum, and G. Aeppli, "Quantum Annealing of a Disordered Magnet", Science **284**, 779 (1999).

[508] C. S. Wu, E. Ambler, R. W. Hayward, D. D. Hoppes, and R. P. Hudson, "Experimental Test of Parity Conservation in Beta Decay", Phys. Rev. **105**, 1413 (1957).

[509] A. G. Fowler, M. Mariantoni, J. M. Martinis, and A. N. Cleland, "Surface codes: Towards practical large-scale quantum computation", Phys. Rev. A **86**, 032324 (2012).

[510] A. Córcoles, E. Magesan, S. J. Srinivasan, A. W. Cross, M. Steffen, J. M. Gambetta, and J. M. Chow, "Demonstration of a quantum error detection code using a square lattice of four superconducting qubits", Nat. Comm. **6**, 6979 (2015).

[511] M. Takita, A. D. Córcoles, E. Magesan, B. Abdo, M. Brink, A. Cross, J. M. Chow, and J. M. Gambetta, "Demonstration of weight-four parity measurements in the surface code architecture", ArXiv e-prints: 1605.01351 (2016).

[512] N. Ofek, A. Petrenko, R. Heeres, P. Reinhold, Z. Leghtas, B. Vlastakis, Y. Liu, L. Frunzio, S. M. Girvin, L. Jiang, M. Mirrahimi, M. H. Devoret, and R. J. Schoelkopf, "Extending the lifetime of a quantum bit with error correction in superconducting circuits", Nature **536**, 441 (2016).

[513] I. I. Rabi, "On the Process of Space Quantization", Phys. Rev. **49**, 324 (1936).

[514] S. Felicetti, T. Douce, G. Romero, P. Milman, and E. Solano, "Parity-dependent State Engineering and Tomography in the ultrastrong coupling regime", Sci. Rep. **5**, 11818 (2015).

[515] J. Braumüller, M. Sandberg, M. R. Vissers, A. Schneider, S. Schlör, L. Grünhaupt, H. Rotzinger, M. Marthaler, A. Lukashenko, A. Dieter, A. V. Ustinov, M. Weides, and D. P. Pappas, "Concentric transmon qubit featuring fast tunability and an anisotropic magnetic dipole moment", Appl. Phys. Lett. **108**, 032601 (2016).

[516] A. Fedorov, P. Macha, A. K. Feofanov, C. J. P. M. Harmans, and J. E. Mooij, "Tuned Transition from Quantum to Classical for Macroscopic Quantum States", Phys. Rev. Lett. **106**, 170404 (2011).

[517] D. Porras and J. J. García-Ripoll, "Shaping an Itinerant Quantum Field into a Multimode Squeezed Vacuum by Dissipation", Phys. Rev. Lett. **108**, 043602 (2012).

[518] M. del Rey, D. Porras, and E. Martin-Martinez, "Simulating Accelerated Atoms Coupled to a Quantum Field", Phys. Rev. A **85**, 022511 (2012).

[519] F. Quijandría, D. Porras, J. J. García-Ripoll, and D. Zueco, "Circuit QED Bright Source for Chiral Entangled Light Based on Dissipation", Phys. Rev. Lett. **111**, 073602 (2013).

[520] J.-M. Reiner, M. Marthaler, J. Braumüller, M. Weides, and G. Schön, "Emulating the one-dimensional Fermi-Hubbard model by a double chain of qubits", Phys. Rev. A **94**, 032338 (2016).

[521] M. Germann, X. Tong, and S. Willitsch, "Observation of electric-dipole-forbidden infrared transitions in cold molecular ions", Nat. Phys. **10**, 820 (2014).

[522] N. S. Shiren and E. B. Tucker, "Selection Rule for the Interaction of Microwave Ultrasonics with Spins", Phys. Rev. Lett. **6**, 105 (1961).

[523] D. P. Franke, F. M. Hrubesch, M. Künzl, H.-W. Becker, K. M. Itoh, M. Stutzmann, F. Hoehne, L. Dreher, and M. S. Brandt, "Interaction of Strain and Nuclear Spins in Silicon: Quadrupolar Effects on Ionized Donors", Phys. Rev. Lett. **115** (2015).

[524] D. P. Franke, M. P. D. Pflüger, P.-A. Mortemousque, K. M. Itoh, and M. S. Brandt, "Quadrupolar effects on nuclear spins of neutral arsenic donors in silicon", Phys. Rev. B **93**, 161303 (2016).

[525] M. Abdi, M. Pernpeintner, R. Gross, H. Huebl, and M. J. Hartmann, "Quantum State Engineering with Circuit Electromechanical Three-Body Interactions", Phys. Rev. Lett. **114**, 173602 (2015).

[526] L. Dreher, M. Weiler, M. Pernpeintner, H. Huebl, R. Gross, M. S. Brandt, and S. T. B. Goennenwein, "Surface acoustic wave driven ferromagnetic resonance in nickel thin films: Theory and experiment", Phys. Rev. B **86**, 134415 (2012).

[527] H. Maier-Flaig, M. Harder, R. Gross, H. Huebl, and S. T. B. Goennenwein, "Spin pumping in strongly coupled magnon-photon systems", Phys. Rev. B **94**, 054433 (2016).

[528] S. G. Bhongale, L. Mathey, E. Zhao, S. F. Yelin, and M. Lemeshko, "Quantum Phases of Quadrupolar Fermi Gases in Optical Lattices", Phys. Rev. Lett. **110**, 155301 (2013).

[529] H. Yuen, "Two-photon coherent states of the radiation field", Phys. Rev. A **13**, 2226 (1976).